Application of Black-Hole Physics to Vortex Dynamics in Superfluids

Paul Dieter Wittmer

Heidelberg, October 2020

Dissertation

submitted to the

Combined Faculties of Natural Sciences and Mathematics of the Ruperto-Carola-University of Heidelberg, Germany

for the degree of

Doctor of Natural Sciences

Put forward by

Paul Dieter Wittmer

born in Arolsen

Oral examination: 16.12.2020

Application of Black-Hole Physics to

Vortex Dynamics in Superfluids

Referees: Prof. Dr. Carlo Ewerz

Prof. Dr. Jan M. Pawlowski

Anwendung der Physik schwarzer Löcher auf Vortexdynamik in Suprafüssigkeiten

Diese Dissertation befasst sich mit der Untersuchung von Nichtgleichgewichtsdynamik und Turbulenz in zwei- und dreidimensionalen Suprafüssigkeiten. Wir verwenden eine intrinsisch nicht-perturbative, holographische Beschreibung durch Feldtheorien in höher-dimensionalen Anti-de-Sitter-Raumzeiten mit einem schwarzen Loch. Es werden numerische Echtzeitsimulationen beider Systeme durchgeführt. In einem ersten Teil berechnen wir die Kinematik von Vortexdipolen in zwei Raumdimensionen, wozu wir eine hochpräzise Methode zur Positionsbestimmung einführen. Indem wir Lösungen der dissipativen Gross–Pitaevskii-Gleichung sowie von Gleichungen für Punkt-Vortizes an die Trajektorien anpassen, quantifizieren wir die starke Dissipation der Suprafüssigkeit. Wir finden, dass Holographie auf Vortexdynamik in suprafüssigen Heliumfilmen und flachen, kalten Quantengasen anwendbar sein kann. In einem zweiten Teil untersuchen wir erstmals Vortexlinien und -ringe in der dreidimensionalen holographischen Suprafüssigkeit. Wir betrachten deren Dynamik und Wechselwirkungen, darunter Leapfrogging und Streuung von Ringen, sowie ihre Anregungen durch Kelvinwellen. Für Anfangsbedingungen fern des Gleichgewichts zeigt das Skalierungsverhalten von Korrelationsfunktionen Signaturen universellen turbulenten Verhaltens in verschiedenen Intervallen der Zeitentwicklung. Die genannten Phänomene werden hier erstmals in einer stark dissipativen dreidimensionalen Suprafüssigkeit im Rahmen einer fundamentalen Theorie untersucht.

Application of Black-Hole Physics to Vortex Dynamics in Superfluids

This thesis is concerned with the investigation of non-equilibrium dynamics and turbulence in two- and three-dimensional superfluids using an intrinsically non-perturbative holographic description in terms of field theories in higher-dimensional black-hole-anti-de Sitter spacetimes. We perform numerical real-time simulations of these systems on large numerical domains. In a first part, we study the kinematics of vortex dipoles in two dimensions. To this end, we introduce a high-precision tracking routine to locate their cores. By matching to the vortex trajectories solutions of the dissipative Gross–Pitaevskii equation and of equations for the motion of point vortices, we quantify the strong dissipation of the superfluid, which in holography is related to the absorption of modes by the black hole. We conjecture holography to be applicable to vortex dynamics in films of superfluid helium and in oblate cold quantum gases. In a second part, we study for the first time vortex lines and rings in the three-dimensional holographic superfluid. We investigate their dynamics, and interactions, including the famous leapfrogging motion and scattering events of rings, as well as Kelvin-wave excitations of their cores. Further, we study the evolution of the superfluid starting from far-from-equilibrium initial conditions characterised by dense vortex tangles. We analyse the dynamics in terms of scaling behaviour in correlation functions and observe signatures of universal turbulent behaviour during different regimes of the evolution. This work constitutes the first *ab initio* study of the mentioned phenomena in a strongly dissipative three-dimensional superfluid.

Publications

This thesis contains results from collaborative work. The following jointly authored publications are, at the time of completion of this thesis, in preparation:

1. C. Ewerz, P. Wittmer, "Turbulence in a Three-Dimensional Holographic Superfluid", *in preparation.*

2. P. Wittmer, C.-M. Schmied, T. Gasenzer and C. Ewerz, "Vortex motion quantifies strong dissipation in a holographic superfluid', *in preparation.*

3. C. Ewerz, A. Samberg, P. Wittmer, "Dynamics of a Vortex Dipole in a Holographic Superfluid", *in preparation.*

The following statement summarises my respective contributions to these projects.

1. I have done the analytical part, developed the numerical code for the real-time simulations of the three-dimensional superfluid, and analysed the data. Both authors jointly conceived the idea, discussed the results, and wrote the manuscript.

2. I have performed the numerical simulations of the holographic superfluid. C.-M. Schmied has performed the (D)GPE simulations. C.-M. Schmied and I jointly worked on the numerical analysis of the data. All authors jointly devised the main conceptual ideas, performed the analytic calculations, discussed the results, and wrote the manuscript.

3. I have performed all numerical simulations and the data analysis, including the implementation of the tracking routine. The numerical code for the real-time simulation of the two-dimensional superfluid was developed by M. Karl and A. Samberg (see [150]), I adapted it for the purposes of this thesis. All authors jointly conceived the idea, planned the implementation, discussed the results, and wrote the manuscript.

Further publications (some jointly with C. Ewerz) based on some of the findings presented in this thesis are planned.

Contents

Contents

1 Introduction

Our current understanding of nature is encapsulated in two grand theories, the Standard Model of particle physics (SM) and Einstein's General Relativity (GR). Both of these theories are incredibly well tested and have in particular been confirmed and consolidated by a number of recent experimental breakthroughs, including the discovery of the Higgs boson and the detection of gravitational waves. The SM governs the physics of microscopic scales and describes three of the four fundamental forces of nature, the strong, weak and electromagnetic force. It is formulated in the language of quantum field theory (QFT). GR, on the other hand, is the theory of the fourth fundamental force of nature, gravity, and governs the physics of macroscopic scales. It is formulated in terms of a classical field theory. Thus far, GR has withstood a formulation in terms of a renormalisable quantum field theory and hence a unified framework with the SM does not exist. In fact, the search for a unified theory of the four fundamental forces of nature still poses one of the most challenging problems of modern-day physics.

An unforeseen and very intriguing link between gauge theories, akin to the SM, and theories of gravity was discovered in 1997 by Maldacena [1] and further developed by others [2, 3], and is nowadays known as the concept of *gauge/gravity duality*. The duality was originally derived from a string-theory setup upon noticing that the physics of certain fundamental higher-dimensional objects gives rise to gauge theories in one and theories of gravity in another limit. Generically, gauge/gravity duality equates non-gravitational quantum field theories with string theories that naturally incorporate gravity. It becomes most relevant for practical applications in a special limit in which the string-theory side reduces to classical Einstein gravity while the field-theory side is rendered strongly coupled. A particularly intriguing feature of gauge/gravity duality is that the spacetime dimensionality of the non-gravitational gauge theories is lower than that of the corresponding dual gravity theories. For practical purposes, the difference in spacetime dimensions is typically one and gauge/gravity duality thus a direct realisation of the *holographic principle* which posits that a region of spacetime in a (quantum) gravitational theory can be described by a non-gravitational quantum field theory defined on the by one lower-dimensional boundary of that region [4, 5]. The duality is therefore also referred to as *holography* or *holographic duality*. In light of the holographic principle, the gravitational spacetime is often referred to as 'bulk' and the quantum field theory as 'boundary theory'.

The original and best understood instance of gauge/gravity duality is the Anti-de Sitter/Conformal Field Theory duality, in short *AdS/CFT duality* or *correspondence*, between a conformal gauge theory and a theory of gravity in an AdS spacetime which

has a negative cosmological constant and is negatively curved. Gauge/gravity duality generalises the AdS/CFT correspondence to a duality between non-conformal (mostly gauge) QFTs and higher dimensional gravity theories in asymptotically AdS spacetimes. For all types of such dualities, holography asserts that the complete dynamics of the field theory is mapped to the complete dynamics of the gravity theory and vice versa. In this sense, the theories are said to be *dynamically equivalent.* The degrees of freedom of the two theories related by the duality, on the other hand, are in general very different. A further remarkable feature of gauge/gravity duality is that thermal physics in the boundary field theory is gravitationally encoded in terms of black-hole physics in the bulk spacetime.

In a special limit, gauge/gravity duality maps a strongly coupled QFT in flat spacetime to weakly coupled Einstein gravity in an asymptotically AdS spacetime. This form of the duality is most useful for many practical purposes, including in particular our applications of holography in this thesis. It is important to appreciate that for the type of applications of holography we have in mind it is utterly irrelevant whether or not string theory ultimately turns out to be the fundamental unified theory of nature. While string theory is indeed used in the derivation of certain instances of gauge/gravity duality, in the above mentioned limit it only acts as a mathematical tool.

Strongly coupled QFTs appear in all fields of physics and their description requires inherently non-perturbative methods since standard perturbation theory breaks down at large coupling. A prominent example where the emergence of strong coupling poses a great challenge is quantum chromodynamics (QCD), the theory of the strong interaction of quarks and gluons in particle physics. At intermediate and small momentum transfers, relevant for instance in the description of the quark–gluon plasma (QGP, see *e. g.* [6] as well as the reviews [7–9]), the QCD coupling constant grows large and renders conventional perturbation theory inapplicable. While other conventional methods, such as lattice gauge theory [10] (see *e. g.* [11, 12] for reviews) or the functional renormalisation group [13] (see *e. g.* [14, 15] for reviews), are powerful alternatives, their applicability is also often plagued by a number of severe obstacles. Lattice gauge theories, for instance, face the so-called sign-problem at finite net density. Gauge/gravity duality by contrast has proven to be a very successful tool for investigating strongly coupled QFTs since it maps the inherently non-perturbative regime to classical gravity calculations which are in principle straightforward to perform by means of numerical methods or in some cases even analytically.

By now, holographic methods have been applied to various physical systems. Examples include applications to QCD and in particular the quark–gluon plasma (see *e. g.* [16] for a review), ultracold quantum gases (see *e. g.* [17] for a review) and condensed matter systems[1] (see *e. g.* [18, 19] for an overview). Hence, gauge/gravity duality links fields of physics, *viz.* gravity to the above mentioned, that had no prior

---

[1]It is interesting to note that the experimentally realisable real-world systems akin to the holographic models, span a temperature range of more than twenty orders of magnitude.

relationship. Moreover, the classical gravity description provides new perspectives on strongly coupled field theories and allows to access quantities that are notoriously difficult to study with conventional methods. This opens many new and exciting possibilities, making gauge/gravity duality arguably one of the most remarkable and influential discoveries of the previous decades with an incredibly wide range of applications. For completeness, we point out that gauge/gravity duality can also be used in the opposite limit with regard to the physical parameter regimes of the dual theories. In particular, upon studying weakly coupled field theories by employing standard QFT methods, one can learn about the nature of (quantum) gravity.

A specific instance of gauge/gravity duality can either be derived from a string-theory setup, like in the case of the original AdS/CFT correspondence, or by constructing a phenomenological model akin to the real-world physical system that one intends to describe ('bottom-up' ansatz). In the vast majority of these models, however, the simplicity of the gravitational description does not come without a price. Namely, the field-theory side does typically not agree exactly with the real-world system of interest. Nonetheless, there are several reasons why the application of holographic methods is a very valuable tool, and we will discuss two of them in the following. First, holography can be employed to learn about generic strongly coupled QFTs. In particular, one may hope that certain infrared observables are insensitive to the details of the field-theory Lagrangian in the ultraviolet and therefore, to some degree, universally valid. The most prominent example for such an observable is the ratio of shear viscosity η to entropy density s which has been found to equal $\eta/s = 1/(4\pi)$ in units of $\hbar/k_\mathrm{B}$ for all isotropic field theories in the infinite-coupling limit which are dual to theories of classical Einstein gravity [20–23]. Based on these findings and the fact that finite-coupling corrections only yield positive corrections to the ratio [24], Kovtun, Son and Starinets conjectured that $1/(4\pi)$ is in fact a lower bound [25],

$$\frac{\eta}{s} \geq \frac{1}{4\pi} \, , \tag{1.1}$$

for all relativistic quantum many-body systems. Equation (1.1) is the famous *KSS bound*.

From measurements of so-called flow coefficients in experiments on ultrarelativistic heavy-ion collisions [26, 27], one has inferred that the value of η/s for the quark–gluon plasma is very close to (but above) the KSS bound [28–30]. The smallness of the measured value provides strong evidence that the QGP, for the currently available energies in heavy-ion collisions, is indeed strongly coupled. In fact, the measurements indicate that the QGP is the most ideal fluid ever observed in nature. In particular, it is even more perfect than cold and ultracold quantum gases which have also been found to respect the bound, see *e. g.* the review [17] and references therein. To this day, all known real-world fluids respect the KSS bound.

A second reason why holography is a valuable tool is that it provides an *ab initio* description of strongly coupled theories akin to real-world systems in regimes that cannot be accessed with conventional methods. Moreover, even if a number of alter-

native approaches exist, they typically capture only certain aspects of the strongly-coupled system, making holography the only available method that provides a fundamental description of the quantum theory, and is in principle straightforward to solve. Here, fundamental description has to be understood in the sense that the dual gravitational description is fundamental.

A prominent example demonstrating the benefit of using holography in this spirit is the description of non-equilibrium dynamics in quantum many-body systems, and in particular superfluids. Superfluidity is a macroscopic quantum phenomenon associated with the formation of a Bose–Einstein condensate. In recent years the study of far-from-equilibrium dynamics in superfluid helium and ultracold Bose gases has drawn considerable attention, both experimentally and theoretically [31–41]. In particular the interest in quantum turbulence, associated with the dynamics of ensembles of vortex defects, has strongly increased [42, 43], most notably due to experimental advances and the observation of Kolmogorov scaling in the kinetic-energy spectrum of superfluid helium [44, 45]. Due to strong correlations prevailing in such systems during the non-equilibrium dynamics, non-perturbative methods are required for a theoretical description. In particular, even if the interaction strength between the constituent particles is weak, the strongly non-linear excitations, *e. g.* topological vortex defects and solitary waves, render a description intricate.

Gauge/gravity duality provides a framework in which not only strong couplings but also strong correlations and non-linear dynamics are naturally accounted for in an inherently non-perturbative description. Particular attention has been attracted by holographic models of strongly dissipative bosonic superfluids. Such models have been employed in numerous works to address non-equilibrium dynamics with a special emphasis on quantum-turbulent behaviour. While the superfluids described by holographic models are qualitatively known to be strongly dissipative, it has proven notoriously difficult to quantitatively determine their phenomenological parameters.

In this work, we employ a widely studied bottom-up holographic model of superfluidity [46–48] in two and three spatial dimensions to study the dynamics of vortex defects and quantum turbulence in strongly dissipative bosonic superfluids. In particular, for the first time we quantitatively characterise the two-dimensional holographic system with regard to its dissipative nature and are led to conjecture its applicability in the description of vortex dynamics in real-world superfluids. We infer that it governs regimes that cannot be captured by conventional methods, thus corroborating the benefits of employing the holographic duality to learn about vortex dynamics and quantum turbulence in certain real-world systems. Furthermore, for the first time ever we construct and analyse vortex solutions of the three-dimensional holographic superfluid and investigate the far-from equilibrium dynamics of the system. We study the dynamics and interactions of vortex defects and from our findings infer the superfluid to be strongly dissipative, just like the two-dimensional system. Our studies constitute the first investigation of the behaviour of vortex defects as well as aspects of quantum turbulence in a strongly dissipative three-dimensional superfluid by means of a fundamental method, albeit we solve the model using an approximation that does not self-consistently couple the superfluid component of

the system to the thermal heat bath.

We present a more detailed motivation for studying superfluidity, and in particular non-equilibrium dynamics and quantum turbulence, as well as for employing the holographic framework to this end in chapter 3. Moreover, we present thorough discussions of the specific physical systems we are interested in and a motivation for our work in an introductory chapter at the beginning of each part. In these chapters we also give a more detailed outline of the respective parts. In the following, we therefore present only a brief overview of the organisation of this thesis.

Organisation of this thesis

To set the stage for our investigations in this work, we begin in chapter 2 with an introduction to the original AdS/CFT correspondence and a discussion of crucial aspects of the holographic dictionary relating the dual theories. We also review important features of the duality at finite temperature and chemical potential which are relevant for this thesis. In chapter 3 we lay out our motivation for studying vortex dynamics and in particular quantum turbulence in superfluids. Furthermore, we present a more thorough motivation for employing holography to this end by contrasting it with other conventional methods. Thereafter, we introduce the holographic model of superfluidity in $d + 1$ dimensions and an approximation scheme thereof that we employ throughout this thesis. We review the corresponding equations of motion and the associated boundary conditions and discuss the physical characteristics of the model with a particular focus on the nature of the phase transition. Thereafter, the thesis is split into two main parts. Part I concerns the two-dimensional and Part II the three-dimensional holographic superfluid.

In *Part I* we study the dynamics of vortex dipoles in a two-dimensional holographic superfluid by means of numerical real-time simulations. In particular, we match to the observed dynamics solutions of the dissipative Gross–Pitaevskii equation to quantify the dissipation of the superfluid and compare it to real-world systems such as liquid helium or cold Bose gases.

We begin in chapter 4 by laying out the physical motivation for our studies. In chapter 5, we review the static and spatially homogeneous as well as fully dynamical equations of motion of the gravitational model and discuss in detail the characteristics of the static solution. Moreover, we discuss our numerical implementation of the equations of motion that we employ for the real-time simulations. In chapter 6 we discuss the initial configuration of the vortex dipole that we study and qualitatively analyse the dynamical evolution of the vortices as they approach and annihilate each other. Furthermore, we lay the ground for all following investigations by introducing a high-precision tracking routine for the vortices that allows us to extract their trajectories from our real-time simulations in a quasi-continuous manner. In chapter 7 we first set the stage for our matching procedure by introducing the (dissipative) Gross–Pitaevskii ((D)GP) model and the Hall–Vinen–Iordanskii (HVI) equations for the mechanical motion of point vortices in dissipative superfluids. Thereafter, we

match solutions of the DGP and HVI equations to the dipole dynamics in the holographic superfluid to quantify the dissipation of the system. Eventually, we extract friction coefficients which we compare to experimentally measured values for helium and cold Bose gases. This allows us to assess the applicability of the holographic framework to the description of vortex dynamics in such systems. In chapter 8 we investigate the kinematic aspects of the dipole evolution and study the dependence of the vortex dynamics on the initial dipole configuration and on the chemical potential of the superfluid. Moreover, we also analyse the rarefaction pulse that is created by the annihilating vortices and compare its characteristics to solutions of the GP model. Finally, we summarise our findings and present an outlook for future works in chapter 9.

In *Part II*, we construct and analyse vortex solutions of the three-dimensional holographic superfluid and study the time evolution of the system starting from various far-from-equilibrium initial conditions. Furthermore, we investigate the characteristic behaviour of interacting and excited or perturbed vortex rings.

We begin in chapter 10 by discussing the physical motivation for our studies. In particular, we highlight the historical interest in vortex rings and their interactions, as well as turbulent behaviour of fluids and superfluids. In chapter 11 we review the equations of motion of the gravitational model, for the static and homogeneous as well as fully dynamical system. We solve the static equations and discuss the characteristics of the corresponding solution. In chapter 12, we construct vortex-ring and vortex-line solutions of the superfluid and study their properties. Furthermore, we investigate the dynamics of a single vortex ring, analyse the details of its kinematics, and compare our findings to solutions of the HVI equations for vortex rings. We also study how the dynamics depends on the initial size and alignment of the ring as well as on the chemical potential of the superfluid. In chapter 13, we study the non-equilibrium real-time evolution of the superfluid starting from different far-from-equilibrium initial conditions given by sets of dense vortex configurations. We analyse the dynamics of the system in terms of scaling behaviour in correlation functions and characteristics of the vortex tangles. We find that at intermediate and late times of the evolution, the system exhibits universal scaling behaviour in the radial occupation number spectrum which we interpret as a signature of turbulent transport of energy. In chapter 14 we investigate the behaviour of interacting vortex rings for various types of initial conditions. We study in particular the leapfrogging motion of two coaxial vortex rings as well as head-on colliding and off-centre scattering rings. Remarkably, we find the rings to exhibit behaviour that was predicted more than 150 years ago by Hermann von Helmholtz for vortex rings in classical liquids. In addition, we investigate Kelvin-wave excitations of vortex rings in the holographic superfluid which were first studied by Lord Kelvin for classical vortex rings. We summarise our findings and present an outlook for future studies in chapter 15.

Finally, in chapter 16 we present a discussion of our main results and give an outlook on potential future research on the topics of this thesis. In appendix A we

present details concerning our numerical implementation of the static and homogeneous as well as fully dynamical equations of motion of the gravitational models for the two- and the three-dimensional superfluid. In addition, we comment on numerical evaluation methods that we employ in this thesis, in particular concerning the fitting of power laws in the radial occupation number spectrum, the finite-difference methods that we use to compute the velocities and accelerations of vortices, and the three-dimensional vortex-tracking routine. In appendix B we discuss details concerning the HVI equations for the dynamics of point vortices and derive the relation between the HVI parameters and the parameters of the dissipative Gross–Pitaevskii equation. We also derive the solutions of the HVI equations for a single vortex–anti-vortex pair. Finally, in appendix C we discuss the time evolution of the radial occupation number spectrum for the dynamics of the second set of initial far-from-equilibrium conditions of chapter 13 and the dynamics of a single vortex ring with special emphasis on the scaling behaviour.

2 Introduction to Holographic Duality

In this chapter we review the basic concepts and some important features of gauge/-gravity duality, or more generally holographic duality, relevant for this thesis. We first focus on the original $\text{AdS}_5/\text{CFT}_4$ correspondence that was introduced by Maldacena as a conjectured duality between the four-dimensional $\mathcal{N} = 4$ maximally supersymmetric $SU(N_{\text{c}})$ Yang–Mills (SYM) theory and type IIB supersymmetric string theory in five-dimensional anti-de Sitter (AdS) spacetime times an additional compact manifold. Further, we discuss generalisations of the $\text{AdS}_5/\text{CFT}_4$ duality to the larger class of gauge/gravity or holographic dualities. For many applications the compact manifold can be neglected, in which case gauge/gravity duality relates a four-dimensional quantum field theory to a theory of gravity in an anti-de Sitter spacetime of one higher dimension. We point out that despite many non-trivial consistency checks in favour of the AdS/CFT correspondence (see *e. g.* [49, 50]), a formal mathematical proof of the duality has not been constructed to this day, thus leaving it a conjecture for now.

Maldacena's pathbreaking conjecture was the culmination of a new line of research on black-hole physics and quantum theories of gravity that included a number of early hints towards holography and thus the existence of a duality between gauge and gravity theories. The origin of holography is typically attributed to the work of Bekenstein and Hawking. In a semi-classical calculation, Hawking found that black holes radiate energy at a temperature determined by the surface gravity of the black hole ('Hawking radiation') [51]. His findings complemented the earlier work of Bekenstein [52], making explicit the famous expression for the entropy of a black hole,

$$S_{\text{BH}} = \frac{A}{4G_{\text{N}}} \frac{c^3}{\hbar} \, , \tag{2.1}$$

where A denotes the area of the black-hole event horizon, G_{N} is Newton's constant, $\hbar$ the reduced Planck constant and c is the speed of light. The Bekenstein–Hawking entropy (2.1) thus states that the entropy of a black hole and therefore its number of degrees of freedom scales with the size of its by one lower-dimensional horizon. The remarkable nature of this discovery was a first early hint towards a description of the black-hole interior in terms of the degrees of freedom encoded on its horizon, *i. e.*, its 'boundary'.

Although intriguing, the findings of Bekenstein and Hawking also raised several questions and in particular stood in conflict with well-established quantum-mechanical as well as thermodynamical principles. In non-gravitational systems

an entropy that scales with the area of a system is incompatible with its extensive nature, according to which the entropy should scale with the volume instead. Moreover, an immediate consequence of Hawking radiation is that black holes evaporate. However, the evaporation of black holes appeared to be incompatible with the unitary evolution of quantum systems. Indeed, if a massive object collapses to a black hole and eventually evaporates, a pure quantum state evolves into mixed states that can only be described by a density matrix, thus contradicting unitarity. It was Hawking himself who formulated these apparent discrepancies in terms of the *information paradox* [53] (see *e. g.* [54] for a review).

A possible resolution of the information paradox involves the *holographic principle* put forward in the seminal works of 't Hooft [4] and Susskind [5]. The holographic principle asserts that the physics of a $(D+1)$-dimensional theory of quantum gravity, typically referred to as the 'bulk theory', is fully encoded on its D-dimensional boundary and can thus be described by some non-gravitational quantum field theory, typically referred to as the 'boundary theory'. The holographic principle implies in particular that the entropy of some volume of quantum-gravity states must scale with the boundary area of that volume [5]. The holographic principle owes its name to an analogy with our everyday-life where a hologram is a two-dimensional picture that encodes the full phase information of a three-dimensional scene [55]. In this spirit, one may think of the boundary quantum field theory as a projection of the entire dynamics of the higher-dimensional 'bulk' quantum-gravity theory. The AdS/CFT correspondence was the first direct realisation of the holographic principle. To this day, no violation of the principle is known (see *e. g.* [56]). For a detailed discussion of the holographic principle, see for instance [57].

Early hints towards a relation between non-gravitational quantum field theories and theories of quantum gravity were also put forward from the field-theory perspective. In another work, 't Hooft showed that in the limit of large number of colours in non-Abelian gauge theories, Feynman diagrams are organised by their topology [58]. Such topological order has a strong resemblance to the perturbative expansion of closed-string worldsheets in a quantum string theory.

Throughout this thesis, we set $\hbar = c = k_{\mathrm{B}} = 1$, thus working in units specified by this choice. In addition, we mostly set the curvature radius of anti-de Sitter spacetime to unity, $L_{\mathrm{AdS}} = 1$. For all calculation in this thesis, we adapt the mostly-plus metric-signature convention $(-, +, \ldots, +)$, and denote by $D + 1$ the spatio-temporal dimensions of the AdS spacetime. Moreover, we denote by $d+1$ the number of spacetime dimensions of non-gravitational quantum field theories, where, if not stated otherwise, $d = D - 1$. We denote indices of the $D + 1$ bulk coordinates $(t, \boldsymbol{x}, z)$ by capital Latin letters M, N.

The outline of this chapter is as follows. We begin in section 2.1 with a brief review of some important features of string theory (section 2.1.1) as well as anti-de Sitter spacetime and $\mathcal{N} = 4$ supersymmetric Yang–Mills theory (section 2.1.2). Thereafter, in section 2.2, we review the main aspects of the derivation of the original $\mathrm{AdS}_5/\mathrm{CFT}_4$ correspondence (subsection 2.2.1). Subsequently, in subsection 2.2.2, we discuss a number of concepts of the so-called holographic dictionary, an

instructional manual for practical uses of gauge/gravity duality. In particular, these concepts hold more generally than just for the original AdS/CFT correspondence and are thus essential for our studies of holographic superfluids in this thesis. In subsection 2.2.3 we review the two fundamental approaches that are used to construct or derive holographic models, focusing mainly on the 'bottom-up' approach that we employ in this work. Since a superfluid is a physical system with finite temperature and chemical potential, we also review how these features are implemented in the holographic framework (section 2.3). In particular, we review the corresponding spacetime geometries dual to boundary theories at non-zero temperature, as well as at non-zero temperature and non-zero chemical potential.

2.1 Foundations for Gauge/Gravity Duality

Maldacena derived the original AdS/CFT correspondence in the framework of a ten-dimensional supersymmetric string theory. While the details of the derivation are rather involved, some basic knowledge of string theory is sufficient to comprehend the main ideas. In the following subsection 2.1.1 we therefore review a number of features of string theory that we deem relevant for the following sections. In addition, in subsection 2.1.2, we review some aspects of anti-de Sitter spacetime and $\mathcal{N} = 4$ supersymmetric Yang–Mills theory that are necessary to understand the essential concepts of holography and gauge/gravity duality.

2.1.1 Aspects of String Theory

In this section we review some basic concepts of string theory. Since a more thorough discussion goes beyond the scope of this thesis, we refer the interested reader to [59–62] for a number of excellent books on the subject. We closely follow [16, 63] in this subsection.

In string theory, the fundamental objects of nature are strings which are not point-like like but one-dimensional. These one-dimensional objects come in two topologies. They can either be open, with two free endpoints, or closed. As strings propagate through spacetime they trace out a two-dimensional worldsheet, which has no boundaries for closed strings. For a given embedding of the string worldsheet $X^M(\sigma^a)$ into a $(D + 1)$-dimensional ambient spacetime with metric g_{MN} and $M = 0, \ldots, D$, as well as local worldsheet coordinates σ^a, $a \in \{0, 1\}$, the induced metric on the worldsheet is given by

$$g_{ab} = g_{MN} \frac{\partial X^M}{\partial \sigma^a} \frac{\partial X^N}{\partial \sigma^b} \, . \tag{2.2}$$

In terms of this metric, one can now define the action for strings in analogy to the action for point-particles in terms of the area of their worldsheet. The simplest action, invariant under reparameterisations of the worldsheet governing the dynamics

of strings is given by the *Nambu–Goto action,*

$$S_{\mathrm{NG}} = -\frac{1}{2\pi\alpha'} \int \mathrm{d}^2\sigma \sqrt{-\det g_{ab}}\,. \tag{2.3}$$

Here, $1/(2\pi\alpha')$ is the string tension and α' ('alpha prime') is a free parameter. In fact, α' is the only free parameter of string theory and thus sets the length and mass scale of the theory,

$$l_{\mathrm{s}} = \sqrt{\alpha'}\,, \qquad M_{\mathrm{s}} = \frac{1}{\sqrt{\alpha'}}\,, \tag{2.4}$$

with string length l_{s} and string mass M_{s}. A remarkable insight into string theory came from Polchinski who showed that strings are not the only fundamental objects of string theory. Instead, they are accompanied by higher-dimensional membranes, so-called Dirichlet branes (D-branes) [64]. Dp-branes are dynamical objects with p spatial and one temporal dimension on which open strings can end. Transverse to the branes, the open strings satisfy Dirichlet boundary conditions, thus the name. For supersymmetric string (superstring) theories, a consistent quantisation is possible only in ten spacetime dimensions, while bosonic string theories require 26 dimensions. We are interested in superstring theories only. The quantisation of string theory gives rise to a finite number of massless modes and an infinite tower of massive excitations with masses of the order of M_{s}. While open-string quantisation gives rise to Yang–Mills theories, closed-string quantisation gives rise to gravity. In particular, one of the massless closed-string modes is the graviton. Since closed strings can break up and open strings can close onto themselves, string theory unifies gauge theories and gravity. String interactions have a very intuitive geometric interpretation in terms of breaking or joining string worldsheets. Interestingly, unlike in quantum field theories, the string coupling constant g_{s} controlling string perturbation theory is not a free parameter, but instead dynamically controlled by one of the massless closed-string excitations, the dilaton. We will be interested in the low-energy limit of string theory, *i.e.*, $E \ll M_{\mathrm{s}}$, which according to (2.4) is equivalent to $\alpha' \to 0$. In this case, the massive string modes become infinitely heavy and thus decouple. Moreover, the strings essentially appear as point-like objects (since $l_{\mathrm{s}} = \alpha'^{1/2} \to 0$) and string theory thus reduces to Einstein's general relativity with a number of additional massless fields. In total, there exist five types of string theory which can all be related by a number of so-called T- and S-dualities. For us, only type IIB superstring theory is of relevance. In the low-energy limit, this theory reduces to type IIB supergravity (SUGRA).

2.1.2 AdS Spacetime and $\mathcal{N} = 4$ Supersymmetric Yang–Mills Theory

In this subsection we briefly review some essential features of the two theories that the AdS/CFT duality relates. We first discuss anti-de Sitter spacetime and subsequently give a brief account of $\mathcal{N} = 4$ supersymmetric Yang–Mills theory.

Anti-de Sitter Spacetime. In light of our application of gauge/gravity duality to superfluids in two (Part I) as well as three (Part II) spatial dimensions, we keep the following discussion as generic as possible and review anti-de Sitter spacetime in $D+1$ dimensions. Anti-de Sitter spacetime is the maximally symmetric solution of the Einstein–Hilbert action

$$S_{\text{EH}} = \frac{1}{16\pi G_{\text{N}}^{(D+1)}} \int \mathrm{d}^{D+1}x \, \sqrt{-g} \, (\mathcal{R} - 2\Lambda) \,, \tag{2.5}$$

where g is the determinant of the spacetime metric g_{MN}, $\mathcal{R}$ is the associated Ricci scalar, $G_{\text{N}}^{(D+1)}$ Newton's constant in $D+1$ dimensions, and Λ the cosmological constant which is negative,

$$\Lambda = -\frac{D(D-1)}{2L_{\text{AdS}}^2} \,, \tag{2.6}$$

with L_{AdS} the curvature radius of the anti-de Sitter spacetime. This implies, in particular, $\Lambda = -3/L_{\text{AdS}}^2$ for the four-dimensional anti-de Sitter spacetime (AdS$_4$) and $\Lambda = -6/L_{\text{AdS}}^2$ for the five-dimensional anti-de Sitter spacetime (AdS$_5$).

The equations of motion associated with the action (2.5) are given by Einstein's equations with finite cosmological constant,

$$\mathcal{R}_{MN} - \frac{1}{2}\mathcal{R} \, g_{MN} + \Lambda \, g_{MN} = 0 \,, \tag{2.7}$$

formulated in terms of the Ricci tensor $\mathcal{R}_{MN}$. They are solved by the $(D+1)$-dimensional anti-de Sitter spacetime with metric

$$\mathrm{d}s^2 = \frac{L_{\text{AdS}}^2}{z^2} \left(-\mathrm{d}t^2 + \mathrm{d}\boldsymbol{x}^2 + \mathrm{d}z^2 \right) \,, \tag{2.8}$$

where we have employed Poincaré coordinates and have defined $\boldsymbol{x} = (x_1, \ldots, x_{D-1})$.

The metric (2.8) shows that for every fixed-z slice the AdS spacetime is conformally equivalent to a flat Minkowski spacetime. Indeed, under an appropriate scale transformation,

$$(t, \boldsymbol{x}) \to C(t, \boldsymbol{x}), \quad z \to Cz \,, \tag{2.9}$$

for $C > 0$, the $(t, \boldsymbol{x})$-part of the metric can be transformed into the standard Minkowski metric,

$$\mathrm{d}s^2 = -\mathrm{d}t^2 + \mathrm{d}\boldsymbol{x}^2 \,. \tag{2.10}$$

At $z = 0$ the AdS$_{D+1}$ spacetime has a conformal boundary (see *e. g.* [65]) of topology $\mathbb{R}^{1,D-1}$. In the framework of AdS/CFT duality or more generally gauge/gravity duality, the conformal boundary plays a central role as one can think of it as 'host' of the dual (conformal) field theory.

It turns out that the AdS metric (2.8) is not only invariant under scale transformations (2.9) but also under Poincaré and in particular special conformal transformations. The isometry group of the metric (2.8) is therefore given by $SO(2, D)$. For details, see *e. g.* [16, 66].

Finally, in anticipation of the AdS/CFT derivation below, let us perform a coordinate transformation of the AdS metric (2.8) defined by

$$z = \frac{L_{\text{AdS}}^2}{r} \,. \tag{2.11}$$

With the new 'radial' coordinate r, the metric reads

$$\mathrm{d}s^2 = \frac{r^2}{L_{\text{AdS}}^2} \left(-\mathrm{d}t^2 + \mathrm{d}\boldsymbol{x}^2 \right) + \frac{L_{\text{AdS}}^2}{r^2}\, \mathrm{d}r^2 \,. \tag{2.12}$$

$\mathcal{N} = 4$ Supersymmetric Yang–Mills Theory. $\mathcal{N} = 4$ SYM theory in four spacetime dimensions is a maximally supersymmetric and conformal non-Abelian quantum field theory with gauge group $SU(N_{\text{c}})$, where N_{c} denotes the number of colours. The field content of the theory is given by one Abelian gauge field, four Weyl fermions as well as six real scalar fields. Due to the supersymmetry, all fields transform in the adjoint representation and are massless. Associated with the supersymmetry is an $SU(4)$ R-symmetry. Furthermore, the conformal invariance gives rise to an additional $SO(4,2)$ symmetry. The conformal invariance also implies that the beta function of $\mathcal{N} = 4$ SYM is identically zero. Thus, the coupling strength of the fields is constant and does not run. In anticipation of the fact that we will mostly be interested in the large-N_{c} limit of the gauge theory, *i.e.*, the limit of large number of colours, we mention that in this case the coupling strength of the field theory is effectively controlled by the so-called 't Hooft coupling [58],

$$\lambda = g_{\text{YM}}^2 N_{\text{c}} \,. \tag{2.13}$$

For further details of $\mathcal{N} = 4$ SYM theory, see for instance [67], and for a general introduction to supersymmetric field theories, see [68].

2.2 AdS/CFT Duality

We now review the string-theory construction of the original $\text{AdS}_5/\text{CFT}_4$ correspondence. Excellent reviews and books on the subject and on gauge/gravity duality and holography in general include [16, 18, 19, 49, 50, 69]. We closely follow [49, 50] throughout this section.

2.2.1 Maldacena's Conjecture

The AdS/CFT correspondence arises in the framework of supersymmetric string theory upon studying a stack of N_{c} coincident D3-branes. Here, we denote the number of branes N_{c} with an additional subscript 'c' in anticipation of the fact that it will later turn out to coincide with the number of colours of the $\mathcal{N} = 4$ SYM theory.

We study the configuration of D3-branes in type IIB superstring theory in flat ten-dimensional Minkowski spacetime, $\mathbb{R}^{1,9}$. Depending on the string coupling,
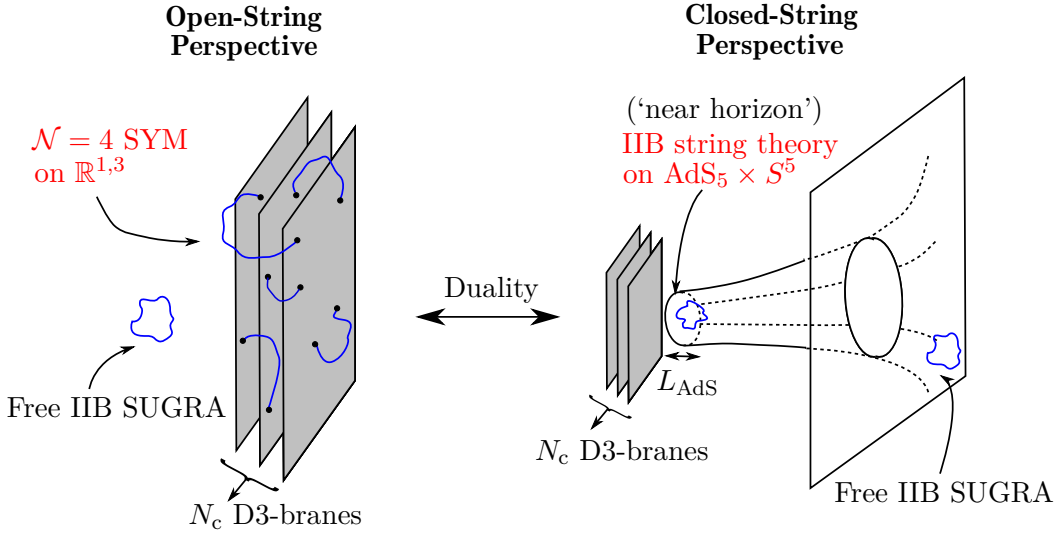
Figure 2.1: Sketch of the string-theory setup that gives rise to the $\mathrm{AdS}_5/\mathrm{CFT}_4$ correspondence. In the low-energy limit, both descriptions of N_c coincident D3-branes factorise into two decoupled theories, with free type IIB SUGRA being one of them in both descriptions. The AdS/CFT duality is the conjecture that the remaining two theories are dynamically equivalent.

the brane configuration must be described from two different perspectives. The AdS/CFT correspondence arises naturally upon studying both perspectives in the low-energy limit and conjecturing that the outcomes are equivalent [1]. Without loss of generality, we take the spacetime coordinates of the branes to coincide with the $(t, \boldsymbol{x}) = (t, x_1, x_2, x_3)$-directions. In figure 2.1 we present a sketch of the two perspectives after the low-energy limit has been taken.

Open-String Perspective. In the first, so-called 'open-string', perspective, the D3-branes are studied as higher-dimensional objects on which open strings can end, as we have mentioned in the previous section. This perspective is appropriate in the limit

$$g_\mathrm{s} N_\mathrm{c} \ll 1 \,. \tag{2.14}$$

The theory contains open strings that end on the branes as well as closed strings propagating in the ten-dimensional spacetime. The action for the string modes splits into three parts, one describing only the open strings, one only the closed strings, and one their interactions,

$$S = S_\mathrm{open} + S_\mathrm{closed} + S_\mathrm{int} \,. \tag{2.15}$$

15

Here, S_{int} governs the interactions between open and closed strings. In the following we discuss the respective actions of the open and closed strings in more detail, beginning with S_{open}. The excitation spectrum of the strings consists of a finite number of massless modes as well as an infinite tower of massive excitations. In the low-energy limit, only the massless excitations survive as the entire tower of massive modes (with masses $m \sim M_{\text{s}} \sim \alpha'^{-1/2}$) decouples from the dynamics. The two endpoints of each open string can end on any of the N_{c} D3-branes, giving rise to a non-Abelian gauge field with gauge group $U(N_{\text{c}})$. The gauge-field components are excitations parallel to the branes. Likewise, there are also excitations transverse to the branes which are given by a collection of six massless scalar fields. One finds that the low-energy effective action of the gauge field, the scalar fields as well as their fermionic superpartners is given by the action of $\mathcal{N} = 4$ supersymmetric Yang–Mills theory with gauge group $U(N_{\text{c}})$ in flat $(3+1)$-dimensional Minkowski spacetime [70]. The $U(N_{\text{c}})$ gauge group can be decomposed as $U(N_{\text{c}}) = SU(N_{\text{c}}) \times U(1)$, where the $U(1)$ subgroup describes the centre-of-mass motion of the branes [71]. Due to the translational symmetry of the underlying system, the $U(1)$ subgroup effectively decouples from the inter-brane dynamics. Hence, the open string sector is effectively governed by $\mathcal{N} = 4$ *SYM theory with gauge group* $SU(N_c)$ *in* $\mathbb{R}^{1,3}$. In terms of the string coupling g_{s}, the coupling constant of $\mathcal{N} = 4$ SYM is given by (see *e. g.* [50])

$$g_{\text{YM}} = 4\pi g_{\text{s}} \,. \tag{2.16}$$

The closed string sector, described by S_{closed}, again consists of a finite number of massless as well as an infinite tower of massive excitations. In the low-energy limit, the massive modes again decouple and can thus be neglected for the same reason as discussed above for the open string spectrum. The massless modes, one of which is the graviton, on the other hand, give rise to type IIB supergravity. The interactions between the (massless) closed strings are governed by Newton's constant (see *e. g.* [50]),

$$G_{\text{N}}^{(10)} = 8\pi^6 g_{\text{s}}^2 \alpha'^4 \,, \tag{2.17}$$

here expressed in terms of the string parameter α'. Since the low energy limit agrees with $\alpha' \to 0$, the interaction between the closed-string modes can be neglected. Hence, the closed string spectrum gives rise to *free type IIB supergravity* in flat $(9+1)$-dimensional Minkowski spacetime. Since the interactions between open and closed strings are also controlled by Newton's constant, S_{int} can be neglected as well, and the open and closed string sectors thus decouple.

Closed-String Perspective. In the second, 'closed string', perspective, the D3-branes are viewed as massive objects that distort their surrounding spacetime. This perspective is therefore also often referred to as supergravity perspective or description. It is appropriate in the limit,

$$g_{\text{s}} N_{\text{c}} \gg 1 \,, \tag{2.18}$$

implying a large tension of the D3-branes and thus a significant backreaction of the branes onto spacetime. Naturally, the description also includes closed strings surrounding the branes. However, due to the large string coupling, they do not break up on the branes to form open strings. The metric corresponding to the distorted spacetime is given by [72]

$$\mathrm{d}s^2 = \frac{1}{\sqrt{H(r)}}\left(-\mathrm{d}t^2 + \mathrm{d}\boldsymbol{x}^2\right) + \sqrt{H(r)}\left(\mathrm{d}r^2 + r^2\,\mathrm{d}\Omega_5^2\right), \qquad (2.19)$$

$$H(r) = 1 + \frac{L_{\mathrm{AdS}}^4}{r^4}, \qquad (2.20)$$

where $r^2 = x_4^2 + \cdots + x_9^2$ is the (squared) radial distance transverse to the branes, $(t, \boldsymbol{x}) = (t, x_1, x_2, x_3)$ are the coordinates of the $(3+1)$-dimensional brane worldvolume and $d\Omega_5$ denotes the angular line-element of a five-sphere. In addition, L_{AdS} is the curvature radius of the spacetime. In anticipation of the fact the L_{AdS} will turn out to be the curvature radius of the AdS spacetime, we have provided it with an additional 'AdS' subscript. In terms of the string-theory parameters g_{s} and α', it is given by

$$L_{\mathrm{AdS}}^4 = 4\pi g_{\mathrm{s}} N_{\mathrm{c}} \alpha'^2. \qquad (2.21)$$

Using equation (2.17), it can also be expressed in terms of Newton's constant as

$$L_{\mathrm{AdS}}^8 = 2\pi^{-4} G_{\mathrm{N}}^{(10)} N_{\mathrm{c}}^2. \qquad (2.22)$$

Far away from the branes, *i.e.*, in the limit $r \gg L_{\mathrm{AdS}}$, the function (2.20) can be approximated by $H(r) \approx 1$, thus reducing the spacetime metric (2.19) to the flat Minkowski metric in $9+1$ dimensions. Close to the branes, *i.e.*, for $r \to 0$, on the other hand, one finds $H(r) \approx L_{\mathrm{AdS}}^4/r^4$. In this, so-called 'near-horizon', limit, the metric reduces to

$$\mathrm{d}s^2 = \left[\frac{r^2}{L_{\mathrm{AdS}}^2}\left(-\mathrm{d}t^2 + \mathrm{d}\boldsymbol{x}^2\right) + \frac{L_{\mathrm{AdS}}^2}{r^2}\,\mathrm{d}r^2\right] + L_{\mathrm{AdS}}^2\,\mathrm{d}\Omega_5^2 = \mathrm{d}s_{\mathrm{AdS}_5}^2 + \mathrm{d}s_{S^5}^2, \quad (2.23)$$

where we have identified $\mathrm{d}s_{\mathrm{AdS}_5}^2$ as the AdS metric (2.12) and $\mathrm{d}s_{S^5}^2$ is the metric of a five-sphere. The geometry close to the branes thus factorises into a five-dimensional anti-de Sitter spacetime and a five-sphere. We point out that r parametrises the radial (normal) distance away from the stack of D-branes. In the context of holography or gauge/gravity duality the additional 'holographic' coordinate of the bulk spacetime is therefore often referred to as 'radial' coordinate. The curvature radii of the AdS spacetime and of the five-sphere agree and are given by L_{AdS}. The two asymptotic spacetime geometries for $r \gg L_{\mathrm{AdS}}$ and $r \ll L_{\mathrm{AdS}}$ are connected by a 'throat'. For a visualisation, see the sketch on the right-hand side of figure 2.1.

The low-energy limit of the closed-string spectrum is taken from the perspective of an observer in the asymptotically flat Minkowski spacetime. From the spacetime metric (2.19) it follows that the proper energy E of a string excitation at a constant

distance r away from the branes is related to the energy of the excitation as measured from an observer at $r \to \infty$ by

$$E_\infty = H(r)^{-1/4} E \,. \tag{2.24}$$

Hence, for an observer at infinity (relative to the branes), the energy of an object appears smaller the deeper it is situated in the spacetime throat, *i.e.*, the closer it is to the branes. Consequently, in the low energy limit, two types of excitations survive. Firstly, massless excitations in the asymptotically flat spacetime. In this region, the massive modes naturally decouple in the low-energy limit. Moreover, interactions between the massless string modes cease as they are again controlled by Newton's constant which vanishes in the limit $\alpha' \to 0$, *cf.* equation (2.17). The string spectrum therefore gives rise to *free type IIB supergravity* in $\mathbb{R}^{1,9}$. Secondly, excitations of arbitrary proper energy deep in the throat for $r \to 0$. These excitations give rise to *type IIB superstring theory* in an $\mathrm{AdS}_5 \times S^5$ spacetime. Since we consider the low-energy limit only, the two asymptotic theories decouple [73, 74] (see *e.g.* [49]).

As a final comment, let us point out that from the relation in equation (2.21) it follows that the low-energy limit $\alpha' \to 0$ is consistent only for $g_\mathrm{s} N_\mathrm{c} \gg 1$, in agreement with our prior assumption for the reliability of the supergravity description of the D3-branes.

The AdS/CFT Conjecture. To summarise, the low-energy descriptions of a stack of N_c coincident D3-branes from an open- and a closed-string perspective, respectively, are given by

(i) $\mathcal{N} = 4$ supersymmetric Yang–Mills theory with gauge group $SU(N_\mathrm{c})$ in $\mathbb{R}^{1,3}$ plus free type IIB supergravity in $\mathbb{R}^{1,9}$.

(ii) Type IIB string theory in $\mathrm{AdS}_5 \times S^5$ plus free type IIB supergravity in $\mathbb{R}^{1,9}$.

Hence, from both perspectives, the description factorises into two decoupled theories. Moreover, in both perspectives, one of the theories is free type IIB supergravity in $\mathbb{R}^{1,9}$. Maldecana conjectured that if the two descriptions are equivalent, the respective remaining theories must be dual to another [1]. In other words,

$\mathcal{N} = 4$ *supersymmetric Yang–Mills theory with gauge group* $SU(N_c)$ *in* $\mathbb{R}^{1,3}$

$$\longleftrightarrow$$

Type IIB string theory in $AdS_5 \times S^5$,

where the arrow denotes the duality. This statement is the famous AdS/CFT-correspondence conjecture.

We have argued in section 2.1.2 that the boundary of anti-de Sitter spacetime at $z = 0$ is conformally equivalent to flat Minkowski spacetime. Thus, for AdS_5, the conformal boundary is given by $\mathbb{R}^{1,3}$, agreeing with the topological domain of the dual $\mathcal{N} = 4$ SYM theory. In light of the holographic principle, the $\mathcal{N} = 4$ SYM

is therefore often referred to as the *boundary theory* and thought of as 'living' on the conformal boundary of the anti-de Sitter spacetime. The latter is referred to as 'bulk' or 'bulk spacetime' in turn. We stress, however, that while this is a very convenient way of thinking about the duality, it is important to appreciate that the two theories are indeed two *independent* and thus dual descriptions of the same physical system.

Before we proceed, a comment is in order. In the 'derivation' of the duality above, we have argued that the two string-theory perspectives are reliable only in different regimes with regard to the effective string coupling $g_s N_c$. The AdS/CFT-duality conjecture does not account for this subtlety in a strict mathematical sense. Consequently, the motivation outlined above must not to be confused with a formal mathematical proof. For further details and a discussion of this aspect, see *e. g.* [50].

A basic consistency check of the AdS/CFT duality is provided by a comparison of the respective symmetry groups. If the two theories are indeed dynamically equivalent, their symmetry groups must coincide. We have discussed above that $\mathcal{N} = 4$ SYM theory is invariant under transformations of the conformal group $SO(4,2)$ as well as its $SU(4)$ R-symmetry group. On the string-theory side, on the other hand, the AdS$_5$ spacetime and the S^5 sphere, have isometry groups $SO(4,2)$ and $SO(6) \sim SU(4)$, respectively. Hence, we find that the symmetry groups on both sides of the duality agree[1]. Since the early works on the AdS/CFT duality, a variety of non-trivial consistency tests has been performed by computing certain observables on both sides of the duality and comparing the outcomes. To this day, every single test has been in favour of the duality and no violation is known.

The duality maps the free parameters of the field-theory side to the parameters of the gravitational theory, *cf.* equations (2.16) and (2.21),

$$g_{\mathrm{YM}}^2 = 2\pi g_s \,, \tag{2.25}$$

$$\lambda = \frac{L_{\mathrm{AdS}}^4}{\alpha'^2} \,, \quad \lambda = g_{\mathrm{YM}}^2 N_c \,. \tag{2.26}$$

Here, g_{YM} is the coupling constant and N_c the number of colours of $\mathcal{N} = 4$ SYM theory. In addition, λ is the 't Hooft coupling which effectively controls the perturbation theory of gauge theories in the large-N_c limit [58]. On the gravity side, g_s is the coupling strength of the strings and α' is related to the string tension and thus the fundamental string length scale $l_s = \sqrt{\alpha'}$.

Despite being very intriguing, the above form of the duality is strongly limited in its applicability. In fact, both sides of the duality are generically very hard to solve. For most practical applications, it would therefore be worthwhile to have one side that is generically hard to solve and one side that is in principle straightforward to solve. The AdS/CFT correspondence is an example of such a duality, if the above statement is mildly weakened. In its strongest form, the AdS/CFT duality is valid

---

[1]In fact, we have only discussed agreement of the bosonic subgroups of the true symmetry groups. However, the supergroups of both theories can also be shown to coincide, see *e. g.* [50]. They are given by $PSU(2,2|4)$.

for all N_c and λ on the field-theory side and g_s and α' on the string-theory side (see *e. g.* [49] for a discussion).

A weaker, however still referred to as strong, form of the duality is obtained upon taking the limit $N_\mathrm{c} \to \infty$ while keeping λ fixed. According to equations (2.25) and (2.26), this corresponds to

$$g_\mathrm{s} = \frac{\lambda}{2\pi N_\mathrm{c}} \to 0 \,, \tag{2.27}$$

while $L_\mathrm{AdS}^4/\alpha'^2$ stays finite. In other words, the coupling strength of the string theory is weak, suppressing all quantum fluctuations and thus leaving only classical tree-level diagrams in g_s. Hence, this *strong form* of the duality relates $\mathcal{N} = 4$ SYM theory in the limit of large number of colours and thus effective field-theory coupling λ to classical type IIB string theory on $\mathrm{AdS}_5 \times S^5$. We point out that the large-N_c limit is in fact inherently taken also in the description of the closed string perspective. Indeed, taking the low-energy limit $\alpha' \to 0$ and thus $G_\mathrm{N}^{(10)} \to 0$, implies $N_\mathrm{c} \to \infty$ according to equation (2.22). For a more thorough discussion of this aspect, see *e. g.* [49].

An even weaker form of the duality is obtained by taking not only the number of colours, but subsequently also the 't Hooft coupling to large values, $\lambda \gg 1$. On the string-theory side, this corresponds to taking the limit

$$\frac{L_\mathrm{AdS}^4}{l_\mathrm{s}^4} = \frac{L_\mathrm{AdS}^2}{\alpha'^2} = \lambda \to \infty \,. \tag{2.28}$$

Thus, the string length scale is much smaller than the curvature radius of the AdS spacetime which essentially reduces the strings to point-particles. Moreover, the limit $l_\mathrm{s} \to 0$ implies that all massive string excitations (with mass $m \sim 1/l_\mathrm{s}$) become infinitely heavy and therefore decouple, leaving only the massless fields, including in particular the graviton. Consequently, the classical type IIB string theory reduces to classical type IIB SUGRA, *i. e.*, classical Einstein gravity plus some additional matter fields. Hence, this *weak form* of the duality relates strongly coupled $\mathcal{N} = 4$ SYM theory for large number of colours to weakly coupled Einstein gravity on $\mathrm{AdS}_5 \times S^5$. The AdS/CFT correspondence is therefore a duality of type *weak/strong*. Namely, if one side is weakly coupled, the other one is strongly coupled and vice versa. The weak/strong nature of the duality makes it a very powerful tool in the description of gauge theories in the inherently non-perturbative regime at strong coupling since the dual description is given in terms of a weakly coupled theory of gravity in a curved background spacetime. In principle, the gravity side is straightforward to solve. We summarise the three forms of the duality in table 2.1. Importantly, the general notion of these different types of the duality hold not only for the original AdS/CFT correspondence but also more generally for gauge/gravity dualities.

For many practical purposes, including in particular the applications of the duality in this thesis, the five-sphere encodes no dynamics and can therefore be neglected, effectively reducing the gravity side to type IIB SUGRA on AdS_5.

Table 2.1: Three different forms of the AdS_5/CFT_4 duality corresponding to different regimes of the respective parameters on both sides. The general notion of these forms holds more generally for gauge/gravity dualities and not only for the original AdS/CFT correspondence.

Form of Duality	QFT side $\mathcal{N} = 4\ SU(N_c)$ SYM theory	Gravity side Type IIB theory on $AdS_5 \times S^5$
Strongest	any N_c and λ	Quantum string theory
Strong	$N_c \to \infty$ for $\lambda = \text{const}$	Classical string theory
Weak	$N_c \to \infty$ and $\lambda \to \infty$	Classical SUGRA

2.2.2 GKPW Formula and the Holographic Dictionary

In the previous subsection, we have reviewed the original idea that led Maldacena to conjecture a duality between a gauge and a gravity theory, the AdS/CFT correspondence. While Maldacena focused mainly on AdS_5/CFT_4, he also paved the way for more general classes of holographic dualities [1] (see *e.g.* [49]). In particular, such dualities are not restricted to four-dimensional field and five-dimensional gravity theories. Instead, upon studying different types of brane configurations in superstring theories, one finds dualities of type AdS_{D+1}/CFT_{d+1}, where the CFT has $d = (D-1)$ spatial dimensions and the anti-de Sitter spacetime D (see *e.g.* [49]). Moreover, such dualities can be further modified in a 'bottom-up' approach by constructing phenomenological models that capture essential aspects of the physical system one is interested in. In the following subsection 2.2.3 we comment further on the different approaches that are typically used in the construction of holographic dualities with special emphasis on the bottom-up approach that we pursue in this thesis.

In order to apply gauge/gravity duality for practical uses, it is necessary to relate not only the parameters of both sides of the duality as we have done above, but also provide a precise mapping of the field- and gravity-theory properties. Such a mapping is provided by the seminal work of Gubser, Klebanov, Polyakov and Witten (GKPW) who developed a rule or 'dictionary' that translates aspects of the gauge theories to dual aspects of the gravitational bulk theories [2, 3]. In particular, these rules apply not only to the AdS/CFT duality but also to the more general notion of gauge/gravity duality. The 'holographic dictionary' thus allows to perform calculations on one side of the duality and relate them to calculations on the other side. Since the seminal works of Maldacena and GKPW, the holographic dictionary has been continuously extended to allow for applications of gauge/gravity duality to various physical systems, such as for instance superconductors or superfluids as

we are interested in in this work.

In the following we discuss a number of important entries of the dictionary relevant for our work. We closely follow [16, 50] throughout this subsection.

UV/IR Relation. A central entry of the holographic dictionary is the ultraviolet/infrared (UV/IR) duality [1, 75, 76]. The UV/IR duality relates energy scales of the field theory to positions along the holographic coordinate z in the AdS spacetime. We recall that the coordinate z is related to the radial coordinate r, used above, by $z = L_{\text{AdS}}^2/r$. Physical processes on the field-theory side at an energy scale E are related to bulk processes localised at

$$z \sim 1/E \,, \tag{2.29}$$

implying that UV (IR) physics in the field theory is dual to bulk physics at small (large) values of z and thus close to (far away from) the boundary.

An important characteristic of gauge/gravity duality is therefore that it provides a natural mapping between the renormalisation group flow of the field theory and an evolution in the bulk along the holographic z-direction. Holographic duality is therefore often referred to as a 'geometrisation of the functional renormalisation group flow' [16, 18]. For details on holographic functional renormalisation, see *e.g.* [77, 78] and references therein.

Global/Local Symmetry Duality. Holographic dualities relate global and local symmetries. A global symmetry of the field theory translates into a local symmetry in the gravitational bulk [1]. For instance, a global spacetime symmetry of the field theory is dual to (local) spacetime isometry in the bulk, in agreement with our discussion of the symmetry groups of both sides of the duality in the previous subsection. Likewise, global internal symmetries with associated conserved currents dualise to local symmetries of (gauge–)matter fields in the gravity theory.

Field-Operator Map. Another concrete realisation of the holographic dictionary that is essential for all practical purposes is the field-operator map [2, 3, 79]. It relates fields on the gravity side to operators on the field-theory side by means of the asymptotic behaviour of the fields at the AdS boundary. A prominent example is the map between fluctuations of the AdS metric, *i.e.*, the graviton, and the field-theory energy-momentum tensor (see *e.g.* [56] for details). Furthermore, a scalar field dualises to a scalar operator and a vector field to a current operator. In accordance with the global/local symmetry duality, such a current operator is conserved if the vector field is gauged under the associated dual local symmetry group. We point out that both scalar and gauge fields are relevant for our studies of holographic superfluids in this thesis. Further details regarding the field-operator map for various types of fields can be found in every review on holographic duality, see for instance [50].

To gain an intuition, let use review the essential features of the field-operator map for the example of a scalar field Φ of mass m which dualises to a scalar operator of scaling dimension Δ. In order to relate the mass to the scalar field in the bulk to the scaling dimension of the field-theory operator, one has to solve its equation of motion, a Klein–Gordon equation in the $(D + 1)$-dimensional spacetime, and study the near-boundary expansion of the corresponding solution. One finds

$$m^2 L_{\text{AdS}}^2 = \Delta_{\pm}(\Delta_{\pm} - D) \,, \tag{2.30}$$

where $\Delta_{\pm}$ are the scaling exponents of the leading and sub-leading coefficient of the near-boundary expansion of the scalar field,

$$\Phi(t, \boldsymbol{x}, z) = (\eta(t, \boldsymbol{x}) + \mathcal{O}(z)) \, z^{\Delta_-} + (\psi(t, \boldsymbol{x}) + \mathcal{O}(z)) \, z^{\Delta_+} \,, \tag{2.31}$$

with boundary fields $\eta(t, \boldsymbol{x})$ and $\psi(t, \boldsymbol{x})$ and $\Delta_- = D - \Delta_+$. Typically, the scaling dimension of the dual scalar operator is given by the larger root of equation (2.30),

$$\Delta \equiv \Delta_+ = \frac{D}{2} + \sqrt{\left(\frac{D}{2}\right)^2 + m^2 L_{\text{AdS}}^2} \,. \tag{2.32}$$

In this case, the leading-order coefficient $\eta(t, \boldsymbol{x})$ in the near-boundary expansion (2.31)) identifies as the source conjugate to the scalar operator and the sub-leading coefficient in the expansion $\psi(t, \boldsymbol{x})$ as its vacuum expectation value in the presence of the source [80, 81]. The relation between operators on the field-theory side and fields on the gravity side makes explicit the interpretation of the AdS boundary (at $z = 0$) as the domain associated with the dual field theory.

While on the gravity side the backreaction of the scalar field induces deformation of the AdS spacetime, on the field-theory side the scalar operator induces deviations from $\mathcal{N} = 4$ SYM theory. If the operator is relevant, *i. e.*, $\Delta < D$, we learn from the near-boundary expansion (2.31) that the scalar field vanishes for $z \to 0$, implying that the associated spacetime metric of the bulk is asymptotically AdS. In accordance with the UV/IR relation, this implies that the dual operator in the boundary theory induces deformations of the field theory only in the infrared and leaves the CFT unchanged in the UV, as would be expected for a relevant field-theory operator. We note that this holds true for all types of bulk fields and associated operators and is not restricted to scalars. On the other hand, a field dual to an irrelevant operator with $\Delta > D$ induces deformations of the AdS spacetime also for $z \to 0$. In this work, we focus only on fields dual to relevant operators. For the bulk scalar field, $\Delta < D$ implies a negative mass-squared $m^2 < 0$. Importantly, in (asymptotically) anti-de Sitter spacetimes the mass-squared of a scalar field may be negative without inducing an instability, provided it is larger than the so-called Breitenlohner–Freedman bound [82–84],

$$m_{\text{BF}}^2 L_{\text{AdS}}^2 = -\frac{D^2}{4} \,. \tag{2.33}$$

Finally, let us point out that there exists an interval for the mass-squared of the scalar field,

$$\frac{D^2}{4} < m^2 L_{\mathrm{AdS}}^2 \leq -\frac{D^2}{4} + 1 \qquad (2.34)$$

for which one has the choice to associate Δ_- with the scaling dimension of the scalar operator instead of Δ_+ [79]. This is called the 'alternative quantisation', as opposed to the 'standard quantisation' we have discussed so far. To be specific, for a mass within the interval (2.34), either coefficient in the near-boundary expansion of the scalar field, *cf.* equation (2.31) can be interpreted as the source conjugate to the scalar operator and the respective other one as its vacuum expectation value. For details, see, *e. g.*, [50]. In this thesis, we will be in a position to choose either quantisation, for both the two- and the three-dimensional holographic superfluid, and chose standard quantisation in both cases.

Generating Functionals.   The final entry of the holographic dictionary we want to mention is the duality of generating functionals which is at the heart of gauge/gravity duality and typically referred to as the *GKPW formula*. It relates the generating functional of the field-theory side to the partition function of the gravity side and may thus be interpreted as the 'mathematical definition' of gauge/gravity duality.

For the strongest form of the duality (see above), the GKPW formula reads,

$$\left\langle \exp\left(\int \mathrm{d}^D x\, \mathcal{O}\phi_{(0)}\right) \right\rangle_{\mathrm{CFT}} = Z_{\mathrm{str}}\Big|_{\lim_{z\to 0} \Phi(t,\boldsymbol{x},z) z^{\Delta-D}=\phi_{(0)}(t,\boldsymbol{x})} \qquad (2.35)$$

where Φ is a generic bulk field, which needs not necessarily be scalar, and $\mathcal{O}$ is the associated dual operator of scaling dimensions Δ. In addition, $\phi_{(0)}$ is the leading-order coefficient in the near-boundary expansion of Φ and thus the source conjugate to $\mathcal{O}$, *cf.* equation (2.31). We note that in equation (2.35) we follow the standard procedure and formulate the statement in the 'standard quantisation'.

In the weak form of the duality (2.35), the string partition function Z_{str} is replaced by its saddle-point approximation, given by

$$Z_{\mathrm{str}} \approx \mathrm{e}^{-S_{\mathrm{SUGRA}}}\,, \qquad (2.36)$$

with S_{SUGRA} the on-shell (extremal) supergravity action. Thus, it follows that

$$\left\langle \exp\left(\int \mathrm{d}^D x\, \mathcal{O}\phi_{(0)}\right) \right\rangle_{\mathrm{QFT}} = \mathrm{e}^{-S_{\mathrm{SUGRA}}}\Big|_{\lim_{z\to 0} \Phi(t,\boldsymbol{x},z) z^{\Delta-D}=\phi_{(0)}(t,\boldsymbol{x})}\,, \qquad (2.37)$$

which is the mathematical formulation of the weak form of gauge/gravity duality. In other words, the generating functional for field-theory correlation functions is given by the supergravity on-shell bulk action with appropriate boundary conditions imposed. In particular, it implies that the computation of correlation functions on the field-theory side essentially reduces to solving a boundary-value problem in the

bulk. Note that we have changed the subscript on the left-hand side from CFT in (2.35) to QFT in (2.37) in order to account for deformed models in which the conformal symmetry is broken.

Another crucial concept of gauge/gravity duality is the relation between finite-temperature field theories and black-hole gravitational geometries. In particular, the introduction of a planar Schwarzschild black hole in the AdS spacetime is dual to a non-zero temperature on the field-theory side [85]. Moreover, upon charging the black hole, *i.e.*, replacing the Schwarzschild by a Reissner–Nordström black hole, one introduces a non-zero density or chemical potential in the dual field theory. We only mention this here in passing as we will cover it more thoroughly in the next section when we review the corresponding gravitational solutions.

2.2.3 Generalisations of the Duality

In the previous subsection we have argued that the original AdS/CFT correspondence can be generalised to dualities in different spacetime dimensions of type $\text{AdS}_{D+1}/\text{CFT}_D$, where on the gravity side there is in general an additional compact manifold. Moreover, we have argued that the gauge/gravity duality can be further generalised in so-called 'bottom-up' models, phenomenological models for the physical systems that one intends to describe. In this subsection, we review the concept of bottom-up constructions of holographic models in more detail. This is also the approach we employ in this thesis. Furthermore, we contrast it with another common method used to construct gauge/gravity-duality models, the so-called 'top-down' approach.

Bottom-Up Approach. In the bottom-up approach of constructing holographic models, one starts from the generic form of the $\text{AdS}_{D+1}/\text{CFT}_D$ duality, which can be derived from a string-theoretical ansatz, and by adding a set of additional fields on the gravity side induces deformations of the AdS spacetime such that the dual field theory incorporates essential features of the physical system that one is interested in. On the gravity side, one typically restricts such models to the AdS spacetime and neglects the five-sphere. In fact, if one starts in the ten-dimensional spacetime, one can simply expand the fields in an appropriate set of basis functions on the compact manifold such that one is effectively left with a field in the AdS spacetime which justifies this restriction. Hence, a typical ansatz for the Einstein–Hilbert action of a bottom-up model is the following[2],

$$S = \frac{1}{16\pi G_{\text{N}}^{(D+1)}} \int \mathrm{d}^{D+1}x \, \sqrt{-g} \left(\mathcal{R} - 2\Lambda + \mathcal{L}_{\text{matter}} \right) , \qquad (2.38)$$

---

[2]Another possibility is to add not only matter fields but also (or instead) corrections to Einstein gravity and study, for instance, Gauss–Bonnet gravity. Interestingly, for field theories dual to Gauss–Bonnet gravity, it has been shown that the ratio of shear viscosity to entropy density violates the KSS bound [86].

with some appropriate matter Lagrangian $\mathcal{L}_{\mathrm{matter}}$. What types of matter fields are required to capture certain features of the physical system one intends to describe is dictated by the holographic dictionary and, in particular, symmetry principles. Crucially, one is in most cases interested in dualities with an asymptotically anti-de Sitter spacetime on the gravity side and thus adds only matter fields that dualise to relevant operators, in accordance with our discussion in the previous subsection. The downside of these models is that one typically loses knowledge of the dual field-theory Lagrangian.

Top-Down Approach. In contrast to the bottom-up approach stands the top-down approach. As the name suggests, in top-down holographic models, one starts with a string theory and some type of brane configuration. From this setup, one 'derives' the dual quantum field theory in a similar fashion as we have outlined above for the original AdS/CFT correspondence. Using the top-down approach, one always knows the exact field-theory Lagrangian and thus has a high degree of control of what physical system one is actually studying. On the downside, employing the top-down approach is typically plagued by the necessary use of very sophisticated string-theory models. Prominent examples of holographic top-down models include, for instance, AdS/QCD models [87–89].

A crucial aspects of all holographic models is that, independent of the details of their construction, they are a fundamental description for some type of, in the weak form of the duality, strongly coupled quantum field theory. In this work, we follow the bottom-up approach for an *ab initio* description of a strongly correlated and dissipative superfluid.

2.3 Duality at Non-Zero Temperature and Chemical Potential

In this section we discuss the generalisation of gauge/gravity duality to the description of field theories at non-zero temperature and chemical potential. The content of this chapter will be a crucial foundation for our investigations of superfluids which are naturally studied at finite temperature and chemical potential.

We have already mentioned in the previous section that finite temperature is realised on the gravity side by introducing a black hole in the AdS spacetime. The Hawking temperature of the black hole [51] corresponds to the temperature of the dual field theory [85]. A very intuitive, though somewhat heuristic, way of thinking of this is that the Hawking radiation emitted by the black hole 'heats up' the boundary theory.

A field theory at non-zero chemical potential, on the other hand, dualises to gravity in a Reissner–Nordström–anti-de Sitter (RN–AdS) spacetime with an additional $U(1)$ gauge field A_M in the bulk. The arguments leading to this gravity solution are as follows. If the field theory has a global $U(1)$ symmetry, a chemical potential can be introduced as the source conjugate to the conserved charge. According

to the holographic dictionary, a conserved $U(1)$ current operator translates into a vector field in the bulk, and since the current is conserved the vector field must be gauged under a $U(1)$ bulk symmetry. The chemical potential then agrees with the leading-order coefficient in the near-boundary expansion of the solution of the corresponding electrostatic potential A_t. Moreover, for the gravity solution to be consistent, the electrostatic potential has to be sourced, thus requiring the black hole to be charged. Hence, the gravitational background must be given by a Reissner–Nordström black hole in an asymptotically anti-de Sitter spacetime. We discuss the boundary conditions for the gauge field in section 2.3.2 below.

In accordance with our discussion above, the gravitational model of the $(D + 1)$-dimensional black-hole spacetime is in this case given by the Einstein–Hilbert–Maxwell action

$$S_{\text{EHM}} = \frac{1}{16\pi G_{\text{N}}^{(D+1)}} \int \mathrm{d}^{D+1}x \, \sqrt{-g} \left(\mathcal{R} + \frac{D(D-1)}{L_{\text{AdS}}^2} - \frac{1}{4} F_{MN} F^{MN} \right) , \quad (2.39)$$

with the same parameters as in the Einstein–Hilbert action (2.5), and F_{MN} the field strength tensor associated with the Abelian gauge field. For vanishing field strength tensor, $F_{MN} = 0$, the action reduces to the Einstein–Hilbert action (2.5) and its zero-temperature solution is the AdS geometry. The equations of motion corresponding to the model (2.39) are given by a set of coupled Einstein and Maxwell equations,

$$\mathcal{R}_{MN} - \frac{1}{2} \mathcal{R} \, g_{MN} + \Lambda \, g_{MN} \;=\; T_{MN} , \quad (2.40)$$

$$T_{MN} \;=\; \frac{1}{2} \left(F_{MA} F_N{}^A - \frac{1}{4} \, g_{MN} F_{AB} F^{AB} \right) , \quad (2.41)$$

$$\nabla_M F^{MN} \;=\; 0 , \quad (2.42)$$

where we have introduced the energy-momentum tensor T_{MN} and the Ricci tensor $\mathcal{R}_{MN}$. For the metric solution of the above equations, we make the following ansatz (assuming isotropy of the underlying system)

$$\mathrm{d}s^2 = \frac{L_{\text{AdS}}^2}{z^2} \left(-h(z) \, \mathrm{d}t^2 + \mathrm{d}\boldsymbol{x}^2 + \frac{1}{h(z)} \, \mathrm{d}z^2 \right) , \quad (2.43)$$

with horizon function $h(z)$. The only boundary condition we impose is $h(z = 0) = 1$ which ensures that in the UV the metric reduces to the AdS metric (2.8) such that the spacetime is asymptotically anti-de Sitter.

In the following we review the solutions of these equations of motion, first for vanishing field strength tensor (section 2.3.1) and subsequently also in its full generality (section 2.3.2). Throughout this section, we assume $D \in \{3, 4\}$.

2.3.1 AdS–Schwarzschild Spacetime

For finite temperature but vanishing chemical potential in the dual field theory, the solution to the equations of motion is given by the *AdS–Schwarzschild* spacetime

with metric

$$\mathrm{d}s^2 = \frac{L_{\mathrm{AdS}}^2}{z^2} \left(-h(z)\,\mathrm{d}t^2 + \mathrm{d}\boldsymbol{x}^2 + \frac{1}{h(z)}\,\mathrm{d}z^2 \right), \tag{2.44}$$

$$h(z) = 1 - \left(\frac{z}{z_{\mathrm{h}}} \right)^D, \tag{2.45}$$

where $h(z)$ is the horizon function, z_{h} the location of the black-hole event horizon, and $\boldsymbol{x} = (x_1, \dots, x_{D-1})$ are the spatial field-theory coordinates. In fact, the horizon of the black hole has an infinite extent along the spatial field-theory directions $\boldsymbol{x}$ and one therefore often refers to it as a black-brane horizon. Importantly, the horizon caps off the AdS geoemtry and restricts the radial holographic interval to $0 \le z \le z_{\mathrm{h}}$.

The Hawking temperature associated with the spacetime metric is given by

$$T = \frac{D}{4\pi z_{\mathrm{h}}}, \tag{2.46}$$

which is also the temperature of the dual boundary theory [85]. A convenient way of deriving the Hawking temperature is by continuing the metric (2.44) to Euclidean spacetime and demanding regularity at the horizon $z = z_{\mathrm{h}}$ [90]. The dependence of the temperature on the black-hole horizon $T \sim 1/z_{\mathrm{h}}$ nicely synchronises with the UV/IR relation discussed in the previous section, *cf.* equation (2.29). In particular, in the zero temperature limit, corresponding to $z_{\mathrm{h}} \to \infty$, the metric reduces to the non-thermal AdS metric (2.8).

We thus find that $\mathcal{N} = 4$ SYM at finite temperature is dual to gravity in a Schwarzschild–anti-de Sitter spacetime. The finite temperature breaks all supersymmetries on the field-theory side and introduces a scale. Nevertheless, the energy-momentum tensor of $\mathcal{N} = 4$ SYM theory remains zero.

Finally, let us note that the finite-temperature duality and in particular the metric solution (2.44) of the Schwarzschild–AdS spacetime can also be derived in a top-down approach by replacing the D-branes in the previously outlined string-theory construction by black D-branes of appropriate dimensionality and then proceeding just as before [85].

2.3.2 AdS–Reissner–Nordström Spacetime

We now generalise the above results by allowing for a finite chemical potential in the dual field theory. In other words, we solve the full set of Einstein–Hilbert–Maxwell equations (2.40)–(2.42). We closely follow [91] in this subsection. Since we are interested in an isotropic dual field theory, it follows that the spatial gauge-field components have to vanish identically,

$$A_i(z) = 0, \tag{2.47}$$

with i charactering the $D-1$ spatial field-theory directions. Moreover, by gauge freedom we set

$$A_z(z) = 0. \tag{2.48}$$

In accordance with the holographic dictionary, the boundary condition for the temporal gauge-field component at the AdS boundary is fixed by the chemical potential μ,

$$A_t(z = 0) = \mu L_{\text{AdS}}\,. \tag{2.49}$$

Here we have used that the chemical potential corresponds to the leading-order coefficient in the near-boundary expansion of A_t (see *e. g.* [92]). Since the equations of motion are of second order, we also impose boundary conditions for the temporal gauge-field component at the black-hole horizon,

$$A_t(z = z_{\text{h}}) = 0\,, \tag{2.50}$$

which follows from demanding[3] that $g^{MN} A_M A_N$ remains finite at the black-hole horizon which ensures the gauge field to be regular at $z = z_{\text{h}}$.

With this set of boundary conditions, we can now solve the equations of motion (2.40)–(2.42). The metric solution is given by the *AdS–Reissner–Nordström* metric,

$$\mathrm{d}s^2 = \frac{L_{\text{AdS}}^2}{z^2}\left(-h(z)\,\mathrm{d}t^2 + \mathrm{d}\boldsymbol{x}^2 + \frac{1}{h(z)}\,\mathrm{d}z^2\right), \tag{2.51}$$

with horizon function

$$h(z) = 1 - \left(1 + \frac{\mu^2 z_{\text{h}}^2}{\gamma^2}\right)\frac{z^D}{z_{\text{h}}^D} + \frac{\mu^2 z_{\text{h}}^2}{\gamma^2}\frac{z^{2D-2}}{z_{\text{h}}^{2D-2}}\,, \tag{2.52}$$

$$\gamma^2 = 2\,\frac{D-1}{D-2}\,. \tag{2.53}$$

The horizon function (2.52) has two zeros, and thus an inner and an outer horizon, and it reduces to the AdS–Schwarzschild solution for $\mu \to 0$. For us, only the outer horizon, denoted by z_{h}, that is the one closer to the AdS boundary, is relevant. The solution for the temporal gauge-field component, which is sourced by the charged black hole, is given by

$$A_t(z) = \mu L_{\text{AdS}}\left(1 - \frac{z^{D-2}}{z_{\text{h}}^{D-2}}\right). \tag{2.54}$$

From the metric (2.51) one finds the associated Hawking temperature to be given by

$$T = \frac{1}{4\pi z_{\text{h}}}\left|D - \frac{(D-2)\mu^2 z_{\text{h}}^2}{\gamma^2}\right|, \tag{2.55}$$

with γ as defined in equation (2.53). In addition, the charge density of the black hole, which corresponds to the vacuum expectation value of the boundary $U(1)$ current

---

[3]Another way to see that A_t has to vanish at the black-hole horizon is by demanding the temporal (in Euclidean time) Wilson loop of the gauge field to be regular at the horizon. For details see *e. g.* [91].

operator, can be read off the near-boundary expansion of the electrostatic potential. We only quote the result here for brevity,

$$\rho = \frac{D}{z_{\mathrm{h}}^{D}}\,\mu\,, \tag{2.56}$$

and refer to, *e. g.*, [91] for details.

In summary, we find that $\mathcal{N} = 4$ SYM theory at finite temperature and chemical potential is dual to gravity in a Reissner–Nordström–AdS (RN–AdS) spacetime with a $U(1)$ gauge field in the bulk. Like for the finite-temperature duality studied in the previous subsection, also the duality at finite chemical potential can be derived from a top-down string-theory construction, given by a stack of D-branes carrying angular momentum [93–96]. In fact, from that derivation one finds that μ corresponds to the chemical potential of a $U(1)$ subgroup of the R-symmetry of $\mathcal{N} = 4$ SYM.

In anticipation of the holographic model of superfluidity that we will study in the following chapters, let us study the high- and low-temperature limits of the RN–AdS spacetime. In the following derivation we follow [91], however, see also [18] for details. We first invert equation (2.55) to obtain the horizon position z_{h} as a function of the temperature and the chemical potential,

$$z_{\mathrm{h}}(T,\mu) = \frac{4\pi\gamma^2}{D-2}\frac{T}{\mu^2}\left[\sqrt{1 + \frac{D(D-2)}{4\pi^2\gamma^2}\left(\frac{\mu}{T}\right)^2} - 1\right]\,. \tag{2.57}$$

For temperatures much higher than the chemical potential, the horizon position reduces to

$$z_{\mathrm{h}} \approx \frac{D}{4\pi T}\,, \qquad \mu \ll T\,, \tag{2.58}$$

and the horizon function approximately agrees with the solution of the Schwarzschild–AdS spacetime, *cf.* equation (2.45). Thus, in the high-temperature limit the RN–AdS solution reduces to the Schwarzschild–AdS (S–AdS) solution, as we would also expect intuitively. However, note that for finite μ the electrostatic potential (2.54) is always non-zero.

In the more interesting low-temperature limit, the horizon position of the black hole is given by

$$z_{\mathrm{h}} \approx \sqrt{\frac{D}{D-2}}\frac{\gamma}{\mu}\,, \qquad \mu \gg T\,, \tag{2.59}$$

which agrees with the solution for the horizon position at identically vanishing temperature, $T = 0$. Hence, the RN–AdS black hole has a finite event horizon even at zero temperature. Let us now study the zero-temperature spacetime geometry and in particular its near-horizon limit in more detail. We first define the zero-temperature horizon position by

$$z_* = \sqrt{\frac{D}{D-2}}\frac{\gamma}{\mu}\,, \tag{2.60}$$
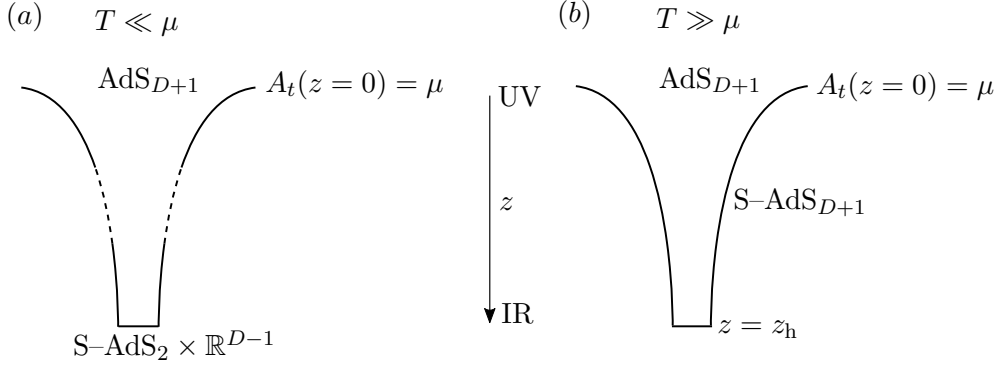
Figure 2.2: Sketch of the AdS–Reissner–Nordström spacetime in the two limits $T \ll \mu$ (left) and $T \gg \mu$ (right), see the main text for further details. Note that the black-hole event horizon for $T \ll \mu$ is not located at $z = z_\mathrm{h}$, see [91] for details.

and furthermore introduce the new coordinate

$$\Xi = \frac{1}{z_* - z} \frac{z_*^2}{D(D-1)} \,. \tag{2.61}$$

In the near-horizon limit $(z_* - z)/z_*^2 \ll 1$, the metric (2.51) reduces to

$$\mathrm{d}s^2 = \frac{L_{\mathrm{AdS}_2}^2}{\Xi^2} \left(-\mathrm{d}t^2 + \mathrm{d}\Xi^2 \right) + \frac{L_{\mathrm{AdS}}^2}{z_*^2} \mathrm{d}\boldsymbol{x}^2 \,, \tag{2.62}$$

where we have switched coordinates from z to Ξ and have defined the length

$$L_{\mathrm{AdS}_2} = \frac{L_{\mathrm{AdS}}}{\sqrt{D(D-1)}} \,. \tag{2.63}$$

We thus find the metric to factorise into an effectively two-dimensional anti-de Sitter metric, described by the first two terms in (2.62), and a flat $(D-1)$-dimensional space, *i.e.*, $\mathbb{R}^{D-1}$, described by the remaining third term. Note that the prefactor of the flat space metric in (2.62) is only a constant which does not change the topology of space. In summary, the zero-temperature Reissner–Nordström–AdS spacetime factorises into an $\mathrm{AdS}_2 \times \mathbb{R}^{D-1}$ spacetime with AdS_2-curvature radius L_{AdS_2} [97, 98]. In the far UV, on the other hand, the metric again reduces to the non-thermal AdS_{D+1} metric (2.8).

Upon increasing the temperature mildly, but still upholding the limit $\mu \gg T$, one finds that the near-horizon geometry changes from non-thermal $\mathrm{AdS}_2 \times \mathbb{R}^{D-2}$ to Schwarzschild–$\mathrm{AdS}_2 \times \mathbb{R}^{D-1}$. We refrain from discussing the details of the associated derivation here and instead refer the interested reader to, for instance, [91] for details. In figure 2.2 we schematically visualise the RN–AdS geometry for both high and low temperatures.

We have now covered all necessary foundations of gauge/gravity duality to proceed to the main parts of this thesis. In particular, in the following chapter we will review the derivation of a holographic model of superfluidity and find that the details of the RN–AdS spacetime geometry just discussed are very important to understand the phenomenology of the system. Subsequently, we apply the holographic duality to the investigation of vortex dynamics in superfluids, in two (Part I) as well as three (Part II) spatial dimensions.

3 Holographic Superfluids

We now start to apply gauge/gravity duality to investigate the dynamics of topological vortex defects in superfluids in two and three spatial dimensions. In this chapter, we first discuss the nature of superfluidity and its relation to Bose–Einstein condensation, and furthermore lay out our motivation for employing the holographic framework to study the non-equilibrium dynamics in superfluids induced by the appearance of quantised vortices (section 3.1). Subsequently, we proceed to setting out the holographic models for the description of superfluids in two as well as three spatial dimensions (sections 3.2–3.3).

3.1 Motivation and Introduction

When liquid helium ^{4}He is cooled below its so-called lambda point at a temperature of $T_\lambda \simeq 2.17$ K, it exhibits remarkable behaviour. The fluid flows frictionless through narrow capillaries, climbs up the walls of its container and remains motionless if the container is rotated [99–101]. In his Nobel Prize winning article [102], Kapitza accounts for such behaviour by introducing a new state of matter, 'superfluidity'. Today, it is recognised that the underlying phenomenon of superfluidity can be associated with the formation of a Bose–Einstein condensate (BEC) which constitutes the true 'new' state of matter. In a gas of bosons, Bose–Einstein condensation is associated with the macroscopic accumulation of atoms in the ground state[1]. Remarkably, while the formation of a BEC is a purely quantum mechanical phenomenon, it manifests itself on the macroscopic level. Experimentally, superfluidity of Bose liquids has to this day only been observed for ^{4}He. In the literature one finds a large number of excellent reviews on superfluidity, specifically superfluid helium, the historical development of a theory thereof and more recently gained insights, also for thin films of superfluid helium, see *e. g.* [105–109].

Experimentally, superfluidity was discovered by Kapitza [102] and independently by Allen and Misener [110] in the late 1930s. Their discoveries came almost 30 years after helium was first liquefied by Kamerlingh Onnes in 1908 [111] and a few years after it was already realised by Keesom and collaborators that helium exhibits unexpected behaviour at temperatures around $T \approx 2.2$ K (see [112] for a review). By gradually cooling the liquid, they found that the specific heat has a sharp peak at this temperature which they, rightly so, associated with a phase transition. Due to

---

[1] Also in Fermi-systems one can find the formation of a macroscopic condensate. In this case, the fermions form either weakly-coupled bound states in momentum space (Cooper pairs) [103] or strongly-bound molecular states in position space which can subsequently condense to form a Bose–Einstein condensate (see *e. g.* [104] for a review).

the characteristic shape of the peak that has strong resemblance to the Greek letter λ, they introduced the terminologies 'lambda point' and 'lambda temperature'. In addition, Keesom also coined the expression helium I for the fluid above T_λ and helium II for the fluid below T_λ. Shortly after the discovery of superfluidity in liquid helium, it was suggested by Fritz London that superfluidity is a manifestation of a Bose–Einstein condensate and that the characteristic behaviour of the liquid is due to a coherent motion of the condensate [113, 114]. At that time, the concept of Bose–Einstein condensation had already been well established for many years (see [115] for a review). Based on the insights of London, Tisza introduced what is nowadays known as the two-fluid model of superfluidity. In his seminal work [116], Tisza elaborated on his idea that below the phase transition temperature, a large number of atoms occupies the ground state and forms a condensate, while all the remaining atoms of the liquid remain in an excited state. Upon decreasing the temperature, the fraction of condensed atoms increases as more excited-state atoms enter the ground state. Hence, Tisza argued that the total liquid consists of the superfluid component, *i. e.*, the atoms in the ground state, and the excited atoms which constitute the 'normal' component. In his picture, the normal fluid is viscous and therefore dissipative while the superfluid component is non-dissipative and flows without friction.

A different, phenomenological, theory of superfluidity was put forward by Landau [117]. Unlike London and Tisza, Landau made no mention of the formation of a condensate and in fact not even of atoms. Instead, he presented a theory purely based on hydrodynamical arguments. Interestingly, despite his fundamentally different approach towards the understanding of superfluidity as compared to London and Tisza, Landau's theory was also based on a two-fluid model which had strong similarities with Tisza's model and led to similar consequences with regard to the characteristic behaviour of the system. Compared to Tisza who laid out his model only on a qualitative basis, Landau was more rigorous in his account and introduced a mathematical framework for the two-fluid model. Moreover, Landau understood (what is nowadays well established) that the normal fluid should be interpreted as collective energy and momentum excitations (quasiparticles) of a system of atoms, *i. e.*, the liquid, rather than a simple accumulation of individual atoms in an excited state. According to Landau, the superfluid component is everything that does not contribute to the normal fluid. Based on energy considerations, he further argued that below a critical velocity, the superfluid component flows frictionless and no collective excitations arise ('Landau criterion'). Above the critical velocity, on the other hand, its superfluid nature ceases. Consequently, above the phase-transition temperature the critical velocity equals zero, $v_c = 0$. A crucial success of Landau's description has been his prediction of the existence of additional types of sound excitations [118] which arise quite naturally in his two-fluid model and have since then also been observed in experiments [119].

Today, the two-fluid model is typically referred to as the Tisza–Landau model. It is generally accepted that while Landau's account correctly captures the hydrodynamics of superfluidity, its nature is associated with a Bose–Einstein condensate.

Interestingly, Landau did not appreciate the fundamental relation of superfluidity to BECs until the late 1950s after the theory of superconductivity was introduced [103]. An essential concept of the two-fluid model is that the total liquid must not be considered a mixture of two fluids that can in principle be separated. Instead, both fluid components coexist inseparably, having different velocities as well as different mass densities. To be specific, the total mass density is the sum of the mass densities of the superfluid component and the normal component and both of them depend on the temperature of the system. In particular, close to absolute zero the superfluid component makes up 100% of the total liquid. It is further interesting to point out that for liquid helium, even close to absolute zero, the Bose–Einstein-condensate fraction makes up only about 9–10% of the total liquid [120, 121] (see also [122] for further details). Hence, the superfluid component and the Bose–Einstein condensate of the Bose liquid are not the same. Instead, at very low temperatures, the BEC essentially 'locks' the non-Bose–Einstein-condensed atoms to form the superfluid component, albeit the exact mechanism still poses an open equation. For further details, see *e. g.* [105, 123]. Throughout this thesis we frequently refer to the total superfluid component as the superfluid condensate.

Following the original works of London, Tisza and Landau, the quest for a microscopic theory of superfluidity drew much attention. In particular, at that time it was still unclear how one should account for interactions between the atoms as the theory of BEC's was set out only for ideal (non-interacting) gases of bosons. This was remedied by Bogoliubov [124] who built his microscopic theory of superfluidity in light of London's idea, accounting for the existence of a Bose–Einstein condensate. His work set the basis for much research, pursuing the development of a theory for interacting bosons, eventually culminating in the work by Onsager and Penrose [125] who proposed a criterion for the formation of a Bose–Einstein condensate also for interacting constituent particles. Some years later, their proposal was generalised to the, up to this day generally accepted, criterion demanding the existence of off-diagonal long-range order which is applicable also for superfluidity [126]. However, even today, the strongly coupled nature of helium atoms poses a great challenge for theorists and prohibits the use of many standard quantum-field-theory methods such as perturbation theory. Therefore, understanding the microscopic origin of superfluidity of ^{4}He still remains an open problem.

After the theoretical basis was set, an in-depth understanding of Bose–Einstein condensation and thus superfluidity was developed. However, many predictions regarding the thermodynamics and other crucial aspects of Bose–Einstein condensates could not be verified experimentally due to limitations in the access to and control of the underlying BEC of superfluid helium, which constituted the only discovered realisation of a BEC at that time. A new era in the study of Bose–Einstein condensates has begun when in the mid 1990s experimental breakthroughs allowed for the first realisation of Bose–Einstein condensates with rubidium and sodium atoms [127–129]. In particular, in these experiments the highly controllable apparatus allow for the condensation of large numbers of atoms and the subsequent possibility to probe the system. These advances have paved the way for intense investigations

of superfluidity throughout the past two and a half decades. Remarkably, enhanced experimental possibilities in the creation and controllability of Bose–Einstein condensates also allow for the investigation of phenomena in other fields of physics, including, for instance, cosmology [130] or quantum optics [131]. It is further interesting to point out that rather recently much attention has been devoted to the proposal that the dark matter in our universe may be a superfluid [132].

A crucial characteristic of superfluids is the appearance of quantised vortices. The dissipationless flow of a superfluid (component) allows for the occurrence of persistent currents which are naturally induced by quantised vortices. A quantised vortex is a topological defect in the superfluid or condensate order-parameter field of the phase transition with an integer phase winding around its core. Their quantum nature implies that unlike classical vortices, superfluid vortices are protected against decay. Remarkably, the appearance of quantised vortices may be considered as the 'smoking gun' for the formation of a Bose–Einstein condensate and thus superfluidity. Indeed, it can be shown that the Landau criterion of superfluidity is not tantamount to the coherent motion of the condensate ('phase coherence', criterion by London and Tisza). There exist cases for which one criterion is satisfied while the other one is not (see *e. g.* [133] for a discussion and references). Hence, there appears to be some ambiguity in the definition of superfluidity. The appearance of quantised vortices, on the other hand, is universally accepted to be an unambiguous signature of the presence of a superfluid condensate. In particular, quantised vortices have been found in superfluid helium [134, 135] as well as in ultracold atomic gases [136].

The presence of quantised vortices typically induces strongly non-linear and thus far-out-of-equilibrium dynamics of the condensate. In recent years, the time evolution of quantum many-body systems far out of equilibrium, including, but not limited to, vortex dynamics in superfluids, has gained much attention, both experimentally and theoretically [31–40, 137]. Strong correlations prevailing in these systems generically require non-perturbative methods to quantitatively describe the dynamics. In particular, even if the interaction strength between the constituent particles is weak, the interplay between linear and strongly non-linear excitations such as topological defects and solitary waves poses a great challenge for theory.

For dilute Bose–Einstein condensates penetrated by vortex defects, the dynamics of the macroscopic wave function can be described by the Gross–Pitaevskii equation (GPE) [138, 139]. In particular, this holds true for two- as well as three-dimensional systems. The Gross–Pitaevskii equation is a non-linear Schrödinger equation for the condensate wave function and accounts for contact interactions between the constituent bosons. However, its applicability ceases if the density of the gas is increased or the interactions between the bosons become too large. While there indeed exist also other theoretical approaches and methods for the description of interacting or dense condensed Bose gases, they all capture only certain aspects of the physics but typically not the entire system.

Hence, the non-equilibrium dynamics of superfluids and BECs defies a theoretical treatment that is capable of describing the system despite strong correlations and in many cases (such as for superfluid helium) large couplings, ideally in terms of a

fundamental theory. Other examples of quantum many-body systems for which non-equilibrium dynamics has been observed and for which the theoretical description poses a major challenge, include the quark–gluon plasma (see *e. g.* [140]), the dynamics of the early universe after inflation, (see *e. g.* [141, 142]), superfluid phenomena in astrophysics (see *e. g.* [143]) and exciton-polariton superfluids, *cf.* [144–147].

Gauge/gravity duality provides a framework in which both of these challenges, strong correlations as well as large couplings, are naturally accounted for. Indeed, holographic models, at least in the weak form of the respective dualities, inherently capture strong interactions or strong couplings of the quantum field theory. In addition, the classical bulk description dual to the quantum theory is naturally capable of capturing strong correlations and non-linear dynamics. In particular, even during far-from-equilibrium real-time dynamics of the quantum field theory, the equations of motion of the dual gravitational theory remain classical. Moreover, even if in bottom-up holographic models the exact field-theory Lagrangian is unknown, it is nevertheless an *ab initio* description of the quantum theory. The holographic framework further allows for a quite natural and straightforward way of introducing finite temperature and a non-zero chemical potential, *cf.* our discussion in section 2.3.

In recent years, holographic models have proven to be a powerful tool in describing the non-equilibrium time evolution of quantum field theories. In principle, the equations of motion of the classical gravitational model dual to the quantum theory can be straightforwardly solved employing numerical methods. Today, holographic dualities have been applied for studying various physical systems in far-from equilibrium situations, including strongly coupled and dissipative superfluids (see *e. g.* [148–150]) as well as heavy-ion collisions and the quark-gluon plasma where typically shock-wave collisions are studied to investigate the fast equilibration of the systems induced by the intrinsically large couplings of the respective holographic models (see *e. g.* [151–155]). For a review of holographic methods used in the description of far-from-equilibrium dynamics see also [156], and for reviews of applications of holographic systems to strongly coupled and strongly correlated quantum-many body systems in general see [17, 19].

Much attention has in particular been paid to applications of gauge/gravity duality to superfluids and superconductors (see [157] for a review). The gravitational model of a superconductor or a superfluid was first introduced in [46–48]. It is given in terms of an Abelian Higgs model in an asymptotically anti-de Sitter spacetime that has one additional spatial dimension as compared to the dual field theory. With applications to superfluids as well as superconductors, this system has been studied extensively, with particular focus on linear [47, 48, 158, 159] and non-linear excitations such as vortices [148, 150, 160–164]. Remarkably, the gravitational model as well as modifications and generalisations thereof can be applied to superfluids and superconductors in one (see *e. g.* [165]), two [47, 48] as well as three spatial dimensions (see *e. g.* [166, 167]).

In this thesis, we apply a holographic model of superfluidity of type [46–48] to study the dynamics of vortices and aspects of quantum turbulence in strongly cor-

related and dissipative superfluids in $2 + 1$ as well as in $3 + 1$ spacetime dimensions by means of numerical real-time simulations. The holographic framework provides an *ab initio* description of strongly dissipative superfluids. In particular, the dissipation is a feature intrinsic to the system and not put in by hand as in many conventional models used for the description of superfluidity. As such, the holographic model captures regimes of out-of-equilibrium superfluid dynamics, induced by vortices or other topological defects, that cannot be accessed by conventional descriptions such as the Gross–Pitaevskii model. Moreover, even though a number of methods exist that are typically employed to study, *e. g.*, vortex dynamics in dissipative superfluids, they always capture only certain aspects of the dynamics and only with limited accuracy. Since holography by contrast provides a fundamental description, it captures all aspects of the characteristic behaviour of vortex defects as well as the dynamics of the hosting superfluid. While it has been well established that the holographic superfluid in the presence of vortices is strongly dissipative (see *e. g.* [148]), the dissipation has thus far never been quantified. Our work constitutes the first ever quantitative characterisation of the dissipative nature of the holographic superfluid as well as a systematic analysis of the applicability of holography to the description of real-world superfluids. Moreover, for the first time ever we employ a fundamental description to study vortex defects and their dynamics as well as quantum turbulence in a three-dimensional strongly dissipative superfluid.

The two-dimensional holographic superfluid has been subject of many investigations of vortex dynamics and quantum turbulence, see *e. g.* [148, 150, 168, 169]. In Part I we for the first time quantitatively characterise the dissipative nature of the underlying superfluid hosting the vortex dynamics and classify the applicability and relevance of the holographic model of superfluidity to the description of vortex dynamics in experiments on ultracold Bose gases as well as superfluid helium in two spatial dimensions. We study the dynamics of vortex dipoles to infer friction coefficients characterising the dissipation of the superfluid and compare them to measured values in real-world systems. We conjecture holography to be applicable in the description of vortex dynamics in superfluid helium as well as thermally excited Bose–Einstein condensates. In chapter 4 we present a more thorough discussion of our work and the physical motivation for our studies concerning the two-dimensional holographic superfluid.

While the three-dimensional holographic superfluid has also been the subject of many investigations, neither its non-equilibrium dynamics nor vortex solutions of the system have been studied to this day. In this work, we for the first time construct vortex solutions of the strongly dissipative superfluid and analyse their characteristics. Moreover, we study the dynamics of vortex defects, with a special emphasis on vortex rings, and investigate the far-from-equilibrium dynamics and turbulent behaviour of the superfluid induced by dense tangles of vortex lines and rings. Our work thus constitutes the first ever investigation of vortex dynamics and quantum turbulence in a strongly dissipative three-dimensional superfluid employing a fundamental description of the system. On a qualitative level, we also characterise the dissipative nature of the superfluid by analysing the dynamics of vortex rings and in

analogy to the two-dimensional system discuss the applicability of the holographic system to the description of real-world superfluids and Bose–Einstein condensates in three spatial dimensions. We present a more thorough discussion of our work and the physical motivation for our studies concerning the three-dimensional holographic superfluid in chapter 10.

In the next section, we present a detailed account of the holographic model of superfluidity in $d + 1$ dimensions that we apply throughout this thesis and discuss the bulk equations of motion of the Abelian Higgs model. The subsequent chapters are then grouped into two main parts, the first on the two-dimensional and the second on the three-dimensional holographic superfluid. In both parts we start off with an introductory chapter in which we specifically motivate our investigations of the respective part.

3.2 Holographic Model of Superfluidity

In the previous section, we have laid out our motivation for studying holographic superfluids in two and three spatial dimensions. We now proceed to discussing their dual gravitational descriptions and covering all necessary prerequisites for the following chapters. In our presentation we loosely follow [18, 91, 157], however, generalising the discussions in [18, 157] to d spatial field-theory dimensions. We note that unless explicitly stated, all results presented in the present and the following section are valid for both, the two- and three-dimensional holographic superfluid. Due to the historic development of the models, we often refer to works that focus only on the two-dimensional system but keep in mind that the results are universally valid (see *e. g.* [18, 91]).

In holography, the bottom-up construction of the gravitational bulk physics dual to a quantum field theory at the boundary is strongly constrained by the symmetries of the field theory. In the case at hand, superfluidity is commonly associated with the breaking of a global $U(1)$ symmetry. Remarkably, the existence of a conserved boundary $U(1)$ current operator suffices to construct the dual gravitational model. From the holographic dictionary, it is well known that a conserved $U(1)$ current has a dual description in terms of an Abelian gauge field A_M (*cf.* section 2.2.2 for a discussion). Therefore, in order to break the global boundary symmetry, one has to break the local bulk symmetry. This requires the Higgs mechanism [170–174]. Hence, one has to introduce a complex scalar field and couple it to the gauge field.

In his seminal work on Abelian gauge-symmetry breaking in an anti-de Sitter spacetime [46], Gubser laid down the minimal requirements on such a Higgs model for spontaneous symmetry breaking to occur. In particular, his work set the basic concepts for the construction of the holographic superconductor [47] and superfluid model[2] [48]. Gubser showed that only a simple Abelian Higgs model without self-interaction is necessary to spontaneously break the local gauge symmetry in the

---

[2]The work [175] was published at about the same time and has some overlap with [48].

bulk[3]. It was shortly thereafter realised that within the holographic framework, this allows for the description of dual boundary superfluids or superconductors [47, 48]. In fact, in holography the gravitational models dual to a superconductor [47] and a superfluid [48] essentially coincide. We give details concerning the differences between holographic superfluids and holographic superconductors, in particular with regard to the applications of the holographic superfluid model in this thesis, in the final paragraph of this section. The gravitational model dual to a superfluid in $d+1$ dimensions is given in terms of a complex scalar field minimally coupled to an Abelian gauge field in a $(D+1)$-dimensional asymptotically anti-de Sitter spacetime, where $D = d + 1$.

The action of the gravitational model is given by

$$S = \frac{1}{16\pi G_{\mathrm{N}}^{(D+1)}} \int \mathrm{d}^{D+1}x \sqrt{-g} \left(\mathcal{R} - 2\Lambda + \frac{1}{q^2} \mathcal{L}_{\text{gauge–matter}} \right) , \qquad (3.1)$$

where we have introduced the gauge–matter Lagrangian

$$\mathcal{L}_{\text{gauge–matter}} = -\frac{1}{4} F_{MN} F^{MN} - |(\nabla_M - \mathrm{i}A_M)\Phi|^2 - m^2 |\Phi|^2 . \qquad (3.2)$$

Here, $G_{\mathrm{N}}^{(D+1)}$ denotes Newton's constant in $D + 1$ dimensions. The first two terms in the parenthesis in (3.1) correspond to the gravitational part of the action with $\mathcal{R}$ denoting the Ricci scalar of the metric g_{MN} and $\Lambda = -D(D-1)(2L_{\mathrm{AdS}}^2)^{-1}$ is the negative cosmological constant of the anti-de Sitter spacetime, *cf.* section 2.3. Furthermore, L_{AdS} again denotes the curvature radius of the asymptotic AdS spacetime. In the prefactor, we use $g = \det g_{MN}$ to denote the determinant of the metric g_{MN}. The gauge–matter fields in (3.2) are the scalar field Φ and the gauge field A_M, where we use $M = t, \boldsymbol{x}, z$ to characterise the spacetime indices of the gravitational bulk with $\mu = t, \boldsymbol{x}$ the coordinates[4] of the dual field theory. For the two-dimensional superfluid the spatial boundary coordinates are given by $\boldsymbol{x} = (x_1, x_2)$ while in three spatial dimensions $\boldsymbol{x} = (x_1, x_2, x_3)$. As in the previous chapter, we use z to denote the additional holographic bulk direction. The z-direction is not to be confused with the third spatial dimension of the three-dimensional superfluid. The kinetic term of the gauge field in (3.2) is formulated in terms of its field strength tensor $F_{MN} = \nabla_M A_N - \nabla_N A_M$, where ∇_M is the gravitational covariant derivative associated with the Levi-Civita connection of g_{MN}. Left implicit, we define the gauge covariant derivative associated with the local $U(1)$ symmetry[5]

---

[3]In fact, Gubser argued that this should be the case but points to some 'logical gaps' in his arguments [46]. However, these were later remedied. See *e. g.* [18, 91] for details.

[4]In the action (3.1) we use, in a slight abuse of notation, $\mathrm{d}^{D+1}x$ as a short-hand notation in place of $\mathrm{d}t\,\mathrm{d}\boldsymbol{x}\,\mathrm{d}z$.

[5]An alternative holographic superfluid model is obtained by promoting the $U(1)$ Abelian symmetry to the non-Abelian $SU(2)$ gauge symmetry instead of introducing the scalar field Φ [176]. In this case, a component of the $SU(2)$ gauge field A_M constitutes the order parameter of the phase transition. An appealing characteristic of this model for the three-dimensional superfluid is its analytic behaviour in the proximity of the phase transition [177, 178]. For more on this, see also [157] and references therein.

$D_M = \nabla_M - \mathrm{i}A_M$. We note that due to the Abelian nature of the gauge field, the field strength tensor can equivalently be defined in terms of the gauge covariant derivative, $F_{MN} = -\mathrm{i}\,[D_M, D_N]$, where we use a square bracket to denote the commutator. The scalar field Φ is charged. It has mass m and is minimally coupled to the gauge field A_M via its charge q. However, in equations (3.1)–(3.2) we have rescaled the fields appropriately such that the charge q can be pulled out front of the gauge–matter Lagrangian. Written in this form, it becomes evident that q controls the dynamic coupling between the gauge–matter sector and the gravitational part of the action, *cf.* (3.1). According to the holographic dictionary (see also our discussion in section 2.2.2), the Abelian gauge field in the bulk is dual to a conserved global $U(1)$ current operator j^μ in the boundary theory. The scalar field Φ is dual to a complex scalar operator Ψ of the dual quantum theory.

Superfluidity is a low-temperature phenomenon that can be associated with Bose–Einstein condensation [135, 179]. A condensate is described by a non-zero vacuum expectation value of a complex bosonic field operator defined in a $(d+1)$-dimensional spacetime, $\langle\Psi\rangle \neq 0$. The complex-valued classical field

$$\psi(t, \boldsymbol{x}) = \langle\Psi(t, \boldsymbol{x})\rangle = \sqrt{n(t, \boldsymbol{x})}\,\exp\{\mathrm{i}\varphi(t, \boldsymbol{x})\}\,, \tag{3.3}$$

here written in the Madelung representation [134], encodes the superfluid-condensate density $n(t, \boldsymbol{x}) = |\psi(t, \boldsymbol{x})|^2$ of the condensed particles as well as their velocity, the gradient field

$$\boldsymbol{v}(t, \boldsymbol{x}) \sim \boldsymbol{\nabla}\varphi(t, \boldsymbol{x})\,, \tag{3.4}$$

with the phase configuration $\varphi(t, \boldsymbol{x}) = \arg(\psi(t, \boldsymbol{x}))$. Here, we use $\boldsymbol{\nabla}$ to denote the gradient with respect to $\boldsymbol{x}$ in two or three spatial dimensions. We note again that everything presented in this chapter is universally valid for two- as well as three-dimensional superfluids. The field $\psi = \langle\Psi\rangle$ acts as an order parameter which, if non-zero, breaks the $U(1)$ symmetry of the system's vacuum state under global phase rotations $\Psi(t, \boldsymbol{x}) \to \Psi(t, \boldsymbol{x})\exp(\mathrm{i}\,\lambda)$ for $\lambda \in \mathbb{R}$. If the $U(1)$ symmetry is broken, the system is in the superfluid phase.

In the holographic framework, one extracts the superfluid order-parameter field, *i.e.*, the vacuum expectation value $\psi = \langle\Psi\rangle$ of the dual scalar operator Ψ, as the sub-leading coefficient in the near-boundary expansion of the scalar field Φ, *cf.* our discussion of the holographic dictionary in section 2.2.2. To allow for spontaneous symmetry breaking to occur, the leading-order coefficient in the near-boundary expansion, on the other hand, has to vanish as it corresponds to the source conjugate to the scalar operator and thus breaks the global $U(1)$ symmetry explicitly (in standard quantisation, *cf.* section 2.2.2).

To induce the Higgs mechanism in the bulk, the gravitational model (3.1) has to be supplemented with an appropriate set of boundary conditions for the gravitational sector as well as the gauge–matter fields along the holographic z-direction. To be specific, the boundary conditions are imposed at the black-hole horizon $z = z_\mathrm{h}$ as well as at the AdS boundary $z = 0$. The boundary conditions for the gauge–matter

fields determine, *inter alia*, the chemical potential of the superfluid which sources the boundary $U(1)$ current-operator component j^0. If the temperature, determined by z_{h}, and the chemical potential of the superfluid are chosen appropriately, an instability occurs in the bulk, causing the scalar field to condense. This higgsed bulk vacuum state is dual to the superfluid phase of the boundary theory with $\psi \neq 0$, *i. e.*, the state after the $U(1)$ symmetry has been broken spontaneously[6]. In this case, the classical gravitational model (3.1) encodes the full quantum behaviour of the dual superfluid in one lower dimension. Above the critical temperature of the bulk phase transition, by contrast, the boundary $U(1)$ symmetry is intact and the vacuum expectation value of the scalar operator vanishes, *i. e.*, $\psi = 0$.

Having understood the basic concepts of the holographic superfluid model, let us take a short detour into some rather technical details with regard to the occurrence of the bulk instability which triggers the phase transition into the superfluid phase at the boundary. In the following we explain the reason why the scalar field Φ condenses and thus induces the spontaneous breaking of the gauge symmetry. The mechanism was first understood by Gubser [46]. In our discussion we closely follow [18, 91] but focus mainly on the qualitative arguments, leaving out mathematical details. For the interested reader we refer to [91, 182] for subsidiary details. In the symmetric phase of the gravitational model, the scalar field vanishes [47] and the action (3.1) thus reduces to the Einstein–Hilbert–Maxwell action (2.39) studied in section 2.3. The solution to this model is given by the Reissner–Nordström–AdS metric (2.51), *i. e.*, a static charged black hole embedded in an (asymptotically) anti-de Sitter spacetime. Due to isotropy of the underlying system, we can again set the spatial gauge-field components A_i to zero and in addition have the gauge freedom to set $A_z = 0$ as well. One then finds an effective mass-squared for the scalar field Φ, *cf.* the gauge–matter Lagrangian in equation (3.2),

$$m_{\mathrm{eff}}^2 = m^2 - q^2 |g^{tt}| A_t A_t \,, \tag{3.5}$$

with temporal gauge-field component A_t. Here, q denotes again the scalar charge and $g^{tt} = -z^2 h(z)^{-1}$ the time-time component of the inverse AdS–Reissner–Nordström metric (2.51) with $h(z)$ the associated horizon function (2.52). The temporal gauge-field component (or electrostatic potential) thus contributes a negative shift to the scalar mass-squared m^2. If this effective mass drops below the Breitenlohner–Freedman (BF) bound (*cf.* (2.33)), it induces an instability and causes the scalar field to condense. For completeness, let us note again that the mass-squared m^2 may well be negative but still not induce an instability as the AdS geometry allows for tachyonic masses above the BF bound. In the ultraviolet (UV), $|g^{tt}| A_t A_t$ tends to zero and the effective mass-squared thus reduces to the scalar mass-squared at the boundary, *i. e.*, $m_{\mathrm{eff}}^2 = m^2$ at $z = 0$. The same holds true also in the (strong) infrared

---

[6]A comment is in order here. In two spatial dimensions the Mermin–Wagner–Hohenberg (MWH) theorem [180, 181] forbids the spontaneous symmetry breaking (SSB) at non-zero temperatures. However, in the holographic system the MWH theorem is evaded due to the large-N_{c} limit of the boundary theory [47]. Indeed, the large-N_{c} limit allows for a second-order phase transition into the superfluid phase. For further details we refer to chapter 5.

(IR) at the black-hole horizon $z = z_{\mathrm{h}}$ since we have to demand $A_t(z = z_{\mathrm{h}}) = 0$ in order to ensure regularity of the gauge field at the horizon, *cf.* our discussions in section 2.3. Within the holographic z-interval in the bulk, the effective mass-squared is thus bounded by the scalar mass-squared which we assume to be above the BF bound.

In section 2.3 we have argued that in the low-temperature limit, the AdS–Reissner–Nordström spacetime reduces to an S–AdS$_2 \times \mathbb{R}^{D-1}$ geometry in the near-horizon limit and an AdS$_{D+1}$ geometry in the near-boundary limit. This implies that in the UV the negative mass shift vanishes as $|g^{tt}|A_t A_t \sim \mu^2 z^2$ and the effective mass-squared m_{eff}^2 thus stays well above the BF bound. Therefore, no instability occurs in the near-boundary region of the bulk. We stress that this is crucial for the UV theory to be well-defined. In the IR, on the other hand, the S–AdS$_2 \times \mathbb{R}^{D-1}$ geometry contributes a constant or even growing shift to the effective mass. Hence, in the near-horizon limit, for low enough temperatures, the effective mass-squared may drop below the BF bound and thus induce an instability. Notably, the BF bound in the IR and the one in the UV also differ due to the different geometries. After reinstating L_{AdS}, one finds $m_{\mathrm{BF}}^2 L_{\mathrm{AdS}}^2 = -D^2/4$ in the UV, while in the IR the BF bound is reduced[7] to $m_{\mathrm{BF}}^2 L_{\mathrm{AdS}}^2 = -D(D-1)/4$. Once the effective mass-squared of the scalar field drops below the BF bound and induces an instability, the electric field causes the local vacuum near the charged black-hole horizon to discharge. This dynamical process terminates with the formation of a scalar charge cloud, sourcing the electric flux in the bulk. In figure 3.1 we show a sketch of the gravitational model dual to a superfluid. During the formation of the condensate, the backreaction of the gauge–matter fields on the gravitational background causes the geometry to adapt accordingly and thus render the system stable again (see *e. g.* [91, 182]). Also, the formation of the charge cloud corresponds to the scalar field gaining a non-trivial bulk profile. In this sense, one often refers to the black hole 'developing scalar hair'. Because of the geometry of the anti-de Sitter spacetime, the standard no-hair theorem [183] is evaded (see *e. g.* [184]). The modulus of the scalar profile in the bulk reaches a maximum at the horizon and decreases monotonously towards the UV where it vanishes. This agrees with our discussion above, according to which the leading-order coefficient of the near-boundary expansion of Φ has to vanish while the sub-leading coefficient encodes the vacuum expectation value of the dual scalar operator which is non-zero in the symmetry-broken phase (in the standard quantisation).

In a nutshell, we find that spontaneous symmetry breaking occurs due to an instability of the charged black hole and the subsequent formation of a scalar charge cloud. In the dual field theory, this process corresponds to the spontaneous breaking of the global $U(1)$ symmetry and thus a phase transition into the superfluid

---

[7]Here, we have used L_{AdS} to denote the curvature radius of the AdS$_{D+1}$ spacetime as before. In the near-horizon geometry AdS$_2 \times \mathbb{R}^{D-1}$ the BF bound is given by $m^2 L_{\mathrm{AdS}_2}^2 = -1/4$, in terms of the AdS$_2$ curvature radius L_{AdS_2}. The two radii are related by $L_{\mathrm{AdS}_2} = L_{\mathrm{AdS}}/\sqrt{D(D-1)}$, *cf.* (2.63). With this relation, one eventually finds $m_{\mathrm{BF}}^2 L_{\mathrm{AdS}}^2 = -D(D-1)/4$ as stated in the main text.
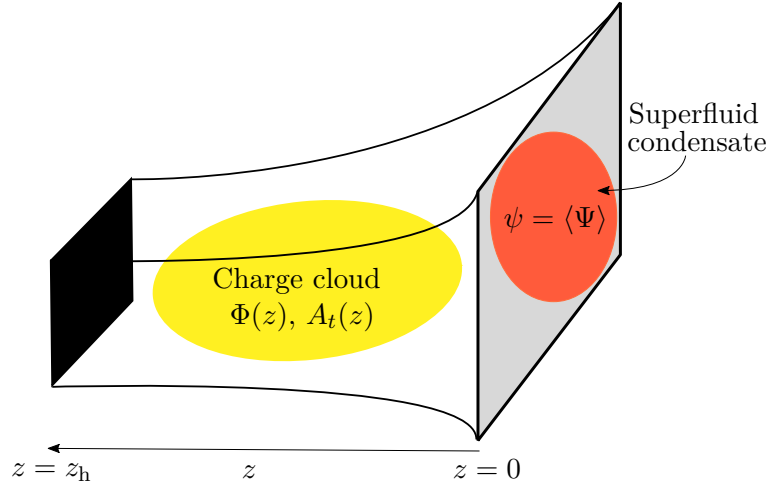
Figure 3.1: Schematic illustration of the holographic superfluid model. In the near-horizon geometry of the AdS spacetime, the occurrence of an instability induces the formation of a scalar charge cloud. The black area at $z = z_\mathrm{h}$ represents the black-hole event horizon. In the dual boundary theory (at $z = 0$), the bulk processes correspond to the formation of a bosonic condensate ψ and thus a phase transition into the superfluid phase.

state, see also figure 3.1. From thermodynamic considerations, one finds the phase transition to be of second order in two [47, 48] as well as three [166] spatial field-theory dimensions. Furthermore, employing the so-called probe-approximation to simplify the equations of motion, the models have been shown to obey mean-field critical behaviour near their respective phase transition [48, 185]. We discuss the probe-approximation in the next paragraph. In other superfluid or superconductor models, the critical exponents of the phase transition have been shown to deviate from mean-field values, *cf.* [186, 187].

In principle, we could now go ahead and derive the equations of motion associated with the action (3.1). However, solving them to simulate the real-time dynamics of the holographic superfluid is notoriously difficult. Therefore, we take a slightly modified route in this work. Instead of solving the full set of coupled gravity–gauge–matter equations of motion, we 'decouple' the gauge–matter system (3.2) from the gravitational sector. To be precise, we first solve the equations of motion corresponding to the gravitational sector only, neglecting the backreaction of the gauge–matter fields. Subsequently, we solve the gauge–matter equations of motion in the fixed background metric determined by the pure gravitational sector. In this so-called probe-approximation, which is applicable if the temperature of the superfluid is below but of the order of the critical temperature of the phase transition [158, 188], the energy of the gauge–matter fields is insufficient to significantly curve the gravitational background. Therefore, the fields may be treated as small

perturbations, so-called 'probes'. The black hole, on the other hand, is static and can absorb energy and momentum modes of the gauge–matter fields. Hence, even in the probe-approximation, there is still an interplay between the gravitational and the gauge–matter sector. Mathematically, the probe-approximation corresponds to taking the scalar charge q to large values. To see this, we recall that the charge q effectively controls the dynamical coupling between the gauge–matter and the gravitational sector in terms of the prefactor $1/q^2$ in the action (3.1). In the limit $q \to \infty$, the two sectors decouple and allow us to first solve the gravitational equations of motion and then use the corresponding metric solution to define the Levi-Civita connection ∇_M in the Lagrangian (3.2). For a more thorough discussion of the probe-approximation, see *e. g.* [148].

The probe-approximation has become very popular over the past decade and proven to be a successful approximation of the fully backreacted theory, see for instance [18]. However, there are severe shortcomings in the low-temperature regime as the large-q limit does not commute with the limit of low temperatures [47]. The fully backreacted solution of the AdS_4 system at finite temperature has first been constructed in [189, 190]. Further (early) works include, *e. g.*, [158, 191]. For the AdS_5 system, see, *e. g.*, [191] for an influential work in which the backreaction of the gauge–matter fields onto the gravitational background is included. However, in [191], a slightly modified model as compared to the one discussed here is used and studied only in the low-temperature limit. For constructions of low- or zero-temperature superfluids or superconductors with very interesting physical properties, see [192–195]. Instead of applying the probe-approximation, there exist also other approximation methods, including *e. g.* [196] where the authors derive and solve an analytic approximation of the gravitational model. Furthermore, it is worth noting that thus far our discussion has evolved only around the bottom-up construction of the holographic superfluid model. Consequently, the exact dual UV quantum field theory is unknown. To gain a deeper understanding of the nature of the holographic superfluid in the UV, one has to rely on top-down constructions which are inherently much more difficult to deal with. These are typically constructed using 'flavour-branes' in the ten-dimensional supersymmetric string theory. For a first construction of a gravitational model, dual to a superconductor with fermions in the fundamental representation, see [56]. Further interesting works include *e. g.* [197, 198].

In the following we make use of the probe-approximation and solve the $(D + 1)$-dimensional gravitational background system. Neglecting the gauge–matter Lagrangian $\mathcal{L}_{\text{gauge–matter}}$ (3.2), the action (3.1) reduces to the Einstein–Hilbert action, *cf.* equation (2.5) of section 2.1.2. Since we have already solved the vacuum Einstein equations for non-zero temperature of the dual field theory in section 2.3, we refrain from going into details here and only review the results for convenience. In $D + 1$ dimensions, the Einstein equations are solved by the $(D + 1)$-dimensional Schwarzschild–anti-de Sitter spacetime with a planar Schwarzschild black hole whose event horizon in the bulk is situated at $z = z_{\text{h}}$. In Poincaré coordinates, the line

element is given by

$$ds^2 = \frac{L_{\mathrm{AdS}}^2}{z^2} \left(-h(z)\,\mathrm{d}t^2 + \mathrm{d}\boldsymbol{x}^2 + \frac{\mathrm{d}z^2}{h(z)} \right) , \tag{3.6}$$

where we again use the mostly-plus sign convention. In the following and throughout this thesis, we set the AdS curvature radius to unity, $L_{\mathrm{AdS}} = 1$. The blackening (or horizon) function $h(z)$ is given by

$$h(z) = 1 - \left(\frac{z}{z_{\mathrm{h}}} \right)^D , \tag{3.7}$$

and the associated temperature is

$$T = \frac{D}{4\pi z_{\mathrm{h}}} , \tag{3.8}$$

which is also the temperature of the dual superfluid.

With the solution for the Einstein–Hilbert part of the action (3.1), we can now derive the equations of motion for the gauge–matter fields in the fixed background metric (3.6). They are given by the Maxwell equations for the gauge-field components and a Klein–Gordon equation for the scalar field

$$\nabla_M F^{MN} = \mathcal{J}^N , \tag{3.9}$$

$$\left(-D^2 + m^2 \right) \Phi = 0 , \tag{3.10}$$

where we have introduced the bulk electromagnetic current

$$\mathcal{J}^N = \mathrm{i} \left(\Phi^* D^N \Phi - \Phi \left(D^N \Phi \right)^* \right) , \tag{3.11}$$

which is not to be confused with the globally conserved field-theory current j^μ, referred to above. The current $\mathcal{J}^N$ couples the Klein–Gordon and Maxwell equations, making (3.9)–(3.11) a system of coupled non-linear partial differential equations in t, $\boldsymbol{x}$ and z. Throughout this work we fix the gauge freedom by setting $A_z = 0$. The z-component of (3.9) can therefore be interpreted as a constraint equation, ensuring the chosen axial gauge. After imposing appropriate boundary conditions, the non-trivial solutions to these equations yield the dual gravitational description of the holographic superfluid. We note that the mass-squared m^2 can be chosen freely so long as it is below zero and above the BF bound, *cf.* our discussions in the previous chapter in section 2.2.2. We choose $m^2 = -2$ and $m^2 = -3$ for the two- and three-dimensional system, respectively.

For the numerical implementation of the equations of motion (3.9)–(3.11), it turns out to be convenient to switch to a different, more appropriate, set of coordinates. Instead of using Poincaré coordinates for the metric (3.6), we employ infalling Eddington–Finkelstein coordinates with respect to the holographic bulk direction z. The infinitesimal coordinate transformation between them is given by

$$\mathrm{d}t_{\mathrm{EF}} = \mathrm{d}t - \frac{\mathrm{d}z}{h(z)} , \tag{3.12}$$

where on the right-hand side Poincaré coordinates are used. If integrated, equation (3.12) shows that the coordinate times at the boundary only differ by a constant offset which can be set to zero. For the boundary superfluid, the coordinates therefore agree. In Eddington–Finkelstein coordinates the metric reads

$$\mathrm{d}s^2 = \frac{L_{\mathrm{AdS}}^2}{z^2} \left(-h(z)\,\mathrm{d}t^2 + \mathrm{d}\boldsymbol{x}^2 - 2\,\mathrm{d}t\,\mathrm{d}z \right), \qquad (3.13)$$

where we have dropped the subscript of the time component. The use of infalling Eddington–Finkelstein coordinates is common for numerical simulations of real-time dynamics in holography [199]. They have two particular advantages over Poincaré coordinates. First, unlike the Poincaré coordinates, they do not have a coordinate singularity at the black-hole horizon. And second, they naturally incorporate that all radial null geodesics fall into the black hole which allows for a so-called characteristic formulation of the dynamics [199]. For a discussion of this type of formulation in a general-relativistic context see for instance [200, 201].

In the previous section we have discussed that at finite temperature the hydrodynamical (or 'quantum hydrodynamical') description of (non-relativistic) superfluidity is encompassed in the Tisza–Landau two-fluid model [116, 117] (see also [202]). In flat space, the relativistic version of this model was introduced in [203–205]. Moreover, the model has also been formulated in a gradient expansion in the gravitational background that is dual to the superfluid discussed above [158, 206–208]. For a review of the so-called fluid/gravity duality in the context of which these calculations were performed, see *e. g.* [209, 210]. A crucial success for holographic superfluids has been to show that to leading order the dual boundary description of the bulk hydrodynamics in [158, 206–208] is governed by the relativistic version of the two-fluid model with only non-dissipative contributions, [158].

Despite [158] being formulated in the fully backreacted theory, it appears likely that an interpretation of the holographic superfluid in terms of the two-fluid model is also valid and indeed useful in the probe-approximation. In the probe-approximation, the black hole is static and does not backreact to dynamical processes of the gauge–matter sector in the bulk. Its dual interpretation is therefore given in terms of a static heat bath, fixing the temperature in the boundary theory (*cf.* our discussion of the holographic dictionary in section 2.2.2). In this sense, it may loosely be interpreted as the normal component of the fluid while the gauge–matter sector is interpreted to constitute the superfluid-condensate component. Since the gauge–matter sector is solved within the fixed gravitational black-hole background, the superfluid component is coupled to the normal component and can dissipate energy and momentum to it. On the gravity side, dissipation corresponds to energy and momentum modes falling into the black hole. Naturally, the holographic superfluid therefore incorporates a dissipation mechanism. Let us further note that the holographic superfluid is in no sense a hydrodynamical expansion of the bulk dynamics at the boundary. Instead, it captures the physics at all scales and is intrinsically relativistic. However, for many applications, the system bears strong resemblance to non-relativistic superfluids. In particular, the dynamics of vortices and other

topological defects is dominated by small, non-relativistic, velocities, *cf.* [148] and our discussions in sections 7.3 and 8.2.

As a final remark of the present section, we want to point to a common misconception regarding the interpretation of the quantum theory, dual to the model discussed above, in terms of a superfluid or superconductor. From a field-theoretical point of view, superfluidity corresponds to the breaking of a global $U(1)$ symmetry while superconductivity corresponds to the breaking of a local $U(1)$ symmetry. By construction, the gravitational model discussed above has a gauged, *i. e.*, local $U(1)$ symmetry with associated gauge field A_M. According to the holographic dictionary, such a gauge field in the bulk is dual to a conserved global $U(1)$ current j^μ. In the bulk, the condensation of the scalar field spontaneously breaks the local bulk $U(1)$ symmetry. In the dual field theory, this corresponds to the breaking of the global $U(1)$ symmetry. Loosely speaking, one therefore finds superconductivity in the bulk and superfluidity at the boundary. However, by 'weakly gauging' the boundary $U(1)$ symmetry, the boundary superfluid can be promoted to a superconductor[8] (see *e. g.* [18]). This is typically done by weakly coupling the scalar operator Ψ in the boundary theory to an additional $U(1)$ gauge field. In this work we are interested in the holographic superfluid and in particular vortex excitations thereof and hence need not worry about the differences between the holographic superfluid and the holographic superconductor since vortices in both systems have a fundamentally different nature. For a discussion of the differences between the holographic superfluid and superconductor with regard to such topological excitations, see [162].

3.3 Boundary Conditions

In the previous section we have reviewed the gravitational model dual to a holographic superfluid in $d+1$ dimensions. Let us now proceed to augmenting the equations of motion for the gauge–matter fields (3.9)–(3.10) with appropriate boundary conditions. Along the spatial field-theory directions, we impose periodic boundary conditions for the two- as well as three-dimensional system. However, we postpone a more thorough discussion of the $(t, \boldsymbol{x})$-dependence of the equations to chapters 5 and 11 and focus here only on the holographic z-direction. The boundary conditions are dictated by the holographic dictionary, *cf.* section 2.2.2, and crucially depend on the dimension. Nevertheless, there are some universal aspects for the two- and the three-dimensional system, and we will discuss these here. For a detailed discussion of the boundary conditions for the two- and three-dimensional superfluid we refer to sections 5.3 and 11.3, respectively.

In agreement with our discussion of the Reissner–Nordström solution in section 2.3, the temporal component of the gauge field fixes the chemical potential μ of the

---

[8]This yields s-wave superconductors [47]. One can also construct more sophisticated gravitational models whose dual condensates carry angular momentum and are thus similar to p-wave superconductors, *cf.* [56, 166, 176, 211, 212].

dual boundary superfluid, *cf.* equation (2.49),

$$A_t(t, \boldsymbol{x}, z = 0) = \mu \, . \tag{3.14}$$

Here and throughout this thesis, we assume the chemical potential of the superfluids (in two and three spatial dimensions) to be independent of time and the boundary spatial coordinates. We therefore suppress any arguments on the right-hand side of equation (3.14). The chemical potential is given by the leading-order coefficient in the near-boundary expansion of the gauge field A_t. Thus, it sources the temporal component of the vector operator j^μ. By fixing it, we allow the sub-leading coefficient, *i. e.*, the charge density which is proportional to the vacuum expectation value of j^0, to be determined dynamically by the equations of motion.

The chemical potential has units of temperature. On dimensional grounds, the introduction of another dimensionful parameter is imperative to ensure the existence of a distinct 'critical' temperature T_c at which the bulk instability occurs. Let us explain this in more detail. Without another scale, the conformal invariance of the dual field theory would imply that all its temperatures are equivalent. Hence, the existence of a preferred critical temperature T_c would be prohibited and there could thus not be a phase transition. This changes with the introduction of the chemical potential, immediately implying that μ sets the scale for the critical temperature T_c, *i. e.*, $T_c \sim \mu$. The conformal invariance of the superfluid further implies that its thermodynamics can only be controlled by the dimensionless parameter μ/T. Indeed, one finds that the instability occurs above a critical value $(\mu/T)_c$ and the scalar field Φ condenses in the bulk [47, 48]. This implies

$$\frac{\mu}{T_c} = \frac{\mu_c}{T} \, , \tag{3.15}$$

where on the right-hand side we have introduced the critical chemical potential μ_c.

For our numerical implementation, we fix the units of the system by setting $z_h = 1$. Let us stress that due to the relativistic nature of the system, this choice simultaneously and uniquely fixes the space as well as time scales of the superfluid. For the absolute temperature of the superfluid, $z_h = 1$ implies

$$T = \frac{D}{4\pi} \, . \tag{3.16}$$

Consequently, from our discussion above we learn that for fixed temperature T the phase transition is solely controlled by the chemical potential μ. Hence, every choice for the chemical potential μ fixes the temperature ratio T/T_c of the system according to $\mu^{-1} = \mu_c^{-1} (T/T_c)$. Above the critical chemical potential[9] μ_c the temperature ratio T/T_c drops below unity and the solution to the above equations is the holographic superfluid [46, 47]. In particular, in equilibrium, $|\psi(\boldsymbol{x})| > 0$ for all $\boldsymbol{x}$.

---

[9]If z_h is reinstated, one finds that there exists a critical value for the dimensionless product μz_h. For $(\mu z_h) > (\mu z_h)_c$ the system is in the superfluid phase with $\psi \neq 0$ (and of course $\Phi(z) \neq 0$). On the other hand, for $(\mu z_h) < (\mu z_h)_c$, the boundary theory is in the normal phase and the scalar field Φ vanishes in the bulk.

The boundary values of the spatial gauge-field components determine the super-fluid velocities along the corresponding directions[10] [48]. We are only interested in vanishing external superfluid velocities and thus choose the boundary conditions

$$A_i(t, \boldsymbol{x}, z = 0) = 0 \,, \tag{3.17}$$

throughout this work. Here, $i = x_1, x_2$ for the two- and $i = x_1, x_2, x_3$ for the three-dimensional system characterises the spatial coordinates of the superfluid. Further-more, we impose $A_i(z = z_{\mathrm{h}}) = 0$ for all i and $A_t(z = z_{\mathrm{h}}) = 0$ to ensure regularity of the gauge field A_M at the black-hole horizon $z = z_{\mathrm{h}}$.

With regard to the scalar field Φ, we have already discussed in the previous section that the boundary condition at $z = 0$ has to ensure that the external source conjugate to the dual scalar operator Ψ vanishes. The source conjugate to the scalar operator typically corresponds to the leading-order coefficient in the near-boundary expansion $(z \to 0)$ of the scalar field, *cf.* equation (2.31). However, for our choices of the scalar mass, it turns out that both the leading as well as the sub-leading coefficient can be interpreted as the source conjugate to and the respective other one as the expectation value of the dual scalar operator, thus allowing for both the standard as well as alternative quantisation, *cf.* our discussion in section 2.2.2. We will comment further on this and also review the explicit near-boundary expansions in the two- as well as three-dimensional system in sections 5.3 and 11.3, respectively. In anticipation of the fact that we choose the standard quantisation in both systems, we can nevertheless quote the boundary condition here,

$$\lim_{z \to 0} \Phi(t, \boldsymbol{x}, z) z^{\Delta - D} = 0 \,, \tag{3.18}$$

with the scaling dimensions Δ defined in equation (2.32). In addition, the scalar field has to be regular at the black-hole horizon at $z = z_{\mathrm{h}}$. This second boundary condition is of behavioural nature, *i. e.*, $|\Phi(z = z_{\mathrm{h}})| < \infty$. In Eddington–Finkelstein coordinates, it corresponds to an infalling boundary condition, *cf.* [213].

We have now augmented the equations of motion discussed in the previous section with a set of boundary conditions that allow us to find a superfluid phase in the dual field theory. In particular, the boundary conditions control the corresponding phase transition. We can now proceed and study the real-time dynamics of the two- and three-dimensional holographic superfluids. While the equations of motion of both systems have strongly resembling structures, a key difference between holographic models lies in the near-boundary expansion of the scalar field Φ. This is crucial as it dictates how we choose our boundary conditions and extract the superfluid order parameter ψ from the solutions of the scalar field. From a systematic perspective concerning the implementation of the equations of motion, however, we proceed

---

[10]These are only externally imposed superfluid velocities. If set to zero, the boundary conditions in no way imply that the system is static. Vortices, for instance, cause the superfluid to have a finite velocity that is completely independent of the boundary conditions for the spatial gauge-field components. For a discussion of superfluids with finite overall superfluid velocity, see *e. g.* [48, 175].

similarly for both systems. We stress that in order to compute the near-boundary expansion of the gauge–matter fields it is important to know their solution in the entire bulk. In particular, despite referring to the dual superfluid as 'boundary theory' or 'boundary superfluid', it must not be thought of as being in some sense trivially given by the scalar field restricted to the boundary. In light of the holographic principle, it should rather be thought of as a projection of the bulk dynamics onto the boundary. In particular, while the gravity equations are purely classical, superfluidity is a quantum phenomenon. Remarkably, the gravity equations capture the exact time evolution of the superfluid density $n(t, \boldsymbol{x}) = |\psi(t, \boldsymbol{x})|$ as well as its velocity field which is encoded in the phase structure of the order parameter $\varphi(t, \boldsymbol{x}) = \arg(\psi(t, \boldsymbol{x}))$.

We have now gathered all necessary ingredients to study the real-time dynamics of holographic superfluids in two and three spatial dimensions. The remainder of this thesis is split into two parts. In Part I we focus on the two-dimensional superfluid and Part II is concerned with the three-dimensional system. Eventually, in chapter 16 we summarise our most important results and present an outlook. Let us note that throughout this thesis, we typically refer to the superfluid model just discussed, for both the two- and three-dimensional system, as *the* holographic superfluid. In doing so, we keep in mind that there are in fact many models for superfluidity within the holographic framework. However, all of them are, in one way or another, modifications of the model introduced in [46–48].

Part I

Two-Dimensional Holographic Superfluid

4 Motivation and Outline

We now begin with our investigations of the dynamics of quantised vortices in the two-dimensional holographic superfluid. We are primarily interested in the physics of vortex dipoles and, most notably, how they can be used to characterise the underlying superfluid with regard to its dissipative nature. In particular, we want to gain insight into the applicability of the holographic framework to the description of vortex dynamics in experimentally accessible systems such as highly oblate ultracold atomic gases [214] and thin films of liquid helium [109, 134].

Only a few years after the discovery of the superfluid phase of liquid helium ^{4}He in the 1930s [102, 110], it was first noticed that the underlying physics of collective phenomena, such as superfluidity, changes fundamentally upon lowering its dimensionality [215]. While it was well understood that in three spatial dimensions long-range order occurs below the critical temperature of a phase transition [125], it was also known that in two spatial dimensions such long-range order is destroyed by thermal fluctuations [180, 181]. However, a quarter of a century later, Berezinskii, Kosterlitz and Thouless (BKT) were the first to predict that also in two spatial dimensions a phase transition into the superfluid phase at finite temperature can in fact exist [216, 217]. For the groundbreaking nature of their discovery, two of these authors were awarded the Nobel Prize in 2016. Soon after BKT published their work, their prediction was experimentally confirmed for liquid helium [218]. For many years thereafter, two-dimensional helium films were intensively studied (see *e. g.* [179]). Moreover, with the experimental breakthrough in the creation of Bose–Einstein condensates at the end of the last century [127–129], new vistas have been opened in the study of two-dimensional collective quantum phenomena. It was quickly understood that trapping potentials allow for the creation of Bose–Einstein condensates also in two spatial dimensions [219] and subsequently it only took a few years until the condensation of Bose gases in two spatial dimensions was first experimentally realised [220, 221] and the BKT phase transition was observed [222–225]. Evidently, these findings have also triggered much theoretical interest in two-dimensional Bose–Einstein condensates. From a theory perspective, the BKT transition was first found for ultracold Bose gases in [226]. Nowadays, refined experimental methods as well as advanced theoretical models break new ground in the study of two-dimensional superfluids and Bose–Einstein condensates. For reviews on two-dimensional Bose gases, see *e. g.* [227, 228].

Much focus in the study of two-dimensional superfluids concerns quantum-turbulent behaviour induced by the appearance of quantised vortices, *e. g.* [229–232]. In an experimental setup, the vortices are free to move only in the plane of the highly oblate condensate or liquid film and can thus, to a good approximation, be considered as

being point-like along the third spatial direction. From a theoretical perspective, vortex dynamics is typically studied in numerical real-time simulations, see *e. g.* [233–237]. For such investigations, the holographic description of a superfluid in $2 + 1$ dimensions has proven particularly successful, see *e. g.* [148, 150] and our discussions in chapter 3. In this work, we use the holographic superfluid to study the real-time dynamics of single vortex–anti-vortex pairs. Such vortex pairs are of particular interest as they constitute the fundamental building blocks of large vortex ensembles as they are typically seen in experiments and numerical simulations (see for instance [229, 232]). Furthermore, while the topological characteristics of vortices are the same in all superfluids and Bose–Einstein condensates, their dynamics is highly dependent on the underlying superfluid. Therefore, gaining an in-depth understanding of the kinematic aspects of the vortex dynamics allows one to deduce properties of and characterise the superfluid hosting the dynamics. We will make use of this fact and characterise the holographic superfluid with regard to its dissipative nature. In two-dimensional systems, the study of interactions between vortices as well as between vortices and the background excitations has drawn much attention, both theoretically and experimentally. Important works include [31, 37, 134, 238–248] for thin films of superfluid helium, [32, 33, 40, 249–251] in the context of cold atomic gases, and [252] for similar scenarios in two-dimensional superconductors.

In this thesis, we build a clean theoretical laboratory to study the dynamics of vortex–anti-vortex pairs in the $(2+1)$-dimensional holographic superfluid. We analyse the dipole dynamics by means of the vortex trajectories, velocities and accelerations and in particular, use the kinematic aspects to quantify the dissipation of the holographic superfluid. For more than a decade now, various aspects of the holographic superfluid have been intensively studied and analysed, see *e. g.* [18]. Yet, it is still an open question how the holographic superfluid compares to experimentally accessible superfluids and cold atomic Bose gases. It is therefore of great interest to gain insight into the characteristics of the holographic superfluid with regard to the physical parameter regime it captures.

We close the aforementioned longstanding gap and for the first time present a quantitative analysis of the dissipative nature of the two-dimensional holographic superfluid in the presence of quantised vortices. We match to the dynamics of a vortex–anti-vortex pair in the holographic superfluid the analogous solution of the dissipative Gross–Pitaevskii equation (DGPE) in two spatial dimensions. The dissipative Gross–Pitaevskii equation is given by the standard Gross–Pitaevskii equation (GPE) [138, 139] supplemented with an additional phenomenological damping term (*cf.* section 7.1 for details). Throughout this thesis we occasionally also refer to the GPE as Gross–Pitaevskii (GP) model. To be specific, we prepare only a single vortex dipole in the initial configuration of both systems and subsequently simulate the respective time evolutions on large numerical grids until the respective vortices annihilate and the superfluids equilibrate. Imprinting only a single dipole, instead of an ensemble of vortices, ensures that we can neglect more complicated many-body interactions. Furthermore, we employ large grids in order to suppress finite-size effects so that we reach the precision we seek for our studies. The basis of our evaluation

method of the dipole dynamics and many further investigations in this work is a high-precision tracking routine which enables us to locate the vortices to inter-mesh precision on the numerical grid. In particular, we introduce a new algorithm that is highly accurate and numerically very efficient. However, while it can be applied for most of the dipole evolution, it breaks down once the vortex-induced density depletions deform and overlap. For those situations, we employ another, well established, albeit slower, tracking routine. Upon combining these algorithms, we extract the vortex trajectories from our numerical simulations of the respective superfluid time evolution in a quasi-continuous manner. For the matching of solutions of the DGP model to the holographic system, we tune the free DGPE parameters such that the sizes of the vortex-induced density depletions around the vortex cores coincide and their quasi-continuous trajectories agree in space and time[1].

Employing known relations between the DGPE and the Hall–Vinen–Iordanskii (HVI) equations describing the mechanical motion of point vortices subject to interactions with the dissipative superfluid hosting the dynamics further allows us to translate the matched DGPE parameters into friction coefficients. These friction coefficients in turn are related to experimentally measurable observables such as the vortex diffusivity. The vortex diffusivity is the key to comparing our findings for the holographic superfluid to experimental results in both cold atomic gases [214] and superfluid helium [134, 135]. The results of this comparison lead us to conjecture that the holographic framework should be applicable to the description of strongly dissipative vortex dynamics in highly dense ultracold alkali gases near a Feshbach scattering resonance[2], thermally excited Bose–Einstein condensates or in superfluid helium at temperatures in the Kelvin regime.

In addition to using the dipole dynamics and specifically the vortex trajectories for the characterisation of the holographic superfluid, we also investigate the kinematic details of the dynamics. In particular, for the first time for vortices in the holographic superfluid, we determine their velocities and accelerations. Indeed, due to the precision gained from our tracking routine as compared to standard plaquette techniques previously used in the literature (see *e. g.* [163]), we can employ finite-difference methods to compute derivatives of the trajectories with respect to time and thus obtain the respective vortex velocities and accelerations[3]. Let us note that

---

[1]See https://www.thphys.uni-heidelberg.de/∼holography/holoDGPE/ for videos demonstrating the matched vortex dynamics and further supplementary material.

[2]In the low-energy (s-wave) scattering of two atoms, a so-called Feshbach resonance occurs when the total energy of the two incoming atoms equals the binding energy of a molecule formed by the two colliding atoms. If the magnetic moments for the molecule and the two incoming atoms differ, the energy difference ΔE between the total energy and the binding energy can be tuned using magnetic fields. Close to a Feshbach resonance ($\Delta E \to 0$), the two channels, *viz.* the open scattering channel of the two atoms and the channel forming a bound state, mix, causing a change in the s-wave scattering length [253]. In particular, this allows for an increase in the scattering length and thus the interaction strength between the constituent atoms. See *e. g.* [254] for a review.

[3]For videos demonstrating the dynamics of vortex dipoles in the holographic superfluid, see https://www.thphys.uni-heidelberg.de/∼holography/DipoleDynamics/.

the trajectories of vortex dipoles in the holographic superfluid[4] have been studied before in [163]. The work presented in this thesis extends and improves on the work in [163] in several ways, most notably by the vast increase in precision of the vortex trajectories due to our improved tracking routine. We further study the dependence of the dipole dynamics on the initial configuration of the vortices on the grid and on the chemical potential of the superfluid. Despite the dipole dynamics itself being our primary focus, we also extend our analysis to times past the annihilation of the vortices and study the nature and behaviour of the rarefaction pulse that is created by the annihilating vortices. In particular, we compare the rarefaction pulse with similar excitations in the GP model, so-called Jones–Roberts solitons, as well as with grey-soliton solutions of the holographic superfluid. Despite the large number of works on vortex dynamics in the two-dimensional holographic superfluid, its rarefaction pulses, created by annihilating vortices, have thus far not been studied in the literature.

Organisation of Part I

In chapter 5 we discuss the details of the two-dimensional holographic superfluid that we have previously left out in chapter 3. In particular, we find the static and homogeneous background solution of the superfluid and derive the full set of dynamical equations of motion which we later use for our numerical real-time simulations.

In chapter 6 we first discuss the initial conditions for the vortex defects used throughout this part, and we present a first qualitative discussion of the dynamics of a single vortex dipole. We then proceed to setting the basis for a more quantitative analysis of the dynamics by introducing a tracking routine that allows us to locate the vortices on the numerical grid to high accuracy. The tracking routine is composed of two separate algorithms, one of which we introduce and apply for the first time in this context. Finally, we comment on a characteristic feature of the vortex trajectories, which is in fact an artefact of the initial preparation of the dipole configuration using a procedure that is also commonly employed in the literature, that has thus far in the literature not been addressed and can only be resolved due to the improved tracking routine.

In chapter 7 we first introduce the (dissipative) Gross–Pitaevskii model and the Hall–Vinen–Iordanskii equations and discuss their relevance in the description of cold Bose gases and vortex dynamics in dissipative superfluids, respectively. We then proceed to matching solutions of the DGPE to the dipole dynamics in the holographic superfluid by tuning the free numerical DGPE parameters. In this context we also discuss the geometric bulk representation of vortices in the holographic framework and comment on the associated geometric interpretation of the superfluid dissipation mechanism. A matching of solutions of the HVI equations to the vortex dynamics finally enables us to convert the extracted parameters of the holographic

---

[4]In addition, similar work to [163] has also been performed in the context of the Gross–Pitaevskii equation in [255].

superfluid to observables that are also measurable in experiments with real-world superfluids and Bose–Einstein condensates.

In chapter 8 we investigate the kinematic aspects of the dynamics of vortex dipoles in the holographic superfluid and interpret our findings in light of the results of chapter 7. To be specific, we study the dependence of the vortex trajectories as well the vortex velocities and accelerations on the initial dipole configuration and on the chemical potential of the superfluid. In the final section of this chapter, we investigate the rarefaction pulse created by the annihilating vortices and show that it strongly resembles soliton solutions in the GP model.

Finally, in chapter 9, we summarise our results and discuss possible directions for future research on the two-dimensional holographic superfluid.

5 Gravitational Model Dual to the Two-Dimensional Superfluid

Having laid out our motivation for studying the two-dimensional holographic superfluid introduced in chapter 3, let us now discuss the missing details of the dual gravitational model, given in terms of an Abelian Higgs model in a $(3+1)$-dimensional asymptotically anti-de Sitter spacetime (*cf.* the action in equation (3.1)). In the following section 5.1, we briefly summarise the most important aspects of section 3.2 with the dimensions fixed to $D = 3$. In section 5.2 we discuss the boundary conditions for the gauge–matter fields. We then proceed to constructing the static and homogeneous background solution of the superfluid (section 5.3) and subsequently derive the full set of dynamical equations of motion that we use in our simulations of the real-time dynamics of the superfluid (section 5.4).

5.1 Gravitational Background Solution

The gravitational model dual to the two-dimensional superfluid is constructed in a bottom-up approach by minimally coupling a scalar field to an Abelian gauge field in an asymptotically anti-de Sitter spacetime in $3+1$ dimensions. However, in this work, we employ an approximation of the model that allows us to distinctly simplify the equations of motion but nevertheless capture the main aspects of the underlying physics. To be specific, we solve the system in the probe-approximation in which the backreaction of the gauge–matter fields on the gravitational sector is neglected. This approximation is applicable if the temperature of the system is close to the phase-transition temperature in which case the energy of the gauge–matter sector is too small to significantly curve the gravitational background, *cf.* [47]. Hence, the gauge–matter Lagrangian (3.2) decouples from the gravitational sector of the action (3.1) and the backreaction of the scalar and gauge field on the metric tensor g_{MN} is negligible. Solving only the gravitational sector of the action (3.1) then yields the $(3+1)$-dimensional Schwarzschild–anti-de Sitter spacetime with metric

$$\mathrm{d}s^2 = \frac{L_{\mathrm{AdS}}^2}{z^2} \left(-h(z)\,\mathrm{d}t^2 + \mathrm{d}x_1^2 + \mathrm{d}x_2^2 - 2\,\mathrm{d}t\,\mathrm{d}z \right) , \qquad (5.1)$$

here written in infalling Eddington–Finkelstein coordinates with respect to the holographic bulk direction z. Henceforth, we set $L_{\mathrm{AdS}} = 1$. Furthermore, we note that throughout Part I we use $\boldsymbol{x} = (x_1, x_2)$ to denote the two spatial boundary coordi-

nates of the superfluid. The horizon function is given by

$$h(z) = 1 - \left(\frac{z}{z_{\mathrm{h}}}\right)^3 , \qquad (5.2)$$

with the black-hole horizon located along the holographic z-direction at $z = z_{\mathrm{h}}$. Using equation (2.46), we find the associated Hawking temperature of the black hole,

$$T = \frac{3}{4\pi z_{\mathrm{h}}} , \qquad (5.3)$$

which is also the temperature of the dual superfluid. To fix units in the gravitational system, we set $z_{\mathrm{h}} = 1$. Thus, the absolute temperature of the superfluid is fixed to $T = 3/(4\pi)$.

In the next section we discuss the boundary conditions for the gauge–matter fields in the AdS$_4$ bulk. Then, in the subsequent two sections, we review the equations of motion of the gauge–matter sector in the fixed gravitational background determined by the metric (5.1). In section 5.3 we study the static and spatially homogeneous solution of the superfluid and discuss details regarding the nature of the phase transition from the normal to the superfluid state. The static solution is important as we will later use it to construct the initial vortex configurations for the non-equilibrium dynamics. In section 5.4, we then proceed to deriving the full set of dynamical equations of motion, without imposing any constraints on their symmetries. As a final comment, let us point out that all results presented in this section are already well established in the literature and we only review them here for completeness.

5.2 Boundary Conditions

In this section we discuss the boundary conditions for the gauge–matter fields of the holographic superfluid model. In a very general dimension-independent form we have already mentioned them briefly in chapter 3.3. Here, we make them explicit for the two-dimensional superfluid. In particular, we give the boundary conditions for the gauge-field components and for the scalar field, at the conformal boundary $z = 0$ and the black-hole horizon $z = z_{\mathrm{h}}$. Moreover, we discuss aspects of the holographic dictionary for the superfluid.

In order to make the boundary conditions at $z = 0$ explicit, we have to study the near-boundary expansion of the fields. Let us start with the gauge field and specifically its temporal component A_t, for which one finds the asymptotic behaviour (see for instance [92])

$$A_t(t, \boldsymbol{x}, z) = \mu(t, \boldsymbol{x}) + \rho(t, \boldsymbol{x})z + \mathcal{O}(z^2) , \qquad (5.4)$$

where μ is again the chemical potential and ρ the charge density of the dual quantum theory. Since we want to describe a superfluid at fixed chemical potential, we fix μ

at the boundary,

$$A_t(t, \boldsymbol{x}, z = 0) = \mu \,, \tag{5.5}$$

and leave ρ to be dynamically determined by the equations of motion. Throughout this thesis, we take the chemical potential to be static and spatially homogeneous and therefore suppress any dependences on the field-theory coordinates on the right-hand side of equation (5.5). In the holographic interpretation, μ is the source conjugate to the temporal component of the boundary $U(1)$ current operator j^μ, and ρ is proportional to its expectation value. Analogously, we find for the gauge-field components parallel to the spatial boundary directions

$$A_i(t, \boldsymbol{x}, z) = \xi_i(t, \boldsymbol{x}) + J_i(t, \boldsymbol{x})z + \mathcal{O}(z^2) \,, \tag{5.6}$$

where ξ_i is the superfluid velocity along the i-th field-theory direction, sourcing j_i, the corresponding component of the dual $U(1)$ current operator, and J_i is proportional to the vacuum expectation value of j_i. We want to study the superfluid without externally imposed velocities and therefore take the boundary conditions to be

$$A_i(t, \boldsymbol{x}, z = 0) = 0 \,. \tag{5.7}$$

For the scalar field Φ, we find the near-boundary expansion from equations (2.31) and (2.32), upon substituting $D = 3$ and our choice for the scalar mass-squared, $m^2 = -2/L^2_{\text{AdS}}$. Importantly, while this mass is slightly tachyonic, it is well above the Breitenlohner–Freedman bound $m^2_{\text{BF}} L^2_{\text{AdS}} = -9/4$. It does therefore not induce an instability. The asymptotic behaviour of the scalar field near $z = 0$ is thus given by

$$\Phi(t, \boldsymbol{x}, z) = \eta(t, \boldsymbol{x})z + \psi(t, \boldsymbol{x})z^2 + \mathcal{O}(z^3) \,. \tag{5.8}$$

In accordance with the holographic dictionary, we now choose the boundary condition at $z = 0$ such that there is no external source conjugate to the dual scalar operator Ψ. There is, however, a subtlety. For our choice of the mass of the scalar field, both coefficients in (5.8) may be interpreted as the source conjugate to the scalar operator Ψ and the respective other one is its vacuum expectation value [79], see also our discussion in section 2.2.2. Hence, there are two possible choices for the boundary condition for the scalar field. Corresponding to these choices, there are also two solutions to the equations of motion and thus, in a sense, two types of superfluids or superconductors for this choice of the scalar mass[1] [47]. Here, we follow [148] and choose the leading-order coefficient η in the expansion (5.8) to be the source conjugate to the dual operator Ψ and $\psi = \langle \Psi \rangle$ to be its vacuum expectation value. Thus, we follow the standard quantisation as opposed to the alternative quantisation for which the roles of η and ψ are reversed. In order to allow for a

---

[1]The two solutions are related by a Legendre transformation [79].

spontaneous breaking of the $U(1)$ symmetry, the source η conjugate to the scalar operator has to vanish. The boundary condition at $z = 0$ for the scalar field is therefore given by

$$\partial_z \Phi(t, \boldsymbol{x}, z)|_{z=0} = 0 \,. \tag{5.9}$$

We have now specified the boundary conditions for the gauge–matter fields at the conformal AdS boundary at $z = 0$. Since the equations of motion (3.9)–(3.11) are of second order, we also need to impose boundary conditions at the black-hole horizon at $z = z_\mathrm{h}$. For the gauge-field components, we take them to be $A_t(z = z_\mathrm{h}) = A_i(z = z_\mathrm{h}) = 0$, and the scalar field has to be regular. For convenience, let us summarise all boundary conditions,

$$A_t(z = 0) = \mu \,, \qquad A_t(z = z_\mathrm{h}) = 0 \,, \tag{5.10}$$

$$A_{x_1}(z = 0) = 0 \,, \qquad A_{x_1}(z = z_\mathrm{h}) = 0 \,, \tag{5.11}$$

$$A_{x_2}(z = 0) = 0 \,, \qquad A_{x_2}(z = z_\mathrm{h}) = 0 \,, \tag{5.12}$$

$$\partial_z \Phi(z)|_{z=0} = 0 \,, \qquad |\Phi(z = z_\mathrm{h})| < \infty \,. \tag{5.13}$$

We use these boundary conditions for the construction of the static and spatially homogeneous solution of the two-dimensional holographic superfluid as well as for the full set of dynamical equations of motion of the system in section 5.4.

5.3 Static and Homogeneous Solution

In this section we explore the equilibrium solution of the holographic superfluid in two spatial dimensions. Since we use this solution for the construction of initial vortex configurations, we sometimes refer to it as background or static background solution of the superfluid. In the probe-approximation, this solution was first constructed in [47, 48]. Including backreaction, on the other hand, the solution was first considered in [189]. We note again that the probe-approximation retains the interesting physics in the parameter regime that we will consider throughout this thesis. We loosely follow [157] in our discussions in this section.

Varying the action (3.1) with respect to the gauge–matter fields yields the Maxwell and Klein–Gordon equations (3.9)–(3.11). To find the static background solution to these equations, we make an ansatz for the fields according to

$$\Phi = \Phi(z) \,, \qquad A_M = A_M(z) \,. \tag{5.14}$$

Hence, in addition to being static, we assume the solution to be spatially homogeneous in $\boldsymbol{x}$. To fix the gauge freedom, we set $A_z = 0$. Using the ansatz (5.14), we obtain a set of ordinary differential equations in the holographic z-direction with the fields defined on the finite domain $0 \leq z \leq z_\mathrm{h}$. In Eddington–Finkelstein coordinates

the equations of motion for the Maxwell field[2] A_M are given by

$$0 = z^2 A_t'' + 2\,\mathrm{Im}(\Phi'\Phi^*)\,, \tag{5.15}$$

$$0 = z^2 (h A_i'' + h' A_i') - 2|\Phi|^2 A_i\,, \tag{5.16}$$

$$0 = 2A_t|\Phi|^2 - \mathrm{i}h\left(\Phi^*\Phi' - \Phi^{*\prime}\Phi\right)\,, \tag{5.17}$$

where we use $i = x_1, x_2$ to denote the spatial field-theory directions and a prime denotes a derivative with respect to z. Since all fields in the above equations depend on z only, we refrain from making this dependence explicit. For the scalar field Φ the Klein–Gordon equation (3.10) reduces to

$$0 = z^2\,h\,\Phi'' - z\left(-2\mathrm{i}z A_t + 2h - zh'\right)\Phi' - \left(2\mathrm{i}z A_t - \mathrm{i}z^2 A_t' + z^2 \boldsymbol{A}^2 + m^2\right)\Phi\,, \tag{5.18}$$

where we have introduced $\boldsymbol{A} = (A_{x_1}, A_{x_2})$ for the spatial gauge-field components.

In the above system of equations, equation (5.17) originates from the z-component of the Maxwell equations. Due to our gauge choice of $A_z = 0$, this equation is not independent of the other equations and should therefore rather be considered as a gauge constraint. Indeed, one can show explicitly that if (5.18) is satisfied and the fields obey their boundary conditions, equation (5.17) is satisfied for every z-slice in the bulk.

Equations (5.15)–(5.16) and (5.18) form a closed system of second-order non-linear ordinary differential equations. Augmented with the set of boundary conditions at the AdS boundary $z = 0$ and the black-hole horizon $z = z_\mathrm{h}$, discussed in the previous section, the holographic superfluid constitutes a one-parameter family of non-trivial solutions to these equations [47, 48]. In the following we solve[3] this boundary-value problem. It turns out that for the solution below the critical temperature, this can only be done numerically [47]. In this work, we employ an iterative Newton–Kantorovich procedure to linearise the equations and then solve the resulting system of linear equations at every iterative step using a collocation method (see *e. g.* [256]). For the latter, we expand the fields in a basis of 32 Chebyshev polynomials and evaluate them on a Gauss–Lobatto grid. In appendix A we give further details on our numerical methods.

In chapter 3 we have argued that the thermodynamics of the gravitational model is uniquely determined by the dimensionless parameter μ/T. Since we have fixed

---

[2]From isotropy of the underlying system, it follows immediately that the spatial gauge-field components A_i vanish identically. For completeness, we nevertheless quote the corresponding equations of motion here.

[3]A comment is in order here. In practice, we derive the solutions of the static and spatially homogeneous system not in Eddington–Finkelstein (EF) but in Poincaré coordinates, *i. e.*, using the metric (3.6). We discuss the corresponding equations of motion and the transformation of the solutions to EF coordinates in appendix A.4. We have checked explicitly that the solutions derived in EF and Poincaré coordinates agree after transforming the fields appropriately and we only use the latter for convenience. To construct the initial conditions for our real-time simulations we use equations (5.15)–(5.18) and then solve the dynamical equations of motion (*cf.* section 5.4) in EF coordinates.
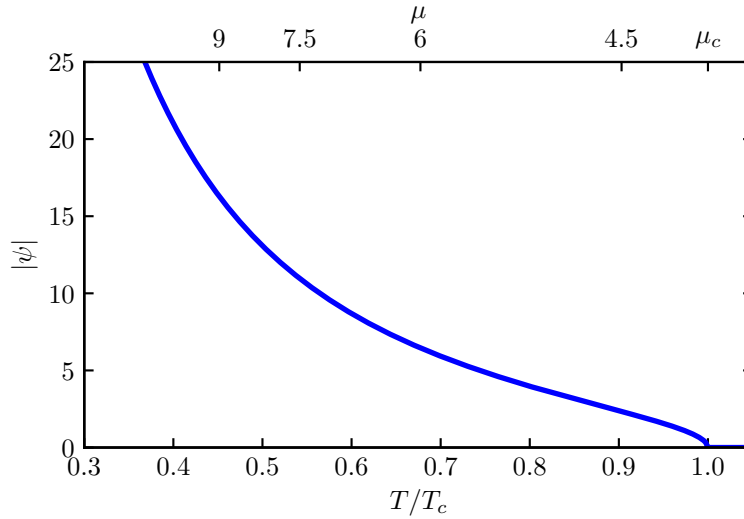
Figure 5.1: Modulus of the superfluid order parameter ψ as a function of T/T_c (lower abscissa) or the chemical potential (upper abscissa), in the probe approximation. The square of the order parameter yields the condensate density of the superfluid $n = |\psi|^2$. Above the critical temperature T_c, the order parameter $|\psi|$ is strictly zero. The chemical potential μ and T/T_c are in one-to-one correspondence, *cf.* (5.20) and the main text.

the temperature by our choice of $z_h = 1$, *cf.* equation (5.3), the chemical potential alone controls the phase transition. Above a critical value μ_c for which the temperature ratio T/T_c drops below unity, the solution to the above equations yields the two-dimensional holographic superfluid with $|\psi| > 0$ [46, 47]. From our numerical implementation of the equations of motion, we find

$$\mu_c \simeq 4.06371\,, \tag{5.19}$$

which agrees with the typical value quoted in the literature [47]. According to (3.15), we can now directly relate the chemical potential to the ratio T/T_c. Throughout this work we use T/T_c and μ interchangeably to characterise the thermodynamic state of the superfluid which is justified by the one-to-one correspondence

$$\mu^{-1} = \mu_c^{-1} \frac{T}{T_c}\,. \tag{5.20}$$

In figure 5.1 we show the modulus of the superfluid order parameter ψ as a function of the chemical potential μ or the temperature ratio T/T_c. The static and homogeneous background solution represents the unperturbed equilibrium superfluid condensate. In general, the density of the condensate is defined as $n = |\psi|^2$ and its phase is given by $\varphi = \arg(\psi)$. Throughout this work we denote the equilibrium density as n_0. The value of the scalar charge q plays no role here since it acts

only as an overall parameter in the action (3.1) and accordingly drops out in the equations of motion. Moreover we use $\mu = 6$ which sets the system into the super-fluid phase at $T/T_{\rm c} = 0.68$ with $n_0 \approx 41.7$ for our studies throughout Part I, except for chapter 7 and section 8.3. In those chapters, on the other hand, we analyse the vortex dynamics in the superfluid for a number of chemical potentials. We mark the corresponding values by ticks on the μ-axis in figure 5.1. The largest chemical potential we employ is $\mu = 9$, corresponding to a ratio of $T/T_{\rm c} = 0.45$. We expect the probe-approximation to be still applicable in this regime. The probe-approximation becomes less trustworthy for increasing chemical potentials or decreasing temperatures.

Before we review the full set of dynamical equations of motion, let us discuss the bulk configuration of the gauge–matter fields in the equilibrium solution. We study both, the low-temperature and the high-temperature branch. Naturally, in this thesis we are most interested in the low-temperature superfluid phase and for our studies we will find it very useful in the following chapters to have a good understanding of the dual bulk configuration of the gauge–matter fields. We therefore begin our discussion with the low-temperature branch for $T/T_{\rm c} < 1$. In figure 5.2 we illustrate the bulk configuration of the fields in this regime. To be specific, we show the profile of the modulus-squared of the scalar field[4] $|\Phi|^2$ (solid blue), the temporal gauge-field component A_t (dotted turquoise), the scalar charge density $\sqrt{-g}|\mathcal{J}^0|$ (dash-dotted red) and the field $|\Phi|^2/z^4$ (dashed green), computed in the probe approximation for a chemical potential of $\mu = 6$. The spatial gauge-field components A_i are zero in the static background solution. In agreement with our discussion in chapter 3, the scalar charge density, also referred to as (scalar) charge cloud, $\sqrt{-g}|\mathcal{J}^0|$ is non-zero at the black-hole horizon, has a maximum in the interior of the bulk and vanishes at the boundary. Due to its profile in the interior of the bulk, it screens the boundary superfluid from the black-hole horizon. At the boundary $z = 0$ the scalar field $|\Phi|^2/z^4$ reduces to the superfluid-condensate density $n = |\psi|^2$. Here $n = n_0$ since we show the equilibrium solution. For different choices of the temperature, or equivalently the chemical potential, of the superfluid, the bulk profiles of the fields are qualitatively similar to those displayed in figure 5.2. However, for decreasing temperature, the absolute value of the scalar field in the bulk grows until it ultimately becomes too large in the vicinity of the black hole (*cf.* figure 5.2) for its backreaction on the gravitational geometry to be negligible. At this point, the probe-approximation breaks down.

Before we proceed to the high-temperature solution, a comment is in order. From a field-theory perspective, one would expect the Mermin–Wagner–Hohenberg (MWH) theorem [180, 181] to prohibit the spontaneous symmetry breaking at non-zero temperatures in the two-dimensional superfluid. Nevertheless, in the holographic setup, a second-order phase transition to a superfluid phase is seen [47, 48, 158]. It has

---

[4]Numerically, one finds that there is more than one non-trivial solution for the scalar field Φ. The solutions differ by additional nods in the bulk profile of $|\Phi|^2$. However, the one presented in figure 5.2 is energetically favoured and believed to be the only stable solution, see *e.g.* [18].
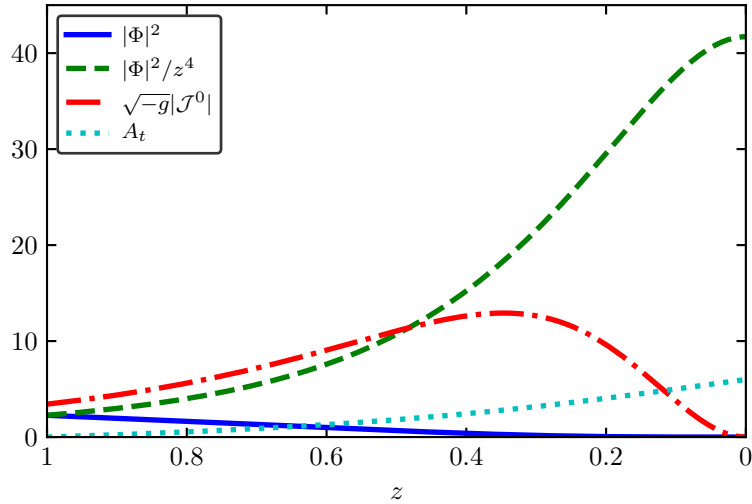
Figure 5.2: Typical bulk profiles of the gauge–matter fields of the holographic superfluid in equilibrium for an exemplary chemical potential of $\mu = 6$. The AdS boundary is at $z = 0$ (right) and the black-hole horizon at $z = z_{\mathrm{h}} = 1$ (left). modulus-squared of the bulk scalar field $|\Phi|^2$ is depicted by the solid blue line and the temporal gauge-field component A_t by the dotted turquoise line. In addition, we show the scalar charge density $\sqrt{-g}|\mathcal{J}^0|$ in red (dash-dotted) and the field $|\Phi|^2/z^4$ (in green, dashed) which reduces to the superfluid density n at the boundary. In equilibrium, $n = n_0 \approx 41.7$. In a related context, a similar version of this figure has been used before in [257].

further been shown that the transition has mean-field critical exponents [48, 185]. The reason the MWH theorem can be evaded in holography is the large-N_{c} limit which suppresses thermal fluctuations that would usually destroy the long-range order. Hence, the nature of the phase transition of the holographic system differs from the BKT transition that is typically seen in conventional two-dimensional field theories. In such systems, long-range order is destroyed by thermal fluctuations and only algebraic long-range order prevails. This is a fundamental difference between the holographic superfluid model we consider in this work and conventional two-dimensional superfluids. However, taking into account gravity corrections dual to $1/N_{\mathrm{c}}$ corrections in the boundary field theory, it has been shown that for all non-zero temperatures in the holographic system, strong infrared fluctuations cause the phase of the order-parameter field to be washed out everywhere and thus prevent the spontaneous breaking of the $U(1)$ symmetry [159]. In this case one also finds algebraic long-range order [159] in the holographic framework. As a result, the critical exponents deviate from their mean-field values. We note that the latter can also be achieved by studying broader classes of holographic superfluid or superconductor

models, *e. g.*, [186, 187].

On the second branch above the critical temperature, for $T/T_{\mathrm{c}} > 1$, there is only a trivial solution for the scalar field, given by $\Phi = 0$. Moreover, a vanishing scalar field implies $A_i = 0$ for the spatial gauge-field components due to isotropy of the underlying system (see also equation (5.16)) and, after reinstating z_{h},

$$A_t = \mu \left(1 - \frac{z}{z_{\mathrm{h}}} \right) , \tag{5.21}$$

for the temporal component of the gauge field. For the gauge field, these configurations agree with the ones we have encountered before in section 2.3, *cf.* equations (2.47) and (2.54), corresponding to solutions of the Einstein–Hilbert–Maxwell action (2.39). However, a non-zero value of the electrostatic potential A_t (5.21) requires the black hole to be charged and thus to be given by a Reissner–Nordström–AdS$_4$ black hole which is not the case in the probe-approximation. Hence, the solution for the gauge field and the solution for the gravitational sector, given by the Schwarzschild–AdS$_4$ spacetime with metric (5.1), are not compatible. Indeed, in the Schwarzschild–AdS$_4$ spacetime there is no charge that can source the electric flux in the bulk and the solution (5.21) is therefore inconsistent and thermodynamically unstable. The thermodynamically stable and 'proper' solution for $T/T_{\mathrm{c}} > 1$ would require taking the backreaction of the gauge–matter fields onto the gravitational sector into account in which case we would find the metric to be given by the Reissner–Nordström–AdS$_4$ metric (2.51), just as in section 2.3 [189].

5.4 Dynamical Equations of Motion and Numerical Implementation

We are ultimately interested in studying the non-equilibrium real-time dynamics of the holographic superfluid. In the previous section we have constructed the static background solution by effectively reducing the equations of motion in (3.9)–(3.11) to a one-dimensional problem in the holographic coordinate z. To evolve the system in time, we have to solve the equations of motion (3.9)–(3.11) in the gravitational background determined by the metric (5.1) without any further simplifying assumptions with regard to symmetries of the respective field configurations. While in the previous section we have left m^2 unspecified in the equations of motion (5.15)–(5.18), here we plug in $m^2 = -2$ explicitly as it allows us to distinctly simplify the dynamical equation of motion for the scalar field.

In light of the boundary condition (5.8) for the scalar field, it turns out to be useful to formulate the equations of motion in terms of the rescaled field $\tilde{\Phi}$,

$$\tilde{\Phi} \equiv \frac{\Phi}{z} . \tag{5.22}$$

We further use the so-called lightcone-derivative defined by

$$\nabla_+ X = \partial_t X - \frac{h(z)}{2} \partial_z X \qquad \text{for} \qquad X \in \left\{ \tilde{\Phi}, A_{x_1}, A_{x_2} \right\} , \tag{5.23}$$

where we have suppressed the arguments of the gauge–matter fields but keep in mind that $X = X(t, \boldsymbol{x}, z)$. By gauge freedom, the z-component of the gauge field is again set to zero, $A_z = 0$.

After some algebra, the equations of motion (3.9)–(3.11) for the spatio-temporal gauge-field components and the scalar field read

$$\partial_z^2 A_t \;=\; \partial_z \boldsymbol{\nabla} \cdot \boldsymbol{A} - 2\,\mathrm{Im}(\tilde{\Phi}^* \partial_z \tilde{\Phi})\,, \tag{5.24}$$

$$\partial_z \nabla_+ A_{x_1} \;=\; \frac{1}{2}\left(\partial_{x_2}^2 A_{x_1} + \partial_{x_1}(\partial_z A_t - \partial_{x_2} A_{x_2})\right) - |\tilde{\Phi}|^2 A_{x_1} + \mathrm{Im}(\tilde{\Phi}^* \partial_{x_1} \tilde{\Phi})\,, \tag{5.25}$$

$$\partial_z \nabla_+ A_{x_2} \;=\; \frac{1}{2}\left(\partial_{x_1}^2 A_{x_2} + \partial_{x_2}(\partial_z A_t - \partial_{x_1} A_{x_1})\right) - |\tilde{\Phi}|^2 A_{x_2} + \mathrm{Im}(\tilde{\Phi}^* \partial_{x_2} \tilde{\Phi})\,, \tag{5.26}$$

$$\partial_z \nabla_+ \tilde{\Phi} \;=\; \frac{1}{2}\boldsymbol{\nabla}^2 \tilde{\Phi} - \mathrm{i}\boldsymbol{A} \cdot \boldsymbol{\nabla}\tilde{\Phi} + \mathrm{i}A_t \partial_z \tilde{\Phi} - \frac{\mathrm{i}}{2}\left(\boldsymbol{\nabla} \cdot \boldsymbol{A} - \partial_z A_t\right)\tilde{\Phi}$$
$$- \frac{1}{2}\left(z + \boldsymbol{A}^2\right)\tilde{\Phi}\,, \tag{5.27}$$

where we have used the two-dimensional gradient $\boldsymbol{\nabla} = (\partial_{x_1}, \partial_{x_2})$. In addition, we find from the z-component of the Maxwell equations

$$0 \;=\; \partial_t \partial_z A_t - \boldsymbol{\nabla}^2 A_t + \partial_t \boldsymbol{\nabla} \cdot \boldsymbol{A} - h\partial_z \boldsymbol{\nabla} \cdot \boldsymbol{A} + 2|\tilde{\Phi}|^2 A_t$$
$$- 2\,\mathrm{Im}\left(\tilde{\Phi}^* \partial_t \tilde{\Phi} - h\tilde{\Phi}^* \partial_z \tilde{\Phi}\right)\,. \tag{5.28}$$

Equations (5.24)–(5.27) form a closed system of non-linear partial differential equations in $(t, \boldsymbol{x}, z)$. Equation (5.28), on the other hand, is by purpose detached from the other dynamical equations as it is not independent of them. Indeed, due to the axial gauge condition, equation (5.28) can be expressed as a linear differential equation in terms of equations (5.24)–(5.27). The boundary conditions for the fields (5.10)–(5.13) further ensure that equation (5.28) is always satisfied at the conformal boundary, $z = 0$. It follows that if equations (5.24)–(5.27) are satisfied, also (5.28) is satisfied in the whole bulk. Hence, equation (5.28) should rather be interpreted as a gauge constraint for the axial gauge condition. Likewise, one could equally well treat the dynamical equation for the temporal gauge-field component (5.24) as the gauge constraint and (5.28) as the dynamical equation for A_t. In this work, we interpret (5.28) as the constraint equation. In our numerical implementation we check explicitly that (5.28) is indeed satisfied throughout the evolution of the superfluid.

Despite their second-order, non-linear and coupled nature, the equations of motion can be solved in a straightforward manner. In the following we lay out the basic scheme of our numerical implementation. We first leave aside equation (5.24) and focus on equations (5.25)–(5.27). In these equations, derivatives with respect to time appear only on the left-hand sides, hidden in the lightcone derivative ∇_+. On every fixed timeslice we can therefore compute the right-hand sides of the equations at every point (x_1, x_2) and then integrate them with respect to z, imposing boundary

conditions for the fields at $z = 0$, to find $\nabla_+ A_{x_1}, \nabla_+ A_{x_2}$ and $\nabla_+ \tilde{\Phi}$. Subsequently, we undo the linear shift of the lightcone derivative (5.23) in each of the equations to obtain expressions for the derivatives of the fields A_{x_1}, A_{x_2} and $\tilde{\Phi}$ with respect to time. Upon using an explicit time-stepping algorithm, we propagate the fields one step forward in time. Eventually, we use these fields on the new timeslice to compute the right-hand side of equation (5.24). Integrating the result with respect to z twice, with boundary conditions imposed at $z = 0$ and $z = z_{\mathrm{h}}$, we also find A_t on the new timeslice. The boundary conditions for the fields are the same as for the static equations of motion, *cf.* equations (5.10)–(5.13).

With regard to technical details, the procedure outlined above is implemented as follows. Like for the static solution, we expand the fields in a basis of 32 Chebyshev polynomials on a Gauss–Lobatto grid along the holographic z-direction. Such an expansion allows for the implementation of derivatives via matrix multiplications. Along the spatial field-theory directions, we use a pseudo-spectral method. We expand the fields in a basis of Fourier polynomials which allows us to implement derivatives with respect to $\boldsymbol{x}$ using discrete Fourier transforms. Throughout Part I, we employ grid sizes of 512×512 points along the (x_1, x_2)-directions. For the time propagation, *i. e.*, to integrate the fields $\partial_t A_{x_1}, \partial_t A_{x_2}$ and $\partial_t \tilde{\Phi}$, we use a fourth-order/fifth-order Runge–Kutta–Fehlberg algorithm with adaptive timestep size. We split one unit timestep (in units of $z_{\mathrm{h}} = 1$) into an adaptive number between 10 and 1000 numerical timesteps. Further details regarding our numerical implementation of the equations of motion and further technical details are presented in appendix A.

6 Holographic Vortex-Dipole Dynamics and Evaluation Method

In the previous two chapters 4 and 5, we have set out our motivation for studying the real-time dynamics of vortex–anti-vortex pairs in a two-dimensional superfluid employing the holographic duality. Moreover, we have discussed the corresponding gravitational model dual to the superfluid in $2+1$ dimensions. In this chapter, we now proceed to introducing quantised vortex excitations of superfluids and analysing their dynamics in the holographic system. To be specific, we qualitatively study the dynamics of vortex dipoles and discuss the basic concepts and quantitative evaluation methods that we employ in our investigations in this chapter and throughout this thesis.

In section 6.1, we first comment on some general characteristics and aspects of topological vortex defects in superfluids and subsequently discuss how we prepare vortex defects and specifically the initial vortex-dipole configuration in the holographic system. Thereafter, in section 6.2, we discuss the time evolution of a vortex dipole and qualitatively analyse the characteristics of its dynamics. The subsequent section 6.3 is concerned with the introduction of tracking algorithms for the vortices on the numerical grid. This is necessary as a quantitative analysis of the dipole dynamics requires us to determine their trajectories to the highest attainable precision. In the final section 6.4 of this chapter, we comment on a characteristic feature of the dipole dynamics in our simulations that becomes evident only once we employ the tracking algorithms. We show that its origin can be attributed to our initial preparation of the vortex configuration. By the end of this chapter, we have introduced and covered all necessary prerequisites needed for the study of the dipole dynamics on a quantitative level. In particular, in the subsequent chapter 7 we use the highly accurate vortex trajectories obtained from the tracking methods to quantitatively characterise the holographic superfluid with respect to its dissipative nature and finally, in chapter 8, to analyse the kinematic aspects of the dipole dynamics itself, including the vortex velocities and accelerations.

Throughout this chapter we fix the chemical potential of the superfluid to $\mu = 6$, which corresponds to a ratio of $T/T_{\rm c} = 0.68$, *cf.* equation (5.20). However, all results, discussions and methods presented in the following are universally valid and applicable for all chemical potentials allowed in the probe-approximation. In particular, in chapter 7 and section 8.3, we are interested in the dependence of various aspects of the dipole dynamics on the chemical potential of the holographic superfluid. For the respective analyses, we employ the same initial conditions and evaluation methods as presented in the present chapter.

The content of this chapter is mainly based on our publications [164, 258] and some parts are taken verbatim from them. For a better embedding in the context of this thesis, we have further added and modified several parts.

6.1 Initial Conditions

Quantised vortices in superfluids, or more generally, in Bose–Einstein condensates are the quantum analogue to classical eddies [259, 260]. They represent topological defects in the complex order-parameter field[1] $\psi(t, \boldsymbol{x}) = \sqrt{n(t, \boldsymbol{x})}\,\mathrm{e}^{\mathrm{i}\varphi(t,\boldsymbol{x})}$. A vortex is characterised by a quantised phase winding around its core. The phase field φ winds around the position $\boldsymbol{x}_0$ of the core by $2\pi w$, with $w = (2\pi)^{-1} \oint \mathrm{d}\varphi \in \mathbb{Z}\backslash\{0\}$, the winding number of the vortex, also commonly referred to as its topological charge. The phase winding gives rise to a non-vanishing curl $\boldsymbol{\nabla} \times \boldsymbol{v}(t, \boldsymbol{x}) \sim w\delta(\boldsymbol{x} - \boldsymbol{x}_0)\hat{\boldsymbol{e}}_\perp$ of the superfluid velocity field $\boldsymbol{v}(t, \boldsymbol{x}) \sim \boldsymbol{\nabla}\varphi(t, \boldsymbol{x})$, where $\hat{\boldsymbol{e}}_\perp$ points in the direction perpendicular to the two-dimensional plane (in an embedding of the system in a three-dimensional space). At the position of the vortex core $\boldsymbol{x}_0$, the quantised phase winding forces the superfluid density $n(t, \boldsymbol{x})$ to drop to zero in order to avoid a phase singularity. Away from the core, the density 'heals' back to the background density n_0 on a characteristic length scale ξ, the healing length[2]. While in the GPE the healing length has an explicit definition (see the next chapter), this is not the case within the holographic framework. Nevertheless, one may think of the healing length as the length scale which determines the width of the superfluid-condensate-density depletion around a vortex core. We will further address this in the next chapter. Finally, a comment is in order here. In agreement with what we have just discussed, throughout Part I, we refer to the point around which the phase winds and at which the condensate density drops to zero as the *core* of a vortex. When we refer to a vortex or a vortex-induced density depletion, on the other hand, we mean not only the core but also the density profile around the core.

The study of quantised vortices in superfluids has been of great interest for many years now, experimentally as well as theoretically [134]. Since the advent of experimentally realised Bose–Einstein condensates [127–129], investigations of vortices, their characteristics, and their interactions with the non-condensed excitations of the system have intensified even more [261]. Nowadays, experimental vortex formation can be achieved by various refined technological methods. A prominent example is the rotation of the condensate by lasers [262–264]. This method is mainly used to create dense vortex lattices, see *e. g.* [263, 265]. In superfluid helium similar vortex lattices can be created by rotating the container, *cf.* [266, 267]. Analogous situations have also been studied theoretically, within the Gross–Pitaevskii equation [268, 269] as well as in the holographic system [169, 270, 271]. Other experiential methods

---

[1]The idea of quantised vortices was first put forward by Onsager [259] and Feynman [260] for three-dimensional vortex rings. We will focus more on this aspect in Part II. Excellent reviews of quantised vortices in ultracold atomic gases and superfluid helium include [134, 261].

[2]We note that the healing length ξ is not to be confused with the externally imposed superfluid velocities ξ_i which we set to zero in the boundary conditions of section 5.2.

include for instance using optical potentials or the flow past obstacles, see *e. g.* [229–231]. For condensates with spin degrees of freedom, vortices can be created by 'topological phase imprinting' [272] (based on the proposals in [273–275]). Despite being applicable only for condensates with internal degrees of freedom, the topological phase-imprinting method resembles the preparation of the initial condition in our theoretical setup which we will discuss in the following paragraph. Before we proceed with this discussion, however, let us briefly mention that refined experimental methods have also been developed to locate vortices in experiments with superfluids or ultracold dilute Bose gases and even to determine their topological charge, which are central prerequisites for a possible comparison of our findings discussed in this thesis with experiments on vortex dynamics. For Bose–Einstein-condensed gases these include, *inter alia*, the use of time-of-flight techniques to measure the condensate's density profile [276–278] and, more recently, spectroscopic methods [232, 279] (based on [280]). For superfluid helium, the use of so-called tracer particles [281] has proven very successful, see *e. g.* [134, 282].

The type of initial condition we have in mind consists of only a single vortex–anti-vortex pair. In the following three chapters, we will find this apparently simple system to offer insights not only into the dynamics of single vortices, but also of large ensembles of vortex defects as well as the holographic superfluid itself. As the name suggests, the system is composed of one vortex of topological charge $w_1 = 1$ and one vortex of topological charge $w_2 = -1$ ('anti-vortex'). In analogy to electrodynamics, the vortex–anti-vortex pair can therefore also be referred to as vortex dipole. In chapter 4 we have set out our motivation for studying the dynamics of such a dipole in a 'clean' theoretical environment. Here, 'clean' refers to the minimisation of uncertainties, of physical as well as numerical nature, in the analysis. From a physics perspective, the dynamics of a vortex dipole is most accurately studied if there are no other vortices present that might cause the occurrence of more complicated many-body interactions which are rather difficult to account for. By our choice for the initial configuration, such effects are avoided. Numerically, the main sources of uncertainty originate from the size of the computational domain as well as the periodicity of the grid. Again borrowing terminology from electrodynamics, due to the periodicity in the (x_1, x_2)-directions, the dipole finds itself surrounded by 'mirror vortices'. Effects on the vortex dynamics originating from the presence of these mirror vortices have to be minimised in order to capture solely the physics of a single dipole. The straightforward way to ensure that this is indeed the case is by choosing the grid size to be, in a sense, sufficiently large. By sufficiently large we mean that an increase in the size of the grid should have no noticeable effect on the physics of the vortex dipole to the precision we seek to achieve in our investigations. In practice, we find that a (x_1, x_2)-grid of 512×512 points, supplemented with our typical choice for the grid spacing of $l = 2/7$ (in units of $z_\mathrm{h} = 1$), is sufficient for our purposes as long as the vortex–anti-vortex separation does not exceed ~ 180 grid points. We give details on our choice for the grid spacing as we go along in this chapter. Along the holographic bulk direction, we find 32 grid points to satisfy our needs. To check that the chosen (x_1, x_2)-grid size is indeed sufficiently

large, we perform one simulation on an additional grid of twice this size, *i. e.*, 1024 grid points along both directions, and find that the dipole dynamics agrees to the desired precision. Thus, we restrict all numerical simulations of Part I to grid sizes of 512×512 points and the corresponding maximal vortex–anti-vortex separation.

We prepare the initial vortex configuration by imprinting the vortices individually onto the homogeneous equilibrium solution of the holographic superfluid at time $t = t_0$. Specifically, we multiply the winding structure of the vortex configuration into the equilibrium solution of the bulk scalar field Φ. For a single vortex of winding number w_i at position $(x_{1,i}, x_{2,i})$, this phase-winding configuration is given by $\varphi(t_0, \boldsymbol{x})_i = w_i \arg(x_1 - x_{1,i} + \mathrm{i}(x_2 - x_{2,i}))$, extending over the entire (x_1, x_2)-grid. To imprint a number of vortices, the individual winding structures are simply added up linearly $\varphi = \sum_i \varphi_i$. Subsequently the total phase configuration is multiplied into the scalar field $\Phi(t_0, \boldsymbol{x}, z) \to \Phi(t_0, \boldsymbol{x}, z)\, \mathrm{e}^{\mathrm{i}\varphi(t_0,\boldsymbol{x})}$ for every slice along the holographic z-direction. In the dual superfluid, this corresponds to multiplying the respective phase configuration into the static background solution of the superfluid order-parameter field $\psi(t_0, \boldsymbol{x}) \to \psi(t_0, \boldsymbol{x})\, \mathrm{e}^{\mathrm{i}\varphi(t_0,\boldsymbol{x})}$. However, we stress that in the holographic framework, it is essential to imprint the phase windings in the entire bulk and not only at the boundary at $z = 0$ [161]. See also our comment in the second to last paragraph of section 3.3. Moreover, we impose the vanishing of the scalar field[3] $\Phi(t_0, \boldsymbol{x}, z)$ at the respective positions $\boldsymbol{x}_i$ of the vortex cores for every fixed-z slice along the holographic direction, *i. e.*, $\Phi(t_0, \boldsymbol{x}_i, z) = 0 \,\forall\, z \in [0, z_\mathrm{h}]$. At all other grid positions, the absolute value of the scalar field remains unchanged. Likewise, also the solutions for the gauge-field components A_M remain unchanged. The vortices then individual build up their density and true phase profile dynamically as we propagate the system in time. For our type of initial configuration, consisting of only two well-separated vortices, the build-up process takes approximately $\Delta t = 5$ unit timesteps. Once the vortices have developed their profile, we reset the time to $t = 0$ and begin our analysis of their dynamics. However, we stress that whenever we quote initial conditions throughout this part, we refer to the configurations at time $t_0 = -5$ and note that at time $t = 0$ the vortices have already slightly moved and therefore changed positions. For our purpose this motion can safely be ignored.

The topological characteristics of vortices are universal to all superfluids or Bose–Einstein-condensed dilute gases. The characteristic shape of the density depletions around the vortex cores as well as the vortex behaviour, on the other hand, is determined by the underlying superfluid. Understanding the details of the dynamics of vortex dipoles in the holographic superfluid is one of our main goals for the next chapters. Vortices in the holographic superfluid were first constructed[4] in [161, 162]

---

[3]In fact, it turns out that presetting the phase-winding configuration only, suffices for the vortex solutions to build up dynamically. In order to accelerate the build-up process, however, we additionally demand the scalar field Φ at the positions of the vortices to vanish along the holographic z-direction.

[4]For the holographic superconductor, vortex solutions have been constructed before in [188, 283]. However, the stability of these solutions requires the presence of an external magnetic field. This is not required for vortices in the holographic superfluid [161, 162].
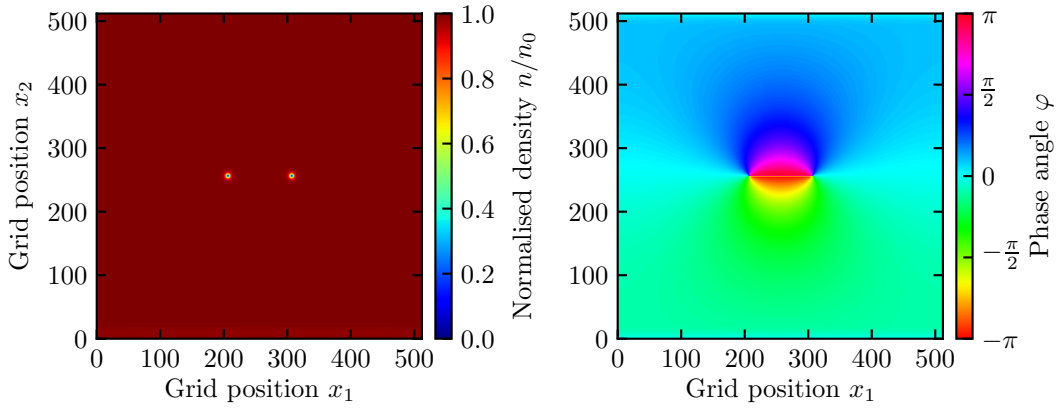
Figure 6.1: Illustration of a typical initial configuration of a vortex dipole studied here. Left: The superfluid density $n(\boldsymbol{x}) = |\psi(\boldsymbol{x})|^2$ normalised to the static background density n_0. The blue dips in the density represent the vortex and anti-vortex at positions $(x_{1,1}, x_{2,1}) = (356, 256)$ and $(x_{1,2}, x_{2,2}) = (156, 256)$, respectively. Right: The corresponding phase-angle configuration $\varphi = \arg(\psi(\boldsymbol{x}))$. Here, the colour map is adapted to the 2π-periodicity of the phase. The snapshot is taken at time $t = 0$, after the vortices have fully developed, *cf.* the main text for details.

and prominent studies of ensembles of vortices in the holographic superfluid include [148, 150, 168]. Furthermore, we point out that also in [163] the authors study the dynamics of single vortex dipoles in the holographic superfluid. However, our investigations extend and improve on their work in several ways. Later in this chapter as well as in chapter 8, we comment in more detail on how our results compare to those presented in [163].

In figure 6.1 we illustrate a typical initial configuration studied throughout the next chapters of this thesis. It shows a single vortex–anti-vortex pair with a separation of $d_0 = 100$ grid points. The individual vortices of winding numbers $w_1 = 1$ and $w_2 = -1$ are imprinted on the quadratic grid at positions $(x_{1,1}, x_{2,1}) = (356, 256)$ and $(x_{1,2}, x_{2,2}) = (156, 256)$ for the vortex and anti-vortex, respectively. The snapshot shown in figure 6.1 is taken at time $t = 0$ when the vortices have fully developed. In the left panel we show the superfluid density $n(t = 0, \boldsymbol{x}) = |\psi(t = 0, \boldsymbol{x})|^2$ normalised to the equilibrated background condensate density n_0. The right panel shows the corresponding phase configuration $\varphi(t = 0, \boldsymbol{x}) = \arg(\psi(t = 0, \boldsymbol{x}))$ of the scalar order-parameter field ψ. Note that both plots in figure 6.1 comprise the full (x_1, x_2)-grid. In our numerical implementation we use a grid spacing of $l = 2/7$, in units of $z_{\mathrm{h}} = 1$. The choice of grid spacing is in principle arbitrary so long as it ensures that a vortex is resolved by an appropriate number of grid points for the purposes of the respective investigations. Given our choice, the diameter of an in-

dividual and isolated vortex-induced density depletion is resolved by approximately 13 grid points at 95% of the background density n_0 which we find very convenient for our purposes. Other choices for which the grid spacing is of the same order of magnitude, however, would also serve our needs. We stress that the physical size of a vortex is determined by the only free parameter of the holographic superfluid, namely the ratio μ/T and specifically in our case, for fixed absolute temperature T, only the chemical potential μ. The choice of the grid spacing only determines to what accuracy we resolve the vortex in our numerical simulations. In the following chapter 7, we find it more convenient to have a higher resolution of the vortices than in the present chapter and therefore choose a smaller grid spacing given by $l = 1/8$. See also section 7.3 and the introduction to chapter 8 for a discussion of this matter.

6.2 Dipole Dynamics

Let us now proceed to studying the dynamics of a vortex dipole in the holographic superfluid. In this section we focus on a qualitative description of the vortex evolution and the underlying physics driving the dynamics. For a detailed and quantitative analysis we refer to the following chapters.

Once the vortices have been imprinted, they move in the flow field of the respective other vortex. If there was no friction, the vortices would simply move on straight lines perpendicular to the dipole vector $\boldsymbol{d}(t) = (\boldsymbol{x}_1 - \boldsymbol{x}_2)(t) = d(t)\,\hat{\boldsymbol{d}}_0$, here defined to be directed from the anti-vortex to the vortex and $\hat{\boldsymbol{d}}_0 = \boldsymbol{d}(0)/|\boldsymbol{d}(0)|$ is the corresponding normal vector. This motion of the vortices in parallel is known as Helmholtz pair propagation[5]. If the superfluid is dissipative, on the other hand, the vortices behave differently. Namely, as a result of friction between the topological defects and the fluid, the vortex velocity decreases relative to the flow field at the position of the respective vortex. This causes the emergence of a Magnus force, directed along (opposite to) the dipole vector for the anti-vortex (vortex). In other words, the Magnus force causes the vortices to approach each other so that they finally annihilate. For a more detailed discussion of this aspect, see chapter 7. After the annihilation, the vortices leave behind a rarefaction pulse (or rarefaction wave) that quickly picks up velocity and eventually decays into sound excitations of the superfluid. In the following we denote the direction perpendicular to the dipole axis as the transverse direction, and the direction parallel to it as the longitudinal direction.

To visualise the vortex behaviour, we consider the vortex-dipole evolution from the exemplary initial configuration displayed in figure 6.1. In figure 6.2 we show snapshots of the corresponding density modulation at four times characteristic for the evolution. Given the initial configuration in figure 6.1, the vortices annihilate after $\Delta t \simeq 2422$ unit timesteps. Before we go into details, we note that the vor-

---

[5]Named after Hermann Ludwig Ferdinand von Helmholtz (1821–1894) who predicted this behaviour for one-dimensionally extended straight vortex lines (*Wirbellinien*) in classical three-dimensional liquids in his celebrated work [284]. See Part II for further details on Helmholtz' contribution to the study of vorticity.
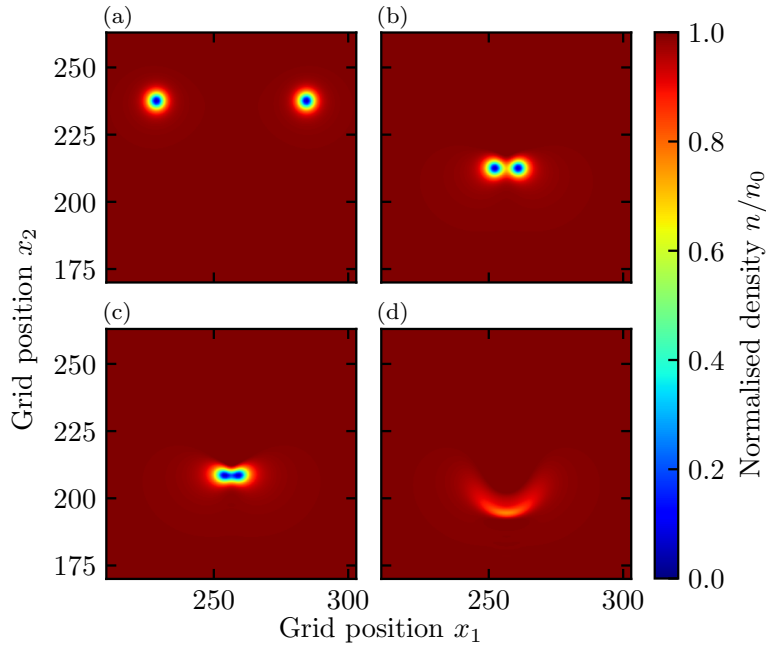
Figure 6.2: Snapshots of the normalised condensate density at four times character-
istic for the evolution of a vortex dipole. The vortices annihilate at time
$t = 2422$. (a) $t = 1600$, early to intermediate stage. The vortex–anti-
vortex separation is still large and the vortices are spherically symmetric
in shape. (b) $t = 2405$, entry stage of the late-time regime. The vortices
have significantly approached each other and their density depletions
mutually deform and merge. (c) $t = 2418$, final stage of the annihila-
tion. The vortices have strongly deformed and their density depletions
overlap. (d) $t = 2427$, propagating rarefaction pulse after the annihila-
tion. At even later times the pulse quickly decays into sound waves and
the superfluid equilibrates.

tices approach each other very quickly with a strong suppression of Helmholtz pair
propagation. This hints towards a strongly dissipative nature of the superfluid. In
the next chapter we will find that the system indeed has a strong dissipation and
quantify it precisely.

We now turn to a more detailed discussion of the vortex evolution presented in
figure 6.2. First, we note that time proceeds from the upper left (a) to the lower
right (d) panel. At the time of the first snapshot ($t = 1600$), the vortices have
already approached each other significantly but are still far apart as compared to
the width of their density depletions. Hence, the vortex diameters are much smaller
than the vortex–anti-vortex separation and their shape is perfectly spherical. In this
limit, the vortices can be approximated as point-like depletions in the background
density with regard to the effect they have on one another. We confirm this explicitly

in the following chapter and find it to be very useful for the quantification of the mutual friction between the superfluid and the defects. Snapshot (*b*) is taken at time $t = 2405$, *i. e.*, only 17 unit timesteps before the vortices annihilate. At this stage of the evolution, the vortex-induced depletions in the superfluid density begin to deform strongly non-elliptically and merge. A notable deformation of the vortices sets in only a few unit timesteps earlier than this. The circular or only elliptically deformed shape of the depletions during most of the vortex evolution is a crucial prerequisite our following analysis of the dipole dynamics. While it takes most of the evolution time for the vortices to approach each other, the final stage during which the vortices deform, merge and eventually annihilate proceeds very quickly, within approximately 30 unit timesteps. This final stage constitutes only $\sim 1.2\%$ of the total evolution time. Henceforth, we denote this time interval as the late-time regime of the evolution. Snapshot (*c*) is taken at time $t = 2418$, four unit timesteps before the vortices annihilate and their phase windings disappear. At this time, the vortices have merged into a peanut-shaped system with strongly overlapping density depletions. However, there are still two distinct zeros in the condensate density corresponding to the vortex cores. Only once the two zeros merge and form a continuum (with the order-parameter field Fourier interpolated at inter-mesh points), the quantised phase windings mutually annihilate. After the annihilation, the vortices leave behind a rarefaction pulse in the superfluid-condensate density, *cf.* panel (*d*) of figure 6.2, which subsequently decays into sound excitations. The snapshot of the rarefaction-pulse configuration is taken at time $t = 2427$. We will study the past-annihilation regime more closely in section 8.4. Once the sound waves have damped out, the system equilibrates and approaches the background solution with homogeneous density n_0.

6.3 Vortex Tracking

In the previous section we have qualitatively described the time evolution of a single vortex–anti-vortex pair. We now want to set out the basis for a more quantitative analysis of the dipole dynamics. We are in particular interested in the trajectories of the vortices. All other observables that we are ultimately interested in, such as the velocities and accelerations of the vortices, can be inferred from their trajectories. In order to extract the trajectories from our numerical simulations, we have to track the vortices on the (x_1, x_2)-grid. Naturally, in light of our matching procedure with the GPE dynamics as well as the computation of derivatives of the trajectories with respect to time, the vortices have to be located to higher than plaquette-precision. Hence, we have to introduce a high-accuracy sub-plaquette tracking routine.

Numerically, there are more than one ways to extract the locations of vortices from simulations of their dynamics. In the literature, one finds that the most common way of tracking vortices is to locate their phase windings on the numerical grid, see *e. g.* [148, 150, 163]. In such procedures, a single vortex is tracked with plaquette resolution. The main advantage of these plaquette-technique methods is

their numerical simplicity. They are mainly used for large ensembles of vortices for which the given precision is sufficient as one is in general not interested in the behaviour of individual vortices but rather ensemble-averaged observables. In contrast, for an in-depth investigation of the dynamics of only two distinct vortices, a tracking algorithm allowing for sub-grid resolution is required. Such a high level of accuracy is necessary in order to resolve the vortex dynamics quasi-continuously. In particular, when the vortices move slower than one grid spacing per unit timestep, which they do for most of their evolution as we will find in chapter 8, derivatives of plaquette-precision trajectories with respect to time either vanish or are equal to unity. Derivatives of trajectories extracted with sub-plaquette precision, on the contrary, allow for the computation of quasi-continuous vortex velocities and accelerations, throughout the entire dipole evolution. For details see also our discussions in sections 6.3.3 and 8.2.

There exists a larger number of different tracking algorithms that allow for a sub-plaquette tracking of vortices. For an incomplete list of methods applied to simulations of various physical superfluid systems, see for instance [285–291]. Each of these methods has its own advantages, drawbacks and limitations. For the purpose of this work, *i. e.*, the tracking of a single vortex–anti-vortex dipole on a two-dimensional background condensate without an external potential, we find that none of those methods fully satisfies our needs. We therefore propose a new tracking algorithm which we employ for most of the dipole evolution and combine it with an existing Newton–Raphson tracking method, used, *e. g.*, in [291] (for a review of various Newton methods, see [292]). Combining the two methods ensures that at each stage of the evolution the vortices are most accurately and numerically efficiently tracked.

In the following subsection we introduce our new tracking algorithm and discuss its applicability. Thereafter, we review the Newton–Raphson method and eventually comment on the advantages of combining both tracking methods. In particular, we contrast the combined routine with a standard plaquette phase-winding technique.

6.3.1 Gaussian Fitting Algorithm

We introduce a new tracking routine that has the advantage of being applicable for most of the dipole evolution and, moreover, being numerically very efficient. We stress that numerical efficiency is crucial for our investigations in the subsequent chapters, as we perform a larger number of simulations for various superfluid parameters and initial vortex–anti-vortex configurations. Furthermore, the sought quasi-continuous nature of the trajectories requires us to track the vortices at every unit timestep or even more frequently. This adds up to several tens of thousands of tracking steps. Hence, we strongly rely on time efficient but still highly accurate tracking algorithms.

In a nutshell, the algorithm we propose tracks the vortices by simultaneously inferring the positions of the minima of the respective vortex-induced density depletions from a simple fitting routine. To be specific, on a fixed timeslice we choose a rectangular subregion of the (x_1, x_2)-grid that contains both vortices. We then apply

a fitting algorithm to the superfluid density $n(\boldsymbol{x})$ in that subregion which captures both vortex-induced density depletions simultaneously and determines the positions of their respective minima. We take these to be the locations of the vortex cores. In practice, we choose the rectangular subregion to be spanned by the vortex dipole plus 40 grid points in the positive and negative x_1- and x_2-directions. We have explicitly checked the independence of our results on the above choice of subregion, given that it is sufficiently large to capture the density depletions of both vortices. For the fitting routine itself, we are free to choose any function that captures the flanks of the vortices sufficiently well. The reason for the independence of the results on the details of the used profile is as follows. Due to the quantised phase windings of the vortices, the superfluid density must vanish at the positions of the vortex cores. Consequently, the density $n(\boldsymbol{x}) = |\psi(\boldsymbol{x})|^2$ has a minimum at this location on the (x_1, x_2)-grid. Furthermore, for spherical or only elliptically deformed vortices, the location of the respective minima can be inferred from the flanks of the density depletions. Therefore, we only have to describe the flanks of the vortices accurately in order to track their locations by subsequent interpolation to the respective minima. Clearly, this yields the vortex locations with sub-grid resolution as the fitting function interpolates between the grid points to the minima.

In practice, we fit a linear combination of two two-dimensional upside down Gaussians according to

$$G(x_1, x_2) = A - A_1 \exp\left\{ -\frac{(x_1 - x_{1,1})^2}{2\sigma_{x_1,1}^2} - \frac{(x_2 - x_{2,1})^2}{2\sigma_{x_2,1}^2} \right\}$$
$$- A_2 \exp\left\{ -\frac{(x_1 - x_{1,2})^2}{2\sigma_{x_1,2}^2} - \frac{(x_2 - x_{2,2})^2}{2\sigma_{x_2,2}^2} \right\} \tag{6.1}$$

to the density profile on the rectangular subregion to determine the core positions $\boldsymbol{x}_i = (x_{1,i}, x_{2,i})$ of the vortices $i = 1, 2$ forming the dipole. The positions $\boldsymbol{x}_i$ are the fitting parameters of interest to us. In addition, the tuple $(\sigma_{x_1,i}, \sigma_{x_2,i})$, $i = 1, 2$, denotes the widths of the Gaussians in the x_1- and x_2-direction. We impose no restrictions on the symmetry of the two Gaussians and thus leave the widths as free fitting parameters. The amplitudes A, A_1 and A_2 are additional fitting parameters to embed the fit of the vortex dipole into the condensate background. This enables us to capture the entire vortex dipole in a single fit. For the fitting routine we use a Levenberg–Marquardt least-squares fitting algorithm. For faster convergence, we provide an initial guess for the vortex locations by locating their phase windings to plaquette precision.

As described above, this choice for the fitting function is only one of many options. Explicit checks with other functions that describe the flanks similarly well show that the results for the vortex-core positions agree to high accuracy. Let us give a specific example. Another choice could, for instance, be the approximate analytic solution for the vortex profile of the Gross–Pitaevskii equation (GPE) [136, 293],

$$n(\boldsymbol{x}) = \frac{n_0(\boldsymbol{x} - \boldsymbol{x}_i)^2}{2\tilde{\xi}^2 + (\boldsymbol{x} - \boldsymbol{x}_i)^2} . \tag{6.2}$$

Here, $n(\boldsymbol{x})$ parametrises the profile of a spherically symmetric vortex -induced density depletion but can straightforwardly be generalised also to elliptically deformed vortices. In addition, n_0 is again the equilibrium superfluid density and $\tilde{\xi}$ is the GPE healing length. In anticipation of our studies in the next chapter, we introduce the tilde notation here for the GPE healing length and reserve ξ for the more generally defined holographic vortex width, *cf.* section 7.3. We discuss the Gross–Pitaevskii equation and its solution for the profile around a vortex core (6.2) in more detail in sections 7.1 and 7.3, respectively. For now, it may suffice to take this solution and proceed as for the Gaussian above by fitting an appropriate linear combination of it to the same rectangular subregion of the superfluid density $n(t, \boldsymbol{x})$.

We find the results for the vortex-core positions to be in excellent agreement with the ones obtained from the Gaussian fitting routine, with discrepancies occurring only on the few-percent level (in grid points). In the following, we take the absolute deviations between the respective positions to be an estimate for the uncertainty of the extracted core positions. The maximal absolute discrepancy we find is given by ± 0.02 grid points. We expect the uncertainty of the vortex positions from the Gaussian fitting routine to be of this order of magnitude. However, we stress that this estimate is solely based on the comparison of the results obtained from both fitting routines. We will later find that discrepancies between the positions extracted from the fitting routines and a second tracking method that we introduce in the next subsection are also of this order of magnitude, thus corroborating our estimate of the uncertainty. Since the exact vortex locations are unknown, it appears not feasible to determine an exact error of the extracted positions. In particular, the uncertainty reported by the fitting routine itself cannot be used for obvious reasons since the shape of the vortex-induced density depletion is clearly not entirely captured by a Gaussian.

To further check if the estimate of ± 0.02 grid points for the error is sensible, we use the following toy model. We take the static background solution for the superfluid density on the quadratic grid and imprint two upside-down Gaussians at random, inter-mesh, positions onto it. For the numerical parameters of the Gaussians we take values similar to the ones we obtain from the fitting routine above. We proceed as if these density depletions were vortices and use the procedure with the approximate analytic GPE vortex solution (6.2) outlined above to find their locations on the numerical (x_1, x_2)-grid and the compare the outcome with the analytically known positions of the density depletions. We repeat this several times for different initial random positions in order to analyse whether the discrepancies depend on the locations of the density depletions relative to the integer grid points. Moreover, we proceed likewise with the roles of the Gaussian and GPE vortex solutions interchanged. We find that for both scenarios the deviations between the analytically known positions and the ones extracted from the fitting routine are again of the order of ± 0.02 grid points. While this is only a toy model, it nevertheless shows that the error estimate for the vortex locations is reasonable.

The reason we use the Gaussian (6.1) for all practical purposes in the fitting routine and not the approximate GPE vortex solution or other alternatives is its

analytical simplicity and the fast numerical convergence of the fitting algorithm. In figure 6.3 we illustrate such an exemplary fit to the superfluid density profile $n(\boldsymbol{x})$. We note that we indeed fit the entire dipole system as explained above but restrict the plots in figure 6.3 to only one of the vortices in order to aid the readability. In the upper panel, the fit (dashed red line) to the condensate-density depletion (blue dots) is shown in a cross section of the vortex along the x_1-axis for fixed x_2 grid position. The chosen value of x_2 is the nearest integer grid position to the x_2-location obtained from the fitting routine. The fit clearly captures the steepest segments of the flanks to high accuracy, but does not reach the minimum of the depletion. Remarkably, this is not necessary to track the location of the minimum. In addition, we point out that only very few data points on the flanks are required to accurately determine the vortex location. In the lower panel of figure 6.3 we show a contour plot of the same fit to the vortex-induced density depletion. The colour coding for the condensate density is the same as above in figure 6.1 and the contour lines of the fit are displayed in grey-scaling. The isolines of the Gaussian are not perfectly circular due to the discrete nature of the numerical grid. This concerns in particular the innermost contour line.

The Gaussian tracking algorithm has the great advantage of being numerically easy to implement and requires very little computation time. It can be applied to vortices that are either spherically symmetric or elliptically deformed as both geometries can be captured by Gaussians. We have seen above in section 6.2 that these requirements are satisfied for most of the dipole evolution. However, as soon as the vortices deform non-elliptically and the density depletions begin to overlap, this tracking algorithm breaks down. The reason for this is simply that a Gaussian can no longer account for such strong non-symmetric deformations. The fits can no longer accurately capture the flanks and thus fail to interpolate to the real minima. For the evolution of a single vortex dipole (with the numerical parameters as discussed above), non-elliptical deformations set in approximately 30 unit timesteps before the vortices annihilate, *cf.* our discussion in section 6.2. At that time, the vortices are approximately eleven grid points apart[6]. To determine the vortex trajectories in the next section, we can therefore rely on the Gaussian-fit tracking routine only for vortex–anti-vortex separations larger than $d(t) = 11$ grid points. As a side remark, we note that we employ our analysis of the dipole dynamics only for times later than $t = 0$, when the vortices have fully developed their characteristic shape in the condensate density.

---

[6]This holds true for our present choice of the grid spacing, given by $l = 2/7$. Upon changing the grid spacing and thus the vortex resolution, the vortex–anti-vortex separation at which the Gaussian fitting routine breaks down changes as well. For $l = 1/8$, our choice in the next chapter, the fitting routine breaks down at a separation of $d(t) = 25$ grid points. This is crucial for our analysis and has to be taken into account in chapter 7.
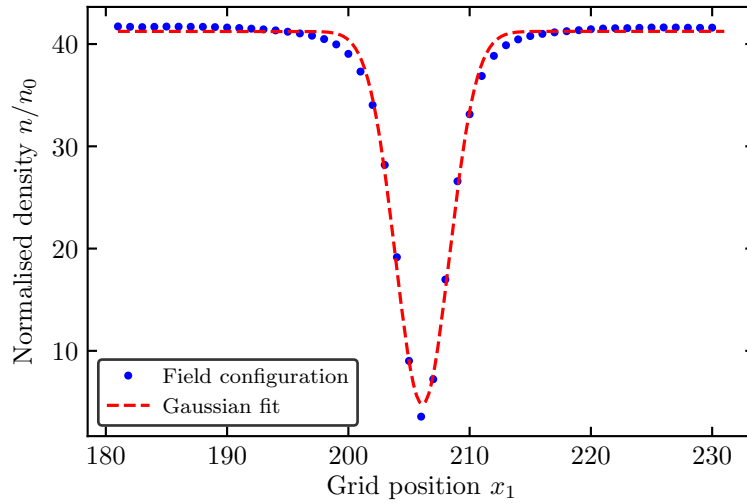
(i) Cross section of the superfluid density (blue dots) and the Gaussian fit (dashed red line) through the vortex along the x_1-axis for fixed $x_2 = 256$.
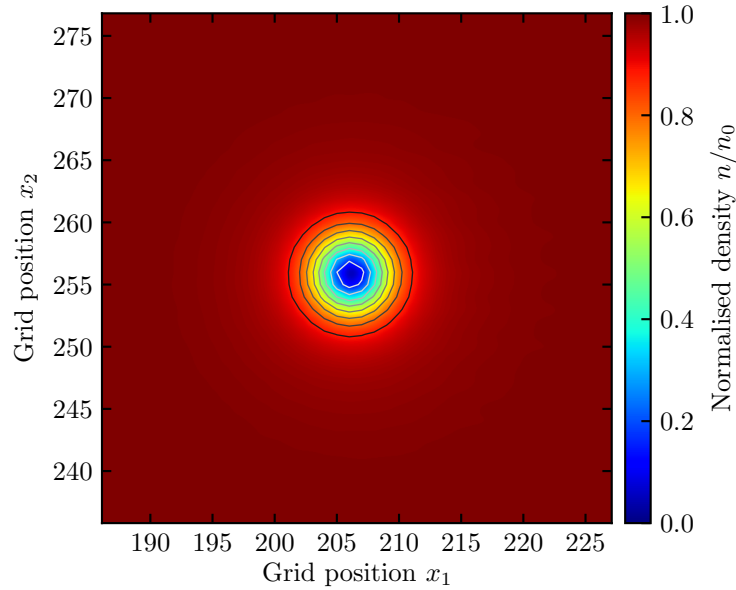
(ii) Two-dimensional contour plot of the Gaussian fit to the vortex. The superfluid density is colour-coded as in the previous figures, and the contour lines of the fit are illustrated in grey-scaling. Due to the discrete nature of the numerical grid the contour lines are not perfectly circular.

Figure 6.3: Illustration of a Gaussian fit to a spherically symmetric vortex-induced density depletion in the superfluid used in the tracking algorithm to locate the vortices on the numerical grid. In the fitting routine we capture the vortex and the anti-vortex simultaneously. For conciseness we only show the anti-vortex here.

6.3.2 Newton–Raphson Tracking Algorithm

In the previous subsection we have seen that there is a need for an alternative vortex tracking algorithm in the regime of overlapping density depletions. A reliable method to locate vortices on the numerical grid even for strongly deformed vortex-induced density depletions around their cores is given by the Newton–Raphson (NR) method. The NR method is a standard algorithm for numerical root-finding and therefore ideally suited to locate vortices on our two-dimensional grid. In the literature, the NR method is already a well-established vortex tracking routine, *cf.* [286, 287, 291]. In the following, we briefly outline the main aspects of the corresponding algorithm and discuss its advantages and drawbacks as compared to the Gaussian fitting routine.

On a fixed timeslice, the Newton–Raphson method locates the vortices by numerically finding the corresponding zeros in the superfluid density $n(\boldsymbol{x}) = |\psi(\boldsymbol{x})|^2$. More specifically, the method is based on an iterative procedure that finds the roots of the complex-valued order-parameter field ψ, where for now we use

$$\psi(\boldsymbol{x}) = \begin{pmatrix} \mathrm{Re}[\psi(\boldsymbol{x})] \\ \mathrm{Im}[\psi(\boldsymbol{x})] \end{pmatrix}, \tag{6.3}$$

instead of $\psi(\boldsymbol{x}) = \mathrm{Re}[\psi(\boldsymbol{x})] + \mathrm{i}\,\mathrm{Im}[\psi(\boldsymbol{x})]$, allowed by the isomorphism between $\mathbb{C}$ and $\mathbb{R}^2$ as additive groups. Starting from an initial guess for the vortex position $\boldsymbol{x}_i^{\mathrm{g}}$, the next better approximation is obtained from a Taylor expansion of $\psi(\boldsymbol{x})$ about $\boldsymbol{x}_i^{\mathrm{g}}$,

$$0 = \psi(\boldsymbol{x}_i) = \psi(\boldsymbol{x}_i^{\mathrm{g}}) + J(\boldsymbol{x}_i^{\mathrm{g}}) \cdot (\boldsymbol{x}_i - \boldsymbol{x}_i^{\mathrm{g}}) + \mathcal{O}\left[(\boldsymbol{x}_i - \boldsymbol{x}_i^{\mathrm{g}})^2\right]. \tag{6.4}$$

Here, we have used $\psi(\boldsymbol{x}_i) = 0$, for $\boldsymbol{x}_i$ the location of the i-th vortex, and introduced the Jacobian matrix,

$$J(\boldsymbol{x}) = \begin{pmatrix} \mathrm{Re}[\partial_{x_1}\psi(\boldsymbol{x})] & \mathrm{Re}[\partial_{x_2}\psi(\boldsymbol{x})] \\ \mathrm{Im}[\partial_{x_1}\psi(\boldsymbol{x})] & \mathrm{Im}[\partial_{x_2}\psi(\boldsymbol{x})] \end{pmatrix}. \tag{6.5}$$

If the Jacobian has full rank it can be inverted to solve (6.4) for the vortex position $\boldsymbol{x}_i$,

$$\boldsymbol{x}_i = \boldsymbol{x}_i^{\mathrm{g}} - J^{-1}(\boldsymbol{x}_i^{\mathrm{g}}) \cdot \psi(\boldsymbol{x}_i^{\mathrm{g}}) + \mathcal{O}\left[(\boldsymbol{x}_i - \boldsymbol{x}_i^{\mathrm{g}})^2\right]. \tag{6.6}$$

Iterating this procedure, $\boldsymbol{x}_i$ converges to the desired true vortex position with subplaquette precision. To evaluate the Jacobian at inter-mesh points, we Fourier interpolate the field ψ on the entire (x_1, x_2)-grid. This also ensures that the tracking algorithm respects the periodicity of the field configuration. Remarkably, the NR algorithm requires no prior assumptions with regard to the shape or symmetry of the density depletions of the vortices. To ensure that the tracked zero $\boldsymbol{x}_i$ indeed corresponds to the location of the i-th vortex, one has to check explicitly if the phase of the order-parameter field winds around this position by $\pm 2\pi$. As initial guess $\boldsymbol{x}_i^{\mathrm{g}}$

for the vortex location, we use the approximate position obtained from tracking its phase winding. It turns out that plaquette-precision for the initial guess is sufficient to ensure convergence of the NR algorithm. We stop the iterative procedure once the condition $n(\boldsymbol{x}_i) < 10^{-8}\, n_0$ is satisfied.

In general, the Newton–Raphson method has the advantage of being universally applicable for the tracking of vortices, independent of the background geometry of the condensate and the vortex shape. This makes the algorithm superior to the Gaussian fitting routine during the late-time regime of the dipole evolution in our studies, when the density depletions strongly deform and overlap. On the downside, the success of the convergence is dependent on the initial guess for the vortex position. If the initial guess deviates too strongly from the real solution, the algorithm might get caught in an infinite loop. Furthermore, to ensure accuracy of the algorithm, the Fourier interpolation of the field ψ and its derivatives requires a large number of grid points. For our purposes in this work, these drawbacks are negligible. Taking the approximate position from locating the phase winding of the vortex core as initial guess ensures convergence of the algorithm. In addition, we find that for grid sizes of 512×512 points the uncertainties from the Fourier interpolation are negligibly small. Nevertheless, the Newton–Raphson method has the disadvantage of being numerically much less efficient than the Gaussian fitting routine. While all steps of the tracking algorithm are in principle straightforward to implement, the number of recurrences of the numerical operations are very time demanding. In particular, at every step of the iterative procedure the three fields $\psi, \partial_{x_1}\psi$ and $\partial_{x_2}\psi$ have to be Fourier interpolated and evaluated at position $\boldsymbol{x}_i$ and, in addition, the 2×2 Jacobian matrix has to be inverted. Despite the fast (in principle) quadratic convergence, this causes the algorithm to be distinctly slower than the Gaussian fitting routine.

In figure 6.4 we directly compare the vortex trajectories extracted from a simulation of the dynamics a vortex dipole using the Newton–Raphson method with those extracted from the same simulation using the Gaussian fitting routine. We apply both algorithms at every unit timestep of the evolution. The initial condition for the dipole evolution is again given by the exemplary configuration of figure 6.1, *i.e.*, a vortex dipole horizontally aligned at $x_2 = 256$ with a size of $d_0 = 100$ grid points. We find that for all vortex–anti-vortex separations larger than eleven grid points, the two tracking algorithms yield the same results for the vortex locations within a maximal absolute deviation of 0.02 grid points. This corroborates our earlier discussion regarding the uncertainty-estimate for the vortex locations from the Gaussian fitting routine. In figure 6.4 the uncertainty is far smaller than the point sizes and therefore not explicitly indicated. During the late-time regime, *i.e.*, for dipole sizes $d(t) < 11$, figure 6.4 clearly displays the break-down of the Gaussian fitting algorithm. The corresponding vortex trajectories continuously bend and finally advance almost in parallel. Evidently, this is not how the vortices behave in our simulation, see also figure 6.2 for comparison. The NR method, on the other hand, accurately captures how the vortices approach and finally annihilate.
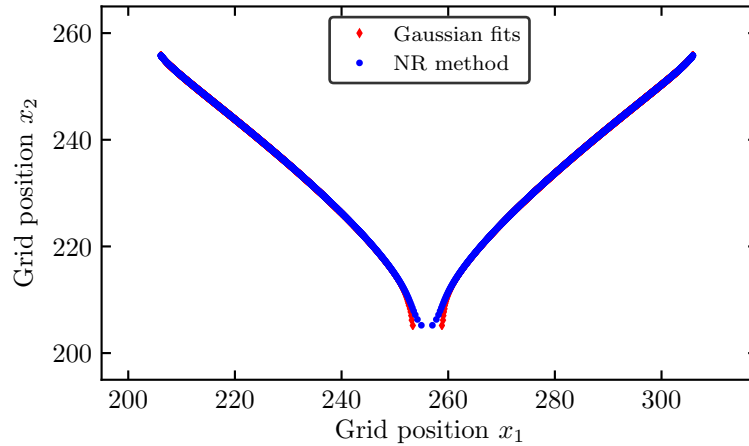
Figure 6.4: Vortex trajectories extracted from the dipole dynamics using the Gaussian fitting routine (red diamonds) and the Newton–Raphson method (blue dots). During the final stage of the evolution the two tracking algorithms yield strongly disagreeing vortex locations, indicating the break-down of the Gaussian fitting routine for strongly deformed and overlapping density depletions. At earlier times, the positions obtained from both methods are in excellent agreement with deviations significantly smaller than the point sizes.

6.3.3 Sub-Plaquette Vortex Tracking

We are now equipped with two tracking algorithms that allow us to determine the grid positions of the moving vortex cores to high accuracy with sub-grid-spacing resolution. To optimise accuracy as well as numerical efficiency, we combine both methods to extract the vortex locations in our investigations in the following chapters. Numerically, the Gaussian fitting routine is distinctly faster then the NR method. Hence, for vortex–anti-vortex separations larger than $d(t) = 11$ grid points we employ the Gaussian fitting routine, as in this regime the two methods yield, within the given uncertainty, the same results for the vortex locations. For smaller separations, on the other hand, when the dipole system merges and the vortices deform, we use the Newton–Raphson method. We recall from our discussion in section 6.2 that this regime makes up only about 1.2% of the total dipole evolution for an initial vortex–anti-vortex separation of $d_0 = 100$ grid points. However, this fraction obviously grows for smaller initial separations.

The combination of the two tracking procedures allows us to determine the positions of the vortices in a precise and quasi-continuous manner throughout their entire evolution, on every fixed timeslice. We contrast this to the standard plaquette technique of locating the phase windings of the vortices, where the positions can
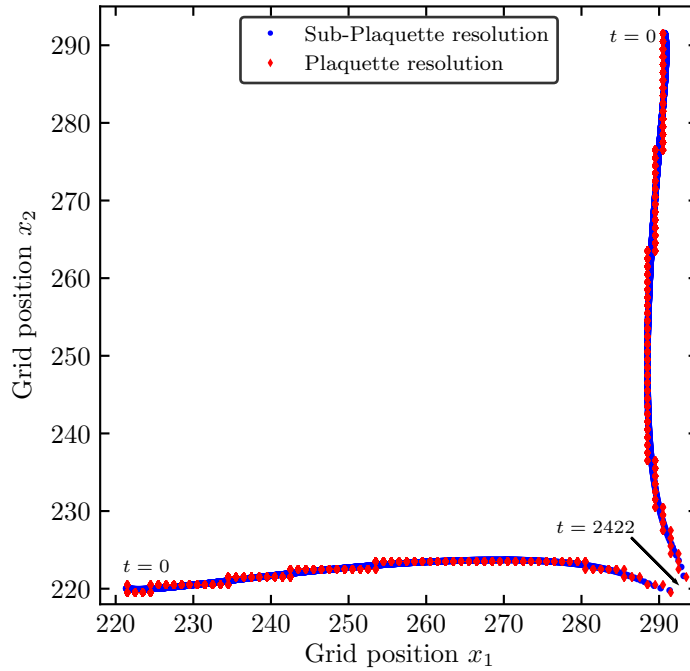
Figure 6.5: Comparison of the vortex trajectories extracted from the dipole dynamics from our combined tracking routine (blue dots) and the standard plaquette technique of locating the phase windings (red diamonds). This illustrates the quasi-continuous nature of the vortex trajectories which is a crucial prerequisite for many investigations throughout this work.

only be extracted with an uncertainty of one grid point. For the trajectories, this implies a stair-like structure since the vortices can only jump from one integer grid point to another. For an exemplary dipole evolution, we show a comparison of the vortex trajectories obtained from our tracking procedure (blue dots) and the standard plaquette technique (red diamonds) in figure 6.5. We apply both algorithms at every unit timestep of the evolution. For a better visualisation of the differences between the two methods, we employ a slightly different initial configuration for the dipole than so far in this chapter. To be precise, we rotate the configuration displayed in figure 6.1 by $\pi/4$ counter-clockwise such that the vortices are aligned along the diagonal of the (x_1, x_2)-grid. Subsequently, we evolve the system in time until the vortices have annihilated. Figure 6.5 clearly illustrates our description of the stair-like and quasi-continuous nature of the respective trajectories. Evidently, the gain due to the sub-plaquette tracking procedures is immense and allows us to resolve the characteristic behaviour of the dipole to much higher accuracy. It also allows us to study the velocities and accelerations of the vortices which would only be discrete for the stair-like trajectories. Furthermore, we will find in chapter 7 below

that only due to the strong increase in precision we can successfully match the dipole dynamics in DGPE and holography. Hence, the tracking procedures set the basis and are a crucial prerequisite for all of our investigations in the following chapters. Henceforth, we refer to the combination of the tracking methods as one tracking routine or tracking procedure. While this eases the notation, we nevertheless keep in mind the change in algorithms at short distances (or late times).

To conclude this section, let us give an empirical estimate for the advantages of the sub-plaquette tracking methods over the phase-winding plaquette-technique. For times distinctly earlier than the late-time regime, it takes approximately 30 unit timesteps for one vortex to move as far as one grid spacing. On average during the early stages of the evolution, every red diamond of the stair-like trajectory in figure 6.5 therefore corresponds to 30 unit timsteps. From the sub-plaquette tracking algorithms, on the other hand, we obtain 30 distinct positions (blue dots) at inter-mesh points, demonstrating the quasi-continuous nature of the extracted trajectories. With proceeding time, however, the vortex velocities increase and the number of timesteps it takes the vortices to move as far as one grid spacing reduces gradually. Consequently, the increasing velocity diminishes the differences between our tracking procedure and the plaquette technique of locating the vortices, *cf.* figure 6.5. In particular, during the late-time regime the vortices move of the order of one grid point per unit timestep as evidenced by the reduced density of data points in this regime in the figure above. In order to track the vortices such that the spatial separation of the vortex locations at two consecutive times is of the same order throughout the evolution, we have to track the vortices more frequently than at every unit timestep during the final stage of the evolution. However, for now the given precision, also during the late-time regime of the evolution, is sufficient for our purposes, and we postpone a discussion of the trajectories in the late-time regime to chapter 8.

Finally, let us stress that we cannot unequivocally validate our results for the vortex locations. However, the strong consistency in the results obtained from the various tracking algorithms, *i. e.*, the fitting routines with different profiles and the NR method, as well as its consistency with our expectation and the observed behaviour of the vortices, provides strong evidence that the results are reliable and highly accurate.

6.4 Phase Healing

In this final section, we want to point to an important feature of the dipole dynamics studied above that is essential also for our investigations in the next chapters and that highlights the increase in precision gained from our tracking routine. Figure 6.5 clearly indicates that during the initial propagation of the vortices their trajectories bend slightly outwards. Only after some time we find the vortices to approach each other on inward-bended curves. The outward bending can only be resolved due to the sub-plaquette resolution of the tracking routine since its magnitude is

smaller than the distance between two grid points (given our choice for the grid spacing of $l = 2/7$). Further investigations of this effect show that it occurs for all initial vortex–anti-vortex separations and arrangements of the vortices on the (x_1, x_2)-grid. A priori, such a behaviour of the vortices is not expected. Indeed, one would intuitively rather expect the vortices to approach each other on inward-bended curves, just like they do after the slight but distinct outward bending. In the following, we present an explanation for the observed behaviour.

The outward bending can be attributed to the preparation of the initial vortex configuration used in our simulations. We imprint the two vortices independently onto the background condensate by linearly superimposing their phase-winding structures and multiplying the sum into the scalar field. For a 'proper' vortex dipole, in contrast, the phase configurations of the vortex and anti-vortex are coupled. A vortex dipole constitutes a unique solution to the equations of motion (3.9)–(3.11), differing from the linear superposition that we imprint in our initial condition. Thus, in our preparation of the initial vortex configuration we omit the important fraction of the dipole phase configuration that couples the vortex and anti-vortex phase configurations. This missing part causes the observed outward bending of the vortices.

As we propagate the system in time, we find that the phase configuration of the dipole 'heals itself'. Indeed, during the evolution of the vortices, the individual vortex and anti-vortex phases dynamically couple and transition into a proper dipole solution. Once this process terminates, the vortices exhibit the expected behaviour of a dipole, with approaching and inward-bended trajectories. We call this initial process 'phase healing' and refer to the corresponding time interval as the early-time regime of the evolution. We stress that the phase healing is not a feature specific to the holographic superfluid, nor does it give any insight into the dynamics of vortices in the holographic superfluid. It has only to do with how we initialise the vortex configuration and we will find below in chapter 7 that it also occurs in the evolution of vortex dipoles in the Gross–Pitaevskii equation. In addition, similar effects have been found before in the preparation of soliton solutions[7] in the GPE [295, 296].

In order to illustrate that the missing fraction of the phase configuration indeed causes the vortices to bend outward, we compare the non-coupled phase structure prepared in the initial dipole configuration to the phase structure of the proper vortex-dipole solution. Our procedure is as follows. We start from a typical initial vortex configuration such as the one we have displayed in figure 6.1 and evolve the dipole system in time until the phase has fully healed and the vortices move along inward-bended trajectories. We then take a snapshot of the phase configuration and compare it with the linearly superimposed phase-winding configuration for the dipole system that we would imprint if the current location of the vortices was taken as new initial configuration. Subtracting the latter from the former yields the initially 'missing' part of the phase configuration, *i. e.*, the component of the proper phase configuration that couples the vortex and anti-vortex phases. If this

---

[7]Solitons are localised depletions in the condensate density with a phase jump across their respective minimum. See *e. g.* [294] for details.
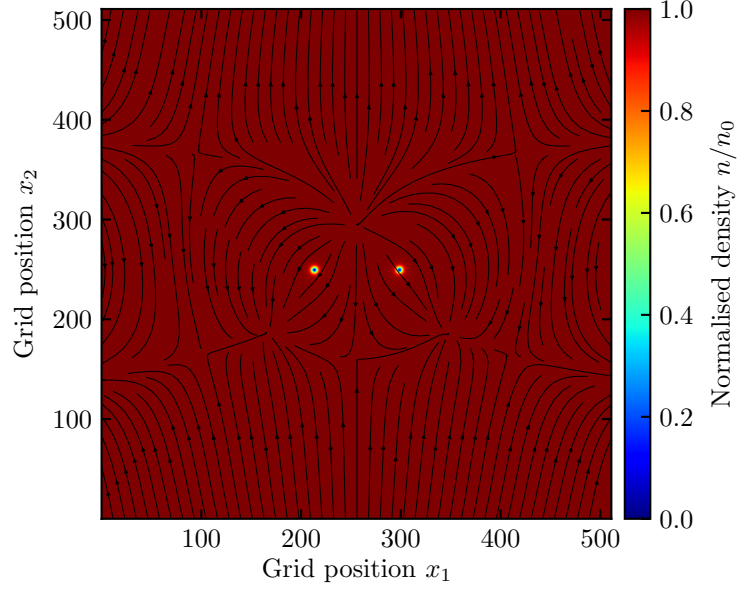
Figure 6.6: Flow lines illustrating the origin of the initial outward bending of the vortex trajectories in the dipole dynamics. In the initial preparation of the vortex configuration we linearly superimpose the phase-winding structures of the vortex and anti-vortex. For a proper vortex dipole, however, the phase structures are coupled, yielding an additional component to the total phase configuration. The shown flow lines result from the negative gradient of this missing component which, if present, would compensate the outward bending.

phase configuration is not taken into account in the preparation of the vortices, the resulting flow field causes the vortex trajectories to initially bend outward. This is illustrated in figure 6.6. Here, we plot the streamlines of the negative gradient field of the missing phase configuration on the (x_1, x_2)-grid. Evidently, if the corresponding sign-reversed phase configuration was included in the initialisation of the vortices, it would counteract the outward-driving flow lines and the vortices would follow inward-bended mutually approaching trajectories. In addition to the phase configuration in figure 6.6, we also plot the normalised density modulation $n(\boldsymbol{x})/n_0$ at the same time at which we take the snapshot of the phase configuration. Another interesting feature of the flow lines in figure 6.6 is that away from the dipole the components of the streamlines along the transverse direction of the vortices point in the direction opposite to the centre-of-mass motion which is directed along the negative x_2-axis. The motion of the vortices along this direction is therefore slowed down. In section 8.2 we show this explicitly. We are not aware of a closed-form expression for the coupled phase configuration of a proper vortex dipole. This is

why, throughout this part of the thesis, we imprint vortices just as discussed above and for the analysis of the dipole motion neglect the early phase-healing regime.

We find that the phase healing depends mildly on the initial separation of the vortices and takes slightly longer if the vortices are further apart. We confirm this explicitly in our quantitative analysis of the dipole kinematics in chapter 8. For the initial vortex configuration of figure 6.1, *i. e.*, a horizontally aligned vortex–anti-vortex pair with a separation of $d_0 = 100$ grid points, the phase healing takes approximately $\Delta t = 600$ unit timesteps. Note that this makes up a considerable fraction, namely $\sim 25\%$, of the total dipole evolution, taking $\Delta t = 2422$ unit timesteps. Since the phase healing is a continuous process, it is not possible to pinpoint an exact endpoint. However, one can estimate it by studying at what point the outward bending ends. In all following investigations of Part I, the consequences of the phase healing on the kinematics of the vortex dipole have to be taken into account. Indeed, if they were not taken into account and therefore not excluded from certain analyses, they would spoil the results. For instance, while the same effect of the phase healing occurs in our GPE simulations in chapter 7 just as in holography, it is naturally not accounted for in the HVI equations. Thus, the phase-healing regime has to be explicitly excluded from the matching procedure with the HVI equations in the next chapter. We comment further on this as we go along in section 7.3.

The above discussion clearly illustrates the great importance of using a sub-plaquette tracking routine to extract the vortex trajectories from the numerical simulations. If we tracked the vortices using plaquette techniques only, we could not resolve the phase-healing regime. Moreover, most the analyses of this thesis would not be possible. Our tracking routine is also a key improvement of our analysis of the dipole dynamics on the results of [163]. Indeed, the authors of [163] only employ a plaquette-precision tracking routine which therefore implies, *inter alia*, that they cannot resolve the phase-healing regime that is present in their simulations as well which we infer from their set of initial vortex configurations. Consequently, they do not exclude the corresponding time interval from their analysis of the vortex–anti-vortex separation and in particular its functional dependence on time. In chapter 8 we show that excluding the early-time regime is in fact an essential aspect of the analysis. For further discussions regarding the comparison of our results with [163], see section 8.1.

7 Quantification of Dissipation in the Holographic Superfluid

In the previous chapter 6, we have qualitatively studied the dynamics of vortex dipoles, and introduced a high-precision tracking routine that allows us extract quasi-continuous vortex trajectories from our real-time simulations. We now begin with our quantitative analysis of the dipole dynamics.

The goal of the present chapter is to quantitatively characterise the holographic superfluid in the presence of vortices with respect to its dissipative nature. The guiding question one should keep in mind throughout the next sections is what physical parameter regime the holographic framework captures and how the observed vortex dynamics compares to the analogue in real-world superfluids such as liquid helium and Bose–Einstein condensates. In order to answer this question, we match solutions of the dissipative Gross–Pitaevskii equation (DGPE) to the dynamics of a vortex dipole in the holographic superfluid. To be specific, we tune the free DGPE parameters so that the vortex sizes as well as the spatio-temporal vortex trajectories in both theories agree to high accuracy. Furthermore, we compare the matched dipole dynamics to solutions of the Hall–Vinen–Iordanskii (HVI) equations for the mechanical motion of point vortices in dissipative superfluids. Using known relations between the DGPE and the HVI equations, we extract friction coefficients characterising the dissipation of the holographic superfluid. Finally, we compare our numerical results for the friction coefficients of the holographic superfluid to experimentally accessible superfluids such as superfluid helium and cold atomic Bose gases. For such systems we infer the friction coefficients from measurements of the vortex diffusivity.

This chapter is organised as follows. In section 7.1, we first introduce the (dissipative) Gross–Pitaevskii model and comment on its applicability in the description of cold Bose gases in two as well as three spatial dimensions. Furthermore, we briefly comment on our numerical implementation of the DGPE. In section 7.2 we shift focus and review the HVI equations for a single vortex dipole. In particular, we use known relations between the DGPE and the HVI equations to relate their parameters. We then proceed to the main part of this chapter in section 7.3 and match solutions of the DPGE to the dipole dynamics in the holographic superfluid. Furthermore, we show that within a certain regime, the matched dipole trajectories also obey the HVI equations. In the final section 7.4, we interpret our results with regard to the experimental relevance of the holographic description of vortex dynamics in a superfluid.

For our investigations in this chapter we slightly adapt the numerical parameters

of the holographic system and change the grid spacing from $l = 2/7$ to $l = 1/8$, while simultaneously keeping the number of grid points fixed. In this setting, vortex-induced density depletions are resolved by a larger number of grid points than in the previous chapter which we find convenient for our matching procedure. With regard to physical observables such a rescaling has no consequence. In order to distinguish parameters denoted by the same letter in holography and DGPE, we denote the respective DGPE parameters with a tilde.

The content of this chapter is mainly based on our publication [258] and some parts are taken verbatim from it. For a better embedding in the context of this thesis, we have further added and modified several parts.

7.1 The (Dissipative) Gross–Pitaevskii Model

In this section, we briefly summarise the implications of the (dissipative) Gross–Pitaevskii model for the description of cold Bose systems. For a concise discussion see, *e. g.*, [214]. The Gross–Pitaevskii equation is a non-linear Schrödinger equation in the mean-field regime for the order-parameter field $\psi(t, \boldsymbol{x})$ of a cold undamped Bose gas. More relevant for our studies in this thesis, the dynamics of a cold Bose gas subject to damping due to interactions between the condensate and the non-condensate excitations, can be described by the dissipative Gross–Pitaevskii equation (DGPE) for the order-parameter field. Reinstating $\hbar$ for the moment, the DGPE for a single-component Bose system is given by

$$\hbar\, \partial_t \psi(t, \boldsymbol{x}) = -\,(\mathrm{i} + \gamma) \left[-\frac{\hbar^2}{2M}\boldsymbol{\nabla}^2 + g\,|\psi(t, \boldsymbol{x})|^2 - \tilde{\mu} \right] \psi(t, \boldsymbol{x})\,. \qquad (7.1)$$

Here, M is the mass of the bosons, g characterises their interactions, γ is a dimensionless phenomenological damping parameter quantifying the dissipation, and $\tilde{\mu}$ is a chemical potential representing a constant shift of the single-particle energy. For $\gamma = 0$, equation (7.1) reduces to the (non-dissipative) standard Gross–Pitaevskii equation (GPE).

To match a solution of the dissipative GP (DGP) model to the dipole dynamics in the holographic superfluid, we numerically solve equation (7.1) in two spatial dimensions. However, as written above, equation (7.1) is likewise applicable in three spatial dimensions if the dimensionality of the fields and parameters is adjusted accordingly. In the following, we set the stage for the matching procedure in this chapter and briefly comment on the conditions under which the DGPE (7.1) or more generally the GPE is applicable to the description of cold Bose gases. Moreover, for a comparison of our numerical simulations with results obtained in experiments on the dynamics of vortices in Bose gases performed in quasi-two-dimensional trapping potentials, we need to distinguish different conditions in the crossover regime between strictly two and strictly three spatial dimensions.

Quite generally, the GP model provides a quantitatively valid description of dilute ultracold, *i. e.*, condensed – or 'degenerate' – Bose gases, typically prepared

with alkali atoms. Dilute means that the length scale characterising the collisional interactions is much smaller than the mean inter-particle spacing. While at very low temperatures ($\tilde{T} \ll \tilde{\mu}$), the GP equation itself provides a good approximation of the condensate dynamics, a self-consistent evaluation of the combined dynamics of the condensate field ψ and the thermal component is required at higher temperatures, and is increasingly difficult the closer $\tilde{T}$ is to the critical temperature of Bose–Einstein condensation. An even more intricate problem is set by non-dilute systems such as superfluid helium where strong quantum fluctuations and depletion of the condensate, also at very low temperatures, limit the applicability of equation (7.1) and one generically resorts to other approaches, in particular the Tisza–Landau two-fluid model, *cf.* our discussion in section 3.1.

The atoms' two-body interactions at the energies prevailing in dilute systems are well captured by a single parameter, the *s*-wave scattering length[1] a, with values of $a \sim 3\,\mathrm{nm}$ and $a \sim 5\,\mathrm{nm}$ for the most commonly used elements sodium ^{23}Na and rubidium ^{87}Rb, respectively. The *s*-wave approximation implies that the two-body interactions entering the many-body field theory are local in space and time, meaning that the ultraviolet length scale below which this locality is violated corresponds to collision energies much higher than those attained in the low-temperature system, see, *e. g.*, [298].

However, the actual value of the respective GP coupling parameter g and the conditions for mean-field and perturbative approximations to be valid depend on the dimensionality of the system. Let us, for simplicity, assume that the Bose system described by (7.1) is confined within a d-dimensional box of volume $\mathcal{V}$ with periodic boundary conditions such that its ground state is characterised by a uniform mean-field condensate density $n_0 = \mathcal{V}^{-1} \int_{\mathcal{V}} \mathrm{d}\boldsymbol{x}\, |\psi(t,\boldsymbol{x})|^2 \equiv \|\psi\|^2$. For gases trapped in three-dimensional volumes $\mathcal{V}$ ranging between 10^{-13} and $10^{-16}\,\mathrm{m}^3$, typical experimental densities $n_{d=3}$ are between 10^{12} and 10^{15} particles per cm^3 [298]. In three spatial dimensions, the interactions are characterised by the coupling constant $g = g_{\mathrm{d}=3} = 4\pi\hbar^2 a/M$, with the three-dimensional *s*-wave scattering length a.

For a given coupling g and a background condensate density n_0 in d dimensions, the characteristic length scale of the condensate is the healing length

$$\tilde{\xi} = \frac{\hbar}{(2Mgn_0)^{1/2}} \,. \tag{7.2}$$

$\tilde{\xi}$ is the scale on which the density rises to the uniform background value n_0 near an infinite potential wall. Likewise, as we have discussed in the previous chapter, $\tilde{\xi}$ sets the length scale on which the density around a vortex core 'heals' to its background value, *i. e.*, it determines the diameter of a vortex-induced density depletion. Note that (7.2) holds for all spatial dimensions, with g and n_0 adjusted accordingly.

An important parameter in three-dimensional cold Bose gases is the diluteness $\zeta = \sqrt{n_{\mathrm{d}=3}a^3}$, which depends on the ratio of the scattering length a and the density of the atoms which is inversely related to the mean inter-particle separation. The

---

[1]For a pedagogical introduction to low-energy quantum-mechanical scattering theory, see [63, 297].

diluteness needs to be small for a mean-field description in terms of the DGPE (7.1) or including perturbative corrections to equation (7.1), to be valid in three spatial dimensions. In dilute alkali gases it is $\zeta \sim 10^{-3}$ while in superfluids like ^{4}He it is of order unity.

More relevant for the settings discussed in this thesis, various experimental realisations with a quasi-two-dimensional trapping geometry have been achieved, with a transverse confinement down to a (atomic) cloud thickness of $\sigma \sim 10^2 \ldots 10^3$ nm [32, 33, 40, 230, 250, 251, 299]. As this thickness is still considerably larger than the respective three-dimensional scattering lengths a of the alkali gases, the coupling entering the DGPE (7.1) in such a quasi-two-dimensional setting is given by $g = \sqrt{8\pi}\hbar^2 a/(M\sigma)$ [40, 219, 300]. We point out that while generic settings are characterised by the small dimensionless ratio a/σ, substantially larger values of g are possible near a so-called confinement-induced resonance [301]. Typical experimental two-dimensional densities are $n \sim 10^{13}$ m^{-2} [32, 33, 40], implying healing lengths (*cf.* equation (7.2)) $\tilde{\xi} = (4\sqrt{2\pi}an/\sigma)^{-1/2}$ between 0.4 and 2 μm, which are usually smaller than or similar to the cloud thickness σ. Such cloud geometries are still three-dimensional for the collisions between particles. Hence, if also the particle motion in the confined direction occupies many transverse trap levels, the validity of mean-field and perturbative approximations is ensured by a small three-dimensional diluteness parameter $\zeta = \sqrt{na^3/\sigma}$, with two-dimensional density n.

In modern experiments, however, only the lowest transverse trap mode is populated in typical quasi-two-dimensional settings and hence the states are strongly localised in the transverse direction. This implies that perturbation theory is controlled by the small dimensionless parameter $\zeta_{d=2} = a/(\sqrt{2\pi}\sigma)$ which typically takes values between 10^{-2} and 10^{-3} and does not depend on the particle density [32, 33, 40, 298]. For even tighter confinement, *i. e.*, approaching the two-dimensional limit, the parameter $\zeta_{d=2}$ becomes sensitive to the density of the condensate. In this case, the expansion parameter is instead of $\zeta_{d=2} = a/(\sqrt{2\pi}\sigma)$ given by $\zeta_{d=2} \sim 1/|\ln(na_{d=2}^2)|$, with $a_{d=2} = \sigma\sqrt{\pi/B}\exp\{-\sqrt{\pi/2}\,\sigma/a\}$, being the respective two-dimensional scattering length, where $B \simeq 0.916$ is Catalan's constant. Thus, $\zeta_{d=2} \sim 1/|\ln(n\sigma^2\pi/B) - \sqrt{2\pi}\,\sigma/a|$, which accounts for the confinement-induced resonance [40, 300–302].

In the following we finally comment on the dissipative damping of the condensate order-parameter field ψ caused by the interactions, which is taken into account in the DGPE (7.1) by a non-zero value of the dimensionless phenomenological damping parameter γ.

If the temperature $\tilde{T}$ of the condensed Bose gas is large compared to the zero-point energy but well below the critical temperature of the phase transition, which in two spatial dimensions is of BKT type, the interactions between the condensed and thermal particles give rise to exponential damping in the limit of long evolution times, once initial effects have been damped out which may arise, *e. g.*, from the particular quench bringing the system out of equilibrium. Within a perturbative expansion of the time-dependent self-energy, the damping parameter γ results, in

two-particle-irreducible two-loop approximation, quadratic in g and thus a, as [249]

$$\gamma \simeq \frac{12\,Ma^2 k_\mathrm{B}\tilde{T}}{\pi\hbar^2}\,.\tag{7.3}$$

Here we have for the moment re-introduced the Boltzmann constant k_B. We note that, if we take the chemical potential $\tilde{\mu}$ in (7.1) to equal the energy eigenvalue $\tilde{\mu} = gn_0$ of the zero-momentum eigenstate of the stationary GPE for a homogeneous gas at zero temperature, all modes except the zero-mode are damped for $\gamma > 0$. Hence, obtaining self-consistent stationary solutions for a condensate at non-vanishing temperatures in general requires to go beyond the DGPE (7.1). One possibility is the inclusion of a noise term and thus the extension of (7.1) to a stochastic differential equation [303, 304], or the coupling of the GPE to the dynamics of higher-order correlators [305, 306] which account for a self-consistent treatment of condensed and non-condensed particles. If the temperature is too high for the perturbative estimate (7.3) of γ to apply, such methods have been used to obtain an estimate. We comment further on this in section 7.4 below.

But even if the estimate (7.3) is not valid, the DGPE can provide a quantitatively good description of dissipative dynamics as long as the system is away from stationarity and as long as the thermal fraction, which gives rise to the dissipation, does not become significantly disturbed by the evolving condensate field. As we are, here, primarily interested in the matching of the vortex dynamics, subject to friction exerted by a static thermal bath, to the analogous dynamics in the holographic superfluid, we make use of equation (7.1) as a phenomenological description of cold Bose gases which we use to determine γ as part of the matching procedure and compare it with experimentally measured values as well as other theoretical approaches.

In our numerical implementation of the DGPE, we solve a dimensionless form of equation (7.1). To transform the DGPE to dimensionless units, we make use of the freedom to choose the temporal and spatial grid units of the GP model independently. To be specific, we introduce the dimensionless (denoted with an overbar) coordinate and time as $\boldsymbol{x} = \bar{\boldsymbol{x}}l$ and $t = \bar{t}Ml^2/\hbar\tau$ in terms of the spatial and temporal grid units l and l^2/τ, respectively. Adopting our language from before, l is the spatial grid spacing and l^2/τ fixes the numerical timestep size. Here, we have introduced the time-rescaling parameter τ. In terms of free parameters of the DGPE (7.1), τ takes the place of the boson mass M. Analogously, for the coupling g and the chemical potential $\tilde{\mu}$, the respective dimensionless parameters are defined by $g = \bar{g}\hbar^2/M$, $\tilde{\mu} = \bar{\tilde{\mu}}\hbar^2/(Ml^2)$. We furthermore define the dimensionless and normalised complex field $u(t, \boldsymbol{x})$ by $\psi(t, \boldsymbol{x}) = \sqrt{n_0}\,u(t, \boldsymbol{x})$, with the background density $n_0 = \bar{n}_0 l^{-2}$. Suppressing the overbar on all quantities measured in grid units yields the dimensionless DGPE in the form

$$\partial_t u(t, \boldsymbol{x}) = \frac{\mathrm{i} + \gamma}{2\tau}\left[\boldsymbol{\nabla}^2 + 2\tilde{\mu}\left(1 - |u(t, \boldsymbol{x})|^2\right)\right]u(t, \boldsymbol{x})\,,\tag{7.4}$$

for the complex field $u(t, \boldsymbol{x})$. From equation (7.2) and the dimensionless chemical defined above, we infer the dimensionless healing length $\tilde{\xi} = (2\tilde{\mu})^{-1/2}$, where we have again suppressed the overbars.

Interestingly, the dimensionless DGPE (7.4) has a rescaling symmetry. Indeed, for a dimensionless parameter $s \in \mathbb{R}$, the equation is invariant under a rescaling of the physical coordinates and parameters according to

$$\boldsymbol{x}' \equiv \boldsymbol{x}s\,, \qquad t' \equiv ts^2\,, \qquad \mu' \equiv \mu/s^2\,, \tag{7.5}$$

where the un-primed parameters are the dimensionless ones defined above (formerly denoted with an overbar) and the primed parameters are the new, rescaled ones. In addition, γ and τ remain unchanged under the rescaling. For the dimensionless healing length, the rescaling implies $\tilde{\xi}' = \tilde{\xi}s$. In section 7.3 we will find the rescaling symmetry to be essential for our comparison of the holographic and matched DGPE vortex dynamics with solutions of the HVI equations.

In our matching procedure, the three free DGPE parameters γ, τ, and $\tilde{\xi}$ are determined by matching the characteristic size of the vortices as well as their dynamics in the DGPE to the respective holographic simulations, see our discussion below. We[2] numerically solve (7.4) by means of a spectral split-step algorithm [307] with fixed timestep on high-performance graphical processing units.

7.2 Vortex Motion in a Dissipative System – the HVI Equations

The overall goal of this chapter is to use the dynamics of vortex dipoles to quantify the dissipation of the holographic superfluid. To this end, we match solutions of the DGPE to the dipole dynamics in the holographic superfluid. However, in order to actually relate the results from the matching procedure to experimentally measurable observables, it turns out to be essential to compare, or better match, the holographic and matched DGPE dynamics of the vortex dipoles also to predictions for the motion of vortices obtained from a more general superfluid-hydrodynamical ansatz. Here, we have in mind the Hall–Vinen–Iordanskii (HVI) equations [238, 239] which describe the mechanical motion of vortices in the point-particle approximation. These equations are derived only from a force balance in a closed system and their general form is therefore independent of the specifics of the respective underlying superfluid. Importantly, the HVI equations account for friction between the vortex defects and the fluid and thus for dissipation. Here, point-particle limit of vortices refers to vortex-induced density depletions of zero width. In their simplest form, the HVI equations describe the mechanical motion of N vortices, accounting for the different forces exerted on the vortices by the fluid and, if present, boundaries. They were originally formulated for superfluids in three spatial dimensions, but can straightforwardly be generalised also to two-dimensional systems.

Specifically, for a number N of elementary vortices in the point-particle limit in two spatial dimensions, the HVI equations determine the velocity $\boldsymbol{v}_i$ of the i-th

---

[2] As stated at the beginning of this thesis, the DGPE simulations were not performed by the author of this thesis, but by C.-M. Schmied.

vortex at position $\boldsymbol{x}_i$ $(i = 1, \ldots, N)$ according to

$$\boldsymbol{v}_i = \frac{\mathrm{d}\boldsymbol{x}_i}{\mathrm{d}t} = \boldsymbol{v}_{\mathrm{s}}^i + C(\boldsymbol{v}_{\mathrm{n}} - \boldsymbol{v}_{\mathrm{s}}^i) + w_i\, C'\hat{\boldsymbol{e}}_\perp \times (\boldsymbol{v}_{\mathrm{n}} - \boldsymbol{v}_{\mathrm{s}}^i)\,, \qquad (7.6)$$

where $\boldsymbol{v}_{\mathrm{s}}^i$ is the superfluid velocity induced by the phase configuration of all vortices but the i-th[3], $\boldsymbol{v}_{\mathrm{n}}$ is the velocity of the normal fluid component, $w_i \in \{1, -1\}$ is the winding number of the vortex, and C and C' are phenomenological friction coefficients. In addition, $\hat{\boldsymbol{e}}_\perp$ is a unit vector perpendicular to the (x_1, x_2)-plane. This should be understood in light of an embedding of the two-dimensional system in a by one higher-dimensional space such that the unit vectors in the x_1- and x_2-direction supplemented with $\hat{\boldsymbol{e}}_\perp$ constitute a right-handed coordinate system. All quantities are taken to be dimensionless in the units of equation (7.4). Equation (7.6) is obtained by balancing the Magnus force[4] resulting from the vortex moving relative to the superfluid velocity induced by all other vortices [238] against the drag forces along and perpendicular to the relative velocity of the vortex and the fluid, and by solving this force-balance equation for the vortex velocity [242, 243].

As we consider the dynamics of the superfluid component of the system only, we neglect the normal-fluid velocity $\boldsymbol{v}_{\mathrm{n}}$. This is consistent with our interpretation of the two-fluid model in the context of the holographic superfluid in section 3.2. Furthermore, also in the DGPE discussed above, the system is not self-consistently coupled to a normal-fluid component. For completeness, we note that a vanishing normal-fluid velocity implies that the Iordanskii force[5] does not affect the vortex velocities, *cf.* [243]. As a result of $\boldsymbol{v}_{\mathrm{n}} = 0$, equation (7.6) takes the simpler form

$$\boldsymbol{v}_i = \frac{\mathrm{d}\boldsymbol{x}_i}{\mathrm{d}t} = (1 - C)\,\boldsymbol{v}_{\mathrm{s}}^i - w_i\, C'\,\hat{\boldsymbol{e}}_\perp \times \boldsymbol{v}_{\mathrm{s}}^i\,. \qquad (7.7)$$

Hence, the motion of the i-th vortex is solely determined by the superfluid velocity

$$\boldsymbol{v}_{\mathrm{s}}^i = 2\pi w_i\, \hat{\boldsymbol{e}}_\perp \times \boldsymbol{\nabla}_{\boldsymbol{x}_i} H_{\mathrm{PV}}(\{\boldsymbol{x}_k, w_k\}) = 2 \sum_{\{j\,|\,j\neq i\}} w_j \frac{\hat{\boldsymbol{e}}_\perp \times (\boldsymbol{x}_i - \boldsymbol{x}_j)}{|\boldsymbol{x}_i - \boldsymbol{x}_j|^2}\,, \qquad (7.8)$$

created by all the other vortices in the system. The superfluid velocity is derived from the Kirchhoff–Onsager point-vortex Hamiltonian [259],

$$H_{\mathrm{PV}}(\{\boldsymbol{x}_k, w_k\,|\,k = 1, \ldots, N\}) = (2\pi)^{-1} \sum_{i \neq j} w_i w_j \ln |\boldsymbol{x}_i - \boldsymbol{x}_j|\,. \qquad (7.9)$$

---

[3] In general there can be further sources that contribute a finite superfluid velocity to $\boldsymbol{v}_{\mathrm{s}}^i$, including in particular an externally imposed superfluid flow. In this work, all additional sources are set to zero (*cf.* equation (5.7)).

[4] For an interesting study of the Magnus force on a vortex in a holographic superfluid see [308]. In that work, the authors show that in the holographic framework the Magnus force serves as a probe for the charge density outside the horizon.

[5] The Iordanskii force accounts for a momentum transfer between the moving vortices and the normal component of the fluid. It arises when the velocity of a vortex deviates from the velocity of the normal fluid, *cf.* [243]. If one assumes the normal component to be static, the Iordanskii force does not contribute to the vortex motion [243].

The theoretical calculation and understanding of the drag entering (7.6) has been the subject of extensive work, see *e. g.* [134, 238–246, 249] and references therein. In this thesis, we are primarily interested in the relation between the HVI equations and the phenomenological description of the superfluid vortex dynamics in terms of the DGPE (7.1). The idea here is as follows. The HVI friction coefficients C, C' can be directly inferred from measurement of the vortex diffusivity (*cf.* section 7.4) in experiments with Bose–Einstein condensates as well as superfluids such as helium ^{4}He. Thus, after matching the DGPE to the holographic simulations, a comparison of the vortex dynamics with the HVI equations in which we determine the friction coefficients allows us to infer the range of applicability of the holographic superfluid in describing experimentally realised superfluids.

The dissipative Gross–Pitaevskii equation as written in (7.1) is just another formulation of the complex Ginzburg–Landau equation (CGLE) (see, *e. g.*, [309]),

$$\left(\delta_{\tilde{\xi}} + \mathrm{i}\alpha\right) \partial_t u_{\tilde{\xi}} = \boldsymbol{\nabla}^2 u_{\tilde{\xi}} + \frac{1}{\tilde{\xi}^2} \left(1 - |u_{\tilde{\xi}}|^2\right) u_{\tilde{\xi}} \,. \tag{7.10}$$

In the literature one therefore often finds these two equations used synonymously. Indeed, after rearranging the terms, the CGLE (7.10) agrees with the DGPE as written in equation (7.1). Interestingly, in [310, 311] it was shown that in the point-vortex limit, *i. e.*, for vortex-induced density depletions much smaller than the distance $d = |\boldsymbol{x}_i - \boldsymbol{x}_j|$ between the defects, the above dynamical HVI equations (7.7) provide an approximate description of the motion of vortices according to the CGLE. The corresponding CGLE solutions $u_{\tilde{\xi}}$ depend on the parameters $\tilde{\xi}$, $\delta_{\tilde{\xi}}$ and α. Solutions $u_{\tilde{\xi}}$ containing N vortices of winding numbers w_i at positions $\boldsymbol{x}_i$ can be written as

$$u_{\tilde{\xi}}(\boldsymbol{x}_i, w_i; N)(\mathfrak{z}) = \prod_{i=1}^{N} f_{1,w_i} \left(\frac{|\mathfrak{z} - \mathfrak{z}_i|}{\tilde{\xi}}\right) \left(\frac{\mathfrak{z} - \mathfrak{z}_i}{|\mathfrak{z} - \mathfrak{z}_i|}\right)^{w_i} \,, \tag{7.11}$$

where we use $\boldsymbol{x} = (x_1, x_2)$ as before and we have further introduced the complex coordinate $\mathfrak{z} = x_1 + \mathrm{i}x_2$, $\mathfrak{z}_i = x_{1,i} + \mathrm{i}\,x_{2,i}$. In addition, the function $f_{1,w_i} : \mathbb{R}^+ \to [0, 1]$, with $f_{1,w_i}(0) = 0$ and $f_{1,w_i}(\infty) = 1$ describes the density profile around the vortex core in the case of $\tilde{\xi} = 1$. As noted before, the healing length $\tilde{\xi}$ controls the size of the vortex-profile solutions of equation (7.10). In the asymptotic limit $\tilde{\xi} \to 0$ (point-vortex limit), with $\delta \equiv \delta_{\tilde{\xi}} |\ln \tilde{\xi}| \in (0, \infty)$ kept fixed, the motion of the vortices (7.11) according to the CGLE (7.10) is well described by the HVI equations (7.7) with friction coefficients C and C' defined given by

$$C = 1 + \frac{\alpha}{\alpha^2 + \delta^2} \,, \qquad C' = \frac{\delta}{\alpha^2 + \delta^2} \,, \tag{7.12}$$

in terms of the CGLE parameters α and δ. We present further details on this in appendix B.

In order to compare the HVI equations to the matched dipole dynamics in the DGPE and holography, we express the parameters $\delta_{\tilde{\xi}}, \alpha$ of the CGLE (7.10) in terms

of the parameters of the DGPE (7.1),

$$\delta_{\tilde{\xi}} = \frac{2\tau\gamma}{1+\gamma^2}\,, \qquad \alpha = -\frac{2\tau}{1+\gamma^2}\,. \tag{7.13}$$

Note that in [310], α was set to unity, which is equivalent to flipping the sign on the left-hand side of equation (7.4) and rescaling time by choosing $\tau = -(\gamma^2+1)/2$, and which yields $\delta_{\tilde{\xi}} = -\gamma$. Hence, the above definitions generalise the expressions given in [310] to the case $\alpha \neq 1$, *i.e.*, they allow us to choose the temporal and spatial grid units independently, as discussed in the previous section. With this, we finally obtain the asymptotically ($\tilde{\xi} \to 0$), valid friction coefficients (7.12)

$$C = 1 - \frac{1}{2\tau}\frac{1+\gamma^2}{1+\gamma^2|\ln\tilde{\xi}|^2}\,, \qquad C' = \frac{\gamma|\ln\tilde{\xi}|}{2\tau}\frac{1+\gamma^2}{1+\gamma^2|\ln\tilde{\xi}|^2}\,, \tag{7.14}$$

expressed in terms of the free DGPE parameters which we will later fix in our matching procedure.

For the case of a vortex dipole, the HVI equations (7.7) can be integrated straightforwardly, even analytically, to provide expressions for the vortex trajectories. Defining, for $N = 2$ vortices with opposite winding numbers $w_1 = -w_2$, the relative and centre coordinates

$$\boldsymbol{d}(t) = (\boldsymbol{x}_1 - \boldsymbol{x}_2)(t) = d(t)\,\hat{\boldsymbol{d}}_0\,, \qquad \boldsymbol{R}(t) = (\boldsymbol{x}_1 + \boldsymbol{x}_2)(t)/2 = R(t)\,\hat{\boldsymbol{d}}_0 \times \hat{\boldsymbol{e}}_\perp\,, \tag{7.15}$$

with $\hat{\boldsymbol{d}}_0 = \boldsymbol{d}(0)/|\boldsymbol{d}(0)|$, $d_0 = d(0)$, one finds the solutions (see appendix B for details)

$$d(t) = \sqrt{d_0^2 - 8\,C'\,t}\,, \qquad R(t) = R(0) + w_1\frac{1-C}{2C'}\,(d_0 - d(t))\,. \tag{7.16}$$

From equations (7.16) we can now straightforwardly compute the explicit closed-form expression of the vortex trajectories according to the HVI equations,

$$\boldsymbol{x}_{1/2}(t) = (R(0) + \Upsilon d_0)\,\hat{\boldsymbol{d}}_0 \times \hat{\boldsymbol{e}}_\perp + d(t)\left(-\Upsilon\hat{\boldsymbol{d}}_0 \times \hat{\boldsymbol{e}}_\perp \pm \frac{1}{2}\,\hat{\boldsymbol{d}}_0\right)\,, \tag{7.17}$$

where we have defined $\Upsilon \equiv w_1(1 - C)/(2C')$. We thus find them to be given by straight lines on the two-dimensional (x_1, x_2)-grid. The intersection of the linear vortex paths occurs at time $t_{\mathrm{a}} = d_0^2/8C'$, enclosing an angle β given by

$$\tan(\beta/2) = \frac{w_1 d_0/2}{R(t_{\mathrm{a}}) - R(0)} = \frac{C'}{1-C} = -\frac{\delta}{\alpha} = \gamma\,|\ln\tilde{\xi}\,|\,. \tag{7.18}$$

We have thus found a solution to the HVI equations for a propagating vortex dipole in a dissipative medium, with the friction coefficients expressed in terms of the free DGPE parameters γ, τ and $\tilde{\xi}$. A main requirement for the applicability of the HVI equations is that the vortices are point-like. In section 7.3 we will show explicitly that for large vortex–anti-vortex separations as compared to the width of the condensate-density depletions around their cores, the vortices in the DGPE

and holography simulations, to a good approximation, behave as being only point-like dips. In this regime, we find that the dipole dynamics is well described by the HVI solutions (7.17). From a direct matching of the dynamics we then infer the friction coefficients C, C' via equation (7.14). Extracting the friction coefficients is essential for a direct comparison to experimental observables. We discuss the physical relevance of the friction coefficients in section 7.4.

7.3 Matching the Dipole Dynamics in DGPE to Holography

In the previous two sections we have covered all necessary prerequisites that we will need as we go along in this chapter. In particular, we have introduced the dissipative Gross–Pitaevskii model and commented on its applicability in the description of two- and quasi-two-dimensional cold Bose gases. Furthermore, we have reviewed the hydrodynamical description of the motion of vortex–anti-vortex pairs in superfluids and solved the corresponding HVI equations. Importantly, we have argued that within the point-particle approximation, the HVI equations coincide with solutions for the motion of vortices according to the DGPE and can thus be expressed in terms of the DGPE's free parameters. After these two rather technical sections, we can now proceed to the main purpose of this chapter, namely matching the vortex dynamics according to the DGPE to the analogous evolution in the holographic superfluid.

To uniquely match the dynamics, we have to fix all three free DGPE parameters, $\tilde{\xi}, \gamma$ and τ. We point out that in principle we could have also chosen a different set of independent parameters. However, this one turns out to be particularly well-suited for our matching procedure. The healing length $\tilde{\xi}$ determines the size of an isolated vortex and has no direct effect on the dynamics of the dipole. The phenomenological damping parameter γ and the time-rescaling parameter τ, on the other hand, have no effect on the shape or size of a vortex. Instead, they determine the kinematic aspects of the dipole dynamics. Hence, in our matching procedure we can proceed in two consecutive steps to fix all three parameters. In a first step, we match the size of the DGPE vortex to the size of the holographic vortex by tuning the healing length $\tilde{\xi}$. Having fixed the healing length, we match as a second step the trajectories of the vortices on the two-dimensional (x_1, x_2)-grid. We use the healing length extracted in the first step as input for the DGPE dynamics of the second step and then tune the free damping parameter γ and the time-rescaling parameter τ until the trajectories agree in space and time to high accuracy.

In the DGPE simulation, we prepare the vortices in a similar way as in the holographic system as far as the phase field is concerned. Namely, we multiply a quantised phase winding of type $\varphi(t_0, \boldsymbol{x})_i = w_i \arg(x_1 - x_{1,i} + \mathrm{i}(x_2 - x_{2,i}))$ into the complex order-parameter field $\psi(t_0, \boldsymbol{x}) \to \psi(t_0, \boldsymbol{x}) \, \mathrm{e}^{\mathrm{i}\varphi(t_0, \boldsymbol{x})_i}$ on the entire (x_1, x_2)-grid, separately for the vortex ($w_i = 1$) and anti-vortex ($w_i = -1$). For the density profile we insert, for each vortex at position $\boldsymbol{x}_i$, the approximate analytic solution of the

non-dissipative ($\gamma = 0$) Gross–Pitaevskii (GP) vortex [136, 293],

$$|u(\boldsymbol{x})|^2 = \frac{(\boldsymbol{x} - \boldsymbol{x}_i)^2}{2\tilde{\xi}^2 + (\boldsymbol{x} - \boldsymbol{x}_i)^2} \, . \tag{7.19}$$

Subsequently, we perform imaginary-time propagation[6] with $\gamma = 1$ for two timesteps $\Delta t_{\mathrm{imag}} = 2/\tau$, to relax the vortex configuration to its full solution, *i. e.*, have the vortices dynamically build up their full characteristic density profile. Here, $\gamma = 1$ is just one choice for the damping parameter, ensuring that the vortex builds up within short time. Once the vortex has built up, we begin with our matching procedure and change γ. In addition, we stress that (7.19) is only chosen as an approximate profile before the imaginary-time propagation causes the field to relax to the actual vortex profile. Nonetheless, the functional form (7.19) in particular matches the actual vortex-profile solution to order $\mathcal{O}((\boldsymbol{x} - \boldsymbol{x}_i)^2)$ around the core. The healing length $\tilde{\xi}$ determines the width of the density depletion around the core and scales as $\tilde{\xi} \sim \tilde{\mu}^{-1/2}$ in the DGPE chemical potential. Note that (7.19) agrees with equation (6.2) of section 6.3 if (6.2) is divided by the equilibrium background condensate density n_0.

The thermodynamic state of the holographic superfluid is controlled by only one free parameter, the dimensionless ratio μ/T. However, since for our numerical simulations we fix the absolute temperature of the superfluid to $T = 3/(4\pi)$ by our choice of $z_{\mathrm{h}} = 1$, μ is effectively the only free parameter controlling the phase transition. Moreover, for fixed scalar mass m, μ controls all variable quantities of the holographic superfluid (in the probe-approximation). This includes, but is not limited to, the background condensate density n_0 (*cf.* figure 5.1), the size of a vortex, the time scales of the system as well as the shape of the vortex trajectories. In order to account for this μ-dependence of the characteristics of the holographic superfluid, we match DGPE solutions to the holographic vortex dynamics for a number of different values of the holographic chemical potential. To be specific, we perform the same matching procedure as we have just described above for four exemplary values of the chemical potential, given by $\mu = 4.5, 6, 7.5, 9$. These values correspond to the temperature ratios $T/T_{\mathrm{c}} = 0.9, 0.68, 0.54, 0.45$. The studied interval of chemical potentials allows for a numerically efficient and stable simulation of the dynamics. Going beyond this interval to even larger chemical potentials, we expect the probe-approximation to no longer accurately capture the physics of the system. A self-consistent analysis for all chemical potentials $0 \leq \mu \leq \mu_{\mathrm{c}}$ would require taking the backreaction of the gauge–matter fields onto the gravitational background into account.

Before we dive into a discussion of the matching procedure, we briefly comment on some important aspects of the numerical implementations of the equations of motion

---

[6]For the imaginary time propagation we use $t = -\mathrm{i}t_{\mathrm{imag}}$ in equation (7.4) and subsequently propagate the system forward in t_{imag}. This damps out all but the ground-state energy modes of the GPE and thus causes the approximate vortex solution used in the initial configuration to relax to the proper low-energy vortex solution.

of the holographic system and the DGPE. We have already covered the basics of the algorithms in sections 5.4 and 7.1, respectively, and hence focus in the following only on the numerical parameters used. For both systems, we employ 512×512 grid points in the (x_1, x_2)-plane as well as a grid spacing of $l = 1/8$ in our numerical simulations, ensuring that the systems are simulated at the same spatial resolution. Likewise, we use an equal number of evaluation points along the time direction. In addition, in both systems the (x_1, x_2)-directions are taken to be periodic.

7.3.1 Matching the Vortex Profiles

In this subsection we focus on the static aspects of the vortex solutions in DGPE and holography and match the sizes of the respective vortex-induced density depletions by tuning the GPE healing length $\tilde{\xi}$ appropriately. Furthermore, once the sizes have been matched, we compare the shapes of the vortices. Our goal is to gain a better understanding of the characteristics of the holographic vortex and how it compares to its DGPE analogue, on a qualitative as well as quantitative level. Since the DGPE damping parameter γ has no effect on the size or the shape of the vortex solution, we set, without loss of generality, $\gamma = 0$. Thus, we match the vortex profile of the non-dissipative GPE to the vortex profile of the holographic system. Likewise, the time-rescaling parameter can be chosen at will.

We point out that in [161] the authors also compare certain aspects of the holographic vortex to its GPE analogue. However, the purpose of the present subsection has to be seen in the broader context of this chapter and the matching procedure as a whole. Furthermore, we present a direct comparison of the vortex shapes after precisely matching their sizes which is new to this work. Also, we extend [161] by studying a much larger range of chemical potentials.

To match the vortex sizes in DGPE and holography and subsequently compare their shapes, we consider a symmetric vortex lattice in accordance with the periodic boundary conditions in our systems. The configuration consists of two vortices and two anti-vortices on a square grid in alternating order evenly spaced around the centre of the two-dimensional grid at $(x_1, x_2) = (256, 256)$. In doing so we ensure a minimal mutual influence onto the individual shape of each vortex, *i.e.*, the shape of the respective vortex-induced density depletion is closest to that of an individual and isolated vortex in an infinite plane. Importantly, this configuration is only used to compare and match the spatial density profiles of the vortices in the two theories. We then use the respective healing length obtained from this matching procedure as input for the simulation of the dynamics of single vortex dipoles.

The quantitative matching of the vortex profiles in holography and DGPE requires adjusting the DGPE healing length $\tilde{\xi}$ such that the vortex sizes agree in both systems. In figure 7.1 we show the density profile of the holographic vortex (blue dots) for an exemplary chemical potential of $\mu = 6$ (corresponding to the ratio $T/T_\mathrm{c} = 0.68$), as well as the (D)GPE vortex (orange diamonds) obtained after tuning $\tilde{\xi}$. In practise, we tune the DGPE healing length $\tilde{\xi}$ such that the density depletions of the vortices are resolved by the same number of grid points at 95% of
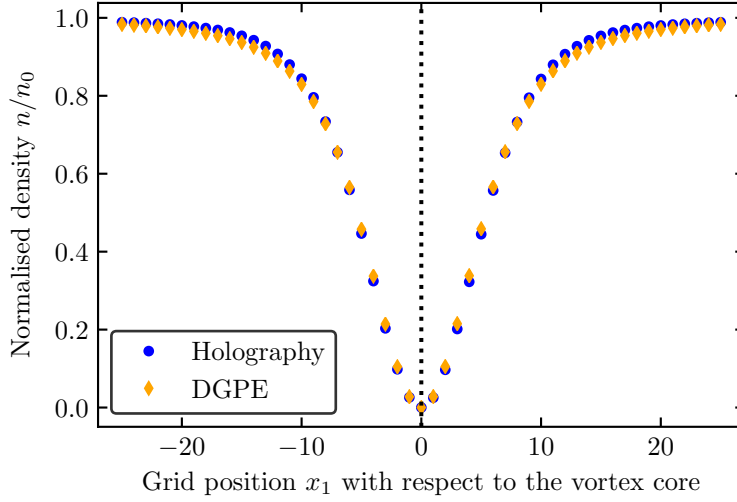
Figure 7.1: Normalised density profile n/n_0 of a single vortex in holography (for an exemplary temperature of $T/T_c = 0.68$) and DGPE as a one-dimensional cut through its centre. The vortices are spherically symmetric and we shift the coordinate axis such that $x_1 = 0$ agrees with the core position. The healing length used to imprint the DGPE vortex is tuned to $\tilde{\xi} = 3.5$ such that, at 95% of the background density, its size agrees with that of the corresponding holographic vortex. After this matching we find that also the shapes of the vortices agree pointwise to within 2% of the background density.

the background density n_0. For the four chemical potentials $\mu = 4.5, 6, 7.5, 9$, we find for the healing length $\tilde{\xi} = 9.25, 3.5, 2.56, 1.93$ in units of grid points, respectively. The results are also summarised in table 7.1 below. The comparison in figure 7.1 shows that after matching the sizes, also the entire spatial profiles of the vortices agree pointwise within 2% of the background density. This holds true for all μ of the holographic system considered. The excellent agreement of the vortex shapes is very remarkable since in the holographic superfluid the density profile around a vortex core is a true solution of the system that builds up in our simulations without any external constraints with regard to its size or shape. We stress that only the γ-independence of the vortex size and shape in DGPE allows us to extract the healing length $\tilde{\xi}$ at $\gamma = 0$ and then subsequently to use this value to match the vortex dynamics to find γ and τ.

In the GP model the healing length $\tilde{\xi}$, *i.e.*, the width of a vortex-induced density depletion scales with the inverse square root of the GPE chemical potential, $\tilde{\xi} \sim \tilde{\mu}^{-1/2}$ with $\tilde{\mu} = n_0 g$. It is interesting to study if the vortex width in the holographic framework has a similar dependence on the holographic chemical potential. In particular, such an analysis might yield new insight into the putative analogy

between the holographic chemical potential μ and the GPE chemical potential $\tilde{\mu}$. For a number of chemical potentials in the interval $4.5 \leq \mu \leq 9$ we therefore study the dependence of the holographic vortex width on μ. To be specific, we supplement the list of chemical potentials for which we have extracted the respective healing lengths in the matching procedure above by six additional values, spread over the considered interval. In light of the increased number of chemical potentials, which is required for a thorough analysis, we extract the width of a vortex for each choice of the holographic chemical potential from a Gaussian fit to its spherically-symmetric density profile instead of matching a GP vortex to the holographic one. In particular, we proceed like this also for the values of the chemical potential for which we have already determined the healing length in our matching procedure discussed above. For the fitting routine, we proceed similarly to our Gaussian tracking procedure. However, here we only fit one vortex. The fitting function is thus given by

$$n(\boldsymbol{x}) = A - A_1 \exp\left\{ -(\boldsymbol{x} - \boldsymbol{x}_i)^2 / 2\xi^2 \right\} , \tag{7.20}$$

where A and A_1 again account for the embedding of the vortex into the condensate background, $\boldsymbol{x}_i$ is the position of the vortex core and ξ is the width in x_1- and x_2-direction. At small $\sqrt{(\boldsymbol{x} - \boldsymbol{x}_i)^2} \lesssim \xi$ and for $A = A_1 = n_0$ equation (7.20) agrees with the approximate GP profile (7.19) to order $\mathcal{O}((\boldsymbol{x} - \boldsymbol{x}_i)^2)$ if one identifies $\xi = \tilde{\xi}$. Since (7.19) agrees with the true GP vortex profile to the same order, so does (7.20). We thus expect the width ξ extracted from the Gaussian fit and the healing length $\tilde{\xi}$ we would extract from a matching procedure with the (D)GPE to approximately coincide. Nonetheless, we denote the width of the holographic vortex extracted from the Gaussian fit (7.20) by ξ (without a tilde), in order to make evident that it is extracted in a different way than $\tilde{\xi}$. For the fitting procedure we prepare the same type of initial condition as for the matching procedure above, *i. e.*, four vortices symmetrically located around the centre of the (x_1, x_2)-grid in such a way that the forces on each individual vortex are balanced. Since the vortex configuration is symmetric, we are free to apply the Gaussian fit to any one of the vortices. For the holographic chemical potentials μ that we also use in the matching procedure above (and below), we can compare the widths ξ extracted from the Gaussian fits with the GPE healing lengths $\tilde{\xi}$ obtained from the matching procedure. For all four values of μ we find excellent agreement. This proves that the width extracted from the Gaussian fit may indeed be associated with the healing length of the holographic system extracted from the matching procedure, just as we have already discussed above. In figure 7.2 we show the dependence of the width ξ on the shifted chemical potential $\delta\mu = \mu - \mu_0$. The double-logarithmic scale clearly demonstrates the power-law scaling of ξ with $\delta\mu = \mu - \mu_0$. To characterise the scaling behaviour we fit the data points with

$$\xi = \frac{a}{(\delta\mu)^b} , \tag{7.21}$$

where a, b and μ_0 are free fitting parameters. Using a Levenberg–Marquardt least-squares fitting algorithm, we find a linear shift of $\mu_0 = 4.06$ and a scaling exponent
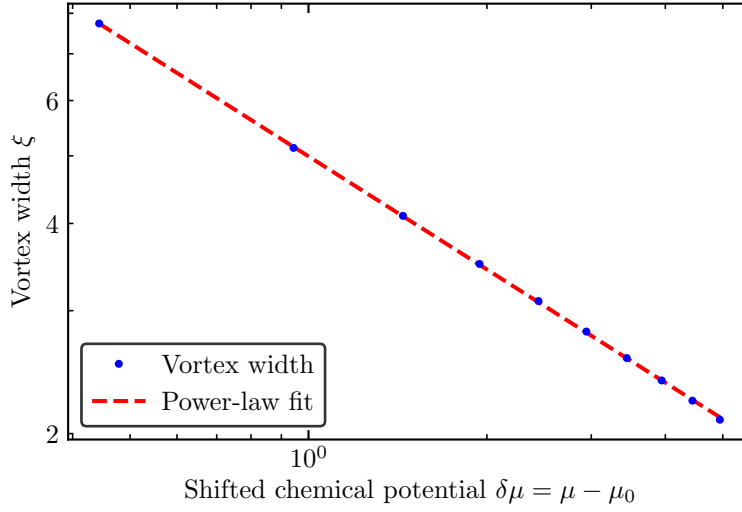
Figure 7.2: Width ξ of the holographic vortex-induced density depletion as a function of the linearly shifted holographic chemical potential $\mu - \mu_0$. The width ξ (blue dots) is extracted from the vortices by a Gaussian fit to their density profiles. The double-logarithmic scale demonstrates that the width depends on $\delta\mu = \mu - \mu_0$ according to $\xi \sim (\delta\mu)^{-b}$, where $\delta\mu$ and b are extracted from a fit to the data points (solid red line). The fitted value $\mu_0 = 4.06$ is close to the critical chemical potential $\mu_{\mathrm{c}} \simeq 4.0637$ and $b = 0.54$. This behaviour coincides with the dependence $\tilde{\xi} \sim \tilde{\mu}^{-1/2}$ of the DGPE healing length on the non-relativistic chemical potential $\tilde{\mu}$.

given by $b = 0.54$. Since a only accounts for an overall normalisation, its exact value is not of interest to us in this context. Error estimates for the parameters are of the order of a few percent, mainly caused by the uncertainties in the determination of the vortex width ξ. Since we are only interested in the qualitative behaviour, we refrain from presenting an in-depth analysis of the errors of ξ and the free fitting parameters in (7.21). Our findings show that the extracted shift μ_0 is very close to the critical chemical potential $\mu_{\mathrm{c}} \simeq 4.0637$ at which the order parameter ψ is found to vanish [48], *cf.* figure 5.1. Such a scaling behaviour has been observed before in a related context for a holographic superconductor in the vicinity of the critical point of the phase transition, where $\delta\mu$ plays a similar role as the gap scale in the Ginzburg–Landau theory which has strong similarities to the boundary theory of the holographic superconductor model [312]. We emphasise that the scaling coincides with the dependence $\tilde{\xi} \sim \tilde{\mu}^{-1/2}$ of the DGPE healing length on the non-relativistic chemical potential $\tilde{\mu}$. This confirms the holographic system to describe, below the critical point, a non-relativistic superfluid [47, 48, 148, 158, 159].

7.3.2 Matching the Trajectories

From the matching of the vortex sizes in the previous subsection we have extracted the DGPE healing length $\tilde{\xi}$ for every value of holographic chemical potential in the list $\mu = 4.5, 6, 7.5, 9$. We now compare and match to each other the time evolution of the vortices in the respective simulations to find the remaining two free DGPE parameters γ and τ. We stress that we are now back to the dynamics of single vortex dipoles. To be specific, we imprint in each system a vortex dipole consisting of two vortices with winding numbers $w_{1,2} = \pm 1$, at positions $(x_{1,1}, x_{2,1}) = (331, 256)$, $(x_{1,2}, x_{2,2}) = (181, 256)$ of our square grid. Thus, the vortices have an initial separation of $d_0 = 150$ grid points. Except for the number of grid points separating the vortices, this configuration agrees with the exemplary initial condition studied in the previous chapter. We use the same procedures of presetting the phase and density and, for the DGPE, a short (imaginary-time) evolution as outlined above. In both theories, holography and DGPE, we then evolve the system in time and track the vortices at every unit timestep using the combined tracking algorithms[7] as explained in section 6.3. Let us stress at this point that the quasi-continuous nature of the trajectories obtained from the tracking routine is indispensable for the success of the matching procedure. Using only plaquette precision for the vortex locations would not suffice to match accurately the two theories.

In our matching procedure we proceed as follows. For every fixed holographic chemical potential, we match the DGPE vortex trajectories to their holographic equivalent in space and time by adjusting the dissipation parameter γ and the time-rescaling parameter τ. Importantly, the matchings in space and time are independent of each other. While variations in γ only affect the shape of the trajectories, variations in τ only affect the time scale of the dynamics.

In table 7.1 we summarise our results. For all four values of the holographic chemical potential, we present the three matched DGPE parameters $\tilde{\xi}, \gamma$ and τ. The parameters in the right columns of this table are extracted from a matching of solutions of the HVI equations to the matched holographic and DGPE dipole dynamics. For details see our discussion below. We find that the phenomenological damping parameter γ depends monotonously but only mildly on the chemical potential of the holographic superfluid. In particular, its order of magnitude is the same for all μ. In figure 7.3 we display the matched vortex trajectories in holography (blue dots) and DGPE (orange diamonds) for an exemplary chemical potential of $\mu = 6$ (corresponding to $T/T_\mathrm{c} = 0.68$). The matched vortex trajectories are in excellent agreement up to very late times of the evolution. Only during the very final stages of the evolution, approximately given by the last three unit timesteps, the trajectories in DGPE and holography can no longer be matched to each other. In figure 7.3 we

---

[7]We note that due to the change in grid spacings from $l = 2/7$ in chapter 6, to $l = 1/8$ in this chapter and the associated increase in the vortex resolution we have to adapt the distance $d(t)$ at which we switch from the Gaussian fitting routine to the NR tracking algorithm. The increase in vortex resolution leads to an earlier onset of the regime of overlapping density depletions. We therefore use the Gaussian fitting routine for $d(t) \geq 25$ (in grid units) and correspondingly the NR method for $d(t) < 25$.

Table 7.1: Summary of the results from the matching procedure. Left columns: Parameters chosen for the holographic simulations. Middle columns: DGPE parameters obtained from matching the vortex sizes and the spatio-temporal trajectories of the vortex dipoles for the respective holographic superfluid parameters. Right columns: Scale parameter s and the friction coefficients, $C = 1 - (1 + \gamma^2)/[2\tau(1 + \gamma^2|\ln \tilde{\xi}'|^2)]$ and $C' = \gamma|\ln \tilde{\xi}'|(1 + \gamma^2)/[2\tau(1 + \gamma^2|\ln \tilde{\xi}'|^2)]$ of the HVI equations governing the mechanical motion of the point vortices, evaluated on a rescaled grid with $\tilde{\xi}' = \tilde{\xi}/s$. We estimate the error of all extracted parameters, in DGPE as well es for the HVI equations, to be of the order of 1–2%.

μ	T/T_c	γ	$\tilde{\xi}$	τ	s	C	C'
4.5	0.9	0.330	9.25	2.85	114	0.88	0.095
6	0.68	0.313	3.50	5.76	116	0.95	0.047
7.5	0.54	0.297	2.56	7.46	116	0.97	0.036
9	0.45	0.281	1.93	9.25	119	0.98	0.029

only display times prior to this point. The minor deviations that are visible in figure 7.3 set in about ten unit timesteps before the vortices annihilate, and their magnitude is smaller than one grid point. At all prior times, including the phase-healing regime, the vortex trajectories match accurately. During the phase-healing regime, the vortices in the DGPE also exhibit the initial outward bending we have seen in the previous chapter for the vortices in the holographic system, *cf.* figure 7.3. In light of the fact the we use the exact same phase configuration in our preparation of the initial condition for the vortex-dipole dynamics in the holographic system and the DGP model, such a behaviour is expected, *cf.* section 6.4 for details. Nevertheless, the fact that the dynamics of the phase healing agrees to the level we observe in figure 7.3 is remarkable. To illustrate the sensitivity of the DGPE trajectories to the phenomenological damping parameter γ we include error bands corresponding to variations of the damping parameter γ by 10% (turquoise-shaded area) and 20% (red-shaded area), respectively. The large deviations from the original (matched) trajectories, caused by only minor variations in γ, highlight the accuracy to which we match the dynamics. As variations in τ only result in a change of the time scale of the DGPE dynamics, we do not illustrate them in figure 7.3. Instead, we only note that a change in τ by $\pm 10\%$ delays or accelerates the dynamics by several unit timesteps. We estimate the errors for all DGPE parameters determined in this way to be of the order of 1–2%. In the next chapter, we will show explicitly that the dynamics of vortex dipoles in the holographic superfluid is independent of the initial alignment of the vortices on the numerical grid and solely parametrised by
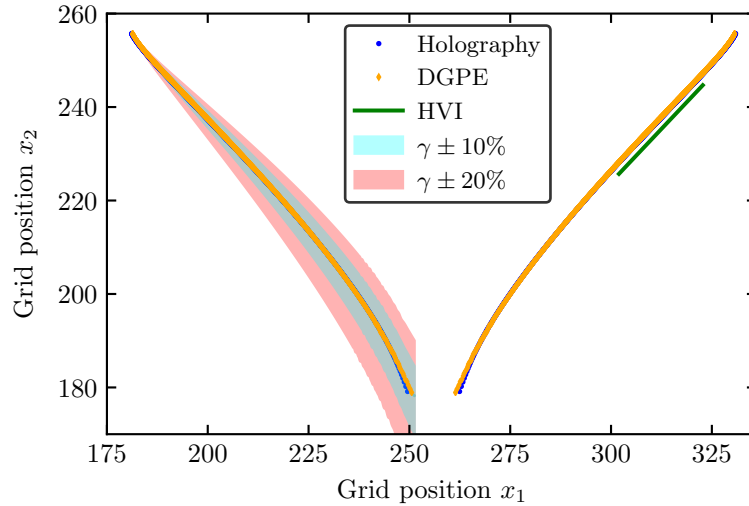
Figure 7.3: Illustration of the matched vortex trajectories from the DGPE (orange diamonds) and holographic (orange diamonds) simulation for an exemplary holographic chemical potential of $\mu = 6$ and an initial vortex dipole separation of $d_0 = 150$ grid points. The DGPE parameters are adjusted such that the trajectories agree to high accuracy in space and time. Both trajectories show a slight initial outward bending which can be attributed to the preparation of the initial vortex configuration, *cf.* section 6.4. At intermediate times ($190 < t < 575$), for large vortex–anti-vortex separations, we additionally illustrate the matching to the HVI equations by the solid green line (deliberately shifted downwards by -2.5 grid points). The error bands correspond to variations of the damping parameter γ by 10% (turquoise-shaded area) and 20% (red-shaded area), respectively.

the dipole size. The same holds true in the GP model. Consequently, it suffices to restrict our matching procedure to only one initial vortex configuration. Using the extracted DGPE parameters for a simulation of the dynamics of more than just two vortices, we again find excellent agreement of the respective vortex trajectories, given the vortex density, globally as well as in local patches, is not 'too large'. In section 7.3.3, we comment further on the dynamics of many-vortex configurations and present a more thorough discussion of what we mean by 'too large' here.

In figure 7.4 we show snapshots of the condensate-density modulation at four characteristic times of the matched DGPE (right panels) and holographic (left panels) dipole dynamics for a holographic chemical potential of $\mu = 6$. For the same simulations we have also presented the trajectories in figure 7.3 above. Given the specific initial vortex configuration and the choice for the chemical potential of the holographic superfluid, it takes approximately $\Delta t = 972$ unit timesteps for the vortices to annihilate. The snapshots in figure 7.4 are taken at times $t = 0, 929, 969, 980,$
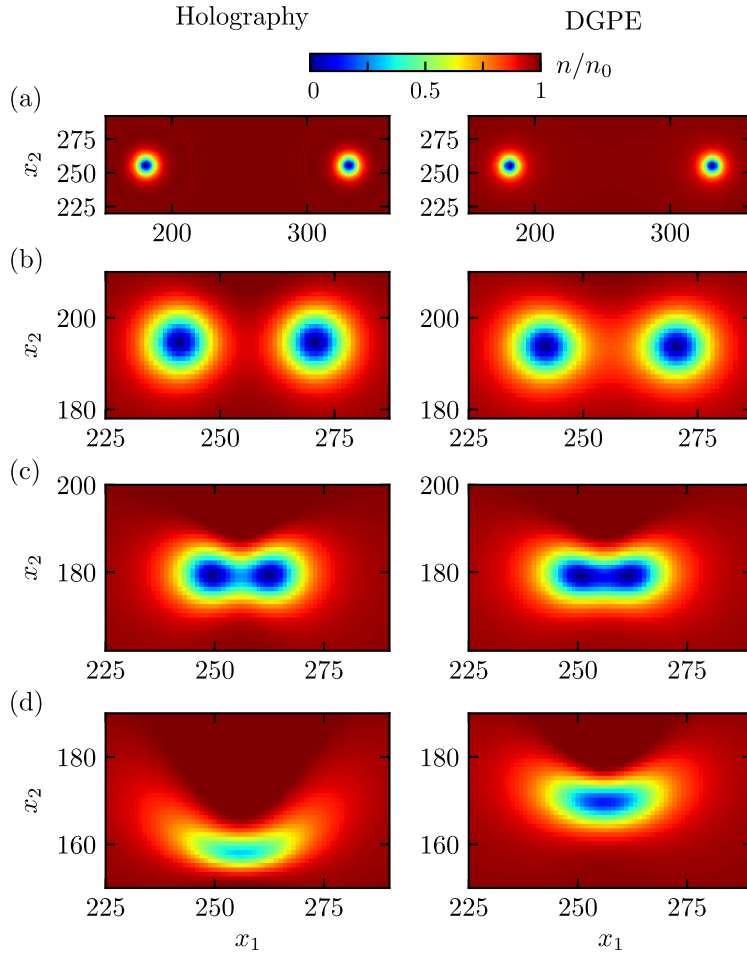
Figure 7.4: Snapshots of the normalised density profile showing the vortex dipole in the holographic superfluid (left panels) and the DGPE (right panels) at subsequent moments of the evolution. The panels clearly indicate strong agreement of the shapes until shortly before the annihilation. (a) Initial configuration at $t = 0$, $d_0 = 150$: The vortices have a circular shape and are well separated from each other. (b) Entry of the late-time regime at $t = 929$: The vortices have significantly approached each other and start to become mutually deformed to an elliptical shape. (c) $t = 969$, three unit timesteps prior to the annihilation (at $t = 972$): The vortices have strongly deformed and their density depressions largely overlap. At this stage of the evolution the dynamics can no longer be matched and the trajectories shown in figure 7.3 end. (d) Rarefaction pulses propagate through the condensates at time $t = 980$ and subsequently damp out, with clear differences in size and shape in the holographic and DGPE cases. Note the different subregions of the (x_1, x_2)-grid as indicated on the axes.

representing the initial configuration and the different regimes of the evolution that we have discussed in the previous chapter. For details see also the figure caption. From our prior matching of the vortex sizes and our discussion of the vortex shapes it is expected that both the shape and the size of the vortices also agree during the early and intermediate stages of the evolution when the vortices are far apart and perfectly spherical. Remarkably, such strong agreement persists for most of the final stage of the evolution and deviations arise only within the last few unit timesteps. In particular, figure 7.4 demonstrates that at prior times the vortices in the two theories deform highly similarly. The onset of the deviations in the vortex shapes coincide with the onset of deviations of the respective trajectories observed in figure 7.3. The differences are largest during the final three unit timesteps, yet again corroborating the matching to break down at these times. In the final snapshot of figure 7.4 the vortices have already annihilated and we display the rarefaction pulse that they have left behind. In the holographic system this pulse picks up velocity very quickly and travels longer in time and further in space than in the DGPE system. In the next subsection we present a possible explanation for this behaviour. Moreover, in section 8.4 of the following chapter, we present a more in-depth analysis of the rarefaction pulse in the holographic superfluid.

Having matched the holographic and DGPE dynamics, we now compare the dipole evolutions of both systems with the corresponding vortex trajectories predicted by the HVI equations, *cf.* equation (7.17). We find it convenient to first discuss the main aspects of such a comparison on a qualitative basis and clarify our expectations before we subsequently turn to a more quantitative analysis. In section 7.2 we have reviewed that the HVI equations (7.6) predict the point vortices to traverse the condensate on straight lines. Thus, in light of the trajectories extracted from our simulations, displayed in figure 7.3, a comparison with the HVI equations must be restricted to a finite segment of the trajectories at intermediate times. Indeed, at early times, the phase-healing regime excludes a straight motion, *cf.* our discussion in section 6.4. During the late-time regime, on the other hand, the vortices can no longer be interpreted as being point-like dips in the condensate density and are thus not expected to follow solutions of the HVI equations which are only applicable in this limit. In fact, the deviations from the HVI trajectories at late times can also be observed in the strong bending of the trajectories in figure 7.3. Hence, if present, a segment in which the vortices follow the HVI trajectories is only expected at intermediate times when the dipole phase has healed and the vortex–anti-vortex separation is still sufficiently large so that the vortices are effectively point-like dips in the condensate density in which case strong bending in the trajectories is avoided. Indeed, in figure 7.3 there appears to be a regime during which the vortices move on straight lines.

In the following we analyse explicitly whether during this regime of the dipole evolution the vortex trajectories indeed follow solutions of the HVI equations. For that, we use the DGPE parameters $\tilde{\xi}, \gamma$ and τ obtained from the matching procedure, compute the HVI friction coefficients C, C' according to equation (7.14) and plug them into the solutions of the HVI equations (7.17). In order to examine if the

straight segments of the holographic and DGPE vortex trajectories agree with these solutions, we have to consider two criteria. First, does the enclosing angle of the straight segments of the trajectories (if extrapolated to their crossing point) agree with the one predicted by the HVI equations, *cf.* equation (7.18)? And second, does the time that passes as the vortices propagate along the segment agree with the HVI result? Explicit calculations show that for the given set of parameters, these criteria are not satisfied. However, there is a caveat in our procedure thus far. Namely, the HVI equations are only approximate solutions of the DGPE vortex dynamics in the $\tilde{\xi} \to 0$ limit, *cf.* section 7.2 for a discussion. In particular, in order for equation (7.14) to be valid, the healing length has to satisfy $\tilde{\xi} \ll 1$ in units of grid points. In contrast, in our DGPE simulations the healing length lies in an interval of $1.93 < \tilde{\xi} < 9.25$, also in units of grid points. Thus, deviations between the HVI solutions and our numerical simulations are expected. However, there is in fact a way to circumvent the disagreement in the healing lengths. Namely, one can make use of the rescaling symmetry of the DGPE (7.5) discussed in section 7.1. This symmetry implies that if we simulate the DGPE vortex dynamics on a rescaled numerical grid with $\boldsymbol{x'} = \boldsymbol{x}s \, , t' = ts^2$ where $s \in \mathbb{R}$ is a constant number and γ and τ are the same as before and we subsequently extract the trajectories and undo the rescaling, the trajectories agree exactly with those extracted from our original DGPE (and thus holography) simulations. Hence, for a comparison of the holographic and DGPE trajectories with solutions of the HVI equations, we can use the parameters obtained from a DGPE simulation on a rescaled numerical grid, including in particular the rescaled healing length $\tilde{\xi}' = \tilde{\xi}s$, to compute the HVI friction coefficients in equation (7.14) and subsequently evaluate the HVI solutions (7.17) with these values for the friction coefficients. Proceeding this way, we find that the two criteria for an agreement discussed above between the DGPE and the HVI solutions are indeed satisfied. That is, the straight segments of the DGPE dipole trajectories agree precisely with the solutions of the HVI equations. Let us give a specific example. We consider the DGPE solution with $\gamma = 0.313$, $\tau = 5.76$ and $\xi = 3.5$ which we have obtained by matching it to the holographic dipole dynamics for a chemical potential of $\mu = 6$, on the original grid with grid spacing $l = 1/8$. On the rescaled grid with a grid spacing of $l' = 14.5$, corresponding to a grid-unit healing length $\xi' = \xi(l/l') \equiv \tilde{\xi}/s = 0.03$, and thus a scale parameter of $s = 116$, the straight segments of the trajectories agree with the solutions of the HVI equations (7.17) (using $\tilde{\xi}'$ to evaluate C, C' in (7.14) and subsequently plugging this into (7.17)). As we have argued above, if one scales the DGPE trajectories extracted on the rescaled numerical grid back to the original grid in space and time, they coincide with the holographic trajectories. Likewise, the straight segments of their trajectories coincide with the solution of the HVI trajectories, with the parameters extracted from the DGPE simulation on the rescaled numerical grid, scaled back in space and time to the original grid.

In figure 7.3 we display the HVI solution for one of the vortices evaluated on the rescaled numerical grid but scaled back in space and time to the original one as a solid straight green line, placed below the holographic and DGPE trajectories on

the right-hand side. As we have discussed above, the time interval during which we evaluate the HVI equations begins only after the phase-healing regime.

We proceed likewise for the DGPE solutions that we have matched to the respective dipole dynamics in the holographic superfluid for all of our other choices for the chemical potential, $\mu = 4.5, 7.5, 9$. In these cases, we find the scale parameter to be $s = 114, 116, 119$. We emphasise again that the HVI equations have been shown to describe the DGPE point-vortex trajectories in the asymptotic limit $\tilde{\xi} \to 0$. Hence, the slightly different scalings with s are due to our matching of the HVI solutions for non-vanishing vortex sizes. With the DGPE parameters γ, τ and $\tilde{\xi}'$ we can now compute the phenomenological friction coefficients C and C', *cf.* equation (7.14), which we later compare to according values measured in experiments. We list the friction coefficients as well as the scale parameters with the other parameters in table 7.1.

In addition to studying the vortex trajectories, it is also interesting to analyse the temporal evolution of the relative distance $d(t)$ and the centre position $R(t)$ of the vortex dipole. For an exemplary holographic chemical potential $\mu = 6$ (the same as we have used in all other figures in this chapter), in figure 7.5 we show a comparison of the evolutions of $d(t)$ and $R(t)$, obtained from the holographic model, the DGPE and the solution of the HVI equations. The solutions of the HVI equations are obtained using $w_1 = 1$, $d_0 = 133.5$, $R(0) = 247.2$ and the respective friction coefficients C and C' stated in table 7.1. Importantly, the HVI solutions do not start at $d_0 = 150$, $R(0) = 256$ to exclude the outward-bended part of the DGPE and holography trajectories at short evolution times up to time $t = 190$ (*i. e.*, the phase-healing regime). Given the excellent agreement of the trajectories extracted from the holographic and DGPE simulations of the vortex dynamics, it is not surprising to find $d(t)$ as well as $R(t)$ to be in excellent agreement in these two theories as well. Like for the trajectories, deviations arise only during the very final stages of the evolution, *cf.* our discussion above. In figure 7.5 we again refrain from showing the final three unit timesteps of the dipole evolution during which the matching breaks down. For the exemplary evolution displayed in figure 7.5, we find that the HVI solution is in good agreement with the results obtained from the DGPE and the holographic model up to times $t \simeq 600$. Deviations arise for $t \gtrsim 600$. At this point the vortex trajectories begin to bend and deviations are thus expected. To ease the interpretation, we recall that the vortices annihilate at time $t = 977$ (again, for the $\mu = 6$ simulation). Except for the specific numbers quoted above, which are only valid for $\mu = 6$, we find, on a qualitative basis, the same results for all other choices of the chemical potential μ, only with adapted DGPE and thus HVI parameters. As a final comment of this subsection, let us note that for the comparison of the matched holographic and DGPE dynamics with the HVI equations it was vital to choose the initial separation of the vortices as large as 150 grid points. For separations distinctly smaller than 150 grid points, one cannot find a straight segment in the trajectories since after the phase-healing regime, the dipole size has already decreased so far as to prohibit an interpretation of the vortices in the point-particle approximation. We will comment further on the presence and
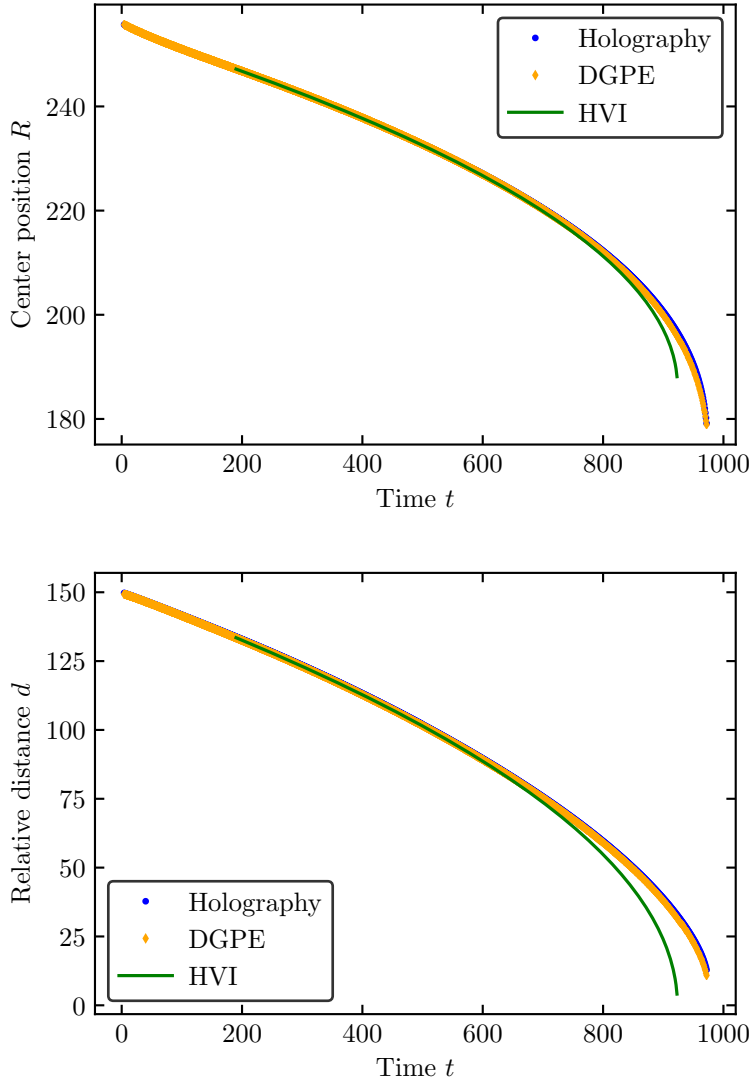
Figure 7.5: Illustration of the temporal evolution of the centre position $R(t)$ (upper panel) and the relative distance $d(t)$ (lower panel) of the vortex dipole with initial separation $d_0 = 150$ as obtained from the holographic model (blue dots), the DGPE (orange diamonds) and the HVI equations (green solid line, *cf.* (7.16)). All quantities are measured in grid units. The starting time of the HVI curves is the same here as in figure 7.3. Up to time $t \simeq 600$, the HVI solution agrees well with the results from the DGPE and the holographic model. For $t \gtrsim 600$, the HVI equations predict a faster approach of the vortex–anti-vortex pair resulting in a shorter lifetime of the vortex dipole. Note that the last point of the HVI trajectory shown in figure 7.3 corresponds to time $t = 575$.

duration of the transient regime after the phase healing and prior to the regime of strongly bent trajectories in the following chapter.

7.3.3 Geometric Interpretation of Dissipation in Holography

We have so far left unanswered the question why the matching of the trajectories breaks down during the very final stages of the evolution. In our analysis presented above, we have found that we cannot tune γ, the relevant DGPE parameter that controls the shape of the respective trajectories, such that the DGPE and holography trajectories agree in the regime of strongly deformed and overlapping vortex-induced density depletions. Moreover, we have found that the deviations between the matched trajectories set in already before the matching breaks down as is clearly discernible in figure 7.3. While the matching breaks down three unit timestep before the respective vortex–anti-vortex pairs annihilate, notable deviations between the trajectories occur approximately ten unit timesteps prior to the annihilation. In addition, we have also observed that, after the vortices have annihilated, the propagating density modulations in holography and DGPE differ strongly, *cf.* figure 7.4. The goal of this subsection is to gain a better understanding of what causes these deviations, in the vortex trajectories as well as in the characteristic behaviour of the rarefaction pulses after the annihilation.

Let us begin by studying the bulk configuration of the gauge–matter fields in the AdS$_4$ background. Within the holographic framework, quite generally, the bulk configuration gives much insight into the dynamics of the dual quantum theory. In figure 7.6 we illustrate the bulk views of the superfluid at a time shortly before the vortex–anti-vortex pair annihilates (upper panel) as well as at a later time when only the rarefaction pulse remains (lower panel). Below the phase-transition temperature, the scalar field condenses near the black-hole horizon, giving rise to the formation of a scalar charge cloud in the bulk [46]. We have elaborated on this in detail in sections 3.1 and 5.3. The charged condensate in the bulk screens the superfluid boundary from the black hole. In both panels of figure 7.6, the scalar charge cloud is depicted by the orange layers which are isosurfaces of the scalar charge density $\sqrt{-g}|\mathcal{J}^0|$ (with defining value 12.3). Here, the determinant g of the metric g_{MN} is not to be confused with the DGPE coupling constant. Since the charge density exhibits a maximum along the holographic z-direction, *cf.* figure 5.2, there are in fact two sheets of $\sqrt{-g}|\mathcal{J}^0|$. Naturally, a larger defining value decreases the separation between them. We also plot isosurfaces of the scalar field $|\Phi(\boldsymbol{x}, z)|^2/z^4$ (blue tubs, defining value 2.2). At the boundary, $|\Phi(\boldsymbol{x}, z)|^2/z^4$ reduces to the superfluid-condensate density $n(\boldsymbol{x})$, illustrated on the $z = 0$ slice with the same colour map as in the previous plots, *i.e.*, red denotes the background density n_0 and blue the respective zeros. In addition, the grey area at $z = z_\mathrm{h}$ in both panels depicts the black-hole horizon.

A vortex in the superfluid has a dual bulk representation in terms of tubes punching through the scalar charge cloud, *cf.* the upper panel of figure 7.6. The scalar field Φ vanishes in the centre of these tubes along the z-direction. Due to the bulk profile of Φ (*cf.* figure 5.1), the tubes increase in radius with increasing proximity
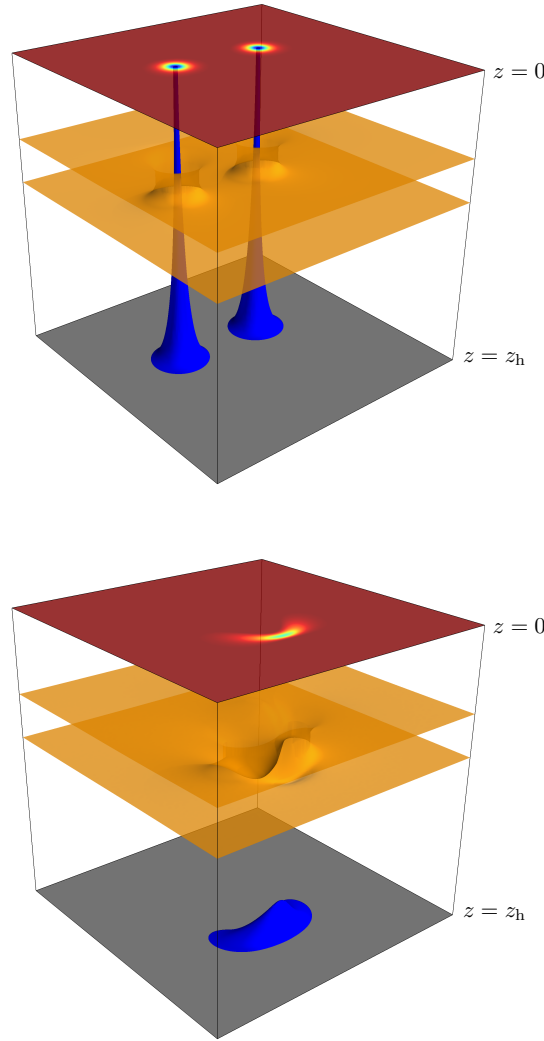
Figure 7.6: Geometric bulk representation of the holographic superfluid in the presence of vortices (upper panel, $t = 500$) and the rarefaction pulses (lower panel, $t = 975$). The blue surfaces are isosurfaces of the scalar field $|\Phi(\boldsymbol{x}, z)|^2/z^4$ and the orange layers are isosurfaces of the charge density $\sqrt{-g}|\mathcal{J}^0|$. The field $|\Phi(\boldsymbol{x}, z)|^2/z^4$ reduces to the superfluid density $n(\boldsymbol{x}) = |\psi(\boldsymbol{x})|^2$ at the boundary at $z = 0$ (illustrated with the same colour map as in Fig. 7.4). The grey area at $z = z_{\mathrm{h}}$ depicts the black-hole horizon. Superfluid vortices form tubes in the bulk field $\Phi(z)$, piercing through the charge density, and thus allow for an energy dissipation mechanism, *cf.* the upper panel. Once the vortices have annihilated, this mechanism ceases to exist as the holes in the charge density heal and the screening is restored (lower panel). For conciseness both panels show a quadratic subregion of the full (x_1, x_2)-domain.

to the black-hole horizon. An interesting consequence of the holes in the charge density is that they allow for energy and momentum excitations near the boundary to 'fall' into the black hole. This is the geometric interpretation of the dissipation mechanism in the holographic superfluid, discussed briefly in section 3.1. Due to the finite width of the tubes, only small wavelengths can fall through the tubes into the black hole and dissipation is thus dominated by ultraviolet (UV) modes [148]. The UV-dominated dissipation in the holographic system is a fundamental difference to the DGPE (7.1). In the DGP model, the dissipation parameter γ damps out modes of all wavelengths equally, including infrared (IR) modes. The deviations seen in the vortex trajectories between the DGPE and holography simulations during the final stages of the evolution may thus be due to the differences in the dissipation mechanisms. In our matching procedure we have matched the infrared physics of both theories. However, once the vortex separation is of the order of the vortex width and the respective density depletions overlap, UV modes strongly dominate the physics. While in the DGPE such modes are just equally damped out as IR modes, which we expect to dominate at earlier times, in holography the dissipation of UV modes strongly dominates over the dissipation of IR modes. Hence, we expect the dissipation in the holographic system to change while it stays the same in the DGP model. This appears to be a likely reason why the vortices deform differently and have deviating trajectories.

Once the vortices in the dipole evolution have annihilated, the respective holes in the charge density close. In particular, the corresponding zeros in Φ and thus $\sqrt{-g}|\mathcal{J}^0|$ disappear instantaneously. Consequently, the screening by the scalar charge cloud increases and energy and momentum modes can no longer as easily dissipate into the black hole. We show the respective bulk configuration in the lower panel of figure 7.6. The snapshot is taken three unit timesteps after the vortices have annihilated. We note that the defining values for the isosurfaces of $|\Phi(\boldsymbol{x}, z)|^2/z^4$ as well as $\sqrt{-g}|\mathcal{J}^0|$ are the same here as in the upper panel. At the boundary, one can clearly discern the propagating rarefaction pulse (the density depletion) which quickly picks up velocity and travels for about $\Delta t \approx 18$ unit timesteps before its density has approximately healed back to its equilibrium value n_0, *cf.* section 8.4 for further details. The holographic bulk representation of the pulse differs distinctly from the configuration dual to the vortices. In particular, the pulse does not punch a hole in the charge density. Instead, as time proceeds and the condensate density at the minimum of the pulse increases, also the charge density evens out. Thus, the geometric bulk interpretation suggests that for the holographic superfluid the presence of vortices strongly increases the dissipation. Nonetheless, it is important to note that the system is not necessarily dissipationless if vortices are not present. In the presence of rarefaction and sound waves the system is also dissipative, however, it appears likely that in these scenarios the dissipation is smaller than in the presence of vortices.

In the DGPE simulation the rarefaction pulse does not accelerate as strongly as in holography and is damped out much sooner. It does therefore not travel as far in space as its holographic analogue. A larger dissipation in the DGPE during this

regime may explain the observed behaviour. However, as in holography, also in the DGP model the dissipation mechanism becomes more relevant in the presence of vortices and is strongest in the vicinity of their cores. Indeed, as we have discussed in section 7.1, the zero mode in the DGPE is not damped. Nevertheless, from our qualitative analysis of the rarefaction pulse, we expect that in the holographic framework the relative decrease in dissipation in the absence of vortices is much more severe than in the DGPE. Otherwise, we would expect the evolution of the rarefaction pulses to have stronger agreement.

The deviations of the vortex dynamics in holography and DGPE during the final stages of the evolution prior to and after the annihilation, have implications also for a comparison of the respective dynamics of many-vortex configurations. If another vortex is located in the vicinity of an annihilating dipole, its subsequent time evolution is affected by the created rarefaction pulse. Since the characteristic behaviour of the pulse differs in DGPE and holography, an interaction between another vortex and the pulse induces deviations of the vortex behaviour in DGPE and holography. Hence, for ensembles of vortices, the trajectory of each individual vortex in DGPE and holography only agrees if the density of the vortices as well as their locations on the grid is such that at no point during the respective evolutions an annihilating dipole affects another vortex in its immediate vicinity. For some exemplary configurations, we have checked and confirmed this explicitly[8].

7.4 Discussion of Experimental Relevance

Let us now compare our findings for the damping parameter and the friction coefficients for the holographic superfluid to experimental realisations of quasi-two-dimensional superfluids and cold Bose gases.

In section 7.1 we have argued that the phenomenological damping parameter of the DGPE γ can be expressed as $\gamma \simeq 12\, M a^2 k_{\mathrm{B}} \tilde{T}/(\pi \hbar^2)$, in terms of the mass of the bosons M, the temperature $\tilde{T}$ of the condensate and the three-dimensional scattering length a. Moreover, for the present section, we have re-introduced $\hbar$ and the Boltzmann constant k_{B}. Taking into account typical temperatures of the order of $\tilde{T} \sim 100\,\mathrm{nK}$ for alkali gases such as ^{23}Na and ^{87}Rb and $a \simeq 3\,\mathrm{nm}$ and $5\,\mathrm{nm}$ for the respective scattering lengths, one infers $\gamma \simeq 12\, M a^2 k_{\mathrm{B}} \tilde{T}/(\pi \hbar^2) \sim 10^{-4} \ldots 10^{-3}$ which is two to three orders of magnitude smaller than the dissipation scale obtained from matching the DGPE to the holographic model, *cf.* table 7.1. To obtain the strong dissipation seen in our holographic simulations in an alkali gas would require increasing the scattering length, *e. g.*, close to a Feshbach resonance, while simultaneously decreasing the density n in order to fix $\tilde{\mu} = \sqrt{8\pi} a n/(M\sigma)$ and thus the healing length $\tilde{\xi} \sim \tilde{\mu}^{-1/2}$ to the value we have extracted from our matching procedure.

---

[8]See https://www.thphys.uni-heidelberg.de/∼holography/holoDGPE/ for a video demonstrating the agreement for an exemplary configuration of four vortices and four anti-vortices.

Hence, we conjecture that the holographic superfluid describes the motion of vortices in a highly dense system, with diluteness $\zeta = \sqrt{na^3/\sigma} \sim 1$, which requires $a \sim \sigma$ in the experimental setups realised thus far. Typically, such a system is difficult to be stabilised with bosons due to three-body-recombination loss prevailing at large scattering lengths [313]. However, this can be remedied by using ultracold paired fermions [314].

A supportive complement to our conjecture is obtained by comparing our results with vortex diffusivities measured in thin films of superfluid ^{4}He [31, 37, 247, 248] and in cold Bose condensates [33, 251]. The dissipative motion of vortices has been studied experimentally and compared with the description in terms of the HVI equations (7.6), (7.7) so far mainly in superfluid helium, in two-dimensional films [31, 37, 247, 248, 315–317] as well as in three-dimensional setups [318, 319]. However, here we are only interest in two- or quasi-two-dimensional systems. In addition, also experiments with atomic Bose–Einstein condensates provide versatile platforms for the study of dissipative vortex dynamics [32, 33, 40, 230, 250, 251, 299, 320–322]. Also a number of theoretical studies has been focused on the effects of dissipation on vortices in such systems, see, e.g., [249, 323–326].

A parameter of interest is the friction coefficient C' in the HVI equations which quantifies the motion of vortices perpendicular to the fluid flow and arises from the drag force created by interactions with the thermal excitations., *i. e.*, the normal component of the system. It is related to the appearance of $\gamma \neq 0$ in the DGPE. The relation of C' to the dissipation of the superfluid is usually being expressed in terms of the vortex diffusivity $\tilde{D}$. Their relation in two spatial dimensions is given by

$$C' = \frac{2\pi\hbar\, n_{\rm s}\sigma}{Mk_{\rm B}\tilde{T}}\, \tilde{D}\,, \tag{7.22}$$

where $n_{\rm s}$ is the three-dimensional superfluid *mass* density, σ is the thickness of the film, M is the particle mass and $\tilde{T}$ the temperature.

On grounds of dimensional arguments the diffusivity has been argued to be of order $\tilde{D} \sim \hbar/M$ near the critical temperature of the BKT transition [240, 242]. At temperatures in the Millikelvin to Kelvin regime, up to the BKT temperature, experiments have confirmed this value to form, by order of magnitude, an upper limit. In general, however, $\tilde{D}$ has been found to be strongly temperature dependent.

In experiments with thin films of superfluid helium, values of $\tilde{D} \sim 10^{-2} \ldots 1\,\hbar/M$, corresponding to $C' \sim 10^{-2} \ldots 1$, have been found [247, 248, 316, 317]. However, in recent experiments with superfluid helium films on silicon chips, coherent dynamics has been found to dominate, that is with very small friction $C' \sim 2 \ldots 3 \times 10^{-6}$ prevailing [31].

In experiments with ultracold dilute atomic gases at temperatures $T \sim 30\,{\rm nK}$ [33], friction coefficients have been measured to be of the order of $C' \sim 10^{-4}$.

For an order of magnitude higher temperatures of the atomic Bose gas, in the range $200\,{\rm nK} \lesssim \tilde{T} \lesssim 450\,{\rm nK}$, on the other hand, friction coefficients of $C' \sim 0.01 \ldots 0.03$ resulting from strong thermal friction, have recently been measured in experiment

Table 7.2: Friction coefficient C'. Left column: of the holographic superfluid, extracted from our matching procedure to the DGPE and HVI vortex dynamics. Centre columns: of thin films of superfluid helium extracted from different experiments. Right columns: of Bose–Einstein condensates, at ultra-low temperatures and including strong thermal friction due to larger temperatures. The extracted friction coefficients of the holographic superfluid are in good agreement with those measured in superfluid helium at $\tilde{T} \sim 1\,\mathrm{K}$ and in thermally excited Bose–Einstein condensates.

Holographic Superfluid	Helium	Helium $\tilde{T} \sim 1\,\mathrm{K}$	BEC $\tilde{T} \sim 30\,\mathrm{nK}$	BEC $\tilde{T} \sim 200\ldots450\,\mathrm{nK}$
	[31]	[247, 248, 316, 317]	[33]	[251]
$0.03\ldots0.1$	3×10^{-6}	$10^{-2}\ldots1$	10^{-4}	$0.01\ldots0.03$

with a dilute ^{23}Na gas [251]. There, the observed nearly linear temperature dependence is consistent with the prediction [323]

$$C' \simeq 0.1 \frac{4\pi\,aM^{1/2}}{\hbar\,\tilde{\mu}^{1/2}} k_\mathrm{B}\tilde{T}\,, \tag{7.23}$$

which is based on a high-temperature $(k_\mathrm{B}\tilde{T} \gg \tilde{\mu})$ evaluation of the analysis of [327]. Moreover, the data of [251] is also matched, at the higher temperatures, by a numerical evaluation of the Zaremba–Nikuni–Griffin kinetic approach [326], in which a generalised GPE is coupled to a Boltzmann equation for the thermal (normal) component [305, 306].

In our numerical matching procedure we extract friction coefficients for the holographic superfluid in the range $C' \simeq 0.03\ldots0.1$, *cf.* table 7.1. For a better overview of how these values compare with the experimentally measured friction coefficients, in various experimental setups, discussed above, we summarise them in table 7.2. The friction coefficients for the holographic superfluid are similar to those observed in strongly dissipative systems, namely in thin films of superfluid ^{4}He at temperatures $\tilde{T} \sim 1\,\mathrm{K}$ [247, 248, 316, 317] and in thermally excited atomic condensates [251]. Based on these findings we conjecture that vortex dynamics in the two-dimensional holographic superfluid should apply to the description of vortex dynamics in such systems.

It is important to appreciate that our findings go beyond the dynamics of vortex dipoles. The friction coefficients we have extracted from our matching procedure characterise not only the dynamics of single vortex dipoles but more generally the dynamics of all vortex ensembles in the holographic superfluid. In particular, only this fact has allowed us to compare the friction coefficients of the holographic superfluid

to values extracted from measurements of the vortex diffusivity in real-world super-fluids and Bose–Einstein condensates. Thus, our findings imply that holography can potentially be used to describe quantum turbulence induced by the appearance of quantised vortex defects in the above discussed experimental systems, *i. e.* superfluid helium and thermally excited Bose gases. In a number of works on turbulence in the two-dimensional holographic superfluid effects such as Kolmogorov scaling [148, 150], the approach to a non-thermal fixed point (see also chapter 13 for a discussion) [150] and many more (*cf.* [148, 150, 168]) have previously been reported. In light of our findings, these results may be considered predictions for turbulent behaviour of the above discussed real-world systems. For the future it would be very interesting to compare the results for the dynamics of vortex dipoles in the holographic superfluid obtained in this thesis as well as results regarding turbulent behaviour of the system directly to experimental findings.

8 Vortex-Dipole Kinematics

In the previous chapter we have used the dynamics of vortex dipoles to quantify the dissipative nature of the holographic superfluid in the presence of vortices. We have inferred the applicability of the holographic framework to experimentally realisable superfluids. In light of our findings and possible future applications of the gravitational model to the description of vortex dynamics in such superfluids, it is interesting to study the dipole dynamics in the underlying superfluid itself in more detail. In particular, despite our matching procedure to DGPE dynamics and our comparison of the vortex trajectories with solutions of the HVI equations, we have yet to fully analyse the kinematic aspects of the dipole evolution. The main goal of the present chapter is therefore to investigate not only the vortex trajectories in more detail but also the vortex velocities and accelerations as well as the respective dependences on the initial configuration of the dipole and on the chemical potential of the superfluid. In addition, we also study the rarefaction pulse that the vortices create as they annihilate. In this chapter we study the kinematic aspects of the dipole dynamics only for vortices in the holographic superfluid. With regard to the rarefaction pulse, on the other hand, we compare our findings with similar excitations in the GP model.

The contents of the following sections is split into three main parts. The first part comprises sections 8.1 and 8.2 and deals mainly with the dependence of the dipole dynamics on the initial vortex configuration. In section 8.1, we study the vortex trajectories for various initial vortex separations and analyse the dipole size $d(t)$ by means of its functional dependence on time. In addition, we comment on a how our findings compare with those of [163]. While the authors of [163] also study the time evolution of vortex dipoles in the holographic framework, our results extend and improve on their work in several ways. In the subsequent section 8.2, we compute derivatives of the trajectories and study the velocities and accelerations of the vortices. In the second part, in section 8.3, we analyse the dipole kinematics with regard to the dependence of the vortex velocities on the chemical potential of the superfluid. Finally, in part three, comprising only section 8.4, we investigate the rarefaction pulse that the vortices transition into after their annihilation and compare the characteristics of the pulse to similar excitations in the holographic superfluid as well as in the GP model.

Throughout sections 8.1, 8.2 and 8.4 we fix the chemical potential of the superfluid to $\mu = 6$ which corresponds to a ratio of $T/T_{\mathrm{c}} = 0.68$. While in the previous two chapters we have presented all our results in units of grid points, we find it convenient in this chapter to adopt physical units. Thus, unless explicitly stated otherwise, we multiply all observables by an appropriate power of the grid spacing l, which we set to

$l = 2/7$ for most of this chapter. The grid spacing l itself is measured in units fixed by our choice of $z_h = 1$. Employing physical units for the vortex–anti-vortex separation for instance, implies $d(t) \to d(t)l$. However, for notational simplicity we henceforth drop l again but keep in mind that we proceed likewise for all other parameters and observables. In our simulations we leave all further numerical parameters such as the number of grid points unchanged.

The content of sections 8.1–8.3 is mainly based on our publications [164, 258] and some parts are taken verbatim from them. For a better embedding in the context of this thesis, we have further added and modified several parts.

8.1 Vortex-Dipole Trajectories

For the success of our studies in the previous chapter it was essential that, after matching the dynamics of vortex dipoles in DGPE and holography for one initial dipole configuration, strong agreement of the vortex dynamics with regard to the vortex trajectories in both theories pertains also for all other initial dipole configurations. If the DGPE parameters extracted from the matching procedure were dependent on the initial dipole size or alignment, we could not have consistently related our findings to experiments on vortex dynamics in real-world superfluids. In this section we analyse explicitly how the vortex trajectories depend on the initial configuration of the dipole and justify that it has been sufficient to perform the matching procedure for only one specific initial condition in the previous chapter.

Due to translational and rotational symmetry of the underlying superfluid, all initial vortex–anti-vortex configurations can be transformed such that the dipole is horizontally aligned along the $x_2 = 256$ axis. Indeed, the vortex dynamics is fully independent of the initial alignment of the dipole on the grid. For a number of exemplary initial configurations of the dipole we have checked and confirmed this explicitly. Henceforth, we therefore focus solely on initial conditions where the vortex dipole is aligned along the $x_2 = 256$ axis and we only vary the initial separation of the vortex–anti-vortex pair.

Including the exemplary simulation of chapter 6, we study the dipole dynamics for five initial separations $d_0/l = 40, 60, 80, 100, 120$ in units of grid points. To be specific, in accordance with our discussion above, we imprint a vortex dipole consisting of one vortex and one anti-vortex onto the static background solution of the superfluid at positions $(x_{1,1}, x_{1,2}) = (256 + d_0/2l, 256)$ and $(x_{2,1}, x_{2,2}) = (256 - d_0/2l, 256)$, respectively. Here, d_0 has physical units which is why we have to divide by the grid spacing l in order to express the vortex–anti-vortex separation in units of grid points. With our choices of d_0/l and the size of the grid, we again suppress unwanted numerical finite-size effects, *cf.* our discussion in section 6.1. In particular, forces exerted on the vortices by the mirror vortices due to the periodicity of the grid are negligibly small.

After we have prepared the initial configurations, we evolve the respective systems in time until the vortices have annihilated. As before, we extract the vortex trajecto-

ries from the simulations using our combined tracking procedure of section 6.3. Thus far, we have employed the tracking routine at every unit timestep of the dipole evolution. Due to the strong increase of the vortex velocities at late times of the dipole evolution, this implies that the spatial separation between the vortex locations at two consecutive tracking steps is not equidistant. While at early times this separation is much smaller than one grid spacing, it distinctly exceeds on grid spacing during the final stages of the evolution, *cf.* figure 6.5. However, for an investigation of the characteristics of the dipole kinematics, it is essential to have an approximately uniform spatio-temporal resolution of the vortex trajectories throughout the entire dipole evolution. Hence, we need to track the vortices more frequently than at every unit timestep shortly before they annihilate. For the matching procedure tracking the vortices only at every unit timestep by contrast was sufficient since our interest concerned mainly the times prior to the annihilation. In fact, we even found that the matching breaks down during the final three unit timesteps of the evolution. In this chapter, on the other hand, we also want to study these times and show that the vortices exhibit very interesting behaviour shortly before they annihilate. In our numerical implementation, one unit timestep is composed of an adaptive number of smaller numerical timesteps. Hence, we can simply apply our tracking procedure at a given number of these numerical timesteps. In practice, we find that tracking the vortices 100 times over the period of one unit timestep is sufficient to re-establish the desired spatio-temporal accuracy of the vortex trajectories. We start applying this version of the tracking routine approximately seven unit timesteps prior to the annihilation. Notably, due to the increase of the temporal resolution, we can also determine the time of the annihilation of the vortex–anti-vortex pair much more precisely and are able to track the vortices even at times later than the endpoint of the evolution we would find if we tracked the vortices only at unit timesteps. A further increase of the number of tracking points would not increase the accuracy of the trajectories due to limitations imposed by the error on each individual vortex location originating from the tracking routine. It would, however, allow us to determine the endpoint of the evolution more precisely since for this it is only essentially whether the vortices have annihilated yet or not.

With the larger number of tracking steps we are able to locate the vortices until their separation is distinctly smaller than one unit grid point. However, as soon as the dipole size drops below one grid point, it is necessary to slightly adapt the NR method since we can no longer use the approximate vortex positions, obtained from locating the respective phase windings of the vortices, as initial guess in the algorithm (unless we Fourier interpolate the field). Indeed, once the vortices are both located within one plaquette of the numerical grid, the total phase winding outside the plaquette vanishes. As an alternative, we employ the vortex locations extracted from the previous tracking step (not unit timestep) as initial guess for the respective next step. This turns out to be an adequate choice to ensure that the NR algorithm quickly converges to the true vortex location.

In figure 8.1 we show the vortex trajectories for the five initial vortex–anti-vortex separations discussed above. For better visualisation, we display only a small sub-
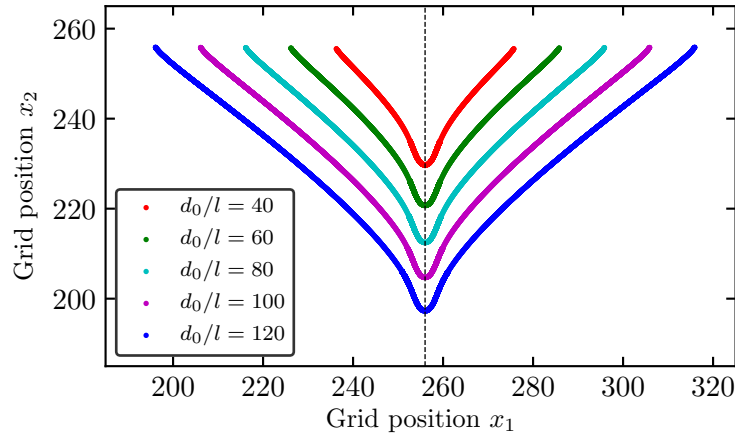
Figure 8.1: Trajectories of the vortex–anti-vortex dipole system in the holographic superfluid with temperature $T/T_{\rm c} = 0.68$ (corresponding to $\mu = 6$) for five different initial separations d_0/l in grid points. The vortices are imprinted along the horizontal $x_2 = 256$-axis and the respective systems evolved in time until the vortices have mutually annihilated. For conciseness we only show a subregion of the full (x_1, x_2)-grid. The slight initial outward bending can be attributed to our procedure of preparing the initial configurations, *cf.* section 6.4. The dashed line separates the trajectories of the vortices from the anti-vortices.

region of the full (x_1, x_2)-grid. The first point of all trajectories corresponds to time $t = 0$ in the respective simulations, when the vortices have fully developed their density profile. Due to the higher time resolution of the enhanced tracking routine (as compared to the previous chapters), we can track the vortices until their separation is distinctly smaller than the marker sizes used in figure 8.1. The increase in resolution during the late-time regime becomes particularly evident upon comparing the corresponding segments in the trajectories in figure 8.1 with those displayed in figure 6.4. Furthermore, the comparison illustrates the necessity of tracking the vortices more frequently than at every unit timestep if one is interested in their late-time behaviour. In order to avoid confusion, we stress that in figure 8.1 we indeed display two trajectories for every fixed initial separation. To aid the identification of the respective trajectories of the vortices and anti-vortices, respectively, we plot a straight vertical line, separating the respective trajectories, and moreover, depicting the x_1-position at which the vortices annihilate. At early times, the trajectories again exhibit a slight outward bending, for all initial vortex separations. We attribute this behaviour to the initially missing phase configuration coupling the vortex and anti-vortex phases, *cf.* our discussion in section 6.4, and thus to our preparation of the superfluid initial conditions. After the phase-healing
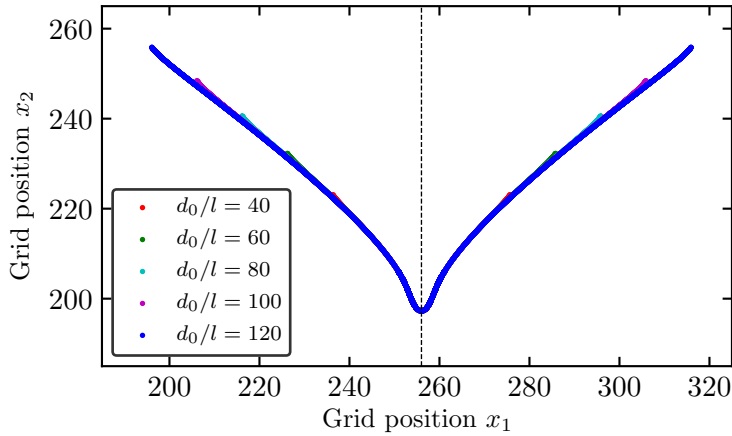
Figure 8.2: Illustration of the same trajectories as depicted in figure 8.1 above, now linearly shifted such that the vortices annihilate at the same (x_1, x_2)-position on the grid. At intermediate and late times, the trajectories are in excellent agreement, while the initial deviations are caused by the preparation of the initial vortex configuration (phase-healing regime). For conciseness we only show a subregion of the full (x_1, x_2)-grid.

regime, the vortices quickly bend inwards, approach and eventually annihilate each other. In the previous chapter we have shown that for large enough vortex–anti-vortex separations, but after the phase-healing regime, the vortices follow solutions of the HVI equations and propagate on straight lines. For the trajectories displayed in figure 8.1 we find that such a behaviour is only discernible for the largest initial vortex–anti-vortex separation given by $d_0/l = 120$ grid points (blue curves). For all smaller initial separations, the trajectories are bent either due to the phase-healing process or due to the finite width of the vortex-induced density depletions. Naturally, for these regimes of the trajectories a description in terms of the HVI equations is precluded.

After the phase-healing regime the vortices follow universal curves. For a better visibility of the universality, we linearly shift the trajectories displayed in figure 8.1 such that all associated vortex–anti-vortex pairs annihilate at the same position on the (x_1, x_2)-grid and we show the resulting curves in figure 8.2. Except for the respective early-time regimes the trajectories for all initial conditions are in excellent agreement. In fact, upon closer inspection we find that the trajectories do not only agree in space but also in time. By agreement in time we mean that at the same vortex–anti-vortex separation for all initial dipole sizes, the spatial distance each vortex travels between two consecutive tracking steps is the same. In other words, the vortex velocities for all initial dipole sizes agree when the vortex–anti-vortex pairs have the same separation. For details, see our discussions in the following

129

section 8.2. Hence, at intermediate and late times of the dipole evolution, the vortex kinematics is independent of the initial dipole size and unambiguously parametrised by the vortex–anti-vortex separation. With regard to the early-time regime of the dipole evolution we find that the phase healing takes slightly longer if the vortices are further apart as evidenced by the deviations of the respective trajectories from the universal curves in figure 8.2.

However, given the similarity of the initial conditions considered above, the strong agreement of the trajectories may not be overly surprising. In order to check if the dynamics is indeed universal, we perform an additional simulation of the dipole dynamics with a distinctly different initial condition and study how the corresponding vortex trajectories compare with those presented above. To be specific, we randomly distribute the vortex and anti-vortex on the quadratic grid and perturb the system with random phase noise[1]. Naturally, the random noise translates into an additional flow or velocity field of the vortices. Thus, at time $t = 0$ the vortices have different locations on the grid as well as an additional velocity component as compared to the vortices studied before. Without the phase noise, each vortex would solely move in the flow field of the respective other vortex and thus follow the curves shown in figure 8.2. We proceed as before and evolve the system in time until the vortices have annihilated. An analysis of the resulting trajectories shows that at intermediate and late times, after appropriate linear shifts and rotations, the trajectories indeed again approach the universal curves displayed in figure 8.2. At early times during the phase-healing regime, on the other hand, the additional phase component induces strong deviations from the trajectories of a dipole that has the same initial separation but in a system that is not initially perturbed by phase noise. However, since we are not particularly interested in this regime, the exact behaviour is not of importance to us. Our findings thus indicate that the additional phase contribution damps out quickly as the system is propagated in time and has no effect on the intermediate- and late-time behaviour of the vortices. We conclude that the physics of vortex dipoles in the holographic superfluid (at intermediate and late times) is indeed universal and depends only on the size of the dipole.

Having studied the vortex trajectories, we now revisit our discussion in section 7.3 concerning the characteristic behaviour of the vortex–anti-vortex separation $d(t)$ as a function of time. In order to motivate our following investigation, we briefly recall the essential statements of that discussion and in particular, review an important aspect of our analysis of the HVI equations in section 7.2. The HVI equations (7.6) predict the dipole size to decrease with the square root of the shifted time, $d(t) \sim \sqrt{t_\mathrm{a} - t}$, where t_a is the time at which the vortex–anti-vortex pair annihilates. In figure 7.5, we have explicitly compared the behaviour of point vortices according to the HVI equations with our results from the holographic and DGPE simulations and found that the curves only agree for a short intermediate period of time. These

---

[1]To perturb the system with random noise, we multiply the phase configuration $\mathrm{e}^{\mathrm{i}\,\mathrm{Re}(\Xi(\boldsymbol{x}))}$ into the bulk scalar field $\Phi(\boldsymbol{x}, z)$ at time $t = 0$, when the vortices have fully developed their density profile, for every fixed-z slice. Here, $\Xi(\boldsymbol{x})$ is obtained by randomly populating modes around the origin in momentum space and subsequently Fourier transforming back to real space.

deviations are expected since the HVI equations only capture the dynamics of point-vortex dipoles, while in the holographic (or DGP) system, the vortices have a finite width, *cf.* our discussion in section 7.3. Nevertheless, it is interesting to analyse if, in the holographic system, the dipole size $d(t)$ also exhibits a power-law behaviour for times after the phase-healing regime. We determine the approximate endpoint of the phase-healing regime by analysing at which point the outward bending ends and the trajectories follow the universal curves. In the following, we analyse the functional dependence of the dipole size on time for the same initial configurations that we have studied above. Naturally, the initial outward-bended part of the dipole evolution has to be excluded as it is an artefact of the preparation of the initial configuration.

In addition, we exclude the final five unit timesteps of the dipole evolution during which the vortices deform strongly and their density depletions overlap in large parts. Once the vortices have significantly merged, an interpretation of their cores and the induced density depletions in terms of quasiparticles (like in the HVI equations) appears to break down. Thus, deviations of $d(t)$ from its behaviour at earlier times are expected. In the following we discuss our explicit analysis and explain why we exclude the final five unit timesteps.

We make an ansatz for the functional dependence of $d(t)$, given by

$$d(t) = A(t_\mathrm{a} - t)^b \,, \tag{8.1}$$

where we have introduced the fitting parameters A, t_a and b. b is the scaling exponent which we are ultimately interested in. Since $d(t)$ changes behaviour during the final stage of the evolution which we exclude from our analysis, we expect t_a to deviate from the actual time of the vortex–anti-vortex annihilation that we extract from our tracking procedure. Thus, we leave it as a free parameter. For the fitting routine we use a Levenberg–Marquardt least-squares fitting algorithm. In figure 8.3 we show the vortex–anti-vortex separation, extracted from the trajectories in figure 8.1, as a function of the shifted time $t_\mathrm{a} - t$.

The double-logarithmic scale demonstrates nicely that the dipole size in the holographic system indeed follows a power-law behaviour according to (8.1). Two comments are in order here. First, despite excluding only the final five unit timesteps of the respective evolutions, the latest time in figure 8.1 corresponds to $t_\mathrm{a} - t \approx 10$. Since t_a must not be confused with the actual time of the annihilation, this is not worrisome. Second, t_a naturally differs for all curves, corresponding to the different initial conditions.

For all initial vortex–anti-vortex separations, the fitting procedure yields a scaling exponent of $b = 0.53 \pm 0.02$. We estimate the uncertainty of b by variations in the boundaries of the interval of the fitted data points at very large and very small separations. Since we cannot precisely pinpoint the end of the phase-healing regime, the upper boundary of the interval (at large separations) constitutes a large source of uncertainty. To determine the corresponding uncertainty of b, we vary the upper endpoint of the interval by ± 20 unit timesteps which we estimate to be the uncertainty in the time marking the end of the phase-healing regime. We find
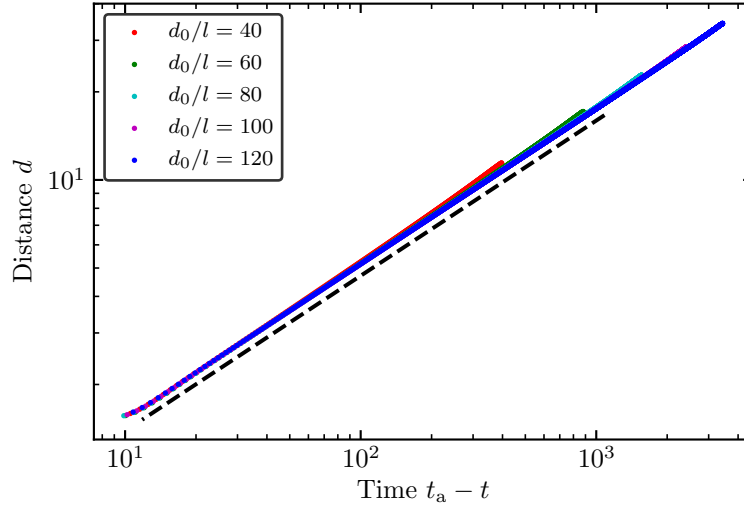
Figure 8.3: Vortex–anti-vortex separation as a function of the shifted time $t_\mathrm{a} - t$, where t_a is extracted from a fit and extrapolates to the annihilation time of the vortices, for five initial vortex configurations, on a double-logarithmic scale. The dashed black line illustrates the power-law behaviour according to $d(t) \sim (t_\mathrm{a} - t)^{0.53}$ (deliberately shifted downwards by one grid points) valid for all initial dipole sizes. After the initial phase-healing regime, the curves are in excellent agreement with the power-law behaviour, except for the final five unit timesteps of the evolution which we do not show here.

$\Delta b = \pm 0.02$. At small vortex–anti-vortex separations, on the other hand, we find the fitting procedure to be insensitive to the exclusion of more than the final five unit timesteps. The inclusion of more data points by contrast severely affects the fit. To be specific, excluding only the final four instead of the final five unit timesteps already alters the scaling exponent by $|\Delta b| = 0.02$. The inclusion of even more data points leads to very poor convergence properties of the fit. Consequently, we exclude $\Delta t = 5$ unit timesteps prior to the vortex–anti-vortex annihilation. The fitting routine itself reports an uncertainty for the scaling exponent of the order of $\Delta b \sim \pm 10^{-4}$ which is clearly negligible as compared to the uncertainties originating from the determination of the boundaries of the fitted interval.

The dashed black line in figure 8.1 illustrates the scaling behaviour according to equation (8.1) with $b = 0.53$, as extracted from the fits. We have deliberately shifted the line downwards from the curves by one grid point to aid the visualisation. At times later than the initial phase-healing regime for each of the initial conditions, the line is in excellent agreement with the respective curves. Hence, we find that as for the HVI equations, the dipole dynamics in the holographic superfluid also exhibits a power-law behaviour in the vortex–anti-vortex separation. The scaling exponents in

holography and the HVI solution agree within two standard deviations. Due to the finite width of the vortex-induced density depletions which render the HVI equations inapplicable exact agreement is not expected.

In [163] the authors study the dynamics of vortex–anti-vortex pairs in a holographic superfluid, with a particular focus on the functional dependence of the vortex–anti-vortex separation $d(t)$ on time. In the following we comment on how their results compare with the ones we have presented above. Before we do an explicit comparison though, let us first consider some general aspects and discuss how the underlying physical systems and the numerical implementations compare.

In both works, ours and [163], the same gravitational model of a two-dimensional superfluid is employed, for the same choice of the scalar mass and the dimensionless parameter μ/T, given by $\mu/T = 8\pi$. In addition, also the numerical methods used to solve the system of partial differential equations are very similar. The authors of [163] also employ a Fourier decomposition in the (x_1, x_2)-plane and a pseudo-spectral method with an expansion in Chebyshev polynomials along the holographic z-direction. However, differences arise in the grid sizes. While we use $512 \times 512 \times 32$ grid points along the (x_1, x_2, z)-directions, in [163] only 241×241 grid points along the (x_1, x_2)-direction and 25 collocation points along the holographic z-direction are used. There are strong differences in the numerical methods used to analyse the dipole dynamics. In [163] the vortices are tracked using a standard plaquette technique of locating their phase windings. As we have discussed in section 6.3, such methods have a significantly lower precision than our tracking algorithms and vortices can only be located with an uncertainty of one grid point.

The main result of [163] is that the dipole evolution splits into two distinct regimes, one for larger and one for smaller dipole sizes than twice the radius of an isolated vortex. The authors of [163] define the latter as the radius of the vortex-induced density depletion at 99% of the background density. They find that in both regimes the vortex–anti-vortex separation exhibits a power-law behaviour in $t_{\mathrm{a}} - t$ with different scaling exponents. For large separations they find a scaling exponent of $b = 1/2$, while at separations smaller than twice the vortex radius, they find $b = 2/5$. The large-distance power law of [163] agrees with the solution of the HVI equations. Above and in section 7.3 we have discussed that for sufficiently large vortex–anti-vortex separations and during a small stage of the dipole evolution, we find a similar behaviour. However, in our analysis we have found that deviations from the HVI solutions set in at significantly larger separations than twice the radius of the vortex-induced density depletions (adopting the definition of [163]). Furthermore, explicit computations show that we cannot find a power law with a scaling exponent of $b = 2/5$ at smaller separations. Neither beginning at the point where deviations from the HVI solutions set in, nor within any other interval at smaller separations.

There might be various reasons for the differences between our results and those presented in [163]. Let us only mention two possible explanations here. We particularly want to highlight the increase in accuracy of the vortex tracking algorithms in our analysis which also implies a distinctly higher precision of $d(t)$. Since fitting a power law of type (8.1) is very sensitive to the given data, it is essential that the un-

certainties in the computation of $d(t)$ are very small. In addition, we want to point to finite volume effects, *i. e.*, effects induced by the periodicity of the numerical grid, which may play a non-negligible role. Since we use distinctly larger grid sizes than [163], such effects may be more strongly suppressed in our results. In particular, we have checked explicitly that finite-volume effects are suppressed by performing one simulation of the dipole dynamics also on a (x_1, x_2)-grid with 1024^2 grid points which gave us the exact same result.

8.2 Vortex Velocities and Accelerations

In this section we continue our investigation of the dipole kinematics and study the vortex and anti-vortex velocities and accelerations as a function of their separation. The quasi-continuous nature of the vortex trajectories allows us to compute their derivatives with respect to time straightforwardly using finite-difference methods. However, due to the adaptive (numerical) timesteps, the common finite-difference methods have to be modified slightly. For details, see appendix A.5. In the following analysis our interest concerns in particular the universality aspect of the dynamics discussed in the previous section and we show that universality holds not only in space but also in time.

8.2.1 Vortex Velocities

We split the dipole motion into a longitudinal component along the dipole axis $\boldsymbol{d}(t)$ and a transverse component orthogonal to it. For our specific choice of initial configurations, the longitudinal component is parallel to the x_1-axis and the transverse component parallel to the x_2-axis. The centre-of-mass of the dipole moves along the transverse component. In the following, the longitudinal and transverse velocities of the vortices are denoted as $v_\parallel$ and $v_\perp$, respectively. In the next subsection we proceed analogously for the accelerations. Along the longitudinal direction, the velocities of the vortex and anti-vortex are opposite in sign but equal in modulus, $|v_\parallel(t)| = |\mathrm{d}\boldsymbol{d}(t)/\mathrm{d}t|/2$. Along the transverse direction, on the other hand, they agree precisely. In order to avoid having to distinguish between the vortex and anti-vortex velocities, we always refer to the modulus $|v_\parallel(t)|$ as the longitudinal velocity component of the vortices.

For the five initial conditions studied in the previous section, we show in figure 8.4 the corresponding vortex-velocity components along the longitudinal (upper panel) and transverse (lower panel) direction. The velocities are expressed in units of $c = 1$, where c is the speed of light. Since we have the freedom to arbitrarily rotate the coordinate system, we take the transverse velocity to be positive, without loss of generality. To wit, the velocity components are presented as a function of the dipole size and time therefore proceeds from right (large vortex–anti-vortex separations) to left (small separations). We furthermore point to the double-logarithmic scale used in both panels. The results agree very well with the intuition for the dipole dynamics gained in the previous section. At intermediate and late times of the
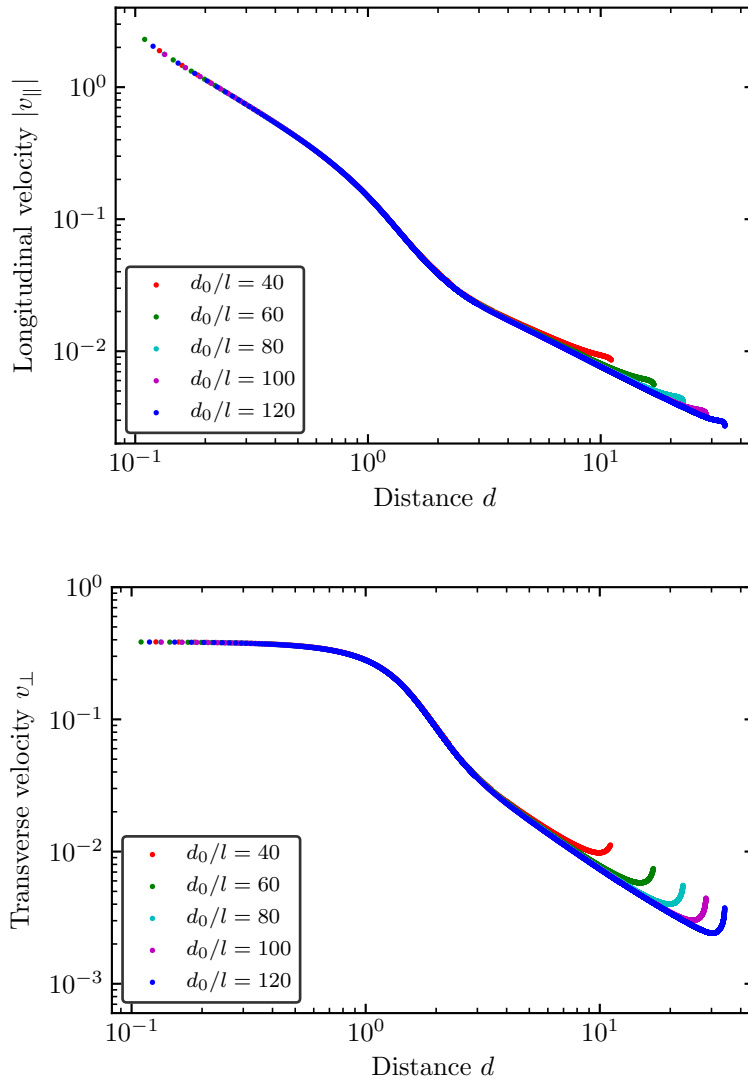
Figure 8.4: Vortex velocities as a function of the respective dipole size for the same five initial vortex configurations as shown in figure 8.1, along the dipole axis (longitudinal direction, upper panel) and orthogonal to it (transverse direction, lower panel). The curves clearly indicate universality of the velocities at intermediate and late times. The behaviour of the velocities at early times can be attributed to our preparation of the initial vortex configuration, *cf.* section 6.4. During the final stages of the vortex annihilation, the transverse velocities saturates to $v_\perp \simeq 0.37$, while the longitudinal velocity increases strongly. Note the double-logarithmic scale in both panels. During the final approximately seven unit timesteps of the respective evolutions the vortices are tracked one hundred times more frequently than at every unit timestep. The final points in both panels correspond to the time of the respective annihilations (determined with the enhanced time resolution).

evolution, the vortex velocities for all initial conditions coincide and thus depend only on the vortex–anti-vortex separation. Before we discuss the specifics of the velocities in more detail, we focus again on the universality aspect of the dynamics.

As for the trajectories, we double-check if independence on the initial configuration is also upheld if the vortices are initially prepared in a distinctly different configuration. To be specific, we consider the same initial configuration as before in section 8.1, given by a randomly distributed vortex–anti-vortex pair perturbed by random Gaussian noise. Proceeding as before, we find that just like the corresponding trajectories, also the velocities approach the universal curves shown in figure 8.4, despite the additional velocity field induced by the imprinted noise. Thus, the noise indeed damps out completely during the early stages of the evolution. While at early times, differences in the velocities are clearly present, they disappear at intermediate and late times. Hence, we find the vortex dynamics to be not only universal in space but also in time. The dipole system completely loses knowledge of its initial configuration, and the dynamics is solely parametrised by the vortex–anti-vortex separation. It follows that after matching the DGPE and holographic dynamics of vortex dipoles for one initial configuration of the vortices, they agree for all other configurations as well. We have checked explicitly that also in DGPE the vortex dynamics is indeed universal. In our studies in chapter 7 agreement of the dynamics independent of the initial configuration has been a crucial prerequisite for a consistent comparison with experimental results.

We now discuss the vortex velocities in more detail. During the initial phase-healing regime, the vortex velocities displayed in figure 8.4 clearly deviate from the universal curves. The transverse velocity even undergoes a phase of deceleration. We have already inferred such a behaviour in section 6.4 from the streamline plot in figure 6.6. Indeed, at short distances away from the vortex cores, the streamlines have components pointing in the direction opposite to the centre-of-mass motion of the vortices, causing the vortices to be slowed down along their transverse direction. Henceforth, we again exclude this phase-healing regime from our analyses and focus on intermediate and late times of the dipole evolution.

Figure 8.4 also illustrates that the transverse velocity of the vortices saturates during the final stages of the evolution. It still increases slightly, but its slope is orders of magnitude smaller than at earlier times. We find the final velocity at the time of the annihilation to be given by $v_\perp \simeq 0.37$. However, the accuracy of the extracted value is limited by the uncertainty of the vortex locations at this stage of the evolution as well as due to limitations in the time resolution resulting from the finite time-stepping scheme of our simulations. Nevertheless, since we are only interested in an estimate here, the precision of $v_\perp = 0.37$ is sufficient for all later purposes (see section 8.4). Unlike the transverse component, the longitudinal velocity does not saturate but increases strongly throughout the evolution at intermediate and late times. In fact, while for most of the dipole evolution, the transverse velocity is larger than the longitudinal velocity, the latter dominates strongly during the final stages shortly before the vortices annihilate, *cf.* figure 8.4. At the time of the annihilation, to our resolution, the longitudinal velocity is about an order of magnitude
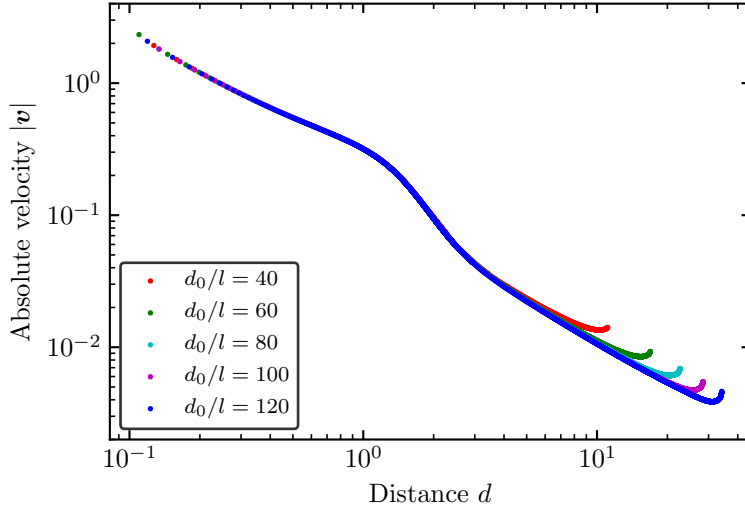
Figure 8.5: Absolute vortex velocity, $|\boldsymbol{v}| = \sqrt{v_\perp^2 + v_\parallel^2}$, as a function of the dipole size for the same five initial configurations as shown in figure 8.1. A comparison with figure 8.4 clearly indicates that at late times the absolute velocity is strongly dominated by the longitudinal velocity component. Note the double-logarithmic scale.

larger than the transverse velocity. In particular, it even exceeds the speed of light. Importantly, such high velocities are not in violation of causality. Due to the strong deformations of the vortex-induced density depletions which largely overlap at these times, the quasiparticle interpretation for the vortices is spoiled. When at late times the longitudinal velocities exceed the speed of sound, the vortices have merged into a peanut-shaped density depletion and the dynamics is strongly dominated by the merging process. Thus, the extracted velocities at these times must not be interpreted as velocities of a mechanical motion in the common sense. On a qualitative level, the observed behaviour of the vortex velocities was expected from the shapes of the trajectories displayed in figure 8.1. Indeed, shortly before the vortices annihilate, their trajectories bend strongly and the vortices eventually annihilate under a very large angle, in particular as compared to the one predicted by the HVI equations or from simple extrapolation of the trajectories at earlier times.

Finally, in figure 8.5 we show the absolute velocity $|\boldsymbol{v}| = \sqrt{v_\perp^2 + v_\parallel^2}$ of the vortices as a function of their separation for the same initial configurations as studied above. Except for the late-time regime, the vortex velocities are very small and well below the speed of light. In particular, the vortex motion is non-relativistic, in agreement with measurements of vortex dynamics in experimentally realised superfluids [134]. These findings again corroborate that the holographic system captures the physics of a non-relativistic superfluid.

8.2.2 Vortex Accelerations

We now proceed to studying the accelerations of the vortices. Our general procedure will be just the same as for the velocities. Namely, we again split the dipole motion into its longitudinal and transverse components and study the accelerations as a function of the vortex–anti-vortex separation.

In figure 8.6 we show the longitudinal (upper panel) as well as transverse (lower panel) acceleration of the vortices for the same five initial dipole configurations as studied before, on double-logarithmic scales. Since the transverse acceleration changes sign after the phase-healing regime, we plot its modulus. In light of our previous findings, it is not surprising to find the vortex accelerations to be universal at intermediate and late times of the evolution. Likewise, also during the early phase-healing regime, the accelerations exhibit the behaviour we have already inferred from the vortex velocities in figure 8.4. Indeed, the transverse accelerations cross zero, which manifests itself as a kink in the curves. The longitudinal component has no zero-crossing. However, it does decrease significantly at early times as figure 8.6 nicely visualises. This decrease in acceleration along the longitudinal direction causes the outward bending of the vortex trajectories.

After the phase-healing regime, the accelerations along both directions of the dipole motion increase monotonously. Only at very late times, we find the transverse acceleration to saturate and become approximately constant. This behaviour agrees well with our findings of the previous sections for the vortex trajectories and velocities, *cf.* figures 8.1 and 8.4, respectively. Along the longitudinal direction, on the other hand, the vortex acceleration increases most strongly during the final timesteps of the evolution and is approximately three orders of magnitude larger than the transverse acceleration.

From the vortex accelerations, we could now in principle infer the forces exerted on each of the vortices. However, that would require an estimate for the vortex masses. Since vortices are depletions in the condensate density, defining their mass in a superfluid or Bose–Einstein condensate is not a straightforward task and has been under debate for many years. Suggestions range from defining it as the kinetic energy of the associated flow field [328–330], over the energy cost of moving it through the condensate [331], the mass of the displaced superfluid condensate [332] or the hydrodynamically defined Kopnin mass for vortices in Fermi superfluids [333–335], to a definition in terms of so-called Kelvin-wave excitations of the quantised vortex. We address Kelvin-wave excitations of vortex defects in superfluids and specifically in the three-dimensional holographic superfluid in section 14.3 of Part II. However, non of the above definitions is directly applicable to our simulations of vortices in a (strictly) two-dimensional system where the vortices are not excited by Kelvin waves. Thus, for now it appears out of reach to define or compute the mass of vortices in the holographic superfluid. Nevertheless, a comment is in order here. Even if the mass of the vortices was known, it would still not make sense to interpret the motion of the vortices in terms of a force field which could, in principle, be computed in this scenario. In classical mechanics, a force field defines the force exerted on a
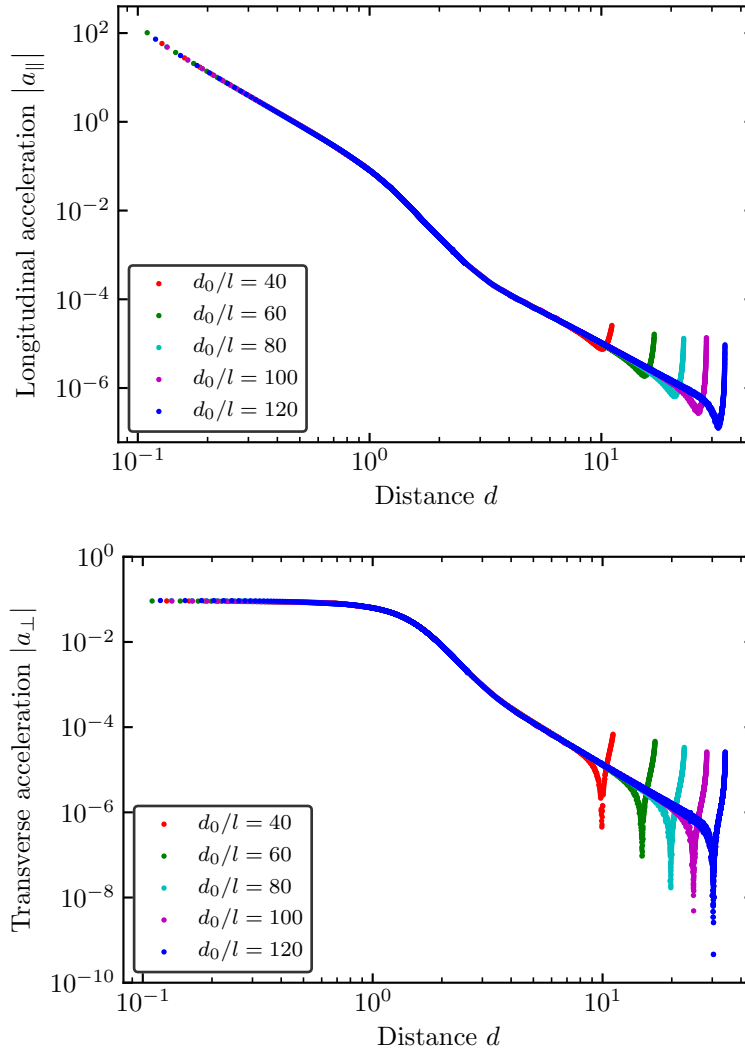
Figure 8.6: Vortex accelerations as a function of the dipole size for the same five initial vortex configurations as shown in figure 8.1 along the dipole axis (longitudinal direction, upper panel) and orthogonal to it (transverse direction, lower panel). The curves clearly indicate universality of the accelerations at intermediate and late times. At early times, the behaviour can again by be attributed to the preparation of the initial vortex configuration, *cf.* section 6.4. At the kinks in the transverse component, the acceleration changes sign. Note the double-logarithmic scale in both panels.

probe-body throughout spacetime. For quantised vortices such an interpretation is not sensible. Indeed, since a vortex naturally has strong long-range effects on the superfluid configuration, it cannot be interpreted as a probe-body.

For a discussion of forces acting on the vortex dipole we therefore refer to our qualitative discussions in section 7.

8.3 Dipole Dynamics at Varying Chemical Potential

In the previous two sections, we have fixed the chemical potential of the holographic superfluid and analysed how the dynamics of vortex dipoles depends on the initial configuration of the vortices. While we have now understood the dynamics of vortex dipoles in general, we have yet to answer the question how exactly the physics of vortex–anti-vortex pairs depends on the chemical potential, or equivalently the temperature, of the holographic superfluid. From our investigations in chapter 7 we already know how the superfluid characteristics, including dissipation, depend on the chemical potential. Likewise, we have studied how the width of a vortex-induced density depletion depends on μ. In this section, we now investigate how the vortex velocities depend on the chemical potential. We expect the universality of the dipole dynamics found in the previous sections to hold also for all other choices of the chemical potential. Thus, throughout this section we only choose on one initial vortex configuration.

8.3.1 General Considerations

In this section, we study the dependence of the dipole dynamics on the chemical potential for the same values that we have also used in our matching procedure in chapter 7, supplemented by one additional value given by $\mu = 5.1$. Thus, we simulate the holographic superfluid for $\mu = 4.5, 5.1, 6, 7.5, 9$ and study how the vortex velocities depend on these choices. All but the additional value of the set of chemical potentials are also marked by the ticks on the μ-axis in figure 5.1. We recall our convention of setting $z_{\mathrm{h}} = 1$ which implies that every choice of μ fixes the critical temperature of the superfluid and thus the ratio T/T_{c}. Our choices for μ discussed above set the system in the superfluid phase at ratios $T/T_{\mathrm{c}} = 0.9, 0.8, 0.68, 0.54, 0.45$. Note that the inclusion of the additional chemical potential ensures that the ratios T/T_{c} are approximately equally spaced ($\mu = 5.1$ corresponds to $T/T_{\mathrm{c}} = 0.8$). In table 8.1 we summarise all chemical potentials, the associated ratios T/T_{c} and further important simulation parameters.

In chapter 7, we have extracted the width ξ of a vortex-induced density depletion in the holographic superfluid from Gaussian fits to the density modulation and found it to scale with the chemical potential μ, *cf.* figure 7.2 (see also [161]). Despite using Gaussian fits, we have argued that the results for ξ agree with those for $\tilde{\xi}$ extracted from matching a GPE solution to the holographic vortex and tuning the healing length $\tilde{\xi}$ until the vortex sizes agree, *cf.* section 7.3. In this light, we will henceforth refer to ξ as the healing length of the holographic superfluid but keep in mind the

Table 8.1: Numerical parameters employed in the simulations of the vortex-dipole dynamics for the given values of the chemical potential. The temperature ratio T/T_c is not independent of μ and can be inferred from equation (5.20). The healing lengths given in the table have physical units, just like the initial dipole size d_0. We also give the values of condensate background density n_0 and L, the size of the computational domain. For details on our procedure, see the main text.

μ	T/T_c	n_0	ξ	d_0/ξ	L/ξ
4.5	0.90	5.5	1.16	39.2	126.5
5.1	0.80	16.1	0.85	39.2	171.1
6	0.68	41.7	0.44	39.2	334.4
7.5	0.54	120.2	0.32	39.2	457.1
9	0.45	265.2	0.24	39.2	606.4

slight abuse of notation. In table 8.1 we also give the values of ξ for the relevant chemical potentials studied in this section. Here, ξ is also expressed in physical units. In order to account for the dependence of the vortex size on the chemical potential, we study the vortex velocities for every choice of μ as a function of the dimensionless distance $d(t)/\xi$. Indeed, for a fixed dipole size $d(t)$ it may happen that for small chemical potentials the vortex-induced density depletions already deform and overlap, while for large chemical potentials they are still well separated and perfectly spherical. Given these circumstances, a straightforward comparison of the respective vortex velocities would not be sensible. It appears more sensible to compare the velocities only for fixed ratios of the dipole size and the healing length.

As we have shown above, the universality of the vortex dynamics allows us to restrict our investigations to only one specific initial configuration of the vortices. For simplicity, we take this configuration to be similar to the ones studied in the previous sections. To be specific, we prepare one vortex and one anti-vortex aligned along the $x_2 = 256$ axis of the quadratic (x_1, x_2)-grid, centred around $x_1 = 256$ with a separation of $d_0/\xi = 39.2$, where ξ is adapted for every choice of the chemical potential. For $\mu = 6$ this corresponds to $d_0/l = 60$ grid points. We stress that a fixed distance $d(t)/\xi$ implies that in physical units the initial vortex–anti-vortex separations differ. For our numerical simulations we again use 512×512 grid points in the (x_1, x_2)-plane and 32 Chebyshev polynomials along the holographic z-direction. Furthermore, we adapt the (x_1, x_2)-grid spacing l for every chemical potential to ensure that the vortices are resolved by a sufficiently large number of grid points. In practice, we resolve each vortex by approximately 13 grid points in diameter at 95% of the background density. Importantly, changing the grid spacing has no effect on the observables. It is, however, essential for our analysis since the Gaussian tracking routine requires a certain width for the respective fits to converge. The

grid spacing also fixes the physical size $L^2 = (N_{\boldsymbol{x}}l)^2$ of the computational domain in the (x_1, x_2)-plane. Here, $L = N_{\boldsymbol{x}}l$ is the side length of the quadratic grid, with $N_{\boldsymbol{x}} = 512$ the number of grid points along the (x_1, x_2)-directions. With our choices of l we ensure that the domain is sufficiently large such that, to the precision we seek for our studies, finite-size effects are suppressed. In the sixth column of table 8.1, we give the side length L of the grid relative to the healing length of the respective system, L/ξ.

8.3.2 Vortex Velocities

We now study the velocities of the vortices for varying chemical potentials of the holographic superfluid. After preparing the initial configurations as explained above, we evolve the system in time and track the vortices using our combined tracking algorithms outlined in section 6.3. The initial time it takes the system to build up the characteristic density profile of the vortices around their cores is slightly dependent on the chemical potential of the superfluid. For all values considered here, we find the process to take less or equal than $\Delta t = 10$ unit timesteps. Once the vortices have fully built up, we 'reset the clock' to $t = 0$ and employ our tracking routine to locate them on the grid. As in the previous sections, we again employ an enhanced version of the tracking routine, locating the vortices during the final stages of the evolution one hundred times more frequently than at every unit timestep. Hereby, we ensure that the vortex velocities are accurately resolved throughout the entire dipole evolution. Due to our choices for the grid spacing, the tracking algorithms work equally well for all chemical potentials. Thus, the uncertainties for the vortex locations and hence for the velocities are of the same order of magnitude. For all choices of the chemical potential, we employ the NR method for dipole sizes smaller than $d(t)/\xi = 7.2$ and for all larger sizes the Gaussian fitting routine. For $\mu = 6$, the transition point specified by $d(t)/\xi = 7.2$ translates into $d(t)/l = 11$ in units of grid points which agrees with our previous choice. In our investigations in chapter 7 we have employed an analogous procedure. To compute the velocities, we again use finite-difference methods, *cf.* appendix A.5, and split them into a longitudinal and transverse component, just as in section 8.2.

In figure 8.7 we show the longitudinal (upper panel) and transverse (lower panel) components of the vortex velocities as a function of the vortex–anti-vortex separation divided by the respective healing length ξ. The velocities are ordered with the chemical potential of the superfluid. For both the longitudinal as well as the transverse component, we find that at a fixed vortex–anti-vortex separation $d(t)/\xi$ the vortex velocities are lager for higher values of the chemical potential of the superfluid. At very late times the transverse component of the velocities flattens and saturates for all μ. The final velocities along the transverse direction at the time of the annihilation are also strongly dependent on the chemical potential. The final velocity is largest for the highest value of μ. Along the longitudinal direction of the dipole motion, on the other hand, the velocities increase strongly, even in the late-time regime. Due to the finite time difference between two consecutive steps in the
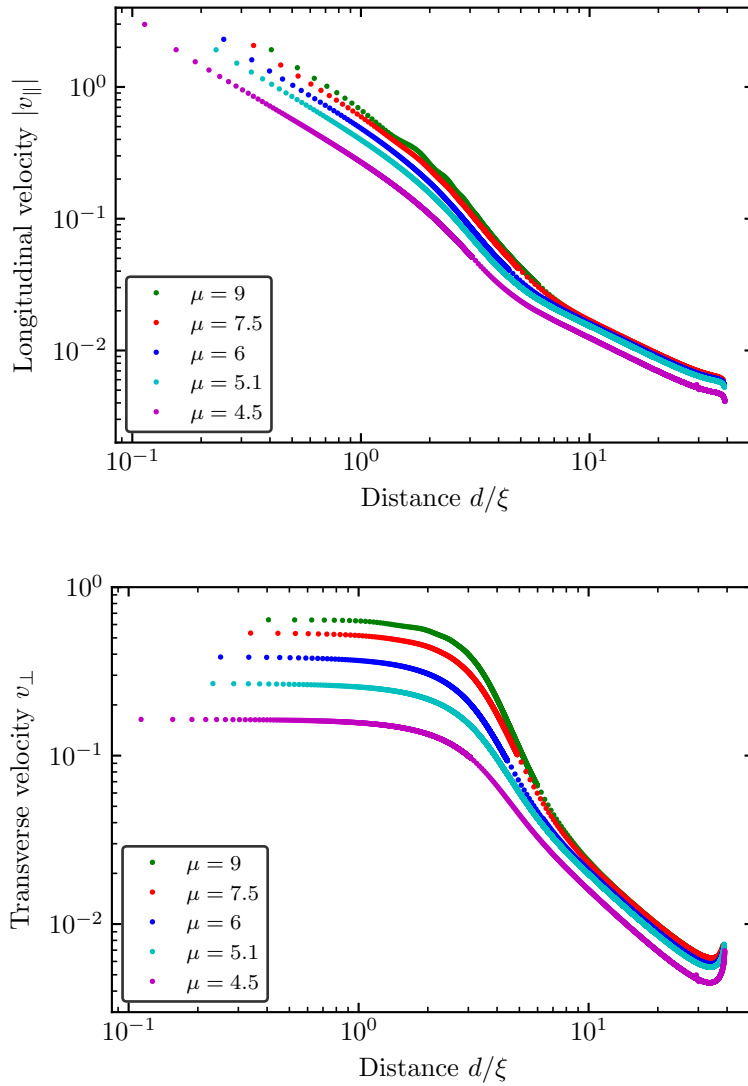
Figure 8.7: Longitudinal (upper panel) and transverse (lower panel) vortex velocities for five values of the chemical potential of the holographic superfluid as a function of $d(t)\xi$. Here, $d(t)$ denotes the vortex–anti-vortex separation in physical units and ξ is the healing length of the holographic superfluid for the respective temperature ratio, *cf.* main text. In the initial configuration, the dipole size is chosen according to $d_0/\xi = 39.2$. At fixed $d(t)/\xi$, both velocity components obey an ordering with the chemical potential of the superfluid and are larger for higher values of μ. For the transverse velocity this results in an ordering of its saturating value during the vortex–anti-vortex annihilation. Note the double-logarithmic scale in both panels. During the final approximately seven unit timesteps of the respective evolutions the vortices are tracked one hundred times more frequently than at every unit timestep. The final points in both panels correspond to the time of the respective annihilations.
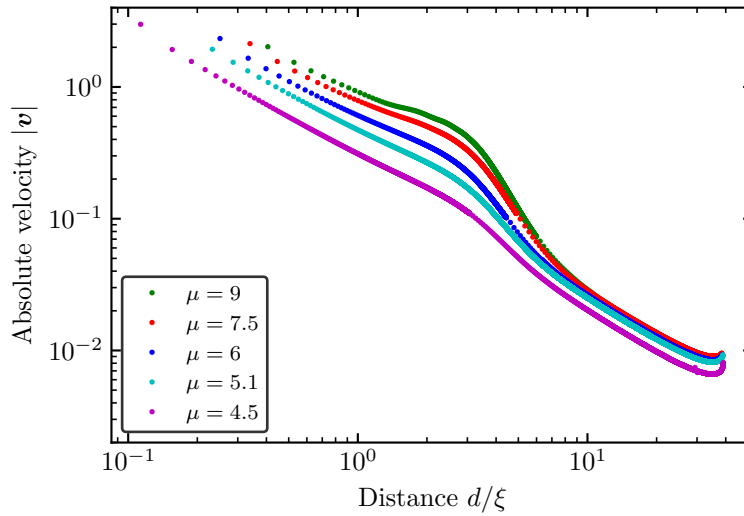
Figure 8.8: Absolute vortex velocities, $|\boldsymbol{v}| = \sqrt{v_\perp^2 + v_\parallel^2}$, as a function of the vortex–anti-vortex separation $d(t)/\xi$ for the same values of the chemical potential μ and initial configurations as in figure 8.7 above. ξ is the healing length of the holographic superfluid for the respective chemical potential, *cf.* main text. Note the double-logarithmic scale.

tracking routine and the strong increase of the velocity shortly before the vortices annihilate, we cannot unambiguously determine an ordering of the final longitudinal velocity with the chemical potential. We stress that the final points of the curves in figure 8.8 correspond to the time of the respective vortex–anti-vortex annihilation in the sense that 0.01 unit timesteps later, we can no longer locate the vortices.

At early times of the evolutions, during the phase-healing regime, we again find the same behaviour for the vortex velocities as in the previous section, induced by the initial preparation of the vortices. Interestingly, the length of the phase-healing regime depends mildly on μ. In our matching procedure of the previous chapter and specifically in the comparison of the dipole dynamics in holography and DGPE with solutions of the HVI equations, we have taken this dependence into account. For completeness, we also show the absolute velocity of the vortices for the various values of the chemical potential in figure 8.8. For all studied values of the chemical potential, the absolute vortex velocity is dominated by its transverse component at early and intermediate times and by its longitudinal component at late times.

We refrain from showing the vortex accelerations here as they yield no new insight into the dependence of the dipole kinematics on the chemical potential. Instead, we only state the important results here for convenience. Naturally, the overall dependence of the accelerations on the vortex–anti-vortex separation is the same for all chemical potentials. In particular, it qualitatively agrees with the accelerations

for the specific choice of $\mu = 6$ displayed in figure 8.6. In addition, like the velocities, also the accelerations along both, the longitudinal as well as transverse direction, are ordered with the chemical potential. At fixed $d(t)/\xi$, they are larger for larger values of μ. We also find the transverse acceleration to saturate for all choices of the chemical potential where, again, the final values are ordered with μ.

8.4 Rarefaction Pulse and Sound Waves

In the previous sections of this chapter we have presented an in-depth study of the dynamics of vortex dipoles. We have tracked their motion, analysed their trajectories and derived their velocities and accelerations. For all of these investigations, we have considered times prior to the annihilation. We proceeded similarly in chapter 7 where we have matched solutions of the dissipative Gross–Pitaevskii equation to the vortex–anti-vortex dynamics in the holographic superfluid. There, we have found that the matching breaks down shortly before the vortices annihilate and ignored all times past that point. In all of these discussions we have swept under the carpet what happens after the vortices annihilate, only briefly mentioning the propagation of some rarefaction pulse (also, rarefaction wave). Hence, there are still several unanswered equations with regard to the excitation that the vortices transition into as they annihilate. Namely, what happens to the density depletions after the phase windings disappear? How long does it take for the system to equilibrate? And most importantly, what can we learn from the dynamics of the rarefaction pulse about the holographic superfluid? The goal of the present section now is to shed light on the superfluid dynamics at times after the annihilation of the vortex–anti-vortex pair and to investigate the vorticity-free excitation left behind by the annihilating vortices. We are interested in the density modulation transverse to the dipole axis, *i. e.*, along the centre-of-mass motion of the vortex–anti-vortex pair. We restrict ourselves to one specific choice of the chemical potential, namely $\mu = 6$ which lies approximately in the centre of the interval of chemical potentials considered in the previous section. As a technical side remark, we note that throughout our following investigations of the rarefaction pulse, we again employ a grid spacing of $l = 2/7$ in our simulations.

We begin our investigation with some general remarks regarding rarefaction pulses and soliton excitations of superfluids (subsection 8.4.1). Subsequently, in subsection 8.4.2, we set out our evaluation method and finally, in subsection 8.4.3, we discuss the observed time evolution and kinematics of a rarefaction pulse in the holographic superfluid.

8.4.1 General Considerations on Rarefaction Pulses and Solitons

In figure 6.2 of section 6.1, we have displayed four characteristic snapshots of the evolution of a vortex–anti-vortex pair. The lower left panel of that figure shows the condensate-density configuration a few unit timesteps before the annihilation. At the time the snapshot is taken, the vortices have already strongly deformed and their

density depletions overlap in large parts and they have merged into a peanut-shaped form. Shortly thereafter, the phase windings of the vortices annihilate each other, leaving behind a strong depletion in the condensate density. We show a snapshot of the evolution of the density depletion, *i. e.*, the rarefaction pulse, in the lower right panel of figure 6.2. At even later times, the depth of the density depletion gradually declines and the superfluid equilibrates. Moreover, in figure 7.6 we have displayed the bulk configuration dual to a propagating rarefaction pulse. For a discussion of the characteristics of the bulk view see section 7.3.3.

To gain an understanding of the nature of rarefaction pulses created by annihilating vortices, let us take a brief detour to the Gross–Pitaevskii model in the context of which much work has been done with regard to such non-vortical superfluid excitations (see *e. g.* [136]). While we have so far exclusively discussed vortex excitations, there exists another important class of topological non-perturbative excitations of superfluids or, more generally, Bose–Einstein condensates, namely solitons [336]. Solitons are localised depletions in the condensate density with a phase jump across their minimum. In their seminal work on two-dimensional axisymmetric solitary-wave solutions in weakly dispersive media [337], Jones and Roberts found that there exist two branches of stable GPE solutions for solitons. In the regime of high velocities and shallow density depletions, they showed that the solitons obey the Kadomtsev–Pitviashvili equation [338] (see also [339] for a closed-form expression of this equation). These so-called lumps propagate the faster the shallower the density minima, with a maximum velocity given by the speed of sound. When reaching the speed of sound, the lumps decay into sound waves. Going to smaller velocities, on the other hand, Jones and Roberts found that there exists a critical velocity at which the soliton density depletion reaches zero. Upon lowering the velocity even further, the zero in the condensate density bifurcates and each of the created zeros carries a quantised phase winding of 2π and -2π, respectively. Thus, the soliton splits into a vortex–anti-vortex pair whose dipole vector is aligned orthogonally to the direction of the soliton propagation. With further decreasing soliton velocity, the vortex–anti-vortex separation increases. Hence, in the GP model, the rarefaction pulses created by annihilating vortices are typically associated with GPE soliton solutions classified by Jones–Roberts, as this is just the reversed process of the one we have just discussed. Importantly, the work of Jones and Roberts concerns only solutions of the non-dissipative GP model, while in the previous chapter 7 we have observed rarefaction pulses in the dissipative GP model, *cf.* panel (*d*) of figure 7.4.

It is now interesting to analyse the characteristics of rarefaction pulses that we find in our simulations of the holographic system and compare them with Jones–Roberts soliton solutions as well as with soliton solutions of the holographic superfluid. In two spatial dimensions, soliton solutions of the holographic superfluid have first been constructed in [340]. Thereafter, numerous properties of solitons in the holographic superfluid have been studied, see *e. g.* [341–345] for an incomplete list. In these works, so-called black- and grey-soliton solutions are investigated. In general, grey solitons are characterised by a non-zero velocity which is directly related to the depth of the density depletion. Black solitons, on the other hand, are static and

their density depletion reaches zero. Black solitons can be thought of as kinks in the condensate density with a phase jump of $\pm\pi$ across their minimum. See also [136] for more on this. In the GP model, a central difference between black and grey solitons, which form a class of so-called dark solitons, and Jones–Roberts solitary waves is that the former are typically unstable while the latter are the only stable soliton solutions of the GPE. In holography, just like in the GP model, dark solitons have been shown to undergo instabilities, *cf.* [343, 344]. Since in our simulations the rarefaction pulse does not undergo an instability, it cannot straightforwardly be associated with grey- or black-soliton solutions of the holographic superfluid studied previously, although in its velocity dependence on the depth of the density depletion it has, to a degree and only at large velocities, a resemblance to the grey-soliton solutions. Instead, at least on a qualitative level, its behaviour is very similar to that of the GPE Jones–Roberts solitary waves [337], at small as well as at large velocities. In our following discussion and quantitative analysis we will confirm this explicitly. In the holographic superfluid, rarefaction pulses created by annihilating vortex–anti-vortex pairs have thus far not been studied in the literature.

8.4.2 Evaluation Method

To study the rarefaction pulse, we first prepare a vortex dipole in the initial condition of the superfluid and subsequently evolve the system in time until the vortices annihilate. With regard to the initial vortex configuration, there is only one restriction. Namely, we need to ensure that the vortices are far enough apart such that the phase healing has completed before the vortices annihilate. Indeed, since the vortex dynamics during the phase-healing regime deviates strongly from the expected dynamics of a proper vortex dipole, we expect that the respective rarefaction pulses would also differ. Therefore, we prepare the vortex–anti-vortex pair in the initial configuration with a separation of $d_0/l = 50$ grid points. In our studies in section 6.2 and 8.2 we have seen that this choice ensures that the phase has fully healed prior to the vortex annihilation. As before, we align the vortices on the horizontal $x_2 = 256$ axis of the quadratic grid, centred around $x_1 = 256$. To ensure a high spatio-temporal resolution of the extracted trajectory of the rarefaction pulse, we again adopt the procedure from above and study its density modulation not only at unit timesteps but also at a number of numerical timesteps. To be specific, we again take one hundred, equally spaced, snapshots of the evolution per unit timestep and analyse the data for each one of them.

For the given initial configuration, the vortices annihilate after 605.26 unit timesteps (to the given enhanced resolution). That means that at time 605.27 we can no longer locate zeros in the density configuration $n(\boldsymbol{x})$ of the superfluid condensate. The chosen initial configuration of the vortex dipole is particularly convenient for the analysis and visualisation of the rarefaction pulse, as the direction of the dipole's centre-of-mass motion, and thus the direction of the subsequent motion of the rarefaction pulse, coincides precisely with the x_2-axis of the grid. By rotational symmetry of the underlying system, we could have also chosen a different initial

configuration and subsequently rotated the field configuration. However, such operations are always accompanied by numerical errors which we care to minimise. In the following, our investigations focus on the time evolution of the condensate-density modulation $n(t, \boldsymbol{x})$ along the x_2-axis at fixed $x_1 = 256$ which is the centre of the rarefaction pulse.

In figure 8.9 we show snapshots of the superfluid density modulation along the x_2-axis at eight times characteristic for the evolution of the rarefaction pulse. The first (upper left panel) snapshot is taken shortly before the vortices annihilate and the last one (lower right panel) in the late-time limit shortly before the density depletion has fully recovered to the background density n_0 and the system has equilibrated. Let us stress that the pulse propagates from right (larger x_2-value) to left (smaller x_2-value). Prior to the vortex annihilation, the condensate density at the minimum of the depletion is still finite. At these times, the vortex cores slightly trail the density depletion along their common direction of propagation (*i. e.*, along the negative x_2-direction). As time proceeds, the vertical separation between the minimum of the pulse and the two vortices, *i. e.*, their cores, and the horizontal separation between the vortices decline and eventually reach zero simultaneously. The merging of the two zeros causes the quantised phase windings of the vortices to annihilate. Following the annihilation, the condensate density at the minimum gradually increases and the pulse accelerates, *cf.* the second to fifth panel in figure 8.9. At times later than $t \approx 612$, the density fluctuations around the pulse, relative to the background condensate n_0, are of the same order of magnitude as the density depletion of the rarefaction pulse itself. Moreover, a second minimum arises as a consequence of the density maximum trailing the rarefaction pulse (relative to the direction of propagation), slowly decaying and thus 'pushing' the remnant condensate into the density depletion. For all later times, it appears no longer sensible to interpret the density depletion as a distinct rarefaction pulse. Instead, several small excitations propagate through the condensate, *cf.* the last three panels in figure 8.9. Below, we will argue that it appears likely that once the background excitations of the condensate are of the same order of magnitude as the density depletion of the rarefaction pulse, the pulse has decayed into sound waves. In the very late-time limit the density slowly equilibrates to its background value n_0. On a qualitative level, we thus find that the behaviour of the rarefaction pulse bears strong resemblance to the characteristics of Jones–Roberts GPE solitary-wave solutions [337].

To quantify the agreement further, let us now analyse the dynamics of the rarefaction pulse on a quantitative level, restricting ourselves to times prior to $t = 612$. We need to find the minimum of the density depletion as well as its depth. Subsequently, we can infer its velocity and compare our findings to the soliton solutions of the GP equation. For the tracking of the density minimum, we employ a slightly modified version of the Newton–Raphson tracking algorithm discussed in section 6.3. In the following we briefly go through the key aspects of the method, adapted to the given scope of application. There are two main adjustments to the NR method of section 6.3 that we have to make. The tracking of the rarefaction pulse reduces to a one-dimensional problem as opposed to the vortex tracking on the two-dimensional
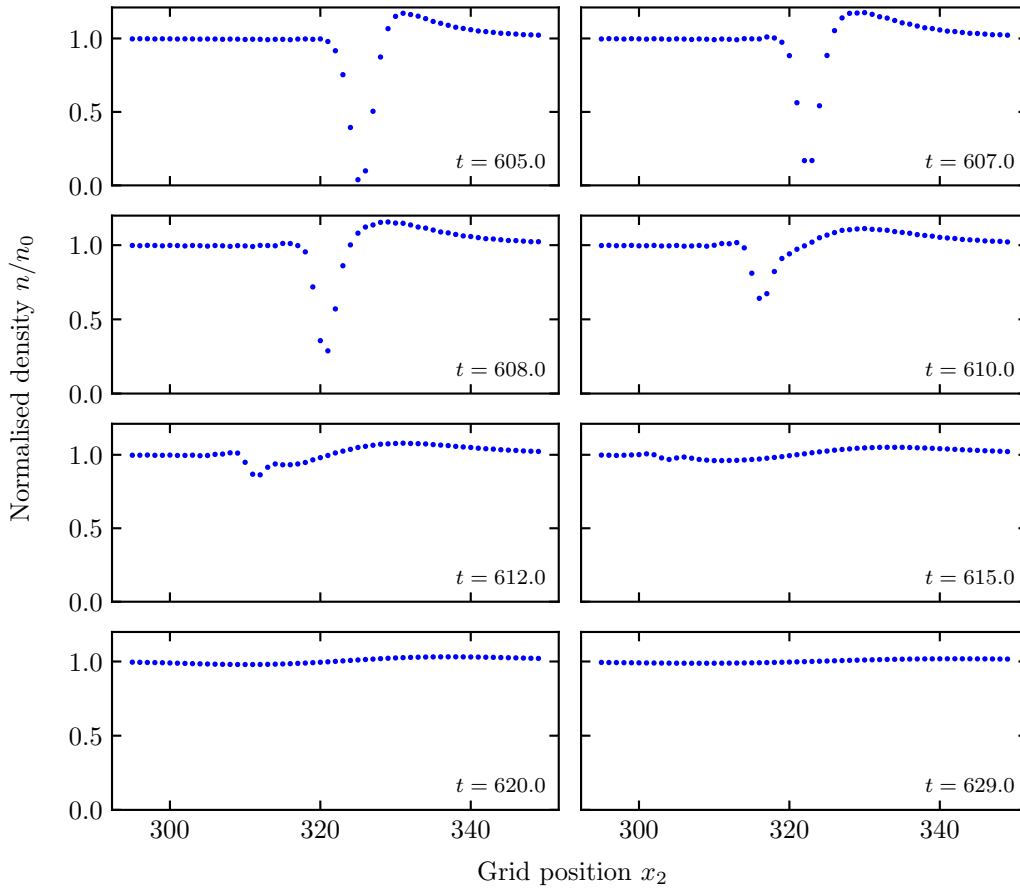
Figure 8.9: Snapshots of the normalised condensate density $n(x_1 = 256, x_2)/n_0$ along the x_2-axis, *i.e.*, perpendicular to the dipole axis at eight consecutive times. The chemical potential of the superfluid is fixed to $\mu = 6$ (corresponding to $T/T_c = 0.68$) and n_0 is the corresponding background condensate density. The snapshot in the upper left panel at time $t = 605.00$ is taken shortly before the vortices annihilate (at time $t = 605.26$). The density depletion at this point is still above zero and can be interpreted as a rarefaction pulse. The snapshots taken at times $t = 607.00, 608.00$ and 610.00 illustrate how the depth of the pulse decreases which results in an increase of its velocity along the negative x_2-direction. At time $t = 612.00$ the depth of the density depletion is approximately of the same order of magnitude as the surrounding density modulations relative to the background density n_0. This indicates that the former depletion can no longer be associated with a single rarefaction pulse, see the main text for further details. At later times, the density modulations damp out and the system equilibrates.

(x_1, x_2)-grid. Furthermore, the density at the requested minimum is not zero. Therefore, instead of searching for zeros in the superfluid density, we instead have to track the zeros in the first derivative of the superfluid density with respect to the coordinate parametrising the direction along which the pulse propagates. Henceforth, we denote this coordinate by x. In our setup, we need to take derivative with respect to $x = x_2$. However, in order to keep the following discussion as general as possible, we use the coordinate x representatively in all equations. Taylor expanding the condensate density about an initial guess x_0^{g} for the position of the minimum yields

$$0 = n'(x_0) = n'(x_0^{\mathrm{g}}) + n''(x_0^{\mathrm{g}})(x_0 - x_0^{\mathrm{g}}) + \mathcal{O}\left[(x_0 - x_0^{\mathrm{g}})^2\right] , \qquad (8.2)$$

where x_0 is the true position of the density minimum and we have suppressed the second argument of the superfluid density (in our case $x_1 = 256$). Furthermore, a prime denotes the derivative with respect to x. (Here, a prime should not be confused with a prime in the equations of motion in section 5.3, denoting the derivative with respect to the holographic coordinate z.) We can now solve equation (8.2) for the position of the density minimum x_0,

$$x_0 = x_0^{\mathrm{g}} - \frac{n'(x_0^{\mathrm{g}})}{n''(x_0^{\mathrm{g}})} + \mathcal{O}\left[(x_0 - x_0^{\mathrm{g}})^2\right] , \qquad (8.3)$$

Upon iterating the procedure, x_0 converges to the desired true position of the rarefaction pulse, to sub-plaquette precision. As before, we evaluate the superfluid density at inter-mesh points by Fourier interpolating the real array. We also use Fourier interpolation to find the density at the position of the minimum. Due to the broadening of the density dip and the decrease in depth, the tracking algorithm becomes less reliable at later times. Gaining higher precision would require a better resolution of the pulse and thus a smaller grid spacing. As for the late-time regime of the vortex-dipole dynamics, we track the minimum one hundred times per unit timestep throughout the evolution, allowing us to extract the trajectory of the pulse in a quasi-continuous manner which is a prerequisite for deriving its velocity. We stress that applying the tracking routine more frequently than at every unit timestep is strictly required here since otherwise (if we tracked only at unit timesteps), we would only have less than ten data points which would certainly not be sufficient for an accurate analysis of the pulse.

8.4.3 Time Evolution of a Rarefaction Pulse

In the left panel of figure 8.10 we show the trajectory (x_2-position) of the density minimum as a function of time. Due to the initial preparation of the vortices, the pulse propagates in the direction of decreasing x_2. In addition, we show the superfluid density at the position of the minimum scaled to the background condensate density n_0 in the right panel of figure 8.10. In both panels, time runs from $t = 605.00$ to $t = 612.00$. The displayed results clearly underpin our qualitative discussion. Indeed, prior to the annihilation of the vortices, the depth of the minimum of the condensate-density depletion increases gradually until it reaches zero
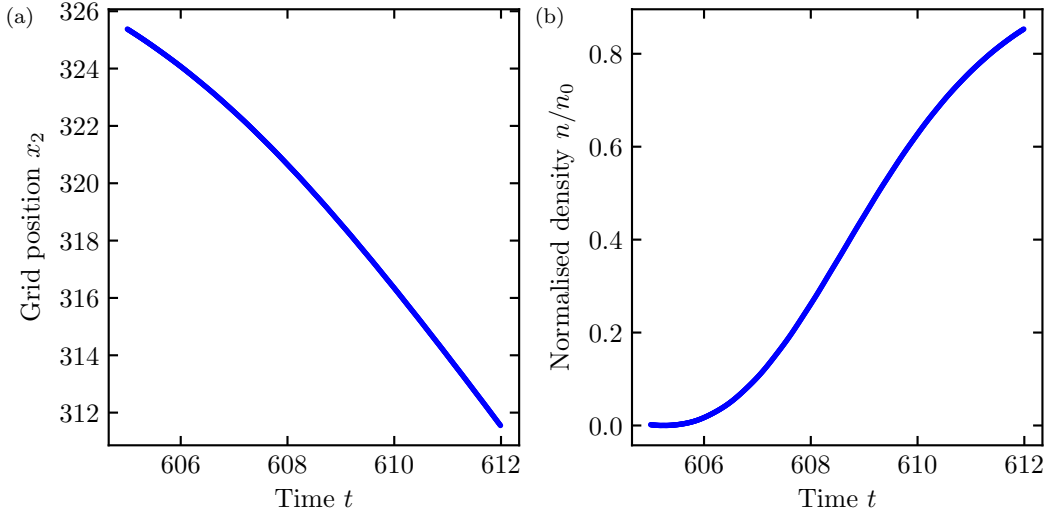
Figure 8.10: Illustration of the temporal evolution of the rarefaction pulse created in the annihilation of a vortex–anti-vortex dipole. In both panels, time starts at $t = 605.00$, shortly before the vortices annihilate at time $t = 605.26$. The final time is given by $t = 612.00$ at which point we can no longer unequivocally identify a rarefaction pulse, *cf.* the main text and figure 8.9. Left panel: The location of the density minimum as a function of time. Due to our choice for the initial configuration of the vortices the wave propagates in negative x_2-direction for fixed $x_1=256$. Right panel: The normalised superfluid density $n(x_2)/n_0$ at the position of the density minimum of the rarefaction pulse as a function of time. The density decreases until the zeros of the vortex-induced density depletions merge and then increases gradually. At time $t = 612$ the density minimum has healed to $n/n_0 \approx 0.85$.

at time $t = 605.26$ when the vortices annihilate. Note that the decrease is visible in figure 8.10 only upon closer inspection. In particular, at time $t = 605.00$ the density at the minimum is less than one percent of the background condensate density n_0. Subsequently, the depth gradually decreases again as the soliton propagates along the symmetry axis of the former vortex dipole. We refrain from showing the full two-dimensional density modulation $n(\boldsymbol{x})$ here, but note that the pulse becomes increasingly one-dimensional as time proceeds, meaning that the spatial extent of the pulse along the x_1-direction decreases. At time $t = 612.00$, the density at the minimum has healed to $\sim 85\%$ of the background condensate density n_0.

Employing finite-difference methods, *cf.* appendix A.5, we can now derive the velocity of the rarefaction pulse along the x_2-axis. The results are illustrated in figure 8.11. The velocity increases gradually as the density at the minimum of the depletion increases. We attribute the minor oscillations in the curve to numerical
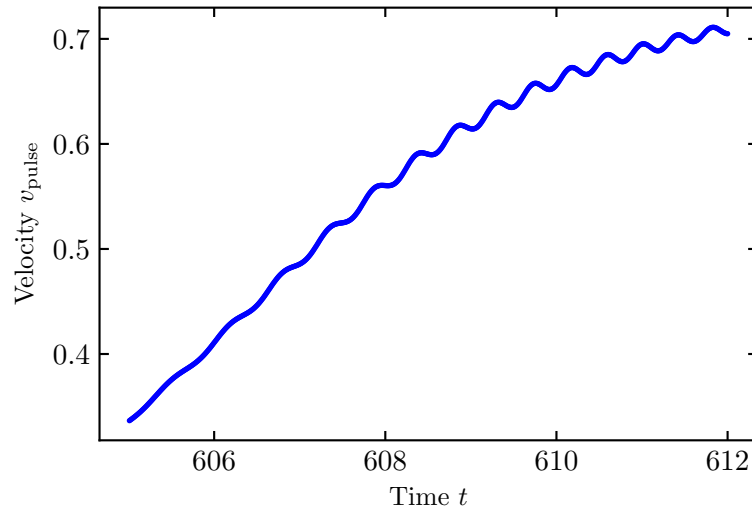
Figure 8.11: Velocity of the rarefaction pulse created in the annihilation of a vortex–anti-vortex dipole. The oscillations are due to uncertainties in the tracking routine used to locate the density minimum of the pulse. At time $t = 612$ the pulse has approximately reached the speed of (first) sound of the holographic superfluid and it appears to have decayed into sonic waves. For details see the main text.

uncertainties in the tracking routine. At times prior to the annihilation, the vortex cores move slightly faster along their transverse direction than the density minimum of the rarefaction pulse. Since the vortices trail the rarefaction pulse at all times prior to the annihilation, they have to 'catch up', which explains the difference in velocities. From section 8.2 we recall that the transverse velocity of the vortices saturates during the finale stages of the evolution. We have found the final velocity to be $v_\perp \simeq 0.37$. For the density minimum, on the other hand, we find the velocity at the time of the annihilation to be $v_{\text{pulse}} \simeq 0.36$. Taking into account the uncertainties in the extraction of the vortex positions as well as of the pulse locations and thus of the respective derivatives of their trajectories, the final velocities of the vortices at the time of their annihilation and the velocity of the pulse at the same time are in excellent agreement. Apart from the small oscillations, we find the velocity to increase monotonously within the considered time interval. At time $t = 612.00$, the pulse has reached a velocity of $v_{\text{pulse}} \simeq 0.7$, coinciding with the speed of (first) sound of the holographic superfluid[2], given by $c_{\text{s}} = \sqrt{2}^{-1} \simeq 0.707$.

Our results suggest a strong similarity of the rarefaction pulse under consideration

---

[2]Due to the conformal invariance of the underlying system, the speed of first sound is given by $c_{\text{s}}^2 = \partial\epsilon/\partial p = 1/d$, where ϵ is the energy density, p the pressure and d the number of spatial dimensions. For $d = 2$ one thus finds $c_{\text{s}} = 1/\sqrt{2}$. See [191] for further details and a thorough discussion of sound modes in the holographic superfluid.

with the Jones–Roberts solitary waves in the GP model [337] discussed above. The saturating velocity of the vortices along the transverse direction of their motion may be associated with the critical velocity separating the two branches of stable GPE soliton solutions in [337]. Furthermore, the density minimum accelerates until it reaches the speed of sound. Once it has reached the speed of sound, we can no longer discern a single density minimum of the rarefaction pulse, see figure 8.9. Instead, we find several small density modulations that are all of approximately the same order of magnitude, including the minimum of the former rarefaction pulse. Hence, it appears most likely that once the pulse reaches the speed of sound, it decays into sound waves. These sound waves subsequently damp out and dissipate their energy into the heat bath, *cf.* the final three panels of figure 8.9. On a qualitative level, the Jones–Roberts solitons behave analogously.

There are, however, several caveats in a comparison of our results with [337]. Most notably, in [337], the medium is non-dissipative. The holographic superfluid, in contrast, is dissipative, even if there are no longer any vortices present, *cf.* our discussions in section 7.3. Naturally, the dissipation has an effect on the dynamics and the behaviour of the propagating rarefaction pulse which renders a direct comparison with [337] intricate. Furthermore, to analyse if the waves, into which the rarefaction pulse supposedly decays, indeed propagate with the speed of sound and may thus be associated with sound waves requires measuring their group velocities. However, to measure group velocities, we would have to track not only the minima of the density depletions but also their centre of mass which is, to the given resolution in terms of grid points, prohibitively difficult in our simulations. It would be interesting to follow up on the investigation of rarefaction pulses in more detail and to analyse if and to what degree their behaviour resembles that of grey solitons, in the holographic superfluid as well as in the GP model. In particular, going beyond the scope of [345], it would be very interesting to study the decay of the rarefaction pulses/solitons into sound waves.

9 Summary of Part I

In the first part of this thesis we have investigated the dynamics of dipoles of quantised vortices in a two-dimensional holographic superfluid. Specifically, we have analysed the interactions between vortices and anti-vortices as well as between vortex defects and the superfluid. Moreover, we have quantified the strong dissipation of the holographic superfluid. Within the holographic framework, the $(2+1)$-dimensional superfluid has a dual description in terms of an Abelian Higgs model in a $(3+1)$-dimensional asymptotically Schwarzschild–anti-de Sitter spacetime. We have prepared a single vortex–anti-vortex pair in the initial configuration of the superfluid and studied its dynamics by means of numerical real-time simulations. For our numerical implementation of the equations of motion we have employed the so-called probe-approximation in which the backreaction of the gauge–matter fields on the gravitational background is neglected.

We started our investigations in chapter 6 with a qualitative discussion of the dynamics of vortex dipoles in the holographic superfluid. In addition, we have discussed a high-precision tracking procedure that allows us to locate the vortices on the numerical grid to sub-plaquette precision and thus to extract their trajectories in a quasi-continuous manner. The tracking routine is composed of two distinct algorithms, operating in different regimes of the dipole evolution. To locate the vortices during the early and intermediate stages of the evolution when the associated density depletions are spherically symmetric, we have introduced a new tracking method that is not only highly accurate but also numerically very efficient. The tracking method employs two-dimensional Gaussian fits to the vortex-induced density depletions on the discrete grid, allowing for the interpolation to the respective minima and thus the extraction of the vortex locations. We have illustrated that during the final stage of the dipole evolution, when the density depletions deform and eventually merge, this fitting routine breaks down. Thus, in order to locate the vortices also at these times to the highest attainable accuracy, we have resorted to a different tracking routine that is based on a two-dimensional Newton–Raphson root-finding algorithm. While this method is capable of locating the vortices even if their density depletions are strongly deformed, it is numerically much less efficient than the Gaussian fitting routine. We have therefore combined the two algorithms and explicitly shown that the resulting tracking routine improves distinctly on standard plaquette techniques that are frequently employed in the analysis of dipole dynamics, also within the holographic framework, *cf.* [163]. We have applied the tracking routine for the extraction of vortex trajectories throughout our studies of Part I and found that it enables breaking new grounds in the investigation of vortex dynamics in superfluids. In particular, the quasi-continuous nature of the trajectories

allows for the computation of quasi-continuous vortex velocities and accelerations. Remarkably, as we will argue in the second part of this thesis, the same tracking routine is also applicable in the analysis of vortex-ring dynamics in three-dimensional superfluids.

In the final section of chapter 6, we have considered the behaviour of the vortex–anti-vortex pair during the early stages of the dipole evolution. The high precision of the tracking routine has allowed us to resolve an initial outward bending of the vortex trajectories which is a priori not expected. We have shown that the outward bending can be attributed to our initial preparation of the vortex configuration and argued that it has to be excluded from most of our investigations in this work. In the literature, the described vortex behaviour has thus far not been investigated to the detail we have presented, although it must be present as can be directly inferred from the method commonly used in the preparation of the initial conditions.

In chapter 7, we have quantified the physical parameter regime of the holographic superfluid and identified experimentally accessible superfluids which in the presence of vortices qualify for a description within the holographic framework. To be specific, we have matched solutions of the dissipative Gross–Pitaevskii equation (DGPE) to the vortex-dipole dynamics in the holographic superfluid. In two consecutive steps, we have unambiguously matched all three free DGPE parameters. First, we have tuned the healing length until the vortex-induced density depletions in both theories have the same size. Remarkably, after this matching, the vortices do not only agree in size but also their shapes are in excellent agreement. A priori, such an agreement is not expected since in the holographic framework the density profile around a vortex core builds up dynamically, with no external constraints imposed. Moreover, we have found that the vortex width scales approximately as $\xi \sim \delta\mu^{-1/2}$, where $\delta\mu = \mu - \mu_0$ is the shifted chemical potential of the holographic superfluid and μ_0 agrees to good approximation with the critical chemical potential of the phase transition. Such a scaling behaviour coincides with the dependence of the GPE healing length on the respective GPE chemical potential and thus corroborates that in the presence of vortices, the holographic framework captures the physics of a non-relativistic superfluid. In a second step, we have employed the matched healing length of the first step in the DGPE simulation of the dipole dynamics and tuned the phenomenological damping parameter as well as a time-rescaling parameter such that the trajectories of the vortices in DGPE and holography agree in space and time. The phenomenological damping parameter quantifies the dissipation of the superfluid. After the matching, the trajectories are in excellent agreement. We have found that minor differences occur only during the very last (unit) timesteps of the evolution and in the behaviour of the rarefaction pulse created by the annihilating vortices. We have argued that these deviations can be attributed to the differences in the underlying dissipation mechanisms in the holographic framework and the DGPE. In particular, we have studied the geometric bulk realisation of the dissipation mechanism in the holographic system and inferred that the dissipation decreases strongly once the vortices have annihilated, while in the DGP model our results suggest that the respective change in dissipation is not significant. Finally,

we have found that up to few restrictions, the excellent agreement of the vortex trajectories pertains also for more complicated many-vortex configurations.

From the damping parameter extracted in the matching procedure we have inferred that the holographic superfluid is strongly dissipative and may therefore be applicable in the description of vortex dynamics in dense Bose gases near a Feshbach resonance. To support this conjecture, we have additionally compared the holographic and the matched DGPE vortex dynamics to solutions of the Hall–Vinen–Iordanskii equations which describe the mechanical motion of point vortices in dissipative superfluids. We have shown that, at intermediate times, the vortices in our simulations are well described by the HVI equations. Using known relations between the DGPE and the HVI equations, we have extracted friction coefficients of the HVI equations which parametrise the mutual friction between the vortices and the superfluid and are therefore a measure for dissipation. While at early times of the evolution, deviations between our simulations and the HVI equations are again due to the initial preparation of the vortex dipoles, deviations during the final stages are due to the finite width of the holographic vortex-induced density depletions. Finally, we have compared the extracted friction parameters to corresponding values measured in experiments with quasi two-dimensional superfluid films and oblate Bose–Einstein condensates. The outcome of this comparison has led us to conjecture that the holographic framework should be applicable to the description of vortex dynamics in very dense or in thermally excited Bose–Einstein condensates, or even in superfluid helium films at temperatures in the Kelvin regime.

In chapter 8, we have analysed the kinematic aspects of the vortex-dipole dynamics in the holographic superfluid. We have studied their trajectories, velocities, accelerations, and the respective dependences on the initial configuration of the dipole as well as on the chemical potential of the superfluid. We have found that except for early times of the evolution, the vortex dynamics is independent of the initial dipole size and its alignment on the grid. Hence, the dynamics of isolated vortex dipoles is solely parametrised by the vortex–anti-vortex separation. At early times, deviations from the universal curves can again be attributed to the initial preparation of the vortices. We have made the interesting observation that the transverse velocity of the vortices is approximately constant during the last few timesteps of the evolution. The longitudinal velocity, on the other hand, has its strongest increase at these times, proving that the dipole dynamics at late times is strongly dominated by the merging of the vortex-induced density depletions. We have argued that, in this regime, the vortices can no longer be interpreted as quasiparticles and their corresponding zeros may thus also travel at velocities faster than the speed of light.

We have also studied how the vortex velocities depend on the chemical potential, or equivalently the temperature, of the superfluid. We have compared the vortex velocities as a function of the vortex–anti-vortex separation in units of the respective healing length, $d(t)/\xi$, for different values of the chemical potential. Our findings show a clear ordering of the velocities with the chemical potential. We have found that both the longitudinal and transverse velocities of the vortices are largest for the highest values of the superfluid chemical potential and lowest for the smallest

values. This dependence on the chemical potential applies in particular to the final transverse velocity of the vortices which exhibits a clear ordering.

Finally, we have also investigated the rarefaction pulse that the vortices create as they annihilate. Despite a large number of works on the dynamics of vortices in holographic superfluid, the rarefaction pulses created in their annihilation have not been studied thus far. We have employed a slightly modified version of our tracking routine to locate the density minimum on the numerical grid, also with sub-grid-spacing resolution. At the time of the annihilation, the velocity of the pulse coincides with the approximately constant transverse velocity of the vortices, and the condensate density at its minimum of the depletion is zero. Subsequently, the pulse gradually accelerates as it travels along the centre-of-mass axis of the former vortex dipole. Simultaneously, the depth of its minimum decreases. After about seven unit timesteps, the velocity of the pulse reaches the speed of sound and the density minimum decays into sound waves. In light of these findings we have argued that rarefaction waves created by annihilating vortices in the holographic superfluid strongly resemble solitary-wave solutions of the GP model, first analysed by Jones and Roberts, *cf.* [337].

For future research it would be very interesting to match in holography and the dissipative Gross–Pitaevskii model not only the dynamics of vortex dipoles, as we we have done in this thesis, but also the dynamics of rarefaction pulses or, more generally, solitons. Such a matching might yield new insights into the applicability of the holographic framework in the description of real-world superfluids. It is interesting to speculate whether in this case the holographic superfluid is applicable also in the description of dilute Bose gases or if the inherently strongly coupled nature of the holographic system excludes such an application. Another pathway for future studies is to include the backreaction of the gauge–matter fields onto the solution of the gravitational sector. In particular, it would allow for a self-consistent treatment of the superfluid and normal component of the system in which case the holographic model has been shown to capture crucial aspects of Tisza–Landau's two-fluid model [158]. The inclusion of backreaction is most important if one wants to study the low-temperature regime of the superfluid. However, also at higher temperatures, a self-consistent treatment of the normal-fluid component appears to be indispensable for a direct comparison of the temperature dependence of the holographic system with the analogous dependence of superfluid helium. It would be interesting to match to the backreacted holographic system solutions of the DGPE including higher-order correlators. In this scenario, both theories account for interactions between the condensate and the normal component. The parameters extracted from such a matching, as well as an additional comparison of the dipole dynamics with solutions of the HVI equations, would likely provide new insights into the applicability of the holographic framework to dense and dissipative real-world superfluids, also in the low-temperature regime.

Part II

Three-Dimensional Holographic Superfluid

10 Motivation and Outline

In the second main part of this thesis, we augment the holographic model of the previous part with one additional spatial direction and use it to investigate the non-equilibrium dynamics induced by the appearance of quantised vortex defects of a strongly correlated and dissipative superfluid in $3+1$ dimensions. The holographic framework provides an inherently non-perturbative approach that allows us to study phenomena such as quantum turbulence, leapfrogging motions of vortex rings, Kelvin excitations of vortex defects and many more, in a strongly dissipative superfluid by means of a fundamental description of the system.

In three-dimensional superfluids, quantised vortices are one-dimensional defects in the order-parameter field with a quantised topological charge. Naturally, the one-dimensional extension of the vortex core allows for new characteristic behaviour of the vortices as compared to their counterparts in two-dimensional superfluids studied in Part I. In particular, the vortex lines typically have segments of finite curvature which opens new possibilities for vortex-vortex interactions and the two ends of one line can even coalesce such that the vortex forms a closed loop, a so-called vortex ring. Historically, there has been an enormous interest in the characteristics and the dynamics of vortex rings ever since Helmholtz[1] first introduced the concept of vorticity in his 1858 seminal work[2] *On integrals of the hydrodynamical equations, which express vortex motion* [284, 348]. His account on what he referred to as *Wirbellinien* (open vortex lines) and *Wirbelfäden* (vortex rings) drew much attention and paved the way for one and a half centuries of intense research which is still ongoing. Today, vortex rings are considered one of the most important aspects of (classical) fluid and superfluid dynamics and highly sophisticated experimental techniques are used to study the details of their dynamics. First and foremost, this is due to the essential role vortex rings play in the hydrodynamics of turbulence, the understanding of which still poses a great challenge for experimentalists and theorists alike. From early on, Helmholtz' findings sparked the interest by many ingenious physicists who would later rise to fame for other groundbreaking discoveries of their own, including W. Thomson (later Lord Kelvin), Maxwell, J. J. Thomson, Kirchhoff, Tait, Lamb, who coined the term vorticity, Taylor, Feynman and many more (see [349] for further details on their contributions). The quickly rising interest in vortex rings was not least due to their simple creation and observation without elaborate laboratory

---

[1]Interestingly, Helmholtz published this work when he was a professor for physiology at Heidelberg University [346]. For a short summary of Helmholtz' remarkable life, we refer the interested reader to [347].

[2]The original work was published in German under the title *Über die Integrale hydrodynamischer Gleichungen, welche den Wirbelbewegungen entsprechen* [284].

experiments. Vortex rings can be created, for instance, by quickly injecting one fluid into another fluid, the splashing of a fluid drop on a liquid surface or simply by rapidly extruding a liquid (or gas) through a narrow hole. By dyeing the liquids or employing smoke instead of liquids, the rings can be made visible to the bare eye. Evidently, the above listed creation mechanisms also occur naturally, making vortex rings ubiquitous in nature and our everyday life. For instance, every time it rains a vortex ring is created when rain drops fall into a puddle [350]. Likewise, when a volcano erupts it typically extrudes vortex rings of ash (see *e. g.* [351]), and dolphins and whales blow out vortex rings of air (see *e. g.* [352]). Furthermore, over the years it has been discovered that vortex rings are crucial for the motion of insects (see *e. g.* [353–355]), the flight of birds (see *e. g.* [356, 356]), fish swimming (see *e. g.* [357]) and especially the manoeuvrability of jellyfish (see *e. g.* [358]). Understanding vortex rings is also important for the safety of helicopter flight in which case they constitute a potential hazard in the so-called vortex-ring state. In addition, in recent years it has even been shown that vortex rings are an essential tool to check for cardiac health (see *e. g.* [359, 360]). Notably, besides vortex rings, also vortex lines can be observed in nature and constitute an intense field of research. Here, we mention in particular the so-called wingtip vortices created by aircraft (see *e. g.* [361]). For more on the omnipresence of vortex rings in nature, see also [362, 363].

Due to their finite curvature, vortex rings travel through the fluid with a self-induced velocity along their axial direction[3]. This holds true for quantised as well as for classical vortex rings. However, while the topological characteristics agree for both, all quantised vortices and all classical vortices, the details of their dynamics depends on the nature of the hosting fluid. Hence, as for vortices in two-dimensional fluids, analysing the dynamics of vortex rings yields insights into the characteristics of the fluid itself. In classical fluids, vortex rings are unstable against decay. Due to the finite viscosity, the rings gradually dissipate energy and momentum which eventually causes them to decay. For textbooks on vortex rings in classical liquids, see *e. g.* [364, 365]. In superfluids, on the other hand, the quantised nature of the vorticity protects rings against decay. This implies that in a dissipationless system, a single and isolated vortex ring has an infinite lifetime. If dissipation is included, on the contrary, the ring gradually shrinks and eventually disappears but remains stable throughout this process. The quantised nature of vortices in superfluids was first understood by Onsager and Feynman [259, 260], and shortly thereafter also verified experimentally in indirect measurements [238, 366] and some years later also directly [367]. The first vortex ring in superfluid helium was later observed in [368] and in Bose–Einstein condensed gases in [369].

While in two spatial dimensions the holographic-superfluid model has proven a very successful and powerful tool to study the dynamics of quantised vortices and the

---

[3]This was also understood by Helmholtz, who describes this motion as follows [284, 348]. *" […] in a circular vortex-filament of very small section in an indefinitely extended fluid, the center of gravity of the section has, from the commencement, an approximately constant and very great velocity parallel to the axis of the vortex-ring, and this is directed towards the side to which the fluid flows through the ring."*

characteristics of superfluid turbulence, in three spatial dimensions neither turbulent behaviour nor the non-equilibrium time evolution of the system in general have thus far been investigated. Moreover, despite a considerable amount of work on the three-dimensional system that one can find in the literature (see *e. g.* the review [91] and references therein), studies of its vortex solutions do not exist. Our goal in this thesis is therefore to construct and analyse, for the first time, vortex solutions of the (3+1)-dimensional holographic superfluid. We consider in particular the structure of the density depletion around a generic vortex core in the condensate density and study its dependence on the chemical potential of the superfluid. Moreover, we compare the shape of the vortex-induced density depletion with the approximate analytic vortex-profile solution of the Gross–Pitaevskii equation. These static aspects of the vortex solutions alone allow us to conclude that, if the system is penetrated by vortex defects, the three-dimensional holographic framework describes a non-relativistic superfluid. Moreover, upon studying the solutions of the bulk fields dual to vortices in the superfluid boundary theory, we find strong evidence suggesting that the superfluid is highly dissipative. Our studies further suggest that, unlike in the two-dimensional system where dissipation is preferred only for ultraviolet (UV) modes, the three-dimensional holographic superfluid allows for the dissipation of energy and momentum modes not only in the UV but also for modes of larger wavelengths towards the infrared regime.

In addition to the static aspects of the vortex solution, we also study the dynamics of single vortex rings in the holographic superfluid, including their trajectories, velocities and accelerations. By comparing these findings to predictions from the Hall–Vinen–Iordanskii equation for the motion of vortex rings, we find further evidence corroborating the holographic superfluid to be strongly dissipative. However, unlike in Part I, here we refrain from a quantitative matching procedure with the DGPE and HVI dynamics of vortex rings and rely only on a qualitative comparison. In order to obtain a thorough characterisation of the vortex-ring dynamics, we also analyse its dependence on the initial radius of the rings as well as on the chemical potential of the superfluid.

In his celebrated work [284], Helmholtz did not only establish the concept of vorticity but he also discussed the dynamics and interactions of vortex rings. It is remarkable that, without performing any explicit calculations, he correctly predicted the qualitative behaviour of two coaxial vortex rings for the two scenarios in which their topological charges have the same or opposite signs. In particular the former scenario in which the vortices travel along a common axis and perform a *leapfrogging*, *i. e.*, reciprocal slip-through, motion, has caught the attention of many researchers and is under intense investigation in classical liquids (for a review see *e. g.* [349]) as well as in superfluids. In the second scenario, on the other hand, the vortices undergo a head-on collision in which they also reveal very interesting behaviour. In this thesis, we employ the holographic framework to study both scenarios for the first time for vortex rings in a strongly dissipative superfluid. Moreover, we do not restrict the analysis to head-on collisions but also study the collision of vortex rings for finite impact parameters. Our investigations allow us to gain crucial

insights into the characteristics of vortex rings in dissipative media and the holographic superfluid itself. Remarkably, we find that despite the strong dissipation and quantumness of the holographic superfluid, the behaviour of the vortex rings is very similar to Helmholtz' predictions. In particular, we find that they indeed perform a leapfrogging motion. We further extend the analysis of two leapfrogging vortex rings to the more complicated scenario of three coaxial vortex rings in the initial configuration and find them to exhibit very interesting behaviour.

The fascinating phenomena involving two vortex rings just mentioned constitute typical interaction processes occurring in the far-from-equilibrium dynamics in superfluid turbulence. Superfluid (or quantum) turbulence is the quantum analogue of turbulence in classical liquids, and a turbulent state is associated with a tangle of vortex defects [42]. While the appearance of vortex tangles is a commonality of classical and quantum turbulence, the fundamental physics in both systems differs significantly [43]. In classical fluids, it is well established that the energy spectrum of the system exhibits Kolmogorov scaling which essentially characterises the turbulent energy transport of the system. In superfluids, on the other hand, comparatively little is known about the energy cascade, and also many further questions are still open. Over the past decades, the interest in superfluid turbulence has strongly increased [42, 43], mainly due to experimental advances and the observation of Kolmogorov scaling in the energy spectrum of superfluid helium [44, 45]. As we have discussed in chapter 3, the holographic duality constitutes a powerful method to investigate far-from-equilibrium dynamics and is capable of describing regimes the Gross–Pitaevskii model and other alternative methods cannot capture (see *e. g.* [370] and references therein for studies of superfluid turbulence in the GP model).

In this light, we study in this thesis not only the interactions of two vortex rings, but also the dynamics of large and dense vortex tangles and the corresponding far-from-equilibrium dynamics of the holographic superfluid. To be specific, we study the time evolution of two initial vortex ensembles consisting of randomly aligned vortex rings and vortex lines, respectively, and analyse the dynamics in terms of scaling laws in correlation functions. We focus in particular on the universal regime of the dynamics at intermediate and late times of the evolution and find the system to exhibit strong signatures of turbulence. It is interesting to note that our results have strong similarity (when accounting for the additional dimension) with previous results found in investigations of the far-from-equilibrium dynamics in the two-dimensional holographic superfluid [150]. However, it is important to appreciate that the underlying processes in the two- and three-dimensional turbulent states are fundamentally different. One particular example is the possibility for vortex rings (and lines) to carry wavy excitations, so-called Kelvin waves. Kelvin waves were first introduced and studied by Lord Kelvin[4] for classical liquids [372] and are known to play a central role in superfluid turbulence as they are responsible for the transport as well as dissipation of energy and momentum [373, 374]. To gain

---

[4]For a short overview of Lord Kelvin's contribution to the study of vortex rings and their dynamics, see [371].

a deeper understanding of Kelvin waves in dissipative superfluids, we also study them in the holographic framework. We study the dynamics of the Kelvin waves themselves as well as the effect they have on the vortex ring carrying them. Among other interesting properties, we find that for helical waves, even though the large dissipation of the superfluid damps the waves, the ring is slowed down relative to an unperturbed circular ring. Thus far, similar results have only been reported in the literature for excited vortex rings in non-dissipative superfluids as well as rings in classical liquids.

Organisation of Part II

In chapter 11 we review the holographic description of a superfluid in three spatial dimensions, mainly filling the missing details left out in chapter 3. We first review the gravitational background solution of the system and subsequently derive the equations of motion of the gauge–matter sector for the static and spatially homogeneous superfluid as well as the fully dynamical system that we employ in our real-time simulations.

In chapter 12 we construct vortex-ring and vortex-line solutions of the holographic superfluid and analyse them with regard to their spatial condensate-density profile as well as their dual representation in the Schwarzschild–AdS$_5$ bulk spacetime. We also investigate the kinematic aspects of the dynamics of vortex rings and compare our findings to solutions of the associated HVI equation. Moreover, in the final section of this chapter, we qualitatively study reconnections of vortex lines and vortex rings in the holographic superfluid.

In chapter 13 we investigate the far-from-equilibrium dynamics of the three-dimensional holographic superfluid induced by initially large and dense tangles of vortex defects. We first discuss the different initial vortex configurations that we employ and subsequently investigate the time evolution of the system on a macroscopic as well as microscopic level. In particular, we compute correlation functions of the superfluid and analyse them with regard to (quasi-)stationary scaling behaviour.

In chapter 14 we study characteristic behaviour of interacting and excited vortex rings. We first investigate the dynamics of two coaxial vortex rings as they leapfrog or collide in a head-on collision. Moreover, we study the dynamics of vortex rings with winding numbers larger than one and in this context also analyse the dynamics of three leapfrogging vortex rings. Thereafter, we analyse the behaviour of vortex rings in off-centre scattering events. Finally, we qualitatively analyse Kelvin-wave excitations of vortex rings and study how they affect the dynamics of the rings.

In chapter 15 we summarise our results and discuss possible pathways for future research on vortex dynamics and quantum turbulence in the three-dimensional holographic superfluid.

11 Gravitational Model Dual to the Three-Dimensional Superfluid

Only a few months after a holographic model for the description of a two-dimensional superconductor or superfluid was first introduced [46–48] it was quickly generalised to three spatial dimensions[1] [167, 375]. In chapter 3 we have already set out the basics of the commonly used holographic model dual to a superfluid in $d + 1$ dimensions (see the action in equation (3.1)). Upon substituting $d = 3$, one finds that it is given in terms of an Abelian Higgs model in a $(4 + 1)$-dimensional anti-de Sitter black-hole spacetime. In this chapter, we fill the missing details of the model for $d = 3$ that we have thus far left out. To be specific, in section 11.1 we briefly review the central aspects of the model and lay out the background solution of the corresponding gravitational sector. In section 11.2 we discuss the boundary conditions for the gauge–matter fields. We then construct and discuss the static and spatially homogeneous equilibrium solution of the superfluid in section 11.3. In the final section 11.4, we derive the full set of dynamical equations of motion of the gauge–matter fields. In sections 11.3 and 11.4 we additionally comment on our numerical implementation of the equations of motion for the static and the dynamical system, respectively.

11.1 Gravitational Background Solution

In the holographic framework, a $(3 + 1)$-dimensional superfluid is gravitationally encoded in terms of a complex scalar field that is minimally coupled to an Abelian gauge field in a $(4 + 1)$-dimensional asymptotically anti-de Sitter spacetime with a planar black hole. For sufficiently low temperatures, the Abelian gauge symmetry breaks spontaneously, triggering the Higgs mechanism and thus the formation of a scalar charge cloud above the black-hole horizon. However, instead of solving the gravitational model (3.1) in its most general form, we again work in the probe-approximation (also referred to as probe-limit) in which the backreaction of the gauge–matter fields on the gravitational sector is neglected. Just like for the model of the two-dimensional superfluid of Part I, this approximation is applicable

---

[1]The authors of [375] construct the static solution of a holographic superconductor for varying masses of the bulk scalar field and compute the associated conductivities of the superconductor. With regard to the description of three-dimensional superfluids, the holographic framework was first applied in [167]. The main focus of [167] concerns the nature of the superfluid phase transition for varying masses of the scalar field and different superfluid velocities. At vanishing superfluid velocities the results of [167] for the superfluid agree with [375] for the superconductor.

if the temperature of the system is below but of the order of the phase-transition temperature.

In the probe-approximation, the gravitational sector of (3.1) is solved by an AdS–Schwarzschild spacetime in $4 + 1$ dimensions. Employing Eddington–Finkelstein coordinates, the corresponding metric reads

$$ds^2 = \frac{L_{\text{AdS}}^2}{z^2} \left(-h(z)\,\mathrm{d}t^2 + \mathrm{d}x_1^2 + \mathrm{d}x_2^2 + \mathrm{d}x_3^2 - 2\,\mathrm{d}t\,\mathrm{d}z \right) , \tag{11.1}$$

where we have explicitly written out the line element of the three spatial field-theory coordinates $\boldsymbol{x} = (x_1, x_2, x_3)$. Henceforth, we again set the AdS curvature radius to unity, $L_{\text{AdS}} = 1$. The horizon function of the metric (11.1) is given by

$$h(z) = 1 - \left(\frac{z}{z_{\text{h}}} \right)^4 , \tag{11.2}$$

where z_{h} again denotes the location of the black-hole horizon along the holographic z-direction. Along the other spatial coordinates $\boldsymbol{x}$, the black hole is infinitely extended. The associated Hawking temperature of the black hole is

$$T = \frac{1}{\pi z_{\text{h}}} , \tag{11.3}$$

which also sets the temperature of the dual superfluid. Throughout this part on the three-dimensional superfluid, we again set $z_{\text{h}} = 1$ to fix our units. This fixes the temperature to $T = 1/\pi$.

In the following section 11.2 we discuss the boundary conditions for the gauge–matter fields. In section 11.3 we then review the static solution of the gauge–matter sector in the fixed gravitational background discussed above. In the literature, these solutions have been discussed in numerous works before, see *e. g.* [167, 375]. Finally, in section 11.4, we discuss the full system of dynamical equations of motion of the gauge–matter fields. To the best of our knowledge, the dynamical equations of motion and thus the time evolution of the three-dimensional superfluid have so far not been studied in the literature.

11.2 Boundary Conditions

In this section we discuss in detail the boundary conditions, which we have briefly mentioned in section 3.3, for the gauge–matter fields of the holographic superfluid model, with the dimensions fixed to $d = 3$. Furthermore, we discuss aspects of the holographic dictionary for the superfluid. We proceed analogously to section 5.3 where we have discussed the boundary conditions for the two-dimensional system. Specifically, we give the boundary conditions for the gauge-field components and for the scalar field, at the conformal boundary $z = 0$ and the black-hole horizon $z = z_{\text{h}}$.

From the holographic dictionary (*cf.* section 2.2.2) it follows that near the conformal boundary of the AdS$_5$ spacetime, the temporal component of the gauge field

has the asymptotic expansion (see *e. g.* [92])

$$A_t(t, \boldsymbol{x}, z) = \mu(t, \boldsymbol{x}) + \rho(t, \boldsymbol{x})z^2 + \mathcal{O}(z^3), \qquad (11.4)$$

where μ is again the chemical potential and ρ the charge density of the dual super-fluid. Here, we are interested in the description of a superfluid at fixed chemical potential. The boundary condition for A_t at the boundary is therefore given by

$$A_t(t, \boldsymbol{x}, z = 0) = \mu. \qquad (11.5)$$

We leave ρ to be dynamically specified by the (dynamical) equations of motion. For our studies of the real-time dynamics of the holographic superfluid in the next chapters, this implies that the charge density is not constant. Throughout this work we study the superfluid only for spatially homogeneous chemical potentials and therefore suppress any argument on the right-hand side of equation (11.5). The charge density, on the other hand, does in general depend on t and $\boldsymbol{x}$. For the spatial components of the gauge field, the near-boundary expansion reads

$$A_i(t, \boldsymbol{x}, z) = \xi_i(t, \boldsymbol{x}) + J_i(t, \boldsymbol{x})z^2 + \mathcal{O}(z^3), \qquad (11.6)$$

where, just as for the two-dimensional superfluid, ξ_i denotes the superfluid velocity along the i-th direction and J_i is proportional to the vacuum expectation value of j_i, the i-th component of the dual boundary $U(1)$ current operator. We are interested in the description of the superfluid without an externally imposed velocity. Hence, we use

$$A_i(t, \boldsymbol{x}, z = 0) = 0 \qquad (11.7)$$

for the boundary condition for the spatial gauge-field components at $z = 0$.

The asymptotic behaviour of the scalar field is determined by equations (2.31) and (2.32), upon substituting $D = 4$ and our choice for the scalar mass. Throughout Part II, we choose $m^2 = -3/L_{\mathrm{AdS}}^2$ which respects the Breitenlohner–Freedman bound given by $m_{\mathrm{BF}}^2 L_{\mathrm{AdS}}^2 = -4$. Consequently, the mass does not trigger an instability. For the near-boundary expansion of the scalar field it follows that

$$\Phi(t, \boldsymbol{x}, z) = \eta(t, \boldsymbol{x})z + \psi(t, \boldsymbol{x})z^3 + \mathcal{O}(z^4). \qquad (11.8)$$

For completeness, we have re-introduced the AdS curvature radius L_{AdS} in the above equations but will henceforth use $L_{\mathrm{AdS}} = 1$ again. In the boundary condition for the scalar field, we have to impose that the source conjugate to its dual operator vanishes identically, ensuring that the $U(1)$ symmetry is not broken explicitly. Typically, the source is associated with the leading-order coefficient in the near-boundary expansion. However, for our choice of the mass of the scalar field both the leading as well as the subleading coefficient in (11.8) can be interpreted as the source conjugate to the dual scalar operator Ψ and the respective other one is its vacuum expectation

value, *cf.* our discussion in section 2.2.2. In order to allow for spontaneous symmetry breaking to occur, one coefficient has to be set to zero[2] [377]. Here, we proceed analogously to Part I and interpret η as the source conjugate to Ψ, *i. e.*, follow the standard quantisation. This implies

$$\partial_z \Phi(t, \boldsymbol{x}, z)|_{z=0} = 0 \tag{11.9}$$

for the boundary condition for the scalar field. Consequently, $\psi = \langle \Psi \rangle$ takes on the role of the superfluid order-parameter field. At the black-hole horizon, we impose the gauge-field components to vanish, *i. e.*, $A_t(z = z_{\mathrm{h}}) = A_i(z = z_{\mathrm{h}}) = 0$, and the scalar field has to be regular. Like for the two-dimensional superfluid model, the use of Eddington–Finkelstein coordinates implies that regularity of Φ at the horizon corresponds to an infalling boundary condition.

In summary, the boundary conditions for the gauge–matter fields are given by

$$A_t(z = 0) = \mu \,, \qquad A_t(z = z_{\mathrm{h}}) = 0 \,, \tag{11.10}$$

$$A_{x_1}(z = 0) = 0 \,, \qquad A_{x_1}(z = z_{\mathrm{h}}) = 0 \,, \tag{11.11}$$

$$A_{x_2}(z = 0) = 0 \,, \qquad A_{x_2}(z = z_{\mathrm{h}}) = 0 \,, \tag{11.12}$$

$$A_{x_3}(z = 0) = 0 \,, \qquad A_{x_3}(z = z_{\mathrm{h}}) = 0 \,, \tag{11.13}$$

$$\partial_z \Phi(z)|_{z=0} = 0 \,, \qquad |\Phi(z = z_{\mathrm{h}})| < \infty \,. \tag{11.14}$$

We employ these boundary conditions to construct the static and spatially homogeneous solution of the superfluid (section 11.3) as well as for the full set of dynamical equations of motion of the system (section 11.4). We note, however, that except for the temporal component of the gauge field, in the time propagation of the system, we need to impose the boundary conditions for the fields only at $z = 0$. For the temporal gauge-field component, on the other hand, we impose boundary conditions at the AdS$_5$ boundary $z = 0$ as well as at the black-hole horizon $z = z_{\mathrm{h}}$. For details see section 11.4.

11.3 Static and Homogeneous Solution

In this section, we review the construction of the static and spatially homogeneous equilibrium solution of the three-dimensional holographic superfluid. In our presentation, we proceed as in section 5.3.

Assuming translational invariance as well as time-independence of the superfluid, we can make an ansatz for the gauge–matter fields in the action (3.1) according to

$$\Phi = \Phi(z) \,, \qquad A_M = A_M(z) \,. \tag{11.15}$$

---

[2]It holds, also for the two-dimensional system with $D = 3$ studied in Part I, that if the mass-squared of the scalar field equals the Breitenlohner–Freedman bound $m_{\mathrm{BF}}^2 = -D^2/4$, both coefficients, η and ψ, have the same scaling dimensions. In this case, there exists a logarithmic branch which has to be set to zero as it would otherwise trigger an instability [376].

We again fix the gauge freedom by setting $A_z = 0$, corresponding to axial gauge. With this ansatz, the equations of motion of the gauge–matter fields, *cf.* equations (3.9)–(3.11), reduce to a coupled system of non-linear ordinary differential equations in the holographic z-coordinate on the finite domain $0 \leq z \leq z_{\mathrm{h}}$. Employing the metric (11.1), we find the equations for the gauge field A_M to be given by

$$0 = z^2 A_t'' - z A_t' + 2 \operatorname{Im}(\Phi' \Phi^*) \,, \tag{11.16}$$

$$0 = z^2 \left(h A_i'' + A_i' h' \right) - z h A_i' - 2 A_i |\Phi|^2 \,, \tag{11.17}$$

$$0 = 2 A_t |\Phi|^2 + 2 \, h \operatorname{Im}(\Phi' \Phi^*) \,, \tag{11.18}$$

where we again use $i = x_1, x_2, x_3$ to denote the spatial directions and a prime to denote derivatives with respect to z. Here, we suppress any arguments of the fields since they all depend only on the holographic coordinate z, including the horizon function h, *cf.* equation (11.2). For the scalar field, we find from the Klein–Gordon equation (3.10)

$$0 = z^2 h \, \Phi'' - z \left(-2\mathrm{i}z A_t + 3h - z h' \right) \Phi' - \left(m^2 + z^2 \boldsymbol{A}^2 + 3\mathrm{i}z A_t - \mathrm{i}z^2 A_t' \right) \Phi \,, \tag{11.19}$$

where we have introduced $\boldsymbol{A} = (A_{x_1}, A_{x_2}, A_{x_3})$.

Equation (11.18) corresponds to the Maxwell equation for the z-component of the gauge field, A_z. Due our choice of axial gauge $A_z = 0$, this equation is not independent of the equations of motion of the other fields. Indeed, one can show that it is trivially satisfied if all fields obey their boundary conditions (*cf.* section 11.2) and equation (11.19) is satisfied. It should therefore rather be interpreted as a gauge constraint.

Equations (11.16), (11.17) and (11.19) form a closed system of second-order ordinary differential equations in the holographic coordinate z. Supplemented with the set of boundary conditions for the gauge-field components and the scalar field at the conformal AdS boundary $z = 0$ and the black-hole horizon $z = z_{\mathrm{h}}$ (11.10)–(11.14), the holographic superfluid constitutes a one-parameter family of non-trivial solutions to these equations. In the following we solve[3] this static boundary-value problem using the same numerical methods as for the two-dimensional system. We linearise the equations of motion by employing a Newton–Kantorovich procedure and in every iteration solve the resulting linear equations of motion by using a collocation method. For the collocation method, we expand the fields in a basis of 32 Chebyshev polynomials and evaluate them on a Gauss–Lobatto grid. See also appendix A for details.

---

[3]A comment is in order here. In practice, as for the two-dimensional system in Part I, we derive the solutions of the static and spatially homogeneous system not in Eddington–Finkelstein (EF) but in Poincaré coordinates, *i. e.*, using the metric (3.6). We discuss the corresponding equations of motion and the transformation of the solutions to EF coordinates in appendix A.4. We have checked explicitly that the solutions derived in EF and Poincaré coordinates agree after transforming the fields appropriately and we only use the latter for convenience. To construct the initial conditions for our real-time simulations we use equations (11.16)–(11.19) and then solve the dynamical equations of motion (*cf.* section 11.4) in EF coordinates.

The thermodynamics of the holographic superfluid model is solely controlled by the dimensionless parameter μ/T, *cf.* our discussion in section 3.2. If this parameter is chosen appropriately, the $U(1)$ symmetry of the gauge–matter sector is broken and the scalar bulk field has a non-trivial bulk profile, $\Phi \neq 0$ [46, 47]. In the dual boundary theory this corresponds to the superfluid phase with non-zero condensate $\psi \neq 0$. In this thesis, we fix the temperature of the superfluid by our choice of $z_{\mathrm{h}} = 1$ which leaves the chemical potential μ as the only free parameter, effectively controlling the phase transition of the superfluid. For further details on this aspect, see our discussion in section 3.2. Upon systematically varying μ, we numerically find the critical chemical potential for the phase transition,

$$\mu_{\mathrm{c}} \simeq 4.1568\,. \tag{11.20}$$

Above μ_{c}, the system is in the symmetry-broken phase. For $\mu < \mu_{\mathrm{c}}$, on the other hand, the symmetry is restored and the unique solution to the equations of motion (11.16)–(11.19) implies $\Phi = 0$ for the scalar field and thus $\psi = 0$ at the boundary. From equation (3.15) we find

$$\mu^{-1} = \mu_{\mathrm{c}}^{-1} \frac{T}{T_{\mathrm{c}}}\,, \tag{11.21}$$

just as for the two-dimensional system (*cf.* section 5.3). Hence, every choice of the chemical potential uniquely fixes the ratio T/T_{c}, where T_{c} is the critical temperature for the phase transition. Since $T = 1/\pi$ is fixed, μ changes the critical temperature of the system.

In figure 11.1 we show the absolute value of the order-parameter field ψ as a function of the chemical potential μ. For completeness, we also add a second horizontal axis displaying the temperature ratio T/T_{c} (corresponding to μ according to equation (11.21)). For most of Part II on the three-dimensional holographic superfluid, we employ a chemical potential of $\mu = 5$ for our studies. This value corresponds to a ratio of $T/T_{\mathrm{c}} = 0.83$. Only in sections 12.1.1 and 12.2 we additionally study the system for various values of the chemical potential. We mark the values used in section 12.2 with ticks on the μ-axis in figure 11.1. The density of the superfluid condensate is given by $n = |\psi^2|$ and the phase configuration of the order-parameter field by $\varphi = \arg(\psi)$. The equilibrium density is denoted by n_0. For our typical choice of $\mu = 5$, we find $n_0 \approx 79.5$.

As for the two-dimensional superfluid, let us briefly comment on the two branches of solutions of the gauge–matter fields above and below the phase-transition temperature. We begin with the superfluid phase for $T/T_{\mathrm{c}} < 1$. Since the scalar field is charged under the local $U(1)$ symmetry, a non-trivial profile of Φ implies the formation of a scalar charge cloud $\sqrt{-g}|\mathcal{J}^0|$ in the bulk. This finite charge density sources the temporal gauge-field component A_t. For the exemplary chemical potential of $\mu = 5$, we illustrate the solutions of the gauge–matter fields in figure 11.2. We show the profile of the modulus-squared of the scalar field $|\Phi|^2$ (solid blue), the temporal gauge-field component A_t (dotted turquoise), the field $|\Phi|^2/z^6$ (dashed green) and
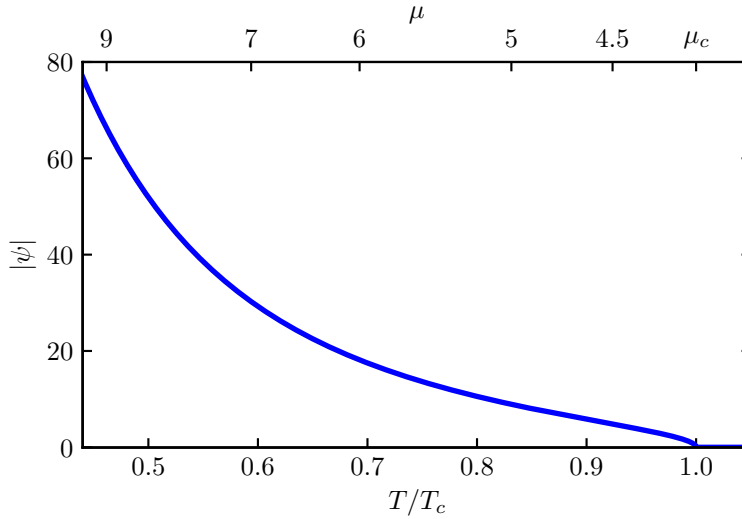
Figure 11.1: Modulus of the complex order parameter $|\psi|$ of the holographic super-
fluid in $3+1$ dimensions as a function of temperature ratio $T/T_{\rm c}$ (lower
abscissa) or chemical potential (upper abscissa), in the probe approxi-
mation. The mass of the bulk scalar field is set to $m^2 = -3$. The square
of the order parameter yields the condensate density of the superfluid
$n = |\psi|^2$. Below the critical temperature $T_{\rm c}$, the order parameter $|\psi|$ in-
creases monotonously and is strictly zero for larger temperatures. The
chemical potential μ and the temperature are in one-to-one correspon-
dence, *cf.* equation (11.21) and the main text for details.

the charge density $\sqrt{-g}|\mathcal{J}^0|$ (dash-dotted red). The spatial gauge-field components
A_i vanish identically in the equilibrium solution. Note that the boundary is to the
right at $z = 0$ and the black-hole horizon to the left at $z_{\rm h} = 1$. At the boundary, the
scalar field vanishes in accordance with the boundary condition (11.9) and increases
monotonously towards the black-hole horizon. For lower temperatures, its profile in
the interior of the bulk increases, which eventually renders the probe-approximation
inapplicable. In this case, the backreaction of the gauge–matter fields on the gravi-
tational sector can no longer be neglected. We avoid this regime in all of our studies
by considering only temperatures for which we expect the probe approximation to
be applicable. The field $|\Phi|^2/z^6$ reduces to the condensate density $n = |\psi|^2$ at the
boundary.

Above the critical temperature, for $T/T_{\rm c} > 1$, the scalar field vanishes identically
in the bulk, *i. e.*, $\Phi = 0$. Likewise, also the spatial components of the gauge field
vanish due to the isotropy of the underlying system, $A_i = 0$. From equation (11.16),
supplemented with the boundary conditions in (11.10), this implies for the temporal
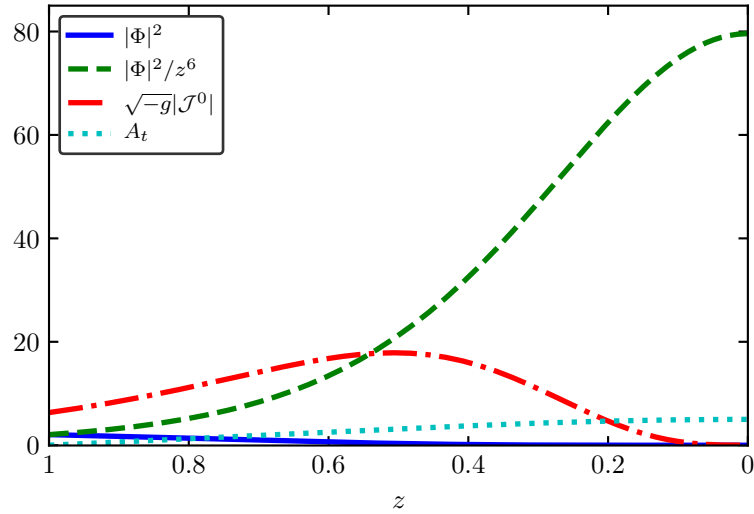
Figure 11.2: Typical bulk profiles of the gauge–matter fields of the holographic superfluid in equilibrium for an exemplary chemical potential of $\mu = 5$. The black-hole horizon is at $z = z_{\mathrm{h}}$ with $z_{\mathrm{h}} = 1$ (left) and the AdS boundary at $z = 0$ (right). The modulus-squared of the bulk scalar field $|\Phi|^2$ is depicted by the solid blue line and the temporal gauge-field component A_t by the dotted turquoise line. In addition, we show the scalar charge density $\sqrt{-g}|\mathcal{J}^0|$ in red (dash-dotted) and the field $|\Phi|^2/z^6$ (in green, dashed), which reduces to the superfluid density n at the boundary. In equilibrium, $n = n_0 \approx 79.5$.

gauge-field component

$$A_t = \mu \left(1 - \frac{z^2}{z_{\mathrm{h}}^2} \right) , \tag{11.22}$$

which again agrees with the gauge-field solution of the Einstein–Hilbert–Maxwell action (2.39) for $d = 3$ discussed in chapter 2. Qualitatively, this is the same result as we have found for the two-dimensional superfluid in Part I. Let us therefore only briefly point out that the solution is not consistent since in the AdS–Schwarzschild spacetime (11.1), there is nothing that carries any charge, including the black hole, that could source the electrostatic potential A_t (unlike in the symmetry-broken phase where the charge density in the bulk sources A_t). For a more thorough discussion of this point, we refer to section 5.3. In this thesis, we are only interested in the symmetry-broken phase below T_{c} and therefore disregard this inconsistency in the symmetric phase.

11.4 Dynamical Equations of Motion and Numerical Implementation

Let us now discuss the full set of dynamical equations of motion for the gauge–matter fields A_M and Φ. To this end, we explicitly write out the Maxwell and Klein–Gordon equations (3.9)–(3.11) in the fixed gravitational background metric (11.1) without any simplifying assumptions with regard to the symmetries of the underlying system. In order to simplify the equations, we explicitly plug in our choice for the mass-squared, $m^2 = -3$.

For the numerical implementation of the boundary condition (11.9) for the scalar field it turns out to be useful to formulate the equations of motion in terms of the rescaled scalar field $\tilde{\Phi}$,

$$\tilde{\Phi} \equiv \frac{\Phi}{z}\,. \tag{11.23}$$

In addition, we again fix the gauge freedom by choosing axial gauge $A_z = 0$. Using the metric (11.1) to define the gravitational covariant derivative, the equations of motion (3.9)–(3.11) for the spatio-temporal components of the gauge field and for the scalar field, after some algebra, reduce to

$$\partial_z A_t - z\partial_z^2 A_t \ = 2z\text{Im}(\tilde{\Phi}^*\partial_z\tilde{\Phi}) - z\partial_z \boldsymbol{\nabla} \cdot \boldsymbol{A}\,, \tag{11.24}$$

$$\begin{aligned}
\partial_t(A_{x_1} - 2z\partial_z A_{x_1}) \ = &\ z\Big[\partial_{x_1}(\partial_{x_2}A_{x_2} + \partial_{x_1}A_{x_3} - \partial_z A_t) - (\partial_{x_2}^2 + \partial_{x_3}^2)A_{x_1}\Big] \\
&+ \partial_{x_1}A_t - 2z\text{Im}(\tilde{\Phi}^*\partial_{x_1}\tilde{\Phi}) \\
&+ (1 + 3z^4)\partial_z A_{x_1} - hz\partial_z^2 A_{x_1} + 2z|\tilde{\Phi}|^2 A_{x_1}\,,
\end{aligned} \tag{11.25}$$

$$\begin{aligned}
\partial_t(A_{x_2} - 2z\partial_z A_{x_2}) \ = &\ z\Big[\partial_{x_2}(\partial_{x_1}A_{x_1} + \partial_{x_3}A_{x_3} - \partial_z A_t) - (\partial_{x_1}^2 + \partial_{x_3}^2)A_{x_2}\Big] \\
&+ \partial_{x_2}A_t - 2z\text{Im}(\tilde{\Phi}^*\partial_{x_2}\tilde{\Phi}) \\
&+ (1 + 3z^4)\partial_z A_{x_2} - hz\partial_z^2 A_{x_2} + 2z|\tilde{\Phi}|^2 A_{x_2}\,,
\end{aligned} \tag{11.26}$$

$$\begin{aligned}
\partial_t(A_{x_3} - 2z\partial_z A_{x_3}) \ = &\ z\Big[\partial_{x_3}(\partial_{x_1}A_{x_1} + \partial_{x_2}A_{x_2} - \partial_z A_t) - (\partial_{x_1}^2 + \partial_{x_2}^2)A_{x_3}\Big] \\
&+ \partial_{x_3}A_t - 2z\text{Im}(\tilde{\Phi}^*\partial_{x_3}\tilde{\Phi}) \\
&+ (1 + 3z^4)\partial_z A_{x_3} - hz\partial_z^2 A_{x_3} + 2z|\tilde{\Phi}|^2 A_{x_3}\,,
\end{aligned} \tag{11.27}$$

$$\begin{aligned}
\partial_t(\tilde{\Phi} - 2z\partial_z\tilde{\Phi}) \ = &\ \Big[\text{i}(\boldsymbol{\nabla} \cdot \boldsymbol{A} - \partial_z A_t)\tilde{\Phi} + 2\text{i}\boldsymbol{A} \cdot \boldsymbol{\nabla}\tilde{\Phi} - h\partial_z^2\tilde{\Phi} - \boldsymbol{\nabla}^2\tilde{\Phi}\Big] \\
&+ \text{i}A_t\tilde{\Phi} - 2\text{i}zA_t\partial_z\tilde{\Phi} + (z^3 + z\boldsymbol{A}^2)\tilde{\Phi} \\
&+ (1 + 3z^4)\partial_z\tilde{\Phi}\,,
\end{aligned} \tag{11.28}$$

where we have suppressed all functional dependences to aid the readability. We stress that the gauge field A_M as well as the scalar field $\tilde{\Phi}$ depend on all five coordinates, $(t, \boldsymbol{x}, z)$, while the horizon function $h = h(z)$ depends only on the

holographic z-coordinate. In the above equations we have introduced the gradient $\boldsymbol{\nabla} = (\partial_{x_1}, \partial_{x_2}, \partial_{x_3})$ with respect to the three spatial field-theory directions.

Finally, we find from the remaining z-component of the Maxwell equations (3.9)

$$
\begin{aligned}
0 \ &= \partial_t \partial_z A_t - \boldsymbol{\nabla}^2 A_t + \partial_t \boldsymbol{\nabla} \cdot \boldsymbol{A} - h \partial_z \boldsymbol{\nabla} \cdot \boldsymbol{A} + 2|\tilde{\Phi}|^2 A_t \\
&\quad - 2 \operatorname{Im} \left(\tilde{\Phi}^* \partial_t \tilde{\Phi} - h \tilde{\Phi}^* \partial_z \tilde{\Phi} \right) .
\end{aligned}
\tag{11.29}
$$

Like for the static system discussed in the previous section, this equation is not independent of equations (11.24)–(11.28). Instead, it can be expressed as differential equation in (11.24)–(11.28). It can be shown that if equations (11.24)–(11.28) are satisfied, equation (11.29) is satisfied for all z if it is satisfied on one fixed-z slice. It should therefore rather be considered a gauge constraint. In our numerical implementation, we have checked explicitly that it is satisfied throughout the entire time evolution of the superfluid. For completeness, let us point out that equation (11.29) could also be treated as a dynamical equation for the temporal gauge-field component A_t in which case equation (11.24) would be a gauge constraint. However, in our numerical implementation we find it more convenient to use (11.29) as the constraint equation.

Equations (11.24)–(11.28) are a closed system of partial non-linear differential equations in the five coordinates $t, \boldsymbol{x}$ and z. While the equations appear rather challenging to solve on first sight, their structure allows an essentially straightforward numerical implementation. We first note that derivatives with respect to time only appear on the left-hand sides of equations (11.25)–(11.28). On a fixed timeslice, we can therefore compute the right-hand sides at every grid position (x_1, x_2, x_3) and then integrate the respective outcomes with respect to time. Subsequently, we solve the remaining linear differential equations in z to obtain the fields $\boldsymbol{A}$ and $\tilde{\Phi}$ on the new timeslice. Finally, we use these fields to solve equation (11.24) to obtain the temporal gauge-field component on the new timeslice. For the boundary conditions for the fields, we again employ equations (11.10)–(11.14). We note that on the respective left-hand sides of the dynamical equations (11.25)–(11.27), for the spatial gauge-field components $\boldsymbol{A}$, and (11.28), for the scalar field $\tilde{\Phi}$, only first-order derivatives with respect to z occur. Consequently, in the intermediate step when we solve the linear differential equations in z for the fields $\tilde{\Phi}$ and $\boldsymbol{A}$, we need to impose boundary conditions only at $z = 0$. For A_t, on the other hand, equation (11.24) is of second order in z and we therefore impose boundary conditions at $z = 0$ and $z = z_{\mathrm{h}}$.

In our numerical implementation of the equations of motion we take the spatial field-theory directions $\boldsymbol{x} = (x_1, x_2, x_3)$ to be periodic and expand the fields in a basis of Fourier polynomials. We employ grid sizes of $96 \times 96 \times 96$ and $128 \times 128 \times 128$ points along the (x_1, x_2, x_3)-directions, depending on the vortex configuration we study. These grid sizes allow us to suppress finite-size effects to below the accuracy we can resolve in our evaluation of the vortex dynamics. We have explicitly checked and confirmed the independence of our results on the size of the computational domain in order to verify that finite-size effects are indeed sufficiently suppressed. The reason we sometimes resort to the smaller numerical grid is the high numerical cost of

simulating the real-time dynamics of the system. For a discussion of the performance of our numerical implementation of the equations of motion see appendix A.2. Along the holographic direction we again expand the fields in a basis of 32 Chebyshev polynomials on a Gauss–Lobatto grid. For the time propagation, we employ a fourth-order fixed-timestep Runge–Kutta algorithm. In units of $z_\mathrm{h} = 1$, we choose the timestep size such that one unit timestep is composed of 250 numerical timesteps. We give further details on our numerical implementation in appendix A.

12 Vortex Solutions of the Holographic Superfluid

In this chapter, we begin our systematic investigation of vortex solutions and the non-equilibrium time evolution of the holographic superfluid in $3+1$ dimensions. In the first section 12.1, we start out with a discussion of the characteristic winding structure of vortex rings in a three-dimensional superfluid. Subsequently, we employ the corresponding phase configuration to construct and analyse vortex-ring solutions of the holographic superfluid. We are particularly interested in the shape and size of the condensate-density profile around the vortex core as well as its dependence on the chemical potential of the superfluid. Moreover, we also investigate the bulk-field configuration dual to the vortex rings in the boundary superfluid. We then proceed to studying the solution of straight vortex-line dipoles. While the underlying translational symmetry of the three-dimensional superfluid implies that such dipoles are simple generalisations of vortex dipoles in two-dimensional superfluids, it is nevertheless interesting to study their construction as we will use them in the next chapter to prepare large ensembles of vortex defects. In section 12.2, we study the time evolution of a single vortex ring and compare its dynamics with solutions of the Hall–Vinen–Iordanskii equation for the mechanical motion of vortex rings in a dissipative superfluid in the point-vortex limit. In addition, we briefly comment on a comparison of our results with numerical simulations of the Gross–Pitaevskii equation. However, we do not present a matching of the dynamics as for vortex dipoles in the two-dimensional holographic superfluid, neither to the dissipative GP model, nor to the HVI equation. In the last part of section 12.2, we investigate the dependence of the vortex-ring dynamics on the chemical potential of the superfluid. Finally, in section 12.3, we study the superfluid dynamics for an initial configuration of vortex lines that allows us to cast a first eye on vortex reconnections in the holographic superfluid.

With our investigations in this chapter, we set the basis for our studies in the following chapter 13, on the far-from equilibrium dynamics of the holographic superfluid and quantum turbulence, and chapter 14, on interactions and further characteristics of vortex rings.

Unless explicitly stated otherwise (in subsections 12.2.2 and 12.1.1), in this chapter we fix the chemical potential of the superfluid to $\mu = 5$, corresponding to a temperature ratio of $T/T_\mathrm{c} = 0.83$. This choice also agrees with our choice in chapters 13 and 14. We recall that we fix the units by our choice of $z_\mathrm{h} = 1$.

12.1 Initial Conditions and Vortex Solutions

We begin this section with a discussion of topological vortex excitations in three-dimensional superfluids. Naturally, in light of our studies in Part I, it is easiest for us to think of vortex lines and vortex rings, in some sense that we will make more precise in the following paragraphs, as extensions of vortices in oblate two-dimensional superfluids. In section 6.1 we have already laid out the basic characteristics of quantised vortices in two spatial dimensions. Let us in the following review the most important aspects of that discussion here and subsequently generalise them to vortex lines and rings in three-dimensional systems. Quantised vortices are topological defects in the superfluid density $n_{d=2}(\boldsymbol{x}) = |\psi_{d=2}(\boldsymbol{x})|^2$, where $n_{d=2}(\boldsymbol{x})$ refers to the condensate density in two spatial dimensions with $\boldsymbol{x} = (x_1, x_2)$. If one integrates along any closed contour $\mathcal{C}$ once enclosing (only) the vortex core, the phase of the order-parameter field $\varphi_{d=2}(\boldsymbol{x}) = \arg(\psi_{d=2}(\boldsymbol{x}))$ winds by integer non-zero multiples of 2π. Whenever $\mathcal{C}$ does not enclose a vortex, or encloses even numbers of vortices and anti-vortices, by contrast, the phase winding around this contour must be zero to ensure single-valuedness of the order-parameter field. Assuming the contour indeed encloses a single vortex, this implies that the condensate density at the location of the vortex core has to vanish. Otherwise, there would be a phase singularity at the core position which can only be remedied by the vanishing of the condensate density and thus the complex order-parameter field ψ. Away from the core, the density heals back to the equilibrium condensate density n_0 on a characteristic scale set by the healing length ξ. We note that, strictly, the healing length is only a parameter of the Gross–Pitaevskii model. Nevertheless, in a slight abuse of notation, we adapt it also for our purposes of this work, defined as outlined in section 7.3, *i. e.*, the width of the vortex-induced density depletion, extracted either from a matching with the GP model or from a fit to the density modulation.

In three-dimensional superfluids, the cores of topological vortex excitations are generalisations of vortex cores in two-dimensional superfluids to one-dimensional lines [134]. The simplest configuration, a straight vortex line, can be thought of as an extension of the topological characteristics of a vortex in $d = 2$ along the $\boldsymbol{e}_\perp$-direction perpendicular to the two-dimensional plane. In other words, the phase structure of the vortex in $d = 2$ is extended to every plane perpendicular to $\boldsymbol{e}_\perp$. Here, $\boldsymbol{e}_\perp$ again refers to the vector which extends the unit vectors of the two-dimensional plane to a right-handed coordinate system. We have introduced this vector before in our discussion of the HVI equations in section 7.2. If we think of the plane as spanned by the (x_1, x_2)-axes, $\boldsymbol{e}_\perp$ is given by the unit vector along the x_3-axis. By construction, on any plane perpendicular to $\boldsymbol{e}_\perp$, the phase of the order-parameter field winds around the vortex-line core by $2\pi w$, where $w \in \mathbb{Z}\backslash\{0\}$ is again the winding number of the vortex in $d = 2$. As for vortices in two spatial dimensions, we refer to straight vortex lines of winding number w as vortices if $w > 0$ and anti-vortices if $w < 0$. Interestingly, the mentioned characteristics in fact imply that the phase of the order-parameter field winds around the vortex-line core on *any* two-dimensional hypersurface of the $(3 + 1)$-dimensional spacetime that is intersected by the core

exactly once. (For a discussion of the definition of the winding number on such hypersurfaces, see the next paragraph.) This is the defining feature of quantised vortex excitations in three-dimensional superfluids. In particular, this definition is not restricted to straight vortex lines but holds for all shapes of one-dimensional vortex cores. Due to the topological constraints imposed by the phase structure, the condensate density has to vanish at the positions of the one-dimensional vortex core to ensure regularity of the order-parameter field. Close to the core, the density drops to zero on a characteristic scale set by the (three-dimensional) healing length ξ.

If the superfluid or Bose–Einstein condensate is bounded by a container or a trapping potential, the open ends of vortex lines are attached to the boundaries. If the system is infinitely extended in space, by contrast, the lines can have infinite length. In general, vortex lines are not straight but instead have segments of non-zero curvature, caused, for instance, by aspect ratios of trapping potentials, the presence of other vortices or externally applied forces that cause vortex lines to bend (see *e. g.* [378, 379]). This may even cause the ends of a vortex line to coalesce and form a loop. Such a closed vortex line is called a vortex ring. We note that for strongly bent vortex lines or vortex rings in three-dimensional superfluids, the notion of vortices and anti-vortices is rather subtle and can be defined consistently only on oriented hypersurfaces. In order to avoid any confusion, we will throughout this work distinguish between them only in the initial preparation of straight vortex lines aligned along any of the coordinate axes or of vortex rings aligned perpendicular to any of the coordinate axes. In these cases, the winding number is indeed straightforward to define. With regard to vortex rings, we comment further on the notion of vortex vs anti-vortex in the next section when we construct their solutions. Before we proceed, an important comment is in order. Throughout this thesis, we study vortex lines and vortex rings whose density depletions in the holographic superfluid have a non-zero width $\xi > 0$. In the literature, on the other hand, one finds that sometimes the name vortex line is associated with what we refer to as point-vortex lines (implying the limit $\xi \to 0$). Vortex defects with $\xi > 0$ are then referred to as vortex tubes. We avoid that notation and refer to vortices in the $\xi \to 0$ limit as point-vortex lines (or rings). Moreover, let us stress that throughout Part II, in analogy to our convention in Part I, we define the core of a vortex line or a vortex ring to be the one-dimensional line of zeros in the superfluid density around which the phase of the order-parameter field winds in the way that we have discussed above.

To find vortex solutions of the two-dimensional holographic superfluid in Part I, we imprinted their winding structure onto the static and homogeneous background solution of the superfluid, imposed the vanishing of the scalar field at the positions of the core along the holographic bulk direction, and subsequently propagated the system in time. The proper vortex solutions of the order-parameter field ψ then built up dynamically within a few unit timesteps. In particular, the initial phase-winding configuration adjusted to the periodic boundary conditions of the computational domain, and the density depletions around the vortex cores relaxed to the proper vortex-profile solution. For vortex-dipole configurations we further found that the

build-up of the proper total phase configuration took distinctly longer than the build-up of the individual density profiles of the vortices, *cf.* our discussion of the phase-healing regime in section 6.4. In this part, we proceed in a similar way to find vortex solutions of the three-dimensional system. To be specific, we first solve the static and homogeneous equations of motion (11.16)–(11.19) to find the equilibrium configuration of the holographic superfluid (*cf.* figure 11.2) and then multiply the winding structure of the topological vortex defects into the solution of the scalar field. Although not required for the solution to build up, for straight vortex lines we additionally demand the scalar field in the bulk to vanish at the respective positions of the vortex cores for all z. For vortex rings we find it more convenient to only imprint their phase-winding structure and leave the absolute value of the bulk fields unchanged. We will address this in more detail in the following two subsections. Once the vortices have been imprinted, we evolve the system in time by solving equations (11.24)–(11.28). During the initial few unit timesteps of this propagation the characteristic vortex solutions build up dynamically. In particular, in the vicinity of the vortex cores the vortex-induced density depletions relax to the characteristic shape of the proper vortex-profile solution. We will argue below that for (single) vortex rings as well as for dipoles of straight-vortex lines we again find a phase-healing regime during which the phase of the respective vortex configuration relaxes to its proper solution. This takes distinctly longer than the build-up of the density profiles.

In the following two subsections 12.1.1 and 12.1.2 we discuss the winding structures of vortex rings and vortex lines, and present the corresponding vortex solutions of the holographic superfluid. We begin with circular vortex rings and then proceed to straight vortex lines.

12.1.1 Vortex-Ring Solutions

In their seminal work on superfluid helium ^{4}He [368], Rayfield and Reif presented the first successful detection of quantised vortex rings. Later, this was also achieved by other groups, most notably in [380]. In Bose–Einstein condensates the first direct detection of vortex rings by Anderson et al. [369] came only shortly after vortex lines had been detected for the first time [276, 277, 381–383] and received a lot of attention. Nowadays, quantised vortex rings in Bose–Einstein condensates as well as in superfluid helium are intensely studied by an increasingly large community. This has also led to numerous technological advances in experimental methods used for the creation and detection of vortex rings. For brevity, we only name a few here. Standard methods include the creation via the decay of grey solitons [369, 384], the collision of solitons [385], density engineering [386, 387] and via quenches through the phase transition [388]. In addition, also from the theoretical perspective, there is an enthusiasm for the investigation of vortex rings. In the literature one finds a large number of numerical simulations that study various methods of how vortex rings could be created and detected in Bose–Einstein condensates. For a selection of theoretical proposals, see *e. g.* [389–393].

In the following we derive the characteristic winding structure of a plane circular single vortex ring. We point out that this derivation is already well established in the literature. For convenience, we review the central aspects of it nonetheless as we find it to be particularly helpful with regard to our following studies of the dynamics of vortex rings as well as in light of our investigations in chapter 14. Due to the azimuthal symmetry of the vortex ring, its phase structure essentially reduces to the rotationally symmetric and superimposed winding structure of a vortex–anti-vortex pair in $d = 2$ as we have studied in Part I. To make this clear, let us consider the order-parameter field configuration $\psi(\boldsymbol{x})$ of the three-dimensional superfluid restricted to a two-dimensional plane vertically intersecting the plane of the circular vortex ring – the 'vortex plane' – with the intersection line going through the centre of the ring. Henceforth, we will frequently employ such a type of two-dimensional intersection of the ring in our analysis. Due to the azimuthal symmetry, there is no need to additionally specify the polar angle of the intersection within the vortex plane. From our discussions above we expect that on any such plane, $\psi(\boldsymbol{x})$ is qualitatively similar to the field configuration of a vortex–anti-vortex pair in a two-dimensional superfluid with background condensate density n_0. Thus, in particular the phase configurations coincide in their general structure. We illustrate the vortex-ring configuration schematically in figure 12.1 for one half of an exemplary ring aligned in the (x_1, x_2)-plane. The vertical intersection agrees with the (x_1, x_3)-plane through the centre of the ring. Furthermore, we denote the radius of the ring by R_0, and its winding number by w.

Having qualitatively understood the winding structure, let us now formulate it in mathematical terms. For simplicity, we restrict the following discussion to the same vortex ring as displayed in figure 12.1 but note that all results presented can be generalised straightforwardly to rings of arbitrary orientation in the three-dimensional superfluid. We begin by reviewing the winding structure of a vortex–anti-vortex pair in a two-dimensional superfluid which we associate with the winding structure of the ring on the (x_1, x_3)-plane intersecting the centre of the ring. Subsequently, we employ the rotational symmetry of the plane circular ring to infer its total three-dimensional winding structure that we use in the preparation of the initial condition of the superfluid.

In section 6.1 we have argued that the winding structure of a single vortex of winding number w_i in a two-dimensional superfluid at position $(x_{1,i}, x_{3,i})$ is given by $\varphi(x_1, x_3) = w_i \arg(x_1 - x_{1,i} + \mathrm{i}(x_3 - x_{3,i})) = w_i \arctan\left(\frac{x_3 - x_{3,i}}{x_1 - x_{1,i}}\right)$. For the total winding structure φ of an elementary ($|w_i| = 1$, $i = 1, 2$) vortex dipole of size $2R_0$ in two spatial dimensions, aligned along the x_1-axis and centred around $(x_{1,0}, x_{3,0})$, this implies $\varphi(x_1, x_3) = \varphi_1(x_1, x_3) + \varphi_2(x_1, x_3)$, where we have introduced

$$\varphi_i(x_1, x_3) = w_i \arctan\left(\frac{x_3 - x_{3,0}}{x_1 - x_{1,0} - \mathrm{sgn}(w_i)R_0}\right), \quad i \in \{1, 2\}, \tag{12.1}$$

for the phase of the vortex ($w_i = 1$) and the anti-vortex ($w_i = -1$), and $\mathrm{sgn}(w_i)$ denotes the sign of the winding number w_i. We point out that upon exchanging
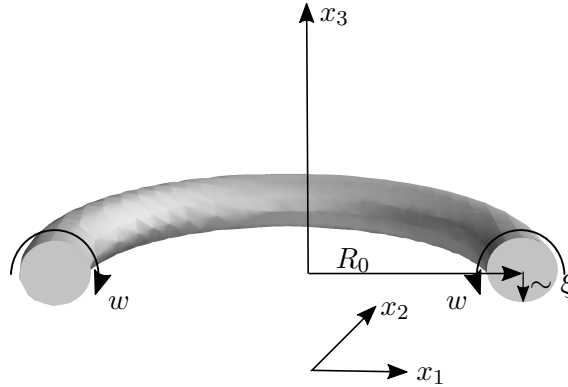
Figure 12.1: Illustration of the geometry of a plane circular vortex ring of radius
R_0 and winding number w in the (x_1, x_2)-plane. The axial direction
of the ring points along the x_3-axis. On the two-dimensional (x_1, x_3)-
slice through its centre, the ring reduces to a vortex–anti-vortex dipole
of size $2R_0$. The healing length ξ sets the scale on which the density
depletion away from the vortex core heals to the background density
n_0.

the roles of the vortex and the anti-vortex, the dipole vector is rotated by 180° and
likewise the direction of its centre-of-mass motion.

We associate the sum $\varphi = \varphi_1 + \varphi_2$ with the winding structure of the vortex ring
on the (x_1, x_3)-plane intersecting its centre. Employing the rotational symmetry of
the vortex ring, we can now generalise this result to find the total three-dimensional
phase-winding configuration of the ring. To this end, it turns out to be useful to
introduce cylindrical coordinates relative to the centre of the vortex ring. Expressed
in terms of the Cartesian coordinates, the radial distance within the vortex plane
away from the centre of the ring is given by

$$\rho(x_1, x_2) = \sqrt{(x_1 - x_{1,0})^2 + (x_2 - x_{2,0})^2} \; . \tag{12.2}$$

The vortex ring we are interested in has winding number w and is coaxially aligned in
parallel to the x_3-axis of the computational domain. Hence, figuratively speaking, we
find its winding structure by rotating the dipole's winding structure on the (x_1, x_3)-
plane intersecting its centre through 180° around the x_3-axis. Expressed in the
cylindrical coordinates, the two phase contributions (12.1) defined on the entire
three-dimensional domain then generalise to

$$\varphi^{\pm}(\boldsymbol{x}) \equiv \pm w \arctan\left(\frac{x_3 - x_{3,0}}{\rho(x_1, x_2) \mp R_0}\right) , \tag{12.3}$$

with $w \equiv w_i = -w_{3-1}$, $i \in \{1, 2\}$. The total phase configuration of the vortex ring is given by the sum of these two contributions. In order to find the vortex-ring solution of the holographic superfluid, we multiply this sum into the background solution of the scalar field Φ

$$\Phi(t_0, \boldsymbol{x}, z) \to \Phi(t_0, \boldsymbol{x}, z) \, \mathrm{e}^{\mathrm{i}\left\{\varphi^+(\boldsymbol{x}) + \varphi^-(\boldsymbol{x})\right\}} \,, \tag{12.4}$$

for the entire (x_1, x_2, x_3)-grid and for all z-slices along the holographic bulk direction. Figure 12.1 illustrates how for the vortex ring the sign of the phase winding w determines whether the phase circulates the ring inside-out or outside-in, relative to the positive x_3-direction. Note that this also determines the direction along which the superfluid flows through the ring.

Unlike for vortices in the two-dimensional superfluid, *cf.* section 6.1, here we do not additionally impose the scalar field to vanish at the respective positions of the vortex core along the holographic z-direction to construct the vortex-ring solution. Due to the strong topological constraints imposed by the quantised phase winding, the density drops to zero dynamically as we propagate the system in time. Interestingly, the same actually holds true also for vortices in $d = 2$. However, there we found it convenient to set the density to zero in order to accelerate the dynamical build-up process of the vortices. For the vortex ring, on the other hand, we find it favourable to imprint only its phase structure. It then takes approximately $\Delta t = 3$ to $\Delta t = 5$ unit timesteps in the initial propagation of the superfluid for the ring to fully develop its density profile. To imprint several vortex rings of winding numbers w_i, whose cores do not intersect, we simply superimpose the phase configurations of the individual rings and multiply the sum into the static background solution of the scalar field Φ.

Once the phase structure of the vortex ring has been imprinted and the system is propagated in time, the ring moves in its own flow field. In other words, the vortex ring has a self-induced velocity pointing along its axial direction. This can be intuitively understood from our discussion of the vortex ring's phase structure. Namely, in analogy to vortex dipoles in $d = 2$ where each vortex moves in the flow field of the respective other vortex, every point of the vortex-ring core moves in the flow field of all other points of the core. While the largest contribution at each point comes from the point on the opposite site of the vortex ring (in radial direction), we stress that also all other points contribute. The sum of all contributions determines the magnitude and orientation of the velocity vector at the specific point. For a plane circular vortex ring, its symmetry implies that all contributions not pointing along the axial direction of the ring cancel. Along the axial direction, on the other hand, the contributions add up to a finite velocity. Naturally, the axial velocity is the same for every point of the circular vortex core. As we have discussed before, the self-induced vortex velocity is determined by the gradient of its phase field,

$$\boldsymbol{v}(t, \boldsymbol{x}) \sim \boldsymbol{\nabla}\varphi(t, \boldsymbol{x}) \,, \tag{12.5}$$

where $\boldsymbol{\nabla}$ is again the three-dimensional gradient. For the vortex ring discussed above, the self-induced velocity points along the negative x_3-direction if $w > 0$, see
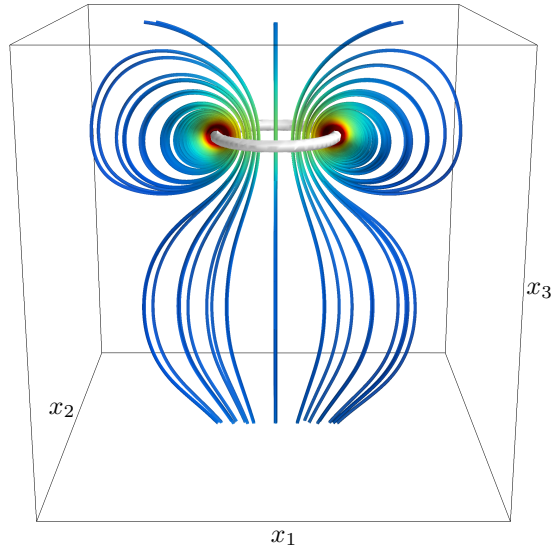
Figure 12.2: Snapshot of an isosurface of the condensate density $n(\boldsymbol{x})$ (grey surface, defining value $n/n_0 = 0.23$) and flow lines of the superfluid velocity field $\boldsymbol{\nabla}\arg(\psi)$ (coloured lines, red denotes the highest and blue the smallest defining velocities) of the vortex-ring solution of the holographic superfluid once the density profile around its core has fully built up. Initially, the ring has a radius of $R_0 = 22$ grid points, a winding number of $w = 1$, and is aligned in the (x_1, x_2)-plane. Due to its phase structure, the ring has a self-induced velocity along the negative x_3-direction.

also figure 12.1. In anticipation of our findings in the following sections, let us point out that due to mutual friction between the fluid and the vortex ring the real velocity of the vortex ring deviates from (12.5). We refer back to this point in section 12.2 where we analyse the dynamics of vortex rings in more detail.

Having discussed the winding structure of a vortex ring, let us now, for the first time in the literature, study the corresponding solution of the three-dimensional holographic superfluid. We imprint the above-discussed winding structure for a vortex ring of initial radius $R_0 = 22$ grid points and centre position[1] $(64, 64, 102)$ onto the static background solution of the superfluid on a cubic grid of size $128 \times 128 \times 128$ and subsequently evolve the system in time until the ring has fully developed its density profile. We illustrate the resulting vortex configuration in figure 12.2. To be specific, we plot an isosurface of the scalar condensate density $n(\boldsymbol{x})$ with a defining value of $n/n_0 = 0.23$ (grey surface). Moreover, we also illustrate a number of flow lines corresponding to the gradient field $\boldsymbol{\nabla}\varphi(\boldsymbol{x})$. In order to aid the readability of

---

[1]For convenience in the graphical illustration as well as the later following analysis of its dynamics, we locate the ring along the x_3-direction in the upper third of the computational domain.

the figure, we plot the flow lines only for the (x_1, x_3)-plane intersecting the centre of the ring. We keep in mind, however, that this configuration is in fact rotationally symmetric around the axial direction of the ring (parallel to the x_3-axis). For the flow lines we employ a colour coding where red denotes the highest and blue the smallest defining values (velocities). The cubic outline depicts the computational domain along the (x_1, x_2, x_3)-directions. We remind the reader that these directions are periodic. Notwithstanding this periodicity, the flow lines are not perfectly symmetric with regard to the axial direction due to minor finite-size effects of the system and numerical uncertainties in the interpolation routine. In practice, we set a number of seed points for the flow lines in the vicinity of the vortex core. We restrict the points to the direct vicinity of the vortex ring in order to aid the readability and since only this region is of interest to us. The choice of seed points is also the reason why the lines at the top and at the bottom do not all have a pendant at the respective other end to close with. Figure 12.2 illustrates nicely what we have discussed above. Namely, as the flow lines indicate, the ring has a self-induced velocity, which causes a motion of the ring along its axial direction. Furthermore, the flow field shows that in every two-dimensional plane the phase configuration is very similar to that of a vortex dipole in two spatial dimensions.

Before we dive into a more quantitative analysis of the vortex-ring solutions of the holographic superfluid, we study their dual bulk representation. To this end, we first recall that the superfluid should be thought of as a projection of the gravitational solution onto the boundary at $z = 0$. In order to gain an understanding of the boundary superfluid, it is therefore essential to first understand its dual bulk representation. For vortices in the two-dimensional holographic superfluid, for instance, the bulk solution provides a geometric interpretation of the dissipation mechanism and has, in our investigations of Part I, allowed us to comprehend the change in dissipation as vortices disappear, *cf.* our discussion in section 7.3.3. For the three-dimensional superfluid, we cannot capture the entire four-dimensional bulk view in a single plot and therefore resort to selected two-dimensional slices of the superfluid and study the bulk representation outgoing from these planes. For the vortex-ring configuration displayed in figure 12.2, there are two natural choices of planes for which it is interesting to study the emanating bulk configuration. First, the plane horizontally intersecting the vortex plane through the centre of the ring, *i. e.*, a fixed-x_3 slice, and second, any plane vertically intersecting the vortex plane through the centre of the ring, *i. e.*, just as the one we have previously employed (a fixed-x_2 slice). Here and in the following, vertical refers to the orientation relative to the vortex plane. We illustrate the geometric bulk representation of the superfluid outgoing from the fixed-x_3 slice and the fixed-x_2 slice of the superfluid in the left-hand panels of figures 12.3i and 12.3ii, respectively. In addition, in both figures in the respective right-hand panels, we show a snapshot of the isosurface of the condensate density $n(\boldsymbol{x})$ for $n/n_0 = 0.23$, depicting the vortex-ring solution (blue surface). In these plots, the transparent red planes indicate the positions of the $z = 0$ slices of the left-hand panels in the three-dimensional superfluid.

Let us now discuss the two figures, 12.3i and 12.3ii, in more detail, beginning with
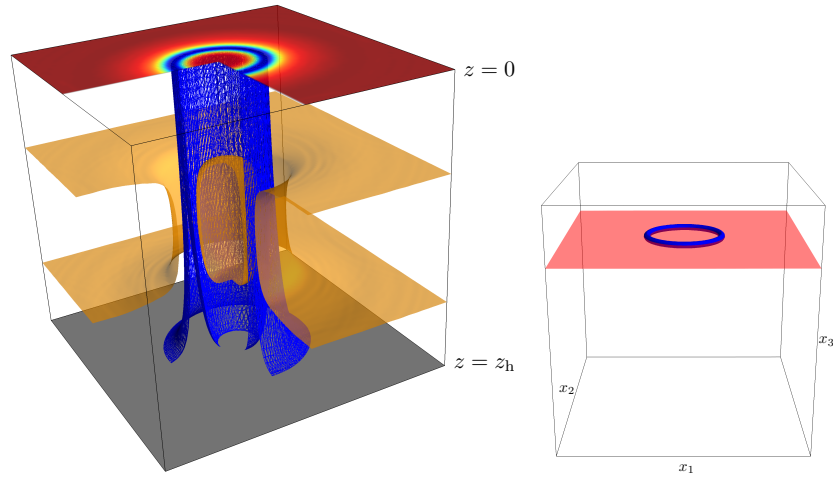
(i) Holographic bulk view outgoing from the horizontal (x_1, x_2)-plane through the centre of the ring. To aid the visualisation, we only show three quarters of the bulk configuration and of the boundary slice.
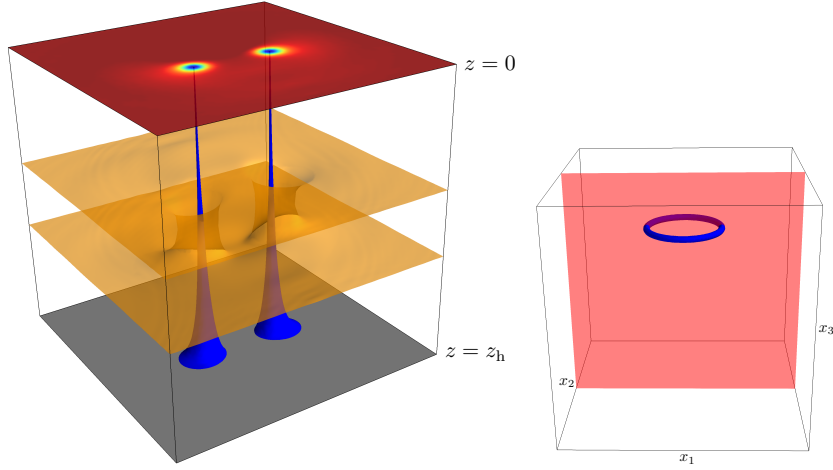
(ii) Holographic bulk view outgoing from the (x_1, x_3)-plane through the centre of the ring. On this two-dimensional slice, the ring reduces to a vortex–anti-vortex pair. The bulk configuration resembles the bulk view of vortex dipoles in Part I, *cf.* figure 7.6.

Figure 12.3: Left panels: Geometric bulk representation dual to the vortex-ring solution, shown for two two-dimensional slices of the superfluid intersecting the vortex plane through the centre of the ring. The blue surfaces are isosurfaces of the scalar field $|\Phi(\boldsymbol{x}, z)|^2/z^6$ (defining value 1.88) and the orange layers are isosurfaces of the scalar charge density $\sqrt{-g}|\mathcal{J}^0|$ (defining value 12.3 for (i) and 16 for (ii)). The field $|\Phi(\boldsymbol{x}, z)|^2/z^6$ reduces to the superfluid density $n(\boldsymbol{x}) = |\psi(\boldsymbol{x})|^2$ at the boundary at $z = 0$ (illustrated with the same colour map as in figure 6.2 Part I). The grey area at $z = z_h$ depicts the black-hole horizon. Right panels: Snapshots of isosurfaces of the condensate density $n(\boldsymbol{x})$ (blue surfaces, defining value $n/n_0 = 0.23$). The transparent red planes indicate the position of the two-dimensional boundary slice of the respective left-hand panels in the three-dimensional superfluid.

some general aspects. The blue meshed surfaces are isosurfaces of the scalar field $|\Phi|^2/z^6$ with a defining value of 1.88. At the boundary at $z = 0$, the field $|\Phi|^2/z^6$ reduces to the superfluid density $n(\boldsymbol{x}) = |\psi(\boldsymbol{x})|^2$. Thus, the boundary slices in the respective left panels of figures 12.3i and 12.3ii show the superfluid-condensate density on the red planes depicted in the corresponding panels on the right. For the condensate density n on the boundary slice we use the same colour coding as in the previous Part (*cf.* figure 6.2), with red denoting the background density n_0 and dark blue denoting zero, corresponding to the vortex core. Note that this should not be confused with the blue isosurfaces in the bulk. Isosurfaces of the scalar charge density $\sqrt{g}|\mathcal{J}^0|$ are depicted by the orange layers with a defining value of $\sqrt{g}|\mathcal{J}^0| = 12.3$ in 12.3i and $\sqrt{g}|\mathcal{J}^0| = 16$ in 12.3ii. For the definition of $\mathcal{J}^0$, see equation (3.11). Since $\sqrt{g}|\mathcal{J}^0|$ has a maximum in the bulk, there are in fact two layers of orange surfaces. The grey areas at $z = z_\mathrm{h}$ depict the black-hole horizon.

From our discussion above we already know that the phase structure of the vortex ring causes the bulk scalar field Φ to vanish along the holographic z-direction for every (x_1, x_2, x_3)-position of the one-dimensional vortex core. Hence, a superfluid vortex ring causes the charge density in the bulk to drop to zero at the respective positions of the ring along the holographic direction. Earlier, we have found the same for vortices in two spatial dimensions whose dual representation is given in terms of tubes, punching through the scalar charge cloud, *cf.* figure 7.6 and, *e. g.*, [148]. Three-dimensional vortex rings now generalise this to one higher dimension. Figure 12.3i shows that outgoing from a horizontal plane intersecting the vortex core, the vortex ring is geometrically represented in terms of a cylinder of zeros in the scalar field Φ and thus the charge density. This implies (see also figure 11.2) that the isosurfaces of $|\Phi|^2/z^6$ are given by two circular funnel-shaped sheets with decreasing separation towards the boundary at $z = 0$. Figure 12.3i also teaches us that 'inside' the cylinder, the charge density does not vanish. Hence, figuratively speaking, the superfluid vortex ring stamps out an annulus of the charge density along the holographic direction outgoing from the two-dimensional vortex-plane. To ensure that this is clearly discernible in figure 12.3i, we plot the field configurations only for three-quarters of the (x_1, x_2)-domain in the bulk as well as at the boundary and omit the fourth quarter such that one has a direct view into the 'inside' bulk perspective of the ring.

The bulk configuration of the vortex ring allows us to gain important insight into the physics of the three-dimensional holographic superfluid. In particular, a direct consequence of the zeros in the charge density is that the screening of the boundary superfluid from the black hole decreases significantly in the presence of vortices which allows for the dissipation of energy and momentum. Due to the holes in the charge density, energy and momentum modes can fall through the charge cloud and into the black hole, which can be interpreted as dissipation into the thermal heat bath. This is the same geometric interpretation of dissipation as before for the two-dimensional system and establishes that the three-dimensional holographic superfluid is dissipative in the presence of vortex excitations. We point out that we have not strictly proven that energy and momentum modes indeed fall through

the charge cloud into the black hole but rather conjecture it to be true. From our investigations of Part I and the similarities between the two- and three-dimensional system, we further expect the dissipation to be very strong. While this statement is somewhat speculative at this point, we will find strong evidence in support of it in the next section. An essential difference between the bulk view in figure 12.3i and the one dual to the vortices in the two-dimensional superfluid (figure 7.6) is the spatial extent (in $\boldsymbol{x}$) of the zeros in the charge density. This has remarkable consequences. Namely, due to the spatial extent of the holes in the charge density, dissipation is no longer restricted to (or rather strongly dominated by) UV modes. Instead, it appears that outgoing from the two-dimensional vortex plane, also modes of larger wavelengths towards the IR regime can fall into the black hole. Hence, vortex rings in the holographic superfluid (and vortex lines, *cf.* below) appear likely to constitute an avenue for the dissipation of energy and momentum modes of wavelengths that go beyond the strict UV regime[2]. We stress that this is a fundamentally new feature of the three-dimensional superfluid with regard to the dissipation of the system in the presence of vortex defects.

The lower panel of figure 12.3 illustrates nicely what we have already discussed above. Namely, the superfluid-field configuration on a plane vertically intersecting the vortex plane through the centre of the ring strongly resembles the configuration of a vortex–anti-vortex pair in $d = 2$, *cf.* the $z = 0$ slice in figure 12.3ii. Moreover, also the bulk view outgoing from the two-dimensional plane is very similar to the one we have found in figure 7.6 of section 7.3 for a vortex–anti-vortex pair in the two-dimensional holographic superfluid. This also implies that outgoing from this plane, preferably UV modes are dissipated into the black hole.

Hence, upon studying the bulk views of the three-dimensional holographic superfluid, we can draw two important conclusions with regard to features we expect the system to exhibit. First, we expect the system to be strongly dissipative. Second, the dissipation is no longer restricted to UV modes like in the two-dimensional superfluid, but instead, under favourable conditions, is allowed also for modes of distinctly larger wavelengths. By favourable conditions we refer to the fact that the dissipation depends on the orientation of the modes in the three-dimensional domain and the exact configuration of the vortex defects. While along some directions dissipation is still preferred only for UV modes, others allow for larger-wavelengths modes to fall into the black hole. There is, however, an important comment in order. If more than one vortex ring is present and the defects interact, they are typically no longer plane circular (see *e. g.* our discussions in chapter 13), which renders an analysis of

---

[2]We base this conjecture on the analysis of the bulk views and the analogy to the two-dimensional system for which it has been well established that dissipation is dominated by UV modes only, *cf.* [148]. Going beyond our qualitative arguments and gaining a more thorough quantitative understanding of the dissipation mechanism, with a special emphasis on the wavelengths of the dissipating modes, would require further studies that go beyond the scope of this thesis. The general way forward for such studies, however, is clear. On would occupy certain momentum modes of the system and study the resulting energy cascade and the dissipation of the system in terms of correlation function.

the dissipation scales intricate. In this thesis, we restrict our investigations of the dissipation mechanism to the qualitative discussion above and leave a quantitative analysis for future work.

After these remarks concerning the bulk representation of the vortex-ring solutions of the holographic superfluid, let us now proceed to a more quantitative investigation of the vortex rings and specifically their density modulation in the boundary superfluid. We are in particular interested in the shape and width of the density depletion around the vortex core of the plane circular ring as well as its dependence on the chemical potential of the superfluid. In the spirit of our investigations in chapter 7, we first compare the shape of the density depletion around the vortex core with the density profile of a vortex according to the Gross–Pitaevskii equation. Here, we restrict our analysis to the approximate analytic Gross–Pitaevskii vortex solution (7.19) instead of directly matching a numerical GPE solution to the holographic vortex. In addition, we study how the width of the holographic vortex-induced density depletion depends on the chemical potential of the superfluid. For our simulations we again employ a grid size of 128^3 points along the (x_1, x_2, x_3)-directions and study the vortex-ring solutions for 10 values of the chemical potentials in the interval $4.5 \leq \mu \leq 9$ (in increments of 0.5). For this interval, we expect the probe-limit to be a good approximation of the holographic model. For every fixed chemical potential, we initially prepare a single vortex ring of radius $R_0 = 22$ grid points and winding number $w = 1$, aligned coaxially with the x_3-axis and with the centre of the ring located at $(x_1, x_2, x_3) = (64, 64, 102)$. We evolve the system in time until the vortex ring has fully developed its density profile. The time this process takes is slightly dependent on the chemical potential. We note that due to the self-induced velocity of the ring, it starts propagating along the negative x_3-direction as soon as we evolve the system in time. However, the change in position has no effect on the following analysis.

For an exemplary chemical potential of $\mu = 5$, corresponding to $T/T_c = 0.83$, we illustrate the normalised density modulation $n(\boldsymbol{x})/n_0$ of the vortex ring in a one-dimensional cut through the centre of the ring along the x_1-axis (blue dots) in figure 12.4. We ensure that we indeed capture the vortex core itself by evolving the system in time until the x_3-position of the core of the vortex ring agrees with a unit grid position. Naturally, the accuracy for this is limited by the uncertainty in the determination of the vortex location as well as the time resolution of our evaluation method. For details on how we extract the location of the vortex ring and in particular its x_3-position, see the next paragraph. In figure 12.4 we clearly identify the two density minima corresponding to the vortex–anti-vortex pair on the fixed-x_2 slice intersecting the vortex core. An important comment is in order here. The density modulation shown in figure 12.4 differs significantly from the analogous configuration of a vortex dipole in the two-dimensional holographic superfluid. In particular, the enhancement of the condensate density in between the vortex-induced density depletions is more pronounced for the ring than for a dipole in $d = 2$. The likely reason is that the superfluid flow through the ring is distinctly larger than the superfluid flow in between the vortex and anti-vortex in the two-dimensional
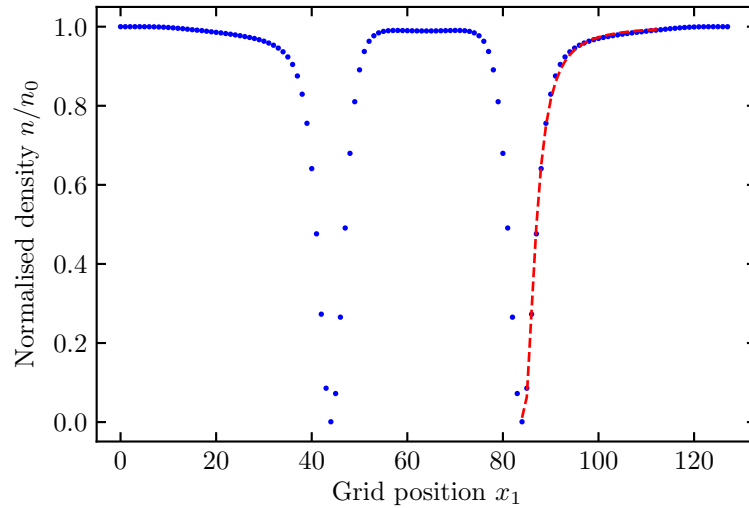
Figure 12.4: Normalised density profile n/n_0 of a vortex ring of radius $R_0 = 22$ in the holographic superfluid for a chemical potential of $\mu = 5$ in a one-dimensional cut through its centre (blue dots). The snapshot is taken once the ring has fully developed its characteristic density profile and its x_3 location agrees with a unit grid point. The dashed red line denotes a fit of the approximate analytic GPE vortex profile (12.6) to the density modulation. The holographic and GPE vortex are in excellent agreement except for intermediate separations, *cf.* the main text for a discussion.

superfluid. As a result, the 'inner' flanks of the vortex-induced density depletions of the ring are distinctly steeper than the 'outer' flanks, *cf.* figure 12.4. Let us therefore point out that despite the fact that we have been using the analogy of the field configuration on the two-dimensional plane to the vortex-dipole configuration in the two-dimensional superfluid, it is important to appreciate that they are not the same. However, since there is a qualitative and conceptual similarity, we find it convenient to make use of this analogy at times. In order to compare the profile for one of the density depletions in figure 12.4 with the typical vortex shape of the GP model, we fit to the data points the approximate analytic GPE vortex-profile solution in $d = 2$ (*cf.* equation (7.19)),

$$n(\boldsymbol{x}) = \frac{n_0(\boldsymbol{x} - \boldsymbol{x}_i)^2}{2\tilde{\xi}^2 + (\boldsymbol{x} - \boldsymbol{x}_i)^2} \; . \tag{12.6}$$

Note that here $\boldsymbol{x}$ and $\boldsymbol{x}_i$ are restricted to the one-dimensional cut through the centre of the ring and $\boldsymbol{x}_i$ is the position of the density depletion. We show the outcome in figure (7.19) (dashed red curve, fitted to both flanks of the right density depletion but shown only for the 'outer' flank, *cf.* below for a discussion). Before

we comment on the comparison of the vortex shapes in more detail, we point out that the vortex profile (12.6) is only an analytical approximation of the GPE vortex solution. It matches the actual vortex-profile solution to order $\mathcal{O}((\boldsymbol{x} - \boldsymbol{x}_i)^2)$, see also our discussions in section 7.3. Figure 12.4 nicely illustrates that the holographic and the approximate GPE vortex solutions are in excellent agreement and minor deviations arise only at intermediate distances away from the core. If we compared the GPE vortex profile to the 'inner' flanks of the density depletions in figure 12.4 we would find larger discrepancies. The reason is yet again the superfluid flow through the ring that causes the profiles of the density modulations inside and outside the ring to differ. Only if the ring was significantly larger we would find the flanks to have the same shape. We find that the strong agreement between the vortex shapes in figure 12.4 persists also for all other choices of the holographic chemical potentials in the interval $4.5 \leq \mu \leq 9$ that we employ throughout this section. In light of our comparison of the vortex shapes in Part I, we suspect the small deviations between the vortex profiles in figure 12.4 to be in part due to the shortcomings of (12.6) to capture the full GPE solution. In addition, we expect the deviations between the vortex solutions in holography and GPE to be enhanced by the finite separation between the vortex and the anti-vortex induced by the ring on the two-dimensional plane. Here, such effects are inevitable because of the limitations in the initial vortex radius imposed by the finite size of the computational domain. We will refer back to this point when we study the solution of straight vortex lines below. The strong resemblance between the holographic and (approximate) GPE vortex is remarkable since the holographic vortex shape is an intrinsic characteristic of the holographic superfluid and builds up dynamically without any external constraints.

We now proceed to a more quantitative investigation of the vortex-ring solution and study the dependence of the width of the vortex-induced density depletion on the chemical potential of the superfluid. For this purpose, we find it most convenient to adapt the method of section 7.3, where we have studied the analogous dependence for vortices in the two-dimensional superfluid. Here, we apply it to the vortex-ring solution on the fixed-x_2 slice intersecting the centre of the ring, on which the superfluid order-parameter field essentially reduces to the solution of a vortex–anti-vortex pair, *cf.* figure 12.3ii. We extract the width ξ of the corresponding density depletion by fitting a two-dimensional Gaussian to the density modulation $n(\boldsymbol{x})$ around one of the vortex cores on this slice. In the same way, we have also extracted the x_3-location of the vortex ring for the analysis described in the previous paragraph. We point out that we find the separation between the vortex cores to be sufficiently large to ensure that the asymmetry of the density depletions visible in figure 12.4 has a negligible effect on the convergence of the Gaussian fit and the extraction of the width of the depletion. The Gaussian is again given by (*cf.* (7.20))

$$n(\boldsymbol{x}) = A - A_1 \exp\left\{-(\boldsymbol{x} - \boldsymbol{x}_i)^2/2\xi^2\right\}, \tag{12.7}$$

with fitting parameters A and A_1, accounting for the embedding of the vortex into the condensate background, $\boldsymbol{x}_i$ is the position of one of the vortex cores on the
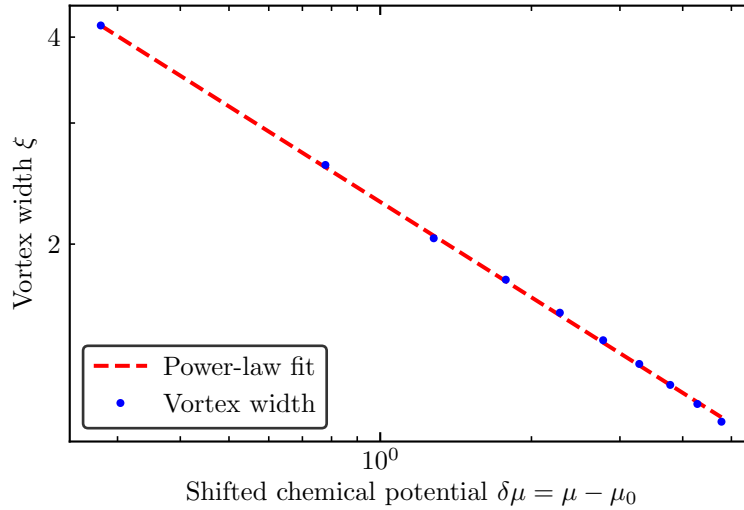
Figure 12.5: Width ξ of the holographic vortex-induced density depletion around the core of a vortex ring (in grid units) as a function of the shifted chemical potential $\delta\mu = \mu - \mu_0$. The width ξ (blue dots) is extracted from the vortex by a Gaussian fit to its two-dimensional profile. The double-logarithmic scale demonstrates that the width depends on $\delta\mu$ according to $\xi \sim (\delta\mu)^{-b}$, where $\delta\mu$ and b are extracted from a fit to the data points (dashed red line). With the fitted values of $\mu_0 = 4.20$, which is close to the critical chemical potential $\mu_c \simeq 4.1568$, and $b = 0.46$, this behaviour approximately coincides with the dependence $\tilde{\xi} \sim \tilde{\mu}^{-1/2}$ of the DGPE healing length on the non-relativistic chemical potential $\tilde{\mu}$.

two-dimensional plane and ξ is the width of the (approximately) circular density depletion. For $A = A_1 = n_0$ and to first order in $(\boldsymbol{x} - \boldsymbol{x}_i)^2$, the Gaussian (12.7) agrees with the approximate analytic density profile of a vortex in the GP model, *cf.* equation (12.6), which we have shown to capture the holographic vortex to high accuracy except for small deviations at intermediate distances away from the core. We have checked and confirmed explicitly that fitting (12.6) to the two-dimensional density profile yields the same width as fitting the Gaussian (12.7) to it. Hence, we strongly expect that to a good approximation, ξ also agrees with the healing length that we would extract from a matching of the GPE solution to the holographic vortex profile. Henceforth, in the present and all following chapters, we will therefore, in a slight abuse of notation, refer to the width ξ as the healing length of the holographic system. From the fitting routine we estimate the uncertainty of ξ to be of the order of a few percent, which can safely be neglected in the following analysis.

In figure 12.5 we show the extracted width ξ as a function of the shifted chemical potential $\delta\mu = \mu - \mu_0$, for chemical potentials $\mu \in [4.5, 9]$ in increments of $\Delta\mu = 0.5$. Note the double-logarithmic scale. The figure clearly indicates the power-law de-

pendence

$$\xi \sim (\delta\mu)^{-b}\,, \tag{12.8}$$

with the linear shift μ_0 given by $\mu_0 = 4.20$ and the scaling exponent b, given by $b = 0.46$. To extract these parameters, we have used Levenberg–Marquardt least-squares fitting algorithm. The dashed red line in figure 12.5 shows the resulting fit to the data points. We find the extracted linear shift to agree well with the critical chemical potential of the three-dimensional holographic superfluid $\mu_{\mathrm{c}} \simeq 4.1568$, for a fixed temperature of $T = (4\pi)^{-1}$. This is analogous to our findings with regard to the two-dimensional system, *cf.* section 7.3.1 and figure 7.2. In particular, the behaviour of the healing length approximately coincides with the dependence of the GPE healing length $\tilde{\xi}$ on the non-relativistic chemical potential $\tilde{\mu}$, $\tilde{\xi} \sim \tilde{\mu}^{-1/2}$ in the GP model independent of the dimension (*cf.* equation (7.2)). Hence, we draw the same conclusion from this analysis as in section 7.3.1. Namely, in the presence of vortices, the holographic framework describes a non-relativistic superfluid.

With this, we conclude our discussion of static aspects of the vortex-ring solutions of three-dimensional holographic superfluid. We follow up on this discussion in section 12.2 where we investigative the dynamics of single vortex rings. For now, we proceed with the construction of straight vortex-line solutions.

12.1.2 Vortex-Line Solutions

To construct straight vortex-line solutions of the three-dimensional holographic superfluid, we proceed as outlined for the vortex rings. Namely, we first imprint their winding structure onto the static and homogeneous background solution of the condensate and subsequently find the solution to build up dynamically as we propagate the system in time. In this subsection we again use $\mu = 5$ for the chemical potential of the superfluid. For simplicity we assume the lines to be oriented in parallel to the x_3-axis and thus perpendicular to the (x_1, x_2)-plane. As for the vortex ring, this assumption can be made without loss of generality due to the underlying rotational and translational invariance of the superfluid. The preparation of all other vortex configurations of straight vortex lines can then be straightforwardly inferred from the procedure discussed in the following.

Figuratively speaking, a straight vortex line can be thought of as a bent-open and straightened vortex ring. In principle, its winding structure can therefore be directly inferred from equation (12.3) for the vortex ring. However, as we have mentioned in the introduction to this section, it turns out to be much simpler than that because straight vortex lines are simple extensions of vortices in $d = 2$ along an axis perpendicular to the two-dimensional plane. To find the phase winding of the straight vortex lines, we can therefore resort to our discussion of the two-dimensional superfluid and vortex excitations thereof. Hence, on every fixed-x_3 slice, the phase configuration parametrising the winding structure of a straight vortex line of winding number w at position $(x_{1,0}, x_{2,0})$ is given by $\varphi(x_1, x_2, x_3, z) = w \arg(x_1 - x_{1,0} + \mathrm{i}(x_2 - x_{2,0}))$, extending over all (x_1, x_2) and along the holographic z-direction. Once we

multiply this phase into the scalar field, *i. e.*, $\Phi(\boldsymbol{x}, z) \rightarrow \Phi(\boldsymbol{x}, z) \, \mathrm{e}^{\mathrm{i}\varphi(\boldsymbol{x})}$ and evolve the system in time, the vortex solution builds up. In the boundary superfluid the build-up process corresponds to the superfluid-condensate density dropping to zero at the position of the one-dimensional core and building up its characteristic density profile in the vicinity of the core. Again, it is not necessary to set the scalar field to zero by hand in the initial condition as the phase winding enforces the density to drop to zero dynamically. Nonetheless, for most applications in this work, we still set it to zero beforehand to reduce the initial time it takes for the solution to build up. Indeed, it takes approximately $\Delta t = 3$ unit timesteps if we set the scalar field to zero at the respective positions and $\Delta t \approx 5$ unit timesteps if not.

For a number of vortex lines of winding numbers w_i we superimpose their phase configurations and multiply the sum into the scalar field. This procedure is just the same as before for the vortices in Part I as well as the vortex rings and holds also if we combine vortex lines and vortex rings in the initial configuration. Due to the periodicity of the computational domain along the (x_1, x_2, x_3)-directions, however, we can only prepare equal numbers of vortex and anti-vortex lines in the initial configuration along a fixed direction. In fact, the same was true also for the two-dimensional system. Two vortex (anti-vortex) lines exclusively along one direction, for instance, would strongly violate the periodicity of the grid and cause the dynamical creation of anti-vortex (vortex) lines at the 'boundaries' of the computational domain where the two incompatible phase configurations come into contact. In order to avoid this, we have to imprint one vortex for every anti-vortex along each direction and vice versa. In other words, vortex line ensembles are again built of vortex–anti-vortex pairs. We stress that the entire procedure just described can also be analogously applied for vortex lines of any other arbitrary orientation in the three-dimensional computational domain, so long as they are straight and come in pairs.

For the remainder of the present subsection, we focus on a single vortex-line dipole and study the characteristics of its solution in the three-dimensional holographic superfluid. We imprint one vortex line and one anti-vortex line in the initial configuration on a grid of size 128^3. We align them along the x_3-axis at positions $(x_1, x_2) = (44, 64)$ and $(84, 64)$, respectively. Subsequently, we evolve the system in time until the lines have fully developed their density profile. In figure 12.6 we show the resulting configuration. The grey surfaces are again the isosurfaces of the condensate density $n(\boldsymbol{x})$ with a defining value of $n/n_0 = 0.23$. On one fixed x_3-slice (for $x_3 = 64$) we also plot the flow lines of the gradient field $\boldsymbol{\nabla}\varphi(\boldsymbol{x})$, where $\varphi(\boldsymbol{x}) = \arg(\psi(\boldsymbol{x}))$ is again the phase configuration of the superfluid order-parameter field ψ. To aid the visualisation, we show the flow lines only in the vicinity of the vortex cores by placing the corresponding seed points appropriately. The colour map for the flow lines is the same as for the vortex ring above in figure 12.2, *i. e.*, red denotes the highest and blue the smallest defining velocities. Here, in a slight abuse of notation, we again refer to $\boldsymbol{\nabla}\varphi(\boldsymbol{x})$ as the velocity of the superfluid but keep in mind that they are in fact only proportional. Due to the alignment of the lines, the centre-of-mass motion of the vortex dipole points along the negative x_2-axis. This choice agrees with the one we previously made for the vortex dipoles in Part I.
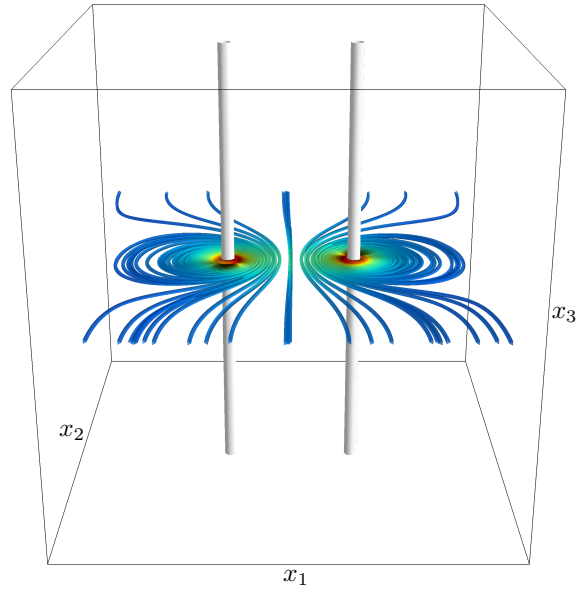
Figure 12.6: Snapshot of an isosurface of the condensate density $n(\boldsymbol{x})$ (grey surface, defining value $n/n_0 = 0.23$) and flow lines of the superfluid velocity field $\boldsymbol{\nabla} \arg(\psi)$ (coloured lines, red denotes the highest and blue the smallest defining velocities) of the vortex-line-dipole solution of the holographic superfluid at time $t = 0$ when the density profile around their cores has fully built up. Each vortex line moves in the flow field of the respective other line as depicted by the flow lines.

Like for the vortex ring, we are particularly interested in the dual bulk configuration of the vortex-dipole solution of the three-dimensional superfluid. To this end, we again need to resort to two-dimensional slices of the superfluid to visualise the corresponding bulk configuration of the charge density and the scalar field Φ along the outgoing holographic z-direction. There are again two natural choices for such slices. First, the x_2-slice vertically intersecting the vortex lines, spanned by the dipole vector, which is oriented perpendicular to the lines and points from the anti-vortex line to the vortex line, and the vortex lines. Second, any (x_1, x_2)-plane that cuts through the lines horizontally. Due to translational invariance of the superfluid configuration along the x_3-axis, any of the x_3-slices has the same geometric bulk representation along the holographic direction.

We use $x_3 = 64$ as for the illustration of the flow lines in figure 12.6 above. We display the geometric bulk views outgoing from the fixed-x_2 slice and the fixed-x_3 slice of the superfluid in the left-hand panels of figures 12.7i and 12.7ii, respectively. In both figures we again plot isosurfaces of the scalar field $|\Phi|^2/z^6$ (meshed blue surfaces, defining value 1.88) and isosurfaces of the scalar charge density $\sqrt{-g}|\mathcal{J}^0|$ (orange layers) with defining values 12.3 and 16 for figures 12.7i and 12.7ii, respec-
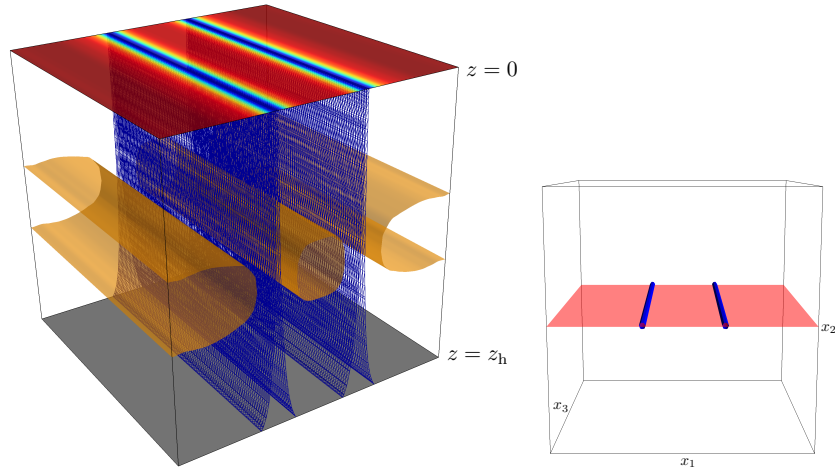
(i) Holographic bulk view outgoing from the two-dimensional x_2-slice spanned by the vortex dipole and the x_3-axis.
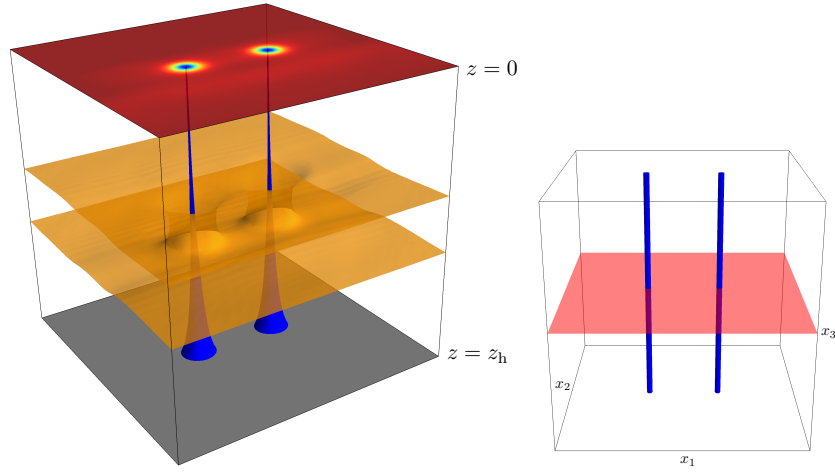
(ii) Holographic bulk view outgoing from the (x_1, x_2)-plane at $x_3 = 64$. On this two-dimensional slice, the vortex lines reduce to a two-dimensional-like vortex–anti-vortex pair. The bulk configuration resembles the bulk view of the vortex dipoles in Part I, *cf.* figure 7.6.

Figure 12.7: Left panels: Geometric bulk representation dual to straight vortex-line solutions, displayed for two two-dimensional slices of the superfluid intersecting the lines. Shown are isosurfaces of the scalar field $|\Phi(\boldsymbol{x}, z)|^2/z^6$ (blue surfaces, defining value 1.88) and the scalar charge density $\sqrt{-g}|\mathcal{J}^0|$ (orange layers, defining value 12.3 for (i) and 16 for (ii)). The field $|\Phi(\boldsymbol{x}, z)|^2/z^6$ reduces to the superfluid density $n(\boldsymbol{x}) = |\psi(\boldsymbol{x})|^2$ at the boundary at $z = 0$ (illustrated with the same colour map as in figure 6.2 in Part I). The scalar charge cloud screens the boundary from the black-hole horizon (grey area at $z = z_{\mathrm{h}}$). Right panels: Snapshots of isosurfaces of the condensate density $n(\boldsymbol{x})$ (blue surfaces, defining value $n/n_0 = 0.23$). The transparent red planes indicate the position of the two-dimensional boundary slice of the respective left-hand panels in the three-dimensional superfluid.

tively. On the boundary slice at $z = 0$, the field $|\Phi|^2/z^6$ reduces to the superfluid density $n(\boldsymbol{x}) = |\psi(\boldsymbol{x})|^2$. To display the density n, we use the same colour coding as in figure 12.3 and the density plots of the two-dimensional superfluid in Part I (see *e. g.* figure 6.2). For a more thorough discussion of the bulk-field configurations see also our description of figure 12.3 in the previous subsection. In addition to the bulk views, in both figures in the respective right-hand panels, we also show a snapshot of the isosurfaces of the condensate density $n(\boldsymbol{x})$ for $n/n_0 = 0.23$, depicting the vortex-dipole (blue surface). In these plots, the transparent red planes indicate the positions of the $z = 0$ slices of the left-hand panels in the superfluid.

In the upper panel of figure 12.7, the bulk view outgoing from the fixed-x_2 slice is very similar to the one we have found above in figure 12.3i for the vortex ring, only with the isosurfaces of $|\Phi|^2/z^6$ bent open and straightened. In other words, the corresponding bulk representation of a straight vortex line outgoing from a plane vertically intersecting the line, is given by a two-dimensional slice of zeros, spanned by the vortex line and the holographic z-direction. Isosurfaces of $|\Phi|^2/z^6$ are thus given by two sheets, approaching each other towards the boundary and enclosing the sheet of zeros in their centre. As we have argued above, the holes in the charge density reduce the screening of the boundary from the black hole and thus allow for an energy and momentum dissipation mechanism, given by modes falling into the black hole. Moreover, just as we have argued for the rings, we expect the spatial extent of the holes to indicate that the dissipation mechanism is possible not only for UV modes, but also for larger wavelengths towards the IR regime.

The bulk configuration outgoing from the fixed-x_3 slice through the superfluid is shown in the lower panel of figure 12.7. It strongly resembles the dual bulk view of a vortex–anti-vortex pair in the two-dimensional superfluid, *cf.* figure 7.6 and thus confirms our expectation. Evidently, by analogy to the two-dimensional system, we expect that outgoing from this plane preferably UV modes fall through the narrow tubes in the bulk and dissipate their energy into the black hole.

We thus find again that the dissipation, including the dissipation scales as well as dissipation strength, depends on the orientation of the wavevectors of the modes in the three-dimensional domain, and on the exact configuration of the vortex defects. For the vortex configuration studied here, for instance, it appears likely that due to the translational symmetry of the configuration there are in the superfluid distinctly less modes occupied along the direction parallel to the lines than transverse to them. Since we expect that only for modes oriented parallel to the vortex lines dissipation is allowed for larger wavelengths (*cf.* figure 12.7i), it appears likely that for this configuration, dissipation takes place only in the UV, outgoing from a fixed-x_3 slice, *cf.* figure 12.7ii. We expect the dissipation mechanism for larger-wavelengths modes to become more important if there are more than just the two straight vortex lines present. Nevertheless, the studied configurations nicely illustrate the general principle and make evident the fundamentally new characteristic behaviour we conjecture the three-dimensional superfluid to exhibit.

Finally, let us comment on the characteristics of the density modulations induced by the straight vortex lines and compare them to the analogous results for the vortex

ring in the previous section. We are again interested in the shape of the vortex-induced density depletions as well as their width and the respective dependences on the chemical potential of the superfluid. To this end, we study the same symmetric vortex-line configuration as for the vortices in the two-dimensional superfluid in section 7.3, but extended along the third spatial direction x_3. To be specific, the configuration is given by two vortex lines and two anti-vortex lines, aligned in a minimal checkerboard configuration so that the forces on every individual line are balanced, ensuring that the vortices are closest in shape and size to an isolated vortex line. Therefore, compared to our fitting procedure of the vortex ring's density depletion in the previous subsection, finite-size effects are much stronger suppressed. We then proceed just like for the vortex ring in the previous subsection and use a two-dimensional Gaussian fit to the density modulation of one vortex line on a fixed-x_3 slice to extract the width of an individual vortex-induced density depletion. We find that for all chemical potentials considered before the extracted width ξ is in excellent agreement with the respective value corresponding to the vortex ring in the previous subsection. Thus, we again find a the power-law behaviour $\xi \sim (\delta\mu)^{-b}$, with linear shift $\mu_0 = 4.17$ and scaling exponent $b = 0.46$. Here, the minor deviation between $\mu_0 = 4.17$, extracted from the vortex lines, and $\mu_0 = 4.20$, extracted from the vortex ring, can be attributed to uncertainties in the fitting routines used to extract ξ from the density depletions as well as the fitting routine of $\xi \sim (\delta\mu)^{-b}$ used to extract μ_0. Furthermore, we also find the shapes of the density depletions, if we restrict the comparison to the outer flanks in figure 12.4, for the lines and the ring to be in excellent agreement for all chemical potentials. This was expected since both, vortex lines and vortex rings, are only two different manifestations of the same underlying topological vortex excitation of the holographic superfluid. However, we stress that, naturally, the agreement pertains only if the studied segments of the vortex lines and rings are only mildly bent and the respective density depletions thus do not overlap and deform.

12.2 Dynamics of Holographic Vortex Rings

In the previous section, we have discussed the type of initial conditions we prepare in order to find topological vortex solutions of the three-dimensional holographic superfluid. We have further presented an in-depth investigation of the corresponding solutions for vortex rings and straight vortex lines and found strong evidence corroborating our expectation that the holographic framework captures, below the phase-transition temperature, the physics of a non-relativistic superfluid. In this section, we now want to study the dynamics of single vortex rings in the three-dimensional holographic superfluid. Understanding the dynamics of a single vortex ring is crucial for all further studies of vortex dynamics within the holographic framework. We first focus on a qualitative description of the vortex-ring dynamics and subsequently perform a more quantitative analysis, including a study of the trajectory of the ring and its velocities and accelerations. In order to draw conclusions with regard to the

characteristics of the holographic superfluid itself, we also compare our findings to well-established results for the dynamics of vortex rings in superfluids obtained from the GP model and the corresponding HVI equation. In the final subsection of this section, we focus on the dependence of the vortex-ring dynamics on the chemical potential of the superfluid. Except for that part, we again fix the chemical potential to $\mu = 5$.

Once a single planar circular vortex ring has been imprinted into the holographic superfluid as outlined in section 12.1.1, its self-induced velocity causes the ring to move along its axial direction, *cf.* figure 12.2. Notably, the orientation of the axial motion perpendicular to the vortex plane is determined by the winding number w of the ring. If there was no dissipation and therefore no mutual friction between the ring and the fluid, the ring would move in its own flow field *ad infinitum*, without any changes in shape or size. In the presence of friction, by contrast, a Magnus force arises which points along the radial direction towards the centre of the ring [134]. Consequently, the vortex ring obtains a radial velocity component and therefore undergoes a gradual and symmetric shrinking. Simultaneously its axial velocity increases. Eventually, the ring shrinks to zero size and its characteristic phase structure disappears. This is the analogous result for vortex rings that we found for vortex dipoles in the two-dimensional superfluid, *cf.* section 6.2. In that case, friction causes each vortex to slow down relative to the velocity induced by the respective other vortex, causing the emergence of a Magnus force along the dipole vector. The vortices therefore obtain a longitudinal velocity component and eventually annihilate. This picture also applies for the vortex ring if we again think of it as vortex–anti-vortex pairs on a continuum of vertical planes vertically intersecting its centre. We stress that this interpretation has its limitations since the topology of the ring imposes strong restrictions on the motion of its core. Nevertheless, it helps to think of the ring in terms of vortex dipoles to understand its shrinking and the annihilation of its phase structure. In this sense, the quantised phase winding around every point of the ring can be thought of as being annihilated by the respective other point on the opposite side of the vortex ring. Hence, in spite of the intrinsic stability of the vortex ring against decay due to its quantised phase winding, it has a finite lifetime nonetheless. Furthermore, it turns out that vortex rings of higher winding number, *i. e.*, $|w| > 1$, quickly decay into elementary vortex rings once the system is propagated in time. Likewise, also higher-wound vortex lines of any other shape decay into elementary vortex lines. In fact, also in the two-dimensional holographic superfluid studied in Part I, higher-wound vortices decay into elementary vortices. In chapter 14 we will show that the decay of vortex rings of higher winding number can lead to very interesting behaviours of the emerging elementary rings.

In figure 12.8 we show four snapshots characteristic for the time evolution of a single vortex ring in the holographic superfluid. We simulate the dynamics of the superfluid on a computational domain of 128^3 grid points along the (x_1, x_2, x_3)-directions until the vortex ring has shrunk to zero size. In the initial configuration, we prepare a ring of winding number $w = 1$ and radius $R_0 = 22$ grid points, aligned in parallel to the (x_1, x_2)-axis and with its centre position located at $(x_1, x_2, x_3) =$
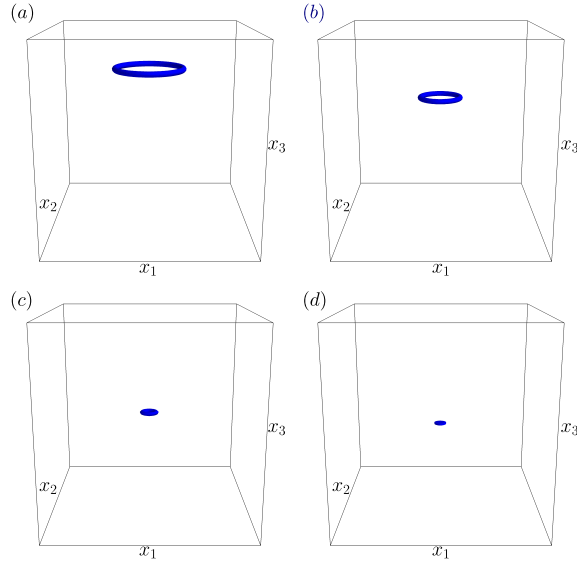
(i) Isosurface plots of the condensate density $n(\boldsymbol{x})$ (for $n/n_0 = 0.23$).
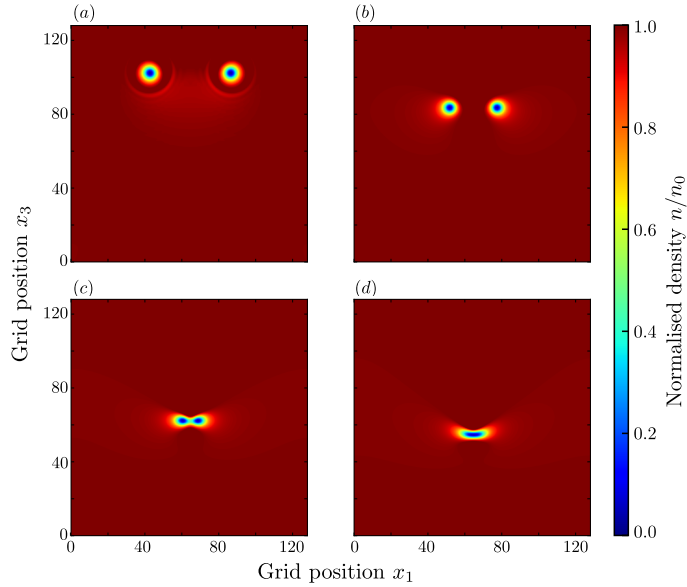
(ii) Condensate-density modulation on the two-dimensional (x_1, x_3)-plane intersecting the vortex plane through the centre of the ring.

Figure 12.8: Four characteristic snapshots of the time evolution of a single vortex ring of winding number $w = 1$ and initial radius $R_0 = 22$. (a), $t = 0$, initial configuration: The density profile around the core has built up. (b) $t = 75$, intermediate time: The ring has shrunk significantly and its density depletions begin to deform mildly. (c) $t = 123$, late time: The ring is about to disappear by shrinking to zero size. While the core itself is still circular, its density profile has strongly deformed and overlaps. (d) $t = 127$, after the annihilation: The ring has disappeared and left behind a rarefaction pulse.

$(64, 64, 102)$. Once the ring has fully developed its density profile, we reset the time to $t = 0$. At this point, the configuration agrees with the one depicted in the previous section in figure 12.2. It then takes approximately $\Delta t = 126$ unit timesteps until the ring has shrunk to zero size and its quantised phase winding has disappeared. In figure 12.8i, we plot isosurfaces of the superfluid-condensate density $n(\boldsymbol{x})$, as before with a defining value of $n/n_0 = 0.23$ (blue surfaces). The black outline in each panel again corresponds to the computational domain. In figure 12.8ii, on the other hand, we depict the superfluid density $n(\boldsymbol{x})$ on the fixed two-dimensional $x_2 = 64$ slice for the same characteristic times as in figure 12.8i. This is the same slice for which we have also studied the dual bulk view of the vortex ring in figure 12.3ii. The snapshots in figure 12.8 are taken at times $t = 0, 75, 123$ and $t = 127$, proceeding from the upper left panel to the lower right. The plots illustrate nicely what we have already formulated in our discussion in the previous paragraph. Namely, the motion of the vortex ring along its axial direction is superimposed by a gradual shrinking of the ring, *i. e.*, a motion opposite to the radial direction, pointing towards the centre of the ring. As the ring shrinks, its velocities in both directions increase with the strongest increase seen along the radial direction during the final stages of the evolution. We will study the velocities in more detail below. Shortly before the ring has shrunk to zero size, the density modulation around the vortex core deforms strongly and the depletions on opposite sides of the ring overlap and merge, *cf.* panels (*c*) of figure 12.8. In figure 12.8i we find that the isosurfaces of $n/n_0 = 0.23$ can no longer resolve the vortex ring at this stage of the evolution. Instead, we only find one large blob. In figure 12.8ii, the time evolution strongly resembles the one for vortices in the two-dimensional superfluid depicted in figure 6.2. In particular, the density depletions of the vortices deform strongly and merge. Once the ring has shrunk to a single-point zero in $n(\boldsymbol{x})$, it leaves behind a rarefaction pulse (*cf.* panel (*d*)), just as we saw for the vortex dipoles in the two-dimensional superfluid. This wave propagates along the x_3-axis but damps out quickly, and eventually decays into sound excitations of the fluid. The rarefaction pulse is clearly visible in the cross section plots of figure 12.8ii, *cf.* the lower right panel. In figure 12.8i, on the other hand, the rarefaction pulse is only discernible as a small blob, distinctly smaller than in panel (*c*) shortly before the annihilation.

Having qualitatively discussed and understood the time evolution of a single vortex ring in the holographic superfluid, let us now proceed to a more quantitative analysis of its dynamics. We are interested in studying the trajectory of the ring as well as its axial and radial velocities and accelerations. In addition, we want to study how these observables compare to results from the Gross–Pitaevskii model and the Hall–Vinen–Iordanskii (HVI) equation for vortex rings. In our analysis, we focus on the same vortex-ring dynamics as depicted in figure 12.8. To extract the trajectory of the ring from our real-time simulation, we have to track the position of its core on the numerical grid. Due to its plane circular geometry, it is not necessary to track the entire one-dimensional vortex core. Instead, it is sufficient to determine the positions of two opposite points of the ring along its radial direction from which we can subsequently infer the location of the centre of the vortex ring as well as its radius.

The most efficient and accurate procedure to locate the two points of the vortex core is yet again given by our tracking routine for vortices in the two-dimensional superfluid introduced in section 6.3 of Part I. The tracking routine, consisting of two separate algorithms, can be applied to the density modulation $n(\boldsymbol{x})$ on any two-dimensional slice vertically intersecting the vortex plane through the centre of the ring, without any need for adaptations since the ring effectively reduces to a vortex–anti-vortex pair for which we have first introduced those algorithms. In particular, since the vortices on this plane also deform in a similar manner as vortex–anti-vortex dipoles in $d = 2$, we can again resort to the combination of the Gaussian fitting routine and the Newton–Raphson method. To be specific, we use the former algorithm for vortex–anti-vortex separations, *i. e.*, vortex-ring diameters, larger than $R(t) = 11/2$ grid points and resort to the NR method for all smaller separations. In addition, we find it convenient for our analysis of the vortex-ring velocities and accelerations to track the ring more frequently than at every unit timestep during the finale stages of its evolution. We recall that in our numerical implementation of the equations of motion, every unit timestep is composed of a number of numerical timesteps, allowing us to analyse the superfluid configuration also at inter-mesh time points without adapting the implementation. Here, we find that tracking the ring fifty times over the course of one unit timestep yields a sufficiently high time resolution. We employ this enhanced tracking routine during the last eight unit timesteps of the ring's evolution. In figure 12.9 we show the resulting trajectories of the induced vortex–anti-vortex pair on the $x_2 = 64$ slice. The time evolution of the density modulation on this slice is illustrated in figure 12.8ii above. The trajectories clearly show how the ring gradually shrinks and eventually annihilates itself. At very early times, we find the trajectories of the vortex ring to exhibit a small outward bending. Like for the vortex dipoles in the previous part, we attribute this to our initial preparation of the phase configuration of the vortex ring. Indeed, the phase-winding structure, *cf.* equation (12.3), that we initially imprint onto the static superfluid solution does not agree with the proper solution for the phase configuration of the ring. Hence, the system undergoes a phase-healing regime at early times. We stress that the phase healing has no effect on our following analysis.

Before we consider the computation of the vortex velocities and accelerations, a comment is in order here. We have thus far in this section restricted our investigations to only one specific initial configuration of the vortex ring. By symmetry considerations, we already know that the dynamics must be independent of the relative orientation of the ring in the three-dimensional superfluid. We have checked and confirmed this explicitly. However, a priori, there may well be a dependence on the initial radius of the ring. We therefore now study if the dynamics indeed depends on R_0 or if it is independent of the initial radius. For this, we simulate the dynamics of a single vortex ring for various initial radii and compare the corresponding trajectories. For simplicity we extract the vortex locations only at every unit timestep, which yields a sufficiently high accuracy for this analysis. In the initial configuration we prepare the rings such that they all have the same centre position and differ only in radius. We then simulate the dynamics of the respective configuration until the ring
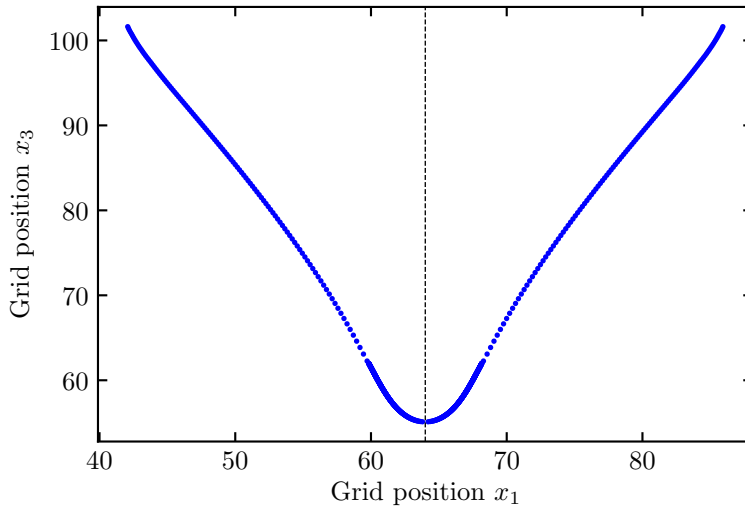
Figure 12.9: Trajectories of the vortex ring on the two-dimensional (x_1, x_3)-plane through the centre of the vortex ring of initial radius $R_0 = 22$. The dashed black line separates the trajectories of the induced vortex and anti-vortex. During the last $\Delta t = 8$ unit timesteps, we track the vortices 50 times per unit timesteps to increase the temporal resolution of the trajectories. The slight initial outward bending can be attributed to our procedure of preparing the vortex ring in the initial superfluid configuration.

has shrunk to zero size. For our simulations we employ slightly smaller grids, given by 96^3 points along the (x_1, x_2, x_3)-directions as opposed to the 128^3 grid points used before. We stress that this choice has no effect on the result. To check this explicitly, we simulate the dynamics of the vortex ring investigated above also on the smaller grid. To the precision we seek, we find the results on the smaller and the larger grid to be in excellent agreement. Returning to the rings of different size on the 96^3 grid, we align each ring in the initial configuration in parallel to the (x_1, x_2)-plane with its centre position located at $(x_1, x_2, x_3)=(64, 64, 77)$. In figure 12.10 we show the vortex-ring trajectories for five different initial radii, $R_0 = 8, 12, 16, 22, 26$ grid points. The left panel shows the corresponding trajectories as we extract them from the simulations by applying our tracking routine. In the right panel, on the other hand, we linearly shift the trajectories along the x_3-axis such that all rings disappear (extrapolated from the displayed trajectories) at the same grid position. We choose this position to coincide with the location where the $R_0 = 26$ vortex ring has shrunk to zero size. The figure clearly illustrates that the trajectories of all vortex rings are in excellent agreement, except for the very early times of the respective evolutions. As we have noted in the previous paragraph, these deviations are due to the initial preparation of the vortex configuration which does not respect
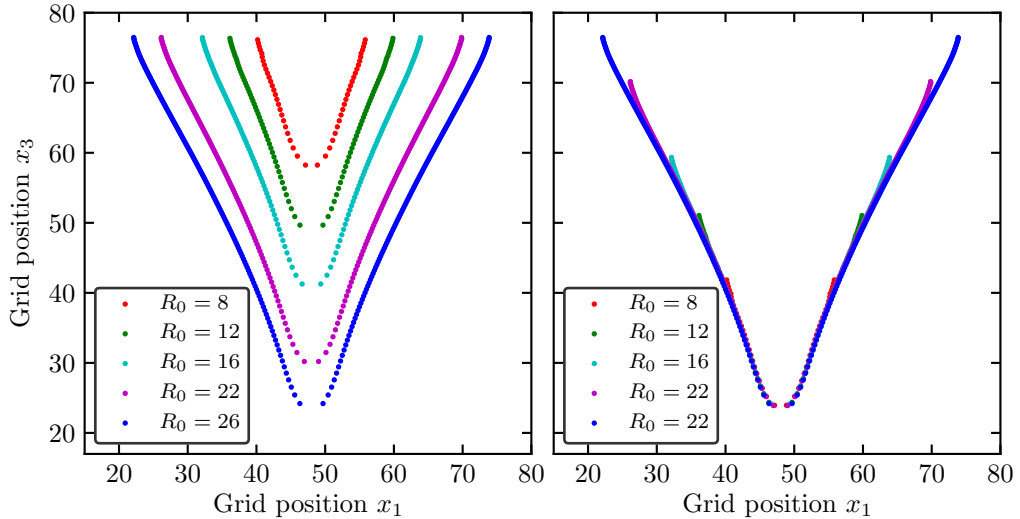
Figure 12.10: Trajectories of the vortex ring for five initial radii on the two-dimensional (x_1, x_3)-plane vertically intersecting the vortex plane through the centre of the ring. In the initial configuration, the centre of the ring is located at $(x_1, x_2, x_3)=(64, 64, 77)$ for all initial radii. Left panel: The trajectories as extracted from the numerical simulations. Right panel: Linearly shifted trajectories such that the ring disappears at the same grid position for all initial radii. This illustrates the universality of the vortex-ring dynamics. Note that the rings are only tracked at unit timesteps.

the periodicity of the grid. Further studies show that the trajectories do not only agree in space but also in time. In other words, also the velocities and accelerations of the vortex rings coincide when they have the same size. This is the same result as for vortex dipoles in the previous Part I. Hence, apart from the early-time regime, the dynamics of vortex rings is universal in the sense that there is no dependence on the initial configuration, and it is solely parametrised by the radius of the ring. This justifies that we restrict our analysis of the vortex-ring kinematics to only one specific initial configuration.

Let us now continue with our study of the vortex-ring velocities and accelerations. We recall that the corresponding simulation domain has a size of 128^3 grid points along the (x_1, x_2, x_3)-directions and the initial vortex-ring radius is $R_0 = 22$ grid points. In the following, we study the velocities and accelerations of the ring. For these observables it turns out to be useful to adapt physical units and thus multiply all observables by an appropriate power of the grid spacing l. For the radius of the vortex ring, for instance, this implies $R \rightarrow Rl$ and the velocity is thus expressed in units of the speed of light. Here, the grid spacing is given by $l = 2/7$, in units specified by $z_\mathrm{h} = 1$. Naturally, we split the motion of the vortex ring into its axial

direction perpendicular to the vortex plane and its radial direction, which accounts for the shrinking of the ring. We can directly extract the corresponding velocities from the trajectories shown in figure 12.9, again employing finite-difference methods, *cf.* appendix A.5. We show the results, reformulated as a function of the radius of the ring, in figure 12.11. Note the double-logarithmic scale in both panels. We further point out that time proceeds from right to left, *i. e.*, with decreasing radius.

Since we have the freedom to arbitrarily rotate the coordinate system, we take the axial velocity to be positive, without loss of generality. We display the axial velocity[3] $v_\perp$ in the upper panel of figure 12.11. At intermediate times, there is a regime during which the velocity approximately follows a power-law behaviour according to

$$v_\perp(R) = \frac{A}{R^b} \, , \tag{12.9}$$

where A is a fitting constant accounting for the normalisation of the velocity and $b = 0.83$ is the scaling exponent, extracted from a fit to the data points. We again employ a Levenberg–Marquardt least-squares fitting algorithm. The fitted power law is depicted by the dashed red line in figure 12.11, deliberately shifted below the velocity curve to aid the visualisation. We estimate the uncertainty of the scaling exponent, by varying the radius interval in the fitting routine, to be of the order of $\Delta b = \pm 0.02$. At later times, the velocity flattens and eventually saturates to $v_\perp \approx 0.39$. Importantly, this is only an estimate and its precision limited by the error estimates on the vortex locations as well as the time resolution of the associated trajectories. The flattening sets in approximately at the time at which the density depletions of the vortex ring strongly deform and overlap. At times prior to the scaling regime, a different behaviour of the axial velocity can again be attributed to the initial preparation of the vortex ring. In the next subsection we present an interpretation of the scaling behaviour and discuss further details.

In the lower panel of figure 12.11, we display the absolute value of the radial velocity v_R. We plot the absolute velocity since v_R accounts for the shrinking of the ring and is therefore negative. While it also (just like $v_\perp$) increases with decreasing radius, we cannot clearly identify any regime during which it would exhibit a scaling behaviour. In particular, during the scaling regime of $v_\perp$, the radial velocity is clearly bent. Upon downsizing this regime from both sides of the radius interval, one may speculate if there exists in fact a distinctly smaller scaling regime. However, for the given set of data points, such a statement is rather speculative and demands further studies of the vortex-ring dynamics for larger initial radii on even larger grids. For most of the evolution, the axial velocity is larger than the radial velocity. This changes during the late-time regime where axial velocity is distinctly smaller than radial velocity. The total motion of the ring during the final timesteps is thus strongly dominated by its shrinking process. We found the same result for the vortex dipoles in the two-dimensional superfluid with regard to their transverse

---

[3]We use $v_\perp$ to denote the axial velocity as it points in the direction perpendicular to the vortex plane. In addition, it highlights the similarity to the transverse velocity of the vortex dipoles of Part I.
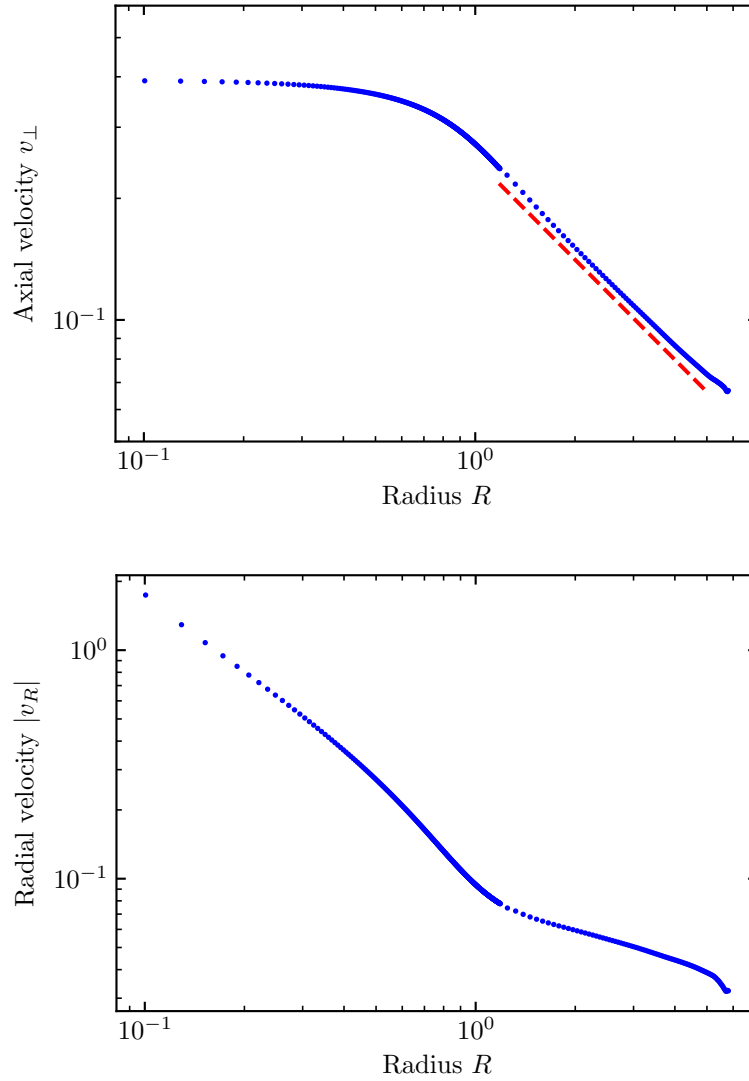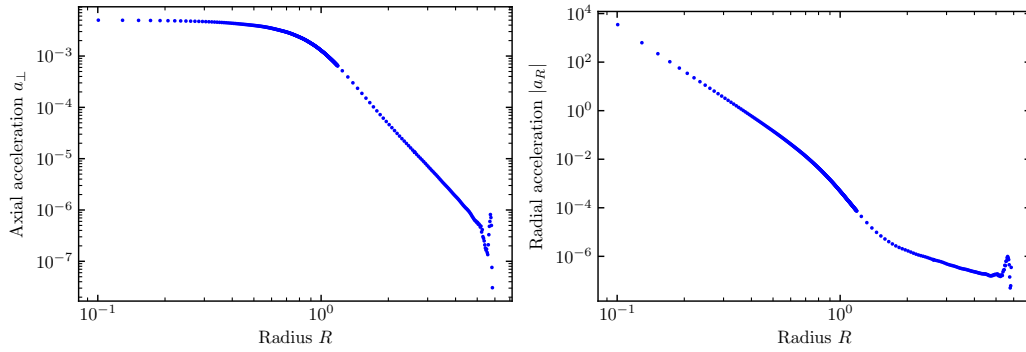
Figure 12.11: Axial (upper panel) and radial (lower panel) velocity of the vortex ring as a function of its radius, on a double-logarithmic scale. The initial radius of the ring is $R_0 = 22/l$ grid points and the corresponding trajectories are shown in figure 12.9. Note that time proceeds from right to left. At intermediate times, the axial velocity approximately increases with a power-law behaviour according to $v_\perp \sim R^{-0.83}$, as indicated by the dashed red line (deliberately shifted below the data points). For very small radii, the axial velocity flattens and saturates to $v_\perp \approx 0.39$. The radial velocity is negative as it accounts for the shrinking of the vortex ring while its magnitude increase strongly throughout the evolution. The behaviour at very early times can be attributed to the initial preparation of the vortex-ring configuration. All quantities are expressed in physical units.

Figure 12.12: Axial (left panel) and radial (right panel) acceleration of the vortex ring as a function of its radius, on a double-logarithmic scale. The initial radius of the ring is $R_0/l = 22$ grid points and the corresponding trajectories are shown in figure 12.9. The behaviour at very early times can be attributed to the initial preparation of the vortex-ring configuration. All quantities are expressed in physical units.

and longitudinal velocity component, see section 8.2. Shortly before the ring has shrunk to zero size, the radial velocity even exceeds the speed of light. As for the vortex dipoles of Part I, this does not violate causality due to the breakdown of the quasiparticle interpretation. For further discussions of this aspect see section 8.2.

Finally, we also compute the accelerations of the vortex ring along its axial and radial direction of motion. We present the results in figure 12.12. The left panel shows the axial and the right panel the radial acceleration. As expected from the velocities discussed in the previous paragraph, we find the axial component to flatten during the final timesteps of the evolution. The radial component, on the other hand, increases strongly at these times and is about six orders of magnitude larger than the axial acceleration. This highlights yet again the rapid shrinking of the vortex ring shortly before it disappears. The behaviour of both acceleration components at early times can again be attributed to the initial preparation of the vortex-ring phase configuration.

12.2.1 Comparison to the Hall–Vinen–Iordanskii Equation

Let us now compare our findings for the dynamics of vortex rings in the holographic superfluid to solutions of the Hall–Vinen–Iordanskii (HVI) equation[4] for a single vortex ring. We have already studied the HVI equations for the special case of

---

[4]In the context of vortex motion in three-dimensional superfluids, the HVI equations [238, 239] is typically referred to as the Hall–Vinen–Bekharevich–Khalatnikov (HVBK) [238, 394, 395] equations. Since the equation of motion for the vortex ring employed in this section is essentially the same as the ones we used in Part I for the vortex dipole, we refer to it as HVI equation throughout this work.

vortices in two-dimensional superfluids in chapter 7. In their original form, they were formulated for three-dimensional vortex excitations. This is the scenario we are interested in here. The HVI equations describe the mechanical motion of vortex defects in the point-particle limit, taking into account interactions between the defects and the superfluid. We refer the interested reader to section 7.2 for more details on the HVI equations and restrict our following remarks to a minimum.

For single and isolated vortex rings in three-dimensional superfluids, the form of the HVI equation is very similar to equation (7.6) in section 7.2. We recall that the phenomenological friction constants C and C' are drag coefficients, parametrising the mutual friction between the superfluid and the vortices. For vortices in two-dimensional superfluids, we have argued that the superfluid velocity $\boldsymbol{v}_s^i$ at the position of one vortex is induced by the flow field of the respective other vortices. For a single vortex ring in three-dimensional superfluids the superfluid velocity at the position of the ring is replaced by the self-induced velocity of the vortex ring itself, *i. e.*, $\boldsymbol{v}_s = \boldsymbol{v}_{\text{self}}$. As we are, here in this section, only interested in the dynamics of plane circular vortex rings of winding number $w = 1$, we restrict the following discussion to such rings. We study the dynamics of the vortex rings in the superfluid-condensate component only and therefore again neglect the normal-fluid velocity $\boldsymbol{v}_n$ in equation (7.6). With this, the HVI equation for a single plane circular vortex ring reduces to

$$\boldsymbol{v} = \frac{\mathrm{d}\boldsymbol{x}}{\mathrm{d}t} = (1 - C)\boldsymbol{v}_{\text{self}} - C' \, \hat{\boldsymbol{e}}_{\text{T}} \times \boldsymbol{v}_{\text{self}} \,, \tag{12.10}$$

where $\boldsymbol{v}$ is the velocity of the ring at its core position $\boldsymbol{x}$, $\boldsymbol{v}_{\text{self}}$ the self-induced velocity of the ring, and $\hat{\boldsymbol{e}}_{\text{T}}$ is the unit vector tangent to the vortex core at position $\boldsymbol{x}$. The orientation of $\hat{\boldsymbol{e}}_{\text{T}}$ is chosen such that $(\hat{\boldsymbol{e}}_R, \hat{\boldsymbol{e}}_{\text{T}}, \hat{\boldsymbol{e}}_\perp)$ constitutes a right-handed coordinate system, where $\hat{\boldsymbol{e}}_\perp$ is the unit vector perpendicular to the vortex plane along the axial direction of motion of the vortex ring, and $\hat{\boldsymbol{e}}_R$ is the unit vector pointing along the radial direction away from the ring's centre. The self-induced velocity for quantised vortex rings is given by [134]

$$\boldsymbol{v}_{\text{self}} = v_{\text{self}}(R)\hat{\boldsymbol{e}}_\perp = \frac{\kappa}{4\pi R} \left[\log\left(\frac{8R}{\tilde{\xi}} \right) - \delta + 1 \right] \hat{\boldsymbol{e}}_\perp \,, \tag{12.11}$$

where κ is related to the winding number of the vortex ring, and δ is an additional parameter, the so-called 'core-parameter', characteristic of the underlying superfluid and the vortex-induced density depletion. The radius is again denoted by R and $\tilde{\xi}$ is the healing length of the superfluid. Here, we again denote the healing length with an additional tilde to clearly distinguish it from the vortex width ξ defined above as a parameter characterising the width of the holographic vortex-induced density depletion. For superfluid helium the self-induced velocity was first computed in [396], after similar expressions were first obtained for classical vortex rings in [397].

From equation (12.10) we can now directly read off the axial and radial velocity components of the vortex ring. We find for the axial component

$$\boldsymbol{v} \cdot \hat{\boldsymbol{e}}_\perp = v_\perp = (1 - C)v_{\text{self}} \tag{12.12}$$

and likewise for the radial component

$$\boldsymbol{v} \cdot \hat{\boldsymbol{e}}_R = v_R = \frac{\mathrm{d}R}{\mathrm{d}t} = -C' \, v_{\text{self}} \,. \tag{12.13}$$

This follows trivially from equation (12.10) since the self-induced velocity points along the axial direction $\hat{\boldsymbol{e}}_\perp$ transverse to the vortex plane, and $\hat{\boldsymbol{e}}_{\mathrm{T}}$ along the direction tangential to the vortex core. This implies that $\hat{\boldsymbol{e}}_{\mathrm{T}} \times \boldsymbol{v}_{\text{self}}$ points along the radial direction of the ring away from the centre , *i. e.*, is parallel to $\hat{\boldsymbol{e}}_R$. Importantly, these equations are only applicable in the limit of vanishing vortex width, *i. e.*, for $\tilde{\xi} \ll R$. We point out that equations (12.12) and (12.13) imply that the induced vortex–anti-vortex pair on the two-dimensional plane intersecting the centre of the ring moves on straight trajectories. This result again agrees with the behaviour of vortex dipoles in the two-dimensional superfluid in the point-particle limit as we have laid out in section 7.3. Notably, equations (12.12) and (12.13) allow for a very intuitive interpretation of the vortex-ring dynamics. Namely, at a fixed radius of the vortex ring, the axial velocity is induced by the self-induced velocity of the ring but slowed down due to friction between its core and the fluid, *cf.* equation (12.12) (note that $C < 1$). The difference between the axial and the self-induced velocity leads to a Magnus force which is proportional to the difference in magnitude and orthogonal in direction. This is reflected in equation (12.13).

Let us now compare these results with our numerical findings for the vortex velocities presented in figure 12.11. We restrict this comparison to a qualitative level. A quantitative matching as in section 7.3 for the vortices in the two-dimensional holographic superfluid and in particular an extraction of the friction coefficients would require a prior matching to the solutions of the dissipative Gross–Pitaevskii model in order to extract the parameters δ, κ and $\tilde{\xi}$ of equation (12.11). In particular, as for vortices in the two-dimensional system, the vortex rings of the holographic system are clearly in violation of the limit of vanishing vortex widths, $\xi \to 0$, *cf.* figure 12.4, which prohibits a direct matching of the holographic dynamics to solutions of the HVI equation. In section 7.3 we have eluded this obstacle for vortices in two dimensions by employing a rescaling symmetry of the DGPE. This, however, is only possible after matching the dynamics to the DGPE first which is thus required also for the three-dimensional system. Here, we leave a more thorough comparison, including a high-precision matching procedure to DGPE and subsequently the HVI equation, for future studies. Such an analysis would in particular enable us to extract the friction coefficients and use them to quantify the dissipation of the three-dimensional holographic superfluid, just as we have done for the two-dimensional system, *cf.* chapter 7.

In the previous subsection we have found the axial velocity of the vortex ring in the holographic superfluid to increase with a power-law behaviour according to $v_\perp \sim R^{-0.83}$. Such a power-law scaling is very similar to the behaviour predicted by the HVI equation, *cf.* equations (12.11) and (12.12). Indeed, for radii R much larger than the healing length $\tilde{\xi}$, the logarithm in (12.11) is sub-dominant and can be approximated by a constant, resulting in an increase of the axial velocity with one

over the radius. For only slightly smaller radii as compared to the healing length, on the other hand, the logarithm yields a correction to the $v_\perp \sim R^{-1}$ behaviour, mildly slowing down the increase. Fitting (12.12) directly to the axial velocity of the holographic vortex ring, in the same regime that we have employed in the fitting routine of the power law, proves that it is in excellent agreement with the data points and, moreover, coincides to high accuracy with the power-law behaviour (12.9) we have extracted earlier. Due to the strong agreement, we refrain from displaying the HVI solution in figure 12.11 explicitly. Upon going to even smaller vortex radii beyond the fitting interval, we find the axial velocity to deviate from the HVI solution. Like for the power-law behaviour, these deviations occur once the density depletions around the vortex core strongly deform, merge, and overlap. In light of the applicability of the HVI equation, the deviations are in fact expected since the HVI equation is valid only for $\tilde{\xi} \ll R$ which is clearly violated once the vortex-induced density depletions deform and overlap.

With regard to the radial velocity, we find our numerical results for vortex rings in the holographic superfluid to deviate from the HVI solution, *cf.* equation (12.13). Notably, the HVI equation predicts the same functional dependence on the vortex radius for the radial as for the axial velocity. The two components only differ in their absolute values. In our studies above, however, we have found the vortex rings in the holographic framework to exhibit a different behaviour. As figure 12.11 clearly illustrates, the two velocity components have a distinctly different dependence on the radius of the vortex ring. In particular, the radial velocity does not follow a power-law behaviour, as would be expected at intermediate times based on the HVI equation. One reason for the different observed behaviour may be that the radial velocity is more sensitive to early deformations of the density depletions which are strongest along the radial direction. Nonetheless, we point out that, in agreement with our early discussion, 12.11 shows that there may in fact be a small interval during which the radial velocity follows a power-law behaviour. However, the regime is distinctly smaller than for the axial velocity and we do not have a sufficient number of data points to ensure proper convergence of a fitting function to verify this explicitly.

Nevertheless, it is interesting to integrate the differential equation for the radial velocity to obtain the direct dependence of the radius of the vortex ring on time. Since we are interested only in the regime of large radii, we again treat the term in brackets in equation (12.11) as being approximately constant. In practice, this corresponds to replacing the radial dependence in the logarithm by $\hat{R}$, the mean radius. Integrating the resulting equation yields

$$C't = \frac{\kappa}{8\pi} \frac{R^2 - R_0^2}{\log\left(\frac{8\hat{R}}{\tilde{\xi}}\right) - \delta + 1} \,, \tag{12.14}$$

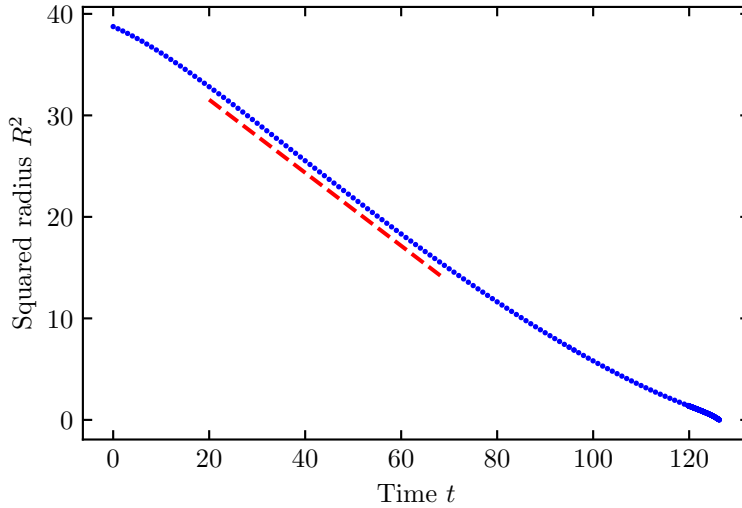with the same parameters as defined above, and R_0 is again the initial radius of the

Figure 12.13: Squared radius of the vortex ring, extracted from the trajectories in figure 12.9, as a function of time. At intermediate times, R^2 decreases linearly with time, as indicated by the dashed red line (deliberately shifted below the data points). Qualitatively, this behaviour agrees with the HVI dynamics of vortex rings.

ring. It follows that

$$\frac{\mathrm{d}R^2}{\mathrm{d}t} = -\Gamma \,, \tag{12.15}$$

where we have introduced the constant $\Gamma > 0$. The exact value of Γ can be inferred from a comparison with equation (12.14). Hence, the squared radius of the vortex ring, according to our approximation of the HVI equation, decays linearly with time. Let us now compare this behaviour with the analogous dependence for the vortex ring in the holographic superfluid. We present the results for the squared radius of the vortex in figure 12.13. The data points are extracted from the trajectories displayed in figure 12.9. In addition, we plot a linear slope (dashed red line) that allows for a better comparison with the HVI solution. We find that at intermediate times, the functional dependence of the holographic system is in excellent agreement with the HVI prediction. Notably, the regime during which agreement persists is much shorter than the scaling regime of the axial velocity as a function of the radius of the vortex ring[5]. Moreover, the scaling regime of $R^2(t)$ sets in at earlier times the scaling regime of $v_\perp$, which we expect to be due the increased sensitivity of the axial velocity on numerical uncertainties. During the late-time regime, we

---

[5]The time interval corresponding to the scaling regime of the axial velocity displayed in figure 12.11 is given by $35 \lesssim t \lesssim 118$, whereas the time interval corresponding to the scaling regime of the radius-squared displayed in figure 12.13 is given by $20 \lesssim t \lesssim 69$.

again find strong differences between our numerical results and the HVI solution which are expected due to the breakdown of the applicability of the HVI equation. Likewise, deviations are also expected at early times due to the initial preparation of the vortex-ring configuration in the holographic system. Before we conclude this subsection, let us point out that $R^2(t)$ appears to be more appropriate for a direct comparison of the two theories than the radial velocity $\mathrm{d}R/\mathrm{d}t$ since it is much less sensitive to minor deviations between the holographic vortex-ring dynamics and the HVI equation. In particular numerical errors are amplified in the computation of the velocity and might therefore spoil the analysis.

The dynamics of vortex rings has also been intensively studied within the Gross–Pitaevskii model. We want to specifically point to one influential work [325] that has a similar focus as our studies in this thesis. The authors of [325] study the dynamics of a single vortex ring in a dissipative condensate and also compare their findings to the HVI (HVBK) equation. Notably, the theoretical framework employed in [325] does not equal the DGPE model outlined in section 7.1. Instead, the non-dissipative GPE is coupled to a bath of thermal excitations which allows for the dissipation of energy and momentum. Just as in the holographic superfluid, the dissipation causes the vortex ring to shrink and eventually annihilate itself. The corresponding decay law found in [325] agrees with the approximate solution of the HVI equation, *cf.* equation (12.15), and thus also our with findings for vortex rings described within the holographic framework. For a non-dissipative Bose gas, on the other hand, the authors of [398] show that a vortex ring traverses the condensate exactly with its self-induced velocity (12.11) and keeps its initial radius throughout the evolution.

12.2.2 Dependence on the Chemical Potential

From our previous studies in this chapter, we have by now established that the holographic superfluid is strongly dissipative. On a qualitative level, we have even understood how the dissipation mechanism is realised within the holographic framework by studying the bulk representation of vortex defects in the superfluid. In particular, we know that this mechanism is the same for all chemical potentials of the superfluid. However, what we do not know yet, is how the strength of the dissipation depends on the chemical potential. Understanding this dependence is the main goal of the present subsection. We focus again on the dynamics of vortex rings. To be specific, we study the kinematics of vortex rings, with special emphasis on the velocities, for various chemical potentials of the superfluid. From our discussions in the previous subsections we know that the vortex-ring velocities are particularly sensitive to the dissipation of the holographic system since they are strongly affected by the mutual friction between the vortex core and the superfluid. Hence, the velocities must, in some way, encode the strength of the dissipation. We expect the details of this dependence to be highly complex. Nevertheless, by comparing the outcomes to our previous findings regarding the vortex-dipole dynamics studied in Part I where we have a much more thorough and quantitative understanding of the dissipation, we gain further insight into the characteristics of the three-dimensional

holographic superfluid.

Let us recall that throughout this work we set $z_{\mathrm{h}} = 1$ and thus fix the absolute temperature of the superfluid to $T = (4\pi)^{-1}$. This leaves the chemical potential μ to be the only free parameter, controlling the temperature ratio T/T_{c} and therefore the phase transition of the superfluid. This implies a one-to-one correspondence between μ and T/T_{c} as discussed above in section 11.3. In section 12.1.1 we have already investigated how the static vortex solution depends on the chemical potential. To be specific, we have extracted the width of the vortex-induced density depletion in $n(\boldsymbol{x})$ and found that it exhibits a power-law behaviour in the shifted chemical potential $\delta\mu = \mu - \mu_0$ with $\mu_0 \approx \mu_{\mathrm{c}}$, where μ_{c} is the critical chemical potential of the holographic system. This has allowed us to substantiate that the three-dimensional holographic model resembles a non-relativistic superfluid.

In the previous subsections we have found the dynamics of plane circular vortex rings to be independent of their initial size. We expect the same to be true also for all other choices of the chemical potential and therefore proceed as above, restricting the analysis to only one specific initial radius of the vortex ring. In light of the highly time-demanding numerics, we simulate the superfluid dynamics on slightly smaller grids than for the single vortex ring studied above, using 96^3 grid points along the (x_1, x_2, x_3)-directions. We stress that we again check explicitly that, to the precision we seek for our investigations, the outcomes are not altered by finite-size effects of the numerical grid. We adapt the convention of the previous subsection and use physical units for all observables, including the healing length which thus has to be multiplied by the grid spacing. Hence, we use $\xi \to \xi l$, where l is again the grid spacing along the (x_1, x_2, x_3)-directions. To account for the change in the vortex size that goes along with the change in μ, we proceed just as for the vortex dipoles in the two-dimensional superfluid and study the vortex velocities as a function of the radius in units of the respective width ξ of the vortex-induced density depletion, *i. e.*, R/ξ. We recall that ξ may be interpreted as the healing length of the superfluid which constitutes the characteristic length scale of the system. Hence, by studying the velocities as a function of the radius in units of ξ, we account for different length scales of the superfluid for different chemical potentials. For every choice of the chemical potential we adapt the grid spacing l such that the vortex-induced density depletions are initially resolved by approximately the same number of grid points as the vortex ring we have studied in the previous subsections, *cf.* figure 12.4. Since we express all observables in physical units (or units of ξ), the grid spacing drops out of all of our results. It is necessary only to ensure that the tracking routine is applicable and locates the vortex rings on the grid to the highest attainable accuracy.

In the initial configuration, we imprint a single vortex ring onto the static background solution of the holographic superfluid for five values of the chemical potential, $\mu = 4.5, 5, 6, 7$ and 9, corresponding to the ratios $T/T_{\mathrm{c}} = 0.92, 0.83, 0.69, 0.59$ and 0.46, respectively. In each system, we prepare the ring of initial radius $R_0/\xi = 8.5$ and winding number $w = 1$, such that its axial direction is aligned in parallel to the x_3-axis and its centre position is located at $(x_1, x_2, x_3) = (48, 48, 77)$. Subsequently, we evolve the respective system in time until the ring has disappeared by shrinking

Table 12.1: Numerical parameters employed in the simulations of the vortex-ring dynamics in the holographic superfluid for various values of the chemical potential μ. The temperature ratio T/T_c is not independent of μ, *cf.* equation (11.21). In addition, ξ is the healing length of the superfluid, expressed in physical units, n_0 the condensate background density, and L the size of the computational domain. For details on our procedure, see the main text.

μ	T/T_c	n_0	ξ	R_0/ξ	L/ξ
4.5	0.92	23.2	1.19	8.5	22.2
5	0.83	97.5	0.74	8.5	36.9
6	0.69	329.1	0.51	8.5	52.1
7	0.59	914.7	0.41	8.5	63.8
9	0.46	4389.9	0.31	8.5	83.4

to zero size. In table 12.1 we summarise the simulation parameters. We also include the superfluid-condensate density n_0 and the length of the computational domain $L = N_{\boldsymbol{x}} l$ in each of the three directions in units of the healing length, where $N_{\boldsymbol{x}} = 96$ is the number of grid points along all three spatial directions. For a more thorough discussion of the aspects addressed in the previous two paragraphs, see also our comments in section 8.3.

To analyse the dynamics of the vortex rings, we proceed as outlined in the previous subsection. We locate the core of the vortex ring using our combined tracking routine to extract its radius as well as its centre position. Since the rings are resolved by the same number of grid points, the tracking routine works equally well and yields similar error estimates of the vortex locations for all choices of the chemical potential. Subsequently, we employ finite-difference methods to derive the velocities of the ring along its axial and radial direction. We again make use of our two-dimensional tracking procedure applied to the induced vortex–anti-vortex pair on the (x_1, x_3)-plane at fixed $x_2 = 48$ intersecting the centre of the ring which allows us to obtain the quasi-continuous trajectories of two opposite points of the vortex core from which we can subsequently derive its velocities. Unlike before, here we only track the vortices at every unit timestep throughout their entire evolution and refrain from tracking them more frequently in the late-time regime.

In figure 12.14 we show the axial (upper panel) as well as radial (lower) velocity of the vortex ring for all five values of the chemical potential, as a function of R/ξ. We find that both velocity components are ordered with the chemical potential (or equivalently the ratio T/T_c) of the superfluid. Indeed, for fixed R/ξ, both velocity components, along the axial as well as the radial direction, are largest for the highest values of the chemical potential (smallest temperature) and then decrease monotonously with decreasing chemical potential (increasing temperature). For the
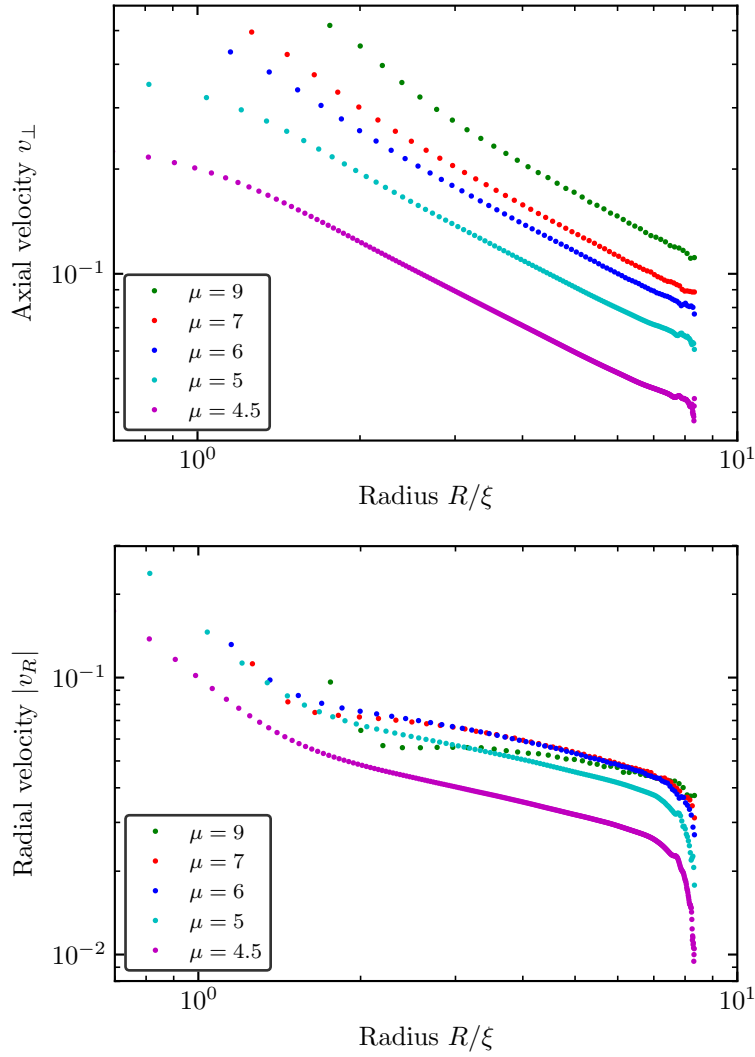
Figure 12.14: Axial (upper panel) and radial (lower panel) velocity of the vortex ring as a function of R/ξ for five values of the chemical potentials of the holographic superfluid μ, on a double-logarithmic scale. Here, R denotes the radius of the vortex ring and $\xi = \xi(\mu)$ the width of the respective vortex-induced density depletion. In order to compare the velocities for different values of the chemical potential we study it as a function of R/ξ. This way, we account for the μ-dependence of the vortex-induced density depletion. In the initial configuration, the radius of the ring is given by $R_0/\xi = 8.5$, for all values of the chemical potential. At fixed R/ξ, both velocity components obey an ordering with the chemical potential of the superfluid and are larger for higher values of μ (only approximately for $|v_R|$). Note that the ring is tracked only at every unit timestep.

axial velocity this dependence is more pronounced than for the radial velocity. Along the axial direction, we find the velocities for all chemical potentials to flatten during the final stages of the evolution. However, unlike for the vortex ring studied in the previous subsection, here the given time resolution of the trajectories does not allow us to extract the saturating velocity. Along the radial direction, we find the vortex-ring velocity for all chemical potentials to increase strongly during the final stages of the evolution and to dominate the total dynamics. We expect the minor deviations from the perfect ordering with μ to be mainly due to numerical uncertainties. On a qualitative level, the strong increase of the radial velocity again agrees with our previous findings in this part as well as for the analogous behaviour of the longitudinal velocity of the vortex dipoles in Part I.

The clear ordering of the velocities with the chemical potential of the superfluid suggests that the dissipation of the system also has a dependence on μ. In particular, by comparing these findings to our results for the vortex-dipole dynamics in section 8.3, we conjecture that the dissipation decreases for increasing chemical potential. Moreover, from the fact that the respective velocities along the axial as well as radial direction are all of the same order of magnitude, we suspect the dissipation to also vary only mildly. This point requests further elaboration. In our matching procedure of Part I, we have found that the dissipation of the two-dimensional holographic superfluid has only a small dependence on the chemical potential. In particular, the dissipation is of the same order of magnitude for all chemical potentials that we have studied and deemed sensible in the probe-approximation. Further studies have then proven that this small dependence of the dissipation on the chemical potential affects the dipole velocities only mildly, *cf.* section 8.3. A comparison of the velocity dependence of figure 8.7 for the vortices in the two-dimensional holographic superfluid with figure 12.14 for the vortex ring, strongly suggests that also in three spatial dimensions the dissipation varies only slightly with μ. We stress that analysing this dependence explicitly would require a direct matching with the dissipative Gross–Pitaevskii equation. Nevertheless, our findings nicely confirm our intuitive understanding that the velocities of vortex defects contains crucial insights into the dissipative nature of the superfluid. As a final comment of this section we point out that it appears likely that a more detailed and quantitative analysis of the μ-dependence of the dissipative nature of the superfluid would require a self-consistent coupling of the superfluid component to the thermal heat bath, *i. e.*, to lift the probe-approximation. Nonetheless, we expect that our studies in the probe-approximation are very useful to give us some intuition about the features of the superfluid and for now, an investigation of the full theory including backreaction appears out of reach due to the enormous numerical costs of solving the equations of motion.

12.3 Vortex Lines and Reconnections

So far in this chapter, we have discussed mainly single vortex ring in the holographic superfluid and their dynamics. In this section, we want to slightly shift focus and investigate the dynamics of vortex lines as well as one crucial aspect of their interactions. To this end, we first recall from our discussions in section 12.1.2 that due to the periodicity of the computational domain, we can only prepare an even number of parallel vortex and anti-vortex lines in the initial configuration. We have further argued that a single vortex line can be thought of as an extension of a vortex in the two-dimensional superfluid along an additional direction perpendicular to the vortex plane. This implies that the dynamics of vortex-line dipoles in three spatial dimensions and of vortex dipoles in two spatial dimensions is very similar and since we have already discussed the latter extensively in Part I, we refrain from presenting an in-depth analysis of the dynamics of straight vortex-line dipoles in this part. Nevertheless, we point out that it would be of great interest to match the dipole-line dynamics with the analogous solution of the three-dimensional Gross–Pitaevskii equation to quantify the dissipation of the holographic superfluid. The procedure would be the same as for the two-dimensional system in chapter 7. In this case, also the HVI equations for the vortex lines take the exact same form as in equation (7.6) for vortices in two-dimensional superfluids. Remarkably, for the three-dimensional holographic superfluid, there are now two ways to quantify the dissipation. First, as discussed above, by employing the dynamics of vortex rings, and second, by using the dynamics of straight vortex-line dipoles. It would be very interesting to study both and compare the outcomes. Such an analysis would in particular allow us to infer how the drag forces on vortex lines compare to those on vortex rings. We leave this investigation for future studies.

In addition to shrinking vortex rings and annihilating vortex lines, three-dimensional superfluids allow for another class of highly interesting interactions between vortex defects – namely, reconnections. Reconnections occur whenever two vortices come into contact but are not aligned anti-parallel to one another along their entire cores, implying that their phase structures cannot mutually annihilate. Instead, the interactions between the vortices cause only segments of the vortex cores to align anti-parallel to one another, resulting in the annihilation of two single points, thus causing the lines to break up and form new vortex lines. In other words, both vortex lines break up into two pieces which then recombine with the pieces of the respective other line. Such a process is called reconnection. It occurs for vortices of all shapes and windings numbers and typically leads to the formation of larger vortex structures. By definition, annihilations of vortex lines are a special type of reconnection where the entire cores are anti-parallel. Over the past decades, vortex reconnections have attracted much interest, mainly due to their immense importance in superfluid turbulence (see *e. g.* [399]). We will comment on this also in the next chapter when we study the dynamics of dense vortex tangles in which the vortices constantly undergo reconnections. Remarkably, it was only in 2007 that vortex reconnections were first observed directly in superfluid helium [400, 401]. However,
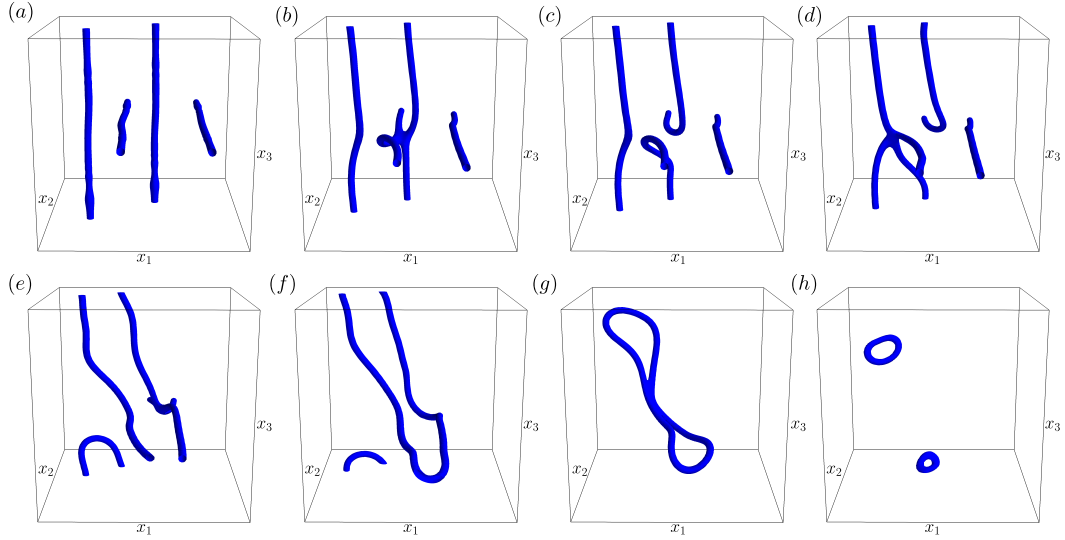
Figure 12.15: Snapshots of isosurfaces of the superfluid density $n(\boldsymbol{x})$ (defining value $n/n_0 = 0.23$) showing the time evolution of four initial vortex lines gradually undergoing reconnections. The initial configuration consists of two vortex dipoles aligned along the x_2- and x_3-axis such that the respective vortex and anti-vortex lines cannot simply annihilate. Instead, the lines deform and reconnect pairwise to form new vortex lines and rings. Eventually, only two vortex rings remain which quickly disappear due to the large dissipation.

prior to the experimental discovery, they were intensively studied by theorists, first within the vortex filament model by Schwarz, *cf.* [402, 403] and references therein, and subsequently also within the Gross–Pitaevskii model [404–406]. The study of vortex reconnections is not restricted to vortex excitations in superfluids but also in, *e. g.*, superconductors [407] or liquid crystals [408]. In classical fluids, on the other hand, vortex reconnections are forbidden due to the helicity conservation theorem [409].

In view of our studies of superfluid turbulence in chapter 13, let us now qualitatively study reconnections of vortex lines in the holographic superfluid. We prepare two vortex lines of winding numbers ± 1 aligned parallel to the x_2-axis and the analogous configuration aligned parallel to the x_3-axis in the initial configuration. By placing them appropriately in the three-dimensional domain we ensure that the respective anti-parallel vortex lines cannot simply annihilate. The vortex configuration at time $t = 5$, when the lines have fully developed their density profile, is displayed in panel (a) of figure 12.15. As the system is propagated in time, each vortex line moves in the flow field of the respective other vortices. Since the alignment of the vortices is not translationally invariant and therefore not analogous to a vortex configuration in a two-dimensional superfluid, the respective flow fields induce a bending of the

vortex lines. An important characteristic of vortex defects in three-dimensional superfluids is that, just like for vortex rings, all segments of finite curvature of generic vortex lines have a self-induced velocity. Hence, the vortex motion induced by the flow fields is superimposed by their own self-induced velocity. In addition, the motion of the vortices is subject to mutual friction which again causes the emergence of Magnus forces. The total vortex-line motion is therefore highly complicated. We illustrate the time evolution in figure 12.15. Note that the computational domain is periodic. Panel (*b*) shows how the two 'innermost' vortex lines attract each other and come into contact. Evidently, in a recombination process first a short segment of each line aligns anti-parallel to the segment of the respective other line. After some time, and upon further approaching each other, the vortex lines break up and form new lines, *i. e.*, they reconnect, *cf.* panels (*b*) and (*c*). As time proceeds, such processes repeat, causing the vortices to reshuffle. At one point during the evolution in this example, the reconnections lead to the formation of one large vortex ring (panel (*f*)). However, since this ring is strongly elongated along one direction, it does not simply shrink to zero size but instead breaks up into two smaller, nearly circular rings. Eventually, these rings disappear by rapidly shrinking to zero size. We point out that just like shrinking vortex rings or annihilating vortex lines, every reconnection induces the emission of rarefaction pulses and sound excitations. Using the GP model, the emission of such sound sound waves was specifically studied in [410, 411].

We stress that vortex reconnections occur independent of whether the underlying superfluid is dissipative or not. In section 7.2 we have found that according to the HVI equations, the approach of two vortices in a dissipative two-dimensional superfluid is governed by $d(t) \sim \sqrt{t_a - t}$, where $d(t)$ is again the distance between the vortices and t_a is the time of annihilation. This power-law behaviour also describes the approach of two annihilating (or reconnecting) vortex lines in three-dimensional (dissipative) superfluids. This has been studied with vortex filament models [412, 413], GPE simulations [404, 406, 414], and has even been extracted from experiments [400, 401]. Remarkably, this power-law behaviour also applies to reconnecting vortex lines in non-dissipative superfluids as was shown numerically in [404, 406] and analytically [414] in the linear regime where the respective density depletions start to overlap. It would be very interesting to study these aspects in the holographic superfluid, a task we leave for future studies.

13 Universal Far-From-Equilibrium Dynamics and Turbulence

In the previous chapter, we have studied various aspects of topological vortex defects in the three-dimensional holographic superfluid. In particular, we have laid down the construction of vortex-ring and straight vortex-line solutions, studied their dual bulk representation, and compared the characteristics of the vortex-induced density depletions to analogous solutions of the Gross–Pitaevskii equation. Furthermore, we have presented a first in-depth analysis of the dynamics of a single vortex ring within the holographic framework. We have shown that it yields convincing arguments suggesting that the underlying superfluid is strongly dissipative. At last, but still very importantly, we have also discussed how vortex defects in the holographic superfluid reconnect.

In this chapter, we now build on those results and study the far-from equilibrium dynamics of the holographic superfluid induced by large ensembles of vortex excitations. For the initial vortex ensembles, we take one configuration consisting of a large number of only circular vortex rings and one consisting of a large number of only straight vortex lines. We imprint these configurations onto the static and homogeneous superfluid solution for a chemical potential of $\mu = 5$, corresponding to a ratio of $T/T_c = 0.83$. On a spatial grid with 128^3 points along the (x_1, x_2, x_3)-directions, we then evolve the system for both initial configurations in time until the last vortex defect has disappeared by shrinking to zero size which takes of the order of 500 unit timesteps in units of $z_h = 1$ for both initial conditions. We are interested in the time evolution of the vortex ensembles on a macroscopic level as well as the physics of the underlying superfluid on microscopic scales which we evaluate by means of correlations functions. In particular, we search for universal scaling laws in these correlation functions which would indicate the superfluid to bear signatures of turbulent behaviour. Analogous studies with similar evaluation methods have been performed before for vortex ensembles in the two-dimensional holographic superfluid in [148, 150].

This chapter is outlined as follows. In section 13.1 we introduce the two sets of initial vortex configurations and briefly comment on how they compare to experimentally created vortex tangles as well as vortex ensembles studied in the GP model. In the following section 13.2, we proceed to a mainly qualitative discussion of the dynamics of the vortex defects with special emphasis on the evolution of the corresponding dual bulk views. In section 13.3, we study the non-equilibrium dynamics and turbulent behaviour of the superfluid in terms of scaling laws in the two-point correlation function.

The content of this chapter is based on our publication [415] and some parts are taken verbatim from it. For a better embedding in the context of this thesis, we have further added and modified several parts.

13.1 Initial Conditions

We study the far-from-equilibrium dynamics of the three-dimensional holographic superfluid induced by two vortex ensembles $\mathcal{A}$ and $\mathcal{B}$ emerging from different initial vortex-ring and vortex-line configurations (also referred to as vortex tangles).

In the initial configuration, the vortex tangle of ensemble $\mathcal{A}$ consists of 18 plane circular vortex rings. We randomly distribute the centres of these vortex rings over the entire three-dimensional domain and align their symmetry axes along the three coordinate axes of the grid, six along each. Of these six vortex rings, three have winding number $w_i = -1$ and the other half has winding number $w_i = -1$. Like for the vortex positions, we also employ a Gaussian random distribution to set the initial radii of the rings. However, we impose the constraint $5 < R_0 < 64$ (in grid points) which ensures that the maximal diameter of every individual ring does not exceed the grid size along any of the three coordinate axes. In addition, the minimal radius ensures that none of the vortex rings disappear before they have even fully developed their density profile. To this end, $R_0 = 5$ grid points are only an approximation, motivated by the results of the previous chapter as well as by experience gained from studying several initial vortex configurations of this type. Indeed, the presence of other vortex rings strongly affects the shrinking of the individual rings and therefore has to be taken into account. The final constraint for the vortex rings in the initial configuration is that we do not allow for any two vortex cores to cross at any point in the computational domain (to inter-mesh accuracy). Intertwined vortex rings, on the other hand, are permitted.

The initial vortex tangle of ensemble $\mathcal{B}$ consists of a total of 24 straight vortex lines, divided into twelve pairs of anti-parallel defects, *i. e.*, the vortex lines of each pair have opposite circulation, with winding numbers $|w_i| = 1$. Of these twelve vortex–anti-vortex pairs, we randomly distribute four along each of the three spatial directions (x_1, x_2, x_3). We recall from the previous chapter that for straight vortex lines, pairs of opposite winding number have to be the fundamental building block in the initial configuration in order to respect the periodicity of the computational domain. The initial configuration of ensemble $\mathcal{B}$ is chosen to conform to this restriction. Like for the vortex rings, also here we ensure that the vortex cores do not intersect at any point, here to grid accuracy.

We prepare the initial configurations by linearly superimposing the phase structures of the individual vortex excitations and subsequently multiply the sum into the static and homogeneous background solution of the superfluid. For the vortex rings of ensemble $\mathcal{A}$ we again refrain from additionally imposing the bulk scalar field Φ to vanish at the respective positions of the vortex cores. For the vortex lines in ensemble $\mathcal{B}$, on the other hand, we find it convenient to punch holes in the profile of the scalar

field along the holographic direction emanating from the vortex-line locations in the superfluid condensate. Given these procedures, we find that for both ensembles it takes approximately $\Delta t = 5$ unit timesteps for the superfluid-condensate density to build up its characteristic profile around the vortex cores. For the vortex rings the build-up process implies in particular that the density at the respective positions of the vortex cores drops to zero. Unlike in our procedures in the previous chapter, we here do not reset the time to $t = 0$ once the density profiles have built up. The reason is that once the vortices have been imprinted their dynamics is strongly affected by the presence of the other vortices which causes them to deform and reconnect with each other. In particular, after the first five unit timesteps, the configurations have already notably departed from their initial state. We thus decide to measure time relative to the time of imprinting the vortex defects.

Experimentally, ensembles of vortex excitations in two- as well as three-dimensional systems can be created by quenching the system through a phase transition or even within the superfluid state. The formation of topological defects induced by a quench across the phase transition is known as the Kibble–Zurek mechanism [416, 417]. Applied to superfluids, one has found, experimentally as well as theoretically within the GP model, that for instance cooling quenches indeed lead to the spontaneous formation of vortex defects [388, 418]. Within the holographic framework, the Kibble–Zurek mechanism has been studied in [149, 165, 419]. Likewise, also for systems already in the superfluid phase, the rapid change of a Hamiltonian parameter can induce the formation of vortices. In addition to quenches, however, also methods previously described in this work can be employed to create vortex ensembles. For references, see *e. g.* [144–147, 229, 369, 420–422] and references therein.

The vortex configurations we study in this chapter can a priori not be associated with a quench in the sense explained above. The reason being simply that it appears unrealistic to create such highly symmetric vortex-line or vortex-ring configurations via quenches. However, as we will find in the following section, it turns out that after some time the vortex ensembles evolve into configurations that resemble those seen in, *e. g.*, cooling quenches studied within the GP model in [388]. Similar configuration have, in addition, also been studied in other GPE simulations, including [233, 234, 234, 423]. For studies of the formation of topological defects in relativistic systems, see [424, 425].

13.2 Time Evolution

We now study the real-time far-from equilibrium dynamics of the holographic superfluid starting from the two initial vortex ensembles discussed in the previous section. For both, ensemble $\mathcal{A}$ as well as $\mathcal{B}$, we evolve the system in time until the last remaining vortex ring has disappeared by shrinking to zero size which takes $t \approx 435$ (ensemble $\mathcal{A}$) and $t \approx 533$ (ensemble $\mathcal{B}$) unit timesteps. In figure 13.1 we show snapshots of the vortex tangles at six times characteristic for the respective evolutions, in figure 13.1i for ensemble $\mathcal{A}$ and in figure 13.1ii for ensemble $\mathcal{B}$. As in the previous
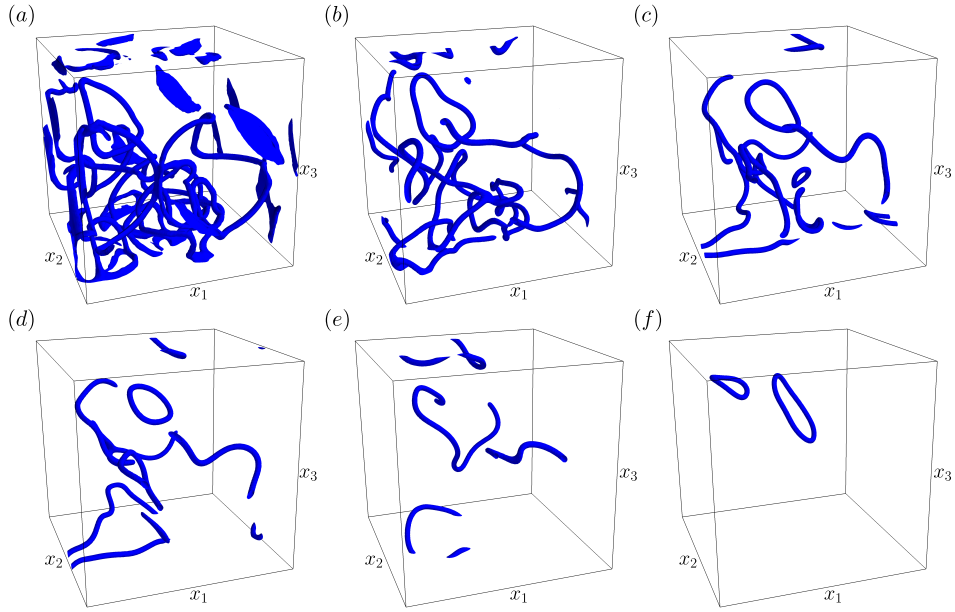
(i) Time evolution of the vortex tangle of ensemble $\mathcal{A}$, with initial condition given by 18 randomly distributed plane circular vortex rings. The snapshots are taken at times (a) $t = 5$, (b) $t = 40$, (c) $t = 100$, (d) $t = 130$, (e) $t = 200$ and (f) $t = 350$.
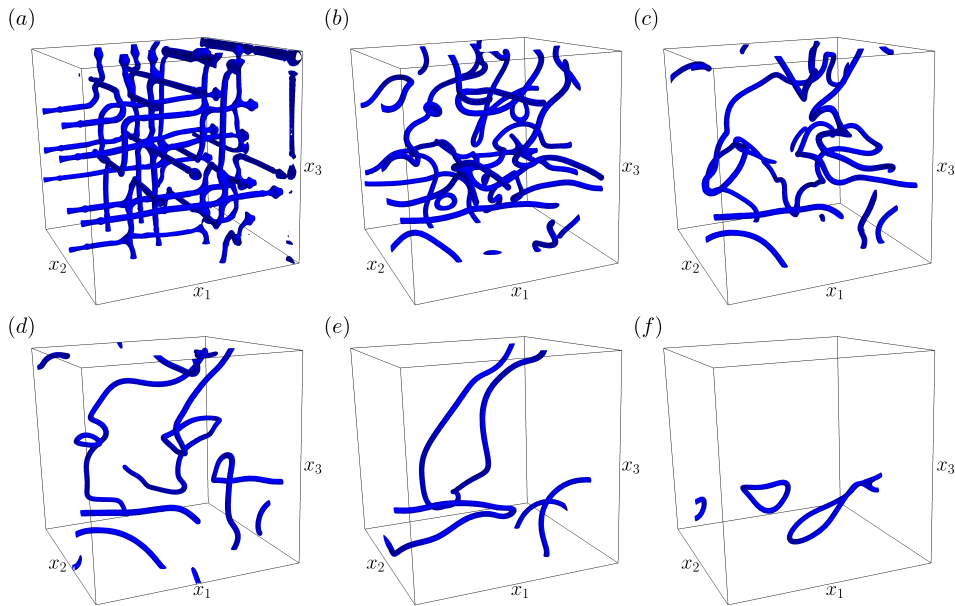
(ii) Time evolution of the vortex tangle of ensemble $\mathcal{B}$, with initial condition given by 24 randomly distributed straight vortex lines. The snapshots are taken at times (a) $t = 5$, (b) $t = 50$, (c) $t = 110$, (d) $t = 150$, (e) $t = 300$ and (f) $t = 450$.

Figure 13.1: Snapshots of isosurfaces of the superfluid-condensate density $n(\boldsymbol{x})$ (defining value $n/n_0 = 0.23$) showing the characteristic stages of the time evolution of vortex ensembles $\mathcal{A}$ (upper panel) and $\mathcal{B}$ (lower panel). For both configurations, the initial vortex tangle gradually decays due to reconnections of the vortex lines and vortex rings and the gradual shrinking and disappearing of vortex rings.

chapter, we plot isosurfaces of the superfluid-condensate density $n(t, \boldsymbol{x}) = |\psi(t, \boldsymbol{x})|^2$ with a defining value of $n/n_0 = 0.23$ to visualise the vortex defects (blue surfaces). With proceeding time, the vortices gradually reconnect and closed vortex structures shrink. As we have seen before in figure 12.15, the reconnections of vortex lines and vortex rings often induce the formation of larger structures, while simultaneously created smaller vortex rings rapidly shrink to zero size and disappear. We note that both, reconnections as well as the shrinking of vortex rings, result in the formation or rarefaction pulses which subsequently decay into sound excitations of the superfluid. While the isosurfaces in our figure cannot resolve these excitations, we have seen the creation of rarefaction and sound waves explicitly for the example of a shrinking and disappearing single vortex ring in figure 12.8. Let us also stress that the energy excess of the superfluid, which we initially inject into the system by imprinting the vortex defects, fully dissipates into the heat bath by modes falling into the black hole. We have discussed the dissipation mechanism in detail in the previous chapter and will again refer to it as we go along in the present section.

The basic principles for the motion of the vortex lines and vortex rings, discussed in chapter 12, hold for such vortex defects in large ensembles in the same way. Namely, the velocity of every individual vortex is induced by the flow fields of the respective other vortices as well as by its own self-induced velocity if it has segments of finite curvature. In addition, once the vortices are set into motion, they experience drag forces due to interactions between themselves and the fluid. This in turn leads to the emergence of Magnus forces, causing the vortices (or rather segments of vortices) to strongly attract or repel each other, depending on their orientation and relative topological charge (locally).

The respective snapshots in panels (*a*) of figures 13.1i and 13.1ii show the vortex configurations of ensembles $\mathcal{A}$ and $\mathcal{B}$ at time $t = 5$. At this time in the evolution, the defects have fully developed their characteristic density profile. Simultaneously, the vortex cores have already moved and some have deformed significantly as compared to their initial configuration. Many of them have even participated in reconnections. In particular, for vortex ensemble $\mathcal{A}$ in figure 13.1i, this implies that one can no longer discern the individual initial vortex rings. For the vortex lines of ensemble $\mathcal{B}$ in figure 13.1ii, on the other hand, an identification of the initial lines is still possible and the configuration at time $t = 5$ strongly resembles the initial configuration. The significant difference in the two ensembles during these early times is mainly due to the self-induced velocities of the rings which cause them to traverse the system much faster during these initial times, thus increasing the probability for reconnections. Compared to the initially straight vortex lines, the frequent reconnections of the vortex rings accelerate the system's departure from its initial condition. For the vortex lines of ensemble $\mathcal{B}$, it takes approximately $\Delta t = 20$ unit timesteps until most of the lines have reconnected at least once and the vortex tangle has significantly departed from its initial condition. Hence, in terms of this characteristic stage of the time evolution, the vortex gas of ensemble $\mathcal{B}$ slightly trails ensemble $\mathcal{A}$.

Notwithstanding this initial delay, for all later times the time evolutions of the vortex tangles emerging from both initial conditions bear strong resemblance. In

particular, upon studying only the time evolution of the vortex tangles, one can no longer trace back the initial vortex configurations, and on a macroscopic level the dynamics appears to be universal. In the following section 13.3 we will analyse the statistical properties of the system during its time evolution in order to gain insight into the superfluid dynamics also from a microscopic perspective. We will find that the system indeed enters a universal stage, characterised by scaling behaviour of a two-point correlation function and setting in at times only slightly later than one would naively expect from an analysis of the (macroscopic) time evolution of the vortex tangles.

With proceeding time, the vortex gases of both ensembles gradually dilute as more and more vortex rings shrink to zero size and disappear. With increasing diluteness, also the number of reconnections decreases, resulting in a slowing down of the evolution as compared to earlier times for denser vortex tangles. We illustrate the time evolution of the diluting vortex gases in panels (*b*) to (*e*) of figure 13.1. Eventually, at very late times, only one or very few (well separated) small vortex rings remain (*cf.* panels (*f*)) which subsequently also quickly shrink and disappear. Once the last vortex ring has disappeared, the remaining rarefaction pulses and sound modes are quickly damped out and the system equilibrates, reaching its static and homogeneous background solution n_0 everywhere. We note that except for panels (*a*), the snapshots of figure 13.1 in the respective panels (*b*)–(*f*) are taken at different times of the evolutions of vortex ensembles $\mathcal{A}$ and $\mathcal{B}$. To be specific, the times are chosen to ensure that for every panel, we show resembling vortex configurations of the two ensembles in terms of the density of the gas and, as we will find in the next section, scaling laws in the two-point function.

Studies of large vortex ensembles have also been performed for the two-dimensional holographic superfluid. In [148, 150, 168] the authors investigate the time evolution of large vortex ensembles in the two-dimensional system. In two spatial dimensions, the vortex gas dilutes due to the mutual annihilation of vortex–anti-vortex pairs. In particular, given the system has periodic boundary conditions, there is always an even number of vortices and anti-vortices and none of each family can vanish without annihilating another vortex of the respective other family. In [150] the authors show that at late times in the evolution, when few vortices are widely spread over the two-dimensional domain, this causes the superfluid vortex dynamics to 'critically slow down', meaning that all length scales in the system decay only algebraically [426]. In [150] the phenomenon of critical-slowing-down dynamics is interpreted as the approach to a non-thermal fixed point [427–429]. The same has also been observed for vortex ensembles in two-dimensional dilute Bose gases described within the Gross–Pitaevskii framework [233–235]. Likewise, also for ensembles of vortex lines and vortex rings in three spatial dimensions described by the (non-dissipative) GPE, the approach to a non-thermal fixed has been observed[1] [233, 234, 388].

---

[1]In recent years, non-thermal fixed points have also been found in various other physical system, including one-dimensional Bose gases [430] and spinor gases [431]. Remarkably, for a one-dimensional Bose gas, the approach to a non-thermal fixed point has even found experimentally [34]. See also [432] for a pedagogical review article.

In our simulations of the vortex dynamics in the three-dimensional holographic superfluid, we cannot find evidence suggesting that the system approaches a non-thermal fixed point. Moreover, based on our discussion of the time evolution of the two vortex ensembles $\mathcal{A}$ and $\mathcal{B}$ above, it appears likely that in these systems a non-thermal fixed point can, in fact, not be found. This does not imply, however, that a non-thermal fixed point of the holographic superfluid does not exist. It only appears likely that it cannot be found employing the vortex dynamics studied in this chapter. Indeed, while we do find the vortex dynamics to slow down, we have also noted that there are always vortex rings present which shrink quickly and eventually disappear. The fact that in three-dimensional systems single vortex excitations can disappear without interacting with another vortex is the crucial difference to the two-dimensional system in which it always takes two vortices, *i. e.*, one vortex and one anti-vortex, to annihilate and thus disappear. Therefore, even if all vortex defects in the three-dimensional system are far apart and only very few remain, which would be the three-dimensional equivalent of the two-dimensional configuration for which the approach to a non-thermal fixed point has been observed in [150], the dynamics does not slow down critically. In particular, spurred by the strong dissipation, the shrinking processes of single vortex rings advance very quickly in the holographic superfluid and therefore prohibits a critical slowing down of the dynamics. In non-dissipative three-dimensional systems as studied in the GP model in [233–235], by contrast, the approach to non-thermal fixed points has been observed. In these systems, single vortex rings also shrink and eventually disappear due to interactions with rarefaction pulses and sound waves. However, unlike in the holographic system, the dynamics proceeds much slower than the rate of change of other length scales present in the system, like for instance the coherence length or the length scale characterising the separations between the defects. For completeness, we point out that in three spatial dimensions, defining a characteristic length scale for the mean-vortex spacings is rather intricate and we therefore refrain from diving into a more detailed discussion. Instead, we refer the interested reader to, *e. g.*, [388].

One may speculate if an increase in grid sizes from 128^3 grid points as before to, of the order of, 504^3 grid points or even larger, would enable us to find the superfluid to approach a non-thermal fixed point. For the simulations of the two-dimensional system in [150], grids of size 504^2 were used. In three spatial dimensions, grid size of the order of 504 points per coordinate direction would certainly allow for the dynamical creation of very large vortex-ring structures which live for much longer than the smaller rings in our simulations before they eventually shrink to zero size and disappear. In addition, several large vortex rings could persist at the same time, even without frequently reconnecting with each other. Since large vortex rings traverse the superfluid much slower than small rings, *cf.* our discussions in chapter 12, the system may indeed, for a short period of time, approach a non-thermal fixed point. However, it appears likely that if such a fixed point is approached at all, the system quickly departs from it again since the large dissipation causes the vortex rings to rapidly shrink and thus pick up large velocities.

A configuration for which we certainly expect to find a non-thermal fixed point is

given by an ensemble of parallel straight vortex lines along only one direction of the grid. Due to the translational symmetry of such a configuration, we expect the vortex dynamics to strongly resemble the dynamics of vortices in the two-dimensional superfluid in [150]. This implies in particular very similar vortex statistics which would imply the approach to a non-thermal fixed point. However, here too, distinctly larger grid sizes are required for concrete computations to corroborate our expectations.

To gain a deeper understanding of the dynamics of vortex ensembles in the holographic superfluid, it is interesting to study not only the superfluid-field configuration itself like we have thus far, but also its dual bulk representation. Here, we want to focus in particular on the bulk scalar charge density $\sqrt{-g}|\mathcal{J}^0|$ which encodes the behaviour of both, the scalar field Φ and the gauge field A_M. It is therefore particularly sensitive not only to vortical excitations of the superfluid, but also to rarefaction pulses and sound waves as we have seen in the previous part of this thesis on the two-dimensional superfluid in chapter 7 (*cf.* figure 7.6). We restrict the following discussion to bulk views corresponding to the superfluid-field configuration of vortex ensemble $\mathcal{A}$. Since the time evolutions of ensembles $\mathcal{A}$ and $\mathcal{B}$ are in strong resemblance, all results presented in the following hold similarly for the dynamics of vortex ensemble $\mathcal{B}$, as we have checked explicitly. In the panels on the left-hand side of figure 13.2, we display snapshots of the bulk-field configuration outgoing from fixed-x_3 slices of the three-dimensional superfluid at two times characteristic for the evolution. The bulk view in figure 13.2i corresponds to an early time $t = 40$ dual to a rather dense vortex gas, and the bulk view in figure 13.2ii to an intermediate time $t = 130$ dual to a strongly diluted vortex gas. The time of the early snapshot lies within the universal regime of the vortex dynamics of the two ensembles $\mathcal{A}$ and $\mathcal{B}$. For the same times, we also show snapshots of isosurfaces of the superfluid-density configuration $n(t, \boldsymbol{x}) = |\psi(t, \boldsymbol{x})|^2$ in the respective right-hand panels of figure 13.2. In these plots, the transparent red planes indicate the position of the $z = 0$ slices of the left-hand panels in the three-dimensional superfluid. Note that the x_3-positions of the two-dimensional slice are not the same for the two times. To illustrate the bulk-field configurations, we again plot isosurfaces of the scalar charge density $\sqrt{-g}|\mathcal{J}^0|$ (orange isosurfaces, defining value 16), on the entire two-dimensional field-theory domain. Comparing the characteristics of the charge density at the two times is our primary goal for the remainder of this section. Nevertheless, for completeness, we also plot isosurfaces of the scalar field $|\Phi|^2/z^6$ (blue surfaces, defining value 1.88). However, in order to not impede the view on the charge density, we restrict these isosurfaces to only half of the two-dimensional domain, for $x_1 < 64$. As we have mentioned before, the field $|\Phi|^2/z^6$ reduces to the condensate density $n(\boldsymbol{x})$ in the limit $z \to 0$. We plot $n(\boldsymbol{x})$ on the $z = 0$ slice with the same colour map as we have used in previous analogous figures. The grey area at $z = z_{\mathrm{h}}$, plotted on the entire two-dimensional domain, again depicts the black-hole horizon. Before we discuss the charge density, we note that the blue isosurfaces, which are again associated with dual vortex excitations, do not fully reach to the boundary if the corresponding two-dimensional slice does not precisely intersect a vortex defect but instead
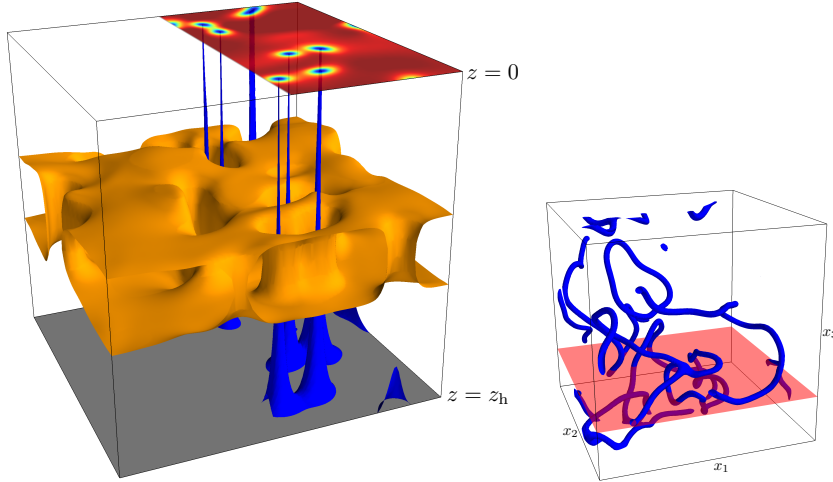
(i) Bulk view of the scalar charge density at an early time of the evolution, $t = 40$. The notches result from rarefaction and sound wave excitations of the superfluid.
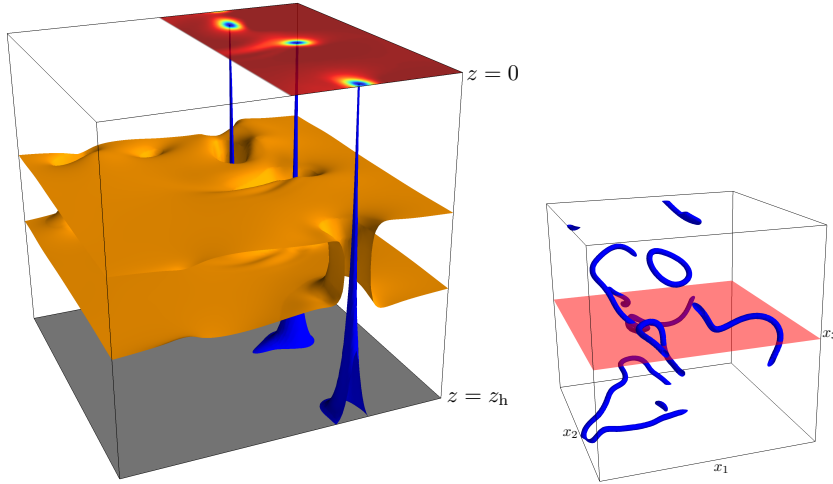
(ii) Bulk view of the scalar charge density at a late time of the evolution, $t = 130$. At this time, the charge density is rather smooth.

Figure 13.2: Left panels: Snapshots of isosurfaces of the bulk scalar charge density $\sqrt{-g}|\mathcal{J}^0|$ (orange layers, defining value 16) at times $t = 40$ (upper panel) and $t = 130$ (upper panel) outgoing from two-dimensional slices (fixed-x_3 slices) of the boundary superfluid, for vortex ensemble $\mathcal{A}$. For $x_1 < 64$, we also plot isosurfaces of the scalar field $|\Phi(\boldsymbol{x}, z)|^2/z^6$ (blue surfaces, defining value 1.88) and the superfluid density $n(\boldsymbol{x}) = |\psi(\boldsymbol{x})|^2$ on the boundary slice. For details see the main text. Note that the domain is periodic in $\boldsymbol{x}$. Right panel: Snapshots of isosurfaces of the superfluid-condensate density $n(\boldsymbol{x})$ (defining value $n/n_0 = 0.23$) at the same times. The transparent red planes indicate the two-dimensional boundary slices of the left panels (rotated by 180° around the x_3-axis).

231

only comes close to it. Close to a vortex core, the superfluid-condensate density at the boundary declines but is still above zero (see *e. g.* figure 12.4). The same holds true for the scalar field Φ in the bulk which is non-zero at this position along the holographic z-direction. Consequently, it may happen that on a fixed-z slice close to the boundary, where the tubes dual to vortices become narrower, the defining value for the isosurfaces of $|\Phi|^2/z^6$ is smaller than the minimal value taken by the field $|\Phi|^2/z^6$ on that slice, implying that the tubes do not fully reach up to that slice and thus the boundary at $z = 0$.

The upper panel of figure 13.2 illustrates that during the early times of the evolution of the vortex ensembles, the scalar charge density is strongly riddled by holes and additionally perturbed by many notches and smaller ripples. The holes are again caused by vortex excitations in the dual superfluid. The notches and ripples, on the other hand, stem from dual rarefaction pulses and sound excitations, respectively. At intermediate to late times, by contrast, the lower panel of figure 13.2 illustrates that these ripples and notches have mostly disappeared and the charge density has smoothed out. Mainly holes corresponding to the vortex defects remain. The same holds true not only for the specific bulk view we display in figure 13.2ii but also for bulk views outgoing from all other two-dimensional slices of the three-dimensional superfluid at intermediate to late times of the evolution. The number of rarefaction pulses and sound excitations has significantly decreased since they are produced predominantly in the rarely occurring reconnections of two vortex lines or rings, or the disappearing of single vortex rings. Nonetheless, in the aftermath of such events, they are also discernible in the charge density, just as at early times. Hence, while at early times short-wavelengths rarefaction pulses and sound waves are very prominent, at intermediate and late times their number has significantly decreased and they are produced only occasionally.

For a final comment of this section, let us specifically focus on the holes in the charge density in figure 13.2i. Evidently, these holes have various sizes as well as shapes, induced by the vortex defects of different shapes in the superfluid and the respective two-dimensional slices thereof. The different-sized holes illustrate once again that in the three-dimensional superfluid it appears likely that not only UV modes but also modes of larger wavelengths can dissipate their energy into the heat bath by falling into the black hole. For the two-dimensional superfluid, *cf.* [150], by contrast, one finds that even in the presence of large vortex ensembles, only small-wavelength modes can dissipate their energy into the black hole because every vortex only pierces a narrow hole through the charge density.

13.3 Observation of Turbulent Behaviour

In the previous chapter we have qualitatively studied the non-equilibrium dynamics of the holographic superfluid induced by the two vortex ensembles $\mathcal{A}$ (random rings) and $\mathcal{B}$ (random lines). We have focused in particular on the time evolution of the vortex gas for both initial configurations as well as its dual bulk representation. We

have found the system to enter a universal stage (on a macroscopic level) once the vortex reconnections and the shrinking of vortex rings have driven the vortex tangle away from its initial configuration. We have identified the universal stage for times $t \gtrsim 20$ and found it to persist until the last vortex ring has disappeared. In this section we dive into a more quantitative analysis of the vortex dynamics. We study correlation functions of the field-theory scalar operator Ψ, whose vacuum expectation value gives the superfluid order-parameter field ψ. This allows us to gain insight not only into the macroscopic dynamics studied in the previous section but also into the microscopic physics of the system. We analyse the correlation functions with regard to algebraic decay which signals the presence of turbulent behaviour of the superfluid. Furthermore, we study if the universal aspects of the superfluid dynamics found in the previous section are also reflected in the microscopic observables.

We are primarily interested in the equal-time two-point correlation function, $\langle \Psi^*(t, \boldsymbol{x}) \Psi(t, \boldsymbol{y}) \rangle$, where $\boldsymbol{x}$ and $\boldsymbol{y}$ are positions of the three-dimensional superfluid. On average, the system we study is translationally invariant which allows us to evaluate the correlation function in momentum space by means of the relative coordinate $\boldsymbol{r} = \boldsymbol{x} - \boldsymbol{y}$. Furthermore, due to the isotropy of the holographic system, we can average over the angular distribution. The corresponding correlation function is then given by[2]

$$ n(t, k) = \int \frac{\mathrm{d}\Omega_k}{4\pi} \langle \Psi^*(t, \boldsymbol{k}) \Psi(t, \boldsymbol{k}) \rangle \tag{13.1} $$

and depends only on the modulus of the radial momentum $\boldsymbol{k}$ (related to $\boldsymbol{r}$ via Fourier transform), $k = |\boldsymbol{k}|$. Here, $\mathrm{d}\Omega_k$ integrates over a two-sphere of surface area 4π. Henceforth, we denote $n(t, k)$ by what it physically represents, namely the radial occupation number spectrum. Likewise, we define the radial kinetic energy spectrum

$$ E(t, k) = \int \frac{\mathrm{d}\Omega_k \, k^2}{4\pi} |\boldsymbol{k}|^2 \langle \Psi^*(t, \boldsymbol{k}) \Psi(t, \boldsymbol{k}) \rangle \,, \tag{13.2} $$

which can also be directly inferred from the radial occupation number spectrum, $E(t, k) = k^4 n(t, k)$.

In the following we investigate the superfluid dynamics of vortex ensembles $\mathcal{A}$ and $\mathcal{B}$ with regard to scaling behaviour in the radial occupation number spectrum. To be specific, we analyse whether certain (infrared) momentum regimes in k exist for which the occupation number becomes (quasi-)stationary in time,

$$ \dot{n}(t, k) = 0 \,, \tag{13.3} $$

---

[2]We point out that in the analysis presented below we approximate the two-point function $\langle \Psi^*(t, \boldsymbol{k}) \Psi(t, \boldsymbol{k}) \rangle$ by the square of the vacuum expectation value of the scalar operator Ψ. Hence, we use $n(t, k) = \int \frac{\mathrm{d}\Omega_k}{4\pi} \langle \Psi(t, \boldsymbol{k}) \rangle \langle \Psi(t, \boldsymbol{k}) \rangle$ to define the angle-averaged momentum-space correlation function, and a similar procedure is used for the kinetic energy spectrum. Since we are interested only in the infrared physics of the superfluid, we expect this to be a reasonable approximation as quantum fluctuations are presumably negligible compared to the vacuum expectation value $\langle \Psi \rangle$.

where the dot denotes a derivative with respect to time, and additionally exhibits a power-law behaviour in momentum space, *i. e.*, a scaling within such an inertial momentum interval according to

$$n(t, \alpha k) = \alpha^{-\zeta} n(t, k), \tag{13.4}$$

where α is an arbitrary positive number and ζ is a scaling exponent. With this procedure we closely follow previous works on turbulence in the two-dimensional holographic superfluid [148, 150] as well as work on dilute Bose gases in two and three spatial dimensions (see *e. g.* [233, 234, 388]). We determine the scaling exponent ζ by fitting a power law according to

$$n(k) = A k^{-\zeta} \tag{13.5}$$

to the radial occupation number spectrum within a certain momentum regime, where A is an additional fitting constant. To determine the momentum interval, we first estimate an upper and lower cutoff by eye and subsequently use our fitting routine for the fine-tuning. The uncertainty stemming from this procedure yields the dominating contribution to the uncertainty of the scaling exponent. For all scaling exponents quoted in this section, the uncertainty is given by $\Delta \zeta = \pm 0.2$. This value exceeds in particular the uncertainty on ζ quoted by the fitting routine itself. We give further details on our fitting procedure as well as the error estimate in appendix A.3.

We find that for both vortex ensembles, $\mathcal{A}$ and $\mathcal{B}$, the superfluid dynamics can be split into four regimes with respect to the time evolution of the radial occupation number spectrum. Remarkably, in three of these regimes we find universal behaviour of the spectrum. The first regime is given by the early times of the evolution, corresponding to the departure of the vortex tangle from its initial configuration. At these times, the spectrum is strongly dependent on the initial vortex configuration and does not exhibit scaling behaviour. Turbulent behaviour of the superfluid is therefore precluded in this regime. At later times, on the other hand, we identify two consecutive universal scaling regimes in (momentum) space and time. For both regimes, equations (13.3) and (13.4) are simultaneously satisfied which is a strong indication that the system has entered a turbulent state. In addition, the extracted scaling exponents and inertial momentum intervals (within the uncertainty) agree for ensembles $\mathcal{A}$ and $\mathcal{B}$. The first regime corresponds to a dense and the second to a strongly diluted vortex gas. Finally, at very late times of the evolution, when only one or very few well-separated vortex rings remain, we identify another universal regime. However, while the spectra for both vortex ensembles agree at these very late times, they do not exhibit scaling behaviour in the above sense. In the following we elaborate on the behaviour of the radial occupation number spectra in each of the universal regimes. For conciseness, we restrict this discussion to spectra corresponding to vortex ensemble $\mathcal{A}$. In order to account for the difference between ensembles $\mathcal{A}$ and $\mathcal{B}$ in the details of the characteristic times at which the regimes are entered an exited, we refer to system $\mathcal{B}$ when necessary. In addition, we show the spectra corresponding to ensemble $\mathcal{B}$ in appendix C.1.

We identify the first universal regime for times $t \gtrsim 40$ ($t \gtrsim 50$ for $\mathcal{B}$) and find it to persist for approximately $\Delta t = 60$ ($\Delta t = 50$ for $\mathcal{B}$) unit timesteps before the spectra deviate and transition into the second scaling regime. We point out that the onset of the first universal scaling regime occurs a short time after the vortex tangles studied in the previous section appear to enter a universal stage at time $t \approx 20$.

During the first regime, the radial occupation number spectrum exhibits a scaling behaviour with an exponent of $\zeta = 5.7$ and the corresponding inertial momentum range is given by $0.34 \leq k \leq 1.43$ (in units of $z_{\mathrm{h}} = 1$). For four exemplary times of this regime, we illustrate the spectrum in the upper panel of figure 13.3. Within the inertial momentum range, the spectra agree to high accuracy, checking off the (quasi-)stationarity condition in equation (13.3). In addition, the spectra are in excellent agreement with the power-law behaviour $n(k) \sim k^{-5.7}$, indicated by the solid black line. Note that the line is deliberately shifted slightly above the corresponding curves to aid the visualisation. We have displayed snapshots of the vortex configurations at the onset and exit times of the scaling regime in panels (b), for $t = 40$, and (c), for $t = 100$, of figure 13.1i in the previous section. From these plots we infer that the exemplary spectra depicted in the upper panel of figure 13.3 and thus the first scaling regime correspond to and are characterised by a rather dense vortex gas with frequently reconnecting defects and rapidly shrinking and disappearing vortex rings. Moreover, due to the frequent reconnections and the shrinking and disappearing rings, the system is also highly excited by a large number of rarefaction pulses and sound waves which we infer from our studies of the dual bulk view of the superfluid configuration at time $t = 40$ in figure 13.2i where we have found the charge density $\sqrt{-g}|\mathcal{J}^0|$ to be strongly perturbed by notches and ripples. In fact, upon closer inspection we find that the gas remains rather dense and perturbed by sound waves and rarefaction pulses throughout the first scaling regime.

For classical turbulence in incompressible fluids, Kolmogorov famously predicted a gradual transfer of energy from small to large momentum scales, bounded by an inertial range. If the system is supplied with energy at large length scales, *i.e.*, small momenta k, the energy gradually cascades to smaller length scales, *i.e.*, large momenta, until it is eventually dissipated into the heat bath due to the viscosity of the fluid. Kolmogorov found this cascade to obey the universal scaling behaviour $E(k) \sim k^{-5/3}$ [433–435].

We find that the scaling behaviour of the radial occupation number spectrum in the first universal regime of the vortex dynamics in the three-dimensional holographic superfluid is consistent with Kolmogorov scaling. Our finding of $n(k) \sim k^{-5.7}$ translates into $E(k) = k^4 n(k) \sim k^{-1.7}$ for the kinetic energy spectrum. Hence, within the uncertainty of the scaling exponent given by $\Delta \zeta = \pm 0.2$, the scaling of the kinetic energy spectrum of the holographic superfluid is consistent with Kolmogorov scaling. Let us stress, however, that the Kolmogorov-like scaling persists only within the first scaling regime and thus only in a transient time interval of the entire evolution. For times $t \gtrsim 100$ for both vortex ensembles, $\mathcal{A}$ and $\mathcal{B}$, the spectra no longer exhibit Kolmogorov-like scaling.

In the literature there is much debate regarding the observation of actual Kol-
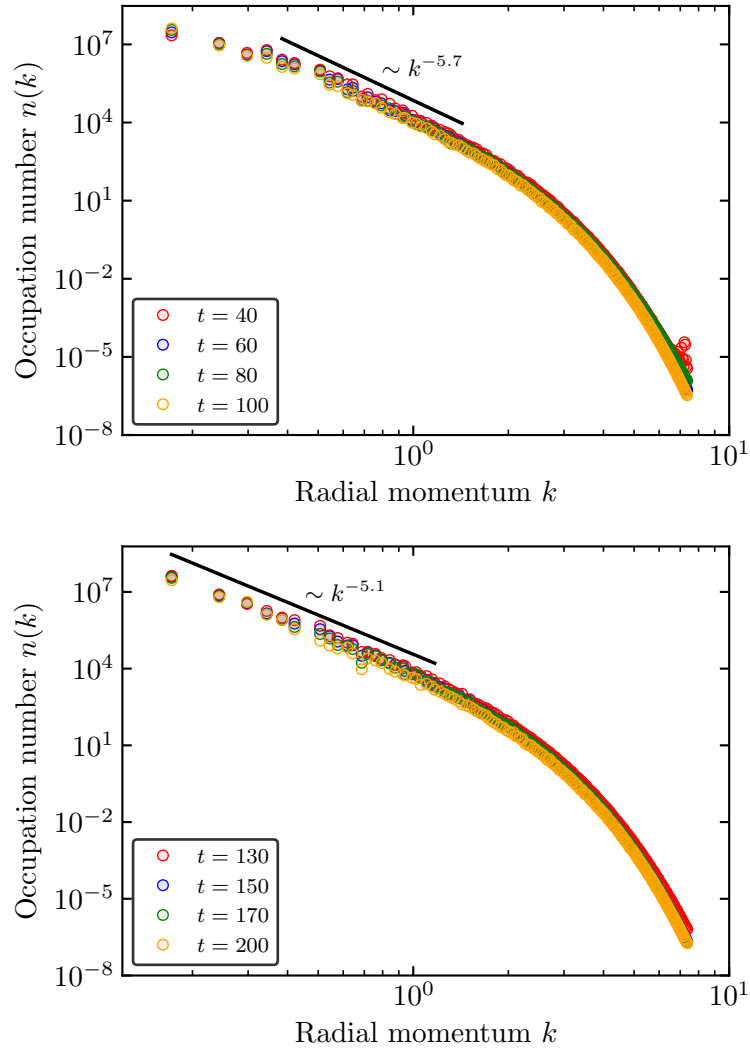
Figure 13.3: Occupation number spectrum $n(k)$ as a function of the radial momentum k at four characteristic times during the first (upper panel) and second (lower panel) universal regime, on a double-logarithmic scale. We show the evolution of the spectrum for system $\mathcal{A}$ (random rings). For system $\mathcal{B}$ (random lines) we find similar behaviour with the same scaling laws (within the error of $\Delta\zeta = \pm 0.2$). The solid black lines depict the fitted power laws in the respective inertial momentum ranges (deliberately shifted above the spectra to aid the visualisation).

mogorov scaling in superfluid turbulence, mainly with regard to simulations of far-from-equilibrium dynamics of Bose gases within the Gross–Pitaevskii model. The interest increased in particular after the scaling behaviour according to Kolmogorov's prediction was measured in superfluid helium [44, 45]. However, despite the observation of a scaling of $E(k) \sim k^{-5/3}$ in the incompressible component of the condensate in GPE simulations of two- as well as three-dimensional systems [234, 436–439], there are still many open questions to be addressed, mainly with regard to the nature of the energy cascade [261]. In this work, we therefore refer to the observed scaling of the holographic superfluid dynamics as Kolmogorov-like scaling and leave open the question whether or not it corresponds to the superfluid-analogue of turbulent transport as envisioned by Kolmogorov. It would be interesting to follow up on this question and study the transfer of energy directly. However, taking into account the recent developments in the study of turbulence in the GP model, it appears likely that such an undertaking would require distinctly larger computational domains along the three spatial field-theory directions (see *e. g.* [440–442]). For now, this appears out of reach for simulations of the holographic superfluid.

After the transient Kolmogorov-like scaling regime, we find that for times $t \gtrsim 130$ ($t \gtrsim 150$ for $\mathcal{B}$), the superfluid dynamics enters a new universal scaling regime. In this regime, the inertial momentum range $0.23 \leq k \leq 1.12$ has shifted deeper into the infrared and the new scaling exponent is given by $\zeta = 5.1$. This scaling persists until at very late times in the evolution only one or very few well-separated vortex rings remain, at times $t \gtrsim 200$ and $t \gtrsim 300$ for ensembles $\mathcal{A}$ and $\mathcal{B}$, respectively. In the lower panel of figure 13.3 we show the spectrum for four exemplary times of the second scaling regime. In addition, the solid black line indicates the power-law behaviour $n(k) \sim k^{-5.1}$ in the corresponding momentum range (deliberately shifted above the curves). The spectra are again stationary within the inertial momentum range in the deep infrared. In addition, we find them to be in excellent agreement with the indicated power law. We note that the lower boundary of the inertial momentum range agrees with the smallest momentum mode of the underlying system. For momenta exceeding the upper boundary of the interval, the spectrum falls off more steeply than with the observed scaling of $n(k) \sim k^{-5.1}$. We have displayed snapshots of the vortex-gas configurations corresponding to the onset and exit times of the scaling regime in panels (d), for $t = 130$, and (e), for $t = 200$, of figure 13.1i in the previous section. At the onset of the scaling regime, the number of vortex excitations has distinctly decreased and likewise has the number of reconnections and disappearing vortex rings. With proceeding time, the vortex gas dilutes even further. However, throughout the time interval of the scaling regime, we still observe vortices reconnecting and forming larger vortex structures. In figure 13.2ii of the previous section we have shown aspects of the bulk view of the superfluid at the onset of this interval, *i. e.* at time $t = 130$. We have checked explicitly that qualitatively, the bulk configuration looks similar for all times during the scaling regime. A comparison with figure 13.2i, at time $t = 40$, illustrates nicely how the differences in the scaling behaviour of the occupation number spectra in this regime and the prior Kolmogorov-like scaling regime reflect in the macroscopic physics of the field

configuration (in particular the charge density) in the bulk.

In two spatial dimensions the statistics of single vortices as well as vortex ensembles, in terms of scaling laws in the radial occupation number spectrum, can be derived within the Onsager point-vortex model[3] [259]. For vortex rings and vortex lines in the point-vortex limit, *i. e.*, $\xi \to 0$, similar formulations exist for three-dimensional superfluids [42, 443–446]. Employing these models, one finds the radial occupation number spectrum for a single plane circular vortex ring to scale according to $n(k) \sim k^{-5.0}$ for momenta larger than the corresponding length scale set by the radius of the ring [234]. The same holds true for single elliptical vortex rings as well as single pairs of straight vortex lines. Likewise, the same scaling behaviour also persists for ensembles of independent vortex excitations for an inertial momentum range bounded below by the momentum corresponding to the mean-vortex separation [234]. As we have noted above, defining the latter length scale is rather intricate, see for instance [388] for a more thorough discussion. Hence, we find the dynamics of a dilute vortex gas in the three-dimensional holographic superfluid during the second scaling regime to resemble the dynamics of independent (point-like) vortex excitations. Indeed, our extracted scaling exponent of $\zeta = 5.1$ agrees within one standard deviation with the predicted exponent of $\zeta = 5.0$. Similar results regarding the scaling behaviour of $n(k)$ of three-dimensional vortex ensembles have been found within the GP model in [233, 234, 388].

Let us note that throughout the system's time evolution, beginning at time $t = 0$, the disappearing of vortex rings is clearly discernible in the spectrum by an increase of the UV modes. This is expected due to the gradually decreasing length scale of the ring.

Once the vortex reconnections cease and the remaining one or few vortex rings have shrunk significantly, the spectrum deviates from the $n(k) \sim k^{-5.1}$ scaling behaviour and enters a third universal regime. At all later times, the spectrum gradually flattens as the rings traverse the superfluid and undergo rapid shrinking. Crucially, this type of characteristic behaviour of the spectrum occurs only if the distance between the vortices is such that they do not come into contact and reconnect. In figure 13.4 we show the spectrum for four exemplary times during the shrinking process of the separated vortex rings, again for vortex ensemble $\mathcal{A}$. For vortex ensemble $\mathcal{B}$ the qualitative behaviour of the spectrum coincides with the one displayed in figure 13.4. As the curves in figure 13.4 indicate, the spectrum is not (quasi-)stationary but changes continuously during the considered time interval, *i. e.*, condition (13.3) is not satisfied. Neither does it, on a fixed timeslice, exhibit a distinct scaling behaviour according to equation (13.4). Nevertheless, we plot the scaling law $n(k) \sim k^{-5.1}$ of the prior scaling regime (solid red line) in order to indicate the deviation of the spectrum from this behaviour. Shortly before the final ring has shrunk to zero size, the spectrum has significantly flattened. In order to quantify

---

[3]The Onsager point vortex model [259] interprets vortices as classical (point-like) objects and employs statistical mechanics to describe their motion. Applied to large vortex ensembles, it turns out to capture crucial aspects of superfluid turbulence.
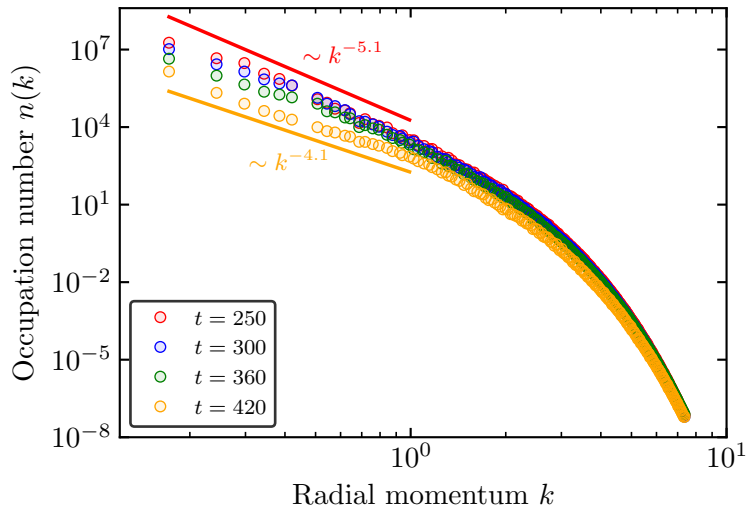
Figure 13.4: Occupation number spectrum $n(k)$ as a function of the radial momentum k at four characteristic times during the third universal regime, on a double-logarithmic scale. We again show the spectra corresponding to the time evolution of system $\mathcal{A}$ (random rings) which qualitatively agree with those of system $\mathcal{B}$ (random lines). The spectrum gradually flattens with proceeding time. The coloured lines depict power laws to indicate the deviation from the scaling behaviour in the prior scaling regime (solid red line) as well as the approximate power law shortly before the final ring in the system's evolution has disappeared (solid orange line).

how much the spectrum has flattened over time, we plot the power law $n(k) \sim k^{-4.1}$ (solid orange line) below the spectrum at time $t = 420$. We stress that we do this only to aid the visualisation. In particular, the spectrum does not exhibit such a scaling behaviour. Upon closer inspection, one finds that the characteristic flattening of the spectrum in an infrared momentum range from a scaling behaviour with an exponent of $\zeta \approx 5.1$ to a spectrum that does no longer exhibit scaling behaviour but is loosely approximated by $n(k) \sim k^{-4.1}$, is similar to the analogous behaviour of the radial occupation number spectrum for the dynamics of a single vortex ring. For further details, we refer the interested reader to appendix C.2 where we present an analysis of the radial occupation number spectrum of a single vortex ring.

The late-time behaviour of the radial occupation number spectrum we observe in our simulations deviates from observations made in the GP model for the dynamics of vortex ensembles. In such simulations, the scaling of $n(k) \sim k^{-5.0}$ persists until the final ring has disappeared by shrinking to zero size. The difference may be rooted in the strong dissipation of the holographic superfluid as compared to the non-dissipative GPE. The dissipation causes the vortex ring in the holographic system

to shrink much more rapidly which may cause a change in the occupation number spectrum. Referring back to our discussion in section 12.2, we point out that, as part of a matching of the DGPE and the holographic dynamics of vortex rings, it would also be very interesting to study explicitly how the spectra depend on the DGPE damping parameter.

To conclude this chapter, let us add two more comments. First, we note that the universal behaviour of the vortex dynamics found in the present and the previous section is indeed universal in a much broader sense than just with regard to the two initial vortex ensembles studied in this work. We have checked explicitly that the results presented above are independent of the number of initial vortex lines and vortex rings as long as the numbers are large enough to create a dense vortex gas but not too large in order to avoid the occurrence of clustering effects which would spoil the observed scaling behaviour. Likewise, the dynamics is also independent of the initial shape and alignment of the vortex defects, including in particular mixtures of the types of initial conditions of vortex ensembles $\mathcal{A}$ and $\mathcal{B}$. Our second comment concerns a comparison of the superfluid dynamics in the three-dimensional holographic system to previous work on analogous simulations of the two-dimensional system in [150]. The authors of [150] show that for large initial vortex ensembles in the two-dimensional superfluid there also exists a transient regime during which the radial occupation number spectrum exhibits a Kolmogorov-like scaling behaviour. However, unlike in three spatial dimensions, the occurrence of the Kolmogorov-like scaling regime depends on the initial vortex configuration [150]. In the late-time regime, on the other hand, the dynamics is universal and follows scaling laws according to $n(k) \sim k^{-\zeta}$ with exponents $4.1 \lesssim \zeta \lesssim 4.2$. Such a scaling behaviour is the analogous result to the $n(k) \sim k^{-5.1}$ scaling we observe for the three-dimensional system in the sense that it agrees with the power law of a single topological vortex defect or a number of independent vortex defects.

14 Interactions of Vortex Rings

So far in the second part of this work on the three-dimensional holographic super-fluid, we have constructed and analysed vortex solutions, studied the dynamics of single vortex rings and investigated the far-from-equilibrium dynamics of the system induced by large ensembles of vortex defects. We have found convincing evidence suggesting that the holographic superfluid is strongly dissipative and captures the physics of a non-relativistic condensate. Furthermore, we have shown that in the presence of many-vortex configurations, the system bears signatures of turbulent behaviour in the transport of energy. However, except for our qualitative discussion of vortex reconnections in section 12.3, we have thus far not investigated the various types of interactions between the vortex defects. Moreover, we have not yet commented on excitations of vortex lines and rings which, in the context of the GP model, have been shown to play a crucial role in the transport of energy and, therefore, turbulent behaviour. In this chapter, we want to make up leeway and study a number of fundamental and non-trivial interactions of vortex rings[1] as well as so-called Kelvin excitations of vortex defects in the holographic superfluid.

We begin our investigations in section 14.1 by studying the leapfrogging motion of two axisymmetric vortex rings of the same winding number. In the same section, we also investigate the behaviour of two head-on colliding rings. In the final subsection of section 14.1, we study vortex rings of higher winding numbers and investigate their solutions and dynamics. We show explicitly that they are unstable against decay into elementary vortex rings which subsequently perform leapfrogging motions. In section 14.2, we dive into a thorough investigation of off-centre colliding vortex rings. In particular, we analyse how the scattering angle of the vortex rings depends on the impact parameter of the collision. Finally, in section 14.3, we qualitatively study Kelvin-wave excitations of vortex rings and comment on their importance with regard to the turbulent behaviour found in the previous chapter.

Throughout this chapter, we study the vortex dynamics of the holographic super-fluid for a chemical potential of $\mu = 5$, which agrees with our choices in the previous chapters. Nevertheless, we note that the qualitative behaviour of the vortex rings is independent of this choice. For all simulations we employ grid sizes of 96^3 points along the (x_1, x_2, x_3)-directions.

---

[1]Remarkably, most phenomena of quantised vortex rings in the holographic superfluid that we study in this chapter can be observed for classical vortex rings as well. It is interesting to note that, with minimal effort, many of them can even be studied at home with vortex rings in water or smoke. For videos demonstrating properties of vortex rings as well as on how to produce vortex rings, see, *e. g.*, [447–450].

14.1 Leapfrogging and Head-On Colliding Vortex Rings

Let us now study the leapfrogging motion as well as the head-on collision of two axisymmetric vortex rings in the holographic superfluid. The qualitative behaviour of the vortex rings for these types of interactions was first predicted more than 150 years ago by H. von Helmholtz in 1858 for vortex rings in classical liquids [284].

14.1.1 Leapfrogging Vortex Rings

> " [...] *zwei ringförmige Wirbelfäden, deren Axe dieselbe ist* [...]. *Haben sie gleiche Rotationsrichtung, so schreiten sie beide in gleichem Sinne fort, und es wird der vorangehende sich erweitern, dann langsamer fortschreiten, der nachfolgende sich verengern und schneller fortschreiten, schließlich bei nicht zu differenten Fortpflanzungsgeschwindigkeiten den andern einholen, durch ihn hindurchgehen. Dann wird sich dasselbe Spiel mit dem andern wiederholen, so daß die Ringe abwechselnd einer durch den andern hindurchgehen.*"
>
> – Hermann von Helmholtz, 1858 [284]

In these concluding remarks[2] of his seminal work [284] on vorticity in classical liquids, Helmholtz first qualitatively describes the leapfrogging motion of two vortex rings. Adapted to the scenario of quantised vortices, his description can also be reformulated as follows. Consider two axisymmetric vortex rings of the same topological charge, *i. e.*, $w_1 = w_2$, moving along the same direction with a finite initial axial separation. As we have outlined before, each vortex ring moves due to its own self-induced velocity as well as the phase configuration of the respective other ring. In particular, the phase configuration of the rear ring causes the radius of the front ring to increase and therefore its velocity to decrease. Simultaneously, the phase structure of the front ring causes the radius of the rear ring to decrease and thus its velocity to increase. Given that the vortices are initially not too far apart and their velocities are not too different, the rear ring catches up and eventually slips through the front ring. Subsequently, the rings reverse roles and repeat the leapfrogging. Under ideal conditions and if the fluid is non-dissipative, this process continuous perpetually.

While Helmholtz was the first to qualitatively lay down the leapfrogging behaviour of vortex rings, he did not present any theoretical calculations. Instead, this was done shortly afterwards by Dyson and Hicks [451, 452] (see also [453]). Other early influential works include *e. g.* [454]. Thereafter, it took over a hundred years before

---

[2]The original work by Helmholtz was translated into English in [348], in which the quote reads: "[···] *two ring-formed vortex-filaments having the same axis* [···]. *If they have the same direction of rotation, they travel in the same direction; the foremost widens and travels more slowly, the pursuer shrinks and travels faster, till finally, if their velocities are not too different, it overtakes the first and penetrates it. Then the same game goes on in the opposite order, so that the rings pass through each other alternately.*".

the leapfrogging motion of two vortex rings in classical liquids was first clearly vi-
sualised and analysed under laboratory conditions [455, 456]. In experiments with
superfluids, on the other hand, leapfrogging vortex rings have not been observed
up to this day. Nevertheless, much theoretical effort has been devoted to under-
standing the leapfrogging motion of quantised vortex rings, mainly within the GP
model (see *e. g.* [398, 457, 458]). In classical liquids, leapfrogging vortex rings have
nowadays been studied in various systems, experimentally as well as theoretically
and in numerical simulations. For a selection of works see *e. g.* [459–462]. For more
on leapfrogging vortex rings in classical liquids, see also [349] and references therein.

In the following we study leapfrogging behaviour of quantised vortex rings in the
holographic superfluid. We first have to find an appropriate initial configuration that
indeed allows for the vortices to slip through each other. Decisive are the size of the
radii and, in particular, the ratio of the two radii as well as the ratios of the radii
and the initial axial separation. Here, we employ a configuration consisting of two
like-sign elementary vortex rings ($w_1 = w_2 = 1$) of equal radii given by $R_0 = 22$ grid
points, coaxially aligned with an initial separation of five grid points along the x_3-
direction. Their centre positions are chosen to be located at $(x_1, x_2, x_3)=(64, 64, 82)$
and $(64, 64, 77)$. As the single ring studied in chapter 12, the vortex rings in this
setup again propagate along the negative x_3-direction. We imprint the vortex-ring
configuration onto the equilibrium superfluid solution at time $t = 0$ and then prop-
agate the system forward in time. As in the previous chapter, we do not reset the
time once the vortex solutions have fully build up.

In figure 14.1 we display the vortex configuration at time $t = 5$ when the vortices
have fully developed their density profile. The grey surfaces are isosurfaces of the
condensate density $n(\boldsymbol{x})$ with a defining value of $n/n_0 = 0.12$. In addition, we
also plot the flow lines corresponding to the gradient field $\boldsymbol{\nabla}\varphi(\boldsymbol{x})$ which is directly
proportional to the velocity field of the superfluid. Here, φ is again the phase of the
superfluid order-parameter field ψ. The colour map employed to visualise the flow
lines is the same as in figures 12.1 and 12.6 for the single vortex ring and the vortex-
line dipole, *i. e.*, red denotes the highest and blue the smallest defining velocities.
Figure 14.1 illustrates nicely how the vortex radius of the rear (upper) ring after
five unit timesteps has already significantly decreased relative to the radius of the
front ring as well as relative to its initial condition. We recall that initially, at time
$t = 0$, the radii of both rings coincide. Likewise, from the flow lines one can clearly
discern the increased velocity of the rear ring relative to the front ring which goes
alongside the decrease in radius.

In figure 14.2i we show snapshots of the vortex rings at eight times characteristic
for their evolution. The first snapshot (panel (a)) agrees with the one displayed
in figure 14.1. Here, we again plot isosurfaces of the condensate density n with a
defining value of $n/n_0 = 0.12$. To aid the identification of the vortex rings through-
out their time evolution, we plot the surfaces in different colours, red for the rear
ring and blue for the front ring of the initial configuration. With proceeding time,
the radius of the rear ring (red), relative to the radius of the front ring, decreases
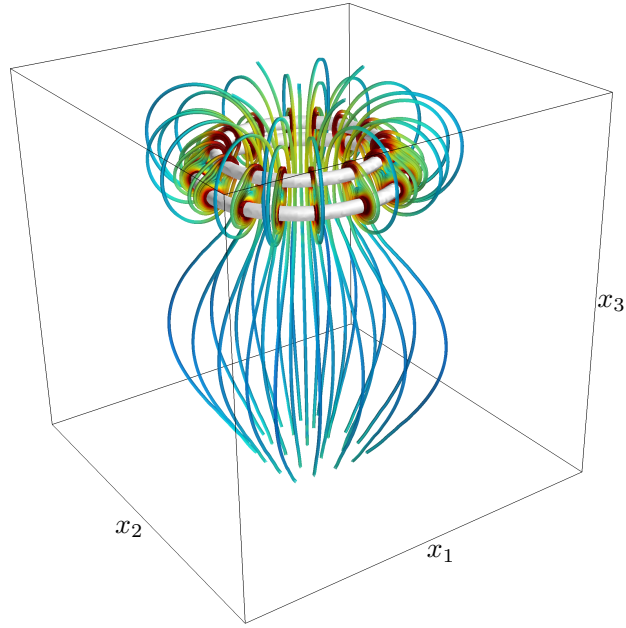even more while its velocity increases. Simultaneously, we find the radius of the

Figure 14.1: Snapshot of isosurfaces of the condensate density $n(\boldsymbol{x})$ (grey surfaces, defining value $n/n_0 = 0.12$) and flow lines corresponding to the velocity field $\boldsymbol{\nabla}\varphi(\boldsymbol{x})$ at time $t = 5$ for two axisymmetric vortex rings. In the initial configuration the vortex rings have the same size ($R_0 = 22$) and a vertical separation of five grid points. The decrease in radius of the rear ring relative to the front ring illustrates the onset of a leapfrogging motion. The flow lines (red denotes the highest and blue the smallest defining velocities), illustrate the larger axial velocity of the rear ring which induces the slip-through motion.

front ring (blue) to increase. Eventually, the rear ring catches up and slips through the front ring, *cf.* panels (b)–(d). This is the famous leapfrogging motion of two vortex rings as predicted by Helmholtz in 1858, here for two vortex rings in the three-dimensional holographic superfluid. Thereafter, we do not find this process to repeat itself with reversed roles of the rings, *i. e.*, the rear ring (blue) does not catch up with the front ring (red) again. Instead, the velocity of the front ring (red) increases strongly while its radius decreases until the ring eventually shrinks to zero size and thus disappears, *cf.* panels (f)–(g). At the same time, the rear ring (blue) gradually shrinks and eventually also disappears (panel (h)).

For the same characteristic times as in figure 14.2i we show snapshots of the density modulation $n(\boldsymbol{x})$ on the two-dimensional plane vertically intersecting the vortex planes through the centres of the rings in figure 14.2ii. As in chapter 12, we take the intersection to agree with (x_1, x_3)-plane at fixed $x_2 = 48$. On this plane, each vortex ring reduces to a vortex–anti-vortex pair. The snapshots illustrate nicely
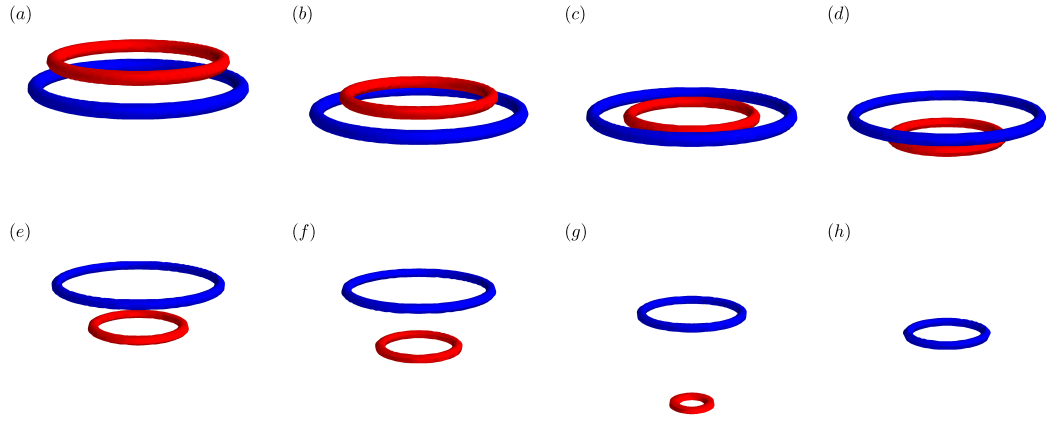
(i) Snapshots of isosurfaces of the superfluid-condensate density $n(\boldsymbol{x})$ for a defining value of $n/n_0 = 0.12$. To aid the identification of the rings, we use different colours for the respective isosurfaces.
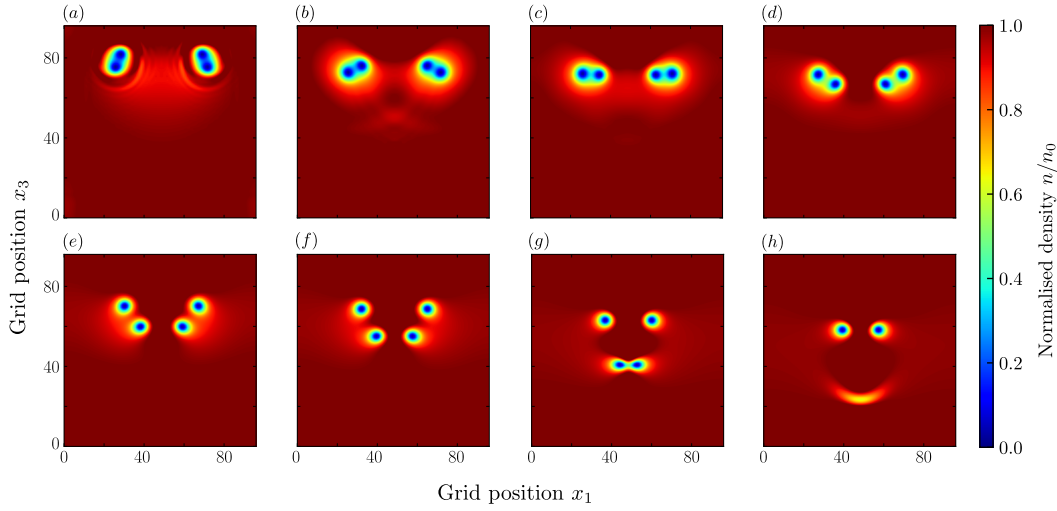
(ii) Snapshots of the normalised superfluid-condensate-density modulation $n(\boldsymbol{x})/n_0$ on the two-dimensional cross section intersecting the vortex plane through the centres of the rings at fixed $x_2 = 48$.

Figure 14.2: Snapshots of the superfluid-condensate density $n(\boldsymbol{x})$ (isosurfaces in the upper panel and modulation on a cross sections in the lower panel) illustrating the time evolution of two leapfrogging vortex rings of the same winding number $w_1 = w_2 = 1$. In the initial configuration, the rings have a radius of $R_0 = 22$ and an axial separation of five grid points. The snapshots in both panels are taken at times (a) $t = 5$, (b) $t = 17$, (c) $t = 24$, (d) $t = 31$, (e) $t = 42$, (f) $t = 50$, (g) $t = 71$, and (h) $t = 84$.

245

how the like-sign vortices rotate around each other as they propagate along the negative x_3-direction. The mutual rotation of the vortices in figure 14.2ii agrees qualitatively with the behaviour of like-sign vortices in two-dimensional superfluids. Once the rear dipole has overtaken the front dipole, its size has already significantly decreased and its velocity is too large to allow for another rotation of the respective vortex pairs on the right and anti-vortex pairs on the left. Instead, the front dipole quickly annihilates and sends out a rarefaction pulse. Shortly thereafter, also the rear dipole disappears by shrinking to zero size.

To analyse the leapfrogging motion also on a quantitative level, we track the vortex rings on the numerical grid and compute their velocities employing finite-difference methods. For the tracking of the rings, we proceed just like for the single vortex ring in section 12.2 by locating the induced vortices and anti-vortices on a two-dimensional plane vertically intersecting the vortex planes through the centres of the rings. Since the vortex rings are plane and circular throughout their evolution, the respective positions on such a two-dimensional plane are sufficient to infer the locations of the entire one-dimensional cores and thus also the radii of the rings. We again make use of our two-dimensional tracking routine of Part I. However, here we employ only the Newton–Raphson method since the density depletions of the vortex rings on the plane are deformed or even overlapping throughout their entire evolution. In particular, while at early times the depletions of one ring overlap with the ones of the respective other ring, at late times the depletions of each ring overlap individually. The NR method is therefore more reliable in locating the exact vortex positions than the Gaussian fitting routine. For the accuracy we seek in the following analysis, tracking the vortices at every unit timestep yields a sufficiently high time resolution.

In figure 14.3 we show the extracted trajectories, employing the same colour coding as in figure 14.2i, *i.e.*, red for the rear and blue for the front ring of the initial configuration. The trajectories confirm nicely what we have already inferred from studying the behaviour of the vortex rings in figure 14.2. Namely, as soon as the vortex rings are initialised, the rear ring picks up velocity and its radius decreases accordingly. Simultaneously, the front ring slows down while its radius increases. The difference in the velocities can qualitatively be inferred from the density of points in the respective trajectories. Subsequently, it only takes a few unit timesteps before the rear ring slips through the front ring. We indicate the x_3-position at which the slip-through occurs by the dashed black line. In particular, the slip-through motion must not be confused with the crossing point of the trajectories. In fact, the crossing point occurs at different times of the respective vortex-ring evolutions. Upon closer inspection of figure 14.3, we also find that shortly after the rear ring has overtaken the front ring, its trajectories bend slightly outwards. This may be interpreted as the onset of a second leapfrogging motion with reversed roles of the rings. However, as noted above, a second slip-through does not occur. Instead, the trajectories of each ring quickly approach each other and eventually concur at the position where the ring shrinks to zero size and disappears. Note that it is only due to the (chosen) limited time resolution of the trajectories that we cannot resolve the final shrinking
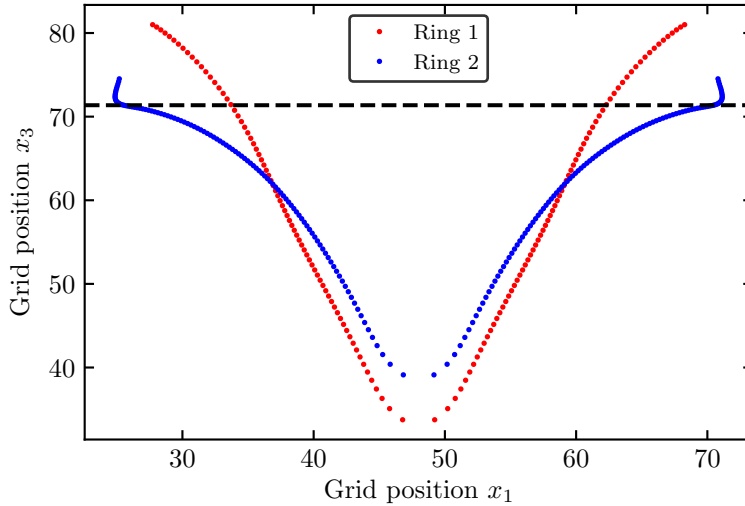
Figure 14.3: Trajectories of the leapfrogging vortex rings on the two-dimensional (x_1, x_2)-plane through the centre of the rings (*cf.* figure 14.2ii). The vortices are tracked at unit timesteps and we use the same colour coding for the rings as in figure 14.2i. The trajectories start once the rings have fully developed their density profile at time $t = 5$. The dashed black line indicates the x_3-position at which the rear ring slips through the front ring.

process of the ring in figure 14.3. For a higher time resolution of the final shrinking process, see figure 12.9.

The failure of the vortex rings to pursue a second leapfrogging motion can be attributed to the strong dissipation of the holographic superfluid. Once the radius of the rear vortex ring has declined relative to the radius of the front vortex ring, the difference gets strongly amplified due to the dissipative nature of the superfluid which causes the smaller ring to shrink even faster as compared to the larger ring. We have seen and analysed the rapid shrinking explicitly in section 12.2 when we studied the behaviour of single vortex rings. In the present scenario, the rapid shrinking of the slipped-through vortex ring prohibits a second leapfrogging motion. At the time the rear ring has slipped through the front ring, its velocity is already too high and its radius too small to be sufficiently impacted by the new rear vortex ring. In other words, the forces emerging from the flow field of the rear vortex, which slow down the axial velocity of the front ring and increase its radius, are much weaker than the Magnus force, arising due to the mutual friction between the vortex itself and the fluid, pointing towards the centre of the ring, thus causing it to undergo rapid shrinking. While Helmholtz could not account for details of the scenario at hand, he nevertheless pointed out that leapfrogging does not occur if the vortex velocities are too different which is essentially what happens here as well. In a system without

dissipation, on the other hand, the vortices would leapfrog perpetually if the initial configuration was chosen appropriately.

From the trajectories we can now also compute the velocities of the vortex rings. We again split the velocity of each ring into its axial component and its radial component, which accounts for growing and shrinking of the vortex ring. We display them both as a function of time in figure 14.4. Unlike before in chapter 12, here we plot $-v_R$ instead of $|v_R|$ in order to account for the growing of the front vortex ring. Given this choice, positive values of the velocity displayed in the lower panel of figure 14.4 therefore correspond to a shrinking motion of the vortex ring which is consistent with our choice in the previous chapter, while negative values correspond to a growing of the ring. Moreover, we use linear instead of log-log scales. The colour coding is again the same as in the figures above. In addition, similarly to figure 14.3, we also plot a vertical dashed black line to indicate the time at which the rear ring slips through the front ring. From the velocities we gain yet another perspective on the behaviour of the vortex rings. For the first leapfrogging motion we find the velocities of the rear and front ring to behave nearly oppositely, just like one would intuitively expect. As the axial velocity of the rear ring (ring 1, red) increases, the axial velocity of the front ring (ring 2, blue) decreases, allowing for the rear ring to slip through. In addition, at early times, prior to the slip-through, the radial velocity of the front ring is positive, accounting for the growing radius of the ring, while the radial velocity of the rear ring is negative and increases in magnitude, *i. e.*, the ring shrinks. Shortly before the rear ring slips through the front ring, the modulus of the radial velocity of the rear ring (ring 1, red) decrease while the radial velocity of the front ring is negative and increases in magnitude. Deviations of the velocities from a perfectly phase-shifted behaviour during the first leapfrogging motion, as seen in particular in the radial velocities, can again be attributed to the strong dissipation of the holographic superfluid. If there was no dissipation, the velocities along both the radial and axial direction would simply oscillate with a phase difference of π between the two rings. In the velocity curves displayed in figure 14.4 we can also clearly discern the onset of the second leapfrogging motion. In particular, here the onset is far easier to detect than in the trajectories displayed above in figure 14.3. Indeed, for the former rear ring (ring 1, red) we find the axial velocity to decrease distinctly after it has slipped through the front ring before it increases strongly due to the large dissipation. Hence, after the first leapfrogging motion, it first decelerates as would be expected for a second slip-through with reversed roles of the rings. However, the large dissipation causes the ring to quickly accelerate again. The new rear ring (ring 2, blue), on the other hand, cannot make up for the strong acceleration and a second leapfrogging motion is prevented.

As a final comment we note that, due to the dissipative nature of the superfluid, it is crucial to prepare the initial vortex configuration such that the axial separation between the rings is much smaller than their radii. If the axial separation was distinctly larger than the radii, the two rings would simply propagate in succession and eventually disappear by shrinking to zero size. It is conceivable that a second leapfrogging motion may occur and indeed complete if the initial radii of the vortex
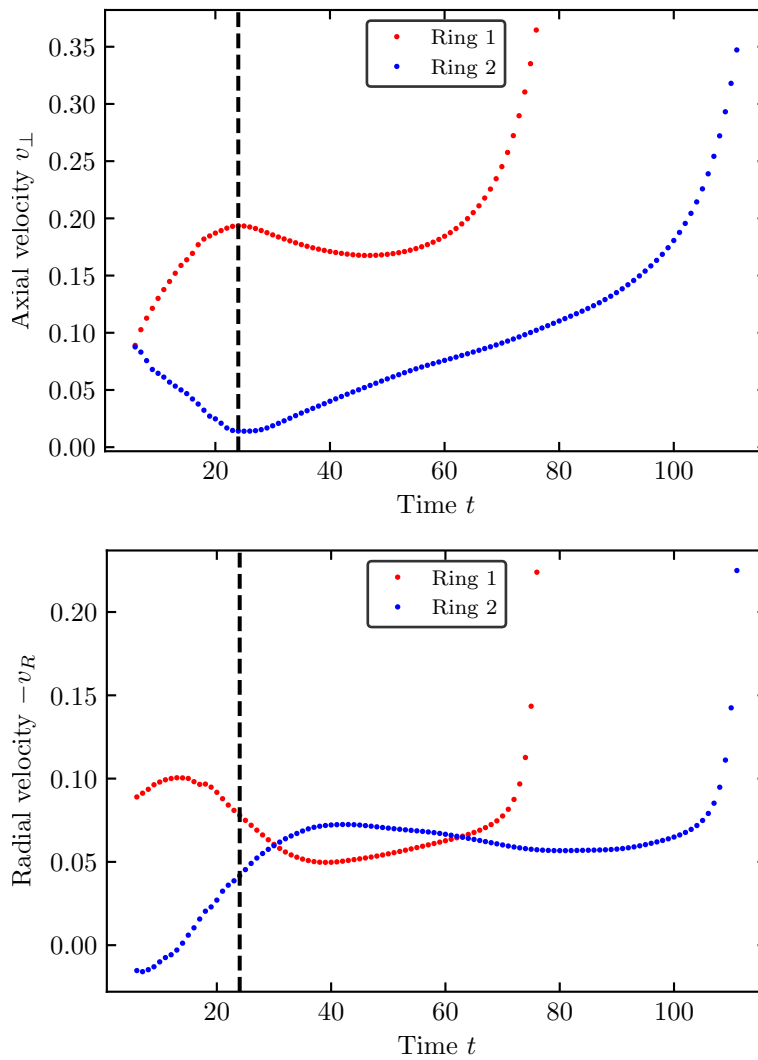
Figure 14.4: Axial (upper panel) and radial (lower panel) velocities of the leapfrogging vortex rings as a function of time, on a linear scale. All quantities are expressed in physical units. Note that we depict the negative of the radial velocity. The negative values for ring 2 therefore correspond to an increase of its radius, while positive values correspond to shrinking radii, consistent with our choice of sign in chapter 12. The colour coding is the same as in figures 14.2i and 14.3. The vertical dashed black line indicates the time at which the rear ring slips through the front ring.

rings are very large, in particular larger than the ones studied here, which implies that their velocities are very small, and their initial axial separation is chosen appropriately. We leave a systematic analysis of the dependence of the dynamics of leapfrogging vortex rings on the initial condition for future work. We will, however, comment further on the scenario of a possible second slip-through motion in section 14.1.3 when we study vortex rings of higher winding numbers.

14.1.2 Head-On Colliding Vortex Rings

In addition to the leapfrogging motion of two coaxial vortex rings, it is also interesting to study two coaxial vortex rings in a head-on collision. For vortex rings in classical liquids, such a scenario was also first discussed by Helmholtz in 1858 who describes the qualitative behaviour of the colliding vortex rings in the following words[3] [284]:

> *"Haben die Wirbelfäden gleiche Radien, gleiche und entgegengesetzte Rotationsgeschwindigkeiten, so werden sie sich einander nähern, und sich gegenseitig erweitern, so daß schließlich, wenn sie sich sehr nah gekommen sind, ihre Bewegung gegen einander immer schwächer wird, die Erweiterung dagegen mit wachsender Geschwindigkeit geschieht."*

> – Hermann von Helmholtz, 1858

Adapted to quantised vortex rings in (non-dissipative) superfluids, Helmholtz' qualitative description of the vortex-ring dynamics can be reformulated as follows. If instead of equal-sign winding numbers, like for the leapfrogging motion studied in the previous section, the vortex rings have opposite-sign winding numbers, the rings approach each other. Due to their phase structures, they both experience an increase in radius which causes their axial velocities to decrease. With increasing proximity, their radial velocities increase even further while their axial velocities decrease gradually.

Let us now study the head-on collision of two quantised plane circular vortex rings in the holographic superfluid. We prepare two coaxial vortex rings of initial radii $R_{1,0} = R_{2,0} = 22$ grid points and winding numbers $w_1 = -w_2 = 1$ with an axial separation of 22 grid points. For simplicity we again align the rings such that their symmetry axis is parallel to the x_3-direction of the computational domain. We imprint the rings onto the equilibrium superfluid solution such that their centres are initially located at $(x_1, x_2, x_3) = (48, 48, 59)$ for the first vortex ring of winding number $w_1 = 1$ and at $(48, 48, 37)$ for the second vortex ring of winding number $w_2 = -1$. Hence, the rings are symmetrically aligned around $x_3 = 48$, which is also where they eventually collide. In the first panel of figure 14.5i we illustrate the vortex-ring configuration after $\Delta t = 5$ unit timesteps when the vortex solutions have

---

[3]Translated into English, the quote reads [348] *"If they have equal radii and equal and opposite angular velocities, they will approach each other and widen one another; so that finally, when they are very near each other, their velocity of approach becomes smaller and smaller, and their rate or widening fast and faster.".*

fully built up their density profile. Here, we again plot isosurfaces of the condensate density $n(\boldsymbol{x})$ with a defining value of $n/n_0 = 0.12$. However, unlike before for the leapfrogging vortex rings we plot here the isosurfaces corresponding to both rings in the same colour. The reason is that at later times, when the rings collide and their density depletions merge and eventually annihilate, a distinction between them in terms of isosurfaces of the condensate density is no longer possible. Before we discuss the time evolution of the rings, let us briefly comment on the chosen initial condition. Evidently, our choice is only one of many that allows for an investigation of the characteristic behaviour of two colliding vortex rings. However, there are indeed certain requirements that have to be satisfied, in particular with regard to the ratio of the two initial radii of the rings, which has to be close to unity, as well as the ratios of the radii to the initial axial separation, which should not be distinctly larger than unity. We will comment further on this as we go along in this section.

In figure 14.5i we show snapshots of the vortex-ring configurations at eight characteristic times of the head-on collision. In all images, we again plot isosurfaces of the condensate density for the same defining value of $n/n_0 = 0.12$. After the vortex rings have been initialised, they quickly approach each other and significantly grow in radius. Interestingly, the increase of the radii sets in as soon as the system is propagated in time. Hence, the radial force acting on each vortex ring induced by the phase configuration of the respective other vortex ring, which causes its radius to increase, is larger than the force originating from the mutual friction between the vortex ring itself with the superfluid, which points along the opposite direction and induces a shrinking. A more thorough investigation of various different initial separations shows that a growth of the vortex rings sets in once their axial separation is of the same order of magnitude as their radii. This also implies that if the initial separation is too large, it may happen that the rings have already shrunk to zero size and thus disappeared before they even come into contact. Thus, the ratio of the axial separation to the radius of the vortex rings is a crucial aspect that has to be taken into account in the preparation of the vortex rings in the initial condition. Shortly before the vortex rings annihilate, their density depletions begin to overlap and merge, *cf.* panels (e)–(f). During that stage, the increase of their radii is strongest and the isosurfaces in figure 14.5i can no longer resolve the two rings separately. Shortly thereafter, the two rings mutually annihilate each other, sending out an azimuthally symmetric rarefaction pulse within their collision plane, *i. e.*, the (x_1, x_2)-plane at fixed $x_3 = 48$, *cf.* panels (g)–(h).

Like for the leapfrogging vortex rings, we gain much insight into the vortex-ring dynamics by studying the superfluid density modulation $n(\boldsymbol{x})$ on a two-dimensional plane vertically intersecting the vortex planes through the centres of the vortex rings. Without loss of generality and just like we have done so far, we take the intersection to agree with the two-dimensional (x_1, x_3)-plane at fixed $x_2 = 48$. For the same characteristic times as in figure 14.5i for the isosurface snapshots, we illustrate the density modulation on the two-dimensional plane in figure 14.5ii. On the plane, the vortex rings reduce to two vortex dipoles with anti-parallel dipole vectors along the x_1-direction. As the dipoles approach each other, their sizes gradually increase until
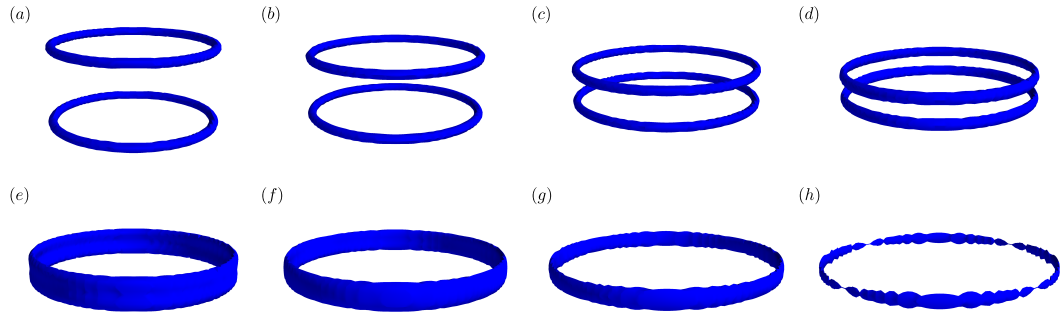
(i) Snapshots of isosurfaces of the superfluid-condensate density $n(\boldsymbol{x})$ for a defining value of $n/n_0 = 0.12$.
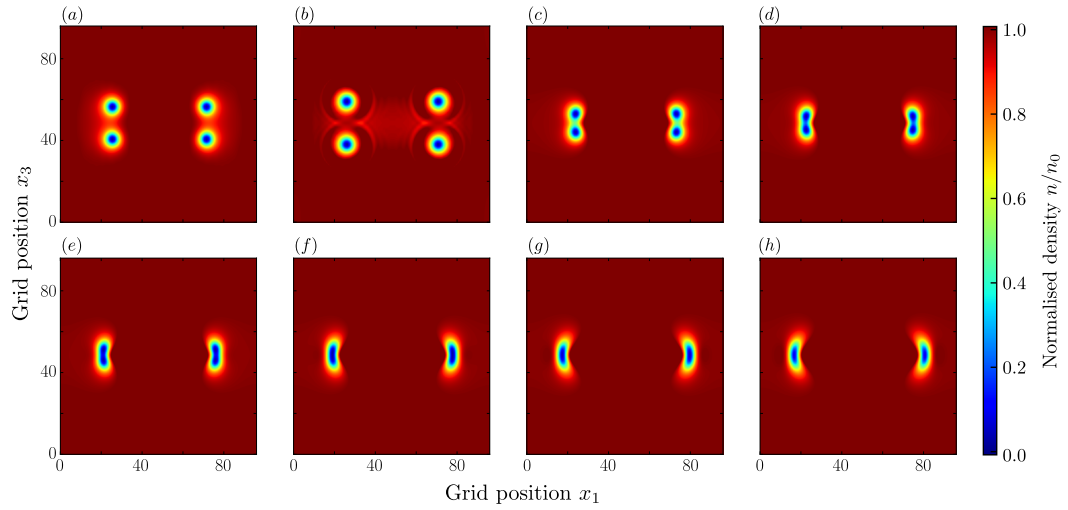
(ii) Snapshots of the normalised superfluid-condensate density $n(\boldsymbol{x})/n_0$ on the two-dimensional plane through the centres of the rings at fixed $x_2 = 48$.

Figure 14.5: Snapshots of the superfluid-condensate density $n(\boldsymbol{x})$ (isosurfaces in the upper panel and modulation on a cross section intersecting the centres of the rings in the lower panel) illustrating the time evolution of two head-on colliding vortex rings of winding numbers $w_1 = -w_2 = 1$. In the initial configuration the rings have a radius of $R_0 = 22$ and an axial separation of 22 grid points. The snapshots in both panels are taken at times (a) $t = 5$, (b) $t = 19$, (c) $t = 38$, (d) $t = 44$, (e) $t = 47$, (f) $t = 50$, (g) $t = 52$, and (h) $t = 53$.

the respective vortex–anti-vortex pairs on the left and right eventually annihilate
and send out a rarefaction pulse. The two-dimensional view of the vortex dynamics
in figure 14.5ii allows for a very intuitive explanation of the observed behaviour
of the rings. For the sake of the following argument, let us briefly disregard the
constraints on the induced vortices in the two-dimensional plane imposed by the
topology of the vortex rings. Thus, we discuss the dynamics in figure 14.5ii as
if it was a purely two-dimensional configuration in which case the behaviour of the
vortices is straightforward to understand. Namely, once the axial separation between
the horizontal dipoles drops below the dipole sizes (which agree by symmetry), the
respective, vertically separated, vortex–anti-vortex pairs on the left and right form
stronger bound pairs. Hence, their mutual attraction (induced by Magnus forces
due to dissipation) is larger than that of the horizontal pairs which causes them
to approach each other and drift outwards. In particular, the approach proceeds
faster than it would be if the velocity was determined only by the separation of
the horizontal vortex–anti-vortex pairs (*cf.* below). The behaviour of the vertical
vortex–anti-vortex pairs is, to some extent, similar to what we have studied in Part
I for isolated dipoles, *cf.* figure 6.2. Evidently, the outward drifting of the respective
pairs on the left and right results in an increase of the horizontal separation between
the former vortex–anti-vortex pairs at the top and bottom. This is precisely what
we observe in figure 14.5ii. Taking into account the three-dimensional setting again,
the outlined interpretation can only be applied with due caution as the horizontal
vortex dipoles are strongly constraint in their behaviour by the topology of the rings.
However, despite these constraints, also for the vortex rings one can interpret the
behaviour in terms of the emergence of a force between every two opposite points
of the respective rings along their axial directions, causing them to behave just like
vortex dipoles in two dimensions and drift outwards. Qualitatively, this explains the
observed behaviour of the two colliding rings in figure 14.5i.

The qualitative behaviour of smoothly merging density depletions and widening
vortex rings agrees with Helmholtz' prediction discussed above. Similar behaviour
has also been observed experimentally for colliding vortex rings in classical liquids
[463, 464] and for vortex rings colliding with a wall [465]. For an incomplete list of
further works regarding various different types of classical liquids and characteristics
of vortex cores, see *e. g.* [464, 466, 467]. The head-on collision of quantised vortex
rings was first studied within the GP model in [468]. In that work the authors find
qualitatively similar behaviour to what we have discussed in the previous paragraphs.
Moreover, in a more recent work, such an investigation of colliding vortex rings
described by the GPE was revisited and, among other investigations of vortex-ring
interactions, also extended to non-central collisions of plane circular vortex rings
[398]. With regard to the qualitative behaviour of the vortex rings in a head-on
collision the results of [398] are also similar to our findings.

We now analyse the collision of the colliding vortex rings in the holographic su-
perfluid also on a quantitative level. We proceed just as for the leapfrogging vortex
rings in the previous subsection 14.1.1 and extract the trajectories of the vortex rings
and subsequently calculate their velocities. We again employ only the NR tracking
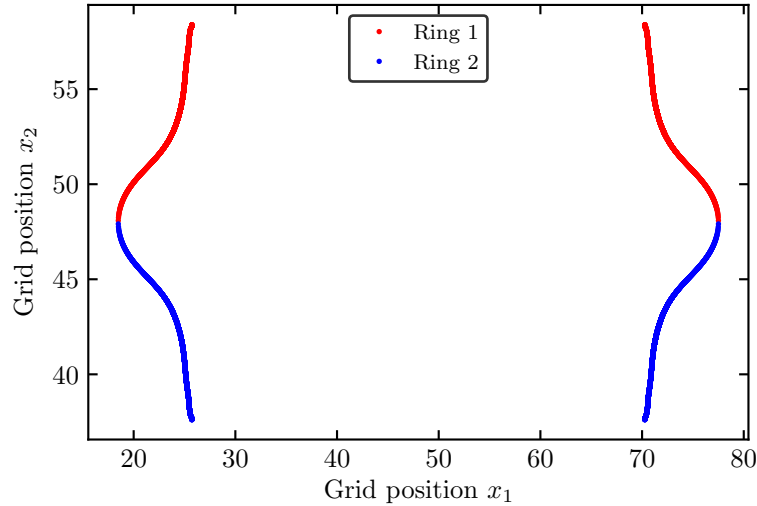
Figure 14.6: Trajectories of the head-on colliding vortex rings on the two-dimensional (x_1, x_3)-plane at fixed $x_2 = 48$ intersecting the centres of the rings (*cf.* figure 14.5ii). To aid the identification, we have introduced a colour coding for the two rings. The trajectories start once the rings have fully developed their density profile at time $t = 5$. Throughout their evolution, the rings are tracked fifty times per unit timesteps.

routine to locate the vortices. To increase the time resolution of the trajectories, we locate the vortices fifty times per unit timestep throughout their entire evolution. We show the resulting trajectories of the induced vortices in the transverse plane in figure 14.6. To aid the identification of the vortex rings, we display the trajectories of the two rings in red and blue, respectively. We stress that here, unlike for the isosurfaces in figure 14.5, a clear distinction between the rings is possible since we only track their zeros and the NR method is not affected by the deformed and over-lapping density depletions. The trajectories nicely illustrate the significant increase in radii the rings undergo as they approach each other. At very late times, the be-haviour of the annihilating vertically separated vortex–anti-vortex pairs on the left and right strongly resembles the behaviour of vortices in the two-dimensional super-fluid studied in Part I, *cf.* figure 8.1. In addition, the trajectories on the left and on the right of the annihilating vertical vortex–anti-vortex pairs also each resemble the trajectories of a single shrinking vortex ring studied in section 12.2, *cf.* figure 12.9. These findings corroborate our qualitative explanations that opposite points of the two vortex rings behave pairwise just like annihilating vortex–anti-vortex dipoles.

From the trajectories it is again straightforward to derive the velocities of the vortex rings by employing finite-difference methods, *cf.* appendix A.5. Due to the symmetry of the configuration, the radial velocities of the vortex rings are symmetric. Likewise, the axial velocities agree in modulus but are opposite in sign. We present
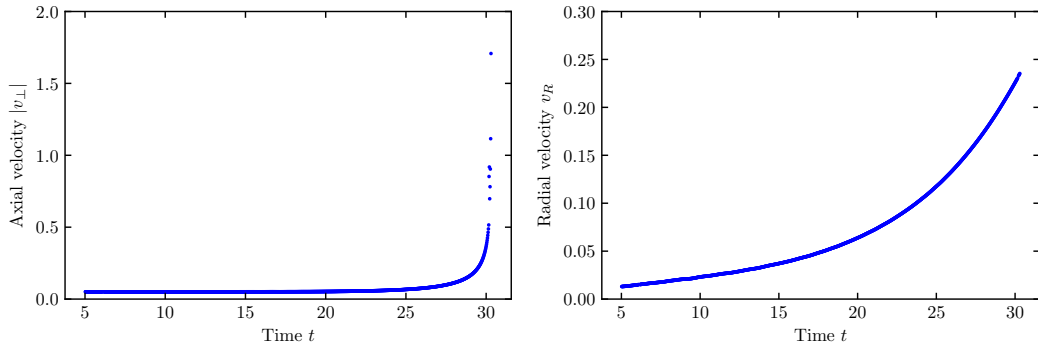
Figure 14.7: Axial (left panel) and radial (right panel) velocities of the head-on colliding vortex rings as a function of time, on linear scales. Due to the mirror symmetry of the configuration, the respective velocities are the same for both vortex rings, except for a relative sign in the axial velocity. We therefore show only the absolute value of the axial velocities of the rings. Both velocity components, the radial and axial, increase monotonously throughout the evolution. All quantities are expressed in physical units.

both velocity components as a function of time in figure 14.7. Note that unlike in before, here we plot v_R and not its negative or its modulus. For conciseness, we only show the modulus of the axial velocities of the rings and henceforth always refer to the modulus as the axial velocity. However, we keep in mind that for one of the rings the axial velocity is in fact negative. As expected, and in agreement with our discussion above, we find the radial velocity to increase strongly as the vortex rings approach each other. For the axial velocity we also find a gradual increase as the axial separation between the rings decreases. In particular during the final stages of the evolution, the axial velocity increases very strongly and is distinctly larger than the radial velocity.

A priori, the observed behaviour of the axial velocity is unexpected. Indeed, the axial velocity of the vortex rings increases despite the increase of the rings' radii. Intuitively, one would rather expect the axial velocity to decrease, just like Helmholtz predicted [284] and as we have argued for the scenario of a single ring in chapter 12. There is, however, a plausible explanation for the behaviour, based on the strong dissipation of the holographic superfluid. Namely, as we have argued above, due to mutual friction between the rings and the fluid a Magnus force acting on both vortex rings, pointing along their respective axial directions, emerges. It is conceivable that due to the strong dissipation of the superfluid, the increase in the axial velocity of the rings, induced by this force, is larger than the decrease one would expect due to the growing radii of the rings and thus the smaller self-induced velocities. Hence, in light of the strong dissipation, the behaviour of the vortex rings does not contradict

Helmholtz' work. However, it requires the inclusion of an additional mechanism. We point out that this is only an intuitive interpretation of the observed behaviour and we have not explicitly evaluated the forces and traced back their origin.

Before we conclude the present subsection, we refer back to our previous discussion concerning the initial configuration of the vortices. In particular, it is also interesting to study the head-on collision of vortex rings with different initial radii. In this scenario, we find the behaviour of the rings to depend crucially on the ratio of their radii. For the following brief discussion, we assume the initial axial separation to always be of the order of the radius of the larger ring. For ratios of the radii close to unity, the behaviour of the rings is essentially the same as outlined above, *i.e.*, they mutually annihilate. The mutual annihilation implies that the sizes of the rings adjust to one another as they grow. An important difference to the scenario studied above is that for non-equal-size vortex rings, their centre-of-mass position is not static. If the ratio of the radii is much larger (or smaller) than unity, on the other hand, the radii of the rings no longer adjust to one another to allow for a mutual annihilation. Instead, the smaller ring typically shrinks to zero size even before the rings come close to one another. If their initial axial separation is distinctly smaller and of the order of the radius of the smaller ring, by contrast, the rings come closer and the smaller one shrinks and disappears as it tries to go through the larger ring.

As compared to head-on colliding vortex rings in classical liquids, there is one feature that we did not find in our simulations described above. In [466] (see also [469] for a follow-up work) the authors collide two vortex rings in water and find that shortly before they collide, the rings form instabilities which eventually has the consequence that they reconnect to a number of much smaller vortex rings. The reason is that due to the growth in diameter, the vortex rings become unstable which manifests itself in the form of wave-like excitations on the rings. Consequently, not all points along the vortex rings annihilate simultaneously. Instead, on several points along the cores they reconnect and form new, distinctly smaller rings. For initially plane circular vortex rings, as studied above, we cannot find this phenomenon in our simulations. Moreover, due to the intrinsic stability of the vortex rings imposed by their quantised phase windings, we also do not expect initially plane circular vortex rings to form such instabilities as they approach each other. We note that also in [468] the authors do not report any such feature for initially plane circular vortex rings in the GP model.

However, in general, also the cores of quantised vortex rings can be excited by wavy excitations. In fact, such excitations are known as Kelvin waves, and we discuss them in more detail in section 14.3 below. While these excitations do not build up dynamically as two initially plane circular vortex rings approach each other, they do typically emerge during the dynamics of large vortex ensembles such as we have studied them in the previous chapter. Moreover, vortex rings perturbed by Kelvin waves can also be directly imprinted in the initial condition of the holographic superfluid (*cf.* section 14.3 for details). If two such vortex rings collide, we expect to find essentially the same behaviour as for the colliding vortex rings in classical liquids. Namely, not all points along the cores simply annihilate simultaneously, but

instead the rings reconnect at several points to form a number of smaller vortex rings. We point out that also in [466, 469] the wavy excitations along the cores are in fact Kelvin waves. Hence, it appears very likely that one could 'recreate' the scattering scenario of classical vortex rings also for quantised vortex rings in the holographic superfluid. It would therefore be very interesting to investigate head-on collisions also for vortex rings carrying Kelvin waves. We leave this for future work.

14.1.3 Non-Elementary Vortex Rings

In our discussion of the vortex-ring solutions in chapter 12 we have argued that non-elementary vortex rings, *i. e.*, rings of winding numbers $|w| > 1$, are unstable against decay into elementary vortex rings of winding numbers $|w| = 1$. However, in our preceding investigations we have deferred a thorough discussion of this matter and focused solely on elementary vortex excitations. In this final subsection of section 14.1, we now want to study the dynamics of vortex rings of higher winding numbers. To be specific, we investigate how single vortex rings of winding numbers $w = 2$ and $w = 3$ behave.

To prepare the respective initial configurations, we proceed just as outlined in section 12.2 and multiply the corresponding winding structure (12.3) of the vortex ring of winding number w into the equilibrium solution of the superfluid. Upon propagating the system in time, the vortex solution then builds up dynamically. In particular, we again refrain from setting the bulk scalar field Φ to zero at the respective positions of the ring along the holographic z-direction. The larger the modulus of the winding number, the longer the build-up takes. The initial configurations we study consist of one vortex ring of radius $R_0 = 22$ grid points each. We again align the ring such that its symmetry axis is oriented in parallel to the x_3-direction of the grid and put its centre at $(48, 48, 77)$. For our simulations we again employ a chemical potential of $\mu = 5$ for the superfluid and solve the equations of motion on a grid of 96^3 points along the (x_1, x_2, x_3)-directions.

We illustrate the time evolution of the vortex rings of winding numbers $w = 2$ and $w = 3$ in eight characteristic snapshots in figures 14.8 and 14.9, respectively. In figures 14.8i and 14.9i we plot isosurfaces of the respective condensate density $n(\boldsymbol{x})$ with a defining value of $n/n_0 = 0.12$. In figure 14.8ii and 14.9ii, on the other hand, we display the respective condensate-density modulation for the same times in a cross section of the ring, here corresponding to the fixed $x_2 = 48$ slice. For both vortex rings, the snapshots displayed in the respective panels (*a*) are taken at time $t = 5$. A direct comparison of figures 14.8 and 14.9 shows that the width of the density depletion around the core of a vortex ring increases with increasing winding number. However, upon closer inspection, one finds that as soon as the systems are propagated in time, the higher-wound vortex rings decay into $|w|$ elementary rings[4]. By bare eye, this is neither discernible in panel (*a*) of figures 14.8i and 14.9i nor in the respective panels of figures 14.8ii and 14.9ii. Remarkably, we find that once the

---

[4]Also in the two-dimensional superfluid studied in Part I one finds that higher-wound vortices decay into elementary vortices as soon as the system is propagated in time.
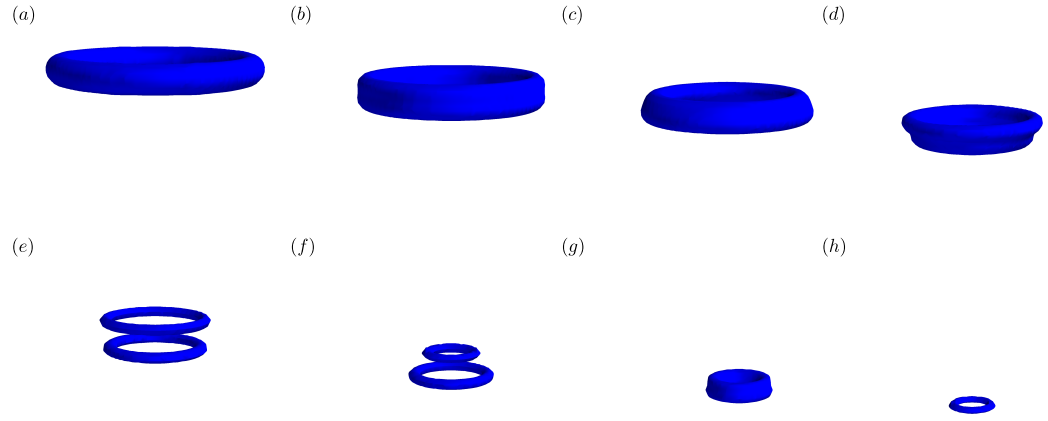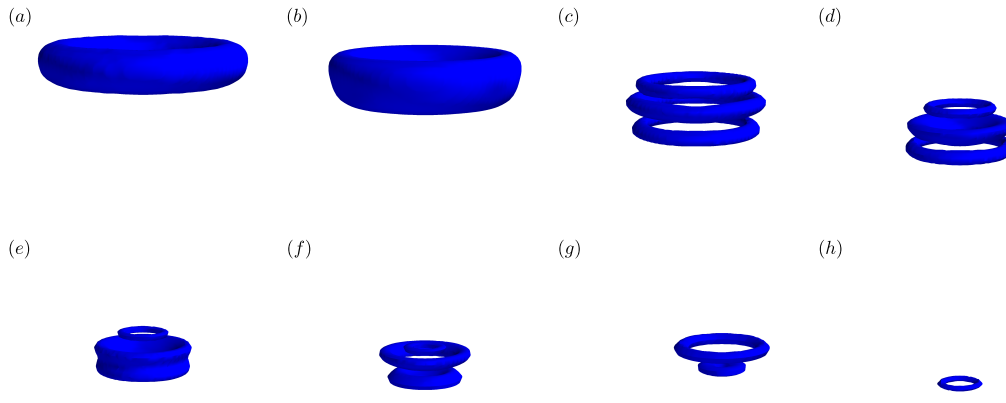
(i) Snapshots of isosurfaces of the superfluid-condensate density $n(\boldsymbol{x})$ for a defining value of $n/n_0 = 0.12$.
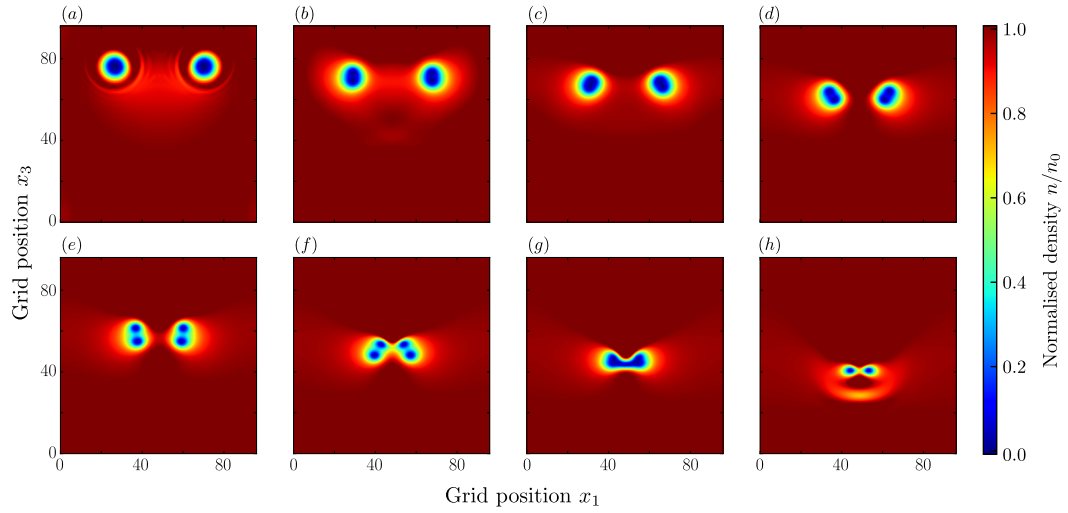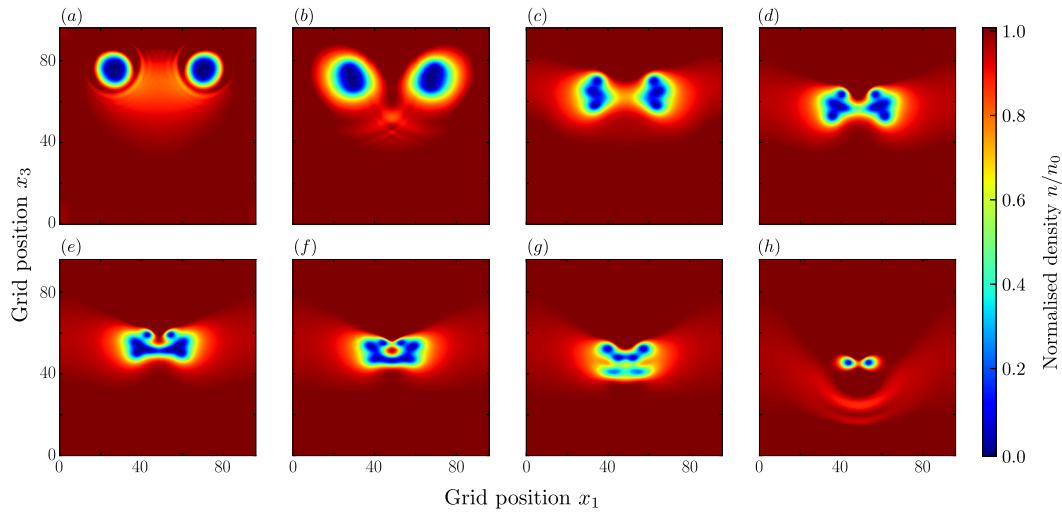

(ii) Snapshots of the normalised superfluid-condensate density $n(\boldsymbol{x})/n_0$ on the two-dimensional plane intersecting the centres of the rings at fixed $x_2 = 48$.

Figure 14.8: Snapshots of the superfluid-condensate density $n(\boldsymbol{x})$ (isosurfaces in the upper panel and modulation on a cross sections in the lower panel) illustrating the time evolution of the initial vortex ring of winding number $w = 2$ and radius $R_0 = 22$. The ring quickly decays into two elementary rings which subsequently perform a leapfrogging motion. The snapshots in both panels are taken at times (*a*) $t = 5$, (*b*) $t = 20$, (*c*) $t = 30$, (*d*) $t = 45$, (*e*) $t = 54$, (*f*) $t = 68$, (*g*) $t = 75$, and (*h*) $t = 85$.

(i) Snapshots of isosurfaces of the superfluid-condensate density $n(\boldsymbol{x})$ for a defining value of $n/n_0 = 0.12$.

(ii) Snapshots of the normalised superfluid-condensate density $n(\boldsymbol{x})/n_0$ on the two-dimensional plane intersecting the centres of the rings at fixed $x_2 = 48$.

Figure 14.9: Snapshots of the superfluid-condensate density $n(\boldsymbol{x})$ (isosurfaces in the upper panel and modulation on a cross sections in the lower panel) illustrating the time evolution of the initial vortex ring of winding number $w = 3$ and radius $R_0 = 22$. The ring quickly decays into three elementary rings which subsequently perform a leapfrogging motion. The snapshots in both panels are taken at times (a) $t = 5$, (b) $t = 14$, (c) $t = 31$, (d) $t = 43$, (e) $t = 49$, (f) $t = 53$, (g) $t = 58$, and (h) $t = 73$.

initially doubly- as well as triply-wound rings have decayed, the elementary rings do not simply fly apart but instead begin to leapfrog. In the following we analyse the leapfrogging behaviour in detail, separately for the $w = 2$ and for the $w = 3$ vortex ring. We track the vortices on the two-dimensional x_2-slice vertically intersecting the respective vortex planes through their centres. We note that throughout the evolution, the rings pertain their plane circular shape which justifies our use of the two-dimensional tracking routine. For both initial vortex rings, we track the elementary vortices on the two-dimensional plane for all times later than $t = 5$ at every unit timestep. We display the resulting trajectories for both initial vortex rings in figure 14.10.

We begin our quantitative analysis of the dynamics for the initial vortex ring of winding number $w = 2$. The snapshots in figure 14.8 are taken at times $t = 5, 20, 30, 54, 68, 75$, and 85. Here, the decay of the initial vortex ring into two elementary rings is clearly discernible in the bifurcation of the zeros in panel (b) of figure 14.8ii. At this time, the vortices have already begun their first leapfrogging motion. We see the following slip-through motion of the rear ring through the front ring in panels (b)–(d). Notably, the slip-through is also discernible in the isosurfaces in the respective panels of figure 14.8i. A short time thereafter at $t = 45$ (panel (d)), the rings have separated far enough such that they are also individually resolved by the isosurfaces of $n(\boldsymbol{x})$. Up to this point in the evolution, we find the qualitative behaviour of the vortex rings to be very similar to the behaviour of the leapfrogging vortex rings that we have studied in subsection 14.1.1. In particular, also the trajectories, displayed in the upper panel of figure 14.10, have a strong resemblance to those shown in figure 14.3. To aid the identification of the two rings, we again use different colours to denote their trajectories.

Shortly after the first leapfrogging motion has completed, a second one sets in, *cf.* panels (e)–(f). After the first slip-through, both vortex rings have already significantly shrunk and therefore picked up large velocities. In fact, it turns out that the vortex-ring configuration after the first leapfrogging motion, characterised by the radii, velocities and the axial separation of the rings, does not allow for the completion of a second leapfrogging motion. What happens instead is that as the rear ring is about to go through the front ring, the density depletions of both rings merge, causing their radii to adjust to an equal size (*cf.* panel (g)), before eventually one of the rings disappears. The other ring remains in the system and still has a finite size (*cf.* panel (h)). Due to the merging of the density depletions we cannot unequivocally identify the rings during this process. In particular, even by employing the NR tracking routine, we cannot unambiguously locate the vortex rings. The reason for this is twofold. First, the respective density depletions of all four vortices on the transverse plane intersecting the centres of the vortex rings deform and overlap severely, and eventually two of these zeros merge to one large continuum, stretching over several grid points (with the field Fourier interpolated at inter-mesh points), *cf.* panel (g). Given this configuration, we find that the approximate locations of the vortices, determined by locating their phase windings to plaquette precision, are not sufficient to ensure proper convergence of the NR algorithm. In particular, we find
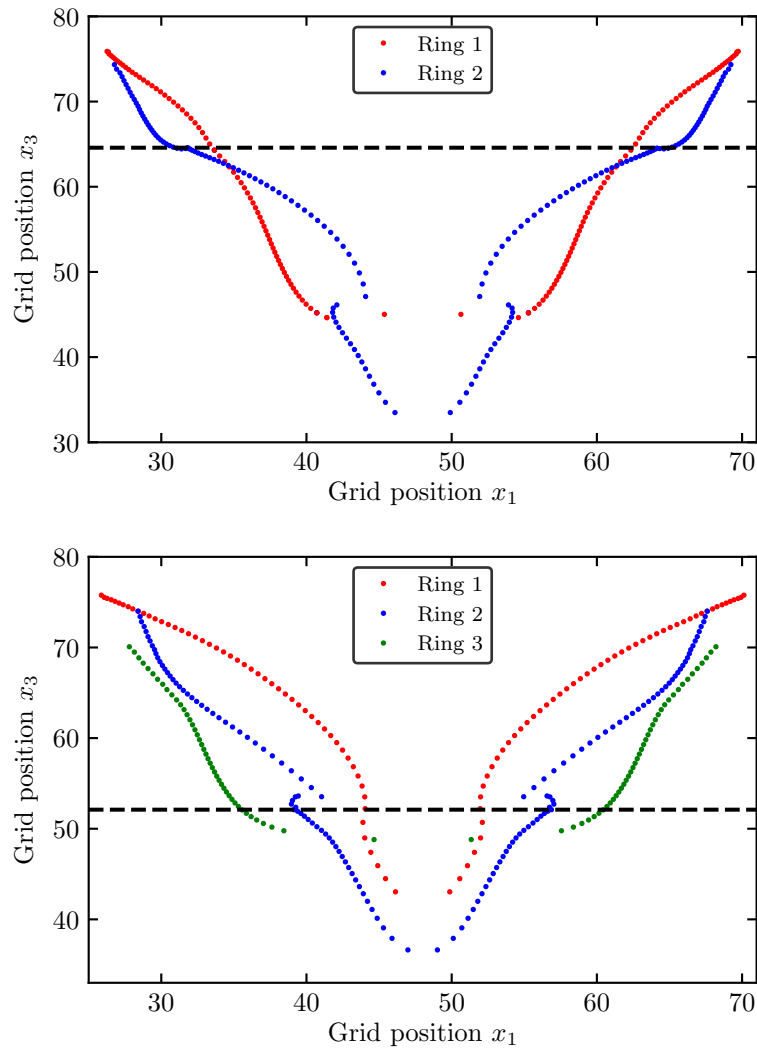
Figure 14.10: Trajectories of the elementary vortex rings the initially doubly-wound (upper panel) and triply-wound (lower panel) vortex ring decays into, on the two-dimensional (x_1, x_3)-plane through the centres of the rings. To aid the identification of the vortex rings, we introduce a colour coding. We track the vortices at every unit timestep, beginning at time $t = 5$ in both systems. In both panels, the dashed black line indicates the x_3-location of the respective successful slip-through motion. In the lower panel, the rear ring slips through the centre ring at this point.

that the Fourier interpolation of the order-parameter field at inter-mesh positions, in the vicinity of the zeros, appears to have large uncertainties and can in fact not fully resolve the structure in the condensate density. Hence, at this stage of the evolution, the trajectories shown figure 14.10 have large uncertainties. What appears to happen is that the formation of the continuum of zeros causes the phase-winding structure of the front vortex ring to disappear while the size of the rear ring increases. We point out that this behaviour of the vortex rings is not in violation with our previous findings in section 14.1 regarding the leapfrogging motion of two plane circular vortex rings as there are several distinct differences between the two vortex-ring configurations, which we deem responsible for the different behaviour. The key difference between the two scenarios is that, here, at the onset of the leapfrogging motion, the sizes of the rings are so small that the density depletions of the rear are already deformed. Moreover, the rings have distinctly larger velocities (due to the smaller radii), and their axial separation is very small. Before the rings even come into contact, the inward-pointing radial force on the front ring, caused by the large dissipation, at the onset of the leapfrogging process is already much larger than the outward pointing force induced by the phase structure of the rear vortex. Hence, the front ring continues to shrink. Simultaneously, the force acting on the rear ring induced by the phase structure of the front ring amplifies the force arising from the mutual friction between the vortex and the superfluid, causing the ring to shrink even faster. This implies that, as the rear ring approaches the front ring and is about to slip through it, both vortex rings are rapidly shrinking. This was not the case for the leapfrogging vortex rings in section 14.1 (*cf.* figure 14.4). It appears as if during the slip-through the front ring accelerates vastly along its radial direction and annihilates itself. The rear ring, on the other hand, survives and its radius increases strongly, as is discernible in the trajectories in figure 14.10. Moreover, the increase in radius can also be inferred from a comparison of the ring sizes in panels (*f*) and (*g*) of figure 14.8i and 14.8ii. We point out that the reason the increase in radius appears to be discontinuous in 14.10 is the time resolution employed in the analysis. We have explicitly checked this by analysing the vortex configuration more frequently than at every unit timestep. However, in figure 14.10 we show the trajectories only at unit timesteps. Eventually, once only one ring remains, it gradually shrinks and eventually disappears, *cf.* panel (*h*).

We now proceed to the triply-wound vortex ring. The snapshots in figure 14.9 are taken at times $t = 5, 14, 31, 43, 49, 53, 58$ and 73. To wit, here the three elementary rings fly apart much faster than the two rings of the initially doubly-wound vortex, *cf.* panels (*a*)–(*c*). This behaviour can be attributed to the distinctly larger repelling forces of three like-sign vortex rings as compared to two rings. Once the rings have significantly flown apart, the first leapfrogging motion sets in, *cf.* panel (*d*). Naturally, in such a process all three rings are involved and the dynamics is therefore much more complicated than for two rings. At first, the centre ring (ring 2, blue) catches up with the front ring (ring 3, green) and tries to go through it. However, what appears to happen is similar to what we have found above for the second leapfrogging motion of the two elementary vortex rings in figure 14.8. Namely,

as the centre ring is about to slip through the front ring, the two rings merge. During this process, a continuum of zeros in the condensate density forms, leading to the annihilation of the front ring, while the centre ring survives, *cf.* panels (*e*) of figure 14.9. This process is also discernible in the trajectories displayed in the lower panel of figure 14.10, which, however, are plagued by large uncertainties in this regime. In particular, the motion of both, the centre as well as the front ring, are very similar to what we have seen for the two elementary rings in the upper panel of figure 14.10. As before, here we also cannot unambiguously assign the zeros in the condensate density to the respective rings which renders an unequivocal identification impossible. Nonetheless, we note that it appears as if the front ring shrinks to zero size and the centre ring survives, while rapidly changing its radius. Again, the apparent discontinuity in the trajectories can be remedied by tracking the rings more frequently than at every unit timestep. As for the two rings, however, we show the trajectories only at unit timesteps. Shortly after the front ring has disappeared, the rear ring (ring 1, red) catches up with the new front ring (ring 2, blue) and slips through it, *cf.* panels (*f*)–(*g*). This leapfrogging motion gets fully completed. Subsequently, the rings do not perform another leapfrogging motion but instead simply shrink to zero size and disappear (panels (*g*)–(*h*)).

As a final comment of this section, we not that the leapfrogging motion of three vortex rings was first studied by J. C. Maxwell, who wrote about it in a letter to W. Thomson (later Lord Kelvin) [470]. Since then, the dynamical behaviour of three vortex rings in classical liquids has been intensively studied, theoretically as well as experimentally in, *e. g.*, [459, 471]. Likewise, also for quantised vortex rings, the leapfrogging motion of three rings has drawn much attention and has been investigated analytically as well as in numerical simulations, see *e. g.* [457, 472].

14.2 Scattering Vortex Rings

In the previous section 14.1, we have studied a head-on collision of two plane circular vortex rings with opposite topological charges, *i. e.*, different-sign winding numbers. We have found that, as the rings approach each other, their radii increase continuously until the two rings eventually mutually annihilate. Once the corresponding phase structures of the vortex rings have disappeared, the rings leave behind an azimuthally symmetric expanding rarefaction pulse. Qualitatively, the behaviour of the rarefaction pulse is very similar to the analogous wave created in the shrinking of a single vortex ring or the annihilation of a vortex–anti-vortex pair in the two-dimensional fluid. Namely, the wave quickly picks up velocity and its depth decreases until it eventually decays into sound excitations of the fluid. However, while head-on collisions, in particular of plane circular rings, are very interesting and reveal much about the dynamics of vortex rings, they are rather unlikely to occur as part of the dynamics of dense vortex tangles such as we have studied them in chapter 13. Instead, in those configurations, one rather finds scattering events where the scattering vortex rings have a finite impact parameter or are tilted relative
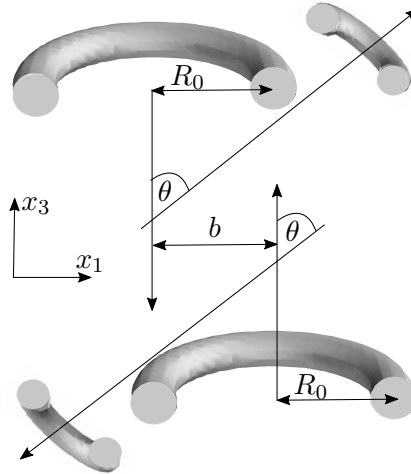
Figure 14.11: Illustration of two scattering vortex rings. In the initial configuration, both rings have a radius of $R_0 = 14$, an axial separation of 14 grid points and are offset by the finite impact parameter b (illustrated by the two large rings). In the post-scattering state, two rings (the two small rings) fly away from the interaction region under a finite angle θ relative to the axial (or longitudinal) direction. The shown rings correspond to isosurfaces of the condensate density $n(\boldsymbol{x})$ (with a defining value of $n/n_0 = 0.23$).

to the vortex plane of the respective other ring. In this section, we are interested in studying the former situation. Our goal is to understand the dynamics of scattering vortex rings, in particular how the dynamics changes as a function of their impact parameter. The vortex-ring configuration we have in mind and want to study in this section consists of two vortex rings, approaching each other along their shared longitudinal (axial) direction with a finite transverse offset given by the non-zero impact parameter b. We prepare the two rings of winding numbers $w_1 = -w_2 = 1$ and radii $R_{1,0} = R_{2,0} \equiv R_0 = 14$ grid points in the initial configuration. We imprint the rings such that their axial directions are aligned in parallel to the x_3-axis of the numerical grid and put their centre positions at $(48 - b/2, 48, 55)$ and $(x_1, x_2, x_3) = (48 + b/2, 48, 41)$ for the vortex ring of winding number $w_1 = 1$ and $w_2 = -1$, respectively. Hence, we choose the rings to be offset by b grid points along the x_1-direction.

We find that for a finite impact parameter, the vortex rings tilt within the (x_1, x_3)-plane before they reconnect and create new vortex rings which eventually fly away from the interaction region under an angle θ relative to the longitudinal direction. Henceforth, we will for obvious reasons refer to the (x_1, x_3)-plane as the reaction plane. In figure 14.11 we schematically illustrate the scattering scenario, with scattering angle θ and impact parameter b. To give an example, an angle of $\pi/2$ corre-

sponds to the limiting scenario of a head-on collision in which case it is the rarefaction pulse which propagates away in a 90 degree angle relative to the longitudinal direction (*i. e.*, the x_3-axis) of the collision. We stress that for the chosen initial configuration of the vortex rings, the scattering takes place solely within the reaction plane vertically intersecting the vortex planes through the centres of the rings at fixed $x_2 = 48$, including the directions of the outgoing vortex rings. This feature of the dynamics simplifies our analysis significantly as it allows us to infer the scattering angle from the behaviour of the induced vortices on the two-dimensional reaction plane. We note that the rings displayed in figure 14.11 are actual solutions of vortex rings in the holographic superfluid and correspond to isosurfaces of the condensate density $n(\boldsymbol{x})$. For a better visualisation, we only show half of the rings.

Our goal for this section is to study the scattering of the two rings as a function of their impact parameter. In particular, we analyse the functional dependence of the scattering angle on the impact parameter b within the interval $b/R_0 \in [0,3]$. Here, $b/R_0 = 0$ corresponds to a head-on collision. In practice, we scan through the values of b/R_0 in increments of $\Delta(b/R_0) = 0.2$, except in the vicinity of points where we find the functional dependence to change, in which case we employ $\Delta(b/R_0) = 0.1$ in order to obtain a higher resolution. To extract the scattering angle from the reconnected vortex rings, we again employ the two-dimensional NR method to locate the induced vortices on the (x_1, x_3)-plane. From the asymptotic positions of the scattered vortex rings, *i. e.*, the positions shortly before the rings shrink to zero size and disappear, we then infer θ. In practice, we extract the scattering angle from the configuration of the vortex rings at one unit timestep before they shrink to zero size and their respective phase-winding structures disappear. We estimate the uncertainty of the scattering angle θ to be of the order of $\Delta\theta = \pm 0.02$. This uncertainty originates from the uncertainty in the tracking procedure used to locate the rings as well as by comparing the results for the two vortex rings flying away from the interaction region.

In figure 14.12 we display our results for the scattering angle θ as a function of the normalised impact parameter b/R_0. We find that the dynamics of the scattering vortex rings can be split into three regimes. In figure 14.12 we mark the transition points between these regimes by the vertical dotted black lines. We note, however, that despite marking distinct points, the transitions are continuous processes which proceed over a short but finite interval of impact parameters. In the following we discuss the qualitative behaviour of the vortex rings as well as the functional dependence of the scattering angle on the impact parameter in all three regimes. In figure 14.13 we show six characteristic snapshots of the time evolution of the scattering vortex rings for one exemplary impact parameter of each of the three regimes. The characteristic times the snapshots are taken at are chosen to best illustrate the details of the respective vortex-ring dynamics. Naturally, the times therefore differ for the respective values of the impact parameters, including in particular the time of the first snapshot. In order to fully capture the dynamics, we choose to show some snapshots even before the vortex rings have fully developed their density profile, which they have after the first five unit timesteps.
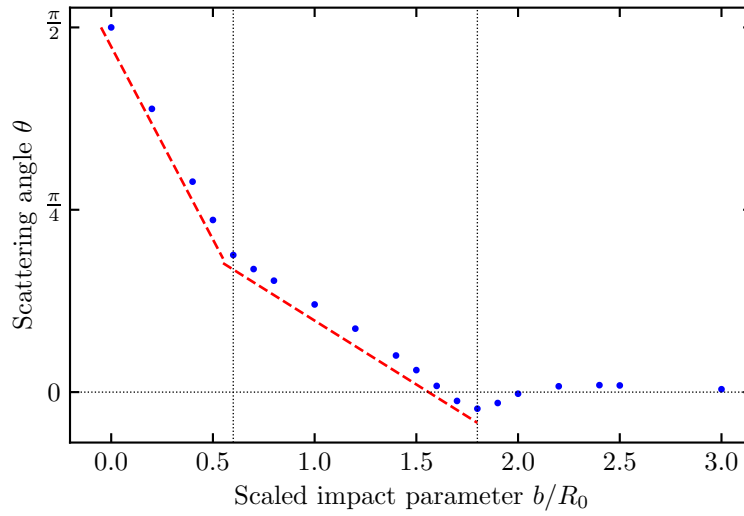
Figure 14.12: Scattering angle θ of the vortex rings as a function of the normalised impact parameter b/R_0, where R_0 denotes the initial radius of the rings. We find three qualitatively and quantitatively different scattering scenarios, separated by the dotted vertical black lines. The dotted horizontal black line depicts a scattering angle of zero. In the first and second scenario, the scattering angle decreases approximately linearly with b/R_0 as illustrated by the dashed red lines (deliberately shifted below the data points).

The first regime comprises all impact parameters in the interval $b/R_0 \in [0, 0.6]$. Here, we include the head-on collision in light of our findings regarding the dependence of the scattering angle on b/R_0, displayed in figure 14.12. Nevertheless, we point out that the qualitative behaviour of the head-on collision is not exactly the same as for the scattering events with a finite impact parameter in this regime. We comment on the differences, but also on the commonalities, as we go along. For an exemplary non-zero impact parameter in the considered interval, given by $b/R_0 = 0.4$, we show eight characteristic snapshots of the scattering process in figure 14.13i. We again plot isosurfaces of $n(\boldsymbol{x})$ with a defining value of $n/n_0 = 0.12$. The snapshots illustrate the qualitative behaviour of the rings for all impact parameters in the interval, except for the head-on collision. The images in figure 14.13i show that the rings tilt within the reaction plane as they approach each other, *cf.* panels (a)–(c). The behaviour of each individual ring is again induced by the phase structure of the respective other ring. As a side remark, we note that in order to aid the visualisation, the camera view used to take the snapshots is slightly tilted relative to the reaction plane, which should not be confused with a motion of the rings out of the reaction plane. As the rings tilt, their radii grow in size, just like we have found for the head-on collision. Interestingly, the tilting causes the rings to experience
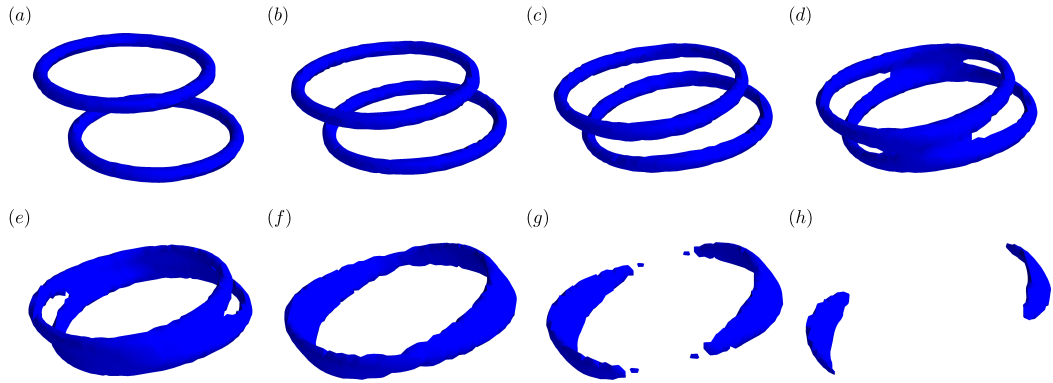
(i) First scenario ($b/R_0 = 0.4$). The snapshots are taken at times (a) $t = 5$, (b) $t = 12$, (c) $t = 16$, (d) $t = 18$, (e) $t = 20$, (f) $t = 23$, (g) $t = 24$, and (h) $t = 26$.
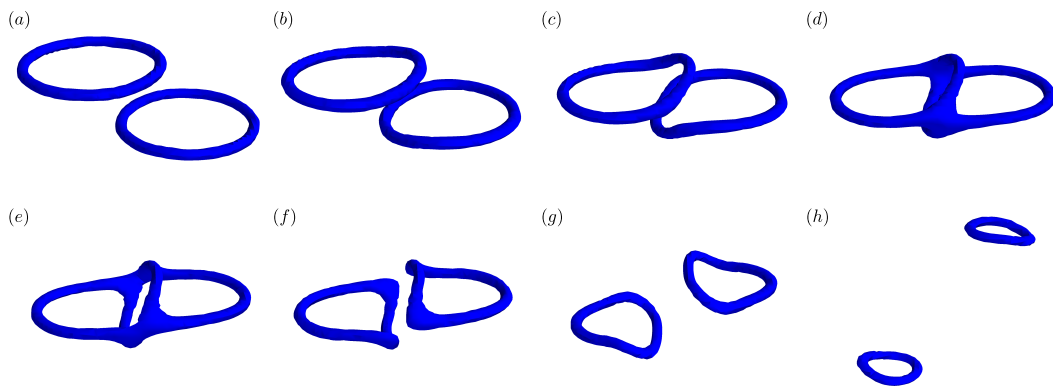
(ii) Second scenario ($b/R_0 = 1.4$). The snapshots are taken at times (a) $t = 3$, (b) $t = 10$, (c) $t = 18$, (d) $t = 21$, (e) $t = 24$, (f) $t = 25$, (g) $t = 31$, and (h) $t = 52$.
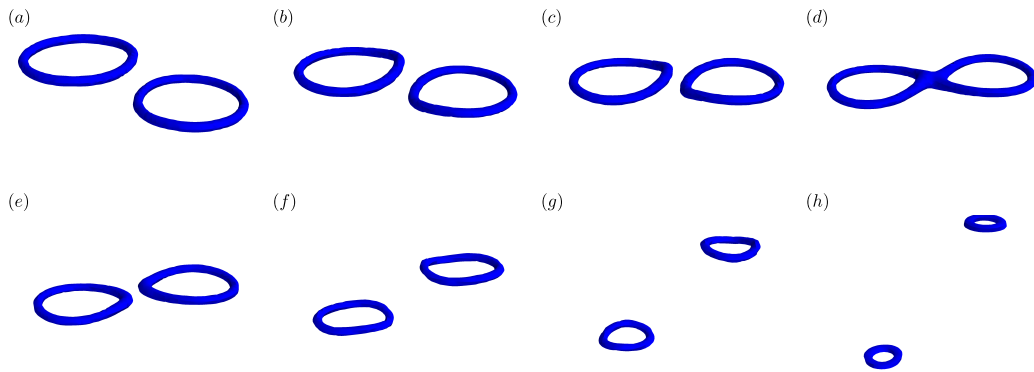
(iii) Third scenario ($b/R_0 = 2.0$). The snapshots are taken at times (a) $t = 4$, (b) $t = 13$, (c) $t = 20$, (d) $t = 24$, (e) $t = 27$, (f) $t = 37$, (g) $t = 48$, and (h) $t = 57$.

Figure 14.13: Snapshots of isosurfaces of the condensate density $n(\boldsymbol{x})$ (defining value $n/n_0 = 0.12$) showing the characteristic stages of the time evolution of scattering vortex rings for three different impact parameters $b/R_0 = 0.4$ (panel (i)), $b/R_0 = 1.4$ (panel (ii)), and $b/R_0 = 2.0$ (panel (iii)), representing the three scattering regimes.

267

deviations from their plane circular shape. As panels (c) and (d) illustrate, the two halves of each ring, to the left and right of the contact axis of the two rings (parallel to the x_2-axis), bend in the direction opposite to the respective other ring. Due to the bending, the rings do not simply annihilate at all point simultaneously as was the case for the head-on collision, but instead reconnect at the two points that come into contact first, *cf.* panels (d)–(f). This results in the formation of two new, strongly deformed, vortex rings which have folded arc-shaped cores, *cf.* panel (d)–(e). Due to the strong bending of these rings, they do not unfold with proceeding time. Instead, they remain folded and gradually shrink due to the annihilation of points on the upper half with opposite points on the lower half of each of the arc-shaped cores, *cf.* panels (d)–(g). Hence, loosely speaking, for each ring the respective upper half annihilates the lower half (as part of a continuous process). Since the two upper halves and the two lower halves of the new rings originate from the former upper ring and the former lower ring in the initial configuration, respectively, each point of a former ring therefore annihilates with another point of the respective other ring. This is a feature the scattering vortex rings have in common with the head-on colliding vortex rings studied in the previous chapter. A difference between the two scenarios, however, is that, unlike in the head-on collision, here, not all points of the cores annihilate simultaneously but instead successively. During the annihilation process of the two vortex rings studied here, they create rarefaction pulses, *cf.* panels (g) and (h), which, however, are not axisymmetric as in the head-on collision. Instead they are (asymptotically) restricted to the reaction plane in which the scattering takes place. The broken axial symmetry is an important difference to the head-on collision. Within the first scattering regime, we find the scattering angle to depend approximately linearly on the impact parameter, *cf.* figure 14.12, following the functional dependence

$$\theta \approx -1.67\frac{b}{R_0} + 1.57\,. \tag{14.1}$$

The second regime comprises all impact parameters in the interval $b/R_0 \in (0.6, 1.8]$. In figure 14.13ii we illustrate eight characteristic snapshots of the scattering process for one exemplary impact parameter of this regime, given by $b/R_0 = 1.4$. Before the rings come into contact, the behaviour is qualitatively the same as in the first regime discussed above. Namely, the rings grow in size and tilt within the reaction plane (the (x_1, x_3)-plane) as they approach each other. In the second regime, however, the bending of the respective halves of the vortex rings is much stronger, *cf.* panels (a)–(c). With proceeding time, the two rings reconnect at the two points that are closest to one another (panels (d) and (e)). Let us stress that despite the appearance in the figure, at every time during the scattering process, there are only two rings present. The reason panels (a)–(c) suggest the existence of three rings is only because the superfluid density between the rings is too small to be resolved by the isosurfaces. Due to the strong bending of the two halves of each vortex ring in the direction opposite to the vortex plane of the other ring, opposite points of these rings do not simply annihilate as in the first regime. Instead, the two rings,

which are highly excited by quadrupole oscillations, unfold and fly apart, *cf.* panels (*f*)–(*g*). With proceeding time, the excitations damp out and the rings gain a plane circular shape, *cf.* panel (*h*). Eventually, the rings shrink to zero size and leave behind rarefaction pulses. These waves are again not azimuthally symmetric but instead concentrated in the reaction plane. We find the scattering angle to depend approximately linearly on the impact parameter,

$$\theta \approx -0.55 \frac{b}{R_0} + 0.94 \,, \tag{14.2}$$

with a different slope and offset than in the first regime, *cf.* figure 14.12. It is interesting to note that for large impact parameters the scattering angle turns negative without changing the qualitative behaviour of the rings or the functional dependence of the scattering angle. This is also nicely visible in figure 14.12.

The third regime comprises all impact parameters $b/R_0 > 1.8$. In this regime, the two vortex rings do not reconnect as in the previous two regimes but instead only interact in a fly-by manoeuvre. For an exemplary impact parameter of $b/R_0 = 2.0$, we illustrate the time evolution of the rings in eight characteristic snapshots in figure 14.13iii. Due to the phase structure of each ring, the respective other ring is again slightly tilted and excited by small oscillations of the vortex core. However, the large transverse separation between the rings prohibits their reconnection. Instead, the rings only interact via their phase structures and then fly off. As they separate from another, the wavy excitations quickly damp out and the rings regain their plane circular shape. If the impact parameter is not too large, the density depletions of the rings overlap, as is clearly discernible in panel (*d*) of figure 14.13iii. Thereafter, the rings fly apart and eventually shrink to zero size and leave behind a rarefaction pulse. Close to the lower cutoff of the impact-parameter interval, the scattering angle is negative and then gradually increases again before it reaches a maximum at very small positive values and subsequently approaches zero. It appears likely that the small positive scattering angles are due to numerical uncertainties. In particular, they are all of the order of the uncertainty of θ.

The qualitative behaviour of the scattering vortex rings in the holographic superfluid is very similar to the analogous behaviour of vortex rings studied in the Gross–Pitaevskii model in [398]. The authors of [398] also find the dynamics of the vortex rings to split into three distinct regimes as a function of their impact parameter. Moreover, the qualitative behaviour of the vortex rings in each regime is similar to the behaviour in the holographic system, described above. Likewise, in [398] the authors also find the scattering angle in the first two regimes to depend approximately linearly on the impact parameter b/R_0. The qualitative agreement of the results is very remarkable since in [398] the studied superfluid is non-dissipative whereas the holographic superfluid is strongly dissipative as our studies in the previous chapters haven shown. However, while the qualitative behaviour agrees, there are indeed some minor differences on the quantitative level which we attribute solely to the dissipative nature of the holographic system. The deviations concern in particular the details of the classification of the three regimes. The authors of [398]

find slightly different transition points as compared to our results depicted in figure 14.12. The reason is that unlike in the GP model, the vortex rings in the holographic superfluid are exposed to an additional Magnus force, caused by the dissipative nature of the system, pointing along the radial direction towards the centre of the respective rings. Consequently, if the radii in the initial vortex-ring configuration agree in the GP model and holography, they are no longer equal during the actual scattering event and thus lead to different qualitative and quantitative behaviour, explaining why the transition points differ slightly. Another difference between the results of [398] and ours concerns the details of the functional dependence of the impact parameter on the scattering angle. We find slightly different slopes and off-sets as compared to [398]. Naturally, such differences are also expected from our previous discussion and can be attributed to the large dissipation in the holographic framework.

14.3 Kelvin-Wave Excitations of Vortex Rings

In the previous section we have found that the scattering of two vortex rings can result in the formation of two new vortex rings which are excited by quadrupole oscillations, *cf.* figure 14.13ii. Likewise, even the mere fly-by manoeuvre of two rings can induce oscillations on the vortex cores, *cf.* figure 14.13iii. In general, such wavy excitations of the vortex cores are known as Kelvin waves. As we have seen in the previous section, for vortex rings in the holographic superfluid, such waves are quickly damped out and the rings become plane circular in shape. Upon closer inspection, we find that we have also encountered Kelvin waves in chapter 13 in our studies of superfluid turbulence. Indeed, after every reconnection of two vortex structures, the new lines and rings carry Kelvin excitations. Our goal for this chapter now is to explicitly investigate Kelvin waves of vortex rings in the holographic superfluid. In particular, we want to gain an understanding of their dynamics in a strongly dissipative superfluid. This is essential also if one wants to investigate the head-on collision of two vortex rings carrying Kelvin-wave excitations discussed in section 14.1.

Only a few years after Helmholtz first introduced vorticity and in particular vortex rings, wavy excitations thereof were first studied by Lord Kelvin [473] to whom they also owe their name. Shortly thereafter, similar studies were performed also by J.J. Thomson [474]. Nowadays, Kelvin waves are known to play a crucial role in classical as well as quantum turbulence [399]. It has been shown that they yield a contribution to the turbulent transport of energy from small to large momentum scales [373, 374, 475]. In addition, Kelvin waves are known to dissipate energy by radiating sound excitations [476, 477]. Understanding their characteristics and impact on the superfluid dynamics is therefore important for a better understanding of the turbulent state of a superfluid.

Our procedure in this section is as follows. Instead of creating the excitations dynamically in the interaction of two vortex rings, we directly imprint them onto

the initial configuration of a vortex ring and subsequently study their evolution as we propagate the system in time. To be specific, we always study single vortex rings which we by hand perturb with various Kelvin waves.

Vortex rings can either be perturbed by Kelvin waves within the vortex plane, out-of-plane, *i. e.*, along their axial direction, or helically, *i. e.*, by a combination of planar and out-of-plane excitations. For a single vortex ring, the respective phase-winding structures can be inferred directly from our discussion in section 12.1. In fact, we only have to slightly modify the phase-winding configuration (12.3) of an unperturbed plane circular vortex ring. To do this explicitly, let us again assume that the vortex ring has an initial radius of R_0, a winding number given by w and is aligned in parallel to the (x_1, x_2)-plane with its centre located at $(x_1, x_2)=(x_{1,0}, x_{2,0}, x_{3,0})$. Accordingly, we denote the amplitude of planar Kelvin waves as A_{x_1,x_2} and the amplitude of out-of-plane excitations as A_{x_3}. Furthermore, we use N_{x_1,x_2} and N_{x_3} to denote the respective wave numbers. The phase configuration of a perturbed vortex ring is then obtained by replacing the radial coordinate

$$\rho(x_1, x_2) \rightarrow \rho(x_1, x_2) - A_{x_1,x_2} \sin(N_{x_1,x_2}\beta) \tag{14.3}$$

for planar oscillations and the axial coordinate

$$x_3 \rightarrow x_3 - A_{x_3} \sin(N_{x_3}\beta) \tag{14.4}$$

for out-of-plane oscillations in equation (12.3). Here, we have introduced the polar angle β of the vortex plane, given by

$$\beta(x_1, x_2) = \arctan\left(\frac{x_2 - x_{2,0}}{x_1 - x_{1,0}}\right), \tag{14.5}$$

and again made use of the planar radius $\rho(x_1, x_2)$, defined as the radial distance away from the centre of the ring within the vortex plane. In their most general form, the two phase contributions (12.3), whose sum yields the total winding structure of the vortex ring, are therefore given by

$$\varphi^{\pm}(\boldsymbol{x}) \equiv \pm w \arctan\left(\frac{x_3 - A_{x_3} \sin(N_{x_3}\beta) - x_{3,0}}{\rho - A_{x_1,x_2} \sin(N_{x_1,x_2}\beta) \mp R_0}\right). \tag{14.6}$$

To find the corresponding vortex solution of the holographic superfluid, we proceed just as before and multiply the total phase configuration of the perturbed ring into the background solution of the scalar field $\Phi(t_0, \boldsymbol{x}, z) \rightarrow \Phi(t_0, \boldsymbol{x}, z)\, e^{i\{\varphi^+(\boldsymbol{x}) + \varphi^-(\boldsymbol{x})\}}$, and upon propagating the system in time the vortex builds up dynamically. As before, we do not additionally set the scalar field to zero in the initial configuration. For all simulations in this section we employ a grid size of 96^3 points along the (x_1, x_2, x_3)-directions and a chemical potential of the holographic superfluid given by our standard choice of $\mu = 5$.

We begin our studies with a vortex ring of radius $R_0 = 18$ grid points, initially perturbed by planar Kelvin waves of amplitude $A_{x_1,x_2}/R_0 = 0.4$ and wave number $N_{x_1,x_2} = 5$. In figure 14.14 we show six characteristic snapshots of the time
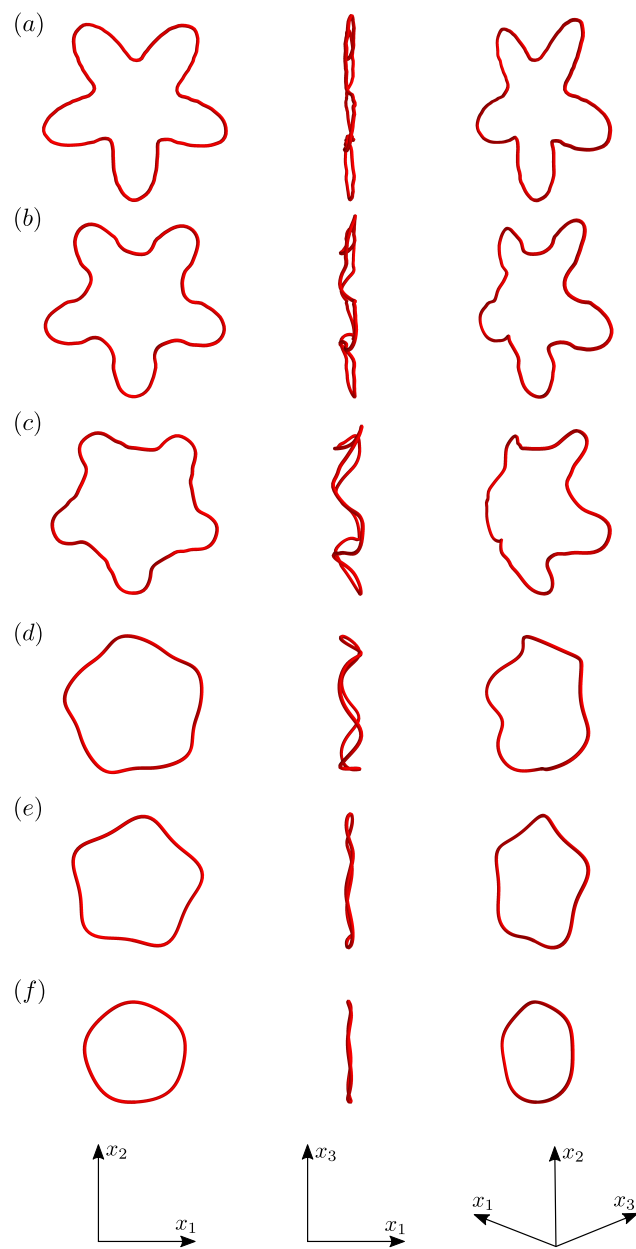
Figure 14.14: Snapshots of the time evolution of a vortex ring initially perturbed by planar Kelvin waves of amplitude $A_{x_1,x_2}/R_0 = 0.4$, where $R_0 = 18$ grid points is the initial radius of the ring, and wave number $N_{x_1,x_2} = 5$. Shown is the vortex core of the ring, obtained from the three-dimensional tracking routine. The snapshots are taken at times (a) $t = 1$, (b) $t = 3$, (c) $t = 7$, (d) $t = 15$, (e) $t = 25$, (f) $t = 56$.

evolution of the ring. We show the ring from three different perspectives, the top view along the axial direction, the side view along the x_2-direction and along the diagonal between the x_1- and x_3-axis. Notably, here we do not plot isosurfaces of the superfluid-condensate density $n(\boldsymbol{x})$. Instead, we plot only the vortex core itself by employing a tracking routine that allows us to locate the one-dimensional core in the three-dimensional computational domain. The tracking routine is a generalisation of the Newton–Raphson method, that we have so far used throughout this thesis, to three spatial dimensions and was first introduced in [291]. We give details on the tracking routine in appendix A.6. The reason we switch our illustration scheme for the vortex rings is that, we find that for large wave numbers or large amplitudes of Kelvin excitations, isosurfaces can no longer properly resolve the vortex core structure. Indeed, resolving them would require going to distinctly smaller defining values of the isosurfaces, which, however, is plagued by numerical errors in the interpolation of the field configuration at inter-mesh grid points. Therefore, we found it easier to employ the tracking routine. Another crucial advantage is that the vortex core builds up within less than one unit timestep (*i. e.*, the density drops to zero) while the density modulation around the core takes distinctly longer to develop its characteristic profile. Hence, the tracking routine allows us to show the vortex-ring configuration for all times $t \geq 1$ unit timesteps.

The images in figure 14.14 illustrate that despite initialising the ring with only planar oscillations (within the (x_1, x_2)-plane), out-of-plane oscillations (along the x_3-axis) build up dynamically. The reason for this is the phase structure of the vortex ring. In chapter 12 we have argued that due to its phase structure, an axisymmetric and circular vortex ring has a self-induced velocity which is the same for every point of the vortex core. For convenience, we also recall that not only rings, but also every finite curvature segment of a one-dimensional vortex core has a local self-induced velocity. For a vortex ring disturbed by Kelvin excitations, the ring is composed of segments of different curvatures, which in particular differ from the curvature of an unperturbed ring. Due to the different curvature of the segments, their velocities along the axial direction of the ring differ from the total axial velocity of the ring. Consequently, out-of-plane oscillations build up. At time $t = 1$, *cf.* panel (*a*), the build-up process has already significantly deformed the ring. Nevertheless, one can still recognise the initial configuration with planar oscillations only. The remaining snapshots are taken at times $t = 3, 7, 15, 25, 56$. Within the first few unit timesteps of the evolution, the amplitude A_{x_3} along the x_3-direction increases gradually, *cf.* panels (*a*)–(*c*). Simultaneously, the planar amplitude A_{x_1, x_2} already decreases and the Kelvin waves are damped out. Only a few unit timesteps later, also the out-of-plane amplitude decreases due to the strong damping. We find that A_{x_3} reaches its maximum at time $t \approx 9$. Furthermore, for the given set of initial parameters, we find that it takes approximately $\Delta t = 65$ unit timesteps before the Kelvin waves are fully damped out and the ring has regained its circular shape. This time interval barely comprises one full period of the Kelvin oscillations. In GPE simulations of Kelvin excitations on vortex rings, one has found the angular frequency ω of the

Kelvin waves to depend on their amplitude[5] [478]. Based on the similarities of the GPE vortices and holographic vortices found in the previous chapters, we expect the same to be true also for the Kelvin excitations of vortex rings in the holographic superfluid. Hence, for the configuration depicted in figure 14.14, we expect the angular frequency to change dynamically as the system is propagated in time due to the decrease in the amplitudes. This gradual change of the Kelvin-wave amplitudes makes it impossible to determine the dependence of ω on the amplitude, which would require the amplitude to be constant for a certain time interval, for vortex rings in the holographic superfluid, as it has been done for vortex rings in a non-dissipative superfluid in [478].

In addition to the initial planar Kelvin-wave excitations, we also study helical Kelvin-wave excitations of vortex rings. To be specific, we study a vortex ring of radius $R_0 = 18$ grid points, perturbed by planar as well as out-of-plane excitations of amplitudes $A_{x_1,x_2}/R_0 = A_{x_3}/R_0 = 0.3$ and wave numbers $N_{x_1,x_2} = N_{x_3} = 10$, respectively. In figure 14.15, we show six characteristic snapshots of the time evolution of the vortex ring. Like before, we employ the three-dimensional tracking routine to locate the ring and correspondingly plot only its one-dimensional core. Moreover, we again show the ring from three different perspective to aid the visualisation of the Kelvin waves. The snapshots are taken at times $t = 1, 4, 10, 14, 20, 34$. Interestingly, we find that the Kelvin waves do not oscillate harmonically. The anharmonicity is most evident in the top view of the ring displayed in panels (a)–(c) on the left-hand side of figure 14.15. In a more systematic investigation of this phenomenon we find that the oscillations become anharmonic if the wave numbers or the Kelvin-wave amplitudes are too large. In particular, the oscillations are not always anharmonic for helical oscillations. If the amplitudes or wave numbers are significantly lowered, the oscillations are harmonic. We refrain from showing examples here explicitly due to their overall similarity to the results displayed in figure 14.14. With proceeding time, the amplitudes of the Kelvin waves quickly damp out, in approximately the same rate for the planar and the out-of-plane oscillations. Once the amplitudes have, in a sense, 'sufficiently' damped out, the oscillations turn harmonic, *cf.* panels (d)–(e). At even later times, the waves are fully damped out and the ring regains its plane circular shape, *cf.* panel (f).

In the literature, one finds that helical Kelvin waves have a very remarkable effect on the motion of the vortex ring itself. Namely, they slow down the axial velocity of the ring relative to an unperturbed ring of the same (initial) radius. This, on the first sight, rather surprising feature of Kelvin waves was first reported for vortex rings in classical liquids in [479] and later confirmed in numerical simulations in [478]. Moreover, it has been shown to hold for quantised vortex rings in non-dissipative condensates [480]. In the following we want to study if the same holds true for vortex rings in dissipative superfluids, such as the holographic system. We compare the

---

[5]In fact, if the amplitude is infinitesimally small, the angular frequency is independent of the amplitude. There is only a dependence for larger amplitudes, see [478] and references therein for details.
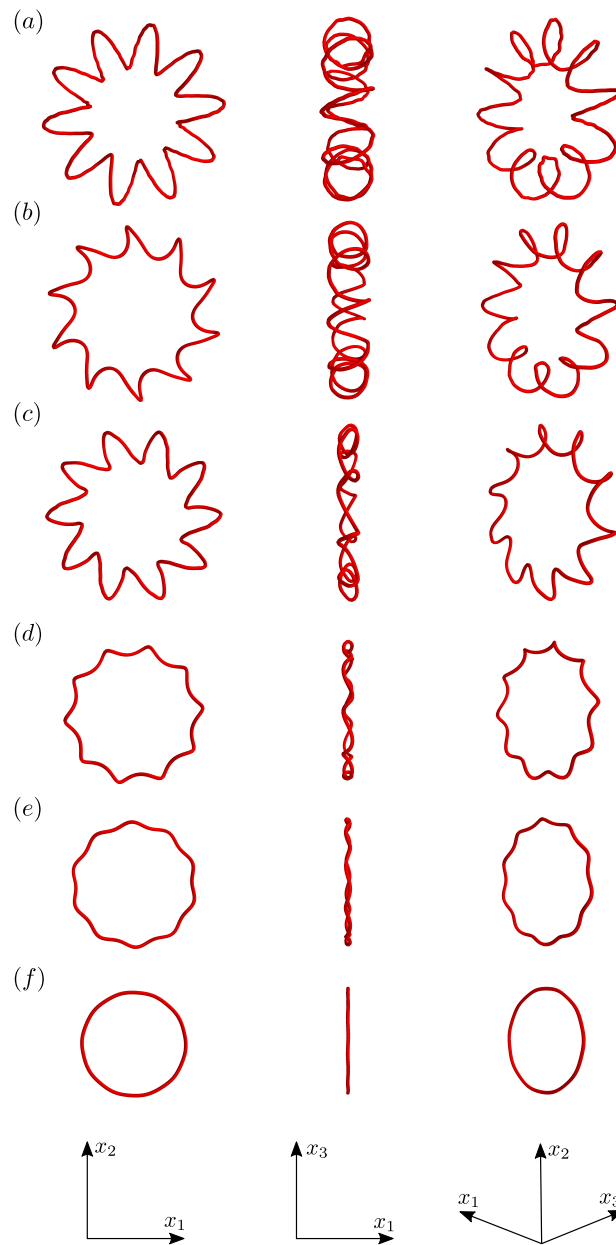
Figure 14.15: Snapshots of the time evolution of a vortex ring initially perturbed by helical Kelvin waves of amplitude $A_{x_1,x_2}/R_0 = A_{x_3}/R_0 = 0.3$, where $R_0 = 18$ grid points is the initial radius of the ring, and wave numbers $N_{x_1,x_2} = N_{x_3} = 10$. Shown is the vortex core of the ring, obtained from the three-dimensional tracking routine. The snapshots are taken at times (*a*) $t = 1$, (*b*) $t = 4$, (*c*) $t = 10$, (*d*) $t = 14$, (*e*) $t = 20$, (*f*) $t = 34$.
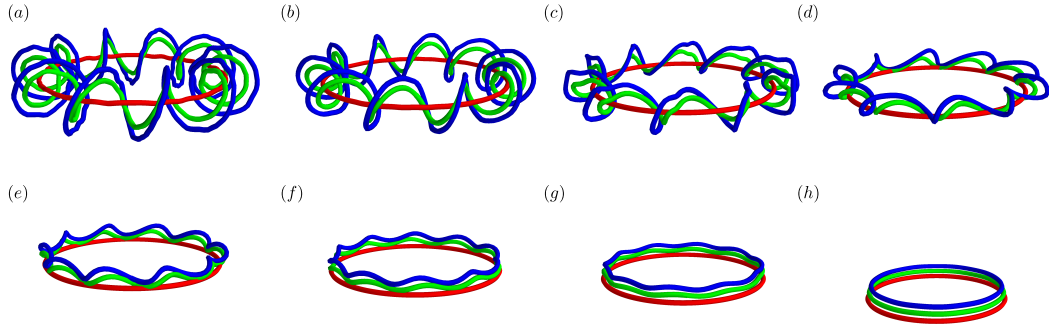
Figure 14.16: Eight characteristic snapshots of the time evolutions of three vortex rings with the same initial radius ($R_0 = 18$ grid points), illustrating the slow-down effect of Kelvin waves. The dynamics of the rings is computed in three different simulations and we show only the vortex cores, obtained from the three-dimensional tracking routine. The blue and green rings are perturbed by Kelvin waves of amplitudes $A_{x_3}/R_0 = A_{x_1,x_2}/R_0 = 0.3$ and $A_{x_3}/R_0 = A_{x_1,x_2}/R_0 = 0.22$, respectively, and both have wave numbers $N_{x_3} = N_{x_1,x_2} = 10$, while the red ring is unperturbed. The perturbed rings are distinctly slower than the unperturbed ring and the larger the amplitude of the Kelvin waves, the slower are the rings. The snapshots are taken at times (*a*) $t = 1$, (*b*) $t = 4$, (*c*) $t = 8$, (*d*) $t = 11$, (*e*) $t = 14$, (*f*) $t = 19$, (*g*) $t = 25$, (*h*) $t = 39$.

vortex-ring dynamics depicted in figure 14.15 with the dynamics of an unperturbed vortex ring with the same initial radius of $R_0 = 18$ grid points. In addition, we add to the comparison another vortex ring of radius $R_0 = 18$ grid points which we initially perturb by helical Kelvin waves of amplitudes $A_{x_1,x_2}/R_0 = A_{x_3}/R_0 = 0.22$ and wave numbers $N_{x_1,x_2} = N_{x_3} = 10$. Note that the wave numbers agree with those of the ring studied above while the amplitudes are smaller. We compute the dynamics of the three vortex rings in three separate simulations and employ the three-dimensional tracking routine to locate their cores. In the respective initial configurations, the centre positions of all three rings agree. In figure 14.16, we show the time evolution of all three vortex rings. For a direct comparison of the vortex-ring dynamics, we display all three rings in the same plot and use different colours to aid the identification. Remarkably, despite the large dissipation in the holographic superfluid and thus the quick damping of the Kelvin waves, the perturbed vortex rings are distinctly slower than the unperturbed ring (red). Moreover, the ring with the larger Kelvin-wave amplitudes (blue) is slower than the one with the smaller amplitudes (green). Our findings therefore show that the prediction in [479], made for classical vortices, is also true for quantised vortex rings in dissipative superfluids.

The reason a perturbed vortex ring is slowed down relative to an unperturbed

ring are yet again the various segments of different curvature of the perturbed ring, induced by the Kelvin waves. Indeed, as we have argued before, due to the Kelvin waves the ring has segments of different curvature which all have their own self-induced velocity, which typically differs in magnitude and direction from the velocity an unperturbed ring of the same radius has. In particular, there typically exist curvature segments for which the axial velocity component points in the direction opposite to the axial vortex-ring motion. As a consequence, the axial motion of the ring is slowed down. For initial planar oscillations, we cannot identify such an effect.

A priori, one might expect that a further increase in amplitude or wave number of the Kelvin waves slows the axial motion of the vortex ring even further. Indeed, this naive expectation has been confirmed for vortex rings in classical liquids [478]. The authors of [478] find that upon gradually increasing the wave numbers or amplitudes of the waves, the rings can be forced to hover or even reverse their motion. It is therefore interesting to study if we find similar effects also for quantised vortex rings with large Kelvin waves in a dissipative superfluid described in the holographic framework. We consider a vortex ring of initial radius $R_0 = 18$ grid points, perturbed by Kelvin waves of amplitudes $A_{x_1,x_2}/R_0 = A_{x_3}/R_0 = 0.56$ and wave numbers $N_{x_1,x_2} = N_{x_3} = 10$. In figure 14.17 we show six characteristic snapshots of the corresponding time evolution of the ring. Given the larger Kelvin waves, we find that it takes distinctly larger for the condensate density to drop to zero at the core of the vortex ring and for the density profile around the core to build up. We attribute this to the high density of Kelvin waves, *i. e.*, their close proximity among another, and thus the associated small structures that have be created dynamically. For times prior to $t = 6$, we find that isosurfaces cannot accurately resolve the ring and neither can the tracking routine unambiguously track its core. The first snapshot of the ring shown in figure 14.17 is therefore taken at time $t = 6$. The remaining images correspond to times $t = 9, 12, 15, 16, 18$. At early times, the Kelvin waves evolve qualitatively similar to what we have found above for the ring with smaller Kelvin-wave amplitudes, *cf.* panels (a)–(c). However, at some later time, but still early in the evolution (at $t \approx 15$), the large-amplitude Kelvin waves induce several reconnections of the vortex ring along its core, *cf.* panels (d)–(e). In these reconnections, one large (main) vortex ring plus ten additional, much smaller, rings are created. Thereafter, the small rings quickly fly away from the main ring and, in the meantime, shrink to zero size and disappear. The main ring, on the other hand, retains only minor Kelvin excitations which are quickly damped out, *cf.* panel (f). Hence, we find that for 'too large' amplitudes, the ring does not simply slow down but instead becomes unstable and undergoes reconnections with itself. The same scenario occurs also if we initially imprint the Kelvin waves with 'too large' wave numbers. In particular, in our studies we did not find a situation in which a ring hovers or even reverses its motion. One may, however, speculate if such effects can found for distinctly larger vortex rings, which, if unperturbed, have a much slower axial velocity which could more easily be reversed, simulated on very large numerical grids. For quantised vortex rings in the GP model [480], similar results to ours presented above have been found. Just like in the holographic system, also in
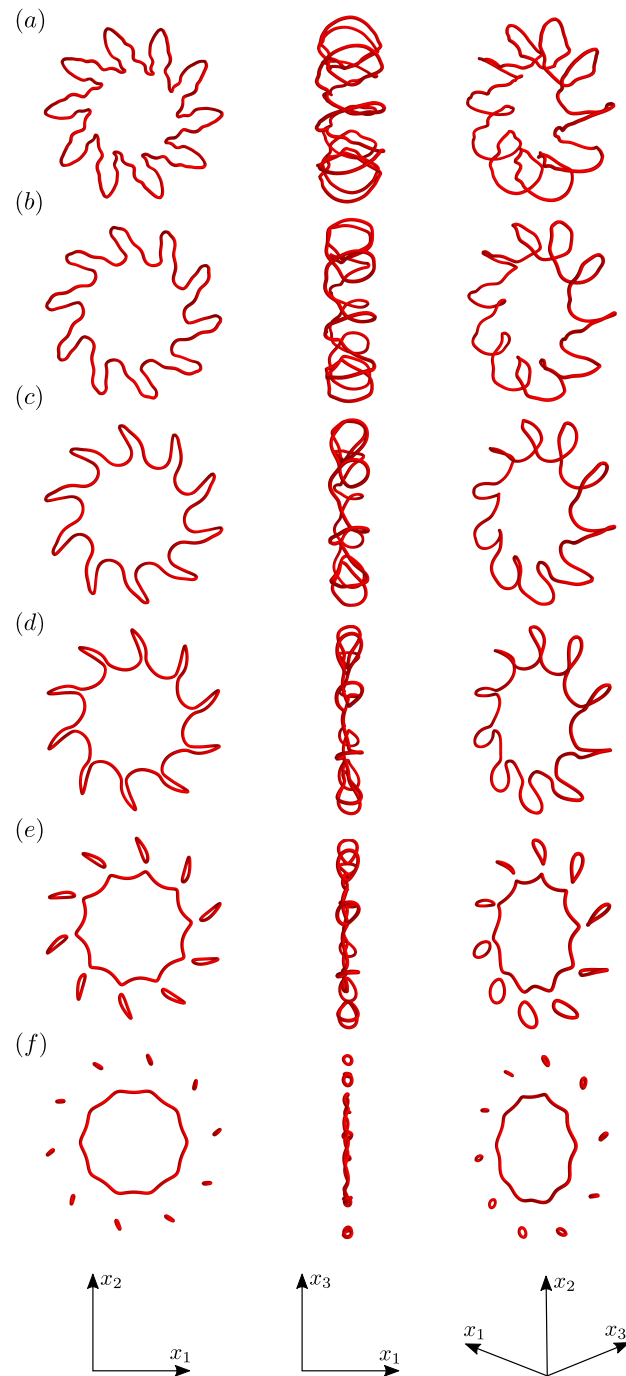
Figure 14.17: Snapshots of the time evolution of a vortex ring initially perturbed by helical Kelvin waves of amplitude $A_{x_1,x_2}/R_0 = A_{x_3}/R_0 = 0.56$, where $R_0 = 18$ grid points is the initial radius of the ring, and wave number $N_{x_1,x_2} = 10$. Note that the amplitude of the Kelvins waves here is distinctly larger than in figure 14.15. Shown is again the vortex core of the ring, obtained from the three-dimensional tracking routine. The snapshots are taken at times (a) $t = 6$, (b) $t = 9$, (c) $t = 12$, (d) $t = 15$, (e) $t = 16$, (f) $t = 18$.

the GP model the rings reconnect with themselves if the excitations are too large. Furthermore, also in [480], the authors could not find hovering vortex rings. The reason such behaviour has been observed for vortex rings in classical liquids is that in those systems, reconnections are prohibited and the type of instabilities we find in the rings are therefore precluded.

In the introduction to this section we have mentioned that in the GP model it has been shown that Kelvin waves send out rarefaction pulses and sound waves [476, 477], and are central for the transport of energy in the system [373, 374, 475]. Based on the similarity between the vortex dynamics in the GP model and the holographic superfluid discussed in this and the previous chapters, we expect that the same holds true also in the holographic framework. In our studies in this thesis we have found first evidence suggesting that Kelvin waves in the holographic superfluid indeed send out sound waves. However, we have not analysed this on a quantitative basis. Instead, we have studied the bulk-field configuration, specifically the bulk scalar charge density, dual to the superfluid in the presence of a vortex ring perturbed by Kelvin waves. Outgoing from certain two-dimensional slices of the superfluid, we have found the charge density to be perturbed by small notches and riddles. As we have argued in chapter 12, this is strong evidence for the presence of sound waves in the superfluid. There is, however, a subtlety. The Kelvin waves in the holographic superfluid are quickly damped out due to the large dissipation. Consequently, there is only a short time period during which one would expect the system to carry sound excitations. We have found the small perturbations of the charge density only during the very early stages of the evolution of the perturbed vortex rings. At these times, however, we expect sound waves to be present also due to the initial build-up of the vortex profile in the condensate density. In our studies, we could not unequivocally exclude the possibility that the perturbations of the charge density are remnants of this build-up process and thus not due to sound waves radiated by the Kelvin waves. It would be very interesting to follow up on this investigation in a future work.

15 Summary of Part II

In the second part of this thesis, we have studied vortex solutions and the far-from-equilibrium dynamics of a three-dimensional holographic superfluid. The holographic framework allows for a fundamental description of a strongly correlated and dissipative superfluid in three spatial dimensions by means of an Abelian Higgs model in a $(4+1)$-dimensional anti-de Sitter-black-hole background. We have for the first time constructed and analysed vortex solutions of the holographic superfluid, investigated the dynamics of single vortex rings, and studied turbulent behaviour of the superfluid induced by complicated tangles of vortex lines and rings. Moreover, we have studied interactions between as well as excitations of vortex rings. For our studies we have developed a fast numerical implementation of the equations of motion in the probe-approximation in which the condensate component of the superfluid is coupled to a static infinitely sized heat bath. In the literature, neither vortex solutions of the considered three-dimensional holographic superfluid nor the real-time non-equilibrium dynamics of the system had thus far been studied.

We started our investigations in chapter 12 with the construction and analysis of vortex-ring and vortex-line solutions of the three-dimensional holographic superfluid. We have argued that the vortex solutions of the superfluid build up dynamically upon multiplying the characteristic winding structure of the respective vortex defect into the static background solution of the dual Abelian Higgs model in the bulk and propagating the system in time. Due to the topological constraints imposed by the initial phase configuration, vortex structures in the gauge–matter sector build up on every fixed-z slice for all points of the dual vortex core in the superfluid. In particular, for every position of the vortex core, the scalar field vanishes along the holographic direction and thus pierces holes through the scalar charge density that screens the boundary from the black hole, *i. e.*, the superfluid from the thermal heat bath. Consequently, vortex defects are avenues for energy and momentum modes, with wavelengths of the order of the diameter of the respective vortex-induced density depletion, to fall into the black hole and thus dissipate. Hence, just like for the two-dimensional superfluid (see *e. g.* [148]), the holographic framework provides a very intuitive geometric interpretation of the dissipation mechanism.

In particular, the bulk configuration of vortices alone establishes that the holographic superfluid is in fact dissipative. Moreover, upon studying the bulk configuration outgoing from two-dimensional slices of the superfluid, we have conjectured that the system does not have a single unique dissipation scale. Instead, the wavelengths of modes that are preferably dissipated depend on the orientation of the wavevectors of these modes in the three-dimensional superfluid as well as on the considered vortex configuration. Outgoing from a two-dimensional plane that con-

tains a one-dimensional vortex core, for instance, the holes in the bulk charge density have a non-zero spatial extent. Thus, for modes oriented parallel to the vortex core, dissipation, unlike in the two-dimensional system, is not restricted solely to short-wavelengths (UV) modes. Instead, it appears likely that under certain favourable conditions, also distinctly larger wavelengths up to the IR scales of the system can dissipate their energy into the black hole. Outgoing from a plane that is intersected by a vortex core only once, on the other hand, the bulk view resembles the dual configuration of a vortex in the two-dimensional system and dissipation thus appears likely to be restricted to UV modes only. In addition to the dissipation scales, it appears likely that also the total energy and momentum flux into the black hole depends on the distribution of modes in the system.

In addition to the dual bulk representation of vortices, we have also analysed the characteristics of their profile in the condensate density of the superfluid. For small-curvature segments of vortex lines or vortex rings, we have found that the width ξ of the induced density depletion scales approximately as $\xi \sim (\delta\mu)^{-1/2}$, where $\delta\mu = \mu - \mu_0$ is the shifted chemical potential of the holographic superfluid and μ_0 agrees approximately with the critical chemical potential of the phase transition for fixed absolute temperature. The scaling behaviour coincides with the dependence of the GPE healing length on the GPE chemical potential and thus signals that in the superfluid phase and in the presence of topological excitations, the holographic framework describes a non-relativistic superfluid. Furthermore, we have found that the shape of the density depletion is in excellent agreement with the approximate solution of the vortex profile in the Gross–Pitaevskii model. Our results are consistent with our previous findings in Part I concerning the agreement of the vortex shapes and the dependences of the vortex width on the respective chemical potential in the two-dimensional holographic superfluid and in the two-dimensional GP model.

Going beyond the static aspects of vortex solutions, we have also investigated the dynamics of single plane circular vortex rings. We have made the interesting observation that vortex rings in the holographic superfluid undergo a rapid shrinking as they traverse the condensate with a velocity self-induced by their own phase configuration. Such a shrinking is characteristic for strongly dissipative superfluids and is caused by mutual friction between the vortex defect and the superfluid. Hence, by studying the dynamics of a single vortex ring we have established that the holographic superfluid in three spatial dimensions is strongly dissipative. For our quantitative analysis of the vortex-ring dynamics, we have extracted the trajectory of the ring from our simulations with inter-mesh accuracy. To be specific, we have applied our combined two-dimensional tracking routine of Part I to the superfluid configuration on a two-dimensional slice perpendicular to the vortex-plane intersecting the centre of the ring, since on such a plane the ring effectively reduces to a vortex–anti-vortex pair. From the quasi-continuous trajectory of the ring we have subsequently derived its velocities and accelerations, along its axial and radial directions. We have found that except for early times of the evolution, the dynamics of a vortex ring is independent of its initial configuration and solely parametrised by its radius. Only at early times, small deviations from the universal behaviour occur as

an artefact due to the way we prepare the initial vortex-ring configuration. During the final stages of the evolution, the vortex-ring dynamics is strongly dominated by the radial shrinking process of the ring and thus by the merging of vortex-induced density depletions. In particular, here the radial velocity is orders of magnitudes larger than the axial velocity which saturates shortly before the ring has shrunk to zero size.

We have also compared the dynamics of vortex rings to solutions of the Hall–Vinen–Iordanskii (HVI) equation for the mechanical motion of point-vortex rings in dissipative superfluids. Despite the limited applicability of this equation due to the finite width of the vortex-induced density depletions in the holographic system, we have found that there exists a regime at intermediate times of the ring's evolution during which the HVI equation describes the dynamics very well. In particular, we have found the dependence of the axial velocity on the radius of the ring in the holographic superfluid and the analogous solution of the HVI equation to coincide. The same holds true for the dependence of the squared radius of the ring on time.

Further in chapter 12, we have studied the dependence of the vortex-ring dynamics, specifically the vortex velocities, on the chemical potential of the holographic superfluid. In order to account for the dependence of the vortex width on the chemical potential in this comparison, we have compared the velocities as a function of the ring's radii expressed in units of the healing length of the respective system. We have found that both velocity components, along the radial as well as the axial direction, are ordered with the chemical potential. At a fixed radius (in units of the healing length), the velocities are larger for higher values of the chemical potential and lower for smaller values. Based on a comparison of these findings with analogous results for vortex dipoles in the two-dimensional holographic superfluid that we have reported on in Part I, we have conjectured that the dissipation strength of the three-dimensional superfluid depends on the chemical potential, albeit we suspect the dependence to small.

In chapter 13 we have studied the non-equilibrium dynamics of the holographic superfluid induced by two types of far-from-equilibrium initial conditions, given by different sets of dense vortex-line and vortex-ring tangles. We have in particular focused on the universal stage of the evolution at intermediate and late times during which the system bears signatures of turbulent behaviour. As soon as the system is propagated in time, the vortices undergo reconnections, inducing the departure of the vortex tangles from their initial configuration and the formation of larger vortex structures. During these early stages of the evolution, the dynamics of the superfluid is strongly dependent on the initial conditions. For times $t \gtrsim 50$, we have found the system to enter a universal stage of the evolution which persists until the final vortex ring has disappeared. The universal behaviour during this stage splits into three distinct regimes with regard to the characteristics of the vortex gas as well as the microscopic physics of the superfluid which we have analysed by means of the occupation number spectrum.

The first universal regime is characterised by a dense tangle of vortex lines and vortex rings which frequently undergo reconnections. In addition, many closed vor-

tex structures shrink and eventually disappear. Consequently, the system is highly excited not only by vortices but also by a large number of rarefaction pulses and sound waves. We have confirmed this by studying aspects of the bulk-field configuration dual to the superfluid. On a microscopic level, the first universal regime is characterised by (quasi-)stationary scaling in the radial occupation number spectrum $n(k)$. Within a certain inertial momentum range, the spectrum is stationary and scales as $n(k) \sim k^{-\zeta}$, with a scaling exponent of $\zeta = 5.7 \pm 0.2$. Such a scaling behaviour coincides with the famous Kolmogorov 5/3-scaling in classical turbulence. We have found the system to remain in this Kolmogorov-like scaling regime for about 60 unit timesteps, independent of the initial conditions we have studied.

At later times, the system enters a second universal (quasi-)stationary scaling regime, characterised by a rather dilute tangle of vortices, with distinctly less frequently reconnecting vortex lines and rings as well as a smaller number of vanishing vortex rings than in the prior regime. Consequently, also the number of rarefaction and sound waves has significantly decreased. We have found that the occupation number spectrum in this regime has a scaling exponent of $\zeta = 5.1$ and the inertial momentum range of the stationary scaling regime has shifted towards the infrared. The power-law spectrum in this regime is consistent with a scaling of $n(k) \sim k^{-5.0}$ for tangles of independent vortex lines and rings in cold Bose gases derived from a statistical approach similar to Onsager's point-vortex model [42] and may be associated with so-called strong-wave turbulence [429]. It has also been observed in several simulations of Bose gases in the non-dissipative GP model [233, 234, 388].

Like the first scaling regime, also the second regime is only transient and transitions into a third universal regime once only one or very few well-separated small vortex rings remain. In this third universal regime, reconnections have ceased and the remaining vortex rings shrink rapidly and eventually disappear. During this process, the spectrum gradually flattens, terminating in a curve that is approximately described by $n(k) \sim k^{-4.1}$ in a finite infrared momentum range. However, this is only an approximate behaviour and we have argued that the spectrum does not exhibit proper scaling behaviour at any time during the third universal regime. In particular, unlike in the two prior regimes, the spectrum is not (quasi-)stationary but instead changes continuously for all momenta throughout this regime.

Finally, in chapter 14, we have built a clean theoretical laboratory to investigate the characteristics of vortex-ring interactions as well as vortex-ring excitations in the holographic superfluid. Remarkably, notwithstanding the large dissipation and quantum nature, we have found the vortex rings to exhibit behaviour that was predicted more than one and a half centuries ago by Helmholtz and Lord Kelvin for vortex rings in classical liquids. We started with an analysis of the behaviour of two coaxial vortex rings of the same radius with like-sign or opposite–sign circulation and an initially finite axial separation. For like-sign topological charges and a suitably chosen initial axial separation, we have observed the vortex rings to perform a leapfrogging motion. The rings slip through each other only once before they both undergo a rapid shrinking and eventually disappear. We have analysed the dynamics by means of the trajectories, velocities and accelerations of the vortex rings. Our

findings show that once the first leapfrogging motion has been completed, a second one sets in but is impeded by the rapid shrinking of both vortex rings. This behaviour is yet another piece of evidence corroborating the holographic superfluid to be strongly dissipative.

Analogously, we have studied and analysed the behaviour of two vortex rings of opposite-sign topological charges in a head-on collision. We have found the rings to experience a strong increase in radius as they approach and eventually annihilate each other. Interestingly, despite the increase in radii, the rings accelerate along their axial direction throughout their entire evolution. We have argued that this behaviour can again be attributed to the large dissipation of the holographic superfluid. After the annihilation, the rings leave behind an azimuthally expanding rarefaction pulse which eventually decays into sound waves.

Furthermore, we have studied the dynamics of vortex rings of higher winding numbers, $|w| > 1$. Such vortex rings quickly decay into $|w|$ elementary vortex rings when the system is evolved in time. We have made the interesting observation that ensuing the decay, these elementary vortex rings perform a leapfrogging motion. We have studied this behaviour explicitly for initial vortex rings of winding numbers $w = 2$ and $w = 3$. In the former case, the two rings successfully complete one slip-through motion but fail to complete a second one. Instead, the two rings merge, eventually causing one of them to disappear by shrinking to zero size while the other one remains with a finite radius. Similarly, also in the more complicated case of three vortex rings, only one slip-through motion is successful while the attempt of a second one fails for the same reason as for the doubly-wound ring, $i.\,e.$, the rings merge which eventually causes on of them to shrink and disappear.

In section 14.2 we have studied off-centre collisions of two equal-size and oppositely-charged circular vortex rings. We have analysed the qualitative behaviour of the rings as well as the dependence of the scattering angle, under which the scattered rings fly off, on the impact parameter of the collision. We have found the behaviour of the scattering vortex rings to split into three regimes, each being characterised by a different functional dependence of the scattering angle on the impact parameter. Likewise, also the qualitative behaviour of the scattering and scattered vortex rings differs in all three regimes. Interestingly, qualitatively similar results have been found before for scattering vortex rings in non-dissipative Bose–Einstein condensates studied in the GP model [398]. We have argued that minor deviations between our results and [398] are expected and consistent with the dissipative nature of the holographic system.

Finally, we have studied the dynamics of Kelvin-wave excitations of circular vortex rings. We have found that for vortex rings perturbed by planar oscillation in the initial configuration, out-of-plane oscillations build up dynamically due to the different curvature-induced and thus locally varying velocities of the ring. However, as a result of the dissipation, the planar as well as the built-up out-of-plane oscillations quickly damp out as the system is further propagated in time. After short time, the waves have therefore disappeared and the ring has regained its circular shape. We have made the interesting observation that despite the strong dissipation

of the holographic superfluid and thus the quick damping of Kelvin waves, a vortex ring with helical Kelvin waves in the initial condition is significantly slowed down relative to an unperturbed ring. We have argued that the slowing-down is due to mutually cancelling velocity contribution of the ring along its axial direction, again induced by segments of different curvature along the core of the ring. The slowing-down effect is notably stronger for larger amplitudes of the Kelvin waves. Similar behaviour of vortex rings has previously been studied in numerical simulations for classical liquids [478] as well as non-dissipative superfluids [480]. Furthermore, we have observed that if the amplitudes of helical Kelvin waves grow too large, the vortex ring experiences instabilities and undergoes several reconnections with itself. At each of these reconnection points, a small vortex ring is created. After the reconnections, the small rings quickly separate from the main ring and eventually disappear. Simultaneously, the remaining excitations of the main ring damp out and the ring regains its circular shape.

A main prospect for future research is the quantification of the dissipative nature of the three-dimensional holographic superfluid by means of a matching procedure with the dissipative Gross–Pitaevskii equation as well as the Hall–Vinen–Iordanskii equations. From a conceptual perspective, our procedure employed in Part I could be used with only little need for modification. Moreover, with our analyses of vortex solutions and the dynamics of vortex rings in the three-dimensional holographic superfluid as well as the development of evaluation methods for the dynamics, we have established excellent starting conditions. Naturally, there are various choices of vortex configurations and their respective dynamics that one could – and in fact should – match, including in particular single plane circular vortex rings as well as isolated vortex dipoles consisting of two straight anti-parallel lines. Such matching procedures would also answer the question whether dissipation equally affects the dynamics of vortex lines and rings or not. To this end, it would also be very interesting to focus more on the dependence of the dissipation scales on the spatial directions for given orientations of vortex lines and vortex rings. To gain a deeper understanding one would have to study quantitatively the energy and momentum flux into the black hole emanating from different coordinate planes and in particular quantify what modes are dominantly dissipated from which plane. Moreover, there is a large number of further aspects regarding the far-from-equilibrium dynamics of the holographic superfluid and especially quantum turbulence that would be very interesting to follow up on. Natural next steps would be to study soliton excitations and in particular instabilities thereof, rarefaction and sound waves, or even quenches from the symmetric to the superfluid phase of the system, to name only a few. For the vast majority of these tasks, our numerical implementation is excellently suitable and thus an optimal starting point. Nonetheless, for certain investigations, including in particular studies of soliton solutions, it would be desirable to implement non-periodic boundary conditions. Furthermore, a long-range objective should be the implementation of backreaction and thus a consistent implementation of the gravity–gauge–matter model without simplifying assumptions.

16 Conclusion and Outlook

In this thesis, we have investigated the real-time non-equilibrium dynamics of a two- and a three-dimensional holographic superfluid by means of numerical simulations. The holographic approach provides an inherently non-perturbative framework to study such strongly non-linear dynamics induced by topological vortex defects. We employ a bottom-up holographic model [46–48] that allows for a fundamental description of a strongly dissipative superfluid, in a parameter regime that cannot be accessed using conventional methods, in terms of a dual classical gravitational theory. While the bottom-up approach does not provide exact knowledge of the superfluid field-theory Lagrangian, it is nonetheless built from first principles and therefore an *ab initio* description of a strongly correlated and dissipative superfluid. In particular, unlike in many conventional descriptions of superfluidity, the dissipation is naturally included in the system and not put in by hand. The model we have employed describes a superfluid in $d + 1$ dimensions by means of an Abelian Higgs model in a $(d + 1 + 1)$-dimensional asymptotically anti-de Sitter black-hole spacetime. The classical gravitational model is in principle straightforward to solve, albeit an efficient numerical implementation is notoriously difficult. We have therefore implemented the equations of motion of the model for both $d = 2$ and $d = 3$ in an approximation that solves the Abelian Higgs model in a static gravitational background spacetime. This approximation captures the underlying physics of the model if the ratio T/T_c is below but close to unity, in which case the energy of the gauge–matter sector is too small to curve the black-hole spacetime. On the field-theory side, the static black hole is dual to a static and infinitely extended heat bath into which the superfluid condensate, dual to the gauge–matter fields in the bulk, can dissipate energy and momentum. In this sense, the black hole may loosely be interpreted as the normal component in the Tisza–Landau two-fluid model of superfluidity at zero velocity while the gauge–matter fields are dual to the condensate component.

In Part I we have investigated the dynamics of vortex dipoles in the two-dimensional holographic superfluid and from our analysis ultimately inferred the physical parameter regime of the superfluid itself. In particular, we have for the first time quantified the dissipative nature of the system and directly compared it with real-world superfluids such as helium or condensed Bose gases. In Part II, we have for the first time constructed and analysed vortex solutions of the three-dimensional holographic superfluid. In addition, we have studied the dynamics of single vortex rings as well as large tangles of vortex lines and rings which we have shown to induce turbulent behaviour of the system. We have also studied a number of different characteristics of vortex-ring excitations and interactions between circular vortex

rings in order to gain a deeper understanding of the behaviour of vortex defects in and the nature of the holographic superfluid as well as its non-equilibrium dynamics.

We have presented in-depth summaries of our findings already at the end of Part I and II in chapters 9 and 15, respectively. In the following, to conclude these discussions, we reiterate the main results, and present a possible roadmap for future research on the topics of this thesis and beyond.

Part I: Two-Dimensional Superfluid

We have investigated the dynamics of a single vortex–anti-vortex pair in the two-dimensional holographic superfluid, focussing mainly on interactions between the vortices and between the vortices and the hosting superfluid. The foundation of our studies has been the introduction of a new, numerically very efficient and highly accurate tracking routine that allows us to extract the vortex trajectories from our simulations in a quasi-continuous manner, *i. e.*, to sub-plaquette precision (chapter 6). Our tracking routine improves distinctly on previously used procedures for similar purposes that one can find in the literature. In order to quantify the dissipative nature of the holographic system and thus to characterise the applicability of the holographic framework to the description of vortex dynamics in real-world superfluids, we have matched solutions of the dissipative Gross–Pitaevskii equation (DGPE), as well as the Hall–Vinen–Iordanskii (HVI) equations for the mechanical motion of point vortices in dissipate superfluids, to the vortex dynamics in the holographic superfluid (chapter 7).

From our matching procedure with the DGPE we have inferred that the holographic superfluid is strongly dissipative over the entire temperature range accessible in the probe-approximation. We have argued that the extracted damping parameter characterising the dissipation is several orders of magnitude larger than in conventional ultracold dilute Bose gases. We have concluded that attaining such high values would require a strong increase of the s-wave scattering length which can be achieved in the vicinity of a Feshbach scattering resonance. We have further supported our conclusion that the system is strongly dissipative by matching to the vortex dynamics also solutions of the HVI equations in order to extract friction coefficients which parametrise the mutual friction between the vortices and the superfluid and are thus another measure for the dissipation. These friction coefficients have allowed for a direct comparison with experiments on vortex dynamics in quasi two-dimensional films of superfluid helium and oblate Bose–Einstein condensates. From this comparison we have conjectured that the holographic framework should be applicable to the description of vortex dynamics in highly dense or thermally excited Bose–Einstein condensates or even to superfluid helium ^{4}He at temperatures in the one-Kelvin range.

Further, in chapter 8, we have analysed the kinematic aspects of the dipole evolution with special emphasis on the vortex velocities and accelerations. In the literature, these observables had not been calculated before. We have found the dynamics

to be parametrised solely by the vortex–anti-vortex separation and thus to be independent of the initial size and alignment of the dipole. This justifies retrospectively the use of only one initial vortex configuration in the matching procedure with the DGPE and the HVI equations. Finally, we have studied the rarefaction pulse created by the annihilating vortices. We have shown that it has strong resemblance with GPE soliton solutions, so-called Jones–Roberts solitons [337]. In particular, we have shown that the wave decays into sound waves once it reaches the speed of sound.

Our results indicate the applicability of the holographic framework for quantitative studies of non-equilibrium phenomena induced by vortex defects in physical parameter regimes where conventional methods cease to be applicable. In particular, since the holographic model is a fundamental description of a superfluid, it is valid at all scales, making it an especially favourable tool to study characteristics of quantum turbulence in dissipative superfluids. Thus, the research presented in this thesis has unfolded and highlighted the vast potential of the holographic description of superfluids for the investigation of aspects of liquid helium and cold Bose gases in certain parameter regimes that conventional methods do not, or only insufficiently, capture.

In view of previous comparisons of holographic models to real-world systems, also beyond superfluids, an important aspect of our matching procedure is that we have matched a theory of real-world cold Bose gases, *viz.* the DGPE, to an existing and intensively studied holographic model. In particular, we have not, as is typically done, build a holographic (bottom-up) model to capture certain aspects of an established theory for a real-world physical system. The latter approach is frequently employed for instance to construct theories akin to quantum chromodynamics (see *e. g.* the review [16] and references therein for details and examples). Instead, we have directly characterised the commonly used model of a superfluid in the holographic framework which has attracted considerably attention in recent years, and has already been studied in numerous publications.

A natural next goal for future research beyond the studies presented in this thesis would be to gain a better understanding of the dissipation mechanism and the dissipation strength of the system in the absence of vortices. We have already qualitatively argued that the dissipation decreases once the vortex–anti-vortex pair has mutually annihilated but we have so far not analysed the decrease on a quantitative level. This could be done by matching DGPE solutions to the dynamics of (grey) solitons in the holographic system. Knowing how the dissipation changes when a vortex–anti-vortex pair annihilates appears likely to be essential also for the purpose of gaining a deeper understanding of quantum turbulence in the holographic superfluid. Moreover, it constitutes an important element that is still missing for a thorough and direct comparison of the vortex-dipole dynamics, including in particular its late-time regime and the rarefaction pulse created in the annihilation of the vortices, in the holographic superfluid with real-world systems. Another extension of our work could be to focus more on the relationship of the holographic model and the (D)GPE. In light of the excellent agreement of the numerical solutions reported

in this work, it appears possible that one can also find an analytic link between the respective theories. To this end, one would study the holographic equations of motion in a suitable series expansion and compare the outcomes at each order with the (D)GPE. Our results suggest that the probe-approximation is a good starting point for this. However, as of now, it is unclear what a suitable expansion parameter for the equations of motion might be. It would also be a very interesting and indeed realistic task for future research to include in the numerical implementation of the equations of motion the backreaction of the gauge–matter fields onto the gravitational sector. The inclusion of backreaction would allow for a fully self-consistent comparison of the holographic model with real-world superfluids, in particular offering a more reliable account of the temperature dependence of the system. There are certainly very exciting times ahead of us with regard to the potential first-time application of holography to the description of vortex dynamics in experimentally realised superfluid, although this will require further advances in the already sophisticated experimental techniques. Nonetheless, from the theory perspective, our work sets a solid foundation for this endeavour.

Part II: Three-Dimensional Superfluid

Neither vortex solutions of the three-dimensional holographic superfluid nor its (non-equilibrium) real-time evolution have previously been studied in the literature. We therefore started our investigations of this part with the (numerical) construction of vortex-line and vortex-ring solutions and a thorough discussion of their basic properties. In addition, we have presented an in-depth analysis of the dynamics of single vortex rings (chapter 12). We have further explored the far-from-equilibrium dynamics of the superfluid induced by different sets of dense tangles of vortex defects with regard to universal and turbulent behaviour (chapter 13). Moreover, in order to gain a deeper understanding of the holographic superfluid and in particular of its vortex dynamics, we have studied a number of non-trivial interactions between and excitations of vortex rings (chapter 14). In particular, we have observed the characteristic behaviour of vortex rings that was first predicted in 1858 by H. von Helmholtz for vortex rings in classical liquids [284], including their famous leapfrogging motion. For our investigations we have developed a fast numerical implementation of the equations of motion that has enabled us to employ grid sizes of up to 128^3 points along the superfluid directions and study even the late-time regime of the many-vortex dynamics.

From a comparison of the static features of vortex solutions with analogous results from the GP model, we have obtained strong evidence corroborating that the holographic model, in the presence of vortex defects, describes a non-relativistic superfluid. Our real-time simulations have further made evident that vortex rings in the holographic superfluid undergo a rapid shrinking as they traverse the system and eventually disappear by shrinking to zero size. This characteristic behaviour establishes that also the three-dimensional holographic superfluid is (strongly) dis-

sipative. We have explicitly shown that the vortex-ring kinematics agrees with the corresponding solution of the HVI equation for point-vortex rings in dissipative superfluids. Moreover, from an investigation of the chemical-potential dependence of the vortex-ring dynamics, we have inferred that the dissipation is of the same order of magnitude for all chemical potentials accessible in the probe-approximation. Upon studying the bulk configurations dual to vortex defects we have found strong evidence suggesting that the dissipation scales of the superfluid depend on the orientation of the dissipating modes relative to the vortices. It appears likely that, under certain conditions, the dissipation is not restricted to UV modes only, like in the two-dimensional holographic superfluid, but also allows for modes of larger wavelengths to dissipate, albeit the details of the dissipation scales and strength are very sensitive to the details of the exact configuration of topological defects.

In addition to single vortex-defect solutions, we have also investigated the far-from-equilibrium dynamics of the three-dimensional holographic superfluid induced by dense tangles of vortex defects with a particular emphasis on universal behaviour of the system at intermediate and late times of the evolution. For a fixed chemical potential of the superfluid and for different types of initial vortex configurations, we have analysed the dynamics of the system with regard to the qualitative behaviour of the vortex tangles as well as (quasi-)stationary scaling behaviour in the radial occupation number spectrum. We have found that the system enters a universal stage with three characteristic regimes once an initial vortex tangle has significantly departed from its initial configuration and most of the vortices have reconnected at least once.

The first universal regime is characterised by a dense tangle of vortices which frequently reconnect and shrink to zero size, thus exciting the system with a large number of additional sound waves and rarefaction pulses. During this transient regime, the occupation number spectrum obeys Kolmogorov's 5/3-scaling in an infrared momentum range, indicating the system to exhibit turbulent behaviour. At later times, the system enters a second universal regime, characterised by a dilute gas of vortices and only a small number of sound waves and rarefaction pulses. In addition, the spectrum exhibits a scaling behaviour of $n(k) \sim k^{-5.1}$ in an infrared momentum range. Such a scaling behaviour coincides with the scaling for a tangle of independent vortex lines in cold Bose gases (see *e. g.* [233, 234, 388] for discussions of this aspect and similar findings in the GP model). The scaling behaviour again indicates turbulent behaviour. Once only very few vortex rings remain and reconnections cease, the system enters a third universal regime which persists until the last ring has disappeared. This regime does not exhibit (quasi-)stationary scaling behaviour.

Finally, we have studied characteristic behaviour of vortex rings in various types of interactions. Interestingly, despite the large dissipation, vortex rings in the holographic superfluid can perform a leapfrogging motion, as was famously predicted for classical vortex rings by Helmholtz [284]. Likewise, also in head-on collisions, the behaviour of vortex rings is in qualitative agreement with Helmholtz' predictions. For off-centre collisions of vortex rings, we have made the interesting observation

that the dependence of the scattering angle on the impact parameter is similar to results from simulations of the non-dissipative GPE, albeit small differences exist and are indeed expected on grounds of the dissipative nature of the holographic system. In addition to interactions, we have also studied Kelvin-wave excitations of vortex rings and found that helical excitations cause the ring's axial velocity to decrease, in agreement with previous findings in the GP model. We have argued that investigating the nature of Kelvin waves is particularly important in order to gain a deeper understanding of quantum turbulence. In particular, in previous work on Kelvin waves in (non-holographic) superfluids it was shown that the waves are central to the transfer of energy, and we expect the same to be true in the holographic system.

The research presented in Part II illustrates the enormous potential of the holographic framework in the study of quantum turbulence and other non-equilibrium phenomena in three-dimensional superfluids. The holographic framework provides a fundamental description of a superfluid in a regime where the applicability of all conventional methods ceases but that is likely to be realised in real-world superfluids characterised by a very large dissipation. While we have not quantified the dissipation precisely, our findings strongly suggest the system to be highly dissipative and, moreover, the holographic framework to be applicable for the description of vortex dynamics in similar experimentally accessible superfluids as the two-dimensional system, namely superfluid helium and thermally excited Bose gases. Furthermore, the geometric bulk realisation of the superfluid provides a new perspectives on the dissipation mechanism of the system and may thus yield many new insights into strongly dissipative superfluids. Our studies constitute a very wide-ranging and thorough 'consistency check' of the model with regard to its description of vortex dynamics. Indeed, in all of our studies, most notably of the single as well as interacting and excited vortex rings, we have found the results on a qualitative level to be consistent with experiments, and wherever experimental results are not available, with our expectations based on studies of non-dissipative superfluids as well as of dissipative superfluids using non-fundamental methods. In particular, there are a number of non-fundamental methods that capture certain aspects of vortex dynamics in dissipative superfluid which are thus ideally suited for comparisons.

A first obvious extension of our work would be a quantitative characterisation of the dissipation of the holographic superfluid by means of a matching procedure of vortex dynamics in the holographic system with solutions of the dissipative GPE and the corresponding HVI equations. Specifically, in a first step one would match the dynamics of a single vortex ring as well as of a dipole consisting of two straight vortex lines. Our studies in this work constitute an excellent starting point for such an undertaking, not least because we have already discussed the HVI equations for both scenarios and, even more, laid out the general procedure for such a matching in Part I which could be adopted with only little need for modification. Another natural extension of our work would be to study further aspects of superfluid turbulence in a three-dimensional system. In three spatial dimensions, a turbulent state of a superfluid exhibits a distinctly richer structure than in two spatial dimensions. One could for instance study the vorticity distribution of the system and analyse the

polarisation of the vortex tangle to learn about possible clustering effects. Likewise, an analysis of the vortex density and total vortex length would be very interesting and could yield new insights into turbulent behaviour. To this end, the three-dimensional tracking routine we have implemented could be employed as an excellent starting point for follow-up studies. Likewise, an analysis of the dynamics of other topological defects such as solitons would be desirable as it provides new insights into the characteristics of the superfluid, including in particular its non-equilibrium dynamics. It would also be very interesting to implement the full set of gravity–gauge–matter equations of motion, *i.e.*, to take into account the backreaction of the gauge–matter fields into the gravitational sector. However, given the enormous need for computational power and the currently available resources, this appears to be a long-term objective. Our studies have certainly set the foundations for many new and very exciting investigations of vortex dynamics and especially quantum turbulence, also beyond the above-mentioned ones, in three-dimensional dissipative superfluids by means of gauge/gravity duality.

Beyond the discussed prospects for future research on holographic superfluids, the numerical and conceptual methods used and developed in this thesis are potentially also useful for applications of holography to other fields of physics, including particle and nuclear physics, in particular the physics of strongly coupled plasmas akin to the quark–gluon plasma, other condensed-matter systems, nuclear astrophysics, and many more. We have discussed the application of holography to the description of such systems in the introduction in chapter 1. The basic framework of our numerical implementation of the equations of motion constitutes an ideal starting point for numerical studies of various holographic systems in two and in three spatial dimensions. Moreover, also the concepts developed in the matching procedure may potentially be applicable in other systems and thus set the basis for further investigations of the applicability of holography to the description of real-world physics.

Appendix

A Numerical Methods

In this appendix we discuss details concerning the numerical methods that we employ in this thesis. This includes the numerical implementation of the equations of motion of the Abelian Higgs model, a statement regarding the performance of our codes, the power-law fitting of the occupation number spectrum, the finite-difference methods that we employ in the computation of vortex velocities and accelerations, and finally the three-dimensional tracking routine that we use to track the cores of vortex rings in the three-dimensional superfluid.

A.1 Implementation of the Equations of Motion

The gravitational models dual to superfluids in two and three spatial dimensions are given by Abelian Higgs models in four- and five-dimensional asymptotically anti-de Sitter spacetime, respectively. We solve the corresponding equations of motion (3.9)–(3.11) in the probe-approximation using similar numerical methods for both systems. For our real-time simulations of both systems we first solve the respective static and spatially homogeneous equations of motion, imprint our initial conditions onto these solutions, and subsequently evolve the systems in time by solving the respective full sets of dynamical equations of motion. In both systems, the holographic z-direction is defined on the finite interval $0 \leq z \leq z_\mathrm{h}$, bounded by the AdS boundary at $z = 0$ and the black-hole event horizon at $z = z_\mathrm{h}$ which we set to unity, $z_\mathrm{h} = 1$. Hence, $0 \leq z \leq 1$.

Unless explicitly stated otherwise, the following discussion holds equally for the two- and the three-dimensional system. For the equilibrium as well as the dynamical system we employ a collocation method with 32 Gauß–Lobatto grid points along the holographic z-direction and expand the fields in a basis of 32 Chebyshev polynomials. Chebyshev polynomials are defined on the finite interval $[-1, 1]$. We therefore perform a coordinate transformation from the holographic z-coordinate to the new rescaled coordinate $\hat{z} \in [-1, 1]$, which is defined by

$$z = \frac{1}{2}(\hat{z} + 1) \,. \tag{A.1}$$

This enables us to implement derivatives with respect to $\hat{z}$ using simple matrix multiplication. For the static and spatially homogeneous systems we linearise the respective equations of motion using a Newton–Kantorovich iteration algorithm and solve the resulting linear equations at each iterative step employing an LU decomposition. For our real-time simulations, we take the spatial field-theory directions $\boldsymbol{x}$ to be period and accordingly expand the fields in a pseudo-spectral basis. Such an expansion

allows us to implement derivatives with respect to $\boldsymbol{x}$ highly efficiently using discrete Fourier transforms. To propagate the two-dimensional system forward in time, we employ a fourth-order/fifth-order Runge–Kutta–Fehlberg algorithm with adaptive timestep size. We implement the algorithm such that each unit timestep, in units of $z_{\mathrm{h}} = 1$, is composed of an adaptive number between 10 and 1000 numerical timesteps. For the three-dimensional system, we employ a fourth-order Runge–Kutta algorithm and we use 250 numerical timesteps to propagate the system forward by one unit timestep (in units of $z_{\mathrm{h}} = 1$). Further discussion concerning the technical details of the implementation of the dynamical equations of motion can be found in chapters 5 and 11 for the two- and the three-dimensional system, respectively.

A.2 Performance

We implement the equations of motion for both systems in C++. For the implementation of discrete Fourier transforms we use the `fftw3` library [481] and implement all linear-algebra operations with help of the `Eigen` library [482]. The codes are parallelised with `OpenMP` [483].

Running the code for the two-dimensional system on the Intel Xeon server architecture using 56 threads, a simulation on a grid with 512×512 grid points along the spatial field-theory directions with grid spacing $l = 2/7$ and 32 collocation points along the holographic direction up to time $t = 972$ (in units timesteps), which corresponds to the time it takes for a vortex dipole with initial separation $d_0 = 150$ grid points to annihilate, takes around 8 hours.

For the three-dimensional system, running the code on the Intel Xeon server architecture using 56 threads, a simulation on a grid with $128 \times 128 \times 128$ grid points along the spatial field-theory directions with a grid spacing of $l = 2/7$ and 32 collocation points along the holographic direction up to time $t = 126$, which corresponds to the time it takes a single vortex ring with initial radius $R_0 = 22$ grid points to shrink to zero size, takes around 400 hours. Accordingly, the simulations of the far-from-equilibrium dynamics and turbulence discussed in chapter 13, which ran for approximately 500 unit timesteps, took around 1500 hours.

We use `Mayavi` [484] for all visualisations of three-dimensional bulk and vortex configurations.

A.3 Power-Law Fits of Occupation Number Spectrum

In chapter 13 we analyse the far-from-equilibrium dynamics of the three-dimensional superfluid in terms of scaling behaviour in the radial occupation number spectrum. Such a scaling behaviour is characterised by $n(t, k) \sim k^{-\zeta}$ within a certain inertial momentum range where ζ is the scaling exponent. We extract the scaling exponent from our data points using a Levenberg–Marquardt least-squares fitting routine.

This procedure is plagued by a number of uncertainties. First and foremost, the determination of the inertial momentum range. We initially choose the endpoints

of the momentum interval by eye and subsequently vary them systematically to estimate the uncertainty of the scaling exponent. We find the uncertainty to be given by $\Delta\zeta = \pm 0.2$. The fitting routine itself, on the other hand, typically reports an uncertainty of $\Delta\zeta = \pm 0.05$ which is clearly subdominant. Yet another source of uncertainty comes from the noise in the set of data points due to the finite size of the computational domain. This uncertainty is the most difficult one to estimate. We proceed as follows. We perform similar simulations to those presented in the main text with analogues initial conditions on smaller grids of size $96 \times 96 \times 96$ points along the spatial field-theory directions and evaluate the sets of data points using the same methods as outlined above. Comparing the results for the scaling exponents yields discrepancies of the order of $\Delta\zeta = \pm 0.1$, which is slightly smaller than the uncertainty originating from the choice of endpoints of the inertial momentum range. Naturally, we expect the finite-size-induced noise to decrease if we work on larger numerical grids or average the results over several simulations with similar initial vortex configurations. As of now, however, both of these methods appear out of reach given the currently available computational resources which strongly constrain the feasible grid sizes and number of simulations we can perform. All uncertainties considered, we therefore quote $\Delta\zeta = \pm 0.2$ for the uncertainty of the scaling exponents throughout chapter 13.

A.4 Equations of Motion in Poincaré Coordinates

We solve the static and homogeneous equations of motion of the superfluids in two and three spatial dimensions not in Eddington–Finkelstein coordinates using the metric (3.13) but instead in Poincaré coordinates, *i. e.*, using the metric (3.6). In this appendix, we discuss the equations of motion for both systems in Poincaré coordinates and lay out how the respective solutions are transformed to Eddington–Finkelstein coordinates which we employ for our real-time simulations.

The content of this section regarding the two-dimensional system agrees with an analogous section in [257] and the discussions are thus very similar. The reason is that in this work we employ the numerical implementation of the two-dimensional system that was developed in [257]. With regard to the three-dimensional system, the numerical implementation of the equations of motion was implemented by the author of this work. The general procedure concerning the use of Poincaré coordinates for the static and spatially homogeneous system as well as the subsequent transformation to Eddington–Finkelstein coordinates is the same as for the two-dimensional system which is why we discuss both systems here in one setting.

In the main text we argue that in the equilibrium solution the spatial components of the gauge field A_M vanish. We therefore set $A_i(z) = 0$ with $i = x_1, x_2$ for the two-dimensional and $i = x_1, x_2, x_3$ for the three-dimensional system throughout this section. We again work in axial gauge and thus set $A_z(z) = 0$ in both systems. Moreover, in light of the boundary condition for the scalar field (5.9), we find it convenient to express both systems of equations of motion in terms of the rescaled

scalar field

$$\tilde{\Phi} \equiv \frac{\Phi}{z} \,. \tag{A.2}$$

Using the metric (3.6) the equations of motion for the scalar field $\tilde{\Phi}$ and the temporal gauge-field component A_t of the two-dimensional system are given by

$$2\tilde{\Phi}^2 A_t = h A_t'' \,, \tag{A.3}$$

$$-A_t^2 \tilde{\Phi} = h^2 \tilde{\Phi}'' - 3z^2 h \tilde{\Phi}' - zh\tilde{\Phi} \,, \tag{A.4}$$

where all fields depend only on the holographic z-direction and we denote derivatives with respect to z by a prime. In addition, we have set $z_{\mathrm{h}} = 1$ and $m^2 = -2$, in agreement with our corresponding choices discussed in the main text.

Similarly, we find for the three-dimensional system

$$2\tilde{\Phi}^2 A_t z = h\left(z A_t'' - A_t'\right) \,, \tag{A.5}$$

$$z A_t^2 \tilde{\Phi} = h\tilde{\Phi}^2 z^3 + \tilde{\Phi}'h(1 + 3z^4) - h^2 z\tilde{\Phi}'' \,, \tag{A.6}$$

where we have again set $z_{\mathrm{h}} = 1$ and plugged in our choice for the scalar mass, $m^2 = -3$.

In both systems, it follows from the z-component of the Maxwell equations that the phase of the scalar field is constant along z. Without loss of generality we have therefore assumed that $\tilde{\Phi}$ is real, for the two- as well as three-dimensional system. The boundary conditions in both systems are given by

$$A_t(z = 0) = \mu \,, \quad A_t(z = z_{\mathrm{h}} = 1) = 0 \,, \tag{A.7}$$

$$\tilde{\Phi}(z = 0) = 0 \,, \qquad |\tilde{\Phi}(z = z_{\mathrm{h}} = 1)| < \infty \,. \tag{A.8}$$

We solve the systems of coupled second-order ordinary differential equations by expanding the fields in a basis of Chebyshev polynomials and employing a Newton–Kantorovich iterative procedure to linearise the equations. See also appendix A.1 for details.

We now discuss the transformation laws for the fields in Poincaré coordinates solving equations (A.3), (A.4), for the two-dimensional system, and (A.5), (A.6), for the three-dimensional system, to Eddington–Finkelstein coordinates such that we can use them to construct the initial conditions for our real-time simulations.

In order to distinguish between the fields in Poincaré and Eddington–Finkelstein coordinates, we denote the fields solving the above systems of equations of motion with an additional subscript 'P', indicating that they are given in Poincaré coordinates, *i.e.*, Φ_{P} and $(A_{\mathrm{P}})_M$ with $M = t, x_1, x_2, z$ for the two- and $M = t, x_1, x_2, x_3, z$ for the three-dimensional system. Moreover, we use $\boldsymbol{A}_{\mathrm{P}} = 0$ due to homogeneity and $(A_{\mathrm{P}})_z = 0$ due to our choice of axial gauge and further denote the Poincaré coordinates themselves by x_{P}^M. Eddington–Finkelstein coordinates by contrast are denoted by x^M without a subscript. Likewise, the fields in Eddington–Finkelstein

coordinates are denoted by $\tilde{\Phi}$ and A_M. The transformation laws for the vector and the scalar field are given by

$$A_M = \frac{\partial x_{\mathrm{P}}^N}{\partial x^M} \left(A_{\mathrm{P}}\right)_N,$$
(A.9)

$$\tilde{\Phi} = \tilde{\Phi}_{\mathrm{P}},$$
(A.10)

where $\partial x_{\mathrm{P}}^N / \partial x^M$ is the Jacobian of the coordinate transformation, given by

$$\frac{\partial x_{\mathrm{P}}^M}{\partial x^N} = \begin{pmatrix} 1 & 0 & 0 & \frac{1}{h(z)} \\ 0 & 1 & 0 & 0 \\ 0 & 0 & 1 & 0 \\ 0 & 0 & 0 & 1 \end{pmatrix},$$
(A.11)

for the two-dimensional and

$$\frac{\partial x_{\mathrm{P}}^M}{\partial x^N} = \begin{pmatrix} 1 & 0 & 0 & 0 & \frac{1}{h(z)} \\ 0 & 1 & 0 & 0 & 0 \\ 0 & 0 & 1 & 0 & 0 \\ 0 & 0 & 0 & 1 & 0 \\ 0 & 0 & 0 & 0 & 1 \end{pmatrix},$$
(A.12)

for the three-dimensional system.

The transformation law for the gauge field (A.9) implies that our choice of axial gauge is lost in Eddington–Finkelstein coordinates, $A_z \neq 0$. In order to restore axial gauge, we employ the gauge symmetry of the system and perform a gauge transformation with generating function $\chi(z)$. Thus, we have to solve the differential equation,

$$0 \overset{!}{=} A_z + \chi' = \frac{(A_{\mathrm{P}})_t}{h(z)} + (A_{\mathrm{P}})_z + \chi' = \frac{(A_{\mathrm{P}})_t}{h(z)} + \chi',$$
(A.13)

where in the first equation we have set the transformed z-component of the gauge field to zero, in the second step we have used equation (A.9) and in the third step we have used that in Poincaré coordinates $(A_{\mathrm{P}})_z = 0$ by axial gauge. Since we choose the generating function $\chi(z)$ of the gauge transformation to be independent of t and $\boldsymbol{x}$, the temporal gauge-field component A_t does not change and neither do the spatial gauge-field components A_i. The scalar field by contrast transforms as

$$\tilde{\Phi} \to \tilde{\Phi} \, \mathrm{e}^{\mathrm{i}\chi}.$$
(A.14)

A.5 Finite-Difference Methods

In this section we give details concerning the finite-difference methods that we employ throughout this thesis to derive the velocities and accelerations of vortices from their quasi-continuous trajectories that we extract from our combined two-dimensional tracking routine. In particular, we also use the method to compute

the velocities and accelerations of vortex rings in the three-dimensional superfluid. Since in both the two- and the three-dimensional system we typically track the vortices during the final phase of their dynamics more frequently than at earlier times, the time difference between two consecutive tracking steps is in general not constant throughout the vortex evolution. In the computation of derivatives of the trajectories using finite differences, this has to be taken into account.

For simplicity, we restrict the following discussion to only one of the spatial direction. We denote the vortex position along that direction at time t_i by $x(t_i)$. The results hold equivalently for all spatial directions. We first Taylor-expand the vortex position around t_{i+1} and t_{i-1},

$$x(t_{i+1}) = x(t_i + \Delta t) = x(t_i) + \dot{x}(t_i)\,\Delta t + \ddot{x}(t_i)\,\frac{(\Delta t)^2}{2} + \mathcal{O}((\Delta t)^3)\,, \qquad \text{(A.15)}$$

$$x(t_{i-1}) = x(t_i - \hat{\Delta} t) = x(t_i) - \dot{x}(t_i)\,\hat{\Delta} t + \ddot{x}(t_i)\,\frac{(\hat{\Delta} t)^2}{2} + \mathcal{O}((\hat{\Delta} t)^3)\,, \qquad \text{(A.16)}$$

where a dot denotes a derivative with respect to time t and we have introduced both $\Delta t = t_{i+1} - t_i$ and $\hat{\Delta} t = t_i - t_{i-1}$ to account for the in general not evenly spaced time differences between two consecutive tracking steps. From the above equations we extract the vortex velocity at time t_i by computing the difference $(\text{A.15}) - (\text{A.16})$ and neglecting all terms of second and higher order in the derivative,

$$v(t_i) = \dot{x}(t_i) = \frac{x(t_{i+1}) - x(t_{i-1})}{t_{i+1} - t_{i-1}}\,. \qquad \text{(A.17)}$$

Likewise, we obtain the acceleration by computing the sum $(\text{A.15})/\Delta t + (\text{A.16})/\hat{\Delta} t$ and neglecting all terms of third and higher order in the derivative,

$$a(t_i) = \ddot{x}(t_i) = \frac{2}{t_{i+1} - t_{i-1}}\left[\frac{x(t_{i+1})}{t_{i+1} - t_i} + \frac{x(t_{i-1})}{t_i - t_{i-1}} - \frac{x(t_i)}{t_{i+1} - t_i} - \frac{x(t_i)}{t_i - t_{i-1}}\right]\,. \quad \text{(A.18)}$$

A.6 Vortex-Core Tracking in Three Spatial Dimensions

In this appendix we give details concerning the three-dimensional tracking routine that we employ in chapter 14 to locate the one-dimensional cores of vortex rings. In fact, the tracking routine enables us to track any vortex line or ring of any shape in the superfluid. Nonetheless, in this thesis we only use this tracking algorithm in section 14.3 in order to visualise the Kelvin-wave excitations of vortex rings. In all other sections and chapters we rather use the two-dimensional routine, applied on a two-dimensional slice intersecting the cores of the vortex rings, which is numerically much more efficient. The algorithm for the tracking in three spatial dimensions was first introduced in [291] and we apply it without any adaptations. In the following discussion we summarise the essential aspects of the algorithm, closely following [291]. For further details, we refer the interested reader to the original work.

While it would be most convenient to simply adopt the two-dimensional Newton–Raphson method to three spatial dimensions and apply it just like we discuss in

section 6.3, it turns out that this is not possible. The reason is that in the three-dimensional system, the superfluid order-parameter field is a map

$$\psi : \mathbb{R}^3 \to \mathbb{C} \cong \mathbb{R}^2 \,, \tag{A.19}$$

which implies that the corresponding Jacobian is not a square matrix like in the two-dimensional system, thus prohibiting an inversion of the matrix which is a key step in the NR procedure, *cf.* equation (6.6). Hence, one has to find another method that circumvents this obstacle. The method we discuss in the following is based on the application of the two-dimensional NR method on suitably chosen two-dimensional slices of the three-dimensional system.

To derive the algorithm, we first point out that along the one-dimensional vortex core that we want to track, the complex order-parameter field ψ vanishes. Consequently, also the projections of the gradient fields $\mathrm{Re}[\boldsymbol{\nabla}\psi(\boldsymbol{x})]$ and $\mathrm{Im}[\boldsymbol{\nabla}\psi(\boldsymbol{x})]$ onto the vortex core vanish. This implies that the cross product of the gradient fields is tangent to the core. In fact, such a vector field has a name, namely *pseudo-vorticity field*. It is defined by

$$\boldsymbol{\omega} = \frac{1}{2}\boldsymbol{\nabla} \times \boldsymbol{j} \,, \tag{A.20}$$

with the density current

$$\boldsymbol{j} = \frac{1}{2\mathrm{i}} \left(\psi^* \boldsymbol{\nabla}\psi - \psi\boldsymbol{\nabla}\psi^* \right) \,, \tag{A.21}$$

which, up to a factor of the condensate density $|\psi|^2$, agrees with the superfluid velocity $\boldsymbol{\nabla} \arg(\psi)$. After some algebra (A.20) can be brought into the desired form

$$\boldsymbol{\omega}(\boldsymbol{x}) = \mathrm{Re}[\boldsymbol{\nabla}\psi(\boldsymbol{x})] \times \mathrm{Im}[\boldsymbol{\nabla}\psi(\boldsymbol{x})] \,. \tag{A.22}$$

Above we have used bold symbols to denote vectors in the three-dimensional system. Since the pseudo-vorticity field is tangent to the vortex core it can be used to define a plane transverse to the vortex core on which the two-dimensional NR method can be applied to locate one point of the vortex core. Subsequently, one can move along the direction of the pseudo-vorticity vector evaluated at the position of the vortex core within the two-dimensional plane and proceed likewise for the new point along the core until the entire core has been tracked. The details of the algorithm are as follows.

Like for the standard NR method, we start from an initial guess $\boldsymbol{x}^{\mathrm{g}}$ for a point, labelled by the index i, along the one-dimensional vortex core. The guess can for instance be obtained by evaluating $|\psi(\boldsymbol{x}^{\mathrm{g}})|^2 < \epsilon n_0$ for sufficiently small $\epsilon \ll 1$, where n_0 is the background density of the condensate. Given the initial guess, we evaluate the pseudo-vorticity field at the respective position $\boldsymbol{\omega}(\boldsymbol{x}^{\mathrm{g}})$. Provided the initial guess is sufficiently close to the real position of the core, the pseudo-vorticity vector points almost in parallel to the vortex core. We now define a plane through $\boldsymbol{x}^{\mathrm{g}}$ and orthogonal to $\boldsymbol{\omega}(\boldsymbol{x}^{\mathrm{g}})$ and extract a set of normalised basis vectors that span

the plane, $(\hat{\boldsymbol{u}}_1, \hat{\boldsymbol{u}}_2)$. On this plane, we can now employ the same NR tracking routine as outlined in section 6.3. To this end, we have to project the gradient fields $\mathrm{Re}[\boldsymbol{\nabla}\psi(\boldsymbol{x})]$ and $\mathrm{Im}[\boldsymbol{\nabla}\psi(\boldsymbol{x})]$ onto the considered two-dimensional plane. Proceeding just as described in section 6.3, this yields

$$\boldsymbol{x}_i = \boldsymbol{x}_i^{\mathrm{g}} - \left[J^{-1}(\boldsymbol{x}^{\mathrm{g}}) \cdot \psi(\boldsymbol{x}^{\mathrm{g}}) \right] \cdot \begin{pmatrix} \hat{\boldsymbol{u}}_1 \\ \hat{\boldsymbol{u}}_1 \end{pmatrix} + \mathcal{O}\left[(\boldsymbol{x}_i - \boldsymbol{x}^{\mathrm{g}})^2 \right] , \qquad (A.23)$$

with the Jacobian matrix

$$J(\boldsymbol{x}) = \begin{pmatrix} \mathrm{Re}[\boldsymbol{\nabla}\psi(\boldsymbol{x}) \cdot \hat{\boldsymbol{u}}_1] & \mathrm{Re}[\boldsymbol{\nabla}\psi(\boldsymbol{x}) \cdot \hat{\boldsymbol{u}}_2] \\ \mathrm{Im}[\boldsymbol{\nabla}\psi(\boldsymbol{x}) \cdot \hat{\boldsymbol{u}}_1] & \mathrm{Im}[\boldsymbol{\nabla}\psi(\boldsymbol{x}) \cdot \hat{\boldsymbol{u}}_2] \end{pmatrix} , \qquad (A.24)$$

for the next better guess for the vortex-core position on the two-dimensional plane. Upon iterating this procedure, $\boldsymbol{x}_i$ converges to the true vortex position. Naturally, the true position is also located on the two-dimensional plane. The index i labels the tracked points along a single one-dimensional vortex core. After storing $\boldsymbol{x}_i$, one proceeds to tracking the next point along the vortex core. The initial guess for that point is given by

$$\boldsymbol{x}^{\mathrm{g}} = \boldsymbol{x}_i + \varsigma \hat{\boldsymbol{\omega}}(\boldsymbol{x}_i) , \qquad (A.25)$$

with an arbitrary but small parameter $\varsigma \in \mathbb{R}$ and the hat over the pseudo-vorticity field indicates that the vector is normalised. The value of ς determines how many points along the one-dimensional vortex core one tracks. It has to be sufficiently small to ensure convergence of the algorithm. Using $\boldsymbol{x}^{\mathrm{g}}$ one then proceeds just like for the previous point. The algorithm terminates once the distance $|\boldsymbol{x}_1 - \boldsymbol{x}_j|$, for $j > 1$, is much smaller than the parameter ς. Where necessary, the periodicity of the grid has to be taken into account. Once the condition is satisfied, the entire vortex core has been located. If two or more vortices are present, one proceeds likewise for all other cores.

In practice, we use $\varsigma = 0.3$ and determine the initial guess by evaluating $|\psi(\boldsymbol{x}^{\mathrm{g}})|^2 < \epsilon n_0$ for $\epsilon = 0.03$.

B Details on the HVI Equations

In this appendix, we discuss details concerning the Hall–Vinen–Iordanskii equations for the mechanical motion of point vortices in two-dimensional superfluids that we employ in chapter 7 to extract friction coefficients from our matching procedure of the vortex-dipole dynamics. We first derive relations between the free parameters of the HVI equations, the complex Ginzburg–Landau equation and the dissipative Gross–Pitaevskii equation that we employ in our matching procedure (appendix B.1) and subsequently present some further details concerning the solutions of the HVI equations for a single vortex dipole (appendix B.2).

B.1 Matching of Parameters between CGLE, HVI and DGPE

In section 7.2 we argue that the dissipative Gross–Pitaevskii equation

$$\partial_t u(t, \boldsymbol{x}) = \frac{\mathrm{i} + \gamma}{2\tau} \left[\boldsymbol{\nabla}^2 + 2\tilde{\mu} \left(1 - |u(t, \boldsymbol{x})|^2 \right) \right] u(t, \boldsymbol{x}) \tag{B.1}$$

is just another formulation of the complex Ginzburg–Landau equation (CGLE),

$$\left(\delta_{\tilde{\xi}} + \mathrm{i}\alpha \right) \partial_t u_{\tilde{\xi}} = \boldsymbol{\nabla}^2 u_{\tilde{\xi}} + \frac{1}{\tilde{\xi}^2} \left(1 - |u_{\tilde{\xi}}|^2 \right) u_{\tilde{\xi}} , \tag{B.2}$$

with $\delta_{\tilde{\xi}} = \delta/|\ln(\tilde{\xi})|$. Comparing the coefficients of the CGLE with the DGPE yields, after some algebra,

$$\delta_{\tilde{\xi}} = \frac{2\tau\gamma}{1 + \gamma^2} , \qquad \alpha = -\frac{2\tau}{1 + \gamma^2} \tag{B.3}$$

for the CGLE parameters expressed in terms of the DGPE parameters.

In [310, 311] it was shown that in the point-vortex limit, *i. e.*, $\tilde{\xi} \to 0$, solutions of the CGLE for the motion of point-vortices coincide with the HVI equations (7.7). In the following we derive how the friction coefficients C, C' of the HVI equations are related to the free parameters of the CGLE (B.2). In [310, 311], the analysis of the vortex dynamics is restricted to $\alpha = 1$. For our purposes in this thesis, we generalise the results to $\alpha \neq 0$. To this end, we define the new parameters

$$\hat{t} \equiv \frac{t}{\alpha} , \qquad \hat{\delta} \equiv \frac{\delta}{\alpha} . \tag{B.4}$$

B Details on the HVI Equations

In terms of these parameters, the CGLE takes the same form as in [310, 311],

$$\left(\frac{\hat{\delta}}{|\ln(\tilde{\xi})|} + \mathrm{i}\right)\partial_{\hat{t}}u_{\tilde{\xi}} = \boldsymbol{\nabla}^2 u_{\tilde{\xi}} + \frac{1}{\tilde{\xi}^2}\left(1 - |u_{\tilde{\xi}}|^2\right)u_{\tilde{\xi}}. \tag{B.5}$$

A solution to (B.5) for the motion of point vortices is given by [310, 311]

$$\boldsymbol{v}_i = \frac{\mathrm{d}\boldsymbol{x}_i}{\mathrm{d}\hat{t}} = -2\pi\mathcal{C}_i\left(\hat{\delta}w_i\mathbb{I}_2 - \mathbb{J}_2\right)\boldsymbol{\nabla}_{\boldsymbol{x}_i}H_{\mathrm{PV}}(\{\boldsymbol{x}_k, w_k\}), \tag{B.6}$$

with the Kirchhoff–Onsager functional [259]

$$H_{\mathrm{PV}}(\{\boldsymbol{x}_k, w_k \,|\, k = 1, \ldots, N\}) = (2\pi)^{-1}\sum_{i \neq j} w_i w_j \ln|\boldsymbol{x}_i - \boldsymbol{x}_j|, \tag{B.7}$$

and we have slightly reorganised factors of 2π as compared to [310, 311]. Moreover, we have adopted the definition

$$\mathcal{C}_i \equiv -\frac{w_i}{1 + \hat{\delta}^2} = -\frac{w_i\alpha^2}{\alpha^2 + \delta^2}, \tag{B.8}$$

and further defined the 2×2 unit matrix $\mathbb{I}_2$ as well as the matrix $\mathbb{J}_2 = \left(\begin{smallmatrix} 0 & -1 \\ 1 & 0 \end{smallmatrix}\right)$. w_i is again the winding number of the i-th vortex. We now manipulate the equations of motion for the vortices (B.6) until we can directly read off the friction coefficients of the HVI equations (7.7) by comparison of coefficients. Using $\mathbb{I}_2 = -\mathbb{J}_2 \cdot \mathbb{J}_2$ as well as $\hat{\delta} = \delta/\alpha$ and slightly reorganising the terms in (B.6) yields

$$\boldsymbol{v}_i = \frac{\mathrm{d}\boldsymbol{x}_i}{\mathrm{d}t} = \left(\frac{\mathcal{C}_i\delta w_i}{\alpha^2}\mathbb{J}_2 + \frac{\mathcal{C}_i}{\alpha}\mathbb{I}_2\right)2\pi\mathbb{J}_2\boldsymbol{\nabla}_{\boldsymbol{x}_i}H_{\mathrm{PV}}(\{\boldsymbol{x}_k, w_k\}). \tag{B.9}$$

We identify the term to the right of the parenthesis to be directly related to the superfluid velocity $\boldsymbol{v}_{\mathrm{s}}^i$ created by all but the i-th vortex (see equation (7.8)),

$$2\pi\mathbb{J}_2\boldsymbol{\nabla}_{\boldsymbol{x}_i}H_{\mathrm{PV}}(\{\boldsymbol{x}_k, w_k\}) = w_i^{-1}\boldsymbol{v}_{\mathrm{s}}^i, \tag{B.10}$$

where we have made use of the identify $\mathbb{J}_2\boldsymbol{\nabla}_{\boldsymbol{x}_i} = \hat{\boldsymbol{e}}_\perp \times \boldsymbol{\nabla}_{\boldsymbol{x}_i}$, where the nabla operator is acting on a scalar field to the right and $\hat{\boldsymbol{e}}_\perp$ is defined as in chapter 7, *i. e.*, as the unit vector perpendicular to the two-dimensional superfluid domain. Hence,

$$\begin{aligned}
\boldsymbol{v}_i &= \frac{\mathrm{d}\boldsymbol{x}_i}{\mathrm{d}t} = \left(\frac{\mathcal{C}_i\delta}{\alpha^2}\mathbb{J}_2 + \frac{\mathcal{C}_i w_i}{\alpha}\mathbb{I}_2\right)\boldsymbol{v}_{\mathrm{s}}^i \\
&= -\frac{\alpha}{\alpha^2 + \delta^2}\boldsymbol{v}_{\mathrm{s}}^i - w_i\frac{\delta}{\alpha^2 + \delta^2}\hat{\boldsymbol{e}}_\perp \times \boldsymbol{v}_{\mathrm{s}}^i,
\end{aligned} \tag{B.11}$$

where in the second step we have used $w_i^2 = 1$ and $\mathbb{J}_2\boldsymbol{v}_{\mathrm{s}}^i = \hat{\boldsymbol{e}}_\perp \times \boldsymbol{v}_{\mathrm{s}}^i$ and furthermore interchanged the positions of the two terms in the parenthesis. Comparing the coefficients of (B.11) with the HVI equations (7.7),

$$\boldsymbol{v}_i = \frac{\mathrm{d}\boldsymbol{x}_i}{\mathrm{d}t} = (1 - C)\,\boldsymbol{v}_{\mathrm{s}}^i - w_i\,C'\,\hat{\boldsymbol{e}}_\perp \times \boldsymbol{v}_{\mathrm{s}}^i, \tag{B.12}$$

yields

$$C = 1 + \frac{\alpha}{\alpha^2 + \delta^2} \,, \qquad C' = \frac{\delta}{\alpha^2 + \delta^2} \,, \tag{B.13}$$

for the friction coefficients of the HVI equations in terms of the free CGLE parameters. Plugging equations (B.3), relating the CGLE and DGPE parameters, into (B.13) finally yields the HVI friction coefficients expressed in terms of the free DGPE parameters,

$$C = 1 - \frac{1}{2\tau} \frac{1 + \gamma^2}{1 + \gamma^2 |\ln \tilde{\xi}|^2} \,, \qquad C' = \frac{\gamma |\ln \tilde{\xi}|}{2\tau} \frac{1 + \gamma^2}{1 + \gamma^2 |\ln \tilde{\xi}|^2} \,. \tag{B.14}$$

B.2 Solution of the HVI Equations

In this section we solve the HVI equations (B.12) for a single vortex–anti-vortex pair with winding numbers $w_i = -w_{3-i}$ ($i \in \{1, 2\}$).

We first write out the superfluid velocity (7.8) created by all but the i-th vortex by plugging in the explicit form of the Kirchhoff–Onsager functional (B.7),

$$\boldsymbol{v}_\mathrm{s}^i = 2 \sum_{\{j \,|\, j \neq i\}} w_j \frac{\hat{\boldsymbol{e}}_\perp \times (\boldsymbol{x}_i - \boldsymbol{x}_j)}{|\boldsymbol{x}_i - \boldsymbol{x}_j|^2} \,. \tag{B.15}$$

Plugging this into the velocity of the i-th vortex (B.12) yields

$$\boldsymbol{v}_i = \frac{\mathrm{d}\boldsymbol{x}_i}{\mathrm{d}t} = -2 \begin{pmatrix} C' & -(1 - C)w_i \\ (1 - C)w_i & C' \end{pmatrix} \frac{\boldsymbol{x}_i - \boldsymbol{x}_{3-i}}{|\boldsymbol{x}_i - \boldsymbol{x}_{3-i}|^2} \,. \tag{B.16}$$

with $i \in \{1, 2\}$ and we have used $w_i \, w_{3-i} = -1$. In order to solve the coupled system of differential equations (B.16), we define the vortex–anti-vortex separation and the centre-of-mass coordinate of the vortices as

$$\boldsymbol{d}(t) = (\boldsymbol{x}_1 - \boldsymbol{x}_2)(t) = d(t) \, \hat{\boldsymbol{d}}_0 \,, \qquad \boldsymbol{R}(t) = (\boldsymbol{x}_1 + \boldsymbol{x}_2)(t)/2 = R(t) \, \hat{\boldsymbol{d}}_0 \times \hat{\boldsymbol{e}}_\perp \,, \tag{B.17}$$

respectively, just like in the main text, *cf.* equation (7.15). We choose the convention that the dipole vector points from the anti-vortex at position $\boldsymbol{x}_2$ to the vortex at position $\boldsymbol{x}_1$. In the following we also use $w_1 = -w_2 = 1$. For the vortex–anti-vortex separation it follows from equation (B.16) that

$$\frac{\mathrm{d}\boldsymbol{d}(t)}{\mathrm{d}t} = -\frac{4}{d(t)^2} \begin{pmatrix} C' & 0 \\ 0 & C' \end{pmatrix} \hat{\boldsymbol{d}}_0 = -\frac{4C'}{d(t)^2} \hat{\boldsymbol{d}}_0 \,, \tag{B.18}$$

and thus

$$\frac{\mathrm{d}d(t)}{\mathrm{d}t} = -\frac{4C'}{d(t)} \,. \tag{B.19}$$

B Details on the HVI Equations

Integrating this equation yields the vortex–anti-vortex separation as a function of time,

$$d(t) = \sqrt{d(0)^2 - 8C't}\,. \tag{B.20}$$

For the centre-of-mass coordinate, on the other hand, we find

$$\begin{aligned}
\frac{\mathrm{d}\boldsymbol{R}(t)}{\mathrm{d}t} &= \frac{4}{d(t)^2} \begin{pmatrix} 0 & (1-C) \\ -(1-C) & 0 \end{pmatrix} \hat{\boldsymbol{d}}_0 \\
&= \frac{4(1-C)}{d(t)}\, \hat{\boldsymbol{d}}_0 \times \hat{\boldsymbol{e}}_\perp\,,
\end{aligned} \tag{B.21}$$

and thus

$$\frac{\mathrm{d}D(t)}{\mathrm{d}t} = \frac{4(1-C)}{d(t)}\,, \tag{B.22}$$

which can be straightforwardly integrated after plugging in the solution for the vortex–anti-vortex separation (B.20),

$$D(t) = D(0) - \frac{1-C}{C'}\left(\sqrt{d(0)^2 - 8C't} - d(0)\right)\,. \tag{B.23}$$

Hence, according to the HVI equations, point vortices in dissipative superfluids move on straight lines which, for an initial separation of d_0, cross at time $t_I = d_0^2/8C'$ under an enclosing angle β given by

$$\tan(\beta/2) = \frac{d_0/2}{R(t_I) - R(0)} = \frac{C'}{1-C} = -\frac{\delta}{\alpha} = \gamma\,|\ln\tilde{\xi}|\,. \tag{B.24}$$

These relations follow immediately from elementary geometric considerations.

C Radial Occupation Number Spectrum

In this appendix we present details regarding the time evolution and characteristic behaviour of the radial occupation number spectrum of the superfluid for vortex ensemble $\mathcal{B}$ discussed in chapter 13. In addition, we also discuss the characteristics of the spectrum for the time evolution of a single vortex ring which qualitatively agrees with the third universal regime of the time evolution of vortex ensembles $\mathcal{A}$ and $\mathcal{B}$.

C.1 Evolution for Vortex Ensemble $\mathcal{B}$

In this appendix we present details concerning the evolution of the radial occupation number spectrum for vortex ensemble $\mathcal{B}$. To be specific, we discuss the time evolution of the spectrum during the universal stage of the superfluid dynamics with special emphasis on the scaling behaviour during the first and the second universal regime as well as on the characteristic flattening of the spectrum during the third universal regime when only one or very few rings remain in the system. We recall that initial vortex ensemble $\mathcal{B}$ is given by 24 vortex lines consisting of twelve straight vortex-line dipoles, *i. e.*, pairs of lines of opposite winding number, aligned along the three coordinate axes of the superfluid, four along each direction. The universal stage of the dynamics sets in at time $t \approx 50$ and lasts until the final ring has disappeared by shrinking to zero size at time $t \approx 533$ (in unit timesteps).

The first universal regime of the superfluid dynamics sets in at time $t \approx 50$ and lasts for about $\Delta t \approx 60$ unit timesteps. In the upper panel of figure C.1 we display the radial occupation number spectrum at four times during this regime. In an infrared inertial momentum range, the system exhibits a (quasi)-stationary scaling behaviour $n(k) \sim k^{-5.7}$ as indicated by the solid black line (deliberately shifted slightly above the data points). The uncertainty of the scaling exponent is given by $\Delta \zeta = \pm 0.2$, *cf.* section 13.3 or appendix A.3. The inertial momentum range, given by $0.34 \leq k \leq 1.43$ (in units fixed by $z_\mathrm{h} = 1$) as well as the scaling exponent agree with the respective results for vortex ensemble $\mathcal{A}$, see section 13.3 for details. With regard to these two ensembles, and in fact a much larger number of initial conditions that we have studied but not discussed in the main text, the dynamics is thus indeed universal. For a more thorough discussion, see section 13.3. We display snapshots of the vortex configurations at onset and exit times of the scaling regime in panels (*b*), for $t = 50$, and (*c*), for $t = 110$, of figure 13.1ii in section 13.2.

At time $t \approx 150$ the system enters a second universal regime of the superfluid dynamics and remains in it for approximately $\Delta t = 150$ unit timesteps. In the lower panel of figure C.1 we display the radial occupation number spectrum at four
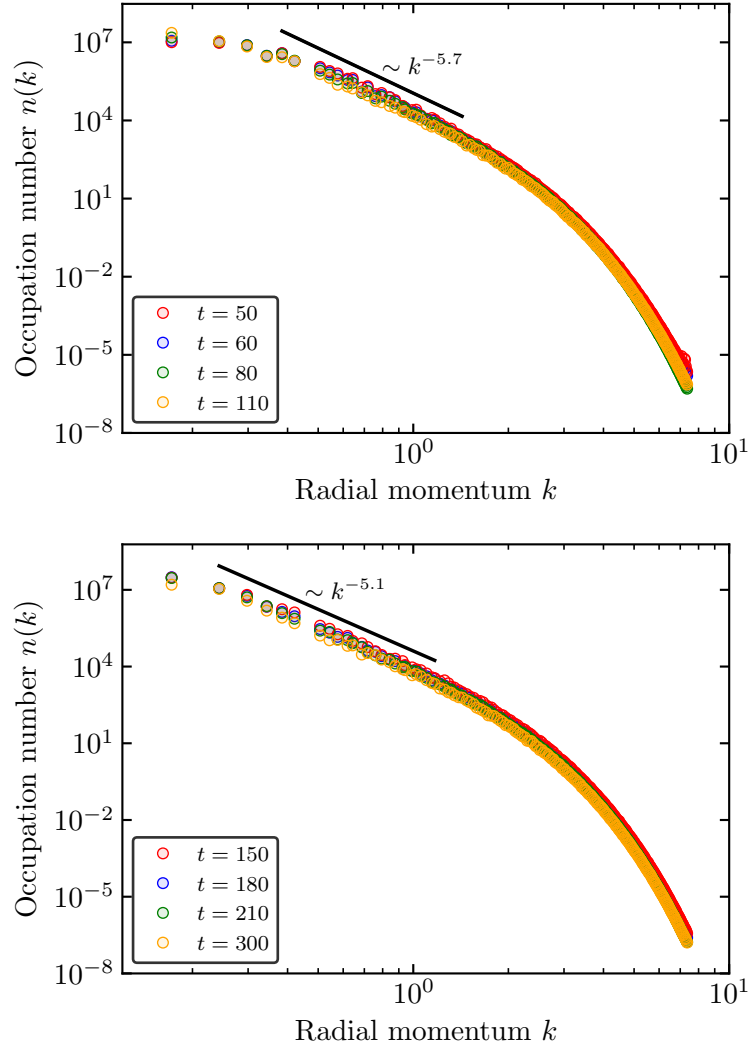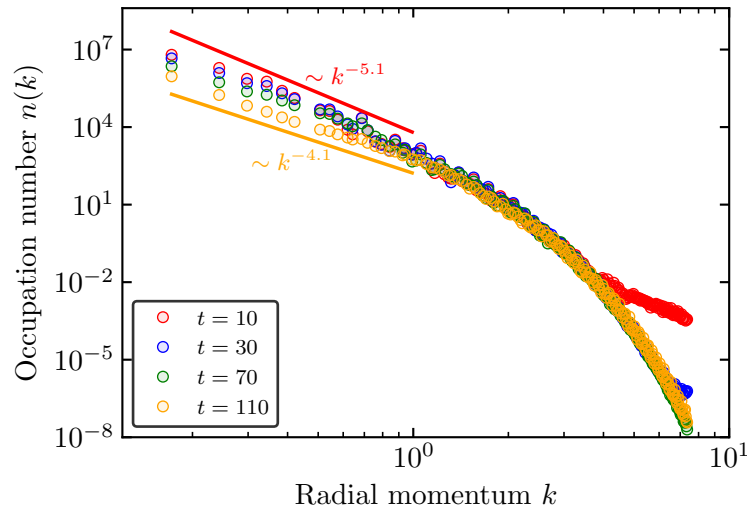
Figure C.1: Occupation number spectrum $n(k)$ as a function of the radial momentum k at four characteristic times during the first (upper panel) and second (lower panel) universal regime, on a double-logarithmic scale, for the evolution of vortex ensemble $\mathcal{B}$. The solid black lines depict the power-law behaviours in the respective regimes and the inertial momentum ranges extracted from a fit to the data points (deliberately shifted above the spectra to aid the visualisation). The scaling behaviour of the spectra in both regimes coincides with the behaviour for vortex ensemble $\mathcal{A}$.
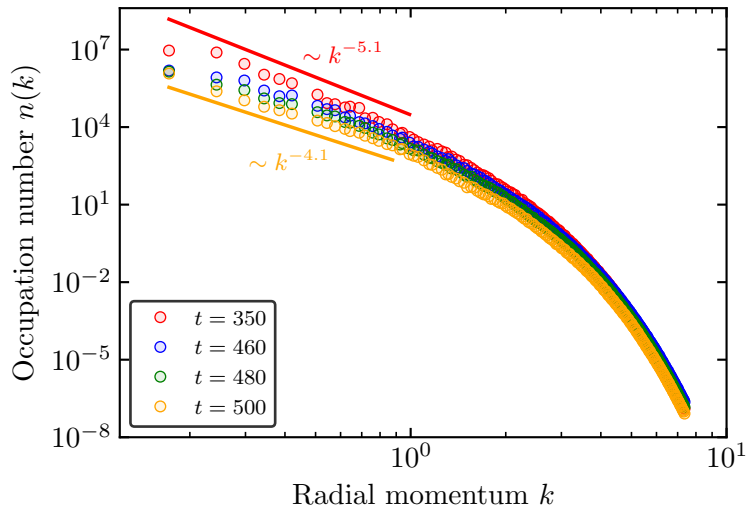
Figure C.2: Occupation number spectrum $n(k)$ as a function of the radial momentum k at four characteristic times during the third universal regime, on a double-logarithmic scale, for the evolution of system $\mathcal{B}$. The spectrum gradually flattens with proceeding time. The red line depicts a power law to indicate the deviation of the data from the scaling behaviour in the prior scaling regime and the solid orange line is plotted to aid the identification of how much the spectrum has flattened during the third scaling regime. In particular, the data points to not obey either power-law behaviour.

times during this regime. The spectrum again exhibits (quasi-)stationary scaling behaviour. As compared to the first regime, the inertial momentum range has shifted further into the infrared ($0.24 \leq k \leq 1.12$) and the scaling exponent is given by $\zeta = 5.1$. We indicate the scaling behaviour by the solid black line which is again deliberately shifted slightly above the data points. We show snapshots of the vortex configurations at onset and exit times of the scaling regime in panels (d), for $t = 150$, and (e), for $t = 300$, of figure 13.1ii in section 13.2. We again find the infrared momentum range (within the uncertainty) as well as the scaling exponent to coincide with the results discussed in the main text for vortex ensemble $\mathcal{A}$.

Once the second universal regime is exited and the final third universal regime is entered, reconnections between the defects cease and only one or very few vortex rings remain in the system and undergo rapid shrinking. At these times, the spectrum gradually flattens and does no longer exhibit any scaling behaviour. In figure C.2 we display the spectrum at characteristic four times during this regime. In order to aid the visualisation and to highlight the deviations of the spectrum from its scaling behaviour in the previous regime, we plot the $n(k) \sim k^{-5.1}$ power law in a similar momentum range as in the second scaling regime (solid red line). More-

Figure C.3: Occupation number spectrum $n(k)$ as a function of the radial momentum k at four characteristic times during the third universal regime, on a double-logarithmic scale, for the evolution of a single vortex ring. The spectrum gradually flattens with proceeding time. Although the system does not exhibit scaling behaviour, we plot the two power laws (red and orange solid lines) to aid the visualisation of the characteristic behaviour of the spectrum and in particular indicate how much the spectrum flattens during the evolution.

over, in order to approximately quantify how much the spectrum flattens during the third regime, we also plot in figure C.2 a power law of $n(k) \sim k^{-4.1}$ below the final curve, which corresponds to the time shortly before the final ring of the system has disappeared. We stress that the spectrum does not exhibit such a scaling behaviour and that it is only plotted here for illustrative purposes as it approximately agrees with the curve at this time. We find analogous behaviour of the spectrum for the superfluid dynamics of system $\mathcal{A}$, *cf.* figure 13.4, indicating the universality of this regime.

C.2 Evolution for a Single Vortex Ring

In this section we discuss the time evolution and the characteristics of the radial occupation number spectrum for the superfluid dynamics of a single vortex ring. To be specific, we analyse the spectrum corresponding to the dynamics of the vortex ring studied in section 12.2. We recall that the ring has an initial radius of $R_0 = 22$ grid points and disappears after $\Delta t = 126$ unit timesteps. In figure C.3 we display the occupation number spectrum at four characteristic times of the evolution of the

vortex ring. We find the spectrum to flatten gradually with proceeding time. In particular, it does not exhibit any (quasi-)stationary scaling behaviour and even at a fixed time, the spectrum does not obey an unequivocal power-law behaviour according to equation (13.4) within a finite inertial momentum range. Nonetheless, to aid the visualisation, we plot two power laws $n(k) \sim k^{-5.1}$ (solid red line) and $n(k) \sim k^{-4.1}$ (solid orange line) shifted slightly above the curve corresponding to the first time and below the curve corresponding to the final time of figure C.3, respectively. In particular, these power-laws aid a comparison of the spectrum with our findings of the characteristic behaviour of the spectrum in the third universal regime of the time evolution of vortex ensembles $\mathcal{A}$ and $\mathcal{B}$ displayed in figures 13.4 and C.2, respectively. The qualitative behaviour of the spectrum displayed in these figures and in figure C.3 is very similar, corroborating that the third universal regime of the superfluid's far-from-equilibrium dynamics approximately coincides with the dynamics of a single vortex ring.

Bibliography

[1] J. M. Maldacena, "The Large-N Limit of Superconformal Field Theories and Supergravity", *Adv. Theor. Math. Phys.* **2** (1998) 231, [`arXiv:hep-th/9711200`].

[2] S. S. Gubser, I. R. Klebanov and A. M. Polyakov, "Gauge Theory Correlators from Non-Critical String Theory", *Phys. Lett.* **B428** (1998) 105, [`arXiv:hep-th/9802109`].

[3] E. Witten, "Anti-de Sitter space and holography", *Adv. Theor. Math. Phys.* **2** (1998) 253, [`arXiv:hep-th/9802150`].

[4] G. 't Hooft, "Dimensional Reduction in Quantum Gravity", `arXiv:gr-qc/9310026`.

[5] L. Susskind, "The world as a hologram", *J. Math. Phys.* **36** (1995) 6377, [`arXiv:hep-th/9409089`].

[6] M. Gyulassy and L. McLerran, "New forms of QCD matter discovered at RHIC", *Nucl. Phys.* **A750** (2005) 30, [`arXiv:nucl-th/0405013`].

[7] P. Braun-Munzinger and J. Stachel, "The quest for the quark-gluon plasma", *Nature* **448** (2007) 302.

[8] P. Braun-Munzinger, V. Koch, T. Schäfer and J. Stachel, "Properties of hot and dense matter from relativistic heavy ion collisions", `arXiv:1510.00442 [nucl-th]`.

[9] A. Andronic, P. Braun-Munzinger, K. Redlich and J. Stachel, "Decoding the phase structure of QCD via particle production at high energy", *Nature* **561** (2018) 321, [`arXiv:1710.09425 [nucl-th]`].

[10] K. G. Wilson, "Confinement of quarks", *Phys. Rev.* **D10** (1974) 2445.

[11] H. J. Rothe, *Lattice Gauge Theories.* World Scientific, 4th ed., 2012.

[12] J. Smit, *Introduction to quantum fields on a lattice*, vol. 15 of *Cambridge Lect. Notes Phys.* Cambridge Univ. Pr., 2002.

[13] C. Wetterich, "Exact evolution equation for the effective potential", *Phys. Lett.* **B301** (1993) 90.

[14] J. Berges, N. Tetradis and C. Wetterich, "Non-perturbative renormalization flow in quantum field theory and statistical physics", *Phys. Rept.* **363** (2002) 223, [`arXiv:hep-ph/0005122`].

[15] J. M. Pawlowski, "Aspects of the functional renormalisation group", *Ann. Phys. (N.Y.).* **322** (2007) 2831–2915, [`arXiv:hep-th/0512261`].

[16] J. Casalderrey-Solana, H. Liu, D. Mateos, K. Rajagopal and U. A. Wiedemann, *Gauge/String Duality, Hot QCD and Heavy Ion Collisions.* Cambridge Univ. Pr., 2014. `arXiv:1101.0618v1 [hep-th]`.

[17] A. Adams, L. D. Carr, T. Schäfer, P. Steinberg and J. E. Thomas, "Strongly Correlated Quantum Fluids: Ultracold Quantum Gases, Quantum Chromodynamic Plasmas, and Holographic Duality", `arXiv:1205.5180 [hep-th]`.

[18] J. Zaanen, Y.-W. Sun, Y. Liu and K. Schalm, *Holographic Duality in Condensed Matter Physics.* Cambridge Univ. Press, 2015.

[19] J. McGreevy, "Holographic duality with a view toward many-body physics", *Adv. High Energy Phys.* **2010** (2010) 723105, [`arXiv:0909.0518 [hep-th]`].

[20] G. Policastro, D. T. Son and A. O. Starinets, "Shear Viscosity of Strongly Coupled $\mathcal{N} = 4$ Supersymmetric Yang-Mills Plasma", *Phys. Rev. Lett.* **87** (2001) 081601, [`arXiv:hep-th/0104066`].

[21] C. P. Herzog, "The Hydrodynamics of M–Theory", *J. High Energy Phys.* **0212** (2002) 026, [`arXiv:hep-th/0210126`].

[22] P. Kovtun, D. T. Son and A. O. Starinets, "Holography and hydrodynamics: diffusion on stretched horizons", *J. High Energy Phys.* **0310** (2003) 064, [`arXiv:hep-th/0309213`].

[23] A. Buchel and J. T. Liu, "Universality of the Shear Viscosity from Supergravity Duals", *Phys. Rev. Lett.* **93** (2004) 090602, [`arXiv:hep-th/0311175`].

[24] A. Buchel, J. T. Liu and A. O. Starinets, "Coupling constant dependence of the shear viscosity in $\mathcal{N} = 4$ supersymmetric Yang–Mills theory", *Nucl. Phys.* **B707** (2005) 56, [`arXiv:hep-th/0406264`].

[25] P. Kovtun, D. T. Son and A. O. Starinets, "Viscosity in Strongly Interacting Quantum Field Theories from Black Hole Physics", *Phys. Rev. Lett.* **94** (2005) 111601, [`arXiv:hep-th/0405231`].

[26] ALICE collaboration, K. Aamodt et al., "Higher harmonic anisotropic flow measurements of charged particles in Pb-Pb collisions at $\sqrt{s_{NN}}$=2.76 TeV", *Phys. Rev. Lett.* **107** (2011) 032301, [`arXiv:1105.3865 [nucl-ex]`].

[27] ATLAS collaboration, G. Aad et al., "Measurement of the azimuthal anisotropy for charged particle production in $\sqrt{s_{NN}} = 2.76$ TeV lead-lead collisions with the ATLAS detector", *Phys. Rev.* **C86** (2012) 014907, [`arXiv:1203.3087 [hep-ex]`].

[28] C. Gale, S. Jeon, B. Schenke, P. Tribedy and R. Venugopalan, "Event-by-event anisotropic flow in heavy-ion collisions from combined Yang-Mills and viscous fluid dynamics", *Phys. Rev. Lett.* **110** (2013) 012302, [`arXiv:1209.6330 [nucl-th]`].

[29] B. Schenke and R. Venugopalan, "Eccentric Protons? Sensitivity of Flow to System Size and Shape in p+p, p+Pb and Pb+Pb Collisions", *Phys. Rev. Lett.* **113** (2014) 102301, [`arXiv:1405.3605 [nucl-th]`].

[30] U. Heinz and R. Snellings, "Collective flow and viscosity in relativistic heavy-ion collisions", *Ann. Rev. Nucl. Part. Sci.* **63** (2013) 123–151, [`arXiv:1301.2826 [nucl-th]`].

[31] Y. P. Sachkou et al., "Coherent vortex dynamics in a strongly interacting superfluid on a silicon chip", *Science* **366** (2019) 1480, [`arXiv:1902.04409 [cond-mat.other]`].

[32] S. P. Johnstone, A. J. Groszek, P. T. Starkey, C. J. Billington, T. P. Simula et al., "Evolution of large-scale flow from turbulence in a two-dimensional superfluid", *Science* **364** (2019) 1267, [`arXiv:1801.06952v2 [cond-mat.quant-gas]`].

[33] G. Gauthier et al., "Giant vortex clusters in a two-dimensional quantum fluid", *Science* **364** (2019) 1264, [`arXiv:1801.06951 [cond-mat.quant-gas]`].

[34] M. Prüfer, P. Kunkel, H. Strobel, S. Lannig, D. Linnemann et al., "Observation of universal dynamics in a spinor Bose gas far from equilibrium", *Nature* **563** (2018) 217, [`arXiv:1805.11881 [cond-mat.quant-gas]`].

[35] C. Eigen, J. A. P. Glidden, R. Lopes, E. A. Cornell, R. P. Smith and Z. Hadzibabic, "Universal prethermal dynamics of Bose gases quenched to unitarity", *Nature* **563** (2018) 221, [`arXiv:1805.09802 [cond-mat.quant-gas]`].

[36] S. Erne, R. Bücker, T. Gasenzer, J. Berges and J. Schmiedmayer, "Universal dynamics in an isolated one-dimensional Bose gas far from equilibrium", *Nature* **563** (2018) 225, [`arXiv:1805.12310 [cond-mat.quant-gas]`].

[37] G. I. Harris, D. L. McAuslan, E. Sheridan, Y. Sachkou, C. Baker and W. P. Bowen, "Laser cooling and control of excitations in superfluid helium", *Nat. Phys.* **12** (2016) 788, [`arXiv:1506.04542 [quant-ph]`].

[38] L. Chomaz, L. Corman, T. Bienaimé, R. Desbuquois, C. Weitenberg et al., "Emergence of coherence via transverse condensation in a uniform quasi-two-dimensional Bose gas", *Nat. Commun.* **6** (2015) 6162, [`arXiv:1411.3577 [cond-mat.quant-gas]`].

[39] A. Polkovnikov, K. Sengupta, A. Silva and M. Vengalattore, "Colloquium: Nonequilibrium dynamics of closed interacting quantum systems", *Rev. Mod. Phys.* **83** (2011) 863, [`arXiv:1007.5331 [cond-mat.stat-mech]`].

[40] Z. Hadzibabic and J. Dalibard, "Two-dimensional Bose fluids: An atomic physics perspective", in *Nano optics and atomics: transport of light and matter waves, Proceedings of the International School of Physics "Enrico Fermi", Course CLXXIII, Varenna, 2009*, IOS Press, Amsterdam, 2009, `arXiv:0912.1490 [cond-mat.quant-gas]`.

[41] D. Kivotides, "Energy spectra of finite temperature superfluid helium-4 turbulence", *Phys. Fluid* **26** (2014) 105105.

[42] M. Tsubota, "Quantum turbulence", *J. Phys. Soc. Jpn.* **77** (2008) 111006.

[43] W. P. Halperin and M. Tsubota, eds., *Progress in Low Temperature Physics Vol. 16: Quantum Turbulence*. Elsevier, Amsterdam, 2008.

[44] J. Maurer and P. Tabeling, "Local investigation of superfluid turbulence", *Europhys. Lett.* **43** (1998) 29.

[45] S. R. Stalp, L. Skrbek and R. J. Donnelly, "Decay of Grid Turbulence in a Finite Channel", *Phys. Rev. Lett.* **82** (1999) 4831.

[46] S. S. Gubser, "Breaking an Abelian gauge symmetry near a black hole horizon", *Phys. Rev.* **D78** (2008) 065034, [`arXiv:0801.2977 [hep-th]`].

[47] S. A. Hartnoll, C. P. Herzog and G. T. Horowitz, "Building a Holographic Superconductor", *Phys. Rev. Lett.* **101** (2008) 031601, [`arXiv:0803.3295 [hep-th]`].

[48] C. Herzog, P. Kovtun and D. Son, "Holographic model of superfluidity", *Phys. Rev.* **D79** (2009) 066002, [`arXiv:0809.4870 [hep-th]`].

[49] O. Aharony, S. S. Gubser, J. M. Maldacena, H. Ooguri and Y. Oz, "Large N field theories, string theory and gravity", *Phys. Rept.* **323** (2000) 183, [`arXiv:hep-th/9905111`].

[50] M. Ammon and J. Erdmenger, *Gauge/Gravity Duality: Foundations and Applications*. Cambridge Univ. Pr., 2015.

[51] S. W. Hawking, "Particle creation by black holes", *Commun. Math. Phys.* **43** (1975) 199.

[52] J. D. Bekenstein, "Black Holes and Entropy", *Phys. Rev. D* **7** (1973) 2333.

[53] S. W. Hawking, "Breakdown of predictability in gravitational collapse", *Phys. Rev.* **D14** (1976) 2460.

[54] A. Dobado, "An elementary introduction to the Holographic Principle", in *32nd International Meeting on Fundamental Physics*, 2005, `arXiv:hep-ph/0506027`.

[55] D. Gabor, "A new microscopic principle", *Nature* **161** (1948) 777.

[56] M. Ammon, J. Erdmenger, M. Kaminski and P. Kerner, "Superconductivity from gauge/gravity duality with flavor", *Phys. Lett.* **B680** (2009) 516, [`arXiv:0810.2316 [hep-th]`].

[57] D. Bigatti and L. Susskind, "TASI lectures on the Holographic Principle", in *Theoretical Advanced Study Institute in Elementary Particle Physics (TASI 99): Strings, Branes, and Gravity*, p. 883, 1999, `arXiv:hep-th/0002044`.

[58] G. 't Hooft, "A planar diagram theory for strong interactions", *Nucl. Phys.* **B72** (1974) 461.

[59] M. B. Green, J. H. Schwarz and E. Witten, *Superstring Theory.* Cambridge Monographs on Mathematical Physics. Cambridge Univ. Pr., 1988.

[60] J. Polchinski, *String Theory.* Cambridge Monographs on Mathematical Physics. Cambridge Univ. Pr., 1998.

[61] R. Blumenhagen, D. Lüst and S. Theisen, *Basic concepts of string theory.* Theoretical and Mathematical Physics. Springer, Heidelberg, Germany, 2013.

[62] K. Becker, M. Becker and J. H. Schwarz, *String theory and M-theory: A modern introduction.* Cambridge Univ. Pr., 2006.

[63] D. Tong, "Lectures on String Theory", `arXiv:0908.0333 [hep-th]`. Lectures in Part III of the Mathematical Tripos at the University of Cambridge.

[64] J. Polchinski, "Dirichlet Branes and Ramond-Ramond charges", *Phys. Rev. Lett.* **75** (1995) 4724, [`arXiv:hep-th/9510017`].

[65] C. Frances, "The conformal boundary of anti-de Sitter space-times", in *IRMA Lectures in Mathematics and Theoretical Physics* (O. Biquard, ed.), vol. 8, p. 205. European Mathematical Society, 2005.

[66] G. Gibbons, "Anti-de-Sitter spacetime and its uses", in *2nd Samos Meeting on Cosmology, Geometry and Relativity: Mathematical and Quantum Aspects of Relativity and Cosmology*, p. 102, 2011, `arXiv:1110.1206 [hep-th]`.

[67] E. D'Hoker and D. Z. Freedman, "Supersymmetric Gauge Theories and the AdS/CFT Correspondence", `arXiv:hep-th/0201253`.

[68] S. P. Martin, *A Supersymmetry Primer*, vol. 21, p. 1. 2010. `arXiv:hep-ph/9709356`.

[69] M. Natsuume, *AdS/CFT Duality User Guide*, vol. 903. 2015. `arXiv:1409.3575 [hep-th]`.

[70] E. Witten, "Bound states of strings and p-branes", *Nucl. Phys.* **B460** (1996) 335–350, [`arXiv:hep-th/9510135`].

[71] G. W. Gibbons and P. K. Townsend, "Vacuum interpolation in supergravity via super p-branes", *Phys. Rev. Lett.* **71** (1993) 3754–3757, [`arXiv:hep-th/9307049`].

[72] G. T. Horowitz and A. Strominger, "Black strings and p-branes", *Nucl. Phys.* **B360** (1991) 197.

[73] I. R. Klebanov, "World volume approach to absorption by nondilatonic branes", *Nucl. Phys.* **B496** (1997) 231, [`arXiv:hep-th/9702076`].

[74] S. S. Gubser, I. R. Klebanov and A. A. Tseytlin, "String theory and classical absorption by three-branes", *Nucl. Phys.* **B499** (1997) 217, [`arXiv:hep-th/9703040`].

[75] L. Susskind and E. Witten, "The Holographic Bound in Anti-de Sitter Space", `arXiv:hep-th/9805114`.

[76] A. W. Peet and J. Polchinski, "UV/IR relations in AdS dynamics", *Phys. Rev.* **D59** (1999) 065011, [`arXiv:hep-th/9809022`].

[77] S. de Haro, K. Skenderis and S. N. Solodukhin, "Holographic Reconstruction of Spacetime and Renormalization in the AdS/CFT Correspondence", *Commun. Math. Phys.* **217** (2001) 595, [`arXiv:hep-th/0002230 [hep-th]`].

[78] K. Skenderis, "Lecture notes on holographic renormalization", *Classical and Quantum Gravity* **19** (2002) 5849, [`arXiv:hep-th/0209067 [hep-th]`].

[79] I. R. Klebanov and E. Witten, "AdS/CFT correspondence and symmetry breaking", *Nucl. Phys.* **B556** (1999) 89, [`arXiv:hep-th/9905104`].

[80] V. Balasubramanian, P. Kraus and A. E. Lawrence, "Bulk versus boundary dynamics in anti-de Sitter spacetime", *Phys. Rev.* **D59** (1999) 046003, [`arXiv:hep-th/9805171`].

[81] V. Balasubramanian, P. Kraus, A. E. Lawrence and S. P. Trivedi, "Holographic probes of anti-de Sitter spacetimes", *Phys. Rev.* **D59** (1999) 104021, [`arXiv:hep-th/9808017`].

[82] P. Breitenlohner and D. Z. Freedman, "Positive energy in anti-de Sitter backgrounds and gauged extended supergravity", *Phys. Lett.* **B115** (1982) 197.

[83] P. Breitenlohner and D. Z. Freedman, "Stability in gauged extended supergravity", *Ann. Phys. (N.Y.)* **144** (1982) 249.

[84] L. Mezincescu and P. Townsend, "Stability at a local maximum in higher dimensional anti-de Sitter space and applications to supergravity", *Ann. Phys. (N.Y.)* **160** (1985) 406.

[85] E. Witten, "Anti-de Sitter space, thermal phase transition, and confinement in gauge theories", *Adv. Theor. Math. Phys.* **2** (1998) 505, [`arXiv:hep-th/9803131`].

[86] M. Brigante, H. Liu, R. C. Myers, S. Shenker and S. Yaida, "Viscosity bound violation in higher derivative gravity", *Phys. Rev.* **D77** (2008) 126006, [`arXiv:0712.0805 [hep-th]`].

[87] T. Sakai and S. Sugimoto, "Low Energy Hadron Physics in Holographic QCD", *Prog. Theor. Phys.* **113** (2005) 843, [`arXiv:hep-th/0412141`].

[88] T. Sakai and S. Sugimoto, "More on a Holographic Dual of QCD", *Prog. Theor. Phys.* **114** (2005) 1083, [`arXiv:hep-th/0507073`].

[89] A. Karch and E. Katz, "Adding flavor to AdS/CFT", *J. High Energy Phys.* **0206** (2002) 043, [`arXiv:hep-th/0205236`].

[90] G. W. Gibbons and S. W. Hawking, "Action integrals and partition functions in quantum gravity", *Phys. Rev.* **D15** (1977) 2752.

[91] S. A. Hartnoll, A. Lucas and S. Sachdev, *Holographic quantum matter*. MIT press, 2018. `arXiv:1612.07324 [hep-th]`.

[92] D. Marolf and S. F. Ross, "Boundary Conditions and New Dualities: Vector Fields in AdS/CFT", *JHEP* **0611** (2006) 085, [`arXiv:hep-th/0606113`].

[93] M. Cvetic and S. S. Gubser, "Phases of R charged black holes, spinning branes and strongly coupled gauge theories", *JHEP* **04** (1999) 024, [`arXiv:hep-th/9902195`].

[94] M. Cvetic, M. Duff, P. Hoxha, J. T. Liu, H. Lu et al., "Embedding AdS black holes in ten and eleven dimensions", *Nucl. Phys.* **B558** (1999) 96, [`arXiv:hep-th/9903214`].

[95] S. S. Gubser, "Thermodynamics of spinning D3-branes", *Nucl. Phys.* **B551** (1999) 667, [`arXiv:hep-th/9810225`].

[96] A. Chamblin, R. Emparan, C. V. Johnson and R. C. Myers, "Charged AdS black holes and catastrophic holography", *Phys. Rev.* **D60** (1999) 064018, [`arXiv:hep-th/9902170`].

[97] T. Faulkner, H. Liu, J. McGreevy and D. Vegh, "Emergent quantum criticality, Fermi surfaces, and AdS(2)", *Phys. Rev.* **D83** (2011) 125002, [`arXiv:0907.2694 [hep-th]`].

[98] G. Gibbons, "Aspects of Supergravity Theories", in *XV GIFT Seminar on Supersymmetry and Supergravity*, 1984.

[99] D. Wilks, J. Wilks and D. Betts, *An Introduction to Liquid Helium.* Oxford Library of the Physical Sciences. Clarendon Press, 1987.

[100] J. Wilks, *The Properties of Liquid and Solid Helium.* International Series of Monographs on Physics. Clarendon Press, 1967.

[101] P. Nozieres and D. Pines, *Theory Of Quantum Liquids, Vol II, Superfluid Bose Liquids.* Advanced Books Classics. Avalon Publishing, 1999.

[102] P. Kapitza, "Viscosity of Liquid Helium below the λ-Point", *Nature* **141** (1938) 74.

[103] J. Bardeen, L. N. Cooper and J. R. Schrieffer, "Theory of Superconductivity", *Phys. Rev.* **108** (1957) 1175.

[104] M. Greiner, C. A. Regal and D. S. Jin, "Fermionic Condensates", *AIP Conf. Proc.* (2005) , [`arXiv:cond-mat/0502539 [cond-mat.other]`].

[105] W. F. Vinen, ed., *The physics of superfluid helium*, p. 414. CERN, 2004.

[106] S. I. Vilchynskyy, A. I. Yakimenko, K. O. Isaieva and A. V. Chumachenko, "The nature of superfluidity and Bose-Einstein condensation: From liquid 4He to dilute ultracold atomic gases (Review Article)", *Low Temp. Phys.* **39** (2013) 724.

[107] A. Griffin, "New light on the intriguing history of superfluidity in liquid 4He", *J. Phys. Condens. Matter* **21** (2009) 164220.

[108] S. Balibar, "The Discovery of Superfluidity", *J. Low Temp. Phys.* **146** (2007) 441, [`arXiv:physics/0611119 [physics.hist-ph]`].

[109] J. M. Kosterlitz, "Superfluidity in Thin Films of 4He", *J. Low Temp. Phys* (2020) .

[110] J. F. Allen and A. D. Misener, "Flow Phenomena in Liquid Helium II", *Nature* **142** (1938) 643.

[111] H. K. Onnes, "The liquefaction of helium", *Koninklijke Nederlandse Akademie von Wetenschappen, Proceedings* **11** (1908) 1908.

[112] W. Keesom, *Helium.* Elsevier, 1942.

[113] F. London, "The λ-Phenomenon of Liquid Helium and the Bose-Einstein Degeneracy", *Nature* **141** (1938) 643.

[114] F. London, "On the Bose-Einstein Condensation", *Phys. Rev.* **54** (1938) 947.

[115] E. A. Cornell and C. E. Wieman, "Nobel Lecture: Bose-Einstein condensation in a dilute gas, the first 70 years and some recent experiments", *Rev. Mod. Phys.* **74** (2002) 875.

[116] L. Tisza, "Transport Phenomena in Helium II", *Nature* **141** (1938) 913.

[117] L. Landau, "Theory of the Superfluidity of Helium II", *Phys. Rev.* **60** (1941) 356.

[118] I. M. Khalatnikov and I. M. Khalatnikov, *An introduction to the theory of superfluidity.* Frontiers in Physics. Benjamin, New York, NY, 1965. Trans. from the Russian.

[119] K. R. Atkins and R. A. Stasior, "First Sound In Liquid Helium At High Pressures", *Can. J. Phys.* **31** (1953) 1156.

[120] I. Bogoyavlenskii, L. Karnatsevich, J. Kozlov and A. Puchkov, "Neutron scattering determination of condensate in liquid 4He", *Physica* **B176** (1992) 151.

[121] A. Griffin, "Condensate forced out of hiding", *Nature* **391** (1998) 25.

[122] A. Griffin, D. Snoke and S. Stringari, *Bose-Einstein Condensation.* Cambridge University Press, 1996.

[123] N. H. March and Z. M. Galasiewicz, "Superfluidity, ground-state wave function and bose condensation in liquid helium four", *Phys. Chem. Liq.* **5** (1976) 103.

[124] N. Bogolyubov, "On the theory of superfluidity", *J. Phys. (USSR)* **11** (1947) 23.

[125] O. Penrose and L. Onsager, "Bose-Einstein Condensation and Liquid Helium", *Phys. Rev.* **104** (1956) 576.

[126] C. N. Yang, "Concept of Off-Diagonal Long-Range Order and the Quantum Phases of Liquid He and of Superconductors", *Rev. Mod. Phys.* **34** (1962) 694.

[127] M. H. Anderson, J. R. Ensher, M. R. Matthews, C. E. Wieman and E. A. Cornell, "Observation of Bose-Einstein condensation in a Dilute Atomic Vapor", *Science* **269** (1995) 198.

[128] C. C. Bradley, C. A. Sackett, J. J. Tollett and R. G. Hulet, "Evidence of Bose-Einstein Condensation in an Atomic Gas with Attractive Interactions", *Phys. Rev. Lett.* **75** (1995) 1687.

[129] K. B. Davis, M. O. Mewes, M. R. Andrews, N. J. van Druten, Durfee et al., "Bose-Einstein Condensation in a Gas of Sodium Atoms", *Phys. Rev. Lett.* **75** (1995) 3969.

[130] P. O. Fedichev and U. R. Fischer, "Gibbons-Hawking Effect in the Sonic de Sitter Space-Time of an Expanding Bose-Einstein-Condensed Gas", *Phys. Rev. Lett.* **91** (2003) 240407, [`arXiv:cond-mat/0304342`].

[131] A. Recati, P. O. Fedichev, W. Zwerger, J. von Delft and P. Zoller, "Atomic Quantum Dots Coupled to a Reservoir of a Superfluid Bose-Einstein Condensate", *Phys. Rev. Lett.* **94** (2005) 040404, [`arXiv:cond-mat/0404533 [cond-mat.other]`].

[132] L. Berezhiani and J. Khoury, "Theory of dark matter superfluidity", *Phys. Rev.* **D92** (2015) 103510, [`arXiv:1507.01019 [astro-ph.CO]`].

[133] J. T. Devreese and J. Tempere, "Superfluidity from He-4 to ultracold atomic condensed systems", *Physica* **C479** 36.

[134] R. J. Donnelly, *Quantized Vortices in Liquid He II*. Cambridge Studies in Low Temperature Physics. CUP, Cambridge, UK, 2005.

[135] D. R. Tilley and J. Tilley, *Superfluidity and Superconductivity*. Institute of Physics Publishing, 2003.

[136] C. Pethick and H. Smith, *Bose-Einstein condensation in dilute gases*. CUP, Cambridge, UK, 2006.

[137] T. Langen, T. Gasenzer and J. Schmiedmayer, "Prethermalization and universal dynamics in near-integrable quantum systems", *J. Stat. Mech.* **1606** (2016) 064009, [`arXiv:1603.09385 [cond-mat.quant-gas]`].

[138] E. P. Gross, "Structure of a quantized vortex in boson systems", *Nuovo Cim.* **20** (1961) 454.

[139] L. P. Pitaevskii, "Vortex Lines in an Imperfect Bose gas", *Sov. Phys. JETP* **13** (1961) 451. [Zh. Eksp. Teor. Fiz. 40 (1961) 646].

[140] J. Berges, J.-P. Blaizot and F. Gelis, "EMMI rapid reaction task force on 'Thermalization in non-Abelian plasmas'", *J. Phys.* **G39** (2012) 085115, [`arXiv:1203.2042 [hep-ph]`].

[141] L. Kofman, A. Linde and A. A. Starobinsky, "Reheating after Inflation", *Phys. Rev. Lett.* **73** (1994) 3195.

[142] R. Micha and I. I. Tkachev, "Relativistic Turbulence: A Long Way from Preheating to Equilibrium", *Phys. Rev. Lett.* **90** (2003) 121301, [`arXiv:hep-ph/0210202 [hep-ph]`].

[143] P. W. Anderson and N. Itoh, "Pulsar glitches and restlessness as a hard superfluidity phenomenon", *Nature* **256** (1975) 25.

[144] J. Kasprzak et al., "Bose–Einstein condensation of exciton polaritons", *Nature* **443** (2006) 409.

[145] K. G. Lagoudakis, M. Wouters, M. Richard, A. Baas, I. Carusotto et al., "Quantized vortices in an exciton–polariton condensate", *Nat. Phys.* **4** (2008) 706, [`arXiv:0801.1916 [cond-mat.other]`].

[146] K. G. Lagoudakis, T. Ostatnický, A. V. Kavokin, Y. G. Rubo, R. André et al., "Observation of Half-Quantum Vortices in an Exciton–Polariton Condensate", *Science* **326** (2009) 974, [`arXiv:0911.2555 [cond-mat.quant-gas]`].

[147] A. Amo et al., "Polariton Superfluids Reveal Quantum Hydrodynamic Solitons", *Science* **332** (2011) 1167, [`arXiv:1101.2530 [cond-mat.quant-gas]`].

[148] A. Adams, P. M. Chesler and H. Liu, "Holographic Vortex Liquids and Superfluid Turbulence", *Science* **341** (2012) 368, [`arXiv:1212.0281 [hep-th]`].

[149] P. M. Chesler, A. M. Garcia-Garcia and H. Liu, "Defect Formation beyond Kibble-Zurek Mechanism and Holography", *Phys. Rev.* **X5** (2015) 021015, [`arXiv:1407.1862 [hep-th]`].

[150] C. Ewerz, T. Gasenzer, M. Karl and A. Samberg, "Non-thermal fixed point in a holographic superfluid", *J. High Energy Phys.* **1505** (2015) 070, [`arXiv:1410.3472 [hep-th]`].

[151] P. M. Chesler, N. Kilbertus and W. van der Schee, "Universal hydrodynamic flow in holographic planar shock collisions", *J. High Energy Phys.* **1511** (2015) 135, [`arXiv:1507.02548 [hep-th]`].

[152] P. M. Chesler and L. G. Yaffe, "Holography and Colliding Gravitational Shock Waves in Asymptotically AdS$_5$ Spacetime", *Phys. Rev. Lett.* **106** (2011) 021601, [`arXiv:1011.3562 [hep-th]`].

[153] J. Casalderrey-Solana, M. P. Heller, D. Mateos and W. van der Schee, "From Full Stopping to Transparency in a Holographic Model of Heavy Ion Collisions", *Phys. Rev. Lett.* **111** (2013) 181601, [`arXiv:1305.4919 [hep-th]`].

[154] M. P. Heller, D. Mateos, W. van der Schee and D. Trancanelli, "Strong Coupling Isotropization of Non-Abelian Plasmas Simplified", *Phys. Rev. Lett.* **108** (2012) 191601, [`arXiv:1202.0981 [hep-th]`].

[155] S. Waeber, A. Rabenstein, A. Schäfer and L. G. Yaffe, "Asymmetric shockwave collisions in AdS$_5$", *J. High Energy Phys.* **1908** (2019) 005, [`arXiv:1906.05086 [hep-th]`].

[156] H. Liu and J. Sonner, "Holographic systems far from equilibrium: a review", `arXiv:1810.02367 [hep-th]`.

[157] C. P. Herzog, "Lectures on holographic superfluidity and superconductivity", *J. Phys.* **A42** (2009) 343001, [`arXiv:0904.1975 [hep-th]`].

[158] J. Sonner and B. Withers, "Gravity derivation of the Tisza-Landau model in AdS/CFT", *Phys. Rev.* **D82** (2010) 026001, [`arXiv:1004.2707 [hep-th]`].

[159] D. Anninos, S. A. Hartnoll and N. Iqbal, "Holography and the Coleman-Mermin-Wagner theorem", *Phys. Rev.* **D82** (2010) 066008, [`arXiv:1005.1973 [hep-th]`].

[160] M. J. Bhaseen, J. P. Gauntlett, B. D. Simons, J. Sonner and T. Wiseman, "Holographic Superfluids and the Dynamics of Symmetry Breaking", *Phys. Rev. Lett.* **110** (2013) 015301, [`arXiv:1207.4194 [hep-th]`].

[161] V. Keranen, E. Keski-Vakkuri, S. Nowling and K. Yogendran, "Inhomogeneous structures in holographic superfluids: II. Vortices", *Phys. Rev.* **D81** (2010) 126012, [`arXiv:0912.4280 [hep-th]`].

[162] O. J. C. Dias, G. T. Horowitz, N. Iqbal and J. E. Santos, "Vortices in holographic superfluids and superconductors as conformal defects", *J. High Energy Phys.* **1404** (2014) 096, [`arXiv:1311.3673 [hep-th]`].

[163] S.-Q. Lan, G.-Q. Li, J.-X. Mo and X.-B. Xu, "Attractive interaction between vortex and anti-vortex in holographic superfluid", *J. High Energy Phys.* **1902** (2019) 122, [`arXiv:1811.00623 [cond-mat.quant-gas]`].

[164] C. Ewerz, A. Samberg and P. Wittmer, "Dynamics of a vortex dipole in a holographic superfluid", *in preparation.*

[165] J. Sonner, A. del Campo and W. H. Zurek, "Universal far-from-equilibrium dynamics of a holographic superconductor", *Nat. Commun.* **6** (2015) 7406, [`arXiv:1406.2329 [hep-th]`].

[166] G. T. Horowitz and M. M. Roberts, "Holographic superconductors with various condensates", *Phys. Rev.* **D78** (2008) 126008, [`arXiv:0810.1077 [hep-th]`].

[167] D. Arean, P. Basu and C. Krishnan, "The many phases of holographic superfluids", *J. High Energy Phys.* **1010** (2010) 006, [`arXiv:1006.5165 [hep-th]`].

[168] Y. Du, C. Niu, Y. Tian and H. Zhang, "Holographic thermal relaxation in superfluid turbulence", *J. High Energy Phys.* **12** (2015) 018, [`arXiv:1412.8417 [hep-th]`].

[169] C.-Y. Xia, H.-B. Zeng, H.-Q. Zhang, Z.-Y. Nie, Y. Tian and X. Li, "Vortex lattice in a rotating holographic superfluid", *Phys. Rev.* **D100** (2019) 061901, [`arXiv:1904.10925 [hep-th]`].

[170] P. W. Higgs, "Broken symmetries, massless particles and gauge fields", *Phys. Lett.* **12** (1964) 132.

[171] P. W. Higgs, "Broken Symmetries and the Masses of Gauge Bosons", *Phys. Rev. Lett.* **13** (1964) 508.

[172] F. Englert and R. Brout, "Broken Symmetry and the Mass of Gauge Vector Mesons", *Phys. Rev. Lett.* **13** (1964) 321.

[173] P. W. Anderson, "Plasmons, Gauge Invariance, and Mass", *Phys. Rev.* **130** (1963) 439.

[174] G. S. Guralnik, C. R. Hagen and T. W. B. Kibble, "Global Conservation Laws and Massless Particles", *Phys. Rev. Lett.* **13** (1964) 585.

[175] P. Basu, A. Mukherjee and H.-H. Shieh, "Supercurrent: Vector hair for an AdS black hole", *Phys. Rev.* **D79** (2009) 045010, [`arXiv:0809.4494 [hep-th]`].

[176] S. S. Gubser, "Colorful Horizons with Charge in Anti-de Sitter Space", *Phys. Rev. Lett.* **101** (2008) 191601, [`arXiv:0803.3483 [hep-th]`].

[177] P. Basu, J. He, A. Mukherjee and H.-H. Shieh, "Superconductivity from D3/D7: holographic pion superfluid", *J. High Energy Phys.* **0911** (2009) 070, [`arXiv:0810.3970 [hep-th]`].

[178] C. P. Herzog and S. S. Pufu, "The second sound of SU(2)", *J. High Energy Phys.* **0904** (2009) 126, [`arXiv:0902.0409 [hep-th]`].

[179] R. J. Donnelly, *Quantized Vortices in Liquid He II*. Cambridge Univ. Pr., 1991.

[180] N. D. Mermin and H. Wagner, "Absence of Ferromagnetism or Antiferromagnetism in One- or Two-Dimensional Isotropic Heisenberg Models", *Phys. Rev. Lett.* **17** (1966) 1133.

[181] P. C. Hohenberg, "Existence of Long-Range Order in One and Two Dimensions", *Phys. Rev.* **158** (1967) 383.

[182] S. A. Hartnoll, *Horizons, holography and condensed matter*, p. 387. 2012. `arXiv:1106.4324 [hep-th]`.

[183] R. Ruffini and J. A. Wheeler, "Introducing the black hole", *Phys. Today* **24** (1971) 30.

[184] S. A. Hartnoll, "Lectures on holographic methods for condensed matter physics", *Class. Quant. Grav.* **26** (2009) 224002, [`arXiv:0903.3246 [hep-th]`].

[185] K. Maeda, M. Natsuume and T. Okamura, "Universality class of holographic superconductors", *Phys. Rev.* **D79** (2009) 126004, [`arXiv:0904.1914 [hep-th]`].

[186] S. Franco, A. Garcia-Garcia and D. Rodriguez-Gomez, "A Ggneral class of holographic superconductors", *J. High Energy Phys.* **1004** (2010) 092, [`arXiv:0906.1214 [hep-th]`].

[187] S. Franco, A. M. Garcia-Garcia and D. Rodriguez-Gomez, " Holographic approach to phase transitions", *Phys. Rev.* **D81** (2010) 041901, [`arXiv:0911.1354 [hep-th]`].

[188] T. Albash and C. V. Johnson, "Vortex and droplet engineering in holographic superconductors", *Phys. Rev.* **D80** (2009) 126009, [`arXiv:0906.1795 [hep-th]`].

[189] S. A. Hartnoll, C. P. Herzog and G. T. Horowitz, "Holographic superconductors", *J. High Energy Phys.* **0812** (2008) 015, [`arXiv:0810.1563 [hep-th]`].

[190] S. S. Gubser and A. Nellore, "Low-temperature behavior of the Abelian Higgs model in Anti-de Sitter space", *J. High Energy Phys.* **0904** (2009) 008, [`arXiv:0810.4554 [hep-th]`].

[191] C. P. Herzog and A. Yarom, "Sound modes in holographic superfluids", *Phys. Rev.* **D80** (2009) 106002, [`arXiv:0906.4810 [hep-th]`].

[192] N. Iqbal, H. Liu and M. Mezei, "Quantum phase transitions in semilocal quantum liquids", *Phys. Rev.* **D91** (2015) 025024, [`arXiv:1108.0425 [hep-th]`].

[193] S. S. Gubser and A. Nellore, "Ground states of holographic superconductors", *Phys. Rev.* **D80** (2009) 105007, [`arXiv:0908.1972 [hep-th]`].

[194] G. T. Horowitz and M. M. Roberts, "Zero temperature limit of holographic superconductors", *J. High Energy Phys.* **0911** (2009) 015, [`arXiv:0908.3677 [hep-th]`].

[195] N. Iqbal, H. Liu, M. Mezei and Q. Si, "Quantum phase transitions in holographic models of magnetism and superconductors", *Phys. Rev.* **D82** (2010) 045002, [`arXiv:1003.0010 [hep-th]`].

[196] R. Gregory, S. Kanno and J. Soda, "Holographic Superconductors with Higher Curvature Corrections", *J. High Energy Phys.* **0910** (2009) 010, [`arXiv:0907.3203 [hep-th]`].

[197] F. Denef and S. A. Hartnoll, "Landscape of superconducting membranes", *Phys. Rev.* **D79** (2009) 126008, [`arXiv:0901.1160 [hep-th]`].

[198] S. S. Gubser, C. P. Herzog, S. S. Pufu and T. Tesileanu, "Superconductors from Superstrings", *Phys. Rev. Lett.* **103** (2009) 141601, [`arXiv:0907.3510 [hep-th]`].

[199] P. M. Chesler and L. G. Yaffe, "Numerical solution of gravitational dynamics in asymptotically anti-de Sitter spacetimes", *J. High Energy Phys.* **1407** (2014) 086, [`arXiv:1309.1439 [hep-th]`].

[200] J. Winicour, "Characteristic Evolution and Matching", *Living Rev. Rel.* **4** (2001) 3, [`arXiv:gr-qc/0102085`].

[201] J. Winicour, "Characteristic Evolution and Matching", *Living Rev. Rel.* **8** (2005) 10, [`arXiv:gr-qc/0508097`].

[202] S. Balibar, "Laszlo Tisza and the two-fluid model of superfluidity", *C. R. Phys.* **18** (2017) 586.

[203] W. Israel, "Covariant superfluid mechanics", *Phys. Lett.* **A86** (1981) 79.

[204] I. Khalatnikov and V. Lebedev, "Relativistic hydrodynamics of a superfluid liquid", *Phys. Lett.* **A91** (1982) 70.

[205] W. Israel, "Equivalence of two theories of relativistic superfluid mechanics", *Phys. Lett.* **A92** (1982) 77.

[206] J. Bhattacharya, S. Bhattacharyya and S. Minwalla, "Dissipative Superfluid dynamics from gravity", *J. High Energy Phys.* **1104** (2011) 125, [`arXiv:1101.3332 [hep-th]`].

[207] C. P. Herzog, N. Lisker, P. Surowka and A. Yarom, "Transport in holographic superfluids", *J. High Energy Phys.* **1108** (2011) 052, [`arXiv:1101.3330 [hep-th]`].

[208] J. Bhattacharya, S. Bhattacharyya, S. Minwalla and A. Yarom, "A theory of first order dissipative superfluid dynamics", *J. High Energy Phys.* **1405** (2014) 147, [`arXiv:1105.3733 [hep-th]`].

[209] M. Rangamani, "Gravity and hydrodynamics: lectures on the fluid-gravity correspondence", *Class. Quant. Grav.* **26** (2009) 224003, [`arXiv:0905.4352 [hep-th]`].

[210] V. E. Hubeny, S. Minwalla and M. Rangamani, *The fluid/gravity correspondence*, p. 348. Cambridge Univ. Pr., 2012. `arXiv:1107.5780 [hep-th]`.

[211] S. S. Gubser and S. S. Pufu, "The gravity dual of a p-wave superconductor", *J. High Energy Phys.* **0811** (2008) 033, [`arXiv:0805.2960 [hep-th]`].

[212] M. M. Roberts and S. A. Hartnoll, "Pseudogap and time reversal breaking in a holographic superconductor", *J. High Energy Phys.* **0808** (2008) 035, [`arXiv:0805.3898 [hep-th]`].

[213] D. T. Son and A. O. Starinets, "Minkowski space correlators in AdS/CFT correspondence: recipe and applications", *J. High Energy Phys.* **0209** (2002) 042, [`arXiv:hep-th/0205051`].

[214] L. P. Pitaevskii and S. Stringari, *Bose-Einstein Condensation*. Clarendon Press, Oxford, 2003.

[215] R. Peierls, "Quelques propriétés typiques des corps solides", *Annales de l'institut Henri Poincaré* **5** (1935) 177.

[216] V. L. Berezinskiǐ, "Destruction of Long-range Order in One-dimensional and Two-dimensional Systems Possessing a Continuous Symmetry Group. II. Quantum Systems", *Sov. Phys. JETP* **34** (1972) 610.

[217] J. Kosterlitz and D. Thouless, "Ordering, metastability and phase transitions in two-dimensional systems", *J. Phys.* **C6** (1973) 1181.

[218] D. J. Bishop and J. D. Reppy, "Study of the Superfluid Transition in Two-Dimensional ^{4}He Films", *Phys. Rev. Lett.* **40** (1978) 1727.

[219] D. S. Petrov, M. Holzmann and G. V. Shlyapnikov, "Bose-Einstein Condensation in Quasi-2D Trapped Gases", *Phys. Rev. Lett.* **84** (2000) 2551, [`arXiv:cond-mat/9909344 [cond-mat.stat-mech]`].

[220] A. Görlitz et al., "Realization of Bose-Einstein Condensates in Lower Dimensions", *Phys. Rev. Lett.* **87** (2001) 130402, [`arXiv:cond-mat/0104549 [cond-mat.soft]`].

[221] D. Rychtarik, B. Engeser, H.-C. Nägerl and R. Grimm, "Two-Dimensional Bose-Einstein Condensate in an Optical Surface Trap", *Phys. Rev. Lett.* **92** (2004) 173003, [`arXiv:cond-mat/0309536 [cond-mat.soft]`].

[222] Z. Hadzibabic, P. Krüger, M. Cheneau, B. Battelier and J. Dalibard, "Berezinskii–Kosterlitz–Thouless crossover in a trapped atomic gas", *Nature* **441** (2006) 1118, [`arXiv:cond-mat/0605291 [cond-mat.other]`].

[223] V. Schweikhard, S. Tung and E. A. Cornell, "Vortex Proliferation in the Berezinskii-Kosterlitz-Thouless Regime on a Two-Dimensional Lattice of Bose-Einstein Condensates", *Phys. Rev. Lett.* **99** (2007) 030401, [`arXiv:0704.0289 [cond-mat.mes-hall]`].

[224] P. Krüger, Z. Hadzibabic and J. Dalibard, "Critical Point of an Interacting Two-Dimensional Atomic Bose Gas", *Phys. Rev. Lett.* **99** (2007) 040402, [`arXiv:cond-mat/0703200 [cond-mat.other]`].

[225] P. Cladé, C. Ryu, A. Ramanathan, K. Helmerson and W. D. Phillips, "Observation of a 2D Bose Gas: From Thermal to Quasicondensate to Superfluid", *Phys. Rev. Lett.* **102** (2009) 170401, [`arXiv:0805.3519 [cond-mat.other]`].

[226] M. Holzmann, G. Baym, J.-P. Blaizot and F. Laloë, "Superfluid transition of homogeneous and trapped two-dimensional Bose gases", *Proc. Natl. Acad. Sci. U.S.A.* **104** (2007) 1476.

[227] Z. Hadzibabic, P. Krüger, M. Cheneau, S. P. Rath and J. Dalibard, "The trapped two-dimensional Bose gas: from Bose-Einstein condensation to Berezinskii-Kosterlitz-Thouless physics", *New J. Phys.* **10** (2008) 045006, [`arXiv:0712.1265 [cond-mat.other]`].

[228] A. Posazhennikova, "Colloquium: Weakly interacting, dilute Bose gases in 2D", *Rev. Mod. Phys.* **78** (2006) 1111, [`arXiv:cond-mat/0506034 [cond-mat.other]`].

[229] T. W. Neely, E. C. Samson, A. S. Bradley, M. J. Davis and B. P. Anderson, "Observation of Vortex Dipoles in an Oblate Bose-Einstein Condensate", *Phys. Rev. Lett.* **104** (2010) 160401, [`arXiv:0912.3773 [cond-mat.quant-gas]`].

[230] T. W. Neely et al., "Characteristics of Two-Dimensional Quantum Turbulence in a Compressible Superfluid", *Phys. Rev. Lett.* **111** (2013) 235301, [`arXiv:1204.1102 [cond-mat.quant-gas]`].

[231] W. J. Kwon, G. Moon, J.-y. Choi, S. W. Seo and Y.-i. Shin, "Relaxation of superfluid turbulence in highly oblate Bose-Einstein condensates", *Phys. Rev.* **A90** (2014) 063627, [`arXiv:1403.4658 [cond-mat.quant-gas]`].

[232] S. W. Seo, B. Ko, J. H. Kim and Y. Shin, "Observation of vortex-antivortex pairing in decaying 2D turbulence of a superfluid gas", *Sci. Rep.* **7** (2017) 4587, [`arXiv:1610.06635 [cond-mat.quant-gas]`].

[233] B. Nowak, D. Sexty and T. Gasenzer, "Superfluid turbulence: Nonthermal Fixed Point in an Ultracold Bose Gas", *Phys. Rev.* **B84** (2011) 020506(R), [`arXiv:1012.4437 [cond-mat.quant-gas]`].

[234] B. Nowak, J. Schole, D. Sexty and T. Gasenzer, "Nonthermal fixed points, vortex statistics, and superfluid turbulence in an ultracold Bose gas", *Phys. Rev.* **A85** (2012) 043627, [`arXiv:1111.6127 [cond-mat.quant-gas]`].

[235] J. Schole, B. Nowak and T. Gasenzer, "Critical dynamics of a two-dimensional superfluid near a nonthermal fixed point", *Phys. Rev.* **A86** (2012) 013624, [`arXiv:1204.2487 [cond-mat.quant-gas]`].

[236] M. Karl, B. Nowak and T. Gasenzer, "Universal scaling at nonthermal fixed points of a two-component Bose gas", *Phys. Rev.* **A88** (2013) 063615, [`arXiv:1307.7368 [cond-mat.quant-gas]`].

[237] T. Simula, M. J. Davis and K. Helmerson, "Emergence of Order from Turbulence in an Isolated Planar Superfluid", *Phys. Rev. Lett.* **113** (2014) 165302, [`arXiv:1405.3399 [cond-mat.quant-gas]`].

[238] H. E. Hall and W. F. Vinen, "The rotation of liquid helium II I. Experiments on the propagation of second sound in uniformly rotating helium II", *Proc. R. Soc. Lond.* **A238** (1956) 204.

[239] S. Iordansky, "On the mutual friction between the normal and superfluid components in a rotating bose gas", *Ann. Phys. (N.Y.)* **29** (1964) 335.

[240] V. Ambegaokar, B. I. Halperin, D. R. Nelson and E. D. Siggia, "Dissipation in Two-Dimensional Superfluids", *Phys. Rev. Lett.* **40** (1978) 783.

[241] E. B. Sonin, "Vortex oscillations and hydrodynamics of rotating superfluids", *Rev. Mod. Phys.* **59** (1987) 87.

[242] V. Ambegaokar, B. I. Halperin, D. R. Nelson and E. D. Siggia, "Dynamics of superfluid films", *Phys. Rev.* **B21** (1980) 1806.

[243] E. B. Sonin, "Magnus force in superfluids and superconductors", *Phys. Rev.* **B55** (1997) 485, [`arXiv:cond-mat/9606099`].

[244] D. J. Thouless, P. Ao and Q. Niu, "Transverse Force on a Quantized Vortex in a Superfluid", *Phys. Rev. Lett.* **76** (1996) 3758, [`arXiv:cond-mat/9603196`].

[245] L. Thompson and P. C. E. Stamp, "Quantum Dynamics of a Bose Superfluid Vortex", *Phys. Rev. Lett.* **108** (2012) 184501, [`arXiv:1110.6386 [cond-mat.mes-hall]`].

[246] T. Cox and P. C. E. Stamp, "Inertial and Fluctuational Effects on the Motion of a Bose Superfluid Vortex", *J. Low Temp. Phys.* **171** (2013) 459, [`arXiv:1207.4237 [cond-mat.quant-gas]`].

[247] M. Kim and W. I. Glaberson, "Vortex Diffusivity in Two-Dimensional Helium Films", *Phys. Rev. Lett.* **52** (1984) 53.

[248] P. W. Adams and W. I. Glaberson, "Vortex dynamics in superfluid helium films", *Phys. Rev.* **B35** (1987) 4633.

[249] R. A. Duine, B. W. A. Leurs and H. T. C. Stoof, "Noisy dynamics of a vortex in a partially Bose-Einstein condensed gas", *Phys. Rev.* **A69** (2004) 053623, [`arXiv:cond-mat/0311651 [cond-mat.stat-mech]`].

[250] Z. Hadzibabic, P. Krüger, M. Cheneau, S. P. Rath and J. Dalibard, "The trapped two-dimensional Bose gas: from Bose–Einstein condensation to Berezinskii–Kosterlitz–Thouless physics", *New J. Phys.* **10** (2008) 045006, [`arXiv:0712.1265 [cond-mat.other]`].

[251] G. Moon, W. J. Kwon, H. Lee and Y.-i. Shin, "Thermal friction on quantum vortices in a Bose-Einstein condensate", *Phys. Rev.* **A92** (2015) 051601, [`arXiv:1509.02236 [cond-mat.quant-gas]`].

[252] G. Blatter, M. V. Feigel'man, V. B. Geshkenbein, A. I. Larkin and V. M. Vinokur, "Vortices in high-temperature superconductors", *Rev. Mod. Phys.* **66** (1994) 1125.

[253] S. Inouye, M. R. Andrews, J. Stenger, H. J. Miesner, D. M. Stamper-Kurn and W. Ketterle, "Observation of Feshbach resonances in a Bose–Einstein condensate", *Nature* **392** (1998) 151.

[254] C. Chin, R. Grimm, P. Julienne and E. Tiesinga, "Feshbach resonances in ultracold gases", *Rev. Mod. Phys.* **82** (2010) 1225, [`arXiv:0812.1496 [cond-mat.other]`].

[255] L. Shanquan, C. Weiru, L. Xiaoying, C. Jiexiang and L. Xiyi, "Annihilation Process of Quantum Vortices in Dissipative Gross-Pitaevskii Equation Model", `arXiv:2003.01376 [cond-mat.quant-gas]`.

[256] J. P. Boyd, *Chebyshev and Fourier Spectral Methods.* Dover Publications, 2nd ed., 2001.

[257] A. W. Samberg, *Applied String Theory, Hot and Cold: A Holographic View on Quark–Gluon Plasma and Superfluids*, Ph.D. thesis, 2015.

[258] P. Wittmer, C.-M. Schmied, T. Gasenzer and C. Ewerz, "Vortex motion quantifies strong dissipation in a holographic superfluid", *in preparation.*

[259] L. Onsager, "Statistical hydrodynamics", *Il Nuovo Cim.* **6** (1949) 279.

[260] R. Feynman, "Chapter II Application of Quantum Mechanics to Liquid Helium", vol. 1 of *Progress in Low Temperature Physics*, p. 17. Elsevier, 1955. DOI.

[261] M. Tsubota, K. Kasamatsu and M. Kobayashi, "Quantized vortices in superfluid helium and atomic Bose-Einstein condensates", `arXiv:1004.5458 [cond-mat.quant-gas]`.

[262] C. Raman, J. R. Abo-Shaeer, J. M. Vogels, K. Xu and W. Ketterle, "Vortex Nucleation in a Stirred Bose-Einstein Condensate", *Phys. Rev. Lett.* **87** (2001) 210402, [`cond-mat/0106235`].

[263] J. R. Abo-Shaeer, C. Raman, J. M. Vogels and W. Ketterle, "Observation of Vortex Lattices in Bose-Einstein Condensates", *Science* **292** (2001) 476.

[264] K. W. Madison, F. Chevy, V. Bretin and J. Dalibard, "Stationary States of a Rotating Bose-Einstein Condensate: Routes to Vortex Nucleation", *Phys. Rev. Lett.* **86** (2001) 4443, [`arXiv:cond-mat/0101051 [cond-mat.stat-mech]`].

[265] V. Bretin, S. Stock, Y. Seurin and J. Dalibard, "Fast Rotation of a Bose-Einstein Condensate", *Phys. Rev. Lett.* **92** (2004) 050403, [`arXiv:cond-mat/0603792 [cond-mat.mes-hall]`].

[266] R. E. Packard and T. M. Sanders, "Detection of Single Quantized Vortex Lines in Rotating He II", *Phys. Rev. Lett.* **22** (1969) 823.

[267] E. J. Yarmchuk, M. J. V. Gordon and R. E. Packard, "Observation of Stationary Vortex Arrays in Rotating Superfluid Helium", *Phys. Rev. Lett.* **43** (1979) 214.

[268] A. L. Fetter, "Rotating trapped Bose-Einstein condensates", *Rev. Mod. Phys.* **81** (2009) 647, [`arXiv:0801.2952 [cond-mat.stat-mech]`].

[269] K. Kasamatsu, M. Tsubota and M. Ueda, "Vortex Phase Diagram in Rotating Two-Component Bose-Einstein Condensates", *Phys. Rev. Lett.* **91** (2003) 150406, [`arXiv:cond-mat/0303125`].

[270] X. Li, Y. Tian and H. Zhang, "Generation of vortices and stabilization of vortex lattices in holographic superfluids", *J. High Energy Phys.* **2002** (2020) 104, [`arXiv:1904.05497 [hep-th]`].

[271] W.-C. Yang, C.-Y. Xia, H.-B. Zeng and H.-Q. Zhang, "Phase Separation and Exotic Vortex Phases in a Two-Species Holographic Superfluid", `arXiv:1907.01918 [hep-th]`.

[272] A. E. Leanhardt, A. Görlitz, A. P. Chikkatur, D. Kielpinski, Y. Shin, D. E. Pritchard et al., "Imprinting Vortices in a Bose-Einstein Condensate using Topological Phases", *Phys. Rev. Lett.* **89** (2002) 190403, [`arXiv:cond-mat/0206303 [cond-mat.soft]`].

[273] M. Nakahara, T. Isoshima, K. Machida, S. ichiro Ogawa and T. Ohmi, "A simple method to create a vortex in Bose–Einstein condensate of alkali atoms", *Physica* **B284-288** (2000) 17, [`arXiv:cond-mat/9905374`].

[274] T. Isoshima, M. Nakahara, T. Ohmi and K. Machida, "Creation of a persistent current and vortex in a Bose-Einstein condensate of alkali-metal atoms", *Phys. Rev.* **A61** (2000) 063610, [`arXiv:cond-mat/9908470 [cond-mat.soft]`].

[275] S.-I. Ogawa, M. Möttönen, M. Nakahara, T. Ohmi and H. Shimada, "Method to create a vortex in a Bose-Einstein condensate", *Phys. Rev.* **A66** (2002) 013617.

[276] M. R. Matthews, B. P. Anderson, P. C. Haljan, D. S. Hall, C. E. Wieman et al., "Vortices in a Bose-Einstein Condensate", *Phys. Rev. Lett.* **83** (1999) 2498, [`arXiv:cond-mat/9908209`].

[277] K. W. Madison, F. Chevy, W. Wohlleben and J. Dalibard, "Vortex Formation in a Stirred Bose-Einstein Condensate", *Phys. Rev. Lett.* **84** (2000) 806, [`arXiv:cond-mat/9912015 [cond-mat.stat-mech]`].

[278] J. R. Abo-Shaeer, C. Raman, J. M. Vogels and W. Ketterle, "Observation of Vortex Lattices in Bose-Einstein Condensates", *Science* **292** (2001) 476.

[279] A. T. Powis, S. J. Sammut and T. P. Simula, "Vortex Gyroscope Imaging of Planar Superfluids", *Phys. Rev. Lett.* **113** (2014) 165303, [`arXiv:1405.4352 [cond-mat.quant-gas]`].

[280] J. Stenger, S. Inouye, A. P. Chikkatur, D. M. Stamper-Kurn, D. E. Pritchard and W. Ketterle, "Bragg Spectroscopy of a Bose-Einstein Condensate", *Phys. Rev. Lett.* **82** (1999) 4569–4573, [`arXiv:cond-mat/9901109`].

[281] G. P. Bewley, D. P. Lathrop and K. R. Sreenivasan, "Visualization of quantized vortices", *Nature* **441** (2006) 588.

[282] G. P. Bewley and K. R. Sreenivasan, "The Decay of a Quantized Vortex Ring and the Influence of Tracer Particles", *J. Low Temp. Phys.* **156** (2009) 84.

[283] M. Montull, A. Pomarol and P. J. Silva, "The Holographic Superconductor Vortex", *Phys. Rev. Lett.* **103** (2009) 091601, [`arXiv:0906.2396 [hep-th]`].

Bibliography

[284] H. Helmholtz, "Über Integrale der hydrodynamischen Gleichungen, welche den Wirbelbewegungen entsprechen", *Journal für reine und angewandte Mathematik* **55** (1858) .

[285] S. Nazarenko and M. Onorato, "Wave turbulence and vortices in Bose-Einstein condensation", *Physica* **D219** (2006) 1, [`arXiv:nlin/0507051 [nlin.CD]`].

[286] G. Krstulovic, "Kelvin-wave cascade and dissipation in low-temperature superfluid vortices", *Phys. Rev.* **E86** (2012) 055301, [`arXiv:1209.3210 [cond-mat.other]`].

[287] G. Krstulovic, M. Brachet and E. Tirapegui, "Radiation and vortex dynamics in the nonlinear Schrödinger equation", *Phys. Rev.* **E78** (2008) 026601.

[288] S. Zuccher, M. Caliari, A. W. Baggaley and C. F. Barenghi, "Quantum vortex reconnections", *Phys. Fluids* **24** (2012) 125108, [`arXiv:1206.2498 [cond-mat.other]`].

[289] A. J. Taylor and M. R. Dennis, "Geometry and scaling of tangled vortex lines in three-dimensional random wave fields", *J. Phys.* **A47** (2014) 465101, [`arXiv:1410.0383 [physics.comp-ph]`].

[290] C. Rorai, J. Skipper, R. M. Kerr and K. R. Sreenivasan, "Approach and separation of quantum vortices with balanced cores", *J. Fluid Mech.* **808** (2016) 641, [`arXiv:1410.1259 [cond-mat.quant-gas]`].

[291] A. Villois, G. Krstulovic, D. Proment and H. Salman, "A vortex filament tracking method for the Gross–Pitaevskii model of a superfluid", *J. Phys.* **A49** (2016) 415502, [`arXiv:1604.03595 [physics.flu-dyn]`].

[292] A. Galántai, "The theory of Newton's method", *J. Comput. Appl. Math.* **124** (2000) 25. Numerical Analysis 2000. Vol. IV: Optimization and Nonlinear Equations.

[293] A. M. J. Schakel, *Boulevard of Broken Symmetries – Effective Field Theories of Condensed Matter*. World Scientific, 2008.

[294] R. S. Drazin, P. G.; Johnson, "Solitons: An Introduction", *J. Appl. Math. Mech.* **70** (1990) 340.

[295] I. C. Christov, R. J. Decker, A. Demirkaya, V. A. Gani, P. Kevrekidis et al., "Kink-Kink and Kink-Antikink Interactions with Long-Range Tails", *Phys. Rev. Lett.* **122** (2019) 171601, [`arXiv:1811.07872 [hep-th]`].

[296] I. C. Christov, R. J. Decker, A. Demirkaya, V. A. Gani, P. Kevrekidis et al., "Long-range interactions of kinks", *Phys. Rev.* **D99** (2019) 016010, [`arXiv:1810.03590 [hep-th]`].

336

[297] D. Tong, "Topics in Quantum Mechanics", 2017. Lectures of the Mathematical Tripos at the University of Cambridge.

[298] I. Bloch, J. Dalibard and W. Zwerger, "Many-body physics with ultracold gases", *Rev. Mod. Phys.* **80** (2008) 885, [`arXiv:0704.3011 [cond-mat.other]`].

[299] W. J. Kwon, G. Moon, J.-y. Choi, S. W. Seo and Y.-i. Shin, "Relaxation of superfluid turbulence in highly oblate Bose-Einstein condensates", *Phys. Rev.* **A90** (2014) 063627, [`arXiv:1403.4658 [cond-mat.quant-gas]`].

[300] P. Naidon, E. Tiesinga, W. F. Mitchell and P. S. Julienne, "Effective-range description of a Bose gas under strong one- or two-dimensional confinement", *New J. Phys.* **9** (2007) 19, [`arXiv:physics/0607140 [physics.atom-ph]`].

[301] D. S. Petrov and G. V. Shlyapnikov, "Interatomic collisions in a tightly confined Bose gas", *Phys. Rev.* **A64** (2001) 012706, [`arXiv:cond-mat/0012091 [cond-mat.stat-mech]`].

[302] C. Mora and Y. Castin, "Ground State Energy of the Two-Dimensional Weakly Interacting Bose Gas: First Correction Beyond Bogoliubov Theory", *Phys. Rev. Lett.* **102** (2009) 180404, [`arXiv:0901.2943 [cond-mat.stat-mech]`].

[303] R. A. Duine and H. T. C. Stoof, "Stochastic dynamics of a trapped bose-einstein condensate", *Phys. Rev.* **A65** (2001) 013603, [`arXiv:cond-mat/0107432 [cond-mat.stat-mech]`].

[304] S. P. Cockburn and N. P. Proukakis, "The Stochastic Gross-Pitaevskii Methodology", in *Quantum Gases: Finite Temperature and Non-Equilibrium Dynamics* (N. Proukakis et al., ed.), p. 177, Imperial College Press, 2013, `arXiv:1207.1216 [cond-mat.quant-gas]`.

[305] E. Zaremba, T. Nikuni and A. Griffin, "Dynamics of Trapped Bose Gases at Finite Temperatures", *J. Low Temp. Phys.* **116** (1999) 277, [`arXiv:cond-mat/9903029 [cond-mat.stat-mech]`].

[306] A. J. Allen, C. F. Barenghi, N. P. Proukakis and E. Zaremba, "A Dynamical Self-Consistent Finite-Temperature Kinetic Theory: The ZNG Scheme", in *Quantum Gases: Finite Temperature and Non-Equilibrium Dynamics*, p. 93, Imperial College Press, 2013, `arXiv:1206.0145 [cond-mat.quant-gas]`.

[307] J. A. Fleck, J. R. Morris and M. D. Feit, "Time-dependent propagation of high energy laser beams through the atmosphere", *Appl. Phys.* **A10** (1976) 129.

[308] N. Iqbal and H. Liu, "Luttinger's theorem, superfluid vortices and holography", *Class. Quantum Gravity* **29** (2012) 194004, [`arXiv:1112.3671 [hep-th]`].

[309] I. S. Aranson and L. Kramer, "The world of the complex Ginzburg-Landau equation", *Rev. Mod. Phys.* **74** (2002) 99, [`arXiv:cond-mat/0106115 [cond-mat.stat-mech]`].

[310] E. Miot, "Dynamics of vortices for the Complex Ginzburg-Landau equation", *Anal. PDE* **2** (2009) 159, [`arXiv:0810.4782 [math.AP]`].

[311] M. Kurzke, C. Melcher, R. Moser and D. Spirn, "Dynamics for Ginzburg-Landau vortices under a mixed flow", *Indiana Univ. Math. J.* **58** (2009) 2597.

[312] K. Maeda and T. Okamura, "Characteristic length of an AdS/CFT superconductor", *Phys. Rev.* **D78** (2008) 106006, [`arXiv:0809.3079 [hep-th]`].

[313] P. Makotyn, C. E. Klauss, D. L. Goldberger, E. A. Cornell and D. S. Jin, "Universal dynamics of a degenerate unitary Bose gas", *Nat. Phys.* **10** (2014) 116, [`arXiv:1308.3696 [quant-ph]`].

[314] D. S. Petrov, C. Salomon and G. V. Shlyapnikov, "Weakly Bound Dimers of Fermionic Atoms", *Phys. Rev. Lett.* **93** (2004) 090404, [`arXiv:cond-mat/0309010 [cond-mat.stat-mech]`].

[315] G. Agnolet, D. F. McQueeney and J. D. Reppy, "Kosterlitz-Thouless transition in helium films", *Phys. Rev.* **B39** (1989) 8934.

[316] D. Finotello, Y. Y. Yu and F. M. Gasparini, "Universal behavior of ^{4}He films as a function of thickness near the Kosterlitz-Thouless transition", *Phys. Rev.* **B41** (1990) 10994.

[317] T. Oda, M. Hieda, R. Toda, T. Matsushita and N. Wada, "Vortex Diffusivity and Core Diameter of 2D Superfluid in 4He Films on Gold and H2 Substrates", *J. Low Temp. Phys.* **158** (2009) 262.

[318] A. I. Golov and P. M. Walmsley, "Homogeneous Turbulence in Superfluid 4He in the Low-Temperature Limit: Experimental Progress", *J. Low Temp. Phys.* **156** (2009) 51.

[319] E. Kozik and B. Svistunov, "Scanning Superfluid-Turbulence Cascade by its Low-Temperature Cutoff", *Phys. Rev. Lett.* **100** (2008) 195302, [`arXiv:0710.4572 [cond-mat.other]`].

[320] P. Rosenbusch, V. Bretin and J. Dalibard, "Dynamics of a Single Vortex Line in a Bose-Einstein Condensate", *Phys. Rev. Lett.* **89** (2002) 200403.

[321] J. R. Abo-Shaeer, C. Raman and W. Ketterle, "Formation and Decay of Vortex Lattices in Bose-Einstein Condensates at Finite Temperatures", *Phys. Rev. Lett.* **88** (2002) 070409.

[322] E. A. L. Henn, J. A. Seman, G. Roati, K. M. F. Magalhães and V. S. Bagnato, "Emergence of Turbulence in an Oscillating Bose-Einstein Condensate", *Phys. Rev. Lett.* **103** (2009) 045301.

[323] P. O. Fedichev and G. V. Shlyapnikov, "Dissipative dynamics of a vortex state in a trapped Bose-condensed gas", *Phys. Rev.* **A60** (1999) R1779, [`arXiv:cond-mat/9902204 [cond-mat.soft]`].

[324] M. Kobayashi and M. Tsubota, "Thermal Dissipation in Quantum Turbulence", *Phys. Rev. Lett.* **97** (2006) 145301.

[325] N. G. Berloff and A. J. Youd, "Dissipative Dynamics of Superfluid Vortices at Nonzero Temperatures", *Phys. Rev. Lett.* **99** (2007) 145301, [`arXiv:0704.1971 [cond-mat.soft]`].

[326] B. Jackson, N. P. Proukakis, C. F. Barenghi and E. Zaremba, "Finite-temperature vortex dynamics in Bose-Einstein condensates", *Phys. Rev.* **A79** (2009) 053615, [`arXiv:0809.4400 [cond-mat.stat-mech]`].

[327] S. V. Iordanskiĭ, "Mutual Friction Force in a Rotating Bose Gas", *Sov. Phys. JETP* **22** (1966) 160.

[328] V. Popov, "Quantum Vortices and Phase Transitions in Bose systems", *Zh. Eksp. Teor. Fiz.* **64** (1973) 672.

[329] J.-M. Duan and A. J. Leggett, "Inertial Mass of a Moving Singularity in a Fermi Superfluid", *Phys. Rev. Lett.* **68** (1992) 1216.

[330] J.-M. Duan, "Mass of a vortex line in superfluid ^{4}He: Effects of gauge-symmetry breaking", *Phys. Rev.* **B49** (1994) 12381.

[331] G. Baym and E. Chandler, "The hydrodynamics of rotating superfluids. I. Zero-temperature, nondissipative theory", *J. Low Temp. Phys.* **50** (1983) 57.

[332] E. Chandler and G. Baym, "The hydrodynamics of rotating superfluids. II. Finite temperature, dissipative theory", *J. Low Temp. Phys.* **62** (1986) 119.

[333] N. B. Kopnin, "Frequency singularities of the dissipation in the mixed state of pure type-II superconductors at low temperatures", *JETP Lett. (USSR) (Engl. Transl.); (United States)* **27** (1978) 417.

[334] E. B. Sonin, "Vortex oscillations and hydrodynamics of rotating superfluids", *Rev. Mod. Phys.* **59** (1987) 87.

[335] E. B. Sonin, "Transverse force on a vortex and vortex mass: Effects of free bulk and vortex-core bound quasiparticles", *Phys. Rev.* **B87** (2013) 134515, [`arXiv:1301.4554 [cond-mat.other]`].

[336] D. J. Frantzeskakis, "Dark solitons in atomic Bose–Einstein condensates: from theory to experiments", *J. Phys.* **A43** (2010) 213001, [`arXiv:1004.4071 [cond-mat.quant-gas]`].

[337] C. A. Jones and P. H. Roberts, "Motions in a Bose condensate. IV. Axisymmetric solitary waves", *J. Phys.* **A15** (1982) 2599.

[338] B. B. Kadomtsev and V. I. Petviashvili, "On the Stability of Solitary Waves in Weakly Dispersing Media", *Sov. Phys. Dokl.* **15** (1970) 539.

[339] S. Manakov, V. Zakharov, L. Bordag, A. Its and V. Matveev, "Two-dimensional solitons of the Kadomtsev-Petviashvili equation and their interaction", *Phys. Lett.* **A63** (1977) 205.

[340] V. Keränen, E. Keski-Vakkuri, S. Nowling and K. P. Yogendran, "Dark solitons in holographic superfluids", *Phys. Rev.* **D80** (2009) 121901, [`arXiv:0906.5217 [hep-th]`].

[341] V. Keränen, E. Keski-Vakkuri, S. Nowling and K. P. Yogendran, "Inhomogeneous structures in holographic superfluids. I. Dark solitons", *Phys. Rev.* **D81** (2010) 126011, [`arXiv:0911.1866 [hep-th]`].

[342] V. Keranen, E. Keski-Vakkuri, S. Nowling and K. Yogendran, "Solitons as probes of the structure of holographic superfluids", *New J. Phys.* **13** (2011) 065003, [`arXiv:1012.0190 [hep-th]`].

[343] M. Guo, E. Keski-Vakkuri, H. Liu, Y. Tian and H. Zhang, "Dynamical Phase Transition from Nonequilibrium Dynamics of Dark Solitons", *Phys. Rev. Lett.* **124** (2020) 031601, [`arXiv:1810.11424 [hep-th]`].

[344] Z. Xu, Y. Du, J. Erdmenger, R. Meyer, Y. Tian and Z.-Y. Xian, "Holographic superfluid solitons with backreaction", *Phys. Rev.* **D101** (2020) 086011, [`arXiv:1910.09253 [hep-th]`].

[345] M. Gao, Y. Jiao, X. Li, Y. Tian and H. Zhang, "Black and gray solitons in holographic superfluids at zero temperature", *J. High Energy Phys.* **1905** (2019) 167, [`arXiv:1903.12463 [hep-th]`].

[346] F. Werner, *Hermann Helmholtz' Heidelberger Jahre (1858–1871)*, vol. 8. Springer, 1997.

[347] O'Connor, J. J. and Robertson, E. F. , "Hermann Ludwig Ferdinand von Helmholtz", `https://mathshistory.st-andrews.ac.uk/Biographies/Helmholtz/`, 2001. [Online; accessed 25-July-2020].

[348] H. Helmholtz, "LXIII. On Integrals of the hydrodynamical equations, which express vortex-motion", *Philos. Mag.* **33** (1867) 485.

[349] V. V. Meleshko, "Coaxial axisymmetric vortex rings: 150 years after Helmholtz", *Theor. Comput. Fluid Dyn.* **24** (2010) 403.

[350] J. S. Lee, S. J. Park, J. H. Lee, B. M. Weon, K. Fezzaa and J. H. Je, "Origin and dynamics of vortex rings in drop splashing", *Nat. Commun.* **6** (2015) 8187.

[351] BBC News Online science editor Dr David Whitehouse, "Etna hoops it up", http://news.bbc.co.uk/2/hi/science/nature/696953.stm, 2000. [Online; accessed 25-July-2020].

[352] K. Marten, K. Shariff, S. Psarakos and D. J. White, "Ring Bubbles of Dolphins", *Sci. Am.* **275** (1996) 82.

[353] G. Gordh, "The evolution of insect flight", *Bull. Entomol. Res.* **87** (1997) 214.

[354] D. L. Grodnitsky and P. P. Morozov, "Vortex formation during tethered flight of functionally and morphologically two-winged insects, including evolutionary considerations on insect flight", *J. Exp. Biol.* **182** (1993) 11.

[355] D. L. Hu, B. Chan and J. W. M. Bush, "The hydrodynamics of water strider locomotion", *Nature* **424** (2003) 663.

[356] J. M. V. Rayner, "A vortex theory of animal flight. Part 1. The vortex wake of a hovering animal", *J. Fluid Mech.* **91** (1979) 697.

[357] E. Drucker and G. Lauder, "Locomotor forces on a swimming fish: three-dimensional vortex wake dynamics quantified using digital particle image velocimetry", *J. Exp. Biol.* **202** (1999) 2393.

[358] B. J. Gemmell, D. R. Troolin, J. H. Costello, S. P. Colin and R. A. Satterlie, "Control of vortex rings for manoeuvrability", *J. R. Soc. Interface* **12** (2015) 20150389.

[359] M. Gharib, E. Rambod, A. Kheradvar, D. Sahn and J. Dabiri, "Optimal vortex formation as an index of cardiac health", *Proc. Natl. Acad. Sci. U.S.A.* **103** (05, 2006) 6305–8.

[360] P. M. Arvidsson, S. J. Kovács, J. Töger, R. Borgquist, E. Heiberg, M. Carlsson et al., "The shape of the healthy heart is optimized for vortex ring formation", *J. Cardiovasc. Magn. Reson.* **18** (2016) .

[361] A. Al-Mahadin and M. Almajali, "Simplified Mathematical Modelling of Wing Tip Vortices", in *2019 Advances in Science and Engineering Technology International Conferences (ASET)*, p. 1, 2019.

[362] K. Shariff and A. Leonard, "Vortex Rings", *Annu. Rev. Fluid Mech.* **24** (1992) 235.

[363] P. G. Saffman, *Vortex Dynamics.* Cambridge Monographs on Mechanics. Cambridge University Press, 1993.

[364] H. Lamb, *Hydrodynamics.* Cambridge University Press, 1924.

[365] G. K. Batchelor, *An Introduction to Fluid Dynamics.* Cambridge Mathematical Library. Cambridge University Press, 2000.

[366] H. E. Hall, "An Experimental and theoretical study of torsional oscillations in uniformly rotating liquid helium II", *Proc. R. Soc.* **A245** (1958) 546.

[367] W. F. Vinen, "The detection of single quanta of circulation in liquid helium II", *Proc. R. Soc.* **A260** (1961) 218.

[368] G. W. Rayfield and F. Reif, "Quantized Vortex Rings in Superfluid Helium", *Phys. Rev.* **136** (1964) A1194.

[369] B. P. Anderson, P. C. Haljan, C. A. Regal, D. L. Feder, L. A. Collins, C. W. Clark et al., "Watching Dark Solitons Decay into Vortex Rings in a Bose-Einstein Condensate", *Phys. Rev. Lett.* **86** (2001) 2926, [arXiv:cond-mat/0012444].

[370] M. Tsubota, K. Fujimoto and S. Yui, "Numerical Studies of Quantum Turbulence", *J. Low Temp. Phys.* **188** (2017) 119, [arXiv:1704.02566 [cond-mat.quant-gas]].

[371] K. Moffatt, "Vortex Dynamics: The Legacy of Helmholtz and Kelvin", in *IUTAM Symposium on Hamiltonian Dynamics, Vortex Structures, Turbulence*, (Dordrecht), p. 1, Springer Netherlands, 2008.

[372] W. Thomson, "On Vortex Motion", *Earth Env. Sci. Trans. Roy. Soc. Edinb.* **25** (1868) 217.

[373] D. Kivotides, J. C. Vassilicos, D. C. Samuels and C. F. Barenghi, "Kelvin Waves Cascade in Superfluid Turbulence", *Phys. Rev. Lett.* **86** (2001) 3080.

[374] W. F. Vinen, M. Tsubota and A. Mitani, "Kelvin-Wave Cascade on a Vortex in Superfluid ^{4}He at a Very Low Temperature", *Phys. Rev. Lett.* **91** (2003) 135301, [arXiv:cond-mat/0306191 [cond-mat]].

[375] G. T. Horowitz and M. M. Roberts, "Holographic superconductors with various condensates", *Phys. Rev. D* **78** (2008) 126008, [arXiv:0810.1077 [hep-th]].

[376] V. E. Hubeny, X. Liu, M. Rangamani and S. Shenker, "Comments on cosmic censorship in AdS / CFT", *J. High Energy Phys.* **0412** (2004) 067, [arXiv:hep-th/0403198].

[377] T. Hertog and G. T. Horowitz, "Towards a big crunch dual", *J. High Energy Phys.* **0407** (2004) 073, [`arXiv:hep-th/0406134`].

[378] A. Aftalion and I. Danaila, "Three-dimensional vortex configurations in a rotating bose-einstein condensate", *Phys. Rev.* **A68** (2003) 023603, [`arXiv:cond-mat/0303416`].

[379] S. Komineas, N. R. Cooper and N. Papanicolaou, "Single vortex states in a confined Bose-Einstein condensate", *Phys. Rev.* **A72** (2005) 053624, [`arXiv:cond-mat/0508562 [cond-mat.other]`].

[380] G. Gamota, "Creation of Quantized Vortex Rings in Superfluid Helium", *Phys. Rev. Lett.* **31** (1973) 517.

[381] J. R. Abo-Shaeer, C. Raman, J. M. Vogels and W. Ketterle, "Observation of Vortex Lattices in Bose-Einstein Condensates", *Science* **292** (2001) 476, [`arXiv:cond-mat/0108195 [cond-mat.soft]`].

[382] F. Chevy, K. W. Madison and J. Dalibard, "Measurement of the Angular Momentum of a Rotating Bose-Einstein Condensate", *Phys. Rev. Lett.* **85** (2000) 2223, [`arXiv:cond-mat/0005221 [cond-mat.soft]`].

[383] D. L. Feder, M. S. Pindzola, L. A. Collins, B. I. Schneider and C. W. Clark, "Dark-soliton states of Bose-Einstein condensates in anisotropic traps", *Phys. Rev.* **A62** (2000) 053606, [`arXiv:cond-mat/0004449 [cond-mat.stat-mech]`].

[384] Z. Dutton, M. Budde, C. Slowe and L. V. Hau, "Observation of Quantum Shock Waves Created with Ultra- Compressed Slow Light Pulses in a Bose-Einstein Condensate", *Science* **293** (2001) 663, [`arXiv:cond-mat/0107310 [cond-mat.soft]`].

[385] N. S. Ginsberg, J. Brand and L. V. Hau, "Observation of Hybrid Soliton Vortex-Ring Structures in Bose-Einstein Condensates", *Phys. Rev. Lett.* **94** (2005) 040403, [`arXiv:cond-mat/0408464 [cond-mat.other]`].

[386] I. Shomroni, E. Lahoud, S. Levy and J. Steinhauer, "Evidence for an oscillating soliton/vortex ring by density engineering of a Bose–Einstein condensate", *Nat. Phys.* **5** (2009) 193, [`arXiv:0805.3263 [cond-mat.other]`].

[387] J. Ruostekoski and Z. Dutton, "Engineering vortex rings and systems for controlled studies of vortex interactions in Bose-Einstein condensates", *Phys. Rev.* **A72** (2005) 063626, [`arXiv:cond-mat/0507032`].

[388] B. Nowak, J. Schole and T. Gasenzer, "Universal dynamics on the way to thermalisation", *New J. Phys.* **16** (2014) 093052, [`arXiv:1206.3181 [cond-mat.quant-gas]`].

[389] B. Jackson, J. F. McCann and C. S. Adams, "Vortex rings and mutual drag in trapped Bose-Einstein condensates", *Phys. Rev.* **A60** (1999) 4882, [`arXiv:cond-mat/9901087 [cond-mat.stat-mech]`].

[390] N. G. Berloff and C. F. Barenghi, "Vortex Nucleation by Collapsing Bubbles in Bose-Einstein Condensates", *Phys. Rev. Lett.* **93** (2004) 090401, [`arXiv:cond-mat/0401021 [cond-mat.soft]`].

[391] N. G. Berloff, "Evolution of rarefaction pulses into vortex rings", *Phys. Rev.* **B65** (2002) 174518, [`arXiv:cond-mat/0107148 [cond-mat.soft]`].

[392] R. Carretero-González, N. Whitaker, P. G. Kevrekidis and D. J. Frantzeskakis, "Vortex structures formed by the interference of sliced condensates", *Phys. Rev.* **A77** (2008) 023605, [`arXiv:cond-mat/0610242 [cond-mat.soft]`].

[393] R. Carretero-González, B. P. Anderson, P. G. Kevrekidis, D. J. Frantzeskakis and C. N. Weiler, "Dynamics of vortex formation in merging Bose-Einstein condensate fragments", *Phys. Rev.* **A77** (2008) 033625, [`arXiv:0711.0375 [cond-mat.other]`].

[394] H. E. Hall and W. F. Vinen, "The rotation of liquid helium II II. The theory of mutual friction in uniformly rotating helium II", *Proc. R. Soc. Lond.* **A238** (1956) 215.

[395] H. Bekarevich and M. IKhalatnikov, "Phenomenological Derivation of the Equations of Vortex Motion in He II", *Sov. Phys. JETP* **13** (1961) 643.

[396] P. Roberts and R. Donnelly, "Dynamics of vortex rings", *Phys. Lett.* **A31** (1970) 137.

[397] W. M. Hicks and J. W. L. Glaisher, "VII. On the steady motion and small vibrations a hollow vortex", *Philos. Trans. R. Soc. London* **175** (1884) 161.

[398] R. M. Caplan, J. D. Talley, R. Carretero-González and P. G. Kevrekidis, "Scattering and leapfrogging of vortex rings in a superfluid", *Phys. Fluids* **26** (2014) 097101, [`arXiv:1404.4922 [cond-mat.other]`].

[399] W. F. Vinen and J. J. Niemela, "Quantum Turbulence", *J. Low Temp. Phys.* **128** (2002) 167.

[400] G. P. Bewley, M. S. Paoletti, K. R. Sreenivasan and D. P. Lathrop, "Characterization of reconnecting vortices in superfluid helium", *Proc. Natl. Acad. Sci. U. S. A.* **105** (2008) 13707, [`arXiv:0801.2872 [cond-mat.other]`].

[401] M. Paoletti, M. E. Fisher and D. Lathrop, "Reconnection dynamics for quantized vortices", *Physica* **D239** (2010) 1367, [`arXiv:0810.5521 [cond-mat.stat-mech]`].

344

[402] K. W. Schwarz, "Three-dimensional vortex dynamics in superfluid ^{4}He: Line-line and line-boundary interactions", *Phys. Rev.* **B31** (1985) 5782.

[403] K. W. Schwarz, "Three-dimensional vortex dynamics in superfluid ^{4}He: Homogeneous superfluid turbulence", *Phys. Rev.* **B38** (1988) 2398.

[404] J. Koplik and H. Levine, "Vortex reconnection in superfluid helium", *Phys. Rev. Lett.* **71** (1993) 1375.

[405] M. Gabbay, E. Ott and P. N. Guzdar, "Reconnection of vortex filaments in the complex Ginzburg-Landau equation", *Phys. Rev.* **E58** (1998) 2576.

[406] R. Tebbs, A. J. Youd and C. F. Barenghi, "The Approach to Vortex Reconnection", *J. Low Temp. Phys.* **162** (2011) 314, [`arXiv:1006.3004 [cond-mat.quant-gas]`].

[407] E. H. BRANDT, "Thermal Depinning And "Melting" Of The Flux-Line Lattice In High-Tc Superconductors", *Int. J. Mod. Phys. B* **05** (1991) 751.

[408] I. Chuang, R. Durrer, N. Turok and B. Yurke, "Cosmology in the Laboratory: Defect Dynamics in Liquid Crystals", *Science* **251** (1991) 1336.

[409] H. K. Moffatt, "The degree of knottedness of tangled vortex lines", *J. Fluid Mech.* **35** (1969) 117.

[410] M. Leadbeater, T. Winiecki, D. C. Samuels, C. F. Barenghi and C. S. Adams, "Sound Emission due to Superfluid Vortex Reconnections", *Phys. Rev. Lett.* **86** (2001) 1410, [`arXiv:cond-mat/0009060 [cond-mat.soft]`].

[411] S.-i. Ogawa, M. Tsubota and Y. Hattori, "Study of Reconnection and Acoustic Emission of Quantized Vortices in Superfluid by the Numerical Analysis of the Gross–Pitaevskii Equation", *J. Phys. Soc. Jpn.* **71** (2002) 813, [`arXiv:cond-mat/0104255 [cond-mat.soft]`].

[412] K. W. Schwarz, "Three-dimensional vortex dynamics in superfluid ^{4}He: Homogeneous superfluid turbulence", *Phys. Rev.* **B38** (1988) 2398.

[413] A. T. A. M. de Waele and R. G. K. M. Aarts, "Route to vortex reconnection", *Phys. Rev. Lett.* **72** (1994) 482.

[414] S. Nazarenko and R. West, "Analytical Solution for Nonlinear Schrödinger Vortex Reconnection", *J. Low Temp. Phys.* **132** (2003) 1, [`arXiv:physics/0304110 [physics.flu-dyn]`].

[415] C. Ewerz and P. Wittmer, "Turbulence in a Three-Dimensonal Holographic Superfluid", *in preparation.*

[416] T. W. B. Kibble, "Topology of cosmic domains and strings", *J. Phys.* **A9** (1976) 1387.

[417] W. H. Zurek, "Cosmological experiments in superfluid helium?", *Nature* **317** (1985) 505.

[418] C. N. Weiler, T. W. Neely, D. R. Scherer, A. S. Bradley, M. J. Davis and B. P. Anderson, "Spontaneous vortices in the formation of Bose-Einstein condensates", *Nature* **455** (2008) 948, [`arXiv:0807.3323 [cond-mat.other]`].

[419] M. Natsuume and T. Okamura, "Kibble-Zurek scaling in holography", *Phys. Rev.* **D95** (2017) 106009, [`arXiv:1703.00933 [hep-th]`].

[420] B. Eiermann, T. Anker, M. Albiez, M. Taglieber, P. Treutlein, K.-P. Marzlin et al., "Bright Bose-Einstein gap solitons of atoms with repulsive interaction", *Phys. Rev. Lett.* **92** (2004) 230401, [`arXiv:cond-mat/0402178 [cond-mat.other]`].

[421] L. E. Sadler, J. M. Higbie, S. R. Leslie, M. Vengalattore and D. M. Stamper-Kurn, "Spontaneous symmetry breaking in a quenched ferromagnetic spinor Bose-Einstein condensate", *Nature* **443** (2006) 312, [`arXiv:cond-mat/0605351 [cond-mat.stat-mech]`].

[422] A. Weller, J. P. Ronzheimer, C. Gross, J. Esteve, M. K. Oberthaler, D. J. Frantzeskakis et al., "Experimental Observation of Oscillating and Interacting Matter Wave Dark Solitons", *Phys. Rev. Lett.* **101** (2008) 130401, [`arXiv:0803.4352 [quant-ph]`].

[423] N. G. Berloff and B. V. Svistunov, "Scenario of strongly nonequilibrated Bose-Einstein condensation", *Phys. Rev.* **A66** (2002) 013603, [`arXiv:cond-mat/0107209 [cond-mat.soft]`].

[424] T. Gasenzer, B. Nowak and D. Sexty, "Charge separation in reheating after cosmological inflation", *Phys. Lett.* **B710** (2012) 500, [`arXiv:1108.0541 [hep-ph]`].

[425] T. Gasenzer, L. McLerran, J. M. Pawlowski and D. Sexty, "Gauge turbulence, topological defect dynamics, and condensation in Higgs models", *Nucl. Phys.* **A930** (2014) 163, [`arXiv:1307.5301 [hep-ph]`].

[426] P. C. Hohenberg and B. I. Halperin, "Theory of dynamic critical phenomena", *Rev. Mod. Phys.* **49** (1977) 435.

[427] J. Berges, A. Rothkopf and J. Schmidt, "Non-thermal Fixed Points: Effective Weak-Coupling for Strongly Correlated Systems Far from Equilibrium", *Phys. Rev. Lett.* **101** (2008) 041603, [`arXiv:0803.0131 [hep-ph]`].

[428] J. Berges and G. Hoffmeister, "Nonthermal fixed points and the functional renormalization group", *Nucl. Phys.* **B813** (2009) 383, [`arXiv:0809.5208 [hep-th]`].

[429] C. Scheppach, J. Berges and T. Gasenzer, "Matter-wave turbulence: Beyond kinetic scaling", *Phys. Rev.* **A81** (2010) 033611, [`arXiv:0912.4183 [cond-mat.quant-gas]`].

[430] M. Schmidt, S. Erne, B. Nowak, D. Sexty and T. Gasenzer, "Nonthermal fixed points and solitons in a one-dimensional Bose gas", *New J. Phys.* **14** (2012) 075005, [`arXiv:1203.3651 [cond-mat.quant-gas]`].

[431] C.-M. Schmied, M. Prüfer, M. K. Oberthaler and T. Gasenzer, "Bidirectional universal dynamics in a spinor Bose gas close to a nonthermal fixed point", *Phys. Rev.* **A99** (2019) 033611, [`arXiv:1812.08571 [cond-mat.quant-gas]`].

[432] C.-M. Schmied, A. N. Mikheev and T. Gasenzer, "Non-thermal fixed points: Universal dynamics far from equilibrium", *Int. J. Mod. Phys.* **A34** (2019) 1941006, [`arXiv:1810.08143 [cond-mat.quant-gas]`].

[433] A. N. Kolmogorov, "The local structure of turbulence in incompressible viscous fluid for very large Reynolds numbers", *Proc. USSR Acad. Wissenschaft* **30** (1941) 299. [Proc. R. Soc. Lond. A434 (1991) 9].

[434] A. N. Kolmogorov, "On the degeneration of isotropic turbulence in an incompressible viscous fluid", *Proc. USSR Acad. Wissenschaft* **31** (1941) 538.

[435] A. N. Kolmogorov, "Dissipation of Energy in Locally Isotropic Turbulence", *Proc. USSR Acad. Wissenschaft* **32** (1941) 16.

[436] C. Nore, M. Abid and M. E. Brachet, "Kolmogorov Turbulence in Low-Temperature Superflows", *Phys. Rev. Lett.* **78** (1997) 3896.

[437] C. Nore, M. Abid and M. E. Brachet, "Decaying Kolmogorov turbulence in a model of superflow", *Phys. Fluid* **9** (1997) 2644.

[438] T. Araki, M. Tsubota and S. K. Nemirovskii, "Energy Spectrum of Superfluid Turbulence with No Normal-Fluid Component", *Phys. Rev. Lett.* **89** (2002) 145301.

[439] M. Kobayashi and M. Tsubota, "Kolmogorov Spectrum of Superfluid Turbulence: Numerical Analysis of the Gross-Pitaevskii Equation with a Small-Scale Dissipation", *Phys. Rev. Lett.* **94** (2005) 065302, [`arXiv:cond-mat/0411750 [cond-mat.other]`].

[440] P. Clark Di Leoni, P. D. Mininni and M. E. Brachet, "Finite-temperature effects in helical quantum turbulence", *Phys. Rev.* **A97** (2018) , [`arXiv:1711.08614 [physics.flu-dyn]`].

[441] V. Shukla, P. D. Mininni, G. Krstulovic, P. C. di Leoni and M. E. Brachet, "Quantitative estimation of effective viscosity in quantum turbulence", *Phys. Rev.* **A99** (2019) , [`arXiv:1811.05374 [cond-mat.quant-gas]`].

[442] M. Kobayashi, P. Parnaudeau, F. Luddens, C. Lothode, L. Danaila et al., "Quantum turbulence simulations using the Gross-Pitaevskii equation: high-performance computing and new numerical benchmarks", `arXiv:2003.03590 [physics.flu-dyn]`.

[443] S. K. Nemirovskii, "Gaussian model of vortex tangle in He II", *Phys. Rev.* **B57** (1998) 5972.

[444] S. K. Nemirovskii, M. Tsubota and T. Araki, "Energy Spectrum of the Random Velocity Field Induced by a Gaussian Vortex Tangle in He II", *J. Low Temp. Phys.* **126** (2002) 1535, [`arXiv:cond-mat/0112068 [cond-mat.soft]`].

[445] V. Berdichevsky, "Statistical mechanics of vortex lines", *Phys. Rev.* **E57** (Mar, 1998) 2885.

[446] V. Berdichevsky, "On statistical mechanics of vortex lines", *Int. J. Eng. Sci.* **40** (2002) 123.

[447] Physics Girl, "How to Make VORTEX RINGS in a Pool", `https://www.youtube.com/watch?v=_18avidXxqY`, 2019. [Online; accessed 25-July-2020].

[448] Physics Girl, "Crazy pool vortex", `https://www.youtube.com/watch?v=pnbJEg9r1o8`, 2014. [Online; accessed 25-July-2020].

[449] Physics Girl, "How to Make a SQUARE Vortex Ring! ft. 3blue1brown", `https://www.youtube.com/watch?v=N7d_RWyOv20`, 2018. [Online; accessed 25-July-2020].

[450] The Royal Institution, "The Science of Vortex Rings", `https://www.youtube.com/watch?v=yjgACB7urOo`, 2018. [Online; accessed 25-July-2020].

[451] F. W. Dyson, "The potential of an anchor ring. Part II", *Philos. Trans. Royal Soc.* **A184** (1893) 1041.

[452] W. M. Hicks, "On the mutual threading of vortex rings", *Proc. R. Soc. Lond.* **A102** (1922) 111.

[453] V. V. Meleshko, A. A. Gourjii and T. S. Krasnopolskaya, "Vortex rings: history and state of the art", *J. Math. Sci.* **187** (2012) 772.

[454] A. E. H. Love, "On the Motion of Paired Vortices with a Common Axis", *Proc. London Math. Soc.* **s1-25** (1893) 185.

[455] H. Yamada and T. Matsui, "Preliminary study of mutual slip-through of a pair of vortices", *Phys. Fluids* **21** (1978) 292.

[456] K. Shariff, A. Leonard and J. H. Ferziger, "Dynamics of a class of vortex rings", *Technical Memorandum 102257 NASA* (1989) .

[457] M. Ikuta, Y. Sugano and H. Saito, "Symmetry-breaking instability of leapfrogging vortex rings in a Bose-Einstein condensate", *Phys. Rev.* **A99** (2019) 043610, [`arXiv:1902.00639 [cond-mat.quant-gas]`].

[458] R. L. Jerrard and D. Smets, "Leapfrogging vortex rings for the three dimensional gross-pitaevskii equation", *Ann. PDE* **4** (2017) 4.

[459] M. Cheng, J. Lou and T. T. Lim, "Leapfrogging of multiple coaxial viscous vortex rings", *Phys. Fluids* **27** (2015) 031702.

[460] J. Satti and J. Peng, "Leapfrogging of two thick-cored vortex rings", *Fluid Dyn. Res.* **45** (2013) 035503.

[461] N. Riley and D. P. Stevens, "A note on leapfrogging vortex rings", *Fluid Dyn. Res.* **11** (1993) 235.

[462] B. N. Shashikanth and J. E. Marsden, "Leapfrogging vortex rings: Hamiltonian structure, geometric phases and discrete reduction", *Fluid Dyn. Res.* **33** (2003) 333.

[463] C.-C. Chu, C.-T. Wang, C.-C. Chang, R.-Y. Chang and W.-T. Chang, "Head-on collision of two coaxial vortex rings: experiment and computation", *J. Fluid Mech.* **296** (1995) 39.

[464] Y. Oshima, "Head-on Collision of Two Vortex Rings", *J. Phys. Soc. Jpn.* **44** (1978) 328.

[465] J. D. A. Walker, C. R. Smith, A. W. Cerra and T. L. Doligalski, "The impact of a vortex ring on a wall", *J. Fluid Mech.* **181** (1987) 99.

[466] T. T. Lim and T. B. Nickels, "Instability and reconnection in the head-on collision of two vortex rings", *Nature* **357** (1992) 225.

[467] A. A. Gurzhii and M. Y. Konstantinov, "Head-on collision of two coaxial vortex rings in an ideal fluid", *Fluid Dyn.* **24** (1989) 538.

[468] J. Koplik and H. Levine, "Scattering of Superfluid Vortex Rings", *Phys. Rev. Lett.* **76** (1996) 4745.

[469] R. McKeown, R. Ostilla-Mónico, A. Pumir, M. P. Brenner and S. M. Rubinstein, "Cascade leading to the emergence of small structures in vortex ring collisions", *Phys. Rev. Fluids* **3** (2018) 124702, [`arXiv:1802.09973 [physics.flu-dyn]`].

[470] J. C. Maxwell, "Letter to William Thomson, 6 October 1868.", in *The Scientific Letters and Papers of James Clerk Maxwell: Volume 1, 1846-1862*, vol. 1. CUP Archive, 1990.

[471] A. V. Borisov, A. A. Kilin and I. S. Mamaev, "The dynamics of vortex rings: Leapfrogging, choreographies and the stability problem", *Regul. Chaot. Dyn.* **18** (2013) 33.

[472] V. P. Ruban, "Three-dimensional stability of leapfrogging quantum vortex rings", *Phys. Fluids* **30** (2018) 084104, [`arXiv:1806.08173 [cond-mat.other]`].

[473] S. W. Thomson, "XXIV. Vibrations of a columnar vortex", *Philos. Mag.* **10** (1880) 155.

[474] J. J. Thomson, *A treatise on the motion of vortex rings: An essay to which the Adams prize was adjudged in 1882, in the University of Cambridge.* 1968.

[475] M. Leadbeater, D. C. Samuels, C. F. Barenghi and C. S. Adams, "Decay of superfluid turbulence via Kelvin-wave radiation", *Phys. Rev.* **A67** (2003) 015601, [`arXiv:cond-mat/0205588`].

[476] W. F. Vinen, "Decay of superfluid turbulence at a very low temperature: The radiation of sound from a Kelvin wave on a quantized vortex", *Phys. Rev.* **B64** (2001) 134520.

[477] C. F. Barenghi, N. G. Parker, N. P. Proukakis and C. S. Adams, "Decay of quantised vorticity by sound emission", *J. Low Temp. Phys.* **138** (2005) 629, [`arXiv:cond-mat/0405635 [cond-mat.other]`].

[478] C. F. Barenghi, R. Hänninen and M. Tsubota, "Anomalous translational velocity of vortex ring with finite-amplitude Kelvin waves", *Phys. Rev.* **E74** (2006) 046303, [`arXiv:physics/0604008 [physics.flu-dyn]`].

[479] L. Kiknadze and Y. Mamaladze, "The Waves on the Vortex Ring in HeII", *J. Low Temp. Phys.* **126** (2002) 321.

[480] J. L. Helm, C. F. Barenghi and A. J. Youd, "Slowing down of vortex rings in Bose-Einstein condensates", *Phys. Rev.* **A83** (2011) 045601.

[481] M. Frigo and S. G. Johnson, "The design and implementation of FFTW3", in *Proceedings of the IEEE*, p. 216, 2005.

[482] G. Guennebaud, B. Jacob et al., "Eigen v3", 2010.

[483] L. Dagum and R. Menon, "OpenMP: an industry standard API for shared-memory programming", *Computational Science Engineering, IEEE* **5** (1998) 46.

[484] P. Ramachandran and G. Varoquaux, "Mayavi: 3D Visualization of Scientific Data", *Computing in Science & Engineering* **13** (2011) 40.

Danksagung

An dieser Stelle möchte ich mich herzlich bei all denjenigen bedanken, die mich in den letzten Jahren unterstützt und zum Gelingen dieser Arbeit beigetragen haben.

Mein ganz besonderer Dank gilt meinem Doktorvater Prof. Carlo Ewerz, der mich in den letzten Jahren in allen Belangen gefördert und mir die Möglichkeit gegeben hat, an diesem spannenden Promotionsthema zu forschen. Durch die langjährige Zusammenarbeit und die zahllosen Diskussionen mit ihm habe ich viel über Physik und das wissenschaftliche Arbeiten gelernt. Darüber hinaus danke ich ihm herzlich für die persönliche Komponente der Betreuung und die vielen außerfachlichen Gespräche, aus denen ich viel für mein weiteres Leben mitnehme.

Herzlich bedanken möchte ich mich auch bei Prof. Jan M. Pawlowski für die Übernahme des Zweitgutachtens. Genauso herzlich möchte ich mich bei Prof. Johanna Stachel und Prof. Matthias Bartelmann für ihre Teilnahme an meiner mündlichen Prüfung bedanken. Prof. Johanna Stachel danke ich zudem herzlich für die vielen spannenden Diskussionen im Rahmen der HGS-HIRe-Meetings, aber auch darüber hinaus.

Ebenfalls bedanken möchte ich mich herzlich bei Prof. Thomas Gasenzer für die langjährige Zusammenarbeit zu den Themen dieser Doktorarbeit und insbesondere unserer geplante gemeinsame Veröffentlichung der Ergebnisse aus Kapitel 7.

In diesem Zusammenhang danke ich auch Dr. Christian–Marcel Schmied, der die gesamten DGPE-Simulationen für das Matching durchgeführt hat und ebenfalls maßgeblich zu dem Erfolg dieses Projekts beigetragen hat.

Ein großer und herzlicher Dank gebührt meinen Vorgänger Dr. Andreas Samberg für die persönliche und fachliche Unterstützung in den letzten Jahren. Ich möchte mich insbesondere für die vielen, oft nächtlichen, Diskussionen über Physik und numerische Methoden sowie für das Korrekturlesen der Arbeit bedanken. Zudem bedanke ich mich für die Zusammenarbeit an unserer geplanten Veröffentlichung der Ergebnisse aus Kapitel 6 und 8.

Einen großen Anteil am Gelingen dieser Arbeit und daran, dass ich es bis hierher geschafft habe, haben zudem meine Studien- und Promotionsfreunde. Insbesondere bedanke ich mich bei Alaric, Lennert, Gonzalo und Johannes für die stets angenehme Arbeitsatmosphäre in den Tiefen des Kellers im Philosophenweg 16 und die vielen spannenden Diskussionen. Alaric und Lennert danke ich zudem für das Korrekturlesen dieser Arbeit. Besonders bedanken möchte ich mich bei Jan Trautmann für die langjährige Freundschaft und Unterstützung im Studium und der Promotion und auch für das Korrekturlesen dieser Arbeit. Ein riesiges Dankeschön geht zudem an meine Studienfreunde Erik, Lennart, Linda, Lukas und Sebastian.

I would also like to thank Prof. Alexander Rothkopf, Prof. Otto Nachtmann,

Danksagung